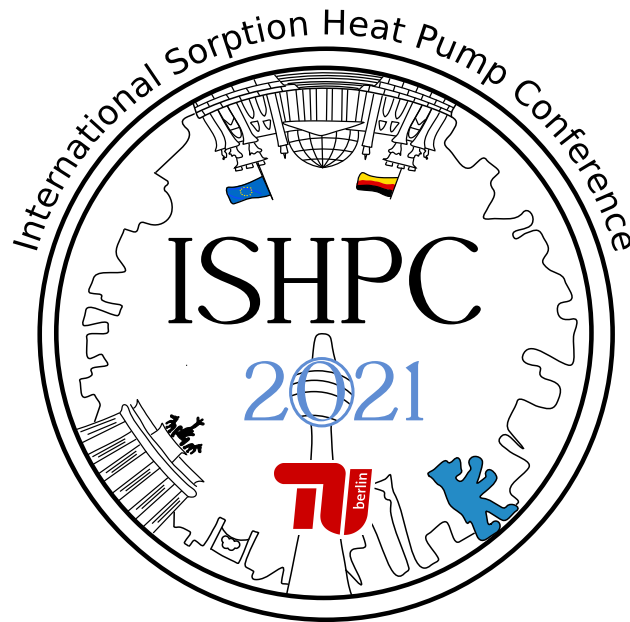


International Sorption 20
Heat Pump Conference 21

ISHPC 2021 Proceedings

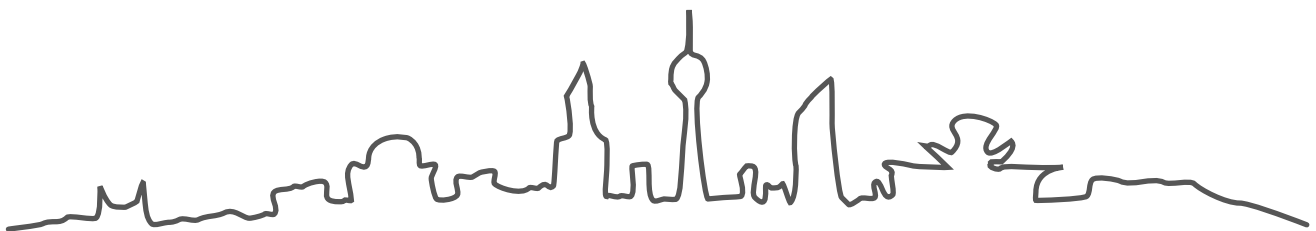
online pre-conference 2020



August 17th, 2020

Technische Universität Berlin
Campus Charlottenburg

Editor	Co-Editors
Thomas Meyer	José Corrales Rupert Graf Walther Hüls Roland Kühn Felix Ziegler



Scientific Committee

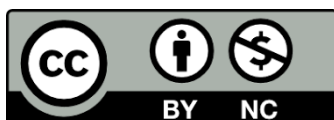
Prof. Dr. Jocelyn Bonjour
Prof. Dr. Keumnam Cho
Prof. Dr. Alberto Coronas
Prof. Dr. Robert Critoph
Prof. Dr. Carlos Infante Ferreira
Prof. Dr. Srinivas Garimella
Dr. Kyle Gluesenkamp
Prof. Dr. Gershon Grossman
Prof. Dr. Marco Guerra
Prof. Dr. Siyoung Jeong
Prof. Dr. Yong Tae Kang
Prof. Dr. Kwang J. Kim

Prof. Dr. Paul Kohlenbach
Prof. Dr. Renato M. Lazzarin
Prof. Dr. Giovanni Antonio Longo
Prof. Dr. Francis Meunier
Prof. Dr. Tetyana Morozyuk
Prof. Dr. Reinhard Radermacher
Prof. Dr. René Rieberer
Prof. Dr. Kiyoshi Saito
Dr. Lena Schnabel
Prof. Dr. Christian Schweigler
Prof. Dr. Ruzhu Wang
Prof. Dr. Felix Ziegler

Organizing Committee

Jan Albers
José Corrales
Rupert Graf
Walther Hüls

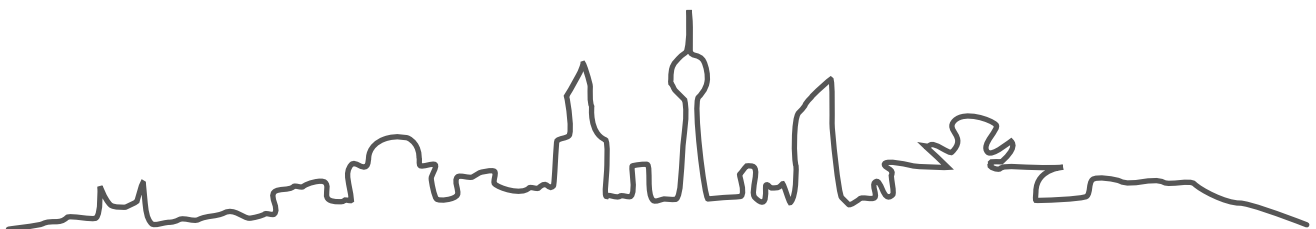
Roland Kühn
Thomas Meyer
Felix Ziegler



These proceedings are published under the
creative commons license CC-BY-NC 4.0.

<https://creativecommons.org/licenses/by-nc/4.0/deed.en>

<http://dx.doi.org/10.14279/depositonce-10430.2>



Foreword

This first part of the proceedings to the International Sorption Heat Pump Conference 2021 is a compendium of all accepted contributions to the online pre-conference starting on August 17th 2020. This online conference is the first part of the on-site conference which has been postponed to August 2021 due to the worldwide COVID-19 pandemic.

All contributions have been peer-reviewed by the scientific committee and other invited sorption scientists.

For decades there has been intense research and development on sorption heat pumping and cooling processes; still, looking at the sales numbers, it is mainly a niche technology. The current transition to an energy system based on renewables changes the boundary conditions. Sorption heat pumps will have an indispensable place in this context, especially for its potential to make use of waste heat.

We want to look at the future of sorption heat pumping devices including the newest research developments, as well as reports about pilots and mature technology.

The dissemination of insights and progress in sorption technology has been one of the major aspects of the International Sorption Heat Pump Conference. Therefore, the editorial board decided to publish this work as open access articles.

The typically rather strict separation of ad- and absorption technologies is avoided by categorizing the articles by five primary research categories:

1. Heat & Mass Transfer
2. Working Media
3. Sorption Cycles
4. Components
5. Technical Application.

The first three categories are subsumed in these proceedings due to their smaller number of contributions.

Conducting this online format of the ISHPC is a measure of coping with vast restrictions in personal contact to confine the spreading of the SARS-CoV2 virus. Nevertheless, we think it is an opportunity to exchange knowledge across borders and to overcome other than the current health-related restrictions.

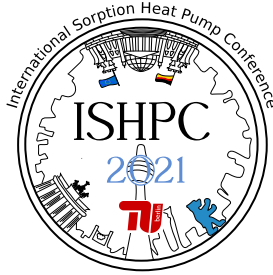
We would like to thank all authors for their contributions, the reviewers for their effort, and wish all participants an insightful experience and a lively discussion during the online conference.

Berlin, July 31st 2020

Contents

1 Heat & Mass Working Media Sorption Cycles	1
1.1 Improved coefficient of performance in sorption systems (#07)	1
1.2 Kinetics research of single/multi-halide sorbents and their simulation comparison in continuous refrigeration cycle (#09)	5
1.3 A numerical study on heat and mass transfer dynamics in sorption cells (#11)	10
1.4 Isotherm relations and COP analysis on silica gel RD with two different adsorptive; acetone and ethanol (#15)	14
1.5 Water and ethanol as refrigerant mixture: Towards adsorption cooling below 0 °C (#25)	19
1.6 Computationally efficient, experimentally validated adsorption chiller model using a plug-flow-based modelling approach (#26)	24
1.7 Experimental Validation of a Dynamic Adsorption Chiller Model Using Optimal Experimental Design (#30)	28
1.8 SorpPropLib: An Open-Source Database for Sorption Equilibrium Properties (#31)	33
1.9 Experimental study on diffusion absorption refrigeration cycle with a low GWP refrigerant-R1234ze(E) (#37)	37
1.10 Modelling ammonia (re-)sorption cycles: An abridged literature review and introduction to an ammonia salt MATLAB model for use in (re)sorption heat pumping (#47)	41
1.11 Measurement of Time Constants of Water Vapor Adsorption Reaction on a Consolidated Silica-gel micro particles using QCM method (#53)	46
1.12 Compact cold storage by means of a closed absorption process with H ₂ O/LiBr and crystallization of the strong absorbent (#54)	51
1.13 Experimental characterization by thermal and mass effectivenesses of plate heat exchangers in NH ₃ -LiNO ₃ absorption chillers (#59)	56
1.14 Hybrid thermochemical cycles for power and cold cogeneration: thermodynamic analysis and dynamic performances (#64)	61
1.15 Heat and Mass Transfer Kinetics of MOF-Coatings from Al-fumarate and CAU-10(Al)-H from IR-LTJ experiments: The Impact of Characteristic Times (#67)	65
1.16 Performance evaluation of a double-lift concept for an adsorption refrigerator for high ambient temperatures (#69)	69
1.17 Experimental investigation of an adsorption module based on heat exchangers with fibrous aluminium structures and the SAPO-34 / water working pair for gas-driven adsorption heat pumps (#70)	74
1.18 Determination of heat and mass transfer parameters of adsorption dynamics in MOF aluminium fumarate coatings with volume swing frequency response measurements (#71)	79
2 Components	84
2.1 A 3D printed capillary-assisted low-pressure evaporator, CALPE, for sorption systems cooling and heat pumps (#08)	84
2.2 Development of novel sorber bed heat and mass exchangers for sorption cooling systems (#13)	88
2.3 Vertical U-pipe Two-phase Flow Characteristics and Refrigerant Vapor Bypass in Absorption Heat Pump and Absorption Heat Exchanger (#33)	92
2.4 Experimental investigation on the dynamic performance of desiccant coated microchannel heat exchangers under condensation conditions (#35)	97
2.5 Heat Transfer and Frictional Pressure Drop Characteristics of H ₂ O/LiBr Solution in Plate Heat Exchanger for Triple Effect Absorption Cycle Application (#42)	101
2.6 Capillary-assisted evaporation of water from finned tubes: Impacts of dynamics and experimental setups (#44)	105
2.7 Absorption of high concentration NH ₃ /H ₂ O in a plate heat exchanger (#49)	110
2.8 Vertical tube evaporator and thermosiphon desorber for a flue gas-condensing heat pump (#52)	115
2.9 Heat Transfer and Flow Characteristics in Thermosiphon Regenerators of Multi-Stage LiBr/Water-Absorption Heat Pumps (#56)	119
2.10 Non-absorbable gasses motor-less purge system for absorption heat transformers (#63)	125

3	Technical Applications	129
3.1	Big-data analytics of the thermo-hygrometric conditions inside a dessicant based and a traditional flower greenhouse (#16)	129
3.2	Heating and Cooling of a Building by Absorption Heat Pumps driven by Evacuated Tube Solar Collectors (ETCs) (#17)	133
3.3	Application of the two-stage absorption heat exchanger in district heating (#19)	137
3.4	Process design and analysis of the zonal absorption heat exchanger for high-rise buildings (#20)	142
3.5	Experimental study on liquid distribution and horizontal motions of droplets in a tube bundle (#21)	147
3.6	Transforming Heat From 90 °C to 110 °C: Demonstration of a Lab-Scale Adsorption Heat Transformer (AdHT) (#22)	152
3.7	Ammonia-salt Large Temperature Jump Experimental Technique Advances (#24)	157
3.8	Integration of absorption chillers in centralized solar heating systems of multifamily buildings. (#27)	162
3.9	Building-level Absorption Heat Exchange Substation Applied in District Heating System (#34)	167
3.10	A miniature 3D printed sorption heat transformer (#55)	172
3.11	Directly Biomass-fired Absorption Heat Pump (#57)	176
3.12	Energy efficient cooling with absorption chillers in a field test (#61)	181
3.13	Electrical, enviromental and economic optimal operation of an absorption heat transformer based industrial heat recovery and upgrade system (#62)	186
3.14	Development and experimental validation of a linear state-space model for absorption heat pumping systems for model-based control strategies (#65)	191
3.15	Explicit calculation of flow rate set values for absorption chiller control (#66)	196
3.16	Chilled Water Flow Rate Control for Chillers in Multiple Producer Cooling Plants. (#68)	200



Improved coefficient of performance in sorption systems

Bahrehmand, Hesam, Bahrami, Majid

Laboratory for Alternative Energy Conversion (LAEC), School of Mechatronic Systems Engineering, Simon Fraser University, 250-13450 102 Avenue, Surrey, BC, V3T 0A3, Canada; Tel.: +1 (778) 782-8538; E-mail addresses: sbahrehm@sfu.ca (H. Bahrehmand) and mbahrami@sfu.ca (M. Bahrami)

Abstract:

A significant portion of the input low-grade heat in adsorption systems is used to overcome the thermal inertia of the sorber bed heat and mass exchangers (S-HMX) when swinging between the sorption and desorption temperatures, which impedes the coefficient of performance (COP). The objective of this study is to enhance the COP of waste-heat driven sorption systems without complicating the system and increasing its mass or volume. The 2-D analytical model presented in our previous study was used to explore the potential improvements for the COP. The effect of thermophysical properties of the heat exchanger (HEX) materials on the COP is investigated. The results show that by decreasing the HEX heat capacity from 2.4 (Al 6061) to 1.2 J/cm³ K (natural graphite sheets), the COP notably increases, by 9%. Also, by increasing the HEX thermal conductivity from 5 to 40 W/m K, the COP increases 21%, whereas further increasing the HEX thermal conductivity from 40 to 167 W/m K, would only increase the COP by 3%. The HEX thermal conductivity after which the COP plateaus depends on the S-HMX geometry and heat transfer characteristics. In addition, an analysis of variance (ANOVA) is conducted to show the potential enhancement of COP with S-HMX design, which amounts to 15%. Finally, the effect of low-grade heat source temperature on the COP is studied; it is shown that there is an optimum temperature to achieve a maximum COP. An optimum heat source temperature range for our design is 75–85 °C.

1. Introduction

Sorption systems can be powered with low-grade thermal energy for air conditioning, heat pumping, heat upgrading and thermal storage. S-HMX adsorbs the sorbate from the evaporator while being cooled with the ambient temperature, e.g. 30 °C. Subsequently, the low-grade heat source, with the temperature 70–90 °C, is connected to the S-HMX to desorb the sorbate to the condenser. The heat source supplies the heat with the heat transfer fluid (HTF) through HEX to the sorbent material. Thus, the heat source needs to overcome the thermal inertia of S-HMX between the ambient temperature and the heat source temperature to continue the desorption process, in the sorption cycle. This sensible energy is wasted and should be minimized to increase the COP and expedite the temperature swing in the sorber bed. This becomes even more crucial where the amount of low-grade heat is limited. For example, in a PEM fuel cell in a 40-foot bus with 50 kW energy input, generates approximately 25 kW electricity and 25 kW heat [1]. The nominal cooling power required for a 40-foot bus AC is 15 kW. Therefore, the required COP of a waste-heat sorption air conditioner (S-AC) should be at least 0.6, which is higher than the COP of the most published studies [2]–[4].

The motivation of this study is to develop a compact S-AC for a PEM fuel cell bus in collaboration with industrial partners, Ballard Power and NewFlyer. The present results are however general and can be used in other sorption system applications. To achieve this goal, we aim to investigate the main hurdles to increase the low COP. Advanced S-AC systems such as thermal regeneration cycles (thermal and forced convective or wave cycle), cascade cycles and multi-stages schemes have been proposed to enhance the COP of S-AC [5]. However, these cycles increase the complexity, and more importantly, the mass, volume, and cost due to their additional HTF circuits, pumps, vacuum pump or compressors, which results in lower specific cooling power (SCP) per overall mass. Therefore, alternative solutions should be explored to increase the COP while keeping the system compact. Table 1 presents a summary of published studies where the effect of S-HMX geometry and operating conditions on COP of S-AC were investigated. It can be observed that most studies did not include the entire S-HMX in their COP enhancement analysis, namely, sorbent, HEX and HTF. Moreover, as noted in Table 1, only off-the-shelf heat exchangers made from aluminum, copper or steel were used in the S-HMX in previous studies. In the present study, first, a detailed breakdown of thermal inertia of various components of S-HMX is presented to investigate the reasons for low COP. Subsequently, a systematic approach is proposed to significantly reduce the thermal inertia of the sorber bed heat transfer fluid and the heat exchanger. Further, the effect of salient thermophysical properties of the heat exchanger material on the COP is investigated. It is followed by a comprehensive analysis of variance (ANOVA) [6] to establish practical solutions to enhance the COP in the present S-HMX design.

Finally, the effects of heat source temperature on SCP and COP are investigated for a range of low-grade heat sources available, i.e. 67 °C from PEM fuel cell and 90 °C from internal combustion engines.

Table 1. Summary of the literature on the effect of S-HMX geometry and operating conditions on COP.

Ref. No.	Parameters	Heat exchanger material	Ref. No.	Parameters	Heat exchanger material
[7]	<ul style="list-style-type: none"> • Cycle time • Mass recovery time 	Steel	[8]	<ul style="list-style-type: none"> • Mass recovery time • switch time • cycle time 	Aluminum fin, copper tube
[9]	<ul style="list-style-type: none"> • Fin height • fin spacing 	Aluminum	[10]	<ul style="list-style-type: none"> • Cycle time • Adsorption/desorption time 	Aluminum
[11]	<ul style="list-style-type: none"> • Desorption temperature • Cycle time • Heat and mass recovery time 	Aluminum	[12]	<ul style="list-style-type: none"> • Cooling time • mass recovery time • heat recovery time 	Aluminum fin, copper tube

2. Background/Fundamentals/Experimental Set-up

A 2-D analytical solution was developed and presented in our recent study and validated using the data collected from: i) an in-house custom-built gravimetric large pressure jump test bed; and ii) two-sorber bed sorption test bed [13]. Figure 1 shows a schematic of the solution domain for S-HMX. Composite sorbents used in the study was silica gel B150/CaCl₂, PVA binder and thermally conductive additives of graphite flakes, see [14] for more details. Our closed-form analytical solution is used to produce the results shown in the present study.

COP is defined as the ratio of evaporative cooling energy (desired effect) to the input energy, Eq. (1). For S-AC with ideal evaporator and condenser, COP can be increased by: i) enhancing the heat and mass transfer processes inside the sorber bed, which

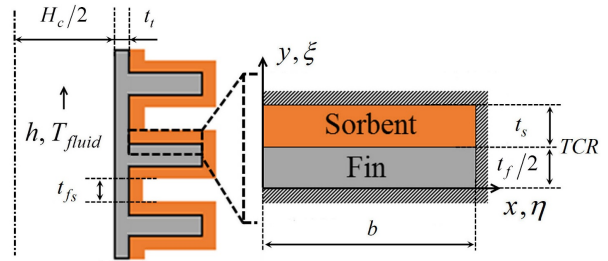


Figure 1. Schematic of the solution domain for a finned-tube S-HMX [13], b : fin height, t_f : fin thickness, t_s : sorbent thickness, TCR : thermal contact resistance, H_c : fluid channel height, t_t : tube thickness, t_{fs} : spacing between adjacent sorbent coatings, h : convective heat transfer coefficient, T_{fluid} : temperature of the HTF, x and y : coordinates, η and ζ : dimensionless coordinates

$$COP = \frac{Q_{evap}}{Q_{input}} = \frac{Q_{evap}}{Q_{sens} + Q_{des}} = \frac{m_{sorb} \int_{ads} \frac{d\omega}{dt} h_{fg} dt}{\int_{des} \left((m_{HEX} c_{p,HEX} + m_{sorb} (c_{p,s} + \omega c_{p,w})) + m_{HTF} c_{p,HTF} \right) \frac{dT}{dt} - m_{sorb} \frac{d\omega}{dt} h_{ads} \right) dt} \quad (1)$$

increases both the evaporative cooling energy and the desorption heat, which overall increases COP, and ii) decreasing the sensible energy required to overcome the thermal inertia of a) the HEX, b) sorbent material, and c) sorbate inside the sorbent and d) HTF

3. Results

Figure 2 shows the impact of HEX thermal conductivity and heat capacity on the COP of S-AC. It can be seen that by increasing the thermal conductivity, COP increases to a certain point and then plateaus. The reason behind this is that by increasing the thermal conductivity, the heat transfer in the S-HMX enhances, which increases both evaporator and desorption heat in Eq. (1), ultimately

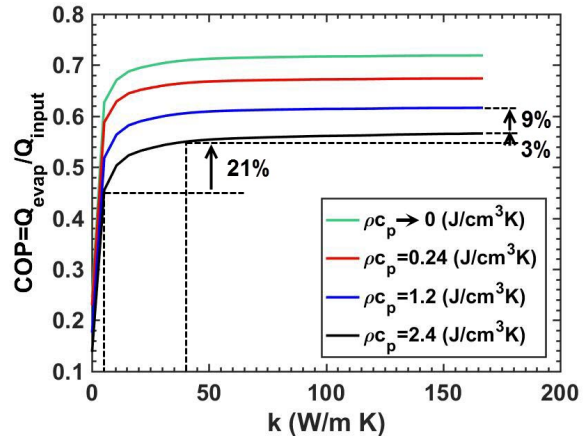


Figure 2. COP vs thermal conductivity and heat capacity of heat exchanger (HEX).

increasing the COP. This trend continues to the point where the heat exchanger heat transfer resistance becomes comparable to that of the sorbent and/or the HTF. Beyond this point, increasing HEX thermal conductivity does not increase COP noticeably because the heat transfer is limited elsewhere, namely the sorbent and/or the HTF. This point depends on the design and the materials of the S-HMX, namely sorbent, HEX and HTF, and should be included in the material selection and the design process. In addition, Figure 2 shows that by reducing the HEX heat capacity while thermal conductivity remains constant, the COP increases as HEX sensible heat in Eq. (1) decreases.

Analysis of variance, ANOVA, is a systematic method that can be used to evaluate the impact of design parameters on the performance by calculating the sums of square, level of contribution, F-statistic ratio and p-value [6]. In this study, the effect of S-HMX design parameters on the SCP and COP is investigated using ANOVA in MATLAB. Box–Behnken design [15] with three levels of design parameters is used to generate the sample points.

Using the Box–Behnken design, an ANOVA is carried out to find which parameters have significant contribution to SCP and COP of S-HMX. Figure 3 shows the level of contribution of each design parameter to SCP and COP of S-HMX. It can be observed that the sorbent thickness and cycle time have the highest level of contribution to SCP. Furthermore, the amount of the additive (graphite flakes) in the sorbent, fin thickness and fin height have the second largest level of contribution to SCP. Finally, the fluid channel height has the lowest impact on SCP. Moreover, it can be observed in Figure 3 that fin thickness and sorbent thickness have the largest impact on the COP. Cycle time, fin height and the amount of graphite flakes in the sorbent have a relatively lower effect on COP. Finally, the fluid channel height has the lowest impact on COP.

Figure 4 shows the effect of desorption temperature on the SCP and COP. It can be observed that by increasing the desorption temperature from 60 °C to about 80 °C, the COP increases, and after about 80 °C, the COP decreases. The reason for this trend is that by increasing the desorption temperature, the p/p₀ range, and thus, the water uptake difference between desorption and sorption processes and SCP increases. However, they increase less for higher desorption temperatures, Figure 4. On the other hand, by increasing the desorption temperature, the sensible heat required to overcome the S-HMX thermal inertia increases, which decreases the COP. Therefore, there exists an optimum desorption temperature corresponding to a maximum COP for each set of S-HMX geometry and operating conditions. This is important because in some low-grade thermal energy sources, e.g. PEM fuel cells, the desorption temperature is about 70 °C and the amount of heat source is limited, which requires a higher COP [1]. As can be seen in Figure 4, the heat source temperature range of 70 °C results in approximately equal COP to that of 90 °C.

4. Conclusions

In this study, it was shown that the HEX thermal inertia could be minimized and the COP maximized by careful material selection of HEX and optimization of S-HMX geometry and cycle time depending on the operating conditions of the S-AC. In the design and optimization process, the entire S-HMX, consisting of the sorbent, HEX and HTF, should be optimized simultaneously to achieve an optimal COP. Finally, the effect of heat source

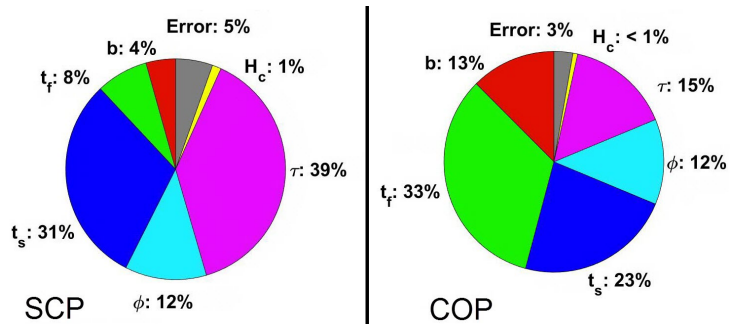


Figure 3. Level of contribution of design parameters to SCP and COP of S-HMX, b : fin height, t_f : fin thickness, t_s : sorbent thickness, ϕ : graphite flake content in the sorbent, τ : cycle time, H_c : fluid channel height, error: (sum of squares of each function minus mean function of each variable)/(sum of squares of each function minus the mean function)

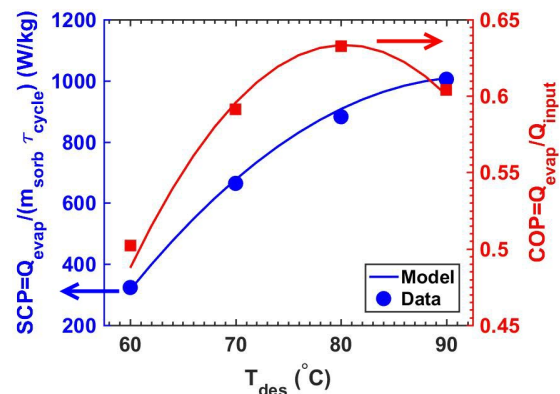


Figure 4. Variation of SCP and COP with desorption temperature

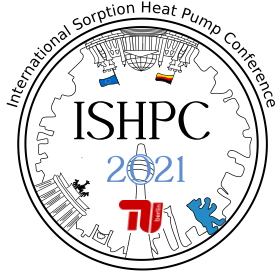
temperature, i.e. desorption temperature, on SCP and COP is studied for different applications of S-AC, and it was demonstrated that there exists an optimum desorption temperature corresponding to a maximum COP for each set of S-HMX geometry and operating conditions.

5. Acknowledgment

The authors gratefully acknowledge the financial support of the Natural Sciences and Engineering Research Council of Canada (NSERC) through Idea to Innovation Grant No. I2IPJ 530368-2018. Also, we would like to acknowledge the support of Ballard Power Systems and New Flyer, NFI Group Inc.

6. List of References

- [1] NFI Group Inc, “f-cell HFC,” in *f-cell + HFC*, 2019.
- [2] A. Freni, L. Bonaccorsi, L. Calabrese, A. Capri, A. Frazzica, and A. Sapienza, “SAPO-34 coated adsorbent heat exchanger for adsorption chillers,” *Appl. Therm. Eng.*, vol. 82, pp. 1–7, 2015.
- [3] U. Wittstadt *et al.*, “A novel adsorption module with fiber heat exchangers: Performance analysis based on driving temperature differences,” *Renew. Energy*, vol. 110, pp. 154–161, 2017.
- [4] Z. He *et al.*, “Study on the performance of compact adsorption chiller with vapor valves,” *Appl. Therm. Eng.*, vol. 126, pp. 37–42, 2017.
- [5] A. Alahmera, S. Ajiba, and X. Wang, “Comprehensive strategies for performance improvement of adsorption air conditioning systems: A review,” *Renew. Sustain. Energy Rev.*, vol. 99, pp. 138–158, 2019.
- [6] O. J. Dunn and V. A. Clark, *Applied Statistics: Analysis of Variance and Regression*. New York: Wiley, 1974.
- [7] Q. W. Pan, R. Z. Wang, Z. S. Lu, and L. W. Wang, “Experimental investigation of an adsorption refrigeration prototype with the working pair of composite adsorbent-ammonia,” vol. 72, 2014.
- [8] B. Zajackowski, “Optimizing performance of a three-bed adsorption chiller using new cycle time allocation and mass recovery,” *Appl. Therm. Eng.*, vol. 100, pp. 744–752, 2016.
- [9] Z. Rogala, “Adsorption chiller using flat-tube adsorbents – Performance assessment and optimization,” *Appl. Therm. Eng.*, vol. 121, pp. 431–442, 2017.
- [10] V. Palomba, B. Dawoud, A. Sapienza, S. Vasta, and A. Frazzica, “On the impact of different management strategies on the performance of a two-bed activated carbon / ethanol refrigerator : An experimental study,” *Energy Convers. Manag.*, vol. 142, pp. 322–333, 2017.
- [11] L. Q. Zhu, Z. W. Gong, B. X. Ou, and C. L. Wu, “Performance Analysis of Four Types of Adsorbent Beds in a Double-Adsorber Adsorption Refrigerator,” *Procedia Eng.*, vol. 121, pp. 129–137, 2015.
- [12] Q. W. Pan, R. Z. Wang, L. W. Wang, and D. Liu, “Design and experimental study of a silica gel-water adsorption chiller with modular adsorbents,” *Int. J. Refrig.*, vol. 67, pp. 336–344, 2016.
- [13] H. Bahrehmand and M. Bahrami, “An analytical design tool for sorber bed heat exchangers of sorption cooling systems,” *Int. J. Refrig.*, vol. 100, pp. 368–379, 2019.
- [14] H. Bahrehmand, M. Khajepour, and M. Bahrami, “Finding optimal conductive additive content to enhance the performance of coated sorption beds: An experimental study,” *Appl. Therm. Eng.*, vol. 143, no. July, pp. 308–315, 2018.
- [15] G. Box and D. Behnken, “Some new three level designs for the study of quantitative variables,” *Technometrics*, vol. 2, pp. 455–475, 1960.



Kinetics research of single- and multi-halide/ammonia working pairs and their simulation comparison in continuous refrigeration cycle

Guoliang An, Liwei Wang*

Institute of Refrigeration and Cryogenics, Key Laboratory of Power Machinery and Engineering of MOE, Shanghai Jiao Tong University, Shanghai, China, 200240.

**Corresponding author. Email: hwwang@sjtu.edu.cn*

Abstract:

Here we research the adaptability of single- and multi-halide/ammonia working pairs on refrigeration cycle after revising the kinetic models coupled with hysteresis effect. For the continuous cycle with two sorption beds, the impact of mass fraction between halides indicates that under the condition of $T_{\text{eva}}=0^{\circ}\text{C}$, $T_{\text{con}}=30^{\circ}\text{C}$ and $T_{\text{heat,in}}=180^{\circ}\text{C}$, both two sorption beds filled with CaCl_2 is optimal for the highest Q_{eva} over 5.8 kW, while one sorption bed should be replaced by multi-halide with mass fraction of 1:1 for the highest COP of 0.57. In between CaCl_2 and MnCl_2 , multi-halide combines the advantages of them: it is not the best in stable conditions, but it is stable enough to counteract the effects of external changes on overall performance.

1 Introduction

Multi-halide is defined as the physical mixture of several types of single halides, while the structure of sorption reactor for multi-halide is the same with that for single-halide. One of the main advantages of multi-halide is the better adaptability to variable heat source when utilized in sorption cycle. If the heat source has a fairly steady temperature, then a properly chosen single halide would be appropriate. If the heat source varies widely, even though not all kinds of halides react at the same time, at least some halides have the ability to react to avoid system invalid. Furthermore, after multi-halide had been reported with better performance than single halide because of less comprehensive hysteresis under non-equilibrium conditions [1], Gao et al. designed a gas heating/cooling sorption refrigeration system with multi-halide of MnCl_2 and CaCl_2 mixed uniformly in one sorption reactor [2], and the results show that with only one sorption bed the maximum specific cooling power (SCP) could get to around $330 \text{ W}\cdot\text{kg}^{-1}$. To optimize the performance, it is not reasonable to test each ratio of multi-halide by experiments. The kinetic study is an important reference for material optimization, cycle verification and reactor design, but it is always a difficult point in this field.

Experimental parameters of existing analogical models are based on a reference volume in scale with the reactor, which indicates that if the reactor structure changes, these kinetic parameters will be invalid for other researchers [3, 4]. The solution is to formulate three-step strategy for overall simulation model establishment. First, conduct kinetic tests with very small mass of sorbents without the limitation of heat and mass transfer in actual reactor. Second, the effect of heat and mass transfer, which could lead to the reaction gradient and consequently influence the specific temperature and pressure of each reaction point, is considered. Third, the models obtained in two previous steps could be coupled together, and thus the simulation for reactor level can be completed accurately.

In order to obtain wide-adaptable kinetic models of halide/ammonia for further simulation, analogical model considering hysteresis effect has been established with refined experimental results of $\text{MnCl}_2/\text{NH}_3$ and $\text{CaCl}_2/\text{NH}_3$ [5]. In this article, based on the former optimal kinetic model, the system simulation of two beds continuous refrigeration cycle with multi-halide ($\text{MnCl}_2\text{-CaCl}_2/\text{NH}_3$) is proposed and the optimal utilization scheme for single- and multi-halide is summarized.

2 Theoretical and simulation models

2.1 Kinetic model coupled with hysteresis effect

The equilibrium state of halide/ammonia characterized by Clapeyron equation is:

$$\ln p_{\text{eq}} = -\frac{\Delta H}{RT_s} + \frac{\Delta S}{R} \quad (1)$$

From the Clapeyron equation, it can be deduced that sorption and desorption processes could occur at the identical state (T_s, p_{eq}), but the threshold desorption temperature should be higher than the threshold sorption temperature because of the hysteresis phenomenon. Therefore, only one Clapeyron line is not sufficient for the overall analysis

of the sorption and desorption characteristics for each halide. As the hysteresis effect has great impact on the threshold temperature and actual reaction enthalpy, the further kinetic model for halide/ammonia working pairs at material level is based on the analogical linear model (Equation 2) and revised with hysteresis effect, which reproduces the relationship among sorbent temperature, ammonia pressure, real-time sorption capacity and sorption rate [5]:

$$\text{Sor: } \frac{dX}{dt} = k_s \left(1 - \frac{p_{\text{eq}}(T_s)}{p_c}\right) (1-X)^m \quad \text{Des: } \frac{dX}{dt} = -k_d \left(\frac{p_{\text{eq}}(T_s)}{p_c} - 1\right) X^m \quad (2)$$

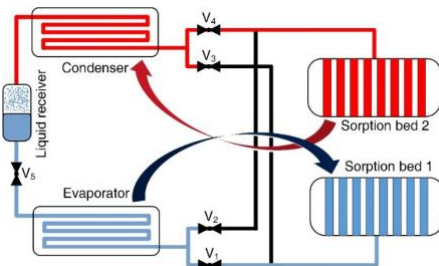
where p_{eq} is the equilibrium pressure corresponding to the temperature of sorbents (T_s), p_c is the constraint pressure of ammonia source, X is the normalization sorption capacity, k_s and k_d are defined as the sorption/desorption rate, and m is the reaction order of sorption/desorption, which are all fitted via experimental kinetic results. The kinetic parameters of $\text{MnCl}_2/\text{ammonia}$ and $\text{CaCl}_2/\text{ammonia}$ are listed in Table 1.

Table 1 - Analogical models for different halide-ammonia working pairs

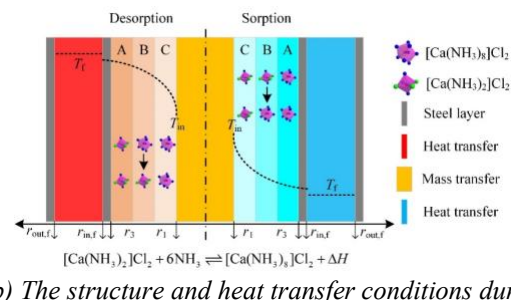
Reaction	Analogical model	Range
Mn2-6	$\frac{dX}{dt} = 1.19 \cdot 10^{-2} \left(1 - \frac{p_{\text{eq}}(T_s)}{p_c}\right) (1-X)^{0.64}$	$X \in (0, 1)$
Mn6-2	$\frac{dX}{dt} = -2.08 \cdot 10^{-3} \left(\frac{p_{\text{eq}}(T_s)}{p_c} - 1\right) X^{0.36}$	$X \in (1, 0)$
Ca2-4	$\frac{dX}{dt} = 2.14 \cdot 10^{-3} \left(1 - \frac{p_{\text{eq}}(T_s)}{p_c}\right) (1-3X)^{0.17}$	$X \in (0, 1/3)$
Ca4-8	$\frac{dX}{dt} = 2.6 \cdot 10^{-3} \left(1 - \frac{p_{\text{eq}}(T_s)}{p_c}\right) \left(\frac{3}{2} - \frac{3}{2}X\right)^{0.50}$	$X \in (1/3, 1)$
Ca8-4	$\frac{dX}{dt} = -9.27 \cdot 10^{-4} \left(\frac{p_{\text{eq}}(T_s)}{p_c} - 1\right) \left(\frac{3}{2}X - \frac{1}{2}\right)^{0.49}$	$X \in (1, 1/3)$
Ca4-2	$\frac{dX}{dt} = -4.30 \cdot 10^{-4} \left(\frac{p_{\text{eq}}(T_s)}{p_c} - 1\right) (3X)^{0.30}$	$X \in (1/3, 0)$

2.2 Cycle model for continuous refrigeration

The continuous refrigeration cycle with two sorption beds, evaporator and condenser is illustrated in Figure 1a, and the working procedure consisting six modes in one cycle is listed in Table 2, with details as follows: (1) Mode A: Through opening V_1 , ammonia is evaporated from the evaporator and sorbed in sorption bed 1, which is cooled by low temperature heat transfer fluid to take away the sorption heat. Meanwhile, V_4 is opened to proceed ammonia desorbed from the sorption bed 2 heated by high temperature heat transfer fluid, and condensed in the condenser. (2) Mode B: When achieving the set desorption time, V_4 is closed and the sorption bed 2 is exchanged into the cooling mode by switching the heat transfer fluid. In this duration, sorption bed 1 keeps the sorption mode. (3) Mode C: If the temperature of sorption bed 2 achieves low enough for the occurrence of the sorption mode Mn2-6, V_2 will be opened to connect the evaporator and sorption bed 2 for sorption. At the same time, V_1 is closed and sorption bed 1 is exchanged into the heating mode by turning on hot fluid. (4) Mode D: When the temperature of sorption bed 1 is elevated high enough for desorption of Ca8-4, V_3 is opened and sorption bed 1 is converted into the desorption mode while sorption bed 2 keeps the sorption mode. (5) Mode E: This model is the converse model of Mode B, i.e., when achieving the set desorption time for sorption bed 1, V_3 is closed and sorption bed 1 is switched into the cooling mode with sorption bed 2 maintaining the sorption mode. (6) Mode F: Similarly, if the temperature of sorption bed 1 decreases low enough for the sorption mode Mn2-6, V_4 is opened for the connection between evaporator and sorption bed 1. Meanwhile, V_2 is closed for sorption bed 2 exchanging into the heating mode.



(a) Schematic diagram of two beds continuous refrigeration cycle



(b) The structure and heat transfer conditions during sorption and desorption stages

Figure 1 - Cycle and reactor models for continuous refrigeration

Table 2 - Operation modes for continuous refrigeration cycle with two beds

Mode	Sorption bed 1	Sorption bed 2	V ₁	V ₂	V ₃	V ₄
A	Sorption	Desorption	√	×	×	√
B	Sorption	Cooling	√	×	×	×
C	Heating	Sorption	×	√	×	×
D	Desorption	Sorption	×	√	√	×
E	Cooling	Sorption	×	√	×	×
F	Sorption	Heating	×	×	×	√

The governing equations of sorption bed, evaporation and condenser are summarized in Equations 3-5, with detailed structure and heat transfer conditions of sorption bed shown in Figure 1b. To simplify the simulation process, the overall performance of the sorption bed is considered equivalent to the superposition of some unit tubes. Because the temperature gradient in the axial direction is much smaller than that in the radial direction for the unit tube, the governing equation can be simplified to the one-dimension unsteady state heat conduction equation with the inner layer (r_1) and outer wall (r_3) given adiabatic and convection boundary conditions, respectively. The analysis of the evaporator and condenser is based on the assumptions that the total mass of ammonia inside the evaporator/condenser is considered to be constant, and the vibration of evaporating/condensing temperature is ignored.

$$\bar{\rho}c \frac{\partial T}{\partial t} = \frac{1}{r} \frac{\partial}{\partial r} \left(\bar{\lambda} r \frac{\partial T}{\partial r} \right) + \beta \rho_{\text{halide}} \left[\alpha \frac{\Delta x_{\text{max,Mn}}}{M_{\text{Mn}}} \Delta H_{\text{Mn}} \frac{dX_{\text{Mn}}}{dt} + (1-\alpha) \frac{\Delta x_{\text{max,Ca}}}{M_{\text{Ca}}} \Delta H_{\text{Ca}} \frac{dX_{\text{Ca}}}{dt} \right] \quad (3)$$

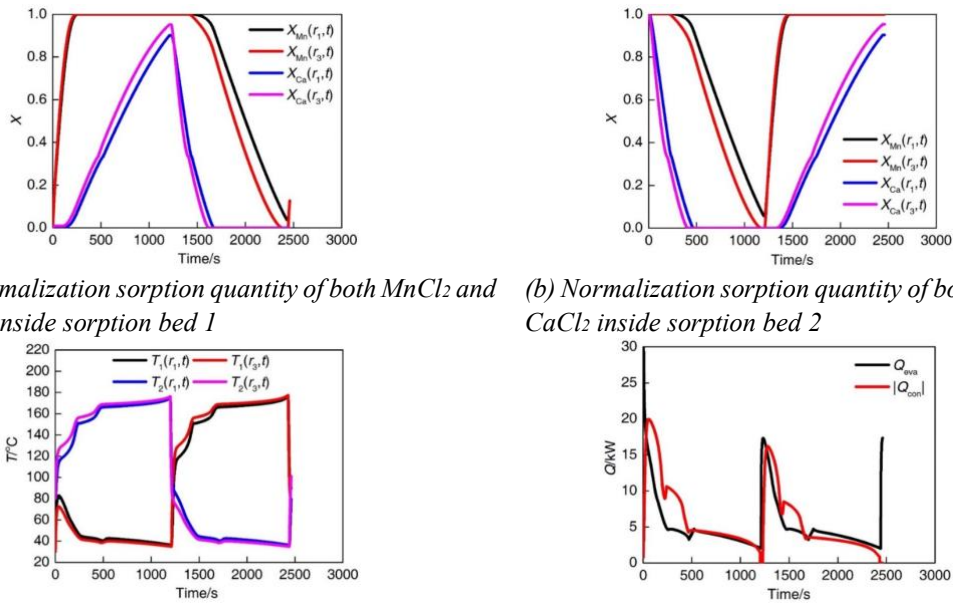
$$m_{\text{NH}_3,\text{eva}} \frac{dT_{\text{eva}}}{dt} = Q_{\text{eva}} - \frac{dm_{\text{receiver,out}}}{dt} \left[\Delta L - c_{\text{NH}_3} (T_{\text{con}} - T_{\text{eva}}) \right] \quad (4)$$

$$m_{\text{NH}_3,\text{con}} \frac{dT_{\text{con}}}{dt} = Q_{\text{con}} + \frac{dm_{\text{receiver,in}}}{dt} \left[\Delta L + c_{\text{NH}_3} (T_{\text{s}} - T_{\text{con}}) \right] \quad (5)$$

where α is the mass ratio of halide, β is the halide ratio inside multi-halide and Δx is the cycle sorption capacity.

3 Simulation results and discussion

The simulation results of the whole cycle with six working modes are illustrated in Figure 2 under the condition of 0°C evaporating temperature, 30°C condensing temperature and mass fraction between halides (both α_1 and α_2) of 0.5. The initial temperatures of sorption bed 1 and 2 set at 30°C and 80°C, respectively. Apparently, the response of sorption/desorption rates and temperatures in the outer layer (r_3) is always faster than that in the inner layer (r_1) due to the difference of boundary conditions. During mode A (1-1200 s), the inlet temperatures of heat transfer fluid of sorption bed 1 and 2 are at $T_{\text{cool,in}}$ and $T_{\text{heat,in}}$, respectively. As for sorption bed 1, since MnCl₂ has much more tremendous pressure potential than CaCl₂, MnCl₂ sorbs NH₃ first (Figure 2a) and causes the vast increase of T_1 (Figure 2c), which prevents CaCl₂ from sorption process (Figure 2a). Because the sorption rate of MnCl₂ keeps declining (Figure 2a), the refrigeration power (Q_{eva}) drops from 34.4 kW to 8.7 kW at 147 s (Figure 2d), after which CaCl₂ could gradually sorb NH₃ (Figure 2a) with T_1 decreasing (Figure 2c). The first inflection point in Q_{eva} line occurs at 264 s (Figure 2d) when X_{Mn} achieves 100% (Figure 2a), while the second and the third inflection points (Figure 2d) represent the reaction exchanging process from Ca₂₋₄ to Ca₄₋₈ between 471 s and 522 s (Figure 2a). From 522 s to 1200 s, Q_{eva} reduces slowly from 4.7 kW to 2.1 kW (Figure 2d) because the sorption rate keeps declining. At 1201 s, V₄ is closed between the condenser and sorption bed 2, and the inlet temperature of heat transfer fluid of sorption bed 2 is changed to $T_{\text{cool,in}}$. After 12 s the threshold sorption temperature of MnCl₂ is achieved (Figure 2c) and then sorption bed 2 is exchanged into the sorption mode, while V₁ is closed and the inlet temperature of heat transfer fluid of sorption bed 1 is set to $T_{\text{heat,in}}$ at 1213 s. Similarly, the heating process of sorption bed 1 is also fast, and T_1 increases to the threshold desorption temperature of CaCl₂ at 1230 s (Figure 2c). During mode B (1201-1212 s), Q_{eva} line maintains stable value around 2.1 kW (Figure 2d) since sorption bed 1 is still connected with the evaporator. However, during mode C (1213-1230 s), sorption bed 2 begins to sorb NH₃ from the evaporator, and the initial sorption rate of MnCl₂ is so large (Figure 2b) that Q_{eva} increases rapidly to 17.3 kW (Figure 2d). The next mode D (1231-2430 s), E (2431-2442 s) and F (2443-2460 s) can be considered as the inverse processes from mode A to C, and variation characteristic of Q_{eva} keeps the same expect for the initial value.



(a) Normalization sorption quantity of both MnCl₂ and CaCl₂ inside sorption bed 1

(b) Normalization sorption quantity of both MnCl₂ and CaCl₂ inside sorption bed 2

(c) Temperature variation of sorption bed 1 and 2 with different cycle stages

(d) Heat transfer power variation of evaporator and condenser with different cycle stages

Figure 2 - Simulation results of continuous refrigeration cycle with two sorption beds, under the condition that $T_{eva} = 0^\circ\text{C}$, $T_{con} = 30^\circ\text{C}$ and $\alpha = 0.5$

Figure 3 depicts the average refrigeration power (Q_{eva}) and coefficient of performance ($COP = Q_{eva} / Q_{heat}$) under the condition of $T_{eva} = 0^\circ\text{C}$, $T_{con} = 30^\circ\text{C}$ and $T_{heat, in} = 180^\circ\text{C}$. To figure out the influence of mass fraction between halides on the overall performance, both α_1 and α_2 are set from 0 to 1. Results show that when both sorption bed 1 and 2 are filled with CaCl₂ [point (0, 0)], Q_{eva} can reach the highest value of over 5.8 kW, and the corresponding COP is around 0.56. However, the optimization condition for COP (0.57) is to fill sorption bed 1 with CaCl₂ and sorption bed 2 with multi-halide [point (0, 0.5)], and the corresponding Q_{eva} is 5.5 kW. The worst performance is at point (1, 1), in which only MnCl₂ is packed inside sorption beds.

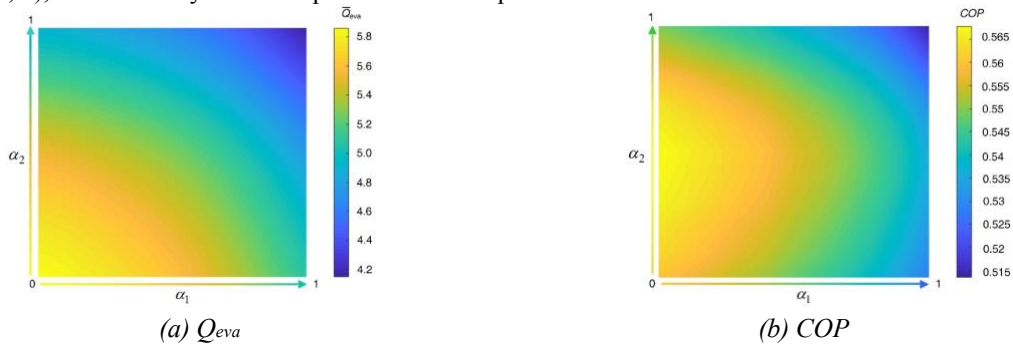


Figure 3 - The influence of mass fraction on Q_{eva} and COP with fixed $T_{eva} = 0^\circ\text{C}$, $T_{con} = 30^\circ\text{C}$ and $T_{heat, in} = 180^\circ\text{C}$

4 Conclusions

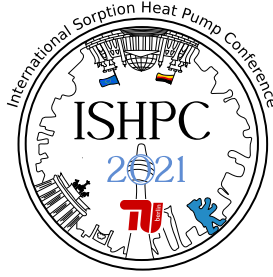
In this article, the adaptability of single- and multi-halide/ammonia on refrigeration cycle is researched after revising the kinetic models. Two sorption beds continuous refrigeration cycle with multi-halide (MnCl₂/CaCl₂) is established and solved based on the above kinetic data. The impact of mass fraction between halides indicates that under the condition of $T_{eva} = 0^\circ\text{C}$, $T_{con} = 30^\circ\text{C}$ and $T_{heat, in} = 180^\circ\text{C}$, both two sorption beds filled with CaCl₂ is optimal for the highest Q_{eva} over 5.8 kW, while one sorption bed should be replaced by multi-halide with mass fraction of 1:1 for the highest COP of 0.57. Even though multi-halide is not the best in stable conditions, it combines the advantages of CaCl₂ and MnCl₂ and reduces the influence of external conditions on overall performance.

5 Acknowledgment

This research was supported by the National Natural Science Foundation of China for the Distinguished Young Scholars (Grant No.51825602).

6 List of References

- [1] Gao J, Wang L, Wang R, Zhou Z. (2017): Solution to the sorption hysteresis by novel compact composite multi-salt sorbents. *Applied Thermal Engineering*, vol.1, pp. 580-585.
- [2] Gao J, Wang L, Gao P, An G, Lu H. (2018): Design and analysis of a gas heating/cooling sorption refrigeration system with multi-salt solid sorbent of CaCl₂ and MnCl₂. *International Journal of Heat and Mass Transfer*, vol.126, pp.39-47.
- [3] Ma Z, Bao H, Roskilly AP. (2019): Seasonal solar thermal energy storage using thermochemical sorption in domestic dwellings in the UK. *Energy*, vol.166, pp.213-222.
- [4] Dutour S, Mazet N, Joly J, Platel V. (2005): Modeling of heat and mass transfer coupling with gas–solid reaction in a sorption heat pump cooled by a two-phase closed thermosiphon. *Chemical Engineering Science*, vol.60, pp.4093-4104.
- [5] An G, Li Y, Wang L, Gao J. (2020): Wide applicability of analogical models coupled with hysteresis effect for halide/ammonia working pairs. *Chemical Engineering Journal*, vol.394, pp.125020.



A numerical study on heat and mass transfer dynamics in sorption cells

Davidesco Avshalom, Tzabar Nir

Thermal Energy Science & Technology (TEST) Laboratory, Faculty of Engineering, Ariel University,
Ariel 40700, Israel

Abstract:

Sorption processes are incorporated in a wide range of applications, aiming to store heat, store mass, manage fluid concentrations, and controlling pressures. In order to design an efficient sorption system for one of the above missions, it is desired to have an effective numerical model which describes the heat and mass transfer inside the system. In this paper, we present some results of a new developed one-dimensional dynamic model for sorption cells, which is based on adsorption isotherm measurements that were generated in the frame of a previous work. The current research focuses on sorption systems which undergo thermal cycles of heating and cooling processes. Four vessels are investigated, and three main parameters are examined: thermal efficiency, average temperature of the adsorbent, and pressure. All the cases refer to nitrogen – activated carbon systems, operating at ambient temperature of 300 K. The results show that a sorption cell design which obtains the highest pressure during the cycle is not necessarily the design which provides the highest thermal efficiency. A clear relation between the pressure and the adsorbent average temperature is obtained, meaning, thermal analysis, which is based on energy equations only, can predict the pressure in the cell.

1. Introduction

Adsorption systems often involve heating and cooling processes of the sorbent beds, therefore, a dynamic heat and mass transfer numerical model is desired to analyze and optimize the processes. Several research groups have published different approaches to simulate adsorption systems [1-7]. The current work is conducted in the frame of our ongoing research on sorption compressors aiming for driving Joule-Thomson cryocoolers in space applications, and in respect to our research on thermal energy storage. Sorption compressors are thermally driven, they don't have moving parts, and therefore they the potential for long-life, reliable, vibration-free, and quiet operation. In the current research, a one-dimensional dynamic numerical heat and mass transfer model for cylindrical cells is developed and published elsewhere [8, 9]. The model allows investigating the effects of using different materials, geometries, dimensions, insulation techniques, and heating and cooling methods. The model has been recently successfully experimentally validated with a nitrogen-activated carbon system. The current paper presents a numerical investigation of the system dimension influence on the thermal efficiency, the average temperature and the maximum pressure in the cell.

2. Method

The current research focuses on cylindrical sorption cells, as shown in figure 1, which consists of a stainless-steel vessel, an insulation layer, an inner heater, an inner cooler, and an adsorbent material. In order to numerically describe the sorption cell, a one-dimensional numerical model is developed, assuming heat transfer and temperature distribution along the radial direction only. This assumption is valid due to a sufficient length over diameter ratio of the cell, normally above 10 [10]. The model consists of a finite differences technique where each section is divided to elements. Each element is defined as a lumped capacity with physical and thermal properties, and it can generate or absorb heat. The numerical energy equation for each element is:

$$\rho_i^n \cdot c_i^n \cdot V_i \frac{T_i^{n+1} - T_i^n}{\Delta t} = \left(\dot{q}_{gen}(i) \cdot V_i + \sum_j^m \frac{T_j - T_i}{R_{ij}} \right) \quad (1)$$

where ρ is the density (kg/m^3), c is the specific heat capacity ($\text{J/kg}\cdot\text{K}$), V is the volume, T is the temperature (K), Δt is the time step (s), \dot{q}_{gen} is the internal heat generation (W/m^3), n is the time step index, m is the number of neighboring elements and R_{ij} is the heat resistance between elements i and j (K/W). There are two types of heat resistances: resistance between elements of the same material, and between elements of different material.

$\eta_{Thermal}$ is the thermal efficiency of the sorption cell, which is the ratio between the heat power that is supplied or rejected from the adsorbent elements and the heat power which is supplied or rejected to the system:

$$\eta_{Thermal} = \frac{\sum_{i=1}^{Ns} (T_i^{n+1} - T_i^n) \cdot C_i}{\dot{Q}_{in} \cdot (t - t_0)} \quad (2)$$

where \dot{Q}_{in} is the power inputed or rejected (W), Ns is the number of adsorbent elements, n is a time step, C_i is the heat capacity of element i (J/K), t_0 is the starting time of the process and t is the end time of the process. An average sorbent temperature, AST , is defined, taking into account the volume significance of each element. AST is calculated as follows:

$$AST = \frac{\sum_{i=1}^{Ns} T_i^n \cdot V_i}{V_s} \quad (3)$$

where V_s is the total adsorbent volume in the cell.

Four sorption cell vessels, which are listed in table 1, are discussed in the current paper. All four vessels consist of a cylindrical heater which is attached to a cooler, a stainless-steel vessel, and an outer insulation layer. The heater and cooler dimensions can vary between a central rod and a cylinder attached to the inner wall of the vessel. Because the heat flux of the heaters and coolers are size dependent, the total heating and cooling powers depend on their dimensions.

The maximum temperature in the cell is limited to comply with different construction materials, especially with seals, insulation materials and instrumentation. The maximum temperature is obtained at the heater elements, meaning, the adsorbent elements are usually at lower temperatures.

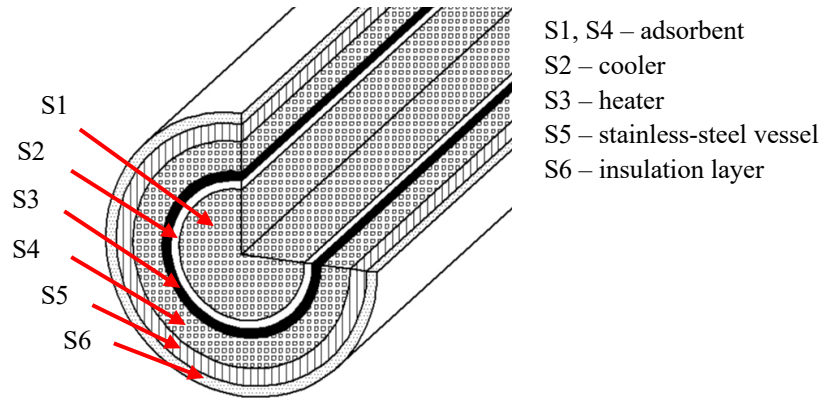


Figure 1 – schematic view of a sorption cell

Table 1 – vessel dimensions

	Vessel-1	Vessel-2	Vessel-3	Vessel-4
Inner vessel radius (mm)	8	15	25	35
Vessel length (mm)	300	430	650	870
Vessel volume (cc)	60	304	1,276	3,348
Vessel thickness (mm)	0.75	1.41	2.35	3.29

3. Results

Figure 2 shows $\eta_{Thermal}$ for the four different vessels, with an initial pressure which equals 0.2 MPa, initial temperature of 300 K, and a maximum temperature of 750 K. Figure 2 (a) presents $\eta_{Thermal}$ at the heating phase as a function of the heater location in the cell. The results show two major trends: a larger vessel provides larger thermal efficiency, and a heater which is close to the center of the vessel yields higher thermal efficiency. Figure 2 (b) shows $\eta_{Thermal}$ at the cooling phase as a function of the cooler location in the cell, with similar nature as for

the heating phase. Figure 3 shows the AST normalized by the maximum temperature, figure 3 (a), and the maximum obtained pressure at the end of the heating phase, figure 3 (b), as a function of the heater location in the cell, and for a maximum temperature of 750 K. The results in figure 3 show that a higher average temperature yields a higher pressure, and that for obtaining high AST and pressure, a small vessel and a heater which is close to the inner vessel wall are desired.

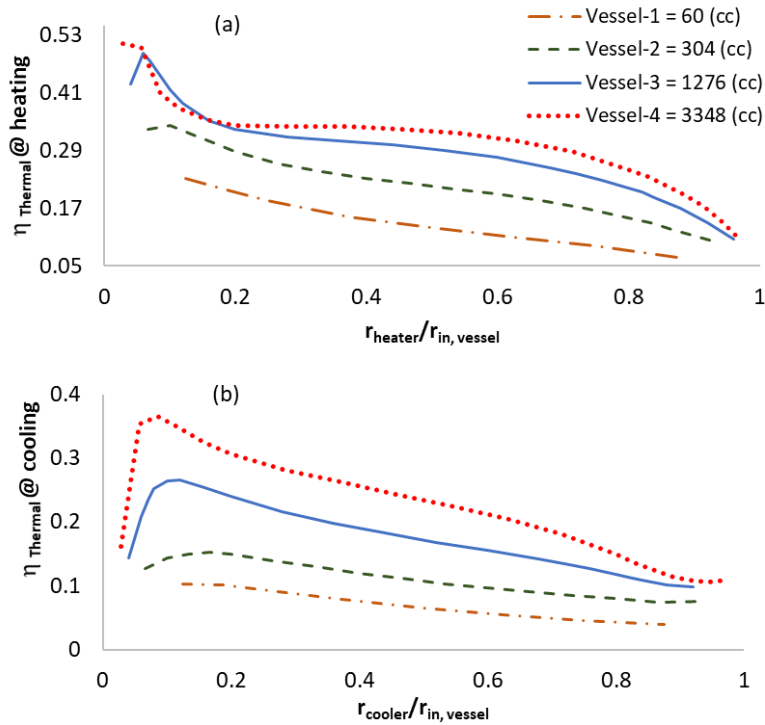


Figure 2 – $\eta_{Thermal}$ of different four cells as a function a relative heater and cooler locations: (a) heating phase, and (b) cooling phase

The results indicate that large vessels with a central heater are desired to obtain efficient sorption compressors, whereas, small vessels generate higher pressures. Moreover, a central heater yields higher thermal efficiency, where a large diameter heater provides higher pressures. Indeed, these trends are somehow intuitive, however, the current model enables the design of systems where compromises are required.

4. Conclusions

A one-dimensional dynamic numerical model of sorption cell is used to investigate the sorption cell performance as a function of the cell dimensions and the heater and cooler configurations. A consistent correlation between the ATS and the maximum pressure is obtained. This means that by a heat transfer analysis only, regardless the adsorption characteristics which determine the mass transfer, the required heater, for obtaining maximum or minimum pressure, can be predicted. Moreover, the design of a sorption cell can be conducted prior to having complete adsorption data of the working pair, where only their thermal characteristics are required.

The optimal configuration of the heater and cooler for obtaining a maximal pressure doesn't necessarily provide the maximum thermal efficiency. The highest values of $\eta_{Thermal}$ is obtained for heaters which are at the center of the cell, while heaters which are located close to the vessel wall, provide higher pressures, relative to central heaters.

These results are only a part of many outcomes of the new developed numerical model, which is an essential tool in our laboratory for developing sorption compressors and thermal energy storage systems, and it is intended to be used for other applications as well.

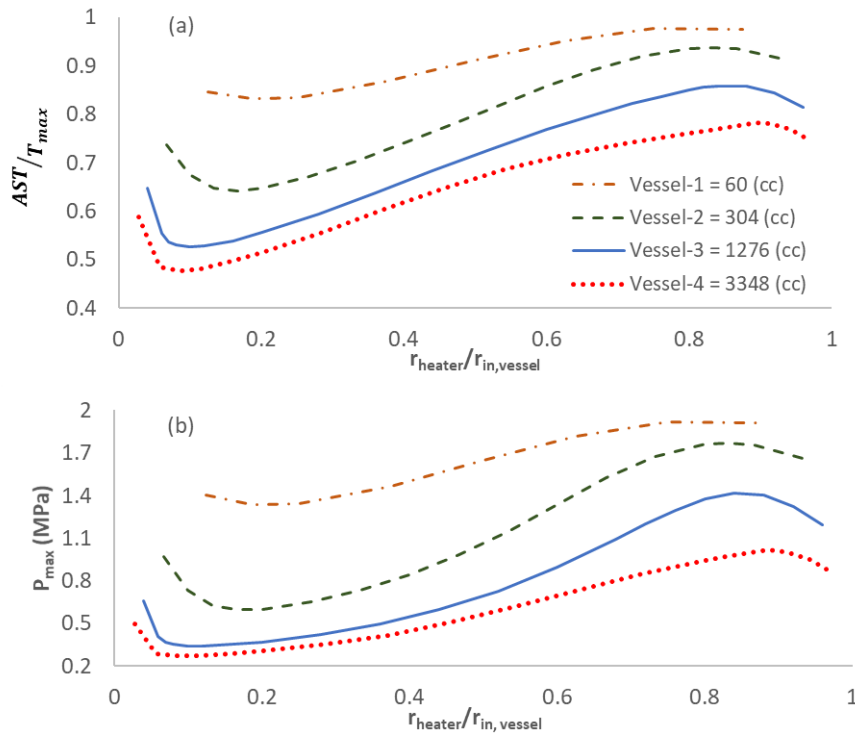


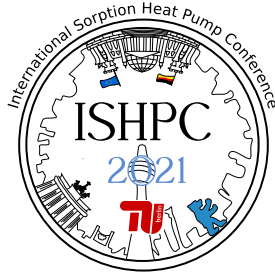
Figure 3 –AST and pressure at the end of the heating phase of different four cells as a function the heater location: (a) AST/T_{max} , and (b) pressure

5. Acknowledgment

The authors acknowledge the Israeli Ministry of Science and Technology for financially supporting the research on sorption Joule-Thomson Cryocoolers for space applications

6. List of References

- [1] Liu H., Nagano K. (2014): Numerical simulation of an open sorption thermal energy storage system using composite sorbents built into a honeycomb structure. *Int. Journal of Heat and Mass Transfer*, vol. 78, pp. 648–661.
- [2] Rahman K.A., Loh W.S., Chakraborty A., Saha B.B., Chun W.G., Ng K.C. (2011): Thermal enhancement of charge and discharge cycles for adsorbed natural gas storage. *Applied Thermal Engineering*, vol. 31, pp. 1630–1639.
- [3] Wu Y., Mulder T., Vermeer C.H., Holland H.J., ter Brake H.J.M. (2017): A 1-dimensional dynamic model for a sorption-compressor cell. *Int. Journal of Heat and Mass Transfer*, vol. 107, pp. 213–224.
- [4] Basumatary R., Dutta P., Prasad M., Srinivasan K. (2005): Thermal modeling of activated carbon based adsorptive natural gas storage system. *Carbon*, vol. 43, pp. 541–549.
- [5] Luo B.J., Wang Z.L., Yan T., Hong G.T., Li Y.L., Liang J.T. (2013): A non-lumped dynamic simulation method of sorption compressor for sorption cryocooler. *Cryogenics*, vol. 58, pp. 14–19.
- [6] Ndiaye K., Ginestet S., Cyr M. (2017): Modelling and experimental study of low temperature energy storage reactor using cementitious material. *Applied Thermal Engineering*, vol. 110, pp. 601–615.
- [7] Bahrehmand H., Ahmadi M., Bahrami M. (2018): Analytical modeling of oscillatory heat transfer in coated sorption beds. *Int. Journal of Heat and Mass Transfer*, vol. 121, pp. 1–9.
- [8] A. Davidesko and N. Tzabar. A one-dimensional heat and mass transfer model of sorption cells. 14th Int. Conference on Heat Transfer, Fluid Mechanics and Thermodynamics (HEFAT), 22-24 July, 2019, Wicklow, Ireland. Pages 74-79.
- [9] A. Davidesko and N. Tzabar (2020): A numerical study on the design of sorption cells for multistage compressors. *Cryogenics*, vol. 108, 103074.
- [10] Holman, J.P., Heat Transfer, Tenth Edition, McGraw-Hill, New York, 2010



Isotherm relations and COP analysis on silica gel RD with two different adsorptive; acetone and ethanol.

Habash, Rami¹, Gedizllis, Gamze^{2,*}, Demir, Hasan³

¹ Istanbul Okan University, Mechatronic Engineering Department, Tuzla Campus, Istanbul, Turkey

^{2,*} Gebze Technical University, Mechanical Engineering Department, Gebze, Turkey

³ OsmaniyeKorkut Ata University, Chemical Engineering Department, Osmaniye, Turkey

Abstract:

One of the most common adsorbents used in adsorption heat pumps (AHP) is silica gel. Many studies on adsorptive working with silica gel such as water, R134a, etc. can be found. On the other hand, the studies for another adsorptive working with silica gel as a pair are limited in the literature. Thus, this study is focusing on the acetone and ethanol adsorption rate on silica gel as an adsorptive. To calculate the COP values of these silica gel RD/acetone and silica gel RD/ethanol pairs, the isotherm equations should be defined, and the necessary calculations should be performed. With the help of the limited studies found in the literature on the adsorption rate of acetone and ethanol on silica gel, the isotherm equations are found, and the COP values are calculated for these pairs.

1. Introduction

The low cooling efficiency of an AHP is due to the slow heat and mass transfer in the adsorbent bed. The development of the AHPs gets the attention of many researchers who focus on accelerating the heat and mass transfer in the adsorbent bed [1,2]. There are many methods for accelerating the heat and mass transfer in an adsorbent bed such as the use of fins or metal additives [3-5]. Besides, new adsorbents are another way to improve performance. These newly developed adsorbents such as SWS-1L, FAM Z01 and Z02, AQSOA-Z05, and metal-organic frameworks (MOFs) [6-13] are new ways to improve the performance of the AHPs. On the other hand, new adsorbents which are suitable for vacuum and AHP working principle are limited in the literature or have not commercialized yet. Thus, the new pairs with common adsorbents should be handled. Due to that reason, new adsorptive scenarios should be studied with the common commercialized adsorbents.

In this study, the use of new adsorptive for AHP such as acetone and ethanol in the adsorbent bed for reducing the cycle time and capability to work with low-temperature waste heat is analyzed. The adsorbent is chosen as Fuji Silica gel RD. The isotherm equations for each silica gel/acetone and silica gel/ethanol were introduced to the literature for the first time. The Coefficient of Performance (COP) of the considered AHP is found for each pair. The scenario is written for a low-temperature heat source for desorption and the necessary mass of silica gel is found to have 3000 kJ cooling capacity.

2. The Thermophysical Properties of Adsorptive and Adsorbent

The thermophysical properties of the considered silica gel RD and the adsorptive; acetone and ethanol are collected from the literature. The thermophysical properties of the silica gel RD and adsorptive are given in Table 1.

3. Isotherm Equations

The most important aim for this paper is to find the isotherm equations of the acetone and ethanol on silica gel RD for AHP modeling. After then, COP values and the mass of silica gel can be estimated for the proper design. The studies on the novel pairs are limited and these properties are found from a detailed literature survey [15-16].

3.1. Silica gel RD / Acetone

The adsorption and desorption behavior of acetone on silica gel is studied by Sui et al. [15]. The amount of adsorbed acetone on silica gel for different three temperatures such as 288, 298, and 308K is shared in their study. They found that Langmuir-Freundlich (L-F) isotherm can be used to determine adsorbate equilibrium concentration in the silica gel particle for a given pressure and temperature [15].

Table 1. Thermophysical Properties of Silica gel RD and adsorptive [14].

Properties	Silica gel RD	Acetone	Ethanol
Density (m3/kg)	670		
Thermal cond (W/mK)	0.0198		
Cp(kJ/kgK)	0.88		
Cpv@ 45C (kJ/kgK)		1.344	0.77
Cpv@15C (kJ/kgK)		1.219	1.318
Cpl@ 45C (kJ/kgK)		2.195	2.811
Cpl@15C (kJ/kgK)		2.1201	2.4496
Heat (enthalpy) of evaporation @15C (kJ/kg)[15]		561.3	42.5
Heat of Adsorption with silica gel RD (kJ/kg)[16]		689	945

$$\bar{W}_\infty = W_m \left[\frac{bP^{1/n}}{1 + bP^{1/n}} \right] \quad (1)$$

Where P represents the equilibrium pressure, Pa, \bar{W}_∞ is the amount of adsorbed acetone, kg/kg, b, n, and W_m are the constants for the specific adsorbent-adsorbate pair. The detailed fitting parameters of L-F model at three different temperatures (i.e., 288 K, 298 K, and 308 K), fitting in a whole pressure range of acetone, adsorbed on silica gel are summarized in Table 2.

Table 2. Fitting parameters of L-F model[15].

Fitting parameters	Acetone		
	288 K	298 K	308 K
W_m	1.43284	1.08684	0.71297
b	0.15895	0.18796	0.22891
n	4.27789	4.14645	2.53781
R^2	0.98598	0.97953	0.96029

In order to find the isotherm of the silica gel/acetone pair, the constants which are given in Table 1 should be extended to all temperature ranges. Thus, the function is found for the fitting parameters by using the parameters at these given temperatures such as 288, 298, and 308K. The isotherm for this pair is found and illustrated in Figure 1 for three different pressures.

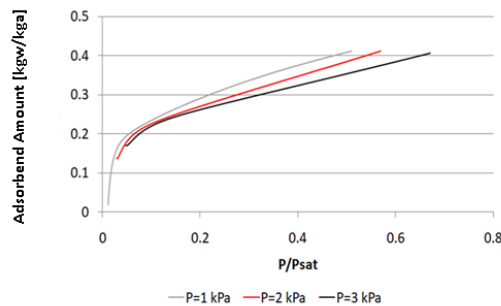


Figure 1–Isotherm of silica gel/acetone pair for three different pressures

3.2. Silica gel RD / Ethanol

The adsorbed ethanol amount on silica gel for different four temperatures such as 301, 311, 321, and 331 K is found by Arnoldsson [16]. Researchers found that Dubinin-Astakhov (DA) isotherm is fit to these four temperatures. The fitting parameters of the model are shared in Table 3.

$$\bar{W}_\infty = W_0 e^{-(A/E)^2} \quad (2)$$

where E is the characteristic energy and A is the adsorption potential and can be found by;

$$A = [RT \ln(P_{sat} / P)] \quad (3)$$

Table 3. Fitting parameters of DAmode [16]

Fitting parameters	Ethanol			
	301 K	311 K	321 K	331 K
W _o (kg/kg)	0.277	0.255	0.227	0.220
E (J/mol)	6700	4900	4000	2750
n	0.8	0.8	0.8	0.8

The same procedure is performed to estimate the isotherm of the silica gel/ethanol pair and to extend it for all temperature ranges. The isotherm for this pair is found and shown in Figure 2 for three different pressures.

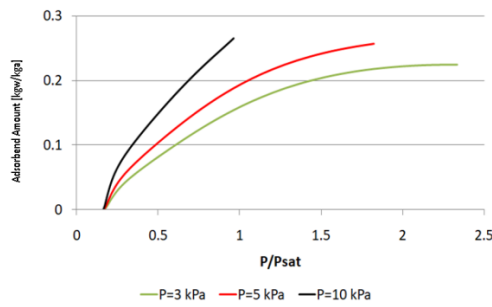


Figure 2–Isotherm of silica gel/ethanol pair for three different pressures

4. COP Calculations

Four processes of the cycle of AHP are shown on the Clausius-Clapeyron diagram in Fig. 3. The adsorbate concentration W_1 and bed temperature T_a are the starting point of the adsorption process of AHP. When the adsorbate concentration (W_2) and the bed temperature (T_b) are attained, the desorption process is started. The temperature approaches T_c then the desorption process is finalized.

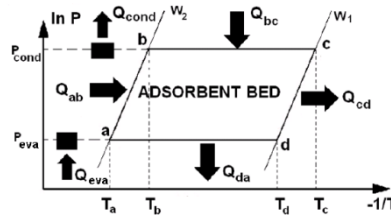


Figure 3. A schematic view of the adsorption-desorption process on the Clausius-Clapeyron diagram.

The cooling capacity of the evaporator and COP of the intermittent AHP can be evaluated by the following equations [17].

$$Q_{eva} = m_a \Delta W \Delta H_v + \int_{T_{cond}}^{T_{eva}} m_a \Delta W C_{p_v} dT \quad (4)$$

$$COP = \frac{Q_{eva}}{Q_{ab} + Q_{bc}} \quad (5)$$

Where

$$Q_{ab} = \int_{T_a}^{T_b} m_a (C_{p_a} + W_2 C_{p_v}) dT \quad (6)$$

$$Q_{bc} = \int_{T_b}^{T_c} m_a (C_{p_a} + W C_{p_v}) dT + \int_a^c m_a \Delta H dW \quad (7)$$

$$SCP = \frac{Q_{eva}}{m_a \tau_{cyc}} \quad (8)$$

Table 4- $Q_{\text{heating}}, Q_{\text{desorption}}, \text{COP}$ values for $Q_{\text{evap}} \sim 3000 \text{ kJ}$.

Properties	Acetone	Ethanol
Mass of silica gel(kg)	112	20
ΔH (kJ/kg)	689	945
Q Heating (kJ)	2305	499
Q Desorption (kJ)	5966	3799
Q_{evap}(kJ)	3023	3031
ΔW	0.0486	0.16
COP	0.37	0.71

Lanzerath et al., (2015) calculated COP values of adsorption chiller from 0.16 to 0.36. Bahrehmand et al. (2018) determined COP values vary from 0.46 to 0.54 and SCP values from 365 to 604 W/kg for 5 min sorption time. Hong et al. (2018) found COP values between 0.24 and 0.35 and SCP as 200 W/kg in their study. The evaluated COP of silica gel RD-ethanol pair adsorption chiller promises for utilizing low grade heat sources on cooling application.

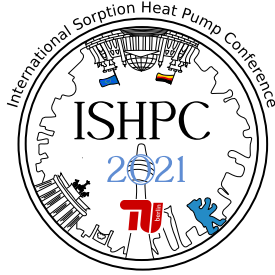
5. Conclusion

RD silica gel/Ethanol and RD silica gel/Acetone are used as adsorbent-adsorbate pair and the characteristics of these pairs are studied in this project. The Langmuir-Freundlich (L-F) isotherm and Dubinin-Astakhov (DA) isotherm are used for RD silica gel/Acetone and RD silica gel/Ethanol pairs, respectively. The necessary calculations are performed, and (COP, Q_{evap}) are calculated. It is observed that isotherm equation of ethanol can be valid at low temperature.

6. List of References

- [1] Ilis, G.G., Mobedi, M., Ülku, S., (2010): A parametric study on isobaric adsorption process in a closed adsorbent bed. *International Communications in Heat and Mass Transfer* 37, 540–547
- [2] Pino, Y., Aristov, Y., Cacciola, G., Restuccia, G., (1996): Composite materials based on zeolite 4A for adsorption heat pump. *Kluwer Academic Publishers Adsorption* 3, 33–40
- [3] Ilis, G.G., Mobedi, M., Ülku, S., (2011): A dimensionless analysis of heat and mass transport in an adsorber with thin fins; uniform pressure approach. *Int. Communications in Heat and Mass Transfer* 38, 790–797
- [4] Demir, H., Mobedi, M., Ülku, S., (2010): The use of metal piece additives to enhance heat transfer rate through an unconsolidated adsorbent bed. *Int. J. Refrigeration* 33, 714–720
- [5] Rezk, A., Al-Dadah, R.K., Mahmoud, S., Elsayed, A., (2013): Effects of contact resistance and metal additives in finned-tube adsorbent beds on the performance of silica gel/water adsorption chiller. *Applied Thermal Engineering* 53, 278–284.
- [6] Aristov YI, Glaznev IS, Freni A, Restuccia G. (2006): Kinetics of water sorption on SWS-1L (calcium chloride confined to mesoporous silica gel): influence of grain size and temperature. *Chemical Engineering Science* 2006; 61:1453e8.
- [7] Kakiuchi H, Shimooka S, Iwade M, Takewaki T. (2005): Novel water vapor adsorbent FAM-Z01 and its applicability to an adsorption heat pump. *Chemical Engineering Japanese*. 2005; 31(5):361e4.
- [8] Kakiuchi H, Shimooka S, Iwade M, Takewaki T. (2005): Water vapor adsorbent FAMZ02 and its applicability to adsorption heat pump. *Chemical Engineering Japanese* 2005; 31(4): 273e7.
- [9] Goldsworthy MJ. (2014): Measurements of water vapour sorption isotherms for RD silica gel, AQSOA-Z01, AQSOA-Z02, AQSOA-Z05 and CECA zeolite 3A. *Microporous Mesoporous Mater* 2014; 196:59e67.
- [10] Ali SM, Chakraborty A. (2016): Adsorption assisted double stage cooling and desalination employing silica gel þ water and AQSOA-Z02 þ water systems. *Energy Conversion and Management* 2016; 117:193e205.
- [11] Girnik IS, Aristov YI. (2016) Dynamic optimization of adsorptive chillers: the “AQSOA™-FAM-Z02/Water” working pair. *Energy* 2016; 106:13e22.
- [12] Kuesgens P, Rose M, Senkovska I, Froede H, Henschel A, Siegle S, et al. (2009): Characterization of metal-organic frameworks by water adsorption. *Microporous Mesoporous Mater* 2009; 120:325e30.
- [13] Ehrenmann J, Henninger SK, Janiak C. (2011): Water adsorption characteristics of MIL-101 for heat-transformation applications of MOFs. *European Journal Inorganic Chemistry* 2011: 471e4.

-
- [14] VDI-Gesellschaft Verfahrenstechnik und Chemieingenieurwesen. (2010): VDI. Heat Atlas. *Springer Link*, 119-614.
- [15] Hong Sui, Jijiang Liu, Lin He, Xingang Li, AmmiJani. (2018): Adsorption and desorption of binary mixture of acetone and ethyl acetate on silica gel. *Chemical Engineering Science, Vol.197, 185-194, 2019*
- [16] Joel Arnoldsson, (2012): Adsorption chillers- uptake of Ethanol on Type RD Silica gel. *Linköping University, Department of Management and Engineering, Energy Systems., p.66*
- [17] Ben Amar N, Sun LM, Meunier F, (1996): Numerical analysis of adsorptive temperature wave regenerative heat pump. *Applied Thermal Engineering 405-18.*
- [18] Lanzerath F, Bau U, Seiler J, Bardow A. (2015) Optimal design of adsorption chillers based on a validated dynamic object-oriented model. *Sci Technol Built Environ. 21:248-57.*
- [19] Bahremand H, Khajepour M, Bahrami M. (2018) Finding optimal conductive additive content to enhance the performance of coated sorption beds: An experimental study. *Appl Therm. Eng 143:308-15.*
- [20] Hong SW, Duong XQ, Chung JD, Kwon OK. (2018) Reassessment on the application of the embossed plate heat exchanger to adsorption chiller. *J Mech Sci Technol 32:1431-6.*



Water and ethanol as refrigerant mixture: Towards adsorption cooling below 0 °C

Entrup, Marten¹, Kappelhoff, Christoph¹, Seiler, Jan¹, Bardow, André^{1,2,3*}

¹ Institute of Technical Thermodynamics, RWTH Aachen University, 52062 Aachen, Germany

² Institute of Energy and Climate Research (IEK-10), Forschungszentrum Jülich, 52425 Jülich, Germany

³ Energy & Process Systems Engineering, ETH Zurich, 8092 Zürich, Switzerland

*Corresponding Author: abardow@ethz.ch

Abstract:

Water is often used as refrigerant in adsorption chillers due to its high enthalpy of vaporization and environmental friendliness. However, water as refrigerant limits the minimal cooling temperature of adsorption chillers to the freezing-point of water. To provide cooling below the freezing-point of water, we propose to use ethanol as anti-freezing agent. Experiments with a water-ethanol refrigerant mixture as refrigerant show that the adsorption chiller process works at cooling temperatures of -5 °C.

1. Introduction

Adsorption chillers can be driven by thermal energy from waste or solar heat and are an environmental friendly alternative to electricity-driven chillers. Moreover, adsorption chillers offer the opportunity to use water as refrigerant [1]. Water has a high enthalpy of vaporization and is environmental friendly. As major downside of using water, water-based adsorption chillers are restricted to a minimal cooling (i.e. evaporation) temperature of about 5 °C due to the freezing-point of water [2]. However, cooling temperatures below 5 °C are required by many applications in industrial refrigeration and food industry [3].

The obvious solution to reach lower cooling temperatures is to use alternative refrigerants like ammonia, methanol or ethanol. Yet, they have their own drawbacks: Ammonia and methanol are incompatible with copper [4] and toxic, thus hampering societal acceptance. Additionally, these three alternative refrigerants are flammable and have a lower enthalpy of evaporation than water. Furthermore, most commercial available adsorption chillers are already based on the refrigerant water.

To retain the good properties of water and extend the working range of available commercial water-based adsorption chillers, an anti-freezing agent can be added. Thus, Seiler et al. suggested and experimentally evaluated ethylene-glycol as anti-freezing agent and achieved a minimal cooling temperature of about 0 °C in their adsorption chiller process [5]. However, ethylene-glycol does not evaporate because of its low vapor pressure. Therefore, the anti-freezing effect is limited to the evaporator and the reflux from the condenser to the evaporator may still freeze at cooling temperatures below 0 °C.

In this study, we use ethanol as an anti-freezing agent. Ethanol has a higher vapor pressure compared to water and therefore also evaporates. Thus, the anti-freezing effect is not limited to the evaporator. However, a water-ethanol-mixtures are still flammable, yet, the flash point depends on the ethanol concentration and is higher compared to pure ethanol [6]. For a one-bed adsorption chiller, we show that the process with a water-ethanol-mixture (22 mol-% Ethanol) still works at evaporation temperatures of -5 °C without freezing. Additionally, we study the effect of the evaporator inlet temperature and the ethanol-concentration on the performance of an adsorption chiller.

2. Experimental Set-up

We performed all experiments using a lab-size one-bed adsorption chiller (Fig. 1). Main components of the adsorption chiller are: a condenser, an adsorber, and an evaporator, which are connected by controllable valves. The inlet temperature of each main component is controlled by thermostats. Heat transfer fluids are water in the condenser and the adsorber and a mixture of water and GlykosolN [7] in the evaporator. We measure the inlet ($T_{i,in}$) and outlet ($T_{i,out}$) temperatures as well as the inlet volume flow rate \dot{V}_i of each main component i . Additionally, the ethanol concentration of the water-ethanol-mixture is measured by sampling and density evaluation in the evaporator $x_{EtOH,evap}$ and the condenser $x_{EtOH,con}$. The performance of the adsorption chiller is evaluated by the Coefficient Of Performance (COP) and Specific Cooling Power (SCP):

$$COP = \frac{\int_{\tau_{start}}^{\tau_{end}} \dot{Q}_{evap} d\tau}{\int_{\tau_{start}}^{\tau_{end}} \dot{Q}_{des} + \dot{Q}_h d\tau} \quad (1)$$

$$SCP = \frac{\int_{\tau_{start}}^{\tau_{end}} \dot{Q}_{evap} d\tau}{\tau_{cycle} * m_{Ads}} \quad (2)$$

\dot{Q}_{evap} is the heat flow in the evaporator, \dot{Q}_{des} is heat flow in the adsorber which is used for desorption and \dot{Q}_h is the heat flow in the adsorber which is used for heating, τ_{start} is the start time and τ_{end} the end time of a cycle, the cycle time τ_{cycle} is the time between τ_{start} and τ_{end} ($\tau_{cycle} = \tau_{end} - \tau_{start}$) and m_{Ads} is the mass of the sorbent zeolithe NaY (here: 5 kg). To determine the heat flows \dot{Q}_j , we use steady-state energy balances taking inlet and outlet temperatures as well as the volume flows into account:

$$\dot{Q}_j = \dot{V}_i \rho_i (T_{i,in}) [h_{i,in}(T_{i,in}) - h_{i,out}(T_{i,out})] \quad (3)$$

The density ρ_i , the specific inlet enthalpy $h_{i,in}$ and the specific outlet enthalpy $h_{i,out}$ of each main component are calculated for water using RefProp with the equation of state ‘‘IAPWS-95’’ [8] and for GlykosolN with data from the manufacturer [7]. We evaluated COP and SCP for cycles, in which the adsorption chiller reached cycle steady-state condition (after at least 3 reproduced cycles). In addition, COP and SCP both depend on cycle time t_{cycle} : In general, long cycle times lead to high COP s and low SCP s, short cycle times lead to low COP s and high SCP s [9]. To consider the trade-off between COP and SCP regarding cycle time, we identified the Pareto-frontiers of SCP vs. COP by controlling the cycle time (for more details see [10]).

To verify the suitability of ethanol as anti-freezing agent, we performed experiments at high ethanol concentration and three evaporator inlet temperatures $T_{evap,in}$ (10, 5 and -5 °C; experiments A, B, C). To study the influence of ethanol on the performance of the adsorption chiller, we considered three overall ethanol-concentrations x_{EtOH} (0, 14 and 22 mol-%) at an evaporator inlet temperature of 10 °C (experiments D, E, A).

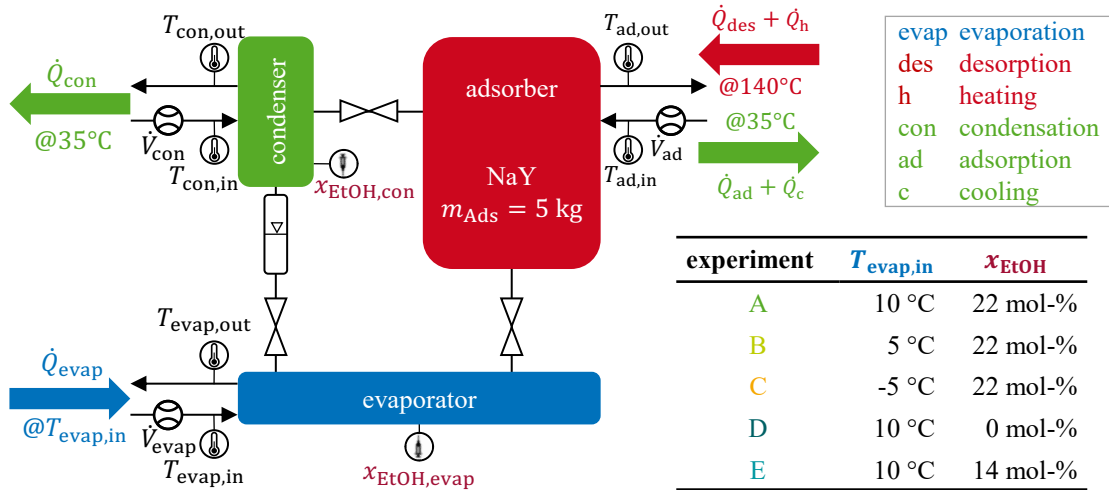


Figure 1: Scheme of the adsorption chiller setup with installed temperature (T) and volume flow rate (\dot{V}) sensors in condenser, evaporator and adsorber, concentration measurement points in condenser ($x_{EtOH,con}$) and evaporator ($x_{EtOH,evap}$), adsorber inlet temperature during desorption and heating (140 °C), adsorber inlet temperature during adsorption and cooling (35 °C) and condenser inlet temperature (35 °C) as well as evaporator inlet temperature $T_{evap,in}$ and overall ethanol-concentration x_{EtOH} of analyzed experimental points A, B, C, D, E.

3. Results

The conducted experiments show that ethanol can be used as anti-freezing agent (Fig. 2 left). Ethanol evaporates and participates in the adsorption process and thus the anti-freezing effect is not limited to evaporator: In all conducted experiments, freezing did not occur. Furthermore, the water-ethanol-mixture as refrigerant (22 mol-%) allows the adsorption chiller process to still work at an evaporator inlet temperature of $-5\text{ }^{\circ}\text{C}$ (Fig. 2 left). In this case, the adsorption chiller process reaches a maximum COP and SCP of 11 % and 18 W/kg, respectively. Compared to the evaporator inlet temperatures of $10\text{ }^{\circ}\text{C}$, the SCP decreases by 29 %, while the COP remains nearly constant. Hence, the evaporator inlet temperature has a larger effect on the SCP than on the COP in the considered temperature range, which is probably caused by lower heat and mass transfer kinetics.

In contrast, the concentration of ethanol in the refrigerant mixture affects both, COP and SCP (Figure 2 right). At evaporation inlet temperature of $10\text{ }^{\circ}\text{C}$, the highest COP and SCP is achieved with an ethanol-concentration of 0 mol-% (26 % resp. 54 W/kg). COP and SCP decrease by 61 % and 55 %, respectively, with increasing ethanol-concentration from 0 mol-% to 22 mol-%. Possible reasons are the lower enthalpy of vaporization of ethanol, a changed adsorption equilibrium due to co-adsorption of ethanol, a lower heat transfer of the water-ethanol-mixture compared to pure water, and slower adsorption kinetics of ethanol. To achieve higher performance, the ethanol concentration should thus be selected as low as possible. Altogether, the achieved COP s and SCP s of all experiments (pure water and water-ethanol-mixture) are very low, since the employed one-bed-adsorption chiller is not optimized and is only used for a first demonstration of the feasibility of water-ethanol mixtures.

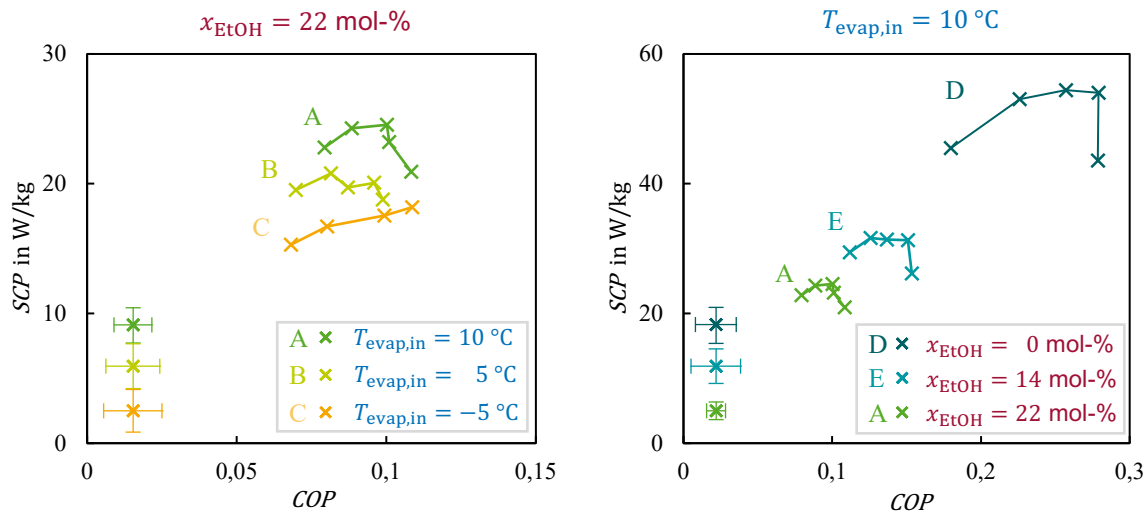


Figure 2: Comparison of Coefficient Of Performance (COP) and Specific Cooling Power (SCP): Effect of evaporator inlet temperature at constant ethanol-concentration (left) and effect of ethanol-concentration at constant evaporator inlet temperature (right). Each shown COP and SCP value is the mean value of at least 3 reproduced cycles. Each of the connected points corresponds to one specific cycle time and the ethanol-concentration and evaporator inlet temperature indicated in the legend. Measurement uncertainties are presented as the maximum value of all points of a specific concentration.

The ethanol-concentration is enriched in ethanol in the condenser (Fig. 3). With an overall ethanol concentration of 22 mol-%, the ethanol concentration in the condenser (38 mol-%) is about 5 times higher than in the evaporator (7 mol-%). Due to the enrichment of the ethanol in the condenser, a higher overall ethanol-concentration is needed to prevent freezing in the evaporator. In general, the enrichment of ethanol could be caused by two mechanisms: evaporation and adsorption. Since the measured ethanol concentration in the condenser and evaporator are in good agreement with the vapor-liquid-equilibrium of water and ethanol, the enrichment of ethanol seems to be mainly caused by the evaporation and not by preferred adsorption of one of both components. However, in a real two-bed adsorption chiller, ethanol-concentration in the evaporator would not decrease as much, since enriched condensate is returned to the evaporator during evaporation.

Furthermore, we used the measured ethanol-concentration in condenser and evaporator as well as the change of the filling level in the condenser during adsorption to calculate the ethanol-concentration of the adsorbed

refrigerant mixture (Fig. 3). The ethanol-concentration of the adsorbed refrigerant mixture is in good agreement with the ethanol-concentration in the condenser. Thus, the adsorption chiller has reached steady-state condition. It should be noted that experiment C shows a lower ethanol-concentration in the evaporator and condenser compared to experiments A and B. Therefore, the overall ethanol-concentration of experiment C is probably lower than the overall ethanol-concentration of experiment A and B. All overall ethanol-concentrations were determined by weighing prior to filling. We suppose an error in the determination of the overall ethanol-concentration of experiment C. A lower overall ethanol-concentration of experiment C would also explain the too high *COP* and *SCP* of experiment C compared to experiment A and B (Fig. 2 left).

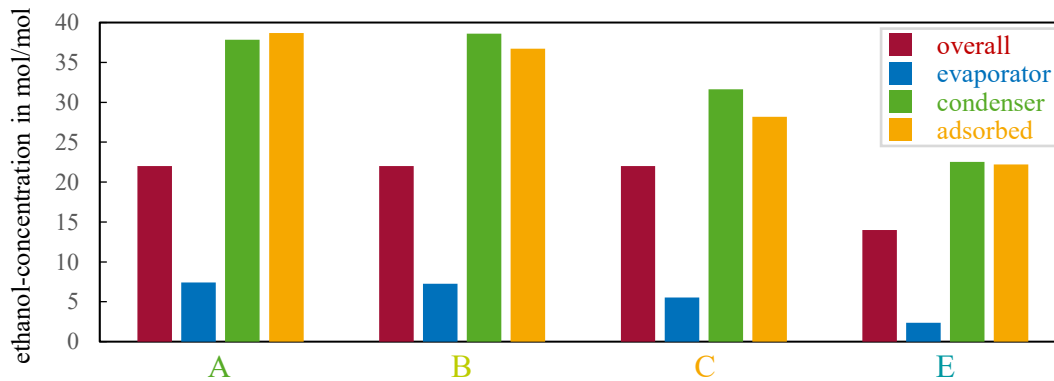


Figure 3: Measured ethanol-concentration in evaporator $x_{EtOH, evap}$, condenser $x_{EtOH, con}$, and overall ethanol-concentration x_{EtOH} as well as the calculated ethanol-concentration of the adsorbed refrigerant mixture of all experiments with a water-ethanol-mixture (A, B, C, E). Experiment D is not shown because the overall ethanol-concentration of experiment D is 0 mol-%.

4. Conclusions

We studied a new refrigerant mixture for adsorption cooling to extend the working range of water-based adsorption chillers below 0 °C. Here, we used ethanol as anti-freezing agent to overcome the limitation of the freezing-point of water. With a mixture with 22 mol-% ethanol, the adsorption chiller process works at an evaporator inlet temperature of -5 °C and reaches a *COP* of 11 % and a *SCP* of 18 W/kg. However, the increased ethanol-concentration reduces *COP* and *SCP*. Thus, ethanol-concentration should be selected as low as possible to prevent freezing while retaining maximum process performance.

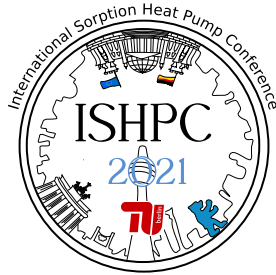
5. Acknowledgment

We thank the German Federal Ministry for Economic Affairs and Energy for funding this work (03EN2002A).

6. List of References

- [1] Fernandes, M. S., Brites, G., Costa, J. J., Gaspar, A. R., Costa, V. (2014): Review and future trends of solar adsorption refrigeration systems. *Renewable & Sustainable Energy Reviews*, vol.39, pp.102-123.
- [2] Freni, A., Dawoud, B., Bonaccorsi, L., Chmielewski, S. (2015): Characterization of Zeolithe-Based Coatings for Adsorption Heat Pumps. *Springer International Publishing*.
- [3] Ammar, Y., Joyce, S., Norman, R., Wang, Y., Roskilly, A. P. (2012): Low grade thermal energy sources and uses from the process industry in the UK: *Applied Energy*, vol.89, pp.3-20.
- [4] Li, T. X., Wang, R. Z., Li, H. (2014): Progress in the development of solid-gas sorption refrigeration thermodynamic cycle driven by low-grade thermal energy. *Progress in Energy and Combustion Science*, vol. 40, pp. 1-58.
- [5] Seiler, J., Hackmann, J., Lanzerath, F., Bardow, A. (2017): Refrigeration below 0°C: Adsorption chillers using water with ethylene glycol as antifreeze. *International Journal of Refrigeration*, vol.77, pp.39-47.
- [6] Martinez, P.J., Rus, E., Compañía, J. M.(2005): Flash point determination of binary mixtures of alcohols, ketones and water. *7th World Congress of Chemical Engineering*, 1-8.

-
- [7] pro Kühlsole GmbH (2016): GlykosolN – datasheet: https://www.prokuehlsole.de/assets/userfiles/prokuehl/dokumente/Glykosol_N_Datenblatt_4S_GB_03_2016.pdf. (Accessed 6 March 2020).
- [8] Wagner, W. and Pruß, A. (2002): The IAPWS Formulation 1995 for the Thermodynamic Properties of Ordinary Water Substance for General and Scientific Use. *Journal of Physical and Chemical Reference Data*, vol.31, pp.387-535.
- [9] Chua, H. T., Ng, K. C., Malek, A., Kashiwagi, T., Akisawa, A., Saha, B. B. (1999): Modeling the performance of two-bed, silica gel-water adsorption chiller. *International Journal of Refrigeration*, vol.22, pp. 194-204.
- [10] Bau, U., Baumgärtner, N., Seiler, J., Lanzerath, F., Kirches, C., Bardow, A. (2019): Optimal operation of adsorption chillers: First implementation and experimental evaluation of nonlinear model-predictive-control strategy. *Applied Thermal Engineering*, vol.149, pp.1503-1521.



Computationally efficient, experimentally validated adsorption chiller model using a plug-flow-based modelling approach

Gibelhaus, Andrej¹, Postweiler, Patrik¹, Seiler, Jan¹ and Bardow, André^{1,2,3*}

¹ Institute of Technical Thermodynamics, RWTH Aachen University, 52062 Aachen, Germany

² Institute of Energy and Climate Research (IEK-10), Forschungszentrum Jülich, 52425 Jülich, Germany

³ Energy & Process Systems Engineering, ETH Zurich, 8092 Zürich, Switzerland

* Corresponding Author: abardow@ethz.ch

Abstract:

State-of-the-art models of adsorption chillers suffer from a trade-off between accuracy and computational efficiency due to the discretization of the heat exchangers. To resolve this trade-off, we present a novel plug-flow-based adsorption chiller model, which is able to accurately represent the flow of the heat transfer fluid in the heat exchangers without the issue of discretization. The results show that the plug-flow based adsorption chiller model achieves the same accuracy as a highly discretized finite-volume-based model, but reduces the simulation time by up to 70 %.

1. Introduction

Design and control of adsorption chiller systems require reliable and computationally efficient dynamic models. However, modelling of adsorption chillers is a challenging task, due to the combination of both, the intrinsic dynamic nature (discontinuous operation) and the interaction of several components (adsorbers, evaporator and condenser) that determine the performance of adsorption chillers. Literature reviews [1] divide adsorption chiller models into 3 main classes: 1) Thermodynamic equilibrium models [2], which are computationally very efficient, but entirely neglect dynamics and, therefore, are not suitable for detailed chiller design and system integration. 2) Distributed-parameter models [3], which provide high accuracy, but at the same time show poor computational efficiency due to spatial resolution of all states, so that these models are too complex for system simulations. 3) As a compromise between model classes 1) and 2), lumped-parameter models [4] have been developed. Lumped-parameter models are computationally efficient and sufficiently accurate to capture trends of the main performance indicators. As main drawback, lumped-parameter models are not capable to accurately describe fast dynamics, which are typical for adsorption chillers, resulting from the periodical operation. To account for the fast dynamics, a 1-d discretization of the heat exchangers is often applied, which enables to accurately fit the model to experimental data [5]. Thus, 1-d discretized lumped-parameter models are most prominent for system simulations of adsorption chillers.

However, the choice of the discretization leads again to a conflict between accuracy and computational efficiency. To improve computational efficiency, rigorous systems optimizations [6] or real-time control applications [7] have to accept inaccuracies (coarse discretization). In this work, we propose a modelling approach for adsorption chillers to resolve the trade-off between accuracy and computational efficiency. The proposed approach replaces the commonly used finite-volume-based heat exchanger models by a thermo-hydraulic pipe model based on the plug-flow approach [8]. The plug-flow approach describes fast dynamics of incompressible fluids accurately and computationally efficiently and, thus, seems appropriate to model the heat exchangers of adsorption chillers.

This paper is structured as follows: The plug-flow based adsorption chiller model is presented in section 2. In section 3, we compare the plug-flow-based model to both, a state-of-the-art finite-volume-based model and experimental data [5], regarding computational efficiency and accuracy. Finally, we summarize the main results in section 4.

2. Plug-flow-based adsorption chiller model

Figure 1 shows the scheme of the adsorption chiller model (a) and of the plug-flow-based heat exchanger model (b). All other sub-models of the adsorption chiller, such as the adsorbent and the VLE volume, are modelled based on our Modelica library SorpLib [9]. Therefore, we focus on the proposed plug-flow based heat exchanger model in the following.

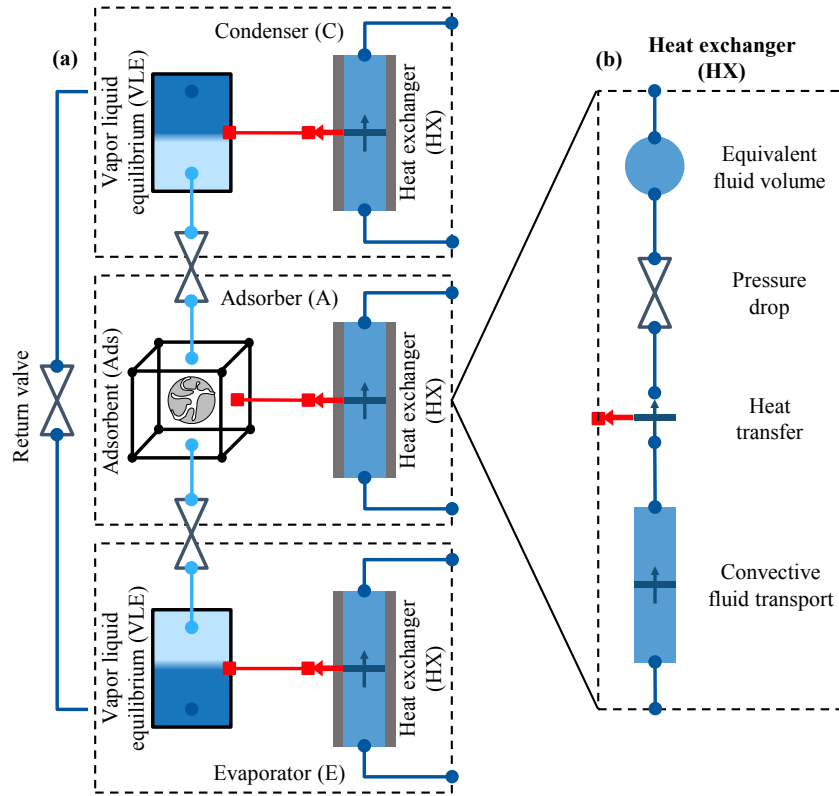


Figure 1: (a) Scheme of 1-bed adsorption chiller consisting of the 3 main components Adsorber (A), Evaporator (E) and Condenser (C) connected via valves. Each component consists of a heat exchanger (HX), which is thermally connected to the adsorbent (Ads) or to the vapor liquid equilibrium (VLE) volume. (b) Scheme of the plug-flow based heat exchanger model. The model consists of 4 sub-models: 1) calculation of the convective fluid transport, 2) calculation of the heat transfer, 3) calculation of the pressure drop, and 4) equivalent fluid volume to account for the thermal inertia of the heat exchanger wall.

Since liquid water is the heat transfer fluid, the heat exchangers of the adsorption chiller can be described by an incompressible, 1-d convective fluid flow. Neglecting axial diffusion and internal sources (e.g. dissipation), the energy balance reads:

$$\rho_{\text{fl}} c_{\text{fl}} \frac{\partial T}{\partial t} + \rho_{\text{fl}} c_{\text{fl}} v \frac{\partial T}{\partial x} = -\dot{q}. \quad (1)$$

The heat transfer $\dot{q} = UA(T - T_s)$ is described by an overall heat transfer coefficient UA consisting of the inner heat transfer coefficient, determined by empirical correlations, and the outer heat transfer coefficient, used as calibration parameter of the model [5].

The main idea of the plug-flow based approach is to decompose the dynamic convection equation (1) into 2 parts (**Figure 1b**) [8]: The first part only describes the convective fluid transport through the heat exchanger without the source term due to heat transfer:

$$\frac{\partial T}{\partial t} + v \frac{\partial T}{\partial x} = 0 \quad (2)$$

This convection equation (2) can be efficiently solved by the Modelica Operator `spatialDistribution()` [10].

The second part of the plug-flow model calculates the heat transfer from or to the connected model (adsorbent or VLE volume, cf. **Figure 1a**) using the Lagrangian approach: For this purpose, the coordinate system is attached to a moving fluid particle flowing through the heat exchanger and, thus, allows to calculate the outlet temperature T_{out} analytically [8]:

$$T_{\text{out}} = T_s + (T_{\text{in}} - T_s) \exp\left(-\frac{UA}{m_{\text{fl}} c_{\text{fl}}}(t_{\text{out}} - t_{\text{in}})\right). \quad (3)$$

The residence time of a fluid particle in the heat exchanger $t_{\text{out}} - t_{\text{in}}$ is calculated by tracking the inflow time of each fluid particle t_{in} as a fluid property, which is convectively transported analogous to Eq. (2).

Subsequently, the pressure drop of the heat exchanger is calculated (e.g. based on empirical correlations) and the thermal inertia of the heat exchanger wall is modelled by an equivalent fluid volume [8].

3. Experimental validation and comparison to a state-of-the-art finite volume based model

Next, we compare the plug-flow-based model to a state-of-the-art finite-volume-based model regarding both, accuracy (measured by agreement with experimental data) and computational efficiency (measured by simulation time). For this purpose, we employ experimental data of Lanzerath et al. [5]. For calibration, we use the temperature triple 90/30/10 °C to estimate the calibration parameters of the model (outer heat transfer coefficients of all heat exchangers and diffusion coefficient of the adsorbent) by minimizing the deviation between modelled and measured heat flows [5]. **Figure 2** shows the excellent agreement between the heat flows of the model and the experimental data for the calibration cycle.

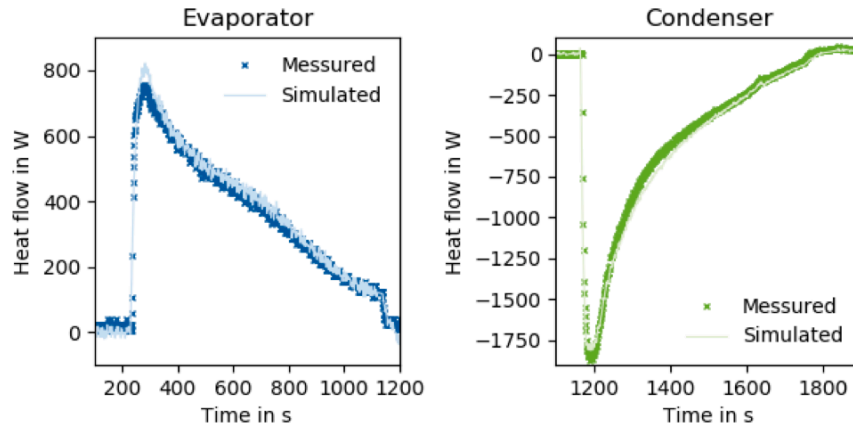


Figure 2: Measured and simulated heat flow curves for the plug-flow based adsorption chiller model in the evaporator and the condenser.

To quantify the accuracy, we use the average Coefficient of Variation \overline{CV} :

$$\overline{CV} = \frac{1}{3} \sum_i CV_i = \frac{1}{3} \sum_i \left(\frac{1}{Q_{\text{meas},i}/\Delta t_{\text{cycle}}} \sqrt{\frac{1}{\Delta t_{\text{cycle}}} \int (\dot{Q}_{\text{meas},i} - \dot{Q}_{\text{sim},i})^2 dt} \right), \quad (4)$$

which sums up the root mean square deviations between simulated heat flows $\dot{Q}_{\text{sim},i}$ and measured heat flows $\dot{Q}_{\text{meas},i}$ in the 3 components (evaporator, condenser and adsorber), normalized by the average measured heat flow of each component $Q_{\text{meas},i}/\Delta t_{\text{cycle}}$. **Figure 3** quantitatively compares the plug-flow based model and the finite-volume-based model regarding both, (a) accuracy (\overline{CV}) and (b) computational efficiency (simulation time). The comparison is shown for the calibration cycle (temperature triple 90/30/10 °C) and for all validation cycles. In the validation cycles, the calibration parameters are fixed but operating parameters are varied: the cycle time (t), the low temperature level (evp), the high temperature level (des) and the medium temperature level (ads). Regarding \overline{CV} , the plug-flow-based model achieves similar or even better results than the highly discretized finite-volume-based model for most cases. However, the plug-flow-based model significantly reduces the simulation time by 65-70 % compared to the highly discretized (40 cells in adsorber, 10 cells in evaporator and condenser) finite-volume-based model. Even if the discretization of the finite-volume-based model is significantly reduced by 75% (10 cells in adsorber, 2 cells in evaporator and condenser), the simulation time is still slightly higher than for the plug-flow-based model. However, the reduced discretization increases the \overline{CV} by up to 78 % in the Des10 cycle.

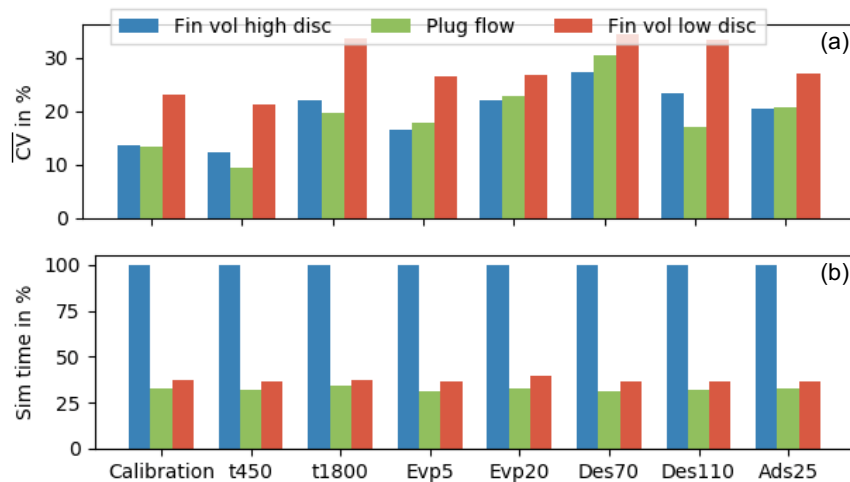


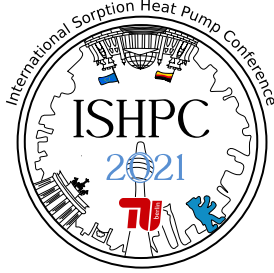
Figure 3: Experimental validation of the plug-flow based adsorption chiller model and comparison to the finite volume (fin vol)-based model for the calibration cycle and all validation cycles. (1) Coefficient of variation \overline{CV} (Eq. (4)) and (2) relative simulation time (sim time) referred to the reference finite volume model with high discretization (high disc). The finite volume model with low discretization (low disc) was chosen to achieve similar simulation times as for the plug-flow-based model.

4. Conclusions

A plug-flow based modelling approach was proposed for adsorption chillers to improve computational efficiency, while ensuring high accuracy. The novel adsorption chiller model proves to be as accurate as an experimentally validated state-of-the-art model. At the same time, the plug-flow-based model reduces the simulation time by up to 70 %. Thus, the presented modelling approach is well suited for complex design and control optimisations of large adsorption chiller systems.

5. List of References

- [1] Pesaran A, Lee H, Hwang Y, Radermacher R, Chun H-H. Review article: Numerical simulation of adsorption heat pumps. *Energy*. 2016;100:310-20. 10.1016/j.energy.2016.01.103
- [2] Meunier F, Neveu P, Castaing-Lasvignottes J. Equivalent Carnot cycles for sorption refrigeration. *International Journal of Refrigeration*. 1998;21(6):472-89. 10.1016/s0140-7007(97)00084-4
- [3] Leong KC, Liu Y. Numerical modeling of combined heat and mass transfer in the adsorbent bed of a zeolite/water cooling system. *Applied Thermal Engineering*. 2004;24(16):2359-74. 10.1016/j.applthermaleng.2004.02.014
- [4] Gong LX, Wang RZ, Xia ZZ, Chen CJ. Design and performance prediction of a new generation adsorption chiller using composite adsorbent. *Energy Conversion and Management*. 2011;52(6):2345-50. 10.1016/j.enconman.2010.12.036
- [5] Lanzerath F, Bau U, Seiler J, Bardow A. Optimal design of adsorption chillers based on a validated dynamic object-oriented model. *Science and Technology for the Built Environment*. 2015;21(3):248-57. <https://doi.org/10.1080/10789669.2014.990337>
- [6] Nienborg B, Dalibard A, Schnabel L, Eicker U. Approaches for the optimized control of solar thermally driven cooling systems. *Applied Energy*. 2017;185:732-44. <http://dx.doi.org/10.1016/j.apenergy.2016.10.106>
- [7] Bau U, Baumgärtner N, Seiler J, Lanzerath F, Kirches C, Bardow A. Optimal operation of adsorption chillers: First implementation and experimental evaluation of a nonlinear model-predictive-control strategy. *Applied Thermal Engineering*. 2019;149:1503-21. <https://doi.org/10.1016/j.applthermaleng.2018.07.078>
- [8] van der Heijde B, Fuchs M, Ribas Tugores C, Schweiger G, Sartor K, Basciotti D, Müller D, et al. Dynamic equation-based thermo-hydraulic pipe model for district heating and cooling systems. *Energy Conversion and Management*. 2017;151:158-69. 10.1016/j.enconman.2017.08.072
- [9] Institute of Technical Thermodynamics, RWTH Aachen University. SorpLib - Adsorption Energy Systems Library, https://git.rwth-aachen.de/ltt_public/SorpLib; 2018 [accessed 06.04.2019]
- [10] Modelica Association. Modelica® - A Unified Object-Oriented Language for Systems Modeling: Language Specifications Version 3.4, <https://www.modelica.org/documents/ModelicaSpec34.pdf>; 2017 [accessed 17.04.2018]



Experimental Validation of a Dynamic Adsorption Chiller Model Using Optimal Experimental Design

Postweiler, Patrik¹, Gibelhaus, Andrej¹, Engelpracht, Mirko¹, Seiler, Jan¹ and Bardow, André^{1,2,3*}

¹ Institute of Technical Thermodynamics, RWTH Aachen University, 52062 Aachen, Germany

² Institute of Energy and Climate Research (IEK-10), Forschungszentrum Jülich, 52425 Jülich, Germany

³ Energy & Process Systems Engineering, ETH Zurich, 8092 Zürich, Switzerland

* Corresponding Author: abardow@ethz.ch

Abstract:

A potential way to reduce the global greenhouse gas emissions for cooling and heating are thermally-driven cooling and heating technologies, such as sorption chillers. However, sorption chillers often suffer from high electricity consumption due to sub-optimal system integration. To optimize system integration, model-based approaches are very promising, but require valid models. For efficient model validation, we present a method based on the Optimal Experimental Design (OED) and apply the method to a dynamic adsorption chiller model. For this purpose, we plan an experiment with OED, execute it and estimate the unknown model parameters. To improve parameter accuracy and thus a valid model, we repeat the procedure iteratively. The results show that the presented method leads to a valid adsorption chiller model with only three optimally planned experiments. Furthermore, we show that the experimental effort decreases by up to 83 % compared to randomly planned experiments.

1. Introduction

Thermally-driven sorption chillers offer an environmentally friendly alternative to conventional compression chillers, by substituting electricity with low-grade thermal energy. However, the electricity saving potential is often not exploited due to sub-optimal system integration [1]. Hence, electrical efficiencies of sorption chillers are often only slightly higher compared to conventional compression chillers [1]. To increase the electrical efficiencies of sorption chillers, dynamic optimization of the whole system is particularly promising as, e.g., shown by Gibelhaus et al. [2]. However, dynamic optimization requires validated models [3].

A key step towards a valid model is to accurately estimate unknown parameters [3]. Accurately parameter estimation often requires a large number of experiments, which can be resource- and time-intensive [3]. Besides, not every experiment offers the same amount of information: poorly or randomly planned experiments often yield little information and are therefore not effective for parameter estimation [3]. For effective parameter estimation, experiments should be planned in such a way that they generate the maximum information and thus minimize the experimental effort. To optimally plan an experiment, Optimal Experimental Design (OED) is particularly promising because it specifies conditions for an experiment where the parameters are determined with the highest accuracy.

OED is already successfully applied in several disciplines, e.g., biochemical networks, biological process kinetics, chemical kinetics, and mass transfer to reduce experimental effort [3]. However, this work is - to the best of the author's knowledge - the first that applies OED for validating an adsorption chiller model and thus to reduce experimental effort. In Section 2, we therefore introduce the procedure for model validation by describing the two main steps: (1) optimal experimental design, and (2) parameter estimation. Section 3 presents the results of the model validation, and main conclusions are drawn in Section 4.

2. Methodology

We implemented a dynamic model of a one-bed adsorption chiller (Fig. 1) in the object-oriented language Modelica based on our open source library SorpLib [4]. The model consists of 1-D discretized finite volume models for the heat exchangers and lumped-parameter models for the vapor liquid equilibrium volume as well as for the adsorbent. The mass transfer is modelled by a linear driving force approach. For a detailed description of the model including model equations, the reader is referred to a prior publication [5]. Model inputs are volume flows to the adsorber \dot{V}_A , the condenser \dot{V}_C , and the evaporator \dot{V}_E as well as the corresponding inlet temperatures T_i , and the cycle time τ . All inputs are

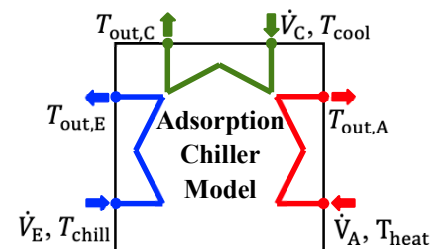


Figure 1 - Scheme of an adsorption chiller model with all inputs and outputs of the main components *evaporator (E)*, *condenser (C)*, and *adsorber (A)*: volume flows (\dot{V}) and temperatures (T).

summarized in the design vector $\boldsymbol{\varphi}$. Model outputs are the outlet temperatures of the components $T_{\text{out},i}$ that shall be accurately predicted after the model validation.

2.1. Sequential approach

The model equations depend on parameters e.g. geometrical data, thermal masses, and heat or mass transfer coefficients. Most of these parameters can be directly determined at the experimental setup or accurately described by correlations. However, the heat transfer coefficients of adsorber, evaporator, and condenser as well as the diffusion coefficient cannot be individually measured with our experimental setup or described precisely by correlations. Therefore, we assume that these coefficients are neither temperature, pressure nor load dependent and treat them as parameters. These parameters need to be estimated for the entire system and are therefore summarized in the parameter vector $\boldsymbol{\theta}$. The parameters are estimated from experimental data. To keep the experimental effort low, the experiments are planned with OED. However, the optimal experiment depends on the current parameter value. Therefore, inaccurate initial parameters may lead to sub-optimal experiments for the true parameter value. Thus, the experimental effort may increase for achieving a given parameter accuracy. To keep the experimental effort low despite uncertain start parameters $\boldsymbol{\theta}_0$, we used a sequential approach (Fig. 2) [3]. Based on an initial parameter vector $\boldsymbol{\theta}_0$, we planned an experiment with OED, carried it out, and estimated the parameters based on the experimental data. The procedure is repeated with the new estimated parameter vector $\hat{\boldsymbol{\theta}}$, until a given accuracy of the estimated parameters is achieved. To quantify the parameter accuracy, we used the Relative Standard Deviation (RSD):

$$\text{RSD}_i = \frac{3 \times \sigma_{\theta_i}}{\theta_i}, \quad (1)$$

where σ_{θ_i} is the standard deviation of the i^{th} parameter and θ_i is the respective parameter value. The factor 3 determines the confidence interval such that the true parameter value is included with a likelihood of 99.7%. As termination criterion of the sequential process, we used a maximum RSD of 2% for every parameter i . Once the required parameter accuracy is achieved, the sequential approach is completed and thus results in a valid model [3]. For the two main steps of the sequential approach 1) OED and 2) parameter estimation, dynamic optimization problems need to be solved. To solve the optimization problems, we used a genetic algorithm [6].

2.2. Optimal experimental design

Since the experimental data is determined with a statistical uncertainty, the estimated parameters are also uncertain. However, the more accurate the parameters are, the more accurate the model outputs. Therefore, OED aims to find the optimal design vector $\boldsymbol{\varphi}$ for an experiment, which maximizes the estimation accuracy of the parameter vector $\boldsymbol{\theta}$. In particular, an experiment should be carried out for a design vector, where the model outputs $T_{\text{out,exp},i}$ are highly sensitive to the estimated parameters. The higher the sensitivity to the estimated parameters, the more precise is the estimation, as a change in the parameters leads to larger changes of the model outputs. Additionally, the measurement variance σ_i^2 of the experimental outputs $T_{\text{out,exp},i}$ should be low. The sensitivity is mathematically the partial derivative of the model output $T_{\text{out,exp},i}$ with respect to the estimated parameters θ_i [3]:

$$\mathbf{Q}_r = \begin{matrix} & \xrightarrow{n_\theta} & \\ \begin{bmatrix} \frac{\partial T_{\text{out,sim},r}}{\partial \theta_1} \Big|_{t_1} & \dots & \frac{\partial T_{\text{out,sim},r}}{\partial \theta_{n_\theta}} \Big|_{t_1} \\ \vdots & \ddots & \vdots \\ \frac{\partial T_{\text{out,sim},r}}{\partial \theta_1} \Big|_{t_{n_{\text{sp}}}} & \dots & \frac{\partial T_{\text{out,sim},r}}{\partial \theta_{n_\theta}} \Big|_{t_{n_{\text{sp}}}} \end{bmatrix} & \cdot & \begin{matrix} \downarrow \\ n_{\text{sp}} \end{matrix} \end{matrix} \quad (2)$$

Eq. 2 presents the dynamic sensitivity matrix of the r^{th} model output \mathbf{Q}_r . The sensitivity matrix \mathbf{Q}_r is a $n_{\text{sp}} \times n_\theta$ matrix, where n_{sp} is the number of time samples and n_θ is the number of the considered estimated parameters [3]. In addition to the sensitivity, the accuracy of the parameter estimation also depends on the measurement variance σ_i^2 of the experimental outputs. Therefore, the Fisher information matrix \mathbf{M} is calculated using the measurement variance σ_i^2 and the dynamic sensitivity matrix \mathbf{Q}_r . Without prior information on the uncertainty of the estimated parameters, the Fisher information matrix \mathbf{M} reads

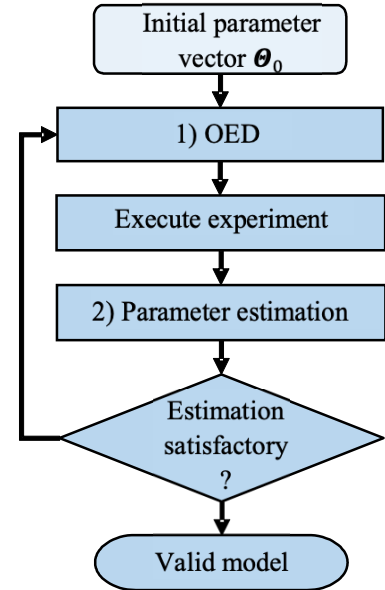


Figure 2 - Scheme of the sequential approach for parameter estimation using the OED. Based on Franceschini & Macchietto 2008 [3].

$$\mathbf{M}(\hat{\boldsymbol{\theta}}, \boldsymbol{\varphi}) = \sum_r^m \sum_s^m \frac{1}{\sigma_{r,s}^2} \mathbf{Q}_r^T \mathbf{Q}_s, \quad (3)$$

where $\hat{\boldsymbol{\theta}}$ is the best parameter vector currently available and $\sigma_{r,s}^2$ is the (r,s)-entry of the measurement variance-covariance matrix. The Fisher information matrix \mathbf{M} is a symmetric $n_{\boldsymbol{\theta}} \times n_{\boldsymbol{\theta}}$ square matrix [3]. The inverse of \mathbf{M} represents the lower boundary of the parameter variance-covariance matrix \mathbf{V} and contains all information about the minimal possible uncertainty of the estimated parameters:

$$\mathbf{V}(\hat{\boldsymbol{\theta}}, \boldsymbol{\varphi}) \geq [\mathbf{M}(\hat{\boldsymbol{\theta}}, \boldsymbol{\varphi})]^{-1}. \quad (4)$$

To keep the wording simple, we refer to the inverse of the Fisher information matrix \mathbf{M} as a parameter variance-covariance matrix, even if it only approximates it. To determine the optimal design vector $\boldsymbol{\varphi}$, the parameter variance-covariance matrix \mathbf{V} needs to be converted into a scalar value to use it in an optimization problem. For this purpose, we use the D-optimality criterion. D-optimality uses the determinant of the parameter variance-covariance matrix \mathbf{V} as the representative scalar and thus geometrically minimizes the volume of the confidence ellipsoid. The dynamic optimization problem for the determination of the optimal experimental design vector $\boldsymbol{\varphi}$ reads [3]:

$$\begin{aligned} \min_{\boldsymbol{\varphi} \in \Phi} \quad & \det(\mathbf{V}(\hat{\boldsymbol{\theta}}, \boldsymbol{\varphi})) \\ \text{s. t.} \quad & \text{model equations.} \end{aligned} \quad (5)$$

The optimal design vector $\boldsymbol{\varphi}$ is determined within the design space Φ . The objective function is minimized subjected to (s.t.) the model equations. The variance-covariance matrix \mathbf{V} is also used for the termination criterion of the sequential approach. On the main diagonal of this variance-covariance matrix are the variances of the parameters $\sigma_{\theta,i}^2$, which are the square of the standard deviation $\sigma_{\theta,i}$ of the parameters used in the RSD (Eq. 1).

2.3. Parameter estimation

The second main step of the sequential approach is the parameter estimation. We estimated the parameters using a weighted least-squares objective function:

$$\begin{aligned} \min_{\boldsymbol{\theta}} \quad & \sum_{i=1}^m \sum_{j=1}^{n_{\text{sp}}} \sum_{k=1}^{n_{\text{exp}}} \frac{(T_{\text{out,sim},i}^k - T_{\text{out,exp},i}^k)^2}{\sigma_i^2} \\ \text{s. t.} \quad & \text{model equation} \\ & \text{inputs.} \end{aligned} \quad (6)$$

The objective function of the optimization problem is the square deviation between the simulated (sim) and measured (exp) outlet temperature, weighted by the inverse measurement variance σ_i^2 . The square deviations are summed up over the number of considered outputs m (here 3, see Fig. 1), the considered time steps n_{sp} , and the number of conducted experiments n_{exp} .

2.4. Case study

Tab. 1 shows the investigated design space Φ of the adsorption chiller model, which is studied in this paper. We chose the input temperatures T_i so that most of the relevant operating conditions are covered. The pumps of the experimental setup limit the volume flows. Further, the cycle time τ covers typical values for a reasonable use of adsorption chillers.

Table 1 – Definition of the design space Φ with lower boundary (LB) and upper boundary (UB)

Input variables	T_{chill}	T_{heat}	T_{cool}	\dot{V}_{E}	\dot{V}_{A}	\dot{V}_{C}	τ
LB	10 °C	60 °C	27 °C	5.3 l/min	4.6 l/min	3.75 l/min	600 s
UB	20 °C	140 °C	45 °C	14.3 l/min	7.9 l/min	6.1 l/min	1260 s

To quantify the accuracy of the model compared to measured data, we used the Coefficient of Variation (CV):

$$\text{CV} = \frac{1}{\tau} \sum_{i=1}^{n_{\text{resp}}} \sum_{j=1}^{\tau} \frac{(T_{\text{out,exp},i}(t_j) - T_{\text{out,sim},i}(t_j))^2}{(T_{\text{out,exp},i,\text{max}} - T_{\text{out,exp},i,\text{min}})}. \quad (7)$$

The normalized residuals are summed up over the number of the considered measurable outcomes n_{resp} and the cycle time τ . We use this normalization since it allows comparing different components and cycle times.

3. Results

The presented method terminates after only 3 iterations. Thereby, the RSD for the worst estimated parameter decreases from 24 % after the 1st iteration to 2 % after the 3rd iteration. To highlight the reduction of the experimental effort, we checked how many random experiments are needed to achieve the same overall parameter accuracy as for one OED experiment. After the 7th random experiment, the overall accuracy of the parameters is higher

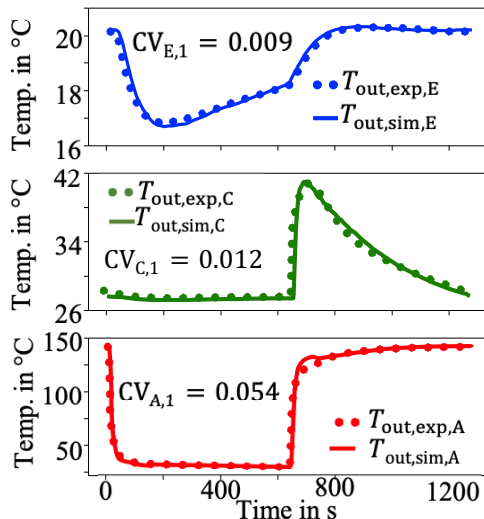


Figure 4 - Experimental (*exp*) and simulated (*sim*) outlet temperatures T_i of evaporator (E), condenser (C), and adsorber (A) of the 1st experiment. The model is parameterized with the estimated parameters by solving Eq. 6.

cycle time τ is at its upper bound. The maximal cycle time results from the asymptotic loading process. Thus, the longer the cycle time is, the larger is the loading difference. A large loading difference leads to higher driving forces and thus also increases process dynamics.

The resulting fit of the parameter estimation (Fig. 4) highlights that the outflow temperatures of the evaporator and the condenser are in very good agreement with the measured data. For the outflow temperatures of the adsorber, a larger difference between experiment and simulation is observed but still provides a qualitatively good agreement (cf. Fig. 4).

The CV for the fits (Fig. 5) proves that a significant part of the lack of fit is due to the adsorber model, which should be further improved in future. The CV increases with the number of iterations since more experiments have to be fitted with the same number of parameters.

4. Conclusion

This work uses the optimal experimental design method in a sequential approach to derive a validated adsorption chiller model while keeping the required experimental effort as low as possible. We successfully applied the method to an adsorption chiller and reduced the experimental effort by up to 83 % compared to randomly planned experiments. The identified parameters lead to excellent agreement between simulation and measurement. Main deviations remain for the adsorber model, which should be improved in future work. The results of this work show that the method of optimal experimental design is a powerful tool to reduce experimental effort for the validation of adsorption chiller models.

5. Acknowledgment

We gratefully acknowledge the financial support from the German Federal Ministry for Education and Research (BMBF) in the founding initiative “KMU-innovativ” via the project Sorb-Zero (01LY1827B). Simulations were performed with computing resources granted by RWTH Aachen University under project thes0615.

than in one OED experiment. Thus, the OED reduces the experimental effort by 83 %. The comparison with random experiments is an extreme case, since experiments are usually better planned with experience than by chance. However, experience does not design a better experiment than the OED, and by applying the method, anyone can determine the optimal experiment.

To reach the desired accuracy, OED chooses the following inputs: The volume flows \dot{V} of the heat transfer circuits of the evaporator and of the condenser are at their lower bound for all iterations. The volume flow of the adsorber heat transfer circuit \dot{V}_A is at the upper bound for the first iteration and at the lower for the following. The volume flows at the lower bounds are preferred due to the variance of the measurable outputs since lower volume flows increase changes in temperatures across the heat exchangers, and larger changes in the temperatures reduce the relative impact of the measurement errors. For all three experiments, the chilling temperature T_{chill} and the heating temperature T_{heat} are at their upper bounds and the cooling temperature T_{cool} is at the lower bound. The chosen temperatures lead to a maximal loading difference of the adsorbent and thus to maximum dynamics of the adsorption and desorption process. Choosing maximum dynamics is reasonable, since the estimated parameters significantly influence the dynamics and thus their impact on the measurement is increased. The cycle

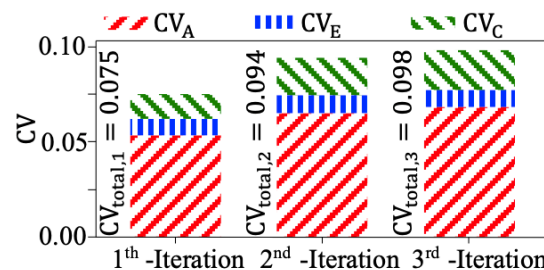
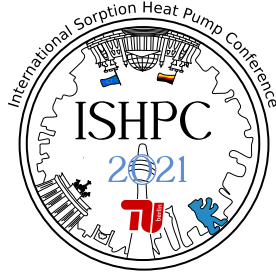


Figure 5 - Coefficient of Variation (CV, Eq. 7) of the adsorber (A), evaporator (E), and condenser (C) model for the three iterations of the presented parameter estimation approach (Fig. 2).

6. List of References

- [1] Weber, C., Mehling, F., Fregin, A., Daßler, I., Schossig, P. (2014): On standardizing solar cooling – field test in the small capacity range. *Energy Procedia*, vol.48, pp.1027–1035.
- [2] Gibelhaus, A., Tangkrachang, T., Bau, U., Seiler J., Bardow, A. (2019): Integrated design and control of full sorption chiller systems. *Energy*, vol.185, pp.409–422.
- [3] Franceschini, G., Macchietto S. (2008): Model-based design of experiments for parameter precision: State of the art. *Chemical Engineering Science*, vol.63, pp.4846–4872.
- [4] Institute of Technical Thermodynamics, RWTH Aachen University. (2018): SorpLib - adsorption energy systems library. URL: <https://git.rwth-aachen.de/lt/SorpLib>. [Accessed: 04 March 2020].
- [5] Lanzerath, F., Bau, U., Seiler J., Bardow, A. (2015): Optimal design of adsorption chillers based on a validated dynamic object-oriented model. *Science and Technology for the Built Environment*, vol. 21, pp.248-257.
- [6] Fortin, F., Rainville, F., Gardner, M., Parizeau, M., Gangne, C. (2012): Deap: Evolutionary algorithms made easy. *Journal of Machine Learning Research*, vol.13, pp.2171-2175.



SorpPropLib: An Open-Source Database for Sorption Equilibrium Properties

Engelpracht, Mirko⁺¹; Yang, Zhiyao^{+2,3}; Gluesenkamp, Kyle R.³; Turnaoglu, Tugba³; Seiler, Jan¹; Bardow, André^{*1,4,5}

¹ RWTH Aachen University, Aachen, Germany

² Purdue University, West Lafayette, IN, USA

³ Oak Ridge National Laboratory, Oak Ridge, TN, USA

⁴ Forschungszentrum Jülich, Jülich, Germany

⁵ ETH Zurich, Zürich, Switzerland

+Both authors contributed equally to this abstract

*Corresponding author: abardow@ethz.ch

Abstract:

Hundreds of sorption working pair equilibrium measurements have been reported in the literature, and many experimental results have been fitted to equilibrium equations. However, an open database does not exist for the equilibrium equations. Therefore, this work compiled 438 published equilibrium equations of sorption working pairs into an open-source database called SorpPropLib. SorpPropLib is accessible from six programming environments commonly used in sorption cycle simulation (C++, Excel®, Python®, Matlab®, Modelica® and LabVIEW™). Plotting capabilities allow fast cycle visualization in each programming environment. Thereby, the open-source database SorpPropLib aims to enable and encourage easy data sharing to advance sorption research.

1 Introduction

The application of sorption processes requires fundamental thermodynamic knowledge of working pairs, such as sorption capacities of a given material. To estimate the phase behavior beyond experiments, the phase equilibrium needs to be described by physically and statistically meaningful mathematical correlations. Today, the literature already reports an exhaustive amount of phase equilibrium measurement and modeling on various working pairs. Undoubtedly, it would be convenient and efficient to have an open-source database that collects the existing data of numerous working pairs. To date, a few studies have been published to compile the current equilibrium data [1-7]. However, the existing collections are either limited to a particular sorbate or sorbent, outdated, or only provided citations without actually presenting the equilibrium equations.

In this work, an open-source database, SorpPropLib, is built on the foundation of a large number of existing equilibrium data of working pairs. SorpPropLib generalizes the equilibrium equations while presenting 438 existing correlations in a user-friendly environment. For solid sorbents, equilibrium correlations are expressed in terms of six functional forms including Toth and Dubinin. For liquid sorbents, equilibrium correlations are expressed in terms of Antoine, Dühring, or one of nine equations of state-type functional forms.

2 Background and Fundamentals

To compile a highly accessible database, the various equations from the diverse sources in the literature need to be generalized. For example, a specific isotherm model such as Toth has a single original form. However, over time, various researchers have made their own tweaks to the form, resulting in a Toth “family” of forms with different numbers and locations of fitting constants. In this work, we have generalized each “family” so that all related data are expressed in one master “family” equation.

In addition, the sorbate or sorbent composition follows different conventions, depending on the field. In general, composition can be expressed as a fraction or ratio; on a sorbent or sorbate basis; and on a mass, molar, or volume basis. In this work, the composition of solid sorbents are presented in terms of mass ratio sorbate, denoted Y [$\text{kg}_{\text{sorbate}}/\text{kg}_{\text{sorbent}}$], and volumetric uptake, denoted y [$\text{m}^3_{\text{sorbate}}/\text{kg}_{\text{sorbent}}$]. Composition of liquid sorbents are presented in terms of mass fraction sorbent, denoted X [$\text{kg}_{\text{sorbent}}/\text{kg}_{\text{total}}$], and molar fraction, denoted x [$\text{mol}_{\text{sorbent}}/\text{mol}_{\text{tot}}$].

3 Results

3.1 General functionality

SorpPropLib offers common equilibrium functions often required for sorption system modeling and optimization. Besides the primary function of calculating equilibrium composition (e.g. Y or X) as a function of pressure

(p) and temperature (T) such as $Y(p, T)$ or $X(p, T)$, SorpPropLib provides inverse functions to obtain pressure as a function of temperature and composition such as $p(Y, T)$ or $p(X, T)$, or functions of partial derivatives such as $dp/dT(Y, T)$ or $dp/dT(X, T)$.

The general working principle of SorpPropLib (Fig. 1) consists of the following two main steps: (a) initialization of a working pair, and (b) calculation based on the initialized working pair.

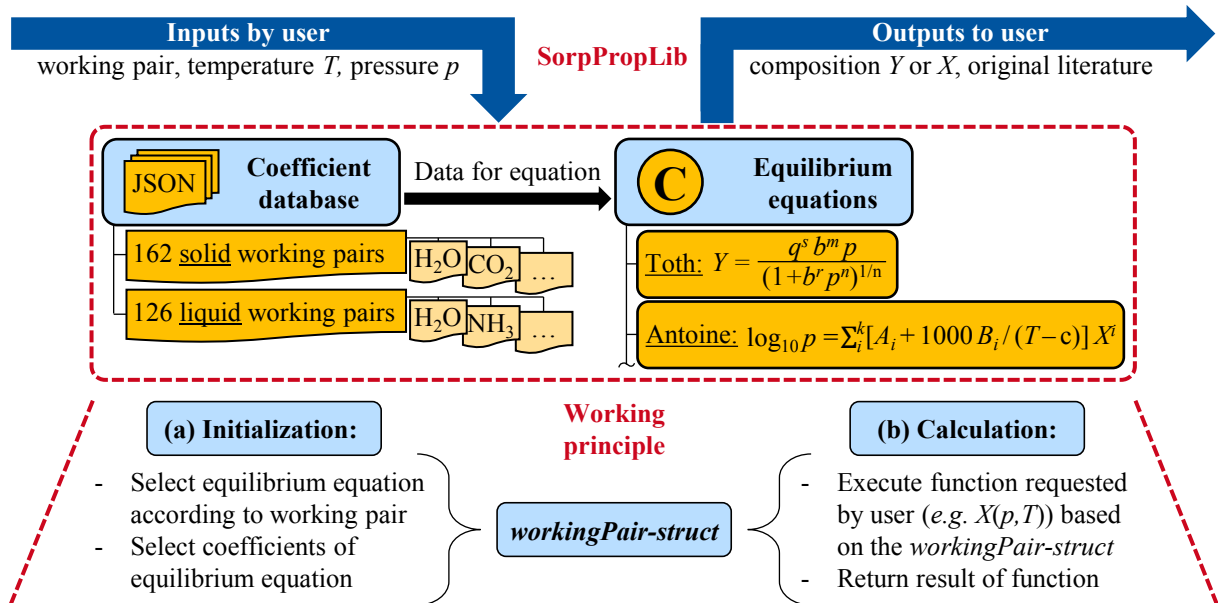


Figure 1 – Data flow and working principle of SorpPropLib showing the two main steps: (a) initialization and (b) calculation.

SorpPropLib currently offers 438 correlations for 288 working pairs and 39 refrigerants as listed in Tab. 1. In the first step (Fig. 1(a)), SorpPropLib initializes a working pair: Based on the user inputs, SorpPropLib selects the required equilibrium equation and its coefficients, which are saved as so-called *workingPair-struct* to computer memory. The equilibrium equations are implemented in the C programming language since it is a highly portable and fast programming language. The coefficients of equilibrium equations are saved into a JSON database as it is very flexible, compact, and fast compared to other databases such as XML.

For equilibrium composition calculations, some functional forms require supporting formulas for the pure sorbate or sorbent. For example, the pure sorbate saturation pressure is necessary for calculating equilibrium pressure based on Dubinin, activity coefficients, and mixing-rule based equilibrium equations. Therefore, SorpPropLib includes pure refrigerant Equations of State (EoS) for common refrigerants. Besides, SorpPropLib also offers the possibility for a user-defined sorbate EoS, which can be passed to equilibrium equations as an additional function argument.

In the second step (Fig. 1(b)), SorpPropLib calculates equilibrium properties such as pressure, temperature, or composition based on both, the *workingPair-struct* and the function (e.g. $Y(p, T)$) requested by the user.

Thus, SorpPropLib searches the equilibrium equation and its coefficients only during initialization. Once the searched data is saved to computer memory, it can be used for further calculations. This speeds the evaluation of equilibrium properties and enables to use SorpPropLib for dynamic simulations or optimizations requiring many property calls.

Table 1 – Working pairs included in SorpPropLib.

Category	Refrigerant	Sorbent Correlation count	Category	Refrigerant	Sorbent Correlation count
Inorganic	Water	33 46	Fluorocarbons	R-12	4 5
	Ammonia	41 76		R-13B1	1 1
	CO ₂	12 12		R-22	4 8
Hydrocarbons	Propane	7 12		R-23	1 1
	Methane	8 8		R-32	16 24
	Propylene	6 11		R-123	1 1

Category	Refrigerant	Sorbent Correlation count	Category	Refrigerant	Sorbent Correlation count
Hydrocarbons	Butane	2 2	Fluorocarbons	R-124	1 1
	Hexane	1 2		R-125	16 20
	Benzene	6 10		R-134a	27 43
	Toluene	1 2		R-143a	9 9
	Cyclohexane	5 9		R-152a	6 6
	Acetone	3 7		R-407C	1 1
	TFE	2 10		R-404A	1 1
	THF	2 2		R-410A	2 3
Alcohol	Ethanol	18 19	R-507A	3 3	
	Methanol	35 36	R-1234ze(E)	4 4	
	2-Propanol	2 6	Others	7 37	

3.2 Wrappers for common sorption programming environments

To expand the capability of SorpPropLib beyond the C programming language, SorpPropLib is linked as Dynamic Link Library (DLL) to the six programming environments shown in Fig. 2(a).

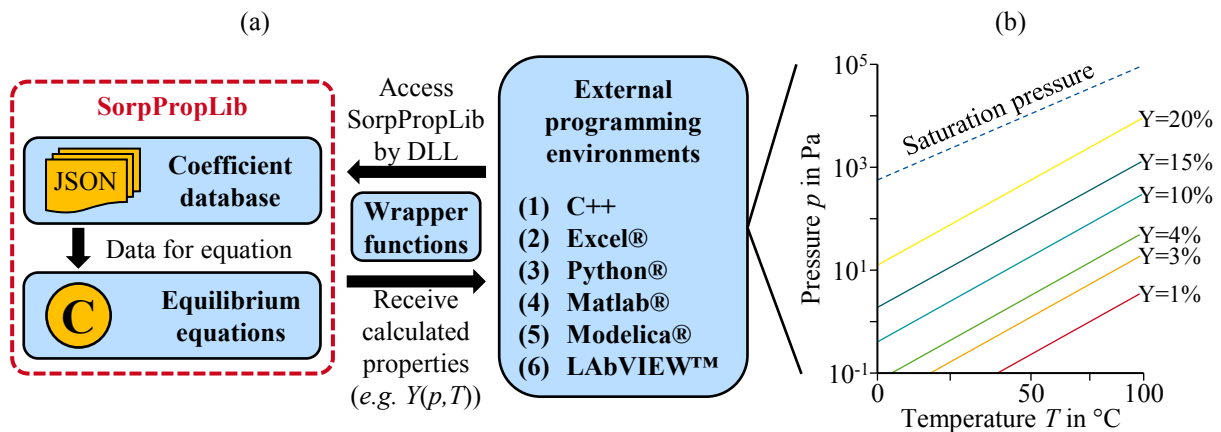


Figure 2 – a) Linking of SorpPropLib to other programming environments, and b) visualization capabilities.

Each programming environment requires corresponding wrapper functions to access functions provided by the DLL. In this work, two approaches are used for the wrapper functions: (1) direct function call, and (2) function call based on the *workingPair-struct*.

- (1) The direct function call approach requires only simple data types (*i.e.* char, int, and double) as function arguments and selects the equilibrium equation and its coefficients in every function call. Thus, this approach needs more computational time and is only suitable when calculating few data points. However, the direct function call approach is easy to implement into various programming environments and allows SorpPropLib to be easily linked to further programming environments than the six environments shown in Fig. 2(a) in future. Therefore, the direct function call approach was implemented in all six programming environments.
- (2) The approach based on the *workingPair-struct* requires complex data types (*e.g.* structures or pointers) as function arguments and selects the equilibrium equation and its coefficients only once during initialization. Thus, this approach is more challenging to implement into other programming environments since the complex data types often need to be mapped manually for each programming environment to ensure the alignment of computer memory. However, the structure-based approach is numerically very efficient and particularly favorable for multiple function calls, as is the case for dynamic modeling and optimization. Therefore, the structure-based approach is being implemented in all programming environments except for Excel®.

3.3 Visualization capabilities

Besides equilibrium property calculation, a visual representation of calculated properties is often desirable, especially when analyzing sorption cycles. For the visual representation of cycle analysis, a Clapeyron or Dühring diagram ((Fig. 2(b)) is implemented for all six programming environments. The Clapeyron diagram shows the

logarithmic pressure versus the negative reciprocal sorbent temperature, whereas the Dühring diagram shows the saturation temperature of the refrigerant versus the sorbent temperature. For both diagrams, the bounds of the chart axis can be changed. Furthermore, the type (*e.g.* mass fraction or ratio), number, and values of the isosteres can be adjusted. In addition to the Clapeyron and Dühring diagrams, the isotherm and isobar diagrams are implemented for all sorbents, and the characteristic curve of the Dubinin model is implemented for solid sorbents. Hence, the equilibrium properties of working pairs can be easily visualized in standard diagrams and compared. Moreover, sorption cycles can be rapidly visualized. Thereby, SorpPropLib facilitates the analysis and improvement of sorption systems.

4 Conclusions

In this work, 438 published equilibrium equations of sorption working pairs were embedded into a single open-source database called SorpPropLib. While SorpPropLib was written in the C programming language, it also works with six commonly used programming environments: C++, Excel®, Python®, Matlab®, Modelica®, and LabVIEW™. Thereby, SorpPropLib can be integrated with existing cycle simulation models programmed in those environments. The plotting capabilities of SorpPropLib allow fast cycle visualization. Besides, SorpPropLib is an open-source project and intended to increase open collaboration in the sorption community.

SorpPropLib is currently under development for inclusion of transport properties and experimental data and shall be updated with new working pairs in the future. Other desirable future additions are information about correlation accuracy and valid ranges. With new wrapper functions, SorpPropLib can also be expanded to other program platforms such as Fortran® or Java™.

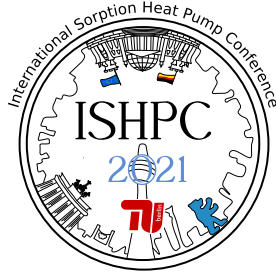
5 Acknowledgment

This material is partially based on work supported by the U. S. Department of Energy's Building Technologies Office under Contract No. DE-AC05-00OR22725 with UT-Battelle, LLC. The authors would also like to acknowledge Mr. Antonio Bouza, Technology Manager – HVAC&R, Water Heating, and Appliance, U.S. Department of Energy Building Technologies Office.

This manuscript has been authored by UT-Battelle, LLC under Contract No. DE-AC05-00OR22725 with the U.S. Department of Energy. The United States Government retains and the publisher, by accepting the article for publication, acknowledges that the United States Government retains a non-exclusive, paid-up, irrevocable, worldwide license to publish or reproduce the published form of this manuscript, or allow others to do so, for United States Government purposes. The Department of Energy will provide public access to these results of federally sponsored research in accordance with the DOE Public Access Plan (<http://energy.gov/downloads/doe-public-access-plan>).

6 List of References

- [1] Boman, D.B., Hoysall, D.C., Staedter, M.A., Goyal, A., Ponkala, M.J., Garimella, S. (2017): A method for comparison of absorption heat pump working pairs. *Int. J. Refrig.*, vol.77, pp.149-175.
- [2] Boman, D.B., Hoysall, D.C., Pahinkar, D.G., Ponkala, M.J., Garimella, S. (2017): Screening of working pairs for adsorption heat pumps based on thermodynamic and transport characteristics. *Appl. Therm. Eng.*, vol.123, pp.422-434.
- [3] Hassan, H., Mohamad, A., Alyousef, Y., Al-Ansary, H. (2015): A review on the equations of state for the working pairs used in adsorption cooling systems. *Renew. Sust. Energ. Rev.*, vol.45, pp.600-609.
- [4] Tamainot-Telto, Z., Metcalf, S.J., Critoph, R.E., Zhong, Y., Thorpe, R. (2009): Carbon–ammonia pairs for adsorption refrigeration applications: ice making, air conditioning and heat pumping. *Int. J. Refrig.*, vol.32, pp.1212-1229.
- [5] Macriss, R., Zawacki, T. (1989;1990): Absorption fluids data survey: 1989 update. NASA STI/Recon Technical Report.
- [6] Macriss, R.A., Gutraj, J., Zawacki, T. (1988): Absorption fluids data survey: final report on worldwide data. Oak Ridge National Lab., TN (USA); Institute of Gas Technology, Chicago, IL (USA).
- [7] Cisternas, L.A., Lam, E.J. (1991): An analytic correlation for the vapour pressure of aqueous and non-aqueous solutions of single and mixed electrolytes. Part II. Application and extension. *Fluid Phase Equilib.*, vol.62, pp.11-27.



Experimental study on diffusion absorption refrigeration cycle with a low GWP refrigerant-R1234ze(E)

Hyung won, Choi¹, Gahyeong, Kim¹, Gawon, Lee¹, JangSeok, Lee², Yong Tae, Kang^{1*}

¹ School of Mechanical Engineering, Korea University

145 Anam-ro, Seongbuk-gu, Seoul, 02841, Republic of Korea, chw000186@korea.ac.kr

(School of Mechanical Engineering, Korea University

145 Anam-ro, Seongbuk-gu, Seoul, 02841, Republic of Korea, ytkang@korea.ac.kr)

² L&A Center, LG Electronics Inc.,

Seoul, 08592, Republic of Korea, jang.lee@lge.com

Abstract:

A diffusion absorption refrigeration cycle (DAR) is purely driven by thermal energy directed to the bubble pump without the mechanical moving part. The performance of the DAR cycle is considerably influenced by the efficiency of the bubble pump. In this study, the experimental evaluations were conducted to figure out the impact of the configuration of the bubble pump on the performance of the DAR cycle. The number of the pump tubes and heat input were changed while measuring the evaporation temperature of the DAR. In addition, as the global warming becomes the serious problem, the low global warming potential (GWP) refrigerants are selected as an alternative. Following this trend, the low GWP refrigerant was employed in this study. R1234ze(E), which is included in HFO series, was used as refrigerant and DMAC was used as an absorbent. Electrical heaters were used to provide the input power, which was varied from 50W to 120W. Pressure value was determined by the saturation temperature of R1234ze(E) at around 30°C, which is estimated at 6.0bar. The lowest evaporation temperature was estimated at -10.2°C at 70W with the two pump tubes with the diameter of 4.76mm.

1 Introduction

A diffusion absorption refrigeration cycle employs the bubble pump to circulate the working fluid instead of the compressor. The bubble pump uses only the thermal energy, so it doesn't demonstrate vibration and noise. However, the DAR has a low Coefficient of Performance (COP). By this reason, many researches have been conducted to enhance the COP of the DAR. Zohar et al. [1] reported that the COP increased by using a partially attached bubble pump, which allows the heat transfer into the rich solution directly from the bubble pump tube. The two phase flow pattern in the bubble pump plays an important role in improving the efficiency of the bubble pump. White et al. [2] reported that it was the slug flow that the most advantageous flow pattern for enhancing the COP for the DAR. Yilidiz et al. [3] analyzed the impact of the insulation on the exergy and energy performances of the DAR. They announced that the COP increased to 21% - 26% by insulating the solution heat exchanger and the rectifier.

Moreover, many researches have been conducted to substitute the conventional working fluids pair, ammonia and water. Zohar et al. [4] simulated the DAR cycle by using the five different refrigerants, such as R23, R22, R124, R134a and R32 with DMAC as an absorbent to compare with the ammonia/water pair. Wang et al. [5] numerically investigated the DAR cycle with binary refrigerant, which consists of R22 and R134a, and DMF as an absorbent. Although many kinds of working fluid pairs were investigated for the DAR applications, these couldn't relieve the environmental problems.

As the global warming becomes the significant problems in the world, the low global warming potential (GWP) refrigerants and the natural refrigerants are considered as the alternatives. In this study, experimental investigation focuses on the operation of the low GWP refrigerants and the natural refrigerants for the DAR applications. R1234ze(E) was used as refrigerant with N,N-dimethylacetamide(DMAC) as an absorbent. Helium is used as an auxiliary gas. The experiments were conducted by focusing on the changes in the evaporation temperature according to the number of the tubes in the bubble pump.

2 Experiment

2.1 Experimental setup and procedure

Fig. 1. represents the schematic diagram of the DAR cycle. The bubble pump, which is insulated, is placed at the right side, and the thermal energy is supplied to generate the vapor of the refrigerant (1). The condenser is at the top side in which the refrigerant vapor is transformed into the liquid state and enters the evaporator (2). After the absorbing process in the absorber, the rest of the gas, which consists of the auxiliary gas and unabsorbed refrigerant enters the evaporator passing through the gas heat exchanger (GHX) (3). The evaporator pressure is charged with the auxiliary gas so that the refrigerant can be easily vaporized because of the low partial pressure in the evaporator, and then the gas mixture flows into the reservoir (4). When some portion of the refrigerant is separated from the absorbent in the bubble pump, the solution is called weak solution (7). The weak solution flows into the solution heat exchanger (SHX), and the heat transfer occurs between weak solution and strong solution in the SHX. After the heat transfer, the weak solution rises to the absorber top side (8) by the potential energy. This weak solution passes through the absorber by the gravity force, absorbing the refrigerant gas flowing upward from the reservoir. As the absorption process is progressing, the weak solution becomes the strong solution and it drops into the reservoir (9). The strong solution is provided into the SHX (5,6) and starts the process (1) repeatedly. The experiments were conducted as follows.

- (1) Mix the refrigerant and the absorbent with a given concentration.
- (2) Make the vacuum state for the experimental setup with the vacuum pump.
- (3) Inject the working fluid and the helium gas into the experimental setup until the pressure reaches a given pressure.
- (4) Supply the heat energy into the bubble pump with the electrical heater.
- (5) Measure the temperature of the DAR cycle components with the thermo couples.

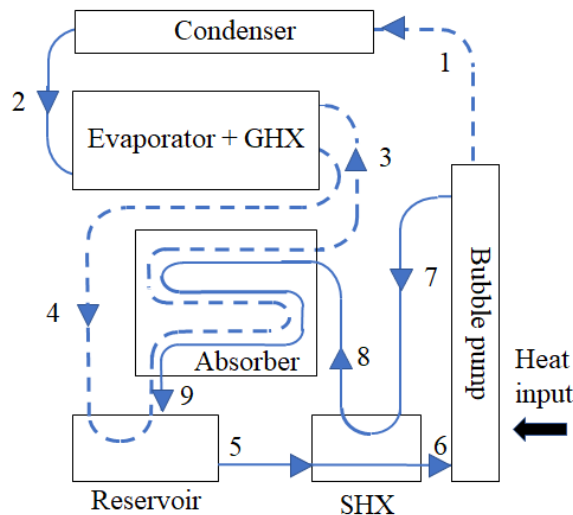


Figure 1-Schematic diagram of the DAR cycle.

2.2 The number of the bubble pumps

To investigate the effect of the number of the bubble pump tubes on the performance of the DAR cycle, experimental investigations were conducted by varying the number of the bubble pump tubes while fixing other conditions. The charge pressure of the DAR cycle was 6.0bar, and the concentration of the working fluid was 35wt%. All the diameters of the bubble pump were the same at 4.7625mm. For each case, bubble pump was changed to a new one with different number of the bubble pump tubes, while other components remained same.

Table 1-. Experimental condition for different number of the pumps.

Number of pumps	Charge pressure [bar]	Concentration [%]	Diameter of pump [mm]	Heat input [W]
1	6.0	35	4.7625	50, 70
2	6.0	35	4.7625	50, 70, 100
3	6.0	35	4.7625	100, 110, 120
4	6.0	35	4.7625	100, 110, 120

3 Results and discussion

The experimental results with respect to the evaporation temperature procured by changing the number of the bubble pump tubes were investigated. The evaporation temperature was measured at the steady state by increasing the number of the bubble pump tubes with the diameter of 4.7625mm. Fig. 2 shows the results for the evaporation temperature of the DAR cycle according to the number of the pump tubes

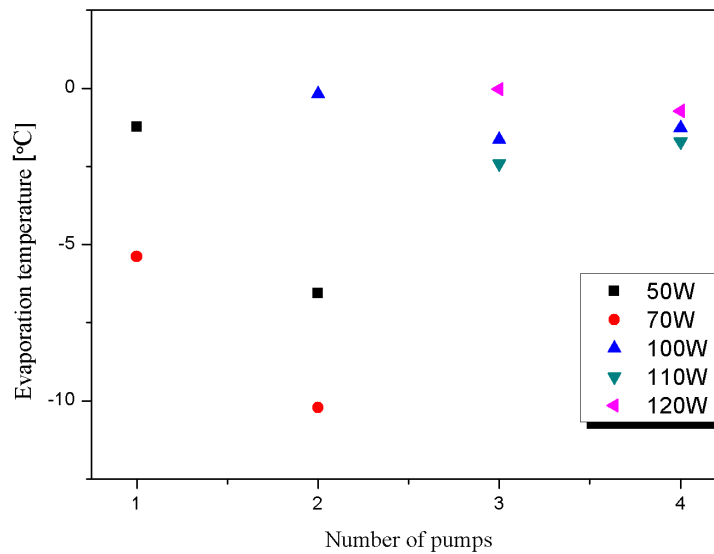


Figure 2– Evaporation temperature variations according to the number of bubble pumps.

It turns out that the evaporation temperature decreases initially as the number of the tube increases from 1 to 2. The minimum temperature is -10.22°C at two bubble pump tubes with 70W heat input. However, when the number of tubes becomes larger than 3, the evaporation temperature begins to rise. The minimum evaporation temperature at each number of pumps are summarized in Table 2. It is found that the minimum heat input to achieve the minimum evaporation temperature increases as the number of the pumps increases. Moreover, the evaporation temperature increases if the heat input becomes larger than the optimum heat input for all the cases of the number of pumps. It seems that when the number of tubes is changed from 1 to 2, the increased mass flow rate of the refrigerant entering the evaporator makes the evaporation temperature decrease. When the number of the tubes is more than 3, because of the limited ability of the absorber, the increased refrigerant isn't absorbed enough by the absorber. This leads to redundant unabsorbed refrigerant passing through the GHX into the evaporator and makes the partial pressure of the refrigerant increase so that the evaporation temperature increases.

Table 2 – The minimum evaporation temperature at given number of bubble pumps and heat input.

Number of bubble pumps	Minimum evaporation temperature [$^{\circ}\text{C}$]	Heat input [W]
1	-5.38	70
2	-10.22	70
3	-2.42	110
4	-1.71	110

4 Conclusions

In this study, the evaporation temperatures of the DAR cycle using R1234ze(E) and DMAC were measured according to the number of the bubble pump tubes and the heat input. The number of the tubes in the bubble pump were varied from 1 to 4. The heat input ranged from 50W to 120W. The following conclusions were drawn from the present study.

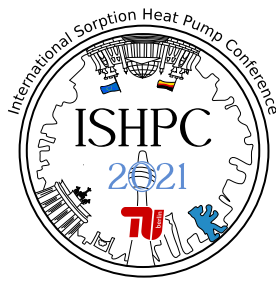
- For the bubble pump with 2 tubes, the evaporation temperature becomes the lowest at the estimated value of -10.22°C with 70W heat input.
- If the number of the bubble pump tubes is more than 3, the increased generated refrigerant is not sufficiently absorbed in the absorber so that the residual refrigerant makes the higher partial pressure in the evaporator. This is the reason why the higher evaporation temperatures are achieved at the tubes with 3 and 4 than 1 and 2.
- It is found that the evaporation temperature decreases when the heat input is increased and after the optimum heat input, the evaporation temperature increases with increasing the heat input. Therefore, to achieve the best performance of the DAR cycle, it is important to set the optimum number of the bubble pump tubes and the amount of heat input.

5 Acknowledgment

This work was supported by Korea Institute of Energy Technology Evaluation and Planning (KETEP) grant funded by the Korea government (MOTIE) (No. 10060218, The development of cooling capacity 200RT class triple effect gas fired absorption chiller). It was also supported by LG Electronics Inc.

6 List of References

- [1] Zohar, A., Jeluinek, M., Levy, A., Borde, I. The influence of the generator and bubble pump configuration on the performance of diffusion absorption refrigeration (DAR) system. *International Journal of Refrigeration* 2008; 31:962-969.
- [2] S.J. White, Bubble pump design and performance, School of Mechanical Engineering, Georgia Institute of Technology, 2001.
- [3] A. Yildiz, M.A. Ersöz, B. Gözmen, Effect of insulation on the energy and exergy performances in Diffusion Absorption Refrigeration (DAR) systems, *International Journal of Refrigeration*, 44 (2014) 161-167.
- [4] Zohar, A., Jelinek, M., Levy, A., Borde, I. Performance of diffusion absorption refrigeration cycle with organic working fluids. *International Journal of Refrigeration* 2009; 32:1241-1246.
- [5] Wang, Q., Gong, L., Wang, J.P., K. Cui, Sun, Chen, G.M. A numerical investigation of a diffusion absorption refrigerator operating with the binary refrigerant for low temperature applications. *Applied Thermal Engineering* 2011; 31:1763-1769.



Modelling ammonia (re-)sorption cycles: An abridged literature review and introduction to an ammonia-salt MATLAB[®] model for use in (re-)sorption heat pumping

Atkinson, G.H.^{1*}, Critoph, R.E.¹ and Hinners, S.¹

¹ The University of Warwick, School of Engineering, Library Road, Coventry, CV4 7AL, UK

* George.H.Atkinson@warwick.ac.uk

1. Introduction

Ammonia sorption cycles can be used in gas-fired heat pumps and offer potential in reducing CO₂ emissions associated with domestic heating. Interest in sorption heat pumps in the UK is related to the commitment by the UK government to 'net zero' by 2050 [1], with the decarbonisation of heat key to achieving emissions targets.

Research at The University of Warwick (Warwick) over recent decades, has focused on the reversible sorption reactions of ammonia (NH₃) as an adsorbate, with applications including waste heat transformation [2, 3], refrigeration [4] and heat pumping (for domestic applications) [5, 6]. Previous work at Warwick has focused on ammonia-carbon physical sorption, although work over recent years has been with ammonia and salts in chemical sorption. The work presented herein focuses on chemical sorption reactions for heat pumping applications.

2. Background and Review of Model Development

2.1. Adsorbate Selection

A good place to start the review of ammonia-salt sorption reactions and their application in heat pumping, is with the adsorbate itself - why ammonia? Amongst others, the desirable characteristics of an adsorbate (refrigerant) are to have: high heats of reaction compared to sensible heating of the adsorbent; thermal stability; environmental harmlessness; and ideally be non-toxic. Work at Warwick has considered water, methanol and ammonia as potential candidates. Specifically, work by Critoph [6] discusses the merits of a series of adsorbates, concluding that methanol and ammonia are strong contenders for heat pumping and refrigeration applications. Ammonia has no ozone depletion potential, no global warming potential and although is toxic, when considering pressure and instability of methanol (above 120 °C), ammonia is determined to have the best potential.

2.2. Historical Experimental Work

In relation to experimental sorption reactions, Hosatte et al. [7] identify that the low heat loss and temperature uplift capabilities of solid-gas reactions (potentially over a wide-temperature range) allow applications to be wide ranging. Worsøe Schmidt [8] also shows the simplicity and reliability of a 'solid-absorption' (adsorption) cycle of ammonia-calcium chloride for solar refrigeration. The advantage of a simple resorption system is also explained, in that the heats of reaction for the 'two steps of reaction ($\text{CaCl}_2 \cdot 8/4\text{NH}_3$ and $\text{CaCl}_2 \cdot 4/2\text{NH}_3$) are almost twice the latent heat of vaporisation.'

With regards salt pairing selection, Neveu and Castaing [9] evaluated the reaction enthalpies and entropies of chloride salts reacting with ammonia, providing a thorough and tabulated appendix to their paper. The tabulated data is valuable in selecting salt combinations for specific applications. The paper begins to review the benefits of a resorption cycle and references a paper by Goetz, Elie and Spinner [10], also useful in understanding initial developments. Both papers recognise that operating two solid-gas reactor beds out of phase with one another will yield 'almost' continuous heating/cooling.

There is a vast number of enthalpy and entropy values for ammonia-salt reactions compiled in work by Touzain [11] and a more recent publication by Donkers et al. [12], which, coupled with the work by Neveu and Castaing [9] and the Clapeyron equation, (2), theoretically enable any salt couple to be evaluated.

Vasiliev et al. [13] apply this knowledge to a barium chloride (as the High Temperature Salt (HTS)) and nickel chloride (as the Low Temperature Salt (LTS)) pair. A conductive carbon fibre (fabric) is used as the host matrix to produce a resorption 'heat pump' in a four reactor configuration, for specific delivery of high temperature heat (steam at $T = 120\text{-}130$ °C) and chilled water ($T = 3\text{-}5$ °C). The stated Coefficient of Performance (COP) is 1.2, although with proposed heat/mass recovery this is posed to be in the region 1.4-1.5.

Trudel, Hosatte and Ternan [14] discuss the development of an ammonia-cobalt chloride chemical heat pump and the hysteresis behaviour exhibited in a number of previous published works. Within the paper the explanations put forward to address hysteresis are first the swelling of the crystal lattice structure as the content of ammonia changes and second is related to the difference in temperature between the gas and solid phases. Alongside hysteresis, Gordeeva and Aristov [15] specifically look at the intricacies for targeted design of composite ‘salts inside porous matrix’ (CSPMs) where the importance of the synthesis method, salt content, and matrix pore size are discussed. The work is a valuable resource when considering the production of CSPMs for heat pumping.

In short, experimental work on ammonia-salt (re-)sorption systems has been promising and significant work has already been invested in characterising salt behaviour (equilibrium lines), understanding hysteresis and the identification that salt swelling, agglomeration and low conductivity in the reactor bed, are all challenges required to be addressed when designing a chemical heat pump.

2.3. Modelling

As research continued at a pace in the early to mid-1990s, work focused on the applications of ammonia-salt reactions, with significant modelling of the behaviour of the reactions taking place. Lebrun and Spinner [16] discuss the two operating modes of a solid-gas reaction, either in a ‘heat pump’ or ‘thermotransformer’ operation, and explain the requirement to understand the heat and mass transfer inside the porous reacting medium. (In the research at Warwick, this constitutes salt impregnated in an Expanded Natural Graphite (ENG) matrix). In relation to modelling of the reactions, Lebrun and Spinner reference a number of analytical models, but relevant to the application at Warwick is the general equation, (1), for the rate of reaction, v .

$$v = \frac{dx}{dt} = f(x) \cdot k_0 \cdot e^{\left(\frac{-E}{T}\right)} \cdot \ln\left(\frac{P}{P_e(T)}\right) \quad (1)$$

where: v = reaction rate, s^{-1} ; x = degree of reaction advancement; k_0 = specific rate of reaction, s^{-1} , $f(P, T)$; E = pseudo energy for activation, K^{-1} ; T = temperature, K ; P = pressure, bar; $P_e(T)$ = equilibrium pressure, bar, calculated from the Clapeyron equation (2);

$$\ln(P_e) = \frac{-\Delta H}{R_0 \cdot T} + \frac{\Delta S}{R_0} \quad (2)$$

where: ΔH = reaction enthalpy change, $J \cdot mol^{-1}$; ΔS = reaction entropy change, $J \cdot mol^{-1} \cdot K^{-1}$ R_0 = universal gas constant, $J \cdot mol^{-1} \cdot K^{-1}$ and finally, in (1), $f(x)$ in the model, describes the reaction kinetics by introducing a ‘pseudo-constant for the order of the reaction by analogy to reactions in a homogenous medium’ [16], formulating in the equation, (3).

$$\frac{dX}{dt} = (1 - X)^n \cdot C \cdot e^{\left(\frac{-E}{T}\right)} \cdot \ln\left(\frac{P}{P_e(T)}\right) \quad (3)$$

where: X = degree of advancement; n = reaction order; and C = kinetic coefficient, s^{-1} . Mazet, Amouroux and Spinner [17] construct a similar model for salts in porous media, however, the exponential term is assumed constant, and the natural log driving pressure term is simplified; (4) shows the simplification.

$$\frac{dX}{dt} = (1 - X)^n \cdot Ar \cdot \left(\frac{P - P_e(T)}{P}\right) \quad (4)$$

where: Ar = Arrhenius term, determined to be approximately constant throughout the reaction [17]. Note that Lebrun and Spinner [16] convert the function $f(x)$ to $f(X, Y)$, to take account of the consecutive nature of two stage salt reactions, for example the decomposition stages of calcium chloride and ammonia, $CaCl_2 \cdot 8/4NH_3$ followed by $CaCl_2 \cdot 4/2NH_3$, where X is the conversion (or advancement) of the first reaction and Y the conversion of the second. For simplicity only the first reaction equation has been summarised.

Goetz and Marty [18] discuss an unreacted-core model for ammonia-manganese chloride reactions, using an inert graphite binder. The paper presents the equilibrium lines and shows the pseudo-equilibrium region where the reaction rate is zero, referencing an earlier German paper by Furrer [19].

Lepinasse, Goetz and Crozat [20] go further and present a thermochemical transformer based on the coupling of two solid-gas reactions, referencing Goetz, Elie and Spinner [10]. Both papers present the coupling of the salt reactions, whereby the working pressure is linked to the coupling of the two reaction rates, encompassing reaction kinetics alongside heat and mass transfer. Goetz et al. also present the idea of four reactors filled with three

different salts, to provide pseudo-continuous cooling, termed a double-effect resorption machine, although the application can be considered for heat pumping.

Further modelling work has been conducted by a number of other sources and although some are listed [21-24], the reference list is by no means exhaustive.

3. Sorption at Warwick

Interest in the reversible reactions of halide-salts with ammonia, has developed at Warwick because of the higher adsorption quantities (up to $1 \text{ kg}\cdot\text{kg}^{-1}$) compared to physical sorption reactions (ammonia-carbon work at Warwick [25]) and working pressures greater than atmospheric pressure, important for good mass transfer [26]. At present a finite element model is being developed to simulate the resorption reaction in a two-reactor configuration, between a HTS and LTS.

The model will build on work conducted by: Hinners and Critoph [2], in modelling the ammoniation of barium chloride for waste heat transformations; Mazet, Amouroux and Spinner [17] and Lebrun and Spinner [16], in the development of the reaction (kinetic) models; Rivero-Pacho, Critoph and Metcalf [25], in developing a finite element model for physical sorption; and Lepinasse, Goetz and Crozat [20] in coupling two solid-gas reactions. The model, developed in MATLAB[®], will simulate a two-reactor (re-)sorption heat pump, for the proposed salt pairing of barium and calcium chloride. The salts have been selected for the range of driving temperatures and pressures considered, with the low temperature range $5 \text{ }^\circ\text{C} - 30 \text{ }^\circ\text{C}$ and high temperature range $150 \text{ }^\circ\text{C} - 200+ \text{ }^\circ\text{C}$ for an operating pressure in the region of 7-8 bar. The model is based on the same geometry used by Hinners and Critoph [2] in their LTJ experiments, **Figure 1**.

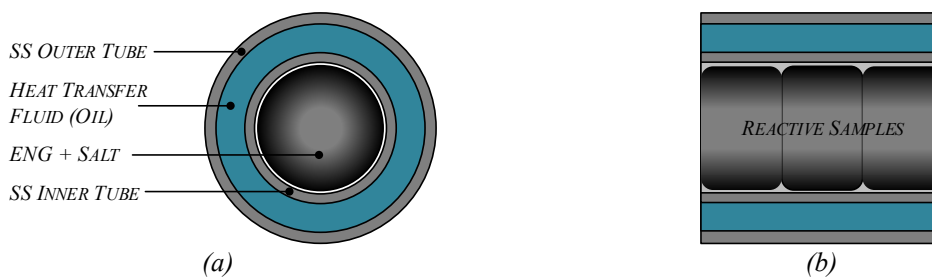


Figure 1: (a) Cross-sectional view of the LTJ geometry and (b) an axial view, showing a series of stacked samples.

Within the proposed MATLAB[®] model, the geometry is discretised axially and radially, **Figure 2**, similar to work by Rivero-Pacho et al. [25]. Each reactive element is considered to be a lumped parameter with temperature, pressure, concentration and heat flow in/out, from which an enthalpy flow is generated from the reaction model.

An equal pressure rise in a small timestep is assumed in the reactive (ENG) elements; knowing the heat flow in addition to the kinetic behaviour, the temperature and mass of the ad/desorbed ammonia can be calculated. With a fixed mass of ammonia in the simulated system, the pressure rise can be iteratively calculated, thus providing the conditions for the next time step.

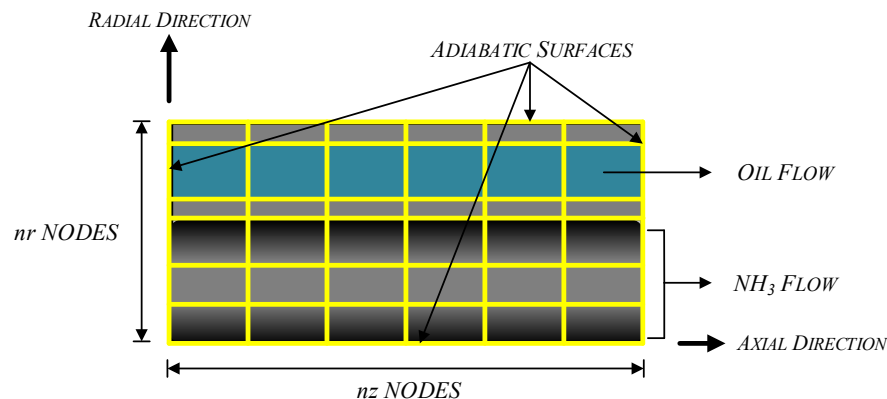


Figure 2: Discretised (half) axial view of the reactor geometry to enable a finite element model to be developed in MATLAB[®]. Each control volume shown (bounded by the yellow boxes) can be considered to have a temperature, pressure and concentration for the model.

The reaction kinetics aspect of the model is based on an adaptation of the work by Mazet, Amouroux and Spinner [17] and Lebrun and Spinner [16], which is summarised in equations (2) and (4), and used to describe the rate of the reaction.

Work to-date has involved developing the model presented in [2] to account for the coupled nature of the two-reactor (two-salt) system and designing a new Large Temperature Jump (LTJ) rig to conduct the experimental validation. Laboratory scale experiments will follow, validating the heat and mass transfer predicted. Further work will then look to optimise the unit-cell reactor designs, before looking ahead in preparation of building a small-scale resorption heat pump.

4. Conclusions

To conclude, both experimental and modelling published works with ammonia-salt systems have been summarised and significant contributions to the research area from a number of prominent sources have been introduced in an abridged literature review. Utilising previous modelling work at Warwick, alongside literature studied, a sorption heat pump MATLAB® model is to be developed to be able to predict the performance of a resorption reaction between a HTS and LTS in a two-reactor heat pumping configuration. Additionally, further work beyond this paper will look to validate the simulations through large temperature jump experiments, before designing a proof-of-concept resorption heat pump.

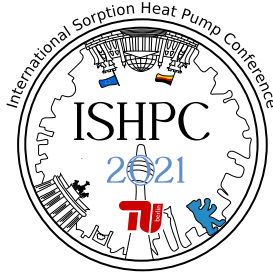
5. Acknowledgements

The work is funded by EPSRC and many thanks go to Robert Critoph, Samuel Hinners and Charles Joyce for their advice and guidance.

6. List of References

- [1] (2018). *Clean Growth: transforming heat - overview of current evidence*. [Online] Available: <https://www.gov.uk/government/publications/heat-decarbonisation-overview-of-current-evidence-base>
- [2] S. Hinners and R. E. Critoph, "Modelling the Ammoniation of Barium Chloride for Chemical Heat Transformations," *Energies*, vol. 12, no. 23, 2019, doi: 10.3390/en12234404.
- [3] J. Locke *et al.*, "Investigation into NH₃-MgCl₂ and NH₃-CaCl₂ reaction rates for the development of a thermal transformer," Coventry, UK, 2018: The University of Warwick.
- [4] Z. Tamainot-Telto, S. J. Metcalf, R. E. Critoph, Y. Zhong, and R. Thorpe, "Carbon-ammonia pairs for adsorption refrigeration applications: ice making, air conditioning and heat pumping," *International Journal of Refrigeration*, vol. 32, no. 6, pp. 1212-1229, 2009, doi: 10.1016/j.ijrefrig.2009.01.008.
- [5] S. J. Metcalf, R. E. Critoph, and Z. Tamainot-Telto, "Optimal cycle selection in carbon-ammonia adsorption cycles," *International Journal of Refrigeration*, vol. 35, no. 3, pp. 571-580, 2012, doi: 10.1016/j.ijrefrig.2011.11.006.
- [6] R. E. Critoph, "Activated carbon adsorption cycles for refrigeration and heat pumping," *Carbon*, vol. 27, no. 1, pp. 63-70, 1989.
- [7] S. Hosatte, F. Rheault, L. Pelletier, and B. Spinner, "A chemical heat pump material characterisation method," in *Biennial Congress on the International Solar Energy Society*, Hamburg, 13th -18th September 1987, in *Advances in Solar Energy Technology*, pp. 2971-2975.
- [8] P. Worsøe-Schmidt, "Solar refrigeration for developing countries using a solid-absorption cycle," *International Journal of Ambient Energy*, vol. 4, no. 3, pp. 115-124, 1983, doi: 10.1080/01430750.1983.9675877.
- [9] P. Neveu and J. Castaing, "Solid-gas chemical heat pumps: Field of application and performance of the internal heat of reaction recovery process," *Heat Recovery Systems & CHP*, vol. 13, no. 3, pp. 233-251, 1993.
- [10] V. Goetz, F. Elie, and B. Spinner, "The structure and performance of single effect solid-gas chemical heat pumps," *Heat Recovery Systems & CHP*, vol. 13, no. 1, pp. 79-96, 1993.
- [11] P. Touzain, "Thermodynamic values of ammonia salt reactions for chemical sorption heat pumps," in *International Sorption Heat Pump Conference*, Munich, Germany, 24-26th March 1999, pp. 225-238.
- [12] P. A. J. Donkers, L. Pel, M. Steiger, and O. C. G. Adan, "Deammoniation and ammoniation processes with ammonia complexes," *AIMS Energy*, vol. 4, no. 6, pp. 936-950, 2016, doi: 10.3934/energy.2016.6.936.
- [13] L. L. Vasiliev, D. A. Mishkinis, A. A. Antukh, A. G. Kulakov, and L. L. Vasiliev, "Resorption heat pump," *Applied Thermal Engineering*, vol. 24, no. 13, pp. 1893-1903, 2004, doi: 10.1016/j.applthermaleng.2003.12.018.

- [14] J. Trudel, S. Hosatte, and M. Ternan, "Solid-gas equilibrium in chemical heat pumps: the $\text{NH}_3\text{-CoCl}_2$ system," *Applied Thermal Engineering*, vol. 19, pp. 495-511, 1999.
- [15] L. G. Gordeeva and Y. I. Aristov, "Composites 'salt inside porous matrix' for adsorption heat transformations: a current state-of-the-art and new trends," *International Journal of Low-Carbon Technologies*, vol. 7, pp. 288-302, 2012, doi: 10.1093/ijlct/cts050.
- [16] M. Lebrun and B. Spinner, "Models of heat and mass transfers in solid-gas reactors used as chemical heat pumps," *Chemical Engineering Science*, vol. 45, no. 7, pp. 1743-1753, 1990.
- [17] N. Mazet, M. Amouroux, and B. Spinner, "Analysis and experimental study of the transformation of a non-isothermal solid/gas reacting medium," *Chemical Engineering Communications*, vol. 99, no. 1, pp. 155-174, 1991, doi: 10.1080/00986449108911585.
- [18] V. Goetz and A. Marty, "A model for reversible solid-gas reactions submitted to temperature and pressure constraints: Simulations of the rate of reaction in solid-gas reactor used as chemical heat pump," *Chemical Engineering Science*, vol. 47, no. 17/18, pp. 4445-4454, 1992.
- [19] M. Furrer, "Thermoanalytical study of selected complexes of inorganic chlorides with ammonia and ammonia derivatives," Switzerland, 1980. Accessed: 22nd March 2020. [Online]. Available: http://inis.iaea.org/search/search.aspx?orig_q=RN:13652849
- [20] E. Lepinasse, V. Goetz, and G. Crozat, "Modelling and experimental investigation of a new type of thermochemical transformer based on the coupling of two solid-gas reactions," *Chemical Engineering and Processing*, vol. 33, pp. 125-134, 1994.
- [21] H.-B. Lu, N. Mazet, and B. Spinner, "Modelling of gas-solid reaction - Coupling of heat and mass transfer with chemical reaction," *Chemical Engineering Science*, vol. 51, no. 15, pp. 3829-3845, 1996.
- [22] N. Mazet and H.-B. Lu, "Improving the performance of the reactor under unfavourable operating conditions of low pressure," *Applied Thermal Engineering*, vol. 18, pp. 819-835, 1998.
- [23] D. Stitou, V. Goetz, and B. Spinner, "A new analytical model for solid-gas thermochemical reactors based on thermophysical properties of the reactive medium," *Chemical Engineering and Processing*, vol. 36, pp. 29-43, 1997.
- [24] V. Goetz, B. Spinner, and E. Lepinasse, "A solid-gas thermochemical cooling system using BaCl_2 and NiCl_2 ," *Energy*, vol. 22, no. 1, pp. 49-58, 1997.
- [25] A. M. Rivero-Pacho, R. E. Critoph, and S. J. Metcalf, "Modelling and development of a generator for a domestic gas-fired carbon-ammonia adsorption heat pump," *Renewable Energy*, vol. 110, pp. 180-185, 2017, doi: 10.1016/j.renene.2017.03.089.
- [26] R. Wang, L. Wang, and W. Jingyi, *Adsorption refrigeration technology theory and application*. Singapore: John Wiley & Sons, 2014.



Measurement of Time Constants of Water Vapor Adsorption Reaction on a Consolidated Silica-gel micro particles using QCM method

Hamamoto, Yoshinori¹, Furuya, Kohei², Miyata, Kazushi¹

¹ Department of Mechanical Eng., Kyushu University, 744, Motooka, Nishi-ku, Fukuoka, 819-0395 Japan
(y-hama@mech.kyushu-u.ac.jp)

² Graduate school of Eng., Kyushu University, 744, Motooka, Nishi-ku, Fukuoka, 819-0395 Japan

Abstract:

Quartz crystal microbalance (QCM) technique was used to measure the adsorption rate of water vapor with a step change of the vapor pressure to silica-gel A-type micro particles consolidated on the QCM sensor. By applying LDF approximation, the time constant for vapor diffusion in a pore of adsorbent was revealed. The effect of the vapor pressure difference before and after the reaction, which is the driving force of the adsorption reaction, on the time constant was confirmed. The time constant increased as the pressure difference decreased. Moreover, the time constant increased as the temperature of the adsorbent decreased.

1 Introduction

Adsorption chiller and heat pump are one of the electric power saving technologies for cooling and heating equipment. For widespread use, it is important to shorten the adsorption and desorption times, that is, increase the reaction rate, in order to reduce the size and increase the output.

Exothermic and endothermic phenomena in the adsorbent due to the vapor adsorption and desorption reactions slow the rate of the reaction. Therefore, the adsorbent is coated thinly on the heat exchanger surface [1-4], and the reaction is accelerated by improving the heat transfer. In addition, since the mass transfer resistance inside the adsorbent greatly affects the progress of the reaction, it is necessary to clarify the effects of the pore structure, diameter and surface state of the adsorbent particles on the internal diffusion resistance.

In this study, a quartz crystal microbalance (QCM) method [5] was used to measure the mass change due to the adsorption of water vapor to the silica gel particle coated on the QCM sensor under isothermal conditions. First, a sample was prepared by bonding adsorbents on a QCM sensor, and then the transient response of the amount of adsorption was measured while increasing the water vapor pressure in a stepwise manner to perform the adsorption reaction, and the time constant was obtained. Finally, the effect of the range of vapor pressure, temperature and relative pressure on the time constant was investigated.

2 Experimental Methods of Measurements

2.1 Measurement principle of QCM method

This method utilizes the phenomenon that the resonance frequency changes when the mass on the crystal unit changes, and the increase or decrease of the mass is measured by measuring the frequency. In general, an equation presented by Sauerbrey [6] is used to convert the frequency change into mass change.

2.2 Sample

The sample was prepared by suspending silica gel micro particles (A type) with an average diameter of about 10 μm and a vinyl acetate resin-based aqueous adhesive with a resin mixing ratio of 41% in distilled water. Ten minutes later, 8 μl of the supernatant of the suspension was dropped onto the gold electrode of the QCM sensor and allowed to dry naturally to bind the fine particles. Figure 1 shows a SEM image of the particles on the sensor. The particles were almost uniformly scattered, and the particle size was found to be less than 2 μm .

Although not shown in a figure, as a result of the measurement experiment of the equilibrium adsorption amount, it was confirmed that the adhesive did not affect the equilibrium adsorption amount.

2.3 Experimental setup and methods

Figure 2 shows an experimental setup consisting of a QCM sensor consolidated with silica-gel micro particles, pressure sensor, thermocouples, vacuum pump, evaporator, temperature-controlled water circulator, valves and tubes. The QCM sensor was installed inside the tube and connected with the evaporator. Vapor pressure was

controlled by valves and the vacuum pump. Pressure sensors measured around the sensor and inside the evaporator by each. Temperature-controlled water circulator kept water temperature in the evaporator. The tube and valves were set in a constant temperature chamber. From the above, pressure and temperature both of vapor and adsorbent were controlled.

Before starting the adsorption experiment, inside the tube was evacuated. Then, the valve 1 and 3 were closed and valve 2 was opened and the tube was filled with water vapor. With the start of the experiment, valve 3 was opened to supply the vapor to the QCM. After the experiment, the valve 2 was closed, the valve 1 was opened, and adsorbed vapor was desorbed from the adsorbent while evacuating by the vacuum pump. In the experiment, the above series of operations was repeated multiple times.

The resonant frequency of the fundamental mode of the QCM sensor was about 5 MHz. Temperature of the sensor T_{ads} was set at 10 °C and 27 °C. Vapor pressure p was set to about 0.3, 0.4 and 1.0 kPa when the temperature T_{ads} was 10 °C, and about 0.7, 1.3 and 2.4 kPa when the temperature 27 °C. Note that the relationship between these pressures and temperatures is often expressed by a single variable called relative pressure. The relative pressure ϕ is the ratio of the vapor pressure of the adsorbent p to the saturated water vapor pressure corresponding to the adsorbent temperature $p_{\text{sat}}(T_{\text{ads}})$. Relative pressure ϕ around the adsorbent by water vapor supply was set to be around 0.2, 0.3 and 0.7.

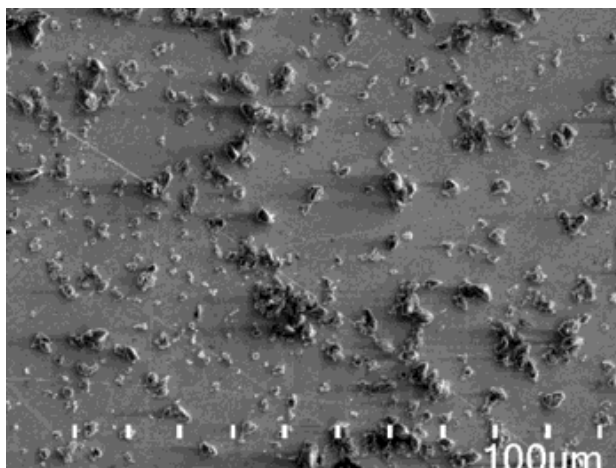


Figure 1 - A SEM image of silica gel particles on the electrode of QCM sensor

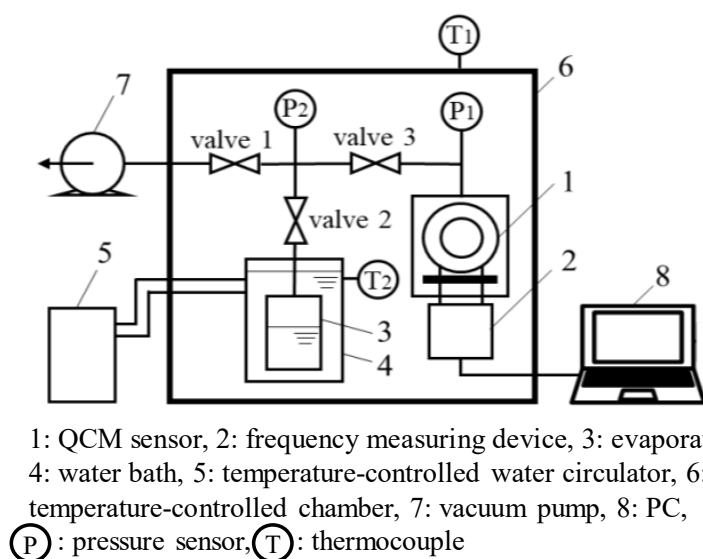


Figure 2 - A schematic of measuring setup

3 Results

3.1 Frequency change and time constant

Figure 3 shows an example of the result when the vapor pressure p changes stepwise from 0 to 2.57 kPa. When the relative pressure ϕ increased, that is, the vapor pressure increased, the frequency also changed, confirming that the mass of the adsorbent increased. The time constant τ of this measurement was about 2 seconds. The time constant represents the resistance value of the vapor transfer rate to the adsorbent. This resistance is due to the diffusion resistance within the pores of the adsorbent particles.

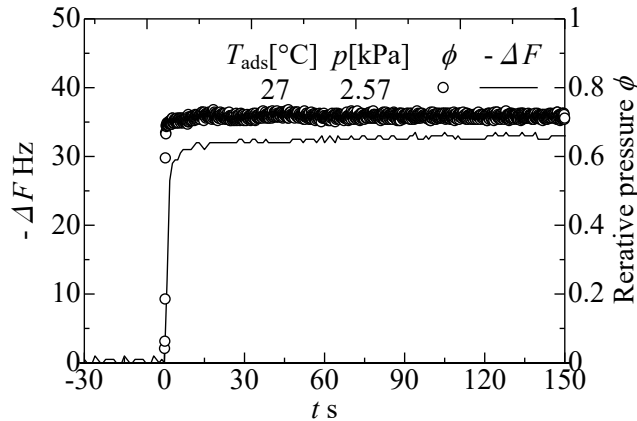


Figure 3 - Frequency change ΔF during adsorption

3.2 Influence of pressure difference on time constant

Figure 4 shows the time constant τ obtained when the vapor pressure p was changed. It was found that the time constant increased when the change in vapor pressure ($p_{\text{end}} - p_{\text{ini}}$) was small. This suggested that the effect of the pressure difference on the vapor transfer in a pore of adsorbent was significant. It was also considered that this was because the number of water vapor molecules was small when the vapor pressure was low, and thus the number of molecules reaching the pore walls was small.

In addition, it was also found that when the temperature of the adsorbent T_{ads} was different, the time constant was different even if the pressure difference of the vapor before and after the reaction was the same, as in around 1 kPa in the figure. This means that when the temperature of adsorbent was low, the saturated vapor pressure on the surface of the pores also decreased and the relative pressure increased. As a result, it was considered that the equilibrium adsorption amount increased, the vapor transfer rate increased, and the time constant decreased.

Next, in order to investigate the time constant dependence of the adsorbent temperature, it is appropriate to compare not only with the vapor pressure difference but also with the relative pressure difference including the effect of temperature.

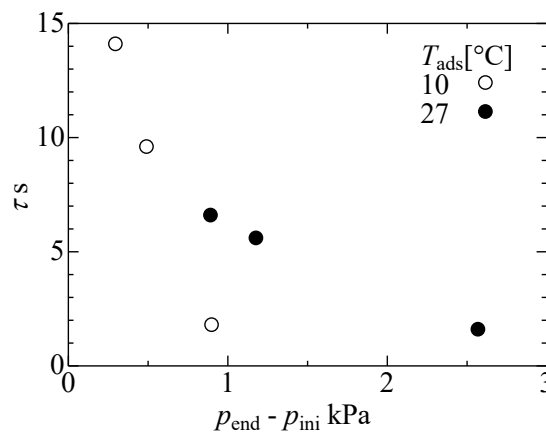


Figure 4 - Influence of pressure difference on time constant

3.3 Influence of temperature of adsorbent on time constant

Figure 5 shows the effect of the relative pressure difference on the time constant. The initial relative pressure ϕ_{ini} ($=p_{ini}/p_{sat}(T_{ads})$) was given as 0 under any conditions, and final relative pressure ϕ_{end} ($=p_{end}/p_{sat}(T_{ads})$) was changed corresponding to vapor pressure p and temperature T_{ads} . It was confirmed that time constant increased as the adsorbent temperature decreased. When the LDF model was applied, the reciprocal of the time constant was proportional to the effective diffusion coefficient in the pores of the adsorbent. Therefore, the above measurement results indicated that the coefficient decreased as the temperature decreased. The qualitative tendency for the effective diffusion coefficient to decrease with decreasing temperature was similar to that for the porous alumina adsorbent [7].

In addition, it seemed that the temperature dependence of the time constant became smaller as the relative pressure change increased. However, when a measurement error of about 1 second was added to the measurement result, the above characteristics disappeared and the temperature dependence appeared to the same degree regardless of the relative pressure difference. It is necessary to verify whether this tendency can be seen in other materials in the future.

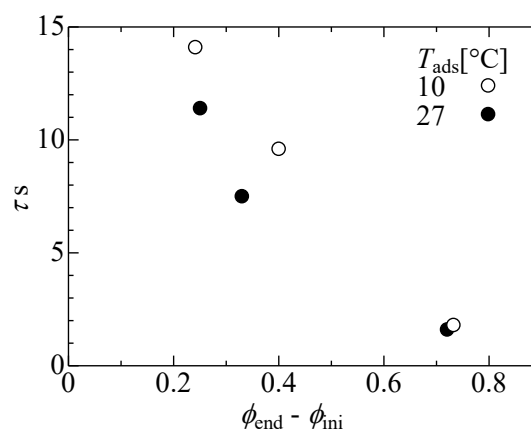


Figure 5 - Influence of relative pressure difference on time constant

4 Conclusions

Time constants of silica-gel (type A) micro particles adsorbing water vapor under several vapor pressure conditions were measured. The influence of the pressure difference on the time constant was significant. This suggested that the effect of the pressure difference on the vapor transfer in a pore of adsorbent was not negligible. Further, the time constant tended to increase as the adsorbent temperature decreased.

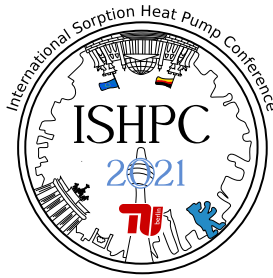
Acknowledgment

This work was supported by [JSPS KAKENHI Grant Number JP19K0423](#). Scanning Electron Microscope (SU3500) in the center of advanced instrumental analysis of Kyushu university was used for SEM imaging.

List of References

- [1] Sortech AG (2007): patent WO2007017015A3.
- [2] Freni, A., Bonaccorsi, L., Calabrese, L., Capri, A., Frazzica A. and Sapienza, A. (2015): SAPO-34 coated adsorbent heat exchanger for adsorption chillers, *Applied Thermal Engineering*, vol.82, pp.1-7.
- [3] Tatlier, M., and Erdem-Senatarlar, A. (2000): Effects of metal mass on the performance of adsorption heat pumps utilizing zeolite 4A coatings synthesized on heat exchanger tubes, *International Journal of Refrigeration*, vol.23, pp.260-268.
- [4] Mori, H., Hamamoto, Y., Yoshida S. and Yonemaru, A. (2000): Experimental study on heat and mass transfer in packed beds adsorbing steam, *Trans. of JSME(B)*, vol.66(649), pp.2463-2470. (in Japanese)

-
- [5] Hamamoto, Y., Nakamori, T. and Mori, H. (2019): Measuring of isothermal water vapor adsorption/desorption rate using QCM method and its mass transfer resistance of a layer coated with silica-gel micro particles in a moist air, *International Journal of Refrigeration*, vol.105, pp.11-18.
- [6] Sauerbrey, G. A. (1959): Verwendung von Schwingquarzen zur Microwagung, *Z.Phys.*, vol.155, pp.206-222.
- [7] Ouchi, T., Hamamoto, Y., Mori, H., Takata, S., Etoh, A. (2014): Water vapor adsorption equilibrium and adsorption/desorption rate of porous alumina film adsorbent synthesized with anodization on heat transfer plate, *Applied Thermal Engineering*, vol.72(2), pp.219-228.



Compact cold storage by means of a closed absorption process with $\text{H}_2\text{O}/\text{LiBr}$ and crystallization of the strong absorbent

Pressl, Dieter¹, Schmidt, Matthias, Castaño Parga, Santiago, Laevemann, Eberhard

Bavarian Center for Applied Energy Research (ZAE Bayern), Division Energy Storage, Walther-Meißner-Straße 6, D-85748 Garching, Germany

¹ Corresponding author: dieter.pressl@zae-bayern.de

Abstract:

Absorption cooling can significantly contribute to industrial energy efficiency by using waste heat, especially if equipped with compact energy storage. Therefore, we developed a novel absorption cold storage process, which includes the formation of $\text{LiBr}\cdot\text{H}_2\text{O}$. First, we motivate the formation of $\text{LiBr}\cdot\text{H}_2\text{O}$ by means of theoretically achievable energy densities, which fundamentally impact both system compactness and economic viability. We also present the results of first experimental investigations, which aimed for an initial assessment of the technical feasibility of the proposed storage process. By means of a 10-kW experimental plant, we experimentally quantified the effect of a low specific salt solution volume flow rate on the heat and mass exchange on a standard tube bundle absorber. Reducing the specific salt solution volume flow rate from 100 L/(h m) to 40 L/(h m) increases the difference in salt mass fraction by 78 %, while the power output is only reduced by 29 %. In laboratory experiments, we achieved salt mass fractions between 73-76 % in a storage tank where saturated salt solution and $\text{LiBr}\cdot\text{H}_2\text{O}$ coexist. This would enable theoretical energy densities up to 300 kWh/m³, whereas an all-liquid-state system cannot achieve more than 135 kWh/m³ when operating under the same temperature conditions.

1. Introduction

Waste heat driven absorption chillers are an effective technology to improve energy efficiency in industry. However, waste heat supply and cooling demand have to fit with respect to time, location, and capacity to maximize the effect. Energy storage can close the gap, if supplied economically. The usual working pair of absorption cooling cycles, $\text{H}_2\text{O}/\text{LiBr}$, can be used as storage material. Since both lithium bromide and industrial space have to be paid for, a high energy density of the storage process is essential. The energy turnover of an absorption cycle is directly proportional to the water evaporated in the evaporator and absorbed in the absorber. Related to the salt solution, it is therefore necessary to achieve a wide spread in the water mass fraction of the solution to maximize its energy storage capacity, which accordingly means a wide spread in the salt mass fraction of the solution. The attempt to increase the spread in the direction of lower salt mass fractions reveals firstly a dependency of the spread of the cooling water temperature and secondly the degradation of the specific absorption capacity of the absorber surface. The attempt to increase the spread in the direction of higher salt mass fractions leads to crystallization of the solution at absorber temperature. Extending previous works [1-3], these challenges were investigated in three phases: First, in a theoretical study, we evaluated the achievable energy density depending on the operational temperatures. Second, in a 10-kW experimental plant, we investigated the absorber performance at increased spread in salt mass fraction. And third, in laboratory experiments, we investigated the handling of partly crystallized solutions.

2. Background/Fundamentals/Experimental Set-up

2.1. Calculation of theoretical energy densities

An ideal storage process is assumed. This mainly includes the achievement of sorptive and thermal equilibrium states and neglecting any losses. Furthermore, we assumed constant temperatures T_E , T_A , T_D , and T_C of the sub-processes evaporation, absorption, desorption, and condensation respectively. The parameters of the calculation model are the temperatures T_E , T_A , and T_C and the maximum salt mass fraction of the strong absorbent after charging w_{max} in order to differentiate between systems without and with crystallization. We analyzed three different process variants, which differ in the salt mass fraction w_{max} achieved after complete charging. In case of the *all-liquid-state* system, w_{max} corresponds to the salt mass fraction at the solubility line at T_A , which is assumed to be the lowest process temperature of the absorbent. For the variants *dihydrate* and *monohydrate*, we assumed that the strong absorbent is completely converted into the corresponding salt hydrate. The values assumed for w_{max} are summarized in Tab. 1.

Table 1 – Maximum salt mass fractions w_{max} assumed for the three process variants analyzed

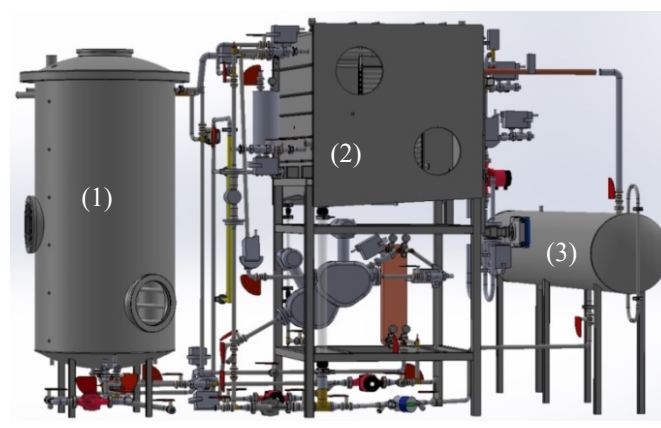
	All-liquid-state	Dihydrate	Monohydrate
w_{max}	62,7 %	70,7 %	82,8 %

By means of the equilibrium state points, the volumetric energy density of the absorption cold storage q_c can be calculated according to Eq. 1, where the heat of evaporation Q_E is related to the maximum volume of the storage material $V_{s,max}$; q_c is defined on the storage material level.

$$q_c = Q_E/V_{s,max} \quad (1)$$

2.2. Experimental investigation of a standard tube bundle absorber for storage application

The experimental investigation of a standard tube bundle absorber was done by means of a 10-kW experimental plant of absorption cold storage. 2-ethyl-1-hexanol was added to the aqueous LiBr-solution. The experimental plant is depicted in Fig. 1 and consists of three major components: A salt solution storage tank (1), a reactor (2), and a water storage tank (3). The reactor contains two standard tube bundle heat exchangers: one operates as evaporator during discharging of the storage and as condenser during charging, the other serves as absorber (discharging) and desorber (charging).



Overall experimental plant	
Volume of salt solution tank	0,5 m ³
Volume of water tank	0,3 m ³
Surface area of evaporator/condenser	0,7 m ²
Mean power at the evaporator	10 kW
Absorber	
Surface area of absorber/desorber	1,5 m ²
Outer diameter of the absorber tubes	0,018 m
Inner diameter of the absorber tubes	0,016 m
Tube rows	3
Tubes per row	20
Length of the absorber tubes	0,44 m

Figure 1: CAD-model and main data of the experimental plant of absorption cold storage

The specific salt solution volume flow rate γ at the absorber was varied between 40 L/(h m) and 100 L/(h m) to analyze its impact on the difference in salt mass fraction Δw and the specific power \dot{Q}_A transferred to the heat transfer fluid at the absorber. The operating conditions were kept constant throughout the complete series of experiments; the most important are summarized in Tab. 2.

Table 2 – Operating conditions of the investigation of the experimental plant of absorption cold storage (T : temperature; w : salt mass fraction)

Internal mean T at the evaporator	Internal mean T at the absorber	T of the salt solution at the reactor inlet	w of the salt solution at the reactor inlet	Theoretical w at the outlet of the reactor
10 °C	35 °C	54 °C	60 %	52 %

2.3. Experimental investigation of the crystallization behavior of LiBr·H₂O

In the intended storage process, both saturated salt solution and LiBr-monohydrate are to be stored in a single storage tank without separation of the two phases. Therefore, first experiments were set out to assess the effective salt mass fraction achievable with this storage principle. The experimental method worked as follows: In a first step, we prepared 100 g samples of LiBr-solution with salt mass fractions of 70 %, 72 %, 75 %, and 78 % by boiling out water on a heating plate. In dependence of the salt mass fraction, the samples had a temperature of

120-140 °C at the end of the heating process. The samples were then brought into a tempered water bath at $T = 95$ °C. The water bath was then cooled down with cooling rates of 60 K/h, 6 K/h, and 1 K/h to $T = 50$ °C, at which the samples were kept for 3 h. Afterwards, we determined the mass ratio of solid sediment (LiBr-H₂O with adherent solution and solution inclusions) and saturated liquid salt solution by means of vacuum filtration. Additionally, we determined the effective salt mass fraction of the solid sediment by the salt and water mass balances of the system.

3. Results

3.1. Theoretical energy densities

The theoretical energy densities q_c calculated under ideal conditions are depicted in Fig. 2 as function of T_E for three process variants: all-liquid-state, dihydrate, and monohydrate. These values are based on a heat rejection temperature at the absorber T_A and the condenser T_C of 35 °C. According to Fig. 2, theoretical energy densities of the all-liquid-state system hardly exceed 200 kWh/m³. For $T_E = 6$ °C, the system with monohydrate achieves 358 kWh/m³, while with dihydrate only 239 kWh/m³ can be obtained. Considering that these values are based on an ideal storage process, formation of LiBr-monohydrate is necessary in order to achieve high energy densities in technical implementation. Thereby, also the specific storage material costs can be minimized.

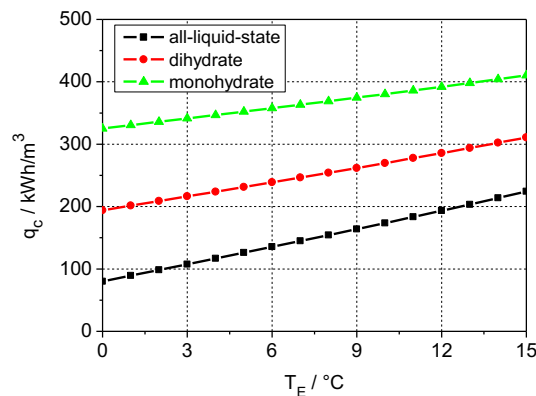


Figure 2: Theoretical energy densities of absorption cold storage with H₂O/LiBr for the process variants all-liquid-state ($w_{max} = 62,7$ %), dihydrate ($w_{max} = 70,7$ %) and monohydrate ($w_{max} = 82,8$ %) for $T_A=T_C=35$ °C

3.2. Experimental investigation of a standard tube bundle absorber for storage application

The experimental results concerning the dependence of the difference in salt mass fraction Δw and the specific power transferred to the heat transfer fluid at the absorber \dot{Q}_A on the specific salt solution volume flow rate γ at a standard tube bundle heat and mass exchanger are presented in Fig. 3. Reducing γ from 100 L/(h m) to 40 L/(h m) results in an increase of Δw of 78 % from 4.0 % to 7.1 %. Simultaneously, \dot{Q}_A decreases by 29 % from 8.9 kW/m² to 6.3 kW/m². These first experimental results indicate that a standard or slightly modified tube bundle absorber might be suitable for storage application.

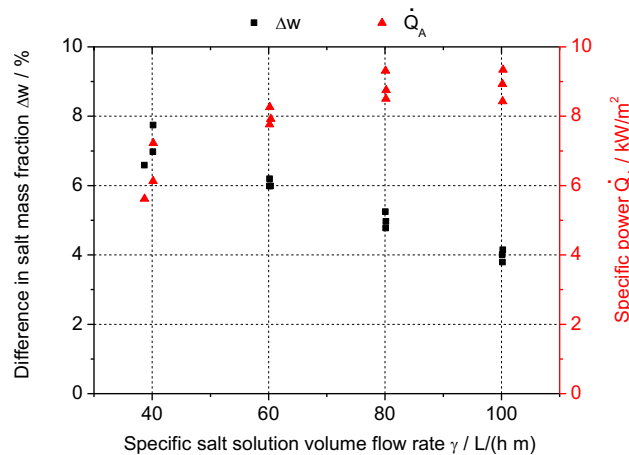


Figure 3: Difference in salt mass fraction Δw and specific power \dot{Q}_A as function of the specific salt solution volume flow rate γ at a tube bundle absorber; initial salt mass fraction = 60 %

3.3. Experimental investigation of the crystallization behavior of LiBr·H₂O

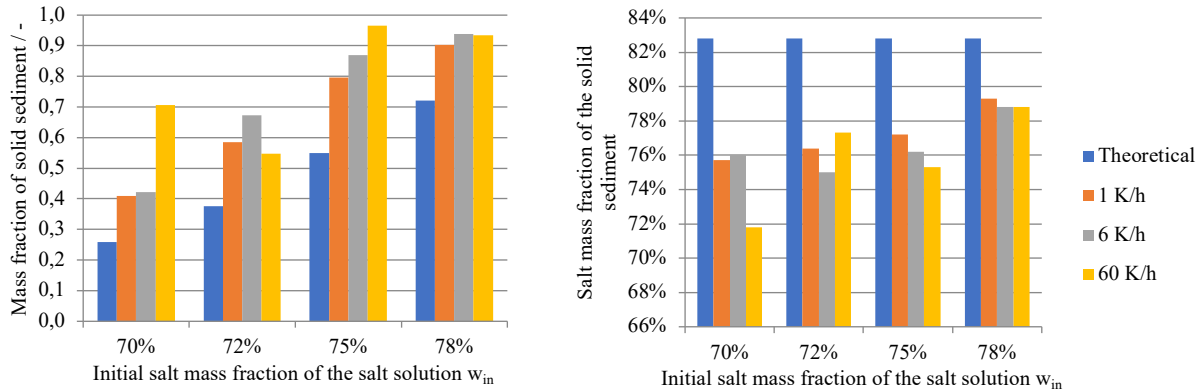


Figure 4: Mass fraction (left) and overall salt mass fraction (right) of the solid sediment for initial salt mass fractions of the liquid salt solution of 70 %, 72 %, 75 %, and 78 % for different cooling rates

The results of the experimental investigation of the crystallization behavior are shown in Fig. 4. Fig. 4 left depicts which part of the initially liquid salt solution is converted into solid sediment after 3 hours at 50 °C. Using the example of an initial salt mass fraction of 72 %, around 60 % of the salt solution is transferred into solid sediment. Theoretically, resulting from the corresponding phase diagram, 38 % of the initial salt solution would be converted into pure LiBr·H₂O. Overall, it can be seen that the fraction of solid sediment tends to increase with rising cooling rate due to a more porous structure of the resulting solid phase. In Fig. 4 right, the overall salt mass fraction of the solid sediment is shown. Accordingly, due to the inclusion of saturated solution in the solid phase, the salt mass fraction is significantly below the theoretically achievable value of pure LiBr·H₂O. Considering again the values for an initial salt mass fraction of 72 %, the results indicate that an overall salt mass fraction of 76 % could technically be feasible.

4. Conclusions

In this study, we presented the results of first theoretical and experimental investigations of a novel absorption cold storage process, which is based on H₂O/LiBr as absorption couple and comprises the formation of LiBr-monohydrate. The formation of monohydrate was first motivated by the calculation of theoretical energy densities of potential process variants. With regard to its technical feasibility, we conducted first experimental investigations. Laboratory-scale experiments indicated that a salt mass fraction of up to 76 % can be achieved in a storage tank where LiBr-monohydrate and saturated salt solution coexist; this would enable theoretical energy densities up to 300 kWh/m³. We also conducted first experiments concerning the heat and mass exchanger, where a significantly higher spread in salt mass fraction of the solution is required compared to an absorption chiller process. In fact, we evaluated the performance of a standard tube bundle absorber at reduced specific salt solution volume flow rates and found that reducing the specific salt solution volume flow rate from 100 L/(h m) to 40 L/(h m) increases the difference in salt mass fraction by 78 %, while the specific power transferred to the heat transfer fluid at the absorber is only reduced by 29 %. This might indicate that a standard tube bundle absorber could also be suitable for storage application, which would e.g. facilitate its integration in industrial waste heat driven absorption chillers. Thereby, potential gaps between waste heat availability and cold demand could be closed. In summary, these results highly motivate the further development of the technology. Therefore, we are planning to implement the proposed storage process in a laboratory plant in a next development step.

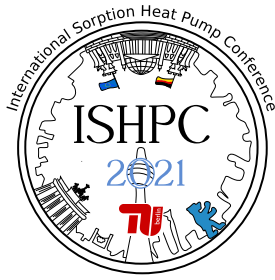
5. Acknowledgment

This work is part of the project MAKSOR^E and was supported by the German Federal Ministry of Education and Research under the project code 03SF0441D. The responsibility for the content of this publication is with the authors.

6. List of References

- [1] Xu, S. M.; Huang, X. D.; Du, R. (2011): An investigation of the solar powered absorption refrigeration system with advanced energy storage technology. In: *Solar Energy* 85 (9), S. 1794–1804. DOI: 10.1016/j.solener.2011.04.022.

-
- [2] N'Tsoukpoe, K. Edem; Le Pierrès, Nolwenn; Luo, Lingai (2012): Numerical dynamic simulation and analysis of a lithium bromide/water long-term solar heat storage system. In: *Energy* 37 (1), S. 346–358. DOI: 10.1016/j.energy.2011.11.020.
- [3] Zhang, Xiaoling; Li, Minzhi; Shi, Wenxing; Wang, Baolong; Li, Xianting (2014): Experimental investigation on charging and discharging performance of absorption thermal energy storage system. In: *Energy Conversion and Management* 85, S. 425–434. DOI: 10.1016/j.enconman.2014.05.100.



Experimental characterization by thermal and mass effectivenesses of plate heat exchangers in NH₃-LiNO₃ absorption chillers

Altamirano, Amín^{1,2}, Stutz, Benoit¹, Le Pierrès, Nolwenn¹, Coronas, Alberto²

¹LOCIE Laboratory, Université Savoie Mont Blanc, CNRS UMR5271, Savoie Technolac, 73376 Le Bourget Du Lac (France) (corresponding author: Benoit.Stutz@univ-smb.fr)

²CREVER—Group of Applied Thermal Engineering, Mechanical Engineering Dept., Universitat Rovira i Virgili, Av. Països Catalans 26, 43007 Tarragona (Spain)

Abstract:

NH₃-LiNO₃ and plate heat exchangers (PHE's) present multiple advantages regarding the conventional working fluids and exchanger technologies used in absorption chillers. The methods used to characterize the absorber and desorber in these systems usually neglect the coupled heat and mass transfer phenomenon. The present work shows the characterization of PHE's used as the absorber and desorber of an NH₃-LiNO₃ absorption chiller through their thermal and mass effectivenesses (ε_{th} and ε_m , respectively), which could help better understand the sorption exchanger performances and serve as a tool for more energy-optimized components. The absorber resulted with a ε_m from 0.31 to 0.76 and a ε_{th} from 0.33 to 0.77, whereas the desorber presented a ε_m from 0.39 to 0.85 and a ε_{th} from 0.63 to 0.92. Results show that ε_{th} and ε_m were mostly impacted by the solution flow regime.

1. Introduction

Absorption chillers possess the potential to fight global warming by the use of renewable energies and waste heat instead of electricity [1]. Nevertheless, they are more complex and expensive when compared to conventional vapor compression systems [2]. Research is ongoing on the study of new working fluids and new compact exchanger technologies to reduce the size and cost of absorption systems. Regarding the former matter, NH₃-LiNO₃ has emerged as a possibility due to its advantages of wide operating temperature conditions and no need of a rectifier [1], whereas plate heat exchangers (PHE) have been investigated for their high performance and compactness [2].

The absorber and desorber have been pointed out as the “bottlenecks” in absorption chillers [3]. Heat/mass transfer coefficients or fluxes are commonly used as parameters to characterize them. However, their effectivenesses is also a fundamental issue towards their size optimization. The present study shows the experimental characterization of PHE used as absorber and desorber for absorption chillers through their thermal and mass effectivenesses (ε_{th} and ε_m , respectively). In the first section, a brief definition of ε_{th} and ε_m is given, after which the studied exchanger geometries and the tested operating conditions are presented. Finally, the results are presented and discussed.

2. Effectivenesses definition and experiments

2.1. Thermal and mass effectivenesses

The studied exchangers (absorber and desorber) possess a counter-current configuration of the liquid phases (solution/heat transfer fluid) and on the two-phase flow side, the NH₃-LiNO₃ solution and the ammonia vapor both flow upwards in a co-current configuration, as represented in Fig. 1 for the case of the absorber. Their performance is defined on the basis of thermal and mass effectivenesses (ε_{th} and ε_m , respectively). The thermal effectiveness (Eq. (1)) is defined as the ratio of the actual transferred heat to the maximum theoretical transferable heat. On the other hand, the mass effectiveness (Eq. (2)) is defined as the ratio of the actual transferred mass (absorbed or desorbed) to the maximum theoretical exchangeable mass.

$$\varepsilon_{th} = \dot{Q}_{sorp} / \dot{Q}_{sorp}^{max} \quad (1)$$

$$\varepsilon_m = \dot{m}_{sorp} / \dot{m}_{sorp}^{max} \quad (2)$$

In the following, the case of the absorber is discussed to explain the procedure. A similar procedure is followed in the case of the desorber. The maximum absorbable mass depends on the solution flow rate and the potential of the heat transfer fluid (HTF) to cool it or heat it. This potential is represented by the equilibrium factor (Eq. (3)), defined as the ratio between the maximum amount of heat that can be transferred to the HTF to the maximum amount of heat that can be transferred by the solution.

$$R_{abs} = \frac{\dot{Q}_{htf,abs}^{max}}{\dot{Q}_{sol,abs}^{max}} = \frac{\dot{m}_{htf}[h_{htf,o}(T_{sol}^{max}) - h_{htf,i}]}{\dot{m}_{sol,i}h_{sol,i} - \dot{m}_{sol,o}h_{sol,o} + \dot{m}_{abs}h_v} \quad (3)$$

The maximum amount of heat that can be transferred to the HTF in an infinitely long exchanger ($\dot{Q}_{htf,abs}^{max}$) is proportional to the maximum enthalpy difference in the HTF itself when achieving an outlet temperature equal to the maximum temperature that the solution side can achieve ($T_{sol}^{max} = \max [T_{sol,i}; T_{sol,o}^{ad}]$). When the inlet solution temperature is lower than the equilibrium solution temperature ($T_{sol,i} < T_{eq}(P_v, x_i)$), it has a tendency to absorb refrigerant (increase its temperature) and the maximum solution temperature ($T_{sol,o}^{ad}$) corresponds to an adiabatic absorption in an infinitely long exchanger. On the other hand, the maximum amount of heat that can be transferred by the solution ($\dot{Q}_{sol,abs}^{max}$) derives from an energy balance for an isothermal absorption in which the outlet solution temperature is equal to the inlet HTF temperature ($T_{sol,o}^{min} = T_{htf,i}$).

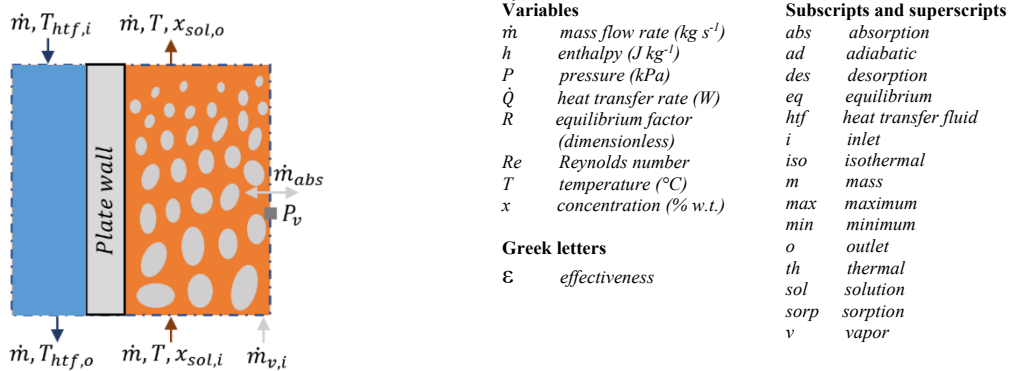


Figure 1 – Control volume of a bubble absorber.

Nomenclature

If the equilibrium factor is higher than one ($R > 1$), then the solution is the limiting fluid and the maximum transferable heat/absorbable mass correspond to an isothermal absorption in an infinitely long absorber where the outlet solution temperature reaches the inlet HTF temperature, in which case $\dot{Q}_{abs}^{max} = \dot{Q}_{sol,abs}^{max}$ and $\dot{m}_{abs}^{max} = \dot{m}_{abs}^{iso}$. On the other hand, if $R < 1$, the HTF is the limiting fluid and the maximum transferable heat/absorbable mass corresponds to an absorption in an infinitely long absorber where the outlet HTF temperature reaches the maximum solution temperature ($\dot{Q}_{abs}^{max} = \dot{Q}_{htf,abs}^{max}$).

2.2. Exchangers' geometries and experimental conditions

PHE and NH₃-LiNO₃ were investigated as the exchanger technology and working fluid, respectively. The PHE technology has been recently investigated owing to its high compactness and low cost. On the other hand, the NH₃-LiNO₃ working pair possesses different advantages over the conventional working pairs (NH₃-H₂O and H₂O-LiBr) such as its wide range of operating conditions without crystallization and no need of a rectifier. The exchangers' geometrical characteristics and operating conditions are presented in Tables 1 and 2, respectively [4,5]. Two tests were conducted to study the absorption performance, the first one (test 1) was aimed to study the effect of the solution flow rate and the HTF inlet temperature, while the second one (test 2) was aimed to study the effect of the HTF inlet temperature and the HTF flow rate [4]. In the experiments performed to characterize the desorber [5], the main interest was to study the heat transfer phenomenon and there was no strict control on the inlet solution temperature, concentration, and operating pressure. Instead, two parameters were changed: the outlet solution temperature, which was fixed at five different values (78, 82, 86, 80, and 95°C), and the solution mass flow rate, which was fixed at three levels (151.2, 208.8, and 298.8 kg h⁻¹). For more details about the experimental set-ups, see the referenced works [4] and [5].

Table 1 – Geometrical characteristics of the studied absorber [4] and desorber [5].

	Absorber	Desorber
Model	Alfa Laval NB51	Alfa Laval AN76
Number of plates	4	20
Absorber length (m)	0.53	0.576
Absorber width (m)	0.112	0.175
Heat transfer effective area (m ²)	0.1	1.8
Spacing between the plates (m)	0.002	0.0024
Plate thickness (m)	0.0004	0.0004
Corrugation angle with horizontal axis (degrees)	30	58.5

Table 2 – Experimental operating conditions of the tested absorber [4] and desorber [5].

	Absorber	Desorber
Inlet solution temperature, $T_{sol,i}$ (°C)	45 (test 1 and test 2)	56 to 69.6
Inlet HTF temperature, $T_{htf,i}$ (°C)	35 and 40 (test 1 and test 2)	80.1 to 100.9
LiNO ₃ inlet solution mass fraction, $x_{sol,i}$ (kg kg ⁻¹)	0.55 (test 1 and test 2)	0.538 to 0.548
Operating pressure (kPa)	510 (test 1 and test 2)	977.7 to 1606
Inlet solution mass flowrate, $\dot{m}_{sol,i}$ (kg h ⁻¹)	10 to 50 (test 1 with $\dot{m}_{htf} =$ 265 kg h ⁻¹)	(151.2, 208.8, 298.8)
HTF mass flowrate, \dot{m}_{htf} (kg h ⁻¹)	132 to 447 (test 2 with $\dot{m}_{sol,i}$ = 40 kg h ⁻¹)	602.36 to 745.64
Outlet solution temperature, $T_{sol,o}$ (°C)	36.9 to 44.2	(78, 82, 86, 90, 95)

3. Results

Fig. 2a shows the impact of the solution flow rate and the HTF inlet temperature on the equilibrium factor (R), or Test 1. During this test, the solution side remains the limiting fluid ($R > 1$). For Test 2 (Fig. 2b), while Re_{sol} remains at values around 35, R increases linearly with the Reynolds number on the heat transfer fluid side (Re_{htf}), varying from 0.9 to 3 with a Re_{htf} from 470 to 1600. The inlet HTF temperature does not seem to have a significant impact on R . This happens because the variation on $T_{htf,i}$ impacts in a similar way the maximum transferable conditions on the HTF side ($\dot{Q}_{htf,abs}^{max}$) as on the solution side ($\dot{Q}_{sol,abs}^{max}$). Figs. 2c and d show the evolution of ε_m and ε_{th} of the studied absorber with Re_{sol} for both tests. The highest effectivenesses are reached at the lowest Re_{sol} due to the low solution velocity that generates two phenomena: a high hydrodynamic bubble disturbance and a high flow residence time in the channel. As Re_{sol} increases, these phenomena decrease and both ε_m and ε_{th} decrease to an asymptote that indicates an approach to a $R=1$ (the solution side is reaching the limit of the maximum potential of transferable heat by the HTF). Moreover, ε_{th} is systematically higher than ε_m . This happens because even though the mass transfer is coupled to the heat transfer, it is also impacted by the driving force of the absorption process (deviation from the equilibrium conditions). Figs. 2c and d show that the variation of Re_{htf} and $T_{htf,i}$ don't significantly impact ε_m and ε_{th} in the studied conditions.

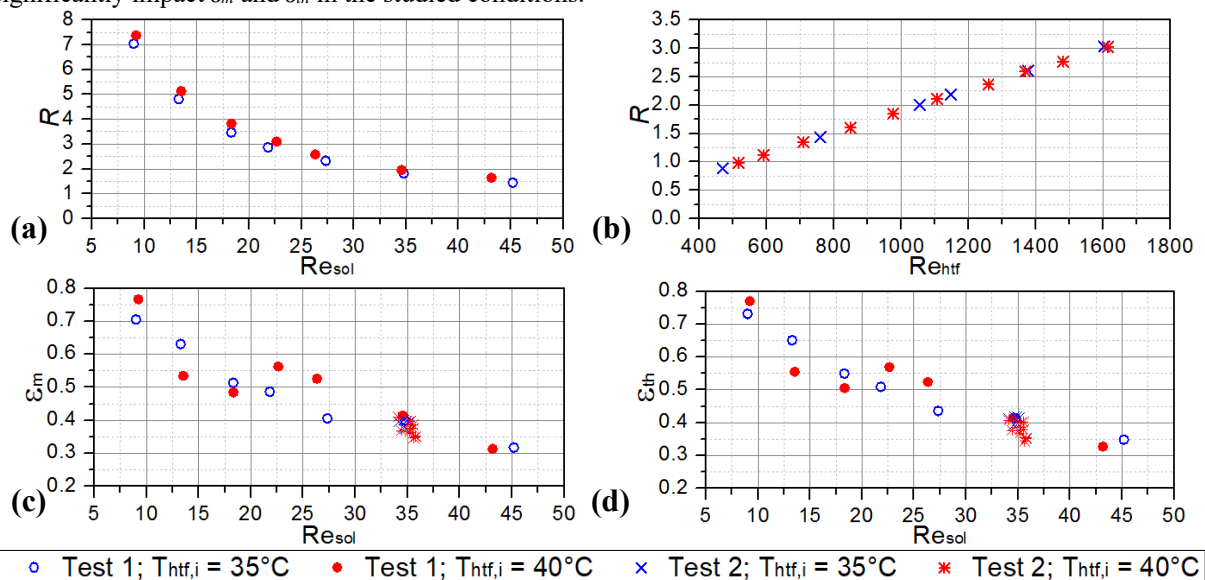


Figure 2 – Evolution of R with (a) Re_{sol} (Test 1) and (b) Re_{htf} (Test 2), and evolution of (c) ε_m and (d) ε_{th} vs Re_{sol} for both Test 1 and Test 2 in the absorber.

Fig. 3a shows the evolution of R with Re_{sol} for the desorber. The three Re_{sol} grouped zones represent the three solution mass flow rates (see Table 2), and the variation in Re in each zone is due to the change in the inlet solution dynamic viscosity. The data is grouped in five outlet solution temperatures (Table 2). The solution side was the limiting fluid in the whole range of tested conditions ($R > 1$), with high R values at low Re_{sol} , and as Re_{sol} increases, R decreases. Moreover, the thermophysical properties' evolution and inlet conditions seem to have a stronger positive impact on R at low Re_{sol} . Regarding the mass and thermal effectivenesses (Fig. 3b and c), the same

tendency as for the absorber can be observed with higher effectivenesses for low Re_{sol} and a decrease approaching an asymptote as R comes close to 1. ε_m is again systematically lower than ε_{th} , however, in this case the gap is much higher due to the high subcooled state of the solution at the inlet of the desorber (subcooling of between 15 and 25°C), leading to poor mass transfer performances. Moreover, for each solution mass flow rate (151.2, 208.8, and 298.8 kg h⁻¹), there is an increase of both ε_{th} and ε_m with Re_{sol} induced by a decrease in the solution's dynamic viscosity. Indeed, a lower viscosity increases the hydrodynamic bubble disturbance, enhancing the mass transfer and increasing ε , which is in agreement with other works that have blamed the elevated viscosity of NH₃-LiNO₃ for its low experimental performance compared with other low viscosity solutions such as NH₃-H₂O [1].

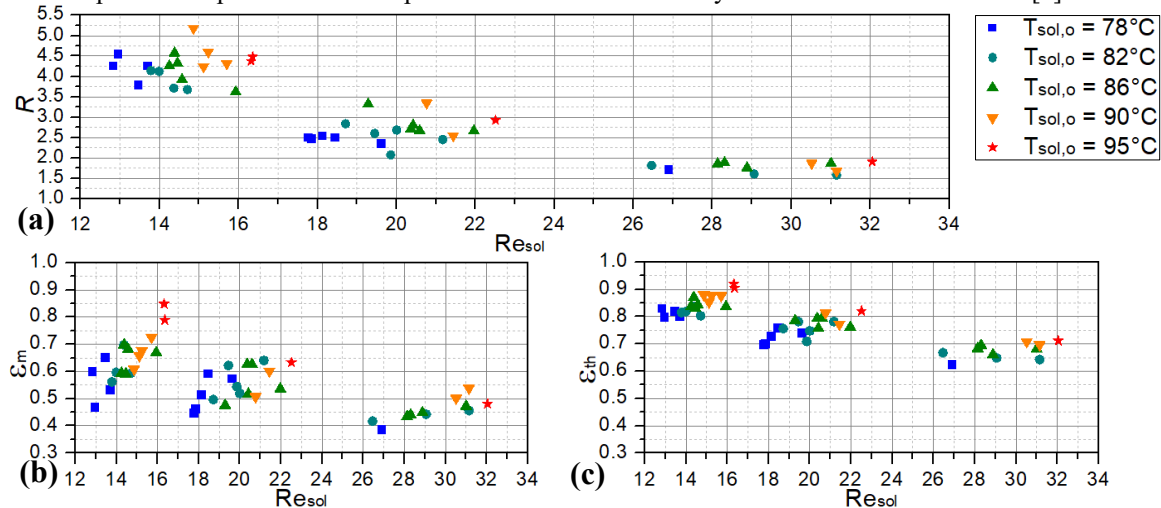


Figure 3 – Evolution of (a) R , (b) ε_m and (c) ε_{th} vs Re_{sol} for the different tested conditions in the desorber.

4. Conclusions

A study of PHE as the absorber and desorber components of an NH₃-LiNO₃ absorption chiller based on their thermal and mass effectiveness was performed. The impact of the different conditions on the effectivenesses was observed. The studied absorber presented a mass effectiveness between 0.31 and 0.76 and a thermal effectiveness between 0.33 and 0.77. On the other hand, the studied desorber presented a mass effectiveness between 0.39 and 0.85 and a thermal effectiveness between 0.63 and 0.92. As the maximum transferable conditions (\dot{Q}_{sorp}^{max} and \dot{m}_{sorp}^{max}) in the studied exchangers were always dependent on the solution side ($R > 1$), ε_{th} and ε_m were mostly impacted by the solution flow regime (Re_{sol}), leading to better performances at low Re_{sol} and lower dynamic viscosities (mainly due to a mass transfer enhancement by hydrodynamic bubble disturbances and an increased bubble residence time in the plate channels). The lowest Re_{hif} in order to maintain $R > 1$ is desirable in the sorption exchangers to have a low pumping energy consumption. Finally, the solution's thermophysical properties and deviation from the equilibrium conditions have a stronger impact on the mass effectiveness than on the thermal effectiveness, especially at low solution flow regimes.

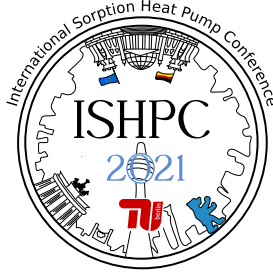
5. Acknowledgments

The authors would like to thank the Mexican sectorial fund “CONACYT-SENER-SUSTENTABILIDAD ENERGÉTICA” and the InnoEnergy PhD School Programme of the European Institute of Technology (EIT) for their support to this research.

6. References

- [1] Altamirano A, Le Pierrès N, Stutz B. Review of small-capacity single-stage continuous absorption systems operating on binary working fluids for cooling: Theoretical, experimental and commercial cycles. *Int J Refrig* 2019;106:350–73. doi:10.1016/j.ijrefrig.2019.06.033.
- [2] Altamirano A, Stutz B, Le Pierrès N. Review of small-capacity single-stage continuous absorption systems operating on binary working fluids for cooling: Compact exchanger technologies. *Int J Refrig* 2020.
- [3] Goyal A, Staedter MA, Hoysall DC, Ponkala MJ, Garimella S. Experimental evaluation of a small-capacity, waste-heat driven ammonia-water absorption chiller. *Int J Refrig* 2017;79:89–100. doi:10.1016/j.ijrefrig.2017.04.006.
- [4] Amaris Castilla C. Intensification of NH₃ Bubble Absorption Process using Advanced Surfaces and Carbon Nanotubes for NH₃/LiNO₃ Absorption Chillers. PhD Universitat Rovira i Virgili, 2013.

-
- [5] Zacarías Santiago A. Transferencia de Masa y Calor en Absorbedores Adiabáticos con Aplicación de la Disolución Nitrato de Litio-Amónico (in Spanish). PhD Universidad Carlos III de Madrid, 2009.



Hybrid thermochemical cycles for power and cold cogeneration: thermodynamic analysis and dynamic performances

Godefroy, Alexis^{1,2}, Perier-Muzet, Maxime^{1,2}, Neveu, Pierre², Mazet, Nathalie¹

¹ CNRS-PROMES Laboratoire PROcédés, Matériaux et Energie Solaire, 66100 Perpignan, France

(corresponding author: alexis.godefroy@promes.cnrs.fr)

² Université de Perpignan Via Domitia, 66100 Perpignan, France

Abstract:

Based on the coupling of a thermochemical sorption cycle with an expansion device, five operating modes are presented for low-grade heat storage and conversion into power and cold. Considering $\text{CaCl}_2(8/4)\text{NH}_3$ as reactant, the performances of these hybrid cycles are presented. The simultaneous power and cold production mode is the most promising one. Its energy and exergy efficiencies reach 0.50 and 0.33, respectively, and its energy storage density $151.4 \text{ kWh/m}^3_{\text{system}}$. The study of the dynamic behavior of this cycle shows that a suitable control of the expander leads to stable power and cold outputs of 490 W and 8 kW for 3 hours, using 0.19 m^3 reactive composite.

1 Introduction

Industrial waste heat at low temperatures (lower than $250 \text{ }^\circ\text{C}$) is a huge heat source. Several cycles have been developed to recover this heat, such as ORC for electricity production or sorption cycles for cold production and storage purposes. The hybrid thermochemical cycles based on solid/gas reactions combine power and cold production with a storage feature, by inserting an expansion device in a thermochemical cycle. So far, very limited research has been carried out on this kind of hybrid cycles, despite their attractive storage ability. In the early work of Ziegler et al. [1], a re-evaluation of the Honigmann process was proposed, leading to a broad approach of hybrid sorption cycles involving an expansion device for power production. Later, Bao et al. [2] investigated their dynamic behavior. Their experimental study [3] showed that power output is very unstable without any external control of the expander behavior, due to the strong coupling between expansion and reaction kinetics. Therefore, managing the dynamic behavior of such hybrid thermochemical cycle is still a key issue. In this paper, 5 ways of hybridizing a thermochemical cycle with an expander are presented. The significant results of the thermodynamic and dynamic studies are depicted, focusing on $\text{CaCl}_2(8/4)\text{NH}_3$ as solid reactant of the sorption process.

2 Operating modes of hybrid thermochemical cycles

Classical thermochemical sorption cycles are characterized by their discontinuous operation, which provides their storage feature: a cycle involves a charging step (endothermal decomposition reaction) and a discharging step (exothermal synthesis reaction). Hybridizing a thermochemical sorption cycle consists in inserting an expansion device on the gas flow between its classical components. Five different operating modes have been identified, they are depicted in Figs. 1 (general working principle) and 2 (thermodynamic paths). They are sorted according to their shares of power and cold in the overall production:

- **Prevailing cold production modes:** the expander is inserted either in the charging step, in the discharging step, or in both steps. These 3 modes are thoroughly investigated in [4]. They are named respectively:
 - **separated** power and cold mode: $W_{ch} \neq 0$ and $W_{disch} = 0$ (in Figure 2: Charge (b) and Discharge (c)),
 - **simultaneous** power and cold mode: $W_{disch} \neq 0$ and $W_{ch} = 0$ (in Figure 2: Charge (a) and Discharge (d)),
 - **combined** power and cold production mode: $W_{ch} \neq 0$ and $W_{disch} \neq 0$ (in Figure 2: Charge (b) and Discharge (d)).
- **Prevailing power generation modes:** in the discharging step, the constraint of cold production is removed, which allows increasing evaporator pressure (point 4') and inserting an expander between evaporator and reactor (points 5'-6'). Heat from the reactor (point 7') is provided to the evaporator to achieve an original autothermal power production step. We note that such autothermal process is close to the above-mentioned Honigmann process for electricity production. A residual cold production occurs at the expander outlet (point 6'). An expander can also be inserted in the charging step, as described above. This leads to two operating modes:
 - **discharge** power generation mode: $W_{disch} \neq 0$ and $W_{ch} = 0$ (in Figure 2: Charge (a) and Discharge (e)),

- **combined** charge and discharge power generation mode: $W_{ch} \neq 0$ and $W_{disch} \neq 0$ (Charge (b) and Discharge (e)).

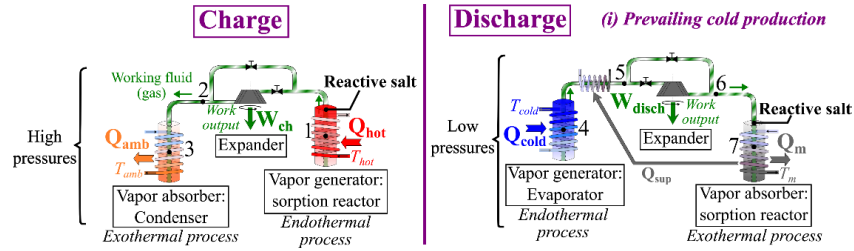


Figure 1 – Operating modes of hybrid thermochemical cycles: working principle. Valves enable the actuation or bypass of the expander.

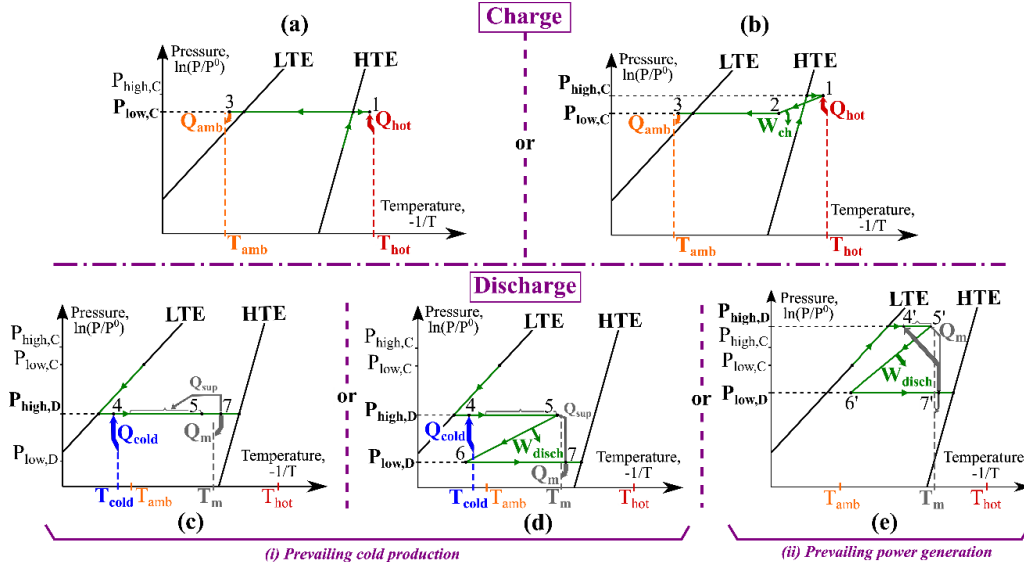


Figure 2 – Operating modes of hybrid thermochemical cycles: thermodynamic paths in Clausius-Clapeyron diagrams. LTE: Low Temperature Equilibrium, liquid/vapor phase change equilibrium of the working fluid. HTE: High Temperature Equilibrium, chemical reaction equilibrium of the reactant.

3 Framework and main results of the study

3.1 Thermodynamic study

The thermodynamic study is based on usual assumptions (steady-state process, heat losses and pressure drops inside components are neglected). It is detailed in a previous work [4]. Several temperature pinches are set for heat exchanges and for the deviation from chemical reaction equilibrium line (HTE line). The cold source and ambient sink temperatures are set at $T_{cold} = 0 \text{ }^\circ\text{C}$ and $T_{amb} = 20 \text{ }^\circ\text{C}$, while the required heat source temperature T_{hot} depends on reactive salt and operating mode. Thermodynamic analyses were conducted for the 5 modes. Four key performance indicators were selected (Table 1). The power production ratio τ_w gives the share of power in the total output. The energy efficiency η_l of these cogeneration cycles involves all energy outputs over one complete cycle ($W = W_{ch} + W_{disch}$ and Q_{cold}). The exergy efficiency η_{ex} allows a fair comparison between the operating modes despite the various shares of cold and mechanical work outputs. The storage performance indicator ESD (Energy Storage Density) involves the production in discharging step and the volume of storage components (reactor – metal wall, anhydrous reactive salt and porous volume, considering a global porosity of 0.7 – and NH_3 tank).

Power production ratio	Energy efficiency	Exergy efficiency	Energy Storage Density
$\tau_w = \frac{ W }{ W + Q_{cold}}$	$\eta_l = \frac{ W + Q_{cold}}{Q_{hot}}$	$\eta_{ex} = \frac{ W + Ex_{cold} }{Ex_{hot}}$	$ESD = \frac{ W_{disch} + Q_{cold}}{V_{stor}}$

Table 1 – Definition of four key performance indicators to characterize the operation of the hybrid thermochemical cycles.

3.2 Dynamic modelling

To predict the dynamics of hybrid thermochemical cycles, models were developed for each component (reactor, condenser, evaporator, expander), accounting for their respective dynamic behaviors. In each component, internal

variables (thermodynamic state of the gas, wall temperature, reaction advancement ...) were considered uniform (0D modelling). The model of the reactor includes energy and mass balances, solid/gas reaction kinetics, and an ideal gas assumption. The works of Castaing et al. [5] and Bao et al. [2] provide more details on such 0D approach for thermochemical systems. Realistic heat transfer coefficients have been used ($100 \text{ W}\cdot\text{m}^{-2}\cdot\text{K}^{-1}$ for reactive bed/wall, $1000 \text{ W}\cdot\text{m}^{-2}\cdot\text{K}^{-1}$ for wall/heat exchanger). As a first approach, the expander is supposed to operate in steady-state and its global performance is described by two efficiencies: isentropic efficiency η_{is} and volumetric efficiency η_v . Moreover, its exhaust pressure is fixed to simulate user control. Finally, $\text{CaCl}_2(8/4)\text{NH}_3$ emerged as a good candidate and a well-known reactant [4]. Thus, the following results are based on this reactive salt.

3.3 Thermodynamic study: results for all operating modes

The main results are gathered in Table 2: heat source temperature T_{hot} and key performance indicators (see §3.1).

	Prevailing cold production			Prevailing power generation	
	Separated mode	Simultaneous	Combined	Discharge mode	Combined
T_{hot} (°C)	138	108	138	108	138
τ_w (%)	10.9	5.0	14.8	53.2	70.7
η_l (-)	0.44	0.42	0.45	0.08	0.12
η_{ex} (-)	0.26	0.22	0.33	0.20	0.31
ESD^* ($\text{kWh}/\text{m}^3_{\text{system}}$)	74.4	151.4	107.9	33.0	28.1

Table 2 – Results of the thermodynamic analyses for the 5 operating modes.
Selected reactant: $\text{CaCl}_2(8/4)\text{NH}_3$. * ESD is computed for $\text{CaCl}_2(8/2)\text{NH}_3$

The 3 operating modes involving a non-isobaric charging step (separated mode, combined power and cold mode, combined charge and discharge mode) require a higher heat source temperature ($T_{hot}=138^\circ\text{C}$) than the other operating modes ($T_{hot}=108^\circ\text{C}$). As expected, power production ratios are higher for prevailing power modes ($\tau_w \approx 53\text{-}71\%$, against $5\text{-}15\%$ for prevailing cold modes). Moreover, energy efficiencies are much higher for prevailing cold modes ($\eta_l \approx 0.42\text{-}0.45$, against $0.08\text{-}0.12$ for prevailing power modes). The difference no longer exists for exergy efficiencies, because this indicator takes account of the high share of power provided by the prevailing power modes. Finally, the highest Energy Storage Density is reached by the simultaneous mode because all useful effects (cold and power) are produced during the discharging step. In view of this good storage performance, simultaneous mode has been selected as case study for the dynamic modelling hereafter.

3.4 Dynamic modelling: results for simultaneous mode

The simultaneous mode appears as the most promising mode. Thus, its dynamic behavior during the discharging step is investigated. The components (evaporator, superheater, expander and reactor with 0.19 m^3 of composite: see Fig. 1) initially rest at ambient temperature. The simulation begins when the evaporator is connected to the cooling loop (at $T_{cold} = 0^\circ\text{C}$) and mass connections between the components (valves) are open. In Fig. 3a, output powers during discharging step (right side) and input thermal power during charging step (right side) are plotted over time. Fig. 3b displays the operating pressures (left side), temperatures and reaction advancement (right side). Regarding output thermal and mechanical powers, a peak is observed at the beginning of the discharging step (Figure 3a: more than 27 kW cold production and 1 kW power production). It lasts less than 2 minutes. Then, the non-equilibrium stage that is reached is close to a steady-state stage: during this stage, cold power mean value is 8 kW and mechanical power mean value is 490 W . Finally, a decrease occurs at about 175 min, caused by the decrease in solid/gas reaction kinetics: the reaction is almost complete (advancement reaches 0.9, see Figure 3b). At the beginning of the simulation, the evaporator temperature T_{ev} suddenly drops (Figure 3b) because of two main factors: (i) the mass connection with the other components (especially the reactor resting at a much lower pressure) which brings the evaporator out of its liquid/vapor equilibrium and creates a suction effect, and (ii) the thermal connection with the cooling loop. This causes the sharp increase in thermal and mechanical powers.

Regarding pressures, a pressure control has been implemented so that the expander low pressure is fixed at 1.9 bar . During the operating stage that is close to a steady-state stage, the evaporator lies at high pressure $P_{high,D} = P_{ev} = 4 \text{ bar}$ and the reactor lies at low pressure $P_{low,D} = P_r = 1.9 \text{ bar}$ (the expander pressure ratio is 2).

Finally, using the data from this dynamic study, the energy and exergy performance indicators listed in Table 1 have been computed: they reach $\eta_I=0.50$, $\eta_{ex}=0.33$ and $\tau_w=5.6$ %. Although relatively close to the estimates derived from thermodynamic study (Table 2, simultaneous mode), these performance values are slightly higher because the temperature pinches are lower than the ones set for the thermodynamic study.

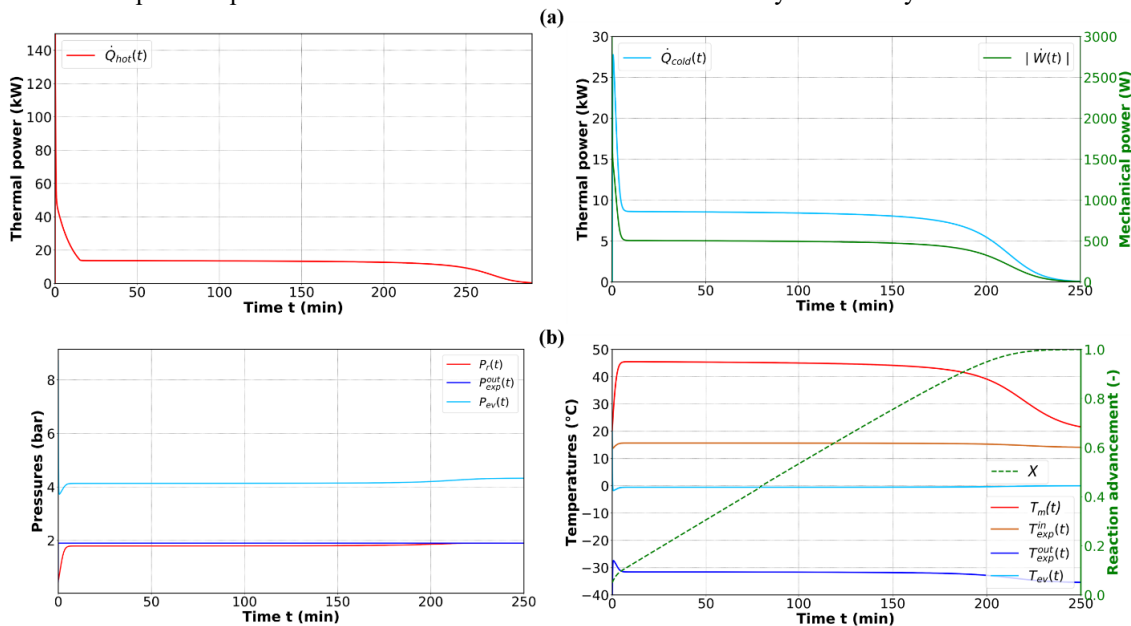


Figure 3 – Simultaneous mode (using $CaCl_2(8/4)NH_3$ as reactant): main results of the dynamic study.

(a) thermal and mechanical powers during charging (left side) and discharging (right side) steps
 (b) Operating pressures (left side), temperatures and reaction advancement (right side) during discharging step.

4 Conclusions

In this paper, five operating modes of hybrid thermochemical cycles were introduced, targeting low-grade heat storage and cogeneration of power and cold. $CaCl_2(8/4)NH_3$ was chosen as reactive salt. A thermodynamic analysis allowed the determination of their energy, exergy and storage performances. The simultaneous power and cold production mode appeared as very promising, especially in terms of energy storage density. The dynamic behavior of this mode was investigated by means of a dynamic model. The first results of this dynamic study highlighted the highly dynamic behavior of the process at the beginning of the discharging step. The global energy and exergy performances obtained with the dynamic study are promising, in line with the results of the thermodynamic analysis: energy and exergy efficiencies reach 0.50 and 0.33, respectively.

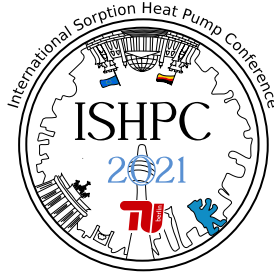
These first results suggest a strong coupling between reactor and expander, which needs further investigations: the increase in pressure ratio across the expander (linked to the increase in mechanical power) is competing with the increase in pressure deviation from the thermodynamic equilibrium of the reactor (linked to the increase in solid/gas chemical reaction kinetics). Using mean mechanical power as objective function, the existence of an optimal exhaust pressure of the expander is under study. An experimental proof-of-concept is currently under development, it will integrate a control of the expander to achieve optimal and stable power output.

5 Acknowledgment

Alexis Godefroy receives a PhD grant from the French Ministry of National Education (No. 2017-09-ED.305).

6 List of References

- [1] Ziegler, F., Jahnke, A., Karow, M. (2009): Re-evaluation of the Honigmann-process: thermo-chemical heat store for the supply of electricity and refrigeration. *Vortrag und Proc. of Heat Powered Cycles Conf.*, Berlin.
- [2] Bao, H., Wang, Y., Roskilly, AP. (2014): Modelling of a chemisorption refrigeration and power cogeneration system. *Applied Energy*, vol. 119, pp. 351-62.
- [3] Bao, H., Wang, Y., Charamboulos, C., Lu, Z., Wang, L., Wang, R., et al. (2014): Chemisorption cooling and electric power cogeneration system driven by low grade heat. *Energy*, vol. 72, pp. 590-8.
- [4] Godefroy, A., Perier-Muzet, M., Mazet, N. (2019): Thermodynamic analyses on hybrid sorption cycles for low-grade heat storage and cogeneration of power and refrigeration. *Applied Energy*, vol. 255.
- [5] Castaing-Lasvignottes, J., Neveu, P. (1997): Development of a numerical sizing tool for a thermochemical transformer (Parts I and II). *Applied Thermal Engineering*, vol. 17, pp. 501-36.



Heat and Mass Transfer Kinetics of MOF-Coatings from Al-fumarate and CAU-10(Al)-H from IR-LTJ experiments: The Impact of Characteristic Times

Henninger, Matthias¹, Gilges, Markus¹, Rustam, Lina², Ernst, Sebastian-Johannes², Velte, Andreas², Seiler, Jan¹, Bardow, André^{1,3,4*}

¹Institute of Technical Thermodynamics (LTT), RWTH Aachen University, 52062 Aachen, Germany

²Fraunhofer Institute for Solar Energy Systems (ISE), 79110 Freiburg, Germany

³Institute of Energy and Climate Research (IEK-10), Forschungszentrum Jülich, 52425 Jülich, Germany

⁴Energy & Process Systems Engineering, ETH Zurich, 8092 Zürich, Switzerland

* Corresponding Author: abardow@ethz.ch

Abstract:

The metal-organic frameworks (MOFs) Al-fumarate and aluminum-isophthalate CAU-10 (CAU = Christian Albrechts University Kiel) are considered for water-based adsorption chillers because of their excellent cyclic stability and high water uptake. However, water uptake captures only the equilibrium behavior, while process performance depends strongly on kinetics. In this work, we, therefore, determine characteristic time constants for water ad- and desorption on Al-fumarate and CAU-10. The MOF coatings are studied by small-scale Infrared Large-Temperature-Jump (IR-LTJ) experiments. Commercially available granular silica gels serve as benchmark. We show that the performance expected from the characteristic time constants depends strongly on the chosen characteristic time as well as the chosen reference in the heat exchanger. For area-specific mean power, silica gel performs best for small time constants, CAU-10 and silica gel both perform best for intermediate time constants, and Al-fumarate performs best for large time constants for the temperature triple 10/30/80 °C. For volume-specific mean powers, silica gels are outperformed by both MOF-coatings with the best results for CAU-10 at intermediate time constants. The results highlight the potential of MOF coatings for adsorption chillers.

1. Introduction

Adsorption chillers can provide environmentally-friendly cooling but are typically limited by low specific cooling power (SCP) and coefficients of performance (COP) [1]. To overcome the limitations of state-of-the-art materials like silica gels or zeolites, advanced materials are developed. Metal-organic frameworks (MOFs) provide improved equilibrium properties such as high water uptake and well-located uptake step [2]. These improved equilibrium properties allow increasing the COP.

Despite promising equilibrium properties, the MOFs MIL-101(Cr) and NH₂-MIL-125 have shown poor specific cooling power SCP in granular form compared to commercial silica gel due to slow heat and mass transfer as well as low densities [3]. To also improve SCP, MOFs have been directly coated on heat exchanger surfaces with promising results [4,5]. However, benchmarking MOFs or comparing coatings with granulates is difficult.

To investigate the kinetic behavior of adsorbents, the Large-Temperature-Jump (LTJ) was developed by Aristov et al. [6] and advanced to the Infrared-LTJ (IR-LTJ) by Graf et al. [7] and Velte et al. [8]. However, different criteria have been employed to extract performance indicators from these LTJ experiments.

In this work, we perform IR-LTJ measurements of granular and coated adsorbents with water for adsorption and desorption. We then discuss two approaches to evaluate the IR-LTJ results.

2. IR-LTJ experiments

IR-LTJ requires less than 100 mg of the adsorbent allowing to benchmark adsorbents at an early development stage. The IR-LTJ setup (Figure 1) employs an IR-camera to monitor the temperature of the investigated adsorbent sample. The adsorbent sample is exposed to a temperature jump so that the kinetic behavior can be determined from the following step responses of pressure in the vapor phase p and temperature of the adsorbent T . The resulting change in loading X is measured indirectly from the change in vapor density in the known

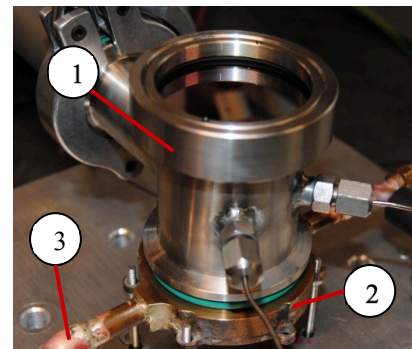


Figure 1 – Experimental IR-LTJ setup: measuring cell with IR-transparent cover (1), copper heat exchanger to control the sample temperature (2), and tubing for the heat exchanger (3).

volume through temperature and pressure measurements. As temperatures, we chose the commonly used triple 10/30/80 °C for evaporation, condensation/adsorption, and desorption, respectively. The refrigerant is water. As promising adsorbents, we selected Al-fumarate [4] and the aluminum-isophthalate CAU-10 [5]. Small samples of 44 mg Al-fumarate and 35 mg CAU-10, were coated on aluminum sheets (Radius $R = 15$ mm) to represent the conditions in a finned heat exchanger. To resolve the impact of the coating thickness, we also investigate two thinner coatings of 22 mg Al-fumarate and 25 mg CAU-10. The reference materials for comparison are the granular silica gels “SG 123” (Grace, 0.5-1.25 mm) and “Siogel” (Oker Chemie, 0-0.71 mm) which are also placed on aluminum sheets of the same size as the MOFs. The adsorbents differ in masses, diameters/coating thicknesses, and bulk densities (Table 1) so the question remains on how to compare these adsorbents.

Table 1 – Overview of the investigated adsorbents.

Material	Supplier	Mass m_{Ads} in mg	Diameter/Thickness in μm	Bulk Density ρ_{Ads} in g/cm^3
SG 123	Grace	1008	500 - 1250	0.710 ± 0.060
Siogel	Oker Chemie	436	0 - 710	0.710 ± 0.090
Al-fumarate	ISE ²	44	181.0 ± 17.5	0.343 ± 0.036
Al-fumarate	ISE ²	22	107.0 ± 12.0	0.291 ± 0.035
CAU-10	ISE ²	35	112.0 ± 22.6	0.442 ± 0.091
CAU-10	ISE ²	25	81.0 ± 11.3	0.437 ± 0.063

3. Interpretation of IR-LTJ experiments: Time constants versus mean powers

The kinetic behavior of the materials can be quantified by characteristic time constants τ as introduced by Aristov et al. [6]: The time constant $\tau_{X/X_{\text{eq}}}$ (X/X_{eq} in %) is the time evolved after the applied temperature jump until the loading X has reached a specified percentage of the equilibrium loading X_{eq} .

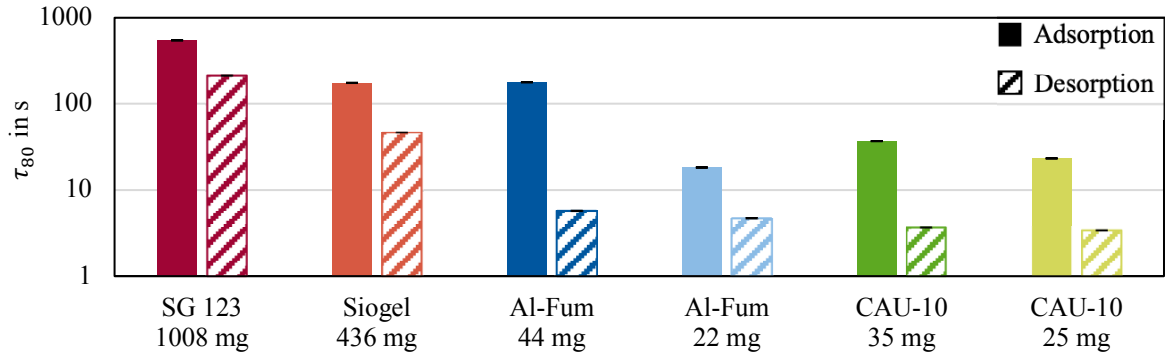


Figure 2 - Resulting characteristic times τ_{80} for 80% relative loading from the IR-LTJ for SG123, Siogel, Al-fumarate, and CAU-10-H for adsorption (filled) and desorption (hatched). Expanded measurement uncertainties are within the drawing accuracy.

The comparison of the characteristic time constants τ_{80} for 80 % relative loading in Figure 2 shows faster desorption than adsorption for all materials. MOF-coatings mostly have lower characteristic times than granular silica gels with the exception that τ_{ads} (for adsorption) of the 44 mg Al-fumarate sample is with 178 s on par with the characteristic time of Siogel (175 s). For desorption, Al-fumarate is the slower MOF (with $\tau_{\text{des}} = 6$ s), but is still 87 % faster than the faster benchmark material Siogel ($\tau_{\text{des}} = 46$ s). CAU-10 performs equally well as Al-fumarate for desorption and is even faster for adsorption.

However, the representation of process performance by characteristic times like τ_{80} can be misleading since the amount of adsorbed refrigerant is not included. Thus, the benefit of a high uptake capacity, which would also result in a high power density, is not considered. Based on Bendix et al. [9] and Ammann et al. [10], we, therefore, propose an alternative analysis of LTJ data by defining an area-specific mean power (Figure 3a)

$$\bar{P}_A = \frac{\Delta h_{\text{evap}} \cdot m_{\text{H}_2\text{O}, X/X_{\text{eq}}}}{A_{\text{hx}} \cdot \tau_{\text{ads}, X/X_{\text{eq}}}}, \quad [\bar{P}_A] = \frac{\text{kW}}{\text{m}^2} \quad (1)$$

with

$$m_{\text{H}_2\text{O}, X/X_{\text{eq}}} = \Delta X_{X/X_{\text{eq}}} \cdot m_{\text{Ads}}, \quad (2)$$

and a volume-specific mean power (Figure 3b)

$$\bar{P}_V = \frac{\Delta h_{\text{evap}} \cdot m_{\text{H}_2\text{O}, X/X_{\text{eq}}}}{V_{\text{Ads}} \cdot \tau_{\text{ads}, X/X_{\text{eq}}}} = \frac{\Delta h_{\text{evap}} \cdot \Delta X_{X/X_{\text{eq}}} \cdot \rho_{\text{Ads}}}{\tau_{\text{ads}, X/X_{\text{eq}}}}, \quad [\bar{P}_V] = \frac{\text{MW}}{\text{m}^3} \quad (3)$$

where Δh_{evap} is the enthalpy of evaporation (2477 kJ/kg at 10 °C) and $m_{\text{H}_2\text{O}, X/X_{\text{eq}}}$ is the adsorbed mass of water at varying relative loadings. Evaluating LTJ-measurements with \bar{P}_A incorporates the adsorbed refrigerant mass $m_{\text{H}_2\text{O}, X/X_{\text{eq}}}$ and the heat exchanger area A_{hx} (Eq. 1). Evaluating \bar{P}_V takes into account the adsorbent volume V_{Ads} (Eq. 3) determined by the bulk densities ρ_{Ads} from Table 1. The two different mean powers lead to a more comprehensive analysis than only the time constants, but still, the choice of time constants (e.g. τ_{50} , τ_{80} , τ_{95}) strongly affects the evaluation of the LTJ-measurements (Figure 3). This effect is similar to the choice of a cycle time which affects the trade-off between SCP and COP in the full-scale adsorption chiller [11]. As adsorption seems to be slower and thus the limiting phase (cf. Figure 2), we only evaluate the adsorption phase.

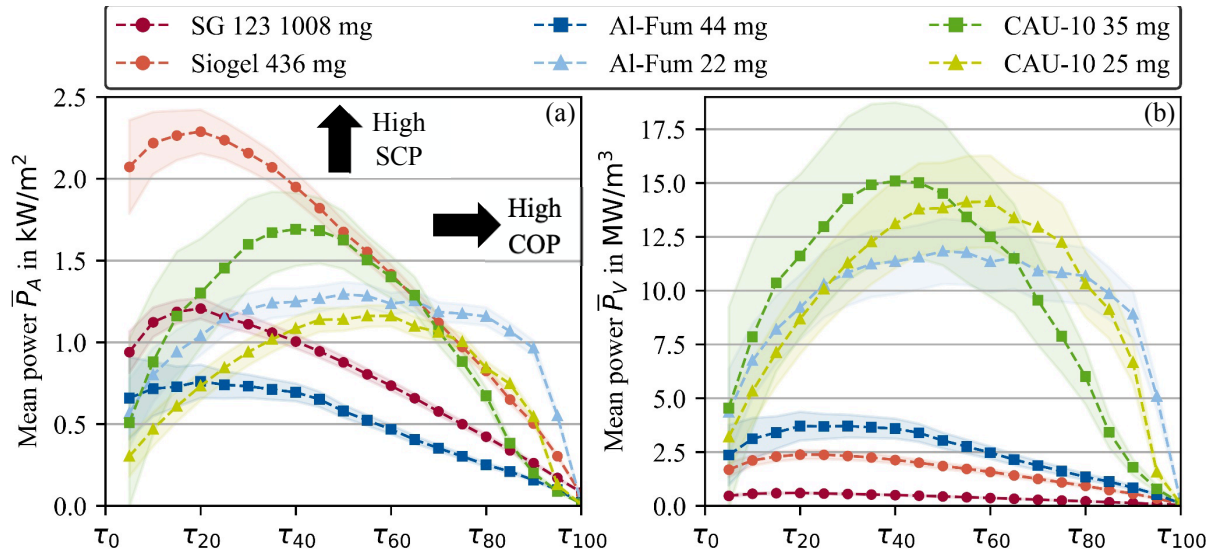


Figure 3 – Area-specific mean power \bar{P}_A (a) and volume-specific mean power \bar{P}_V (b) over different adsorption time constants τ_{ads} for the granular adsorbents SG 123 and Siogel as well as the MOF-coatings CAU-10 and Al-fumarate. Shaded areas represent measurement uncertainty with coverage factor $k = 1$ according to [12].

In Figure 3, small time constants are subject to a larger measurement uncertainty as decreasingly small pressure differences have to be detected with the indirect IR-LTJ experiment. Importantly, each adsorbent shows a distinct optimal relative loading where its mean power is maximal. The highest mean power is also provided by different adsorbents at different time constants τ_{ads} at which the LTJ-measurements are evaluated.

The highest area-specific power (Figure 3a) is provided by Siogel which is thus expected to maximize SCP. For high time constants $\tau_{\text{ads}} > 75\%$, however, the thin Al-fumarate coating yields maximal area-specific mean power. Regarding coating thickness, the thick coating of CAU-10 outperforms its thin coating while Al-fumarate shows the opposite trend. Additional research is needed to optimize coating thickness and to study limits on heat and mass transfer.

In Figure 3b, the volume-specific mean power of the adsorbents also depends on the chosen time constant τ_{ads} . Here, all MOF-coatings outperform the two silica gels with the best results for CAU-10. In contrast to Figure 3a, the volume-specific mean power not only accounts for the adsorbed mass but also for the volumes of the adsorbents (cf. Eq. 3).

While the observations only hold for the chosen temperature triple of 10/30/80 °C, the findings clearly show the importance of the chosen time constant τ_{ads} and the reference for the mean power.

4. Conclusion

The equilibrium properties of new materials are not sufficient to determine the overall performance of adsorption chillers. For this reason, we determine and compare characteristic times for ad- and desorption of Al-fumarate and

CAU-10 coatings to two commonly used granular silica gels by performing IR-LTJ-experiments for the refrigerant water. Our results show that the MOF-coatings can compete with classical granular silica gels with respect to area-specific chilling power and outperform the silica gels with respect to volume-specific chilling power. For the temperature triple 10/30/80 °C, the area-specific mean power is maximal at low relative loadings for Siogel; at intermediate relative loadings for the thick coating of CAU-10 as well as Siogel, and at high relative loadings for the thin coating of Al-fumarate. For the volume-specific mean power, all MOF-coatings outperform the silica gels with the best results for CAU-10. Thus, to exploit the advantages of MOF-coatings over granular silica gels, a dedicated adsorber design is required: An adsorber with the same available heat transfer area for granular and coated materials will not provide higher cooling power for MOF-coatings.

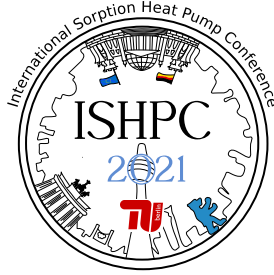
These results indicate the complex trade-offs between kinetic and equilibrium properties, between granulates and coatings as well as between heat transfer area and adsorbent volume. Additional insight could be gained by varying the temperature triple and the coatings' thicknesses. The presented approach shows that such studies should cover the full range of time constants. To study all resulting trade-offs including SCP and COP, heat exchanger metal mass needs to be incorporated into the analysis. For such an analysis the kinetic behavior should be employed as the basis for predictive dynamic models to determine the performance of full-scale adsorption chillers as proposed by Graf et al. [3].

Acknowledgment

We gratefully acknowledge the financial support from the German Federal Ministry for Education and Research (BMBF) in the founding initiative "KMU-innovativ" via the project Sorb-Zero (01LY1827B).

5. References

- [1] Meunier, F. (2013): Adsorption heat powered heat pumps. *Applied Thermal Engineering*, vol.61, pp.830-836.
- [2] deLange, M.F., Verouden, K.J.F.M., Vlugt, T.J.H., Gascon, J., Kapteijn, F. (2015): Adsorption-Driven Heat Pumps: The Potential of Metal-Organic Frameworks. *Chemical reviews*, vol.115, pp.12205-12250.
- [3] Graf, S., Redder, F., Bau, U., deLange, M., Kapteijn, F., Bardow, A. (2019): Toward Optimal Metal-Organic Frameworks for Adsorption Chillers: Insights from the Scale-Up of MIL-101(Cr) and NH₂-MIL-125. *Energy Technology*, vol.341, pp.1900617.
- [4] Jeremias, F., Fröhlich, D., Janiak, C., Henninger, S.K. (2014): Advancement of sorption-based heat transformation by a metal coating of highly-stable, hydrophilic aluminium fumarate MOF. *RSC Advances*, vol.4, pp.24073-24082.
- [5] Fröhlich, D., Pantatosaki, E., Kolokathis, P.D., Markey, K., Reinsch, H., Baumgartner, M., van der Veen, M.A., deVos, D.E., Stock, N., Papadopoulos, G.K., Henninger, S.K., Janiak, C. (2016): Water adsorption behaviour of CAU-10-H: a thorough investigation of its structure–property relationships. *Journal of Materials Chemistry A*, vol.4, pp.11859-11869.
- [6] Aristov, Y.I., Dawoud, B., Glaznev, I.S., Elyas, A. (2008): A new methodology of studying the dynamics of water sorption/desorption under real operating conditions of adsorption heat pumps: Experiment. *International Journal of Heat and Mass Transfer*, vol.51, pp.4966-4972.
- [7] Graf, S., Lanzerath, F., Bardow, A. (2017): The IR-Large-Temperature-Jump method: Determining heat and mass transfer coefficients for adsorptive heat transformers. *Applied Thermal Engineering*, vol.126, pp.630-642.
- [8] Velte, A., Földner, G., Laurenz, E., Schnabel, L. (2017): Advanced Measurement and Simulation Procedure for the Identification of Heat and Mass Transfer Parameters in Dynamic Adsorption Experiments. *Energies*, vol.10, pp.1130.
- [9] Bendix, P., Földner, G., Möllers, M., Kummer, H., Schnabel, L., Henninger, S., Henning, H.-M. (2017): Optimization of power density and metal-to-adsorbent weight ratio in coated adsorbers for adsorptive heat transformation applications. *Applied Thermal Engineering*, vol.124, pp.83-90.
- [10] Ammann, J., Michel, B., Studart, A.R., Ruch, P.W. (2019): Sorption rate enhancement in SAPO-34 zeolite by directed mass transfer channels. *International Journal of Heat and Mass Transfer*, vol.130, pp.25-32.
- [11] Bau, U., Bardow, A. (2019): Pareto-optimal performance of one-bed adsorption chillers by easy-to-implement heat-flow-based control. *Applied Thermal Engineering*, vol.159, pp.113590.
- [12] Joint Committee for Guides in Metrology (2012): Evaluation of measurement data - The role of measurement uncertainty in conformity assessment: JCGM106:2012. 1st ed. *JCGM 100 series - Guides to the expression of uncertainty in measurement (GUM series)*.



Performance evaluation of a double-lift concept for an adsorption refrigerator for high ambient temperatures

Kühn, Roland^{1*}, Göller, Christoph¹, Goerdten, Paul¹, Mähne, Kilian¹, Römer, Julia¹, Schrecker, Stefan¹

¹ Coolar UG (haftungsbeschränkt), Wolfener Str. 32-34/Haus C, 12681 Berlin, roland@coolar.co

Abstract:

The aim of the paper at hand is, to compare experimental data of a single-lift and a double-lift adsorption cycle when used in a refrigerator. The miniature adsorption cycle runs without electricity, water and silica gel is used as the working pair. The objective for this study was to provide 8 °C evaporator temperature at ambient temperatures of up to 43 °C.

Both systems reach the 8 °C evaporator temperature at 43 °C ambient temperature. The double-lift system provided a larger cooling capacity and achieved 2 K lower evaporator temperatures. The maximum cooling capacity of both systems is similar, due to a heat transfer restriction in the adsorber. An improved double-lift system will be used in a future refrigerator prototype designed for off-grid use.

1 Introduction

Nearly one billion people worldwide have no access to electricity [1] and many more have no reliable access. For many of these people this means, that access to basic healthcare services cannot be guaranteed as many critical medicines require reliable cooling which in most cases has to be realized with electricity driven refrigerators. The state-of-the-art medical off-grid refrigerators are “solar direct drive” (SDD) refrigerators. These refrigerators are directly driven by photovoltaic panels and use ice storages as a buffer to provide cooling at night and eliminate the bottlenecks that limited the use of photovoltaic or fossil fuel powered refrigerators for off-grid cooling previously: short battery life-time in hot and arid climate zones [2] or difficulties with the fuel supply [3]. However, the direct connection to the photovoltaic panel is also the major weakness of SDD refrigerators. The photovoltaic system has to be designed very carefully [2]. On the one hand, it must be assured that the starting current of the compressor of the refrigerator can be overcome. Until the intensity of solar irradiation on the photovoltaic panel generates a strong enough current to start the compressor, a significant share of the daily solar energy is wasted [4]. For the same reason, the compressor might stop working when the intensity of solar irradiation on the photovoltaic system drops, e.g. when clouds appear. Then the compressor might not be able to start again during the rest of the day and the refrigerator may become too warm to maintain proper storage temperatures for medicine [4]. This problem is partially mitigated by a new generation of compressors that was released in 2019 and requires a lower starting current [5]. On the other hand, cooling must be produced in a short time during a day, so, that refrigerators often become too cold [2]. Important medical substances like vaccines are spoiled when they are frozen [2]. Current attempts are to insulate the medicine from the walls of the refrigerator compartment via baskets (causing most of the refrigerator’s storage volume to be underutilized) or to integrate a better temperature regulation.

An alternative approach to solving these challenges is to use a completely different technology. Over the past 30 years, several concepts of solar thermally driven adsorption refrigeration units were realized. The solar irradiation during daytime is used to dry an adsorbent and cold is provided overnight to provide either cool water [6,7] or, at best, ice [7,8]. There is no temperature control and methanol is used as the refrigerant [6,7,8]. Unfortunately, in these known concepts, the cold room is often heated by condensing refrigerant during the regeneration of the adsorbent at daytime [8]. Thus, these concepts always require the intervention of the user, who manually transfers either the goods that have to be chilled, or the ice produced by the cooling system [8] into a nearby cool box. Besides, previous concepts have so far only used solar thermal collectors that were directly filled with the sorption medium [6,7,8]. Due to that, the collectors had to be connected to the cooling unit in a vacuum-tight manner. This greatly limits the flexibility to position the refrigerator in relation to the collector and leads to a high risk and vulnerability to leakages in the system. Previous concepts furthermore only achieved sufficient ice production for cooling at ambient temperatures well below 30 °C [7,8].

The team at Coolar UG has developed various prototypes for vaccine refrigerators based on adsorption refrigeration technology. As opposed to the concepts described above, these prototypes cool the cold room directly, use water as refrigerant and just need a simple water circuit heated by a solar thermal collector to drive the system [9]. As a result, the vacuum system can be kept at a compact size while the heat supply can be locally decoupled from the refrigerator. In addition, a good antifreeze-protection for the use-case of storing vaccines can be achieved, due to using water as the refrigerant. In a previous work, test results of a solar thermal off-grid refrigerator for 32 °C ambient temperature were presented, which is able to run without any electricity or batteries [9]. The paper at hand sets out to show first results from a test rig, which runs a standard single-lift adsorption cycle as well as a double-lift cycle. The aim is to show the differences of both processes when cooling a refrigerator at ambient temperatures of up to 43 °C while targeting evaporator temperatures below 8 °C.

2 Background/Fundamentals/Experimental Set-up

2.1 Experimental setup

Figure 1 shows a photograph of the test rig with the medical refrigerator cabinet (left) and a schematic of the internal adsorption refrigeration cycle setup (right), comprising an evaporator, two adsorption chambers and a condenser, separated by three check valves (I-III) and a U-tube. The internals of the adsorbers are finned tube bundle heat exchangers, which are filled with silica gel beads and are optimized for natural circulation in the external water circuit. The internal cycle is comparable to the one presented by Saha et.al [10] but consists of only two instead of four adsorption chambers. Thus, no continuous cooling can be provided. The external circuits and the self-made internal check valves are similar to the ones used in a former prototype [9].

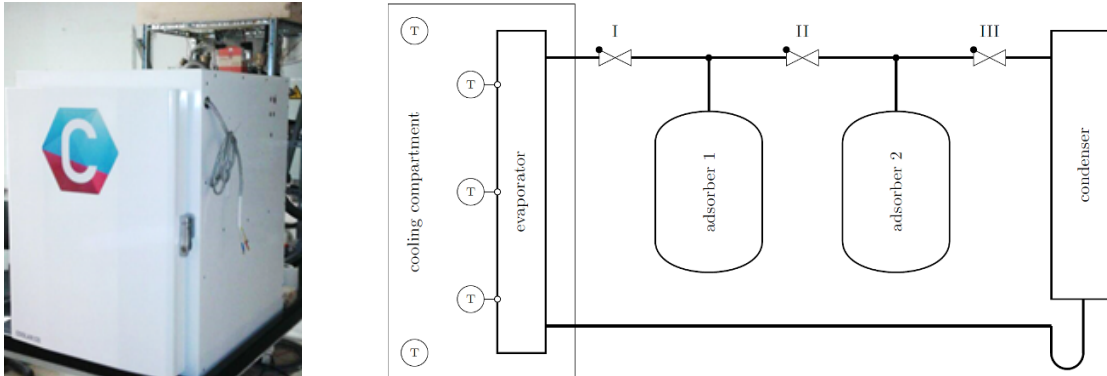


Figure 1 – Photograph of the test rig (left), schematic of the internal adsorption refrigeration cycle setup (right)

The two connected adsorption chambers are located between the evaporator and the condenser. Thereby, either an operation in single-lift or in double-lift mode is possible. In single-lift operation, both adsorbers are heated or cooled simultaneously and hence, operate together like a single adsorber. When both adsorbers are cooled, check valves I and II are open and water vapor flows from the evaporator to the adsorbers; when they are heated, water vapor flows from the adsorbers through valve II and III to the condenser. Depending on the condenser pressure and the liquid water fill level in the condenser during desorption, a certain amount of condensate flows back through the U-tube to the evaporator automatically.

In double-lift operation, the water vapor from the evaporator flows either exclusively to adsorber 1, when the pressure of adsorber 2 is higher than the evaporator pressure, or otherwise to both adsorbers. In contrast to the single-lift operation, in double-lift mode regeneration is done in two steps. In the first step of regeneration, only adsorber 1 is heated and adsorber 2 is still cooled; the water vapor is lifted from adsorber 1 to adsorber 2. In a subsequent step the now much more humid adsorber 2, in comparison to the single-lift operation, is heated and the water vapor flows to the condenser and is condensed and the liquid water flows back to the evaporator. The double-lift operation is intended to be used at high ambient temperatures, when the adsorber pressure would stay below the condenser pressure while regeneration in a single-lift process. However, the additional step where adsorber 1 is heated but adsorber 2 stays cool increases the controlling effort of the cycle.

All tests are performed in a climatic chamber at 43 °C (± 1 K). The adsorbers are unequal: adsorber 1 contains 6.6 kg silica gel while adsorber 2 contains 2kg. In the refrigerator prototypes, which are controlled by the day-night-cycle of the sun, the adsorbent mass is higher. In order to approximate the cooling performance of a full size adsorption cooling system in such a refrigerator prototype, nearly 4 cycles per day are performed in the test rig.

The ratio between adsorption and regeneration time is set in a way that simulates 8 hours per day of sufficient solar irradiation for regeneration.

2.2 Balancing

Several digital temperature sensors of the type Dallas DS18B20 are used for the balancing. The measurement uncertainty given by the manufacturer is 0.5 K.

To determine the cooling capacity, the heat infiltration rate into the refrigerator cabinet (UA) and the heat capacity of the refrigerator compartment (C) are needed. The heat infiltration rate UA is 0.618 W/K and includes the heat transfer through the refrigerator housing and the thermal bridges from the installed components, as well as the air circulation through seals. It was determined by using a constant electric heat source at steady state [9]. The heat capacity of the refrigerator compartment C is approximately 19.1 kJ/K. It results from the masses and heat capacities of the internals and fluids and was determined with warm-up tests at constant ambient temperature based on the known UA-value. When temperature differences between the individual refrigerator compartment components as well as their different rate of temperature change is neglected, the cooling capacity \dot{Q}_0 within a time step ($t_2 - t_1$) can be calculated from the temporal change of the mean cooling compartment temperature T_c and the ambient temperature T_a as follows:

$$\dot{Q}_0 = \frac{1}{t_2 - t_1} \int_{t_1}^{t_2} [UA \cdot (T_c(t) - T_a(t))] dt + C \cdot \frac{T_c(t_2) - T_c(t_1)}{t_2 - t_1} \quad (2)$$

The mean evaporator temperature is determined over the arithmetic mean of three temperature sensors located on the outside of the evaporator in equal vertical spacing above each other (Figure 1, right). The mean internal compartment temperature is given by the arithmetic mean of two sensors, one close to the bottom and one close to the top of the refrigerator compartment.

3 Test results at 43 °C ambient temperature

Figure 2 shows the trend of the cooling capacity over time at the top section and the mean evaporator and mean internal compartment temperature in the section below in comparison between single-lift (SL) and double-lift (DL) operation for three cycles. The process phases are marked on the top right part of Figure 2.

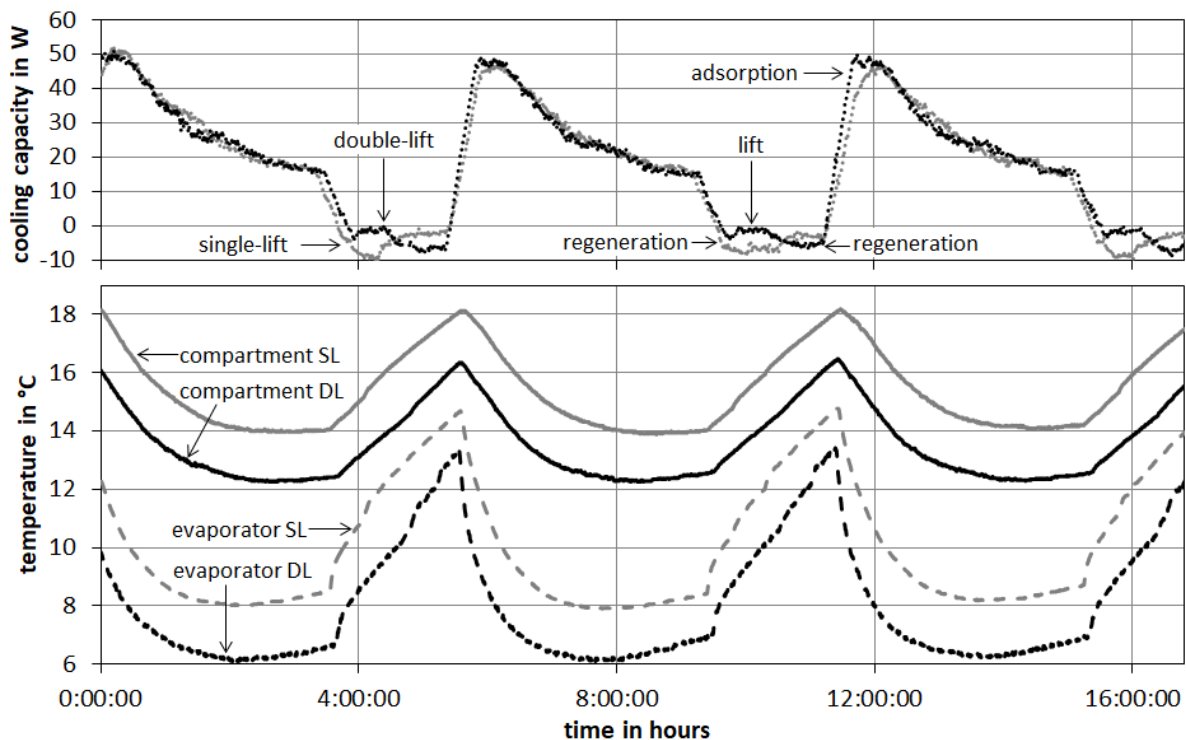


Figure 2 – temporal evolution of cooling capacity (top) and internal temperatures (bottom) during the test

The starting time in Figure 2 is the point at which the cooling capacity during adsorption reaches its maximum. While adsorption takes place the evaporator temperature decreases until a minimum is reached. At that time the compartment temperature is decreasing further and reaches a constant level. The cooling capacity is positive, reaches a rather steep maximum and decreases slightly afterwards while the loading of the adsorbent increases.

When adsorption stops and heating starts (after approx. 3.5 hours), the cooling capacity drops and the internal temperatures increase significantly.

During regeneration the cooling capacity becomes negative because the pressure in the condenser increases and condensed water is forced into the evaporator through the U-tube. During single-lift operation, the cooling capacity becomes negative right after regeneration starts, because both adsorbers are heated and push water vapor into the condenser. In double-lift operation, regeneration starts with the lift of water vapor from adsorber 1 to adsorber 2; adsorber 1 is heated and the generated water vapor is adsorbed by the cool adsorber 2 and no water vapor is condensed in the condenser. After half of the regeneration time has passed, adsorber 2 is heated and consequently starts to release water vapor into the condenser, causing the pressure to rise whereby liquid water is recirculated into the evaporator and the cooling capacity becomes negative. The total heat input into the refrigerator compartment caused by the condensate recirculation is approximately 25% lower for the double-lift than for the single-lift process, mainly due to the later recirculation when the evaporator temperature and pressure have been increased already.

During adsorption, the cooling capacity and the maximum cooling capacity that is reached are nearly the same in both modes of operation. The maximum cooling capacity is most likely restricted by heat transfer constraints as the maximum cooling capacity was similar in the tests at 43 °C and 32 °C (not shown here) ambient temperature. The heat exchanger designs of the adsorbers as well as of the evaporator were adopted from a former prototype, which was intended to run at 24h day-night-cycles [9]; but the test rig was operated about four times faster.

The most noticeable difference in the adsorption phase between single-lift and double-lift operation occurs at the beginning of the adsorption process. There, the cooling capacity curve is steeper and the maximum cooling capacity is reached earlier in double-lift operation than it is the case in single-lift operation. The duration of the cool-down period of adsorber 1 is similar in both modes of operation. However, adsorber 1 is much drier when the system is operated in double-lift mode than in single-lift mode, so that the temporary available adsorption capacity increases stronger with decreasing adsorber temperature. Hence, it can be noticed, that the decrease in evaporator temperature at the beginning of the adsorption is stronger in double-lift operation. Obviously, the total absorption capacity is also bigger in double-lift operation than in single-lift operation so that the total amount of cold generated during adsorption is also higher in double-lift mode. Hence, a 2 K lower mean evaporator and compartment temperature are achieved during double-lift operation compared to the single-lift operation. However, a much bigger difference between both processes was to be expected from the theoretically much bigger achievable difference in loading in the double-lift process.

For future investigations the components will be more harmonized to each other, especially regarding cycle times. Further tests on a fully functional stand-alone refrigerator prototype for 43 °C ambient temperature are planned for the summer of 2020.

4 Conclusions

A single-lift and a double-lift process were investigated on a test rig, which cools a medical refrigerator compartment. The experiments were performed in a climatic chamber, maintaining ambient temperature of 43 °C. The aim was to reach a temperature of 8 °C or below at the evaporator of the refrigerator.

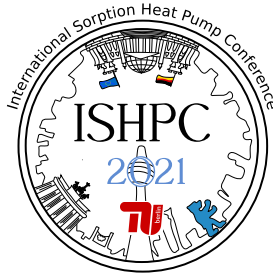
Using the single-lift process a mean evaporator temperature of 8 °C was reached. With the double-lift process a lower mean evaporator temperature just slightly above 6 °C is achieved, due to less internal process losses during regeneration and a higher adsorption capacity of the adsorber. However, restrictions, due to unfavorable component designs, were detected and a more significant difference between the two operation modes is to be expected in future setups.

5 Acknowledgment

The research was performed in the sub-project 01QE1916 “aDLA” funded by the German Federal Ministry of Education and Research within the project E!12900 “ARCTICOOL” funded and executed under the framework of the EU joint program Eurostars-2 with co-funding from the European Union Horizon 2020 research and innovation program. The team at Coolar expresses their thanks to them, the teams at the supervising Eureka! secretariat and the Eurostars office at DLR as well as to our partner Arctiko for their support.

6 List of References

- [1] International Energy Agency (2018): World Energy Outlook 2018, vol.1.
- [2] World Health Organization/UNICEF (2017): Solar direct-drive vaccine refrigerators: evidence brief.
- [3] McCarney S., Robertson, J., Arnaud, J., Lorenson, K., Lloyd, J. (2013): Using solar-powered refrigeration for vaccine storage where other sources of reliable electricity are inadequate or costly. *Vaccine*, vol.31 (51), pp.6050-6057.
- [4] World Health Organization (2020): E003 – Refrigerators and Freezers. *PQS devices catalogue: pre-qualified equipment for the Expanded Programme on Immunization (EPI)*, pp.28-181.
- [5] Pedersen, P., Katic, I, Markussen, W.B. Jensen, J.K., Cording, C., Moeller, H. (2019): Direct drive solar coolers, *Refrigeration Science and Technology Proceedings*, pp.3468-3475
- [6] Nwamba, K.J. (2008): The design and evaluation of a solar-powered adsorption refrigerator for African conditions. *Magisterial Thesis Dissertation, Tshwane University of Technology*.
- [7] Anyanwu, E.E., Ezekwe, C.I. (2003): Design, construction and test run of a solid adsorption solar refrigerator using activated carbon/methanol, as adsorbent/adsorbate pair. *Energy Conversion and Management*, vol.44 (18), pp.2879-2892.
- [8] Boubakri, A., Arsalane, M., Yous, B., Ali-Moussa, L., Pons, M., Meunier, F., Guillemot, J.J. (1992): Experimental study of adsorptive solar-powered ice makers in Agadir (Morocco) - 1. Performance in actual site. *Renewable Energy*, vol.2(1), pp.7-13
- [9] Kühn, R., Mähne, K., Düwel, K., Göller, C., Römer, J. (2019): First field test results of a solar thermal off-grid refrigerator for vaccines. *Refrigeration Science and Technology Proceedings*, pp. 3484-3492
- [10] Saha, B.B, Akisawa, A, Kashiwagi, T. (2001): Solar/waste heat driven two-stage adsorption chiller: the prototype. *Renewable Energy*, vol.23, pp.93-101.



Experimental investigation of an adsorption module based on heat exchangers with fibrous aluminium structures and the SAPO-34 / water working pair for gas-driven adsorption heat pumps

Velte, Andreas^{1*}, Joos, Lukas¹, Kostmann, Cris², Fink, Marcel², Földner, Gerrit¹

¹ Fraunhofer Institute for Solar Energy Systems (ISE), Heidenhofstrasse 2, 79111 Freiburg

* Corresponding author: andreas.velte@ise.fraunhofer.de

² Fraunhofer Institute for Manufacturing Technology and Advanced Materials (IFAM), Winterbergstraße 28, 01277 Dresden

Abstract:

Gas driven adsorption heat pumps require compact, efficient and cost effective adsorption modules. The design studied here is based on aluminum fiber heat exchangers. This technology is currently under development and only two modules with different size were studied up until now. The evaporator / condenser of the large scale module has the same size as the adsorption heat exchanger. In case of the downsized module, the adsorption heat exchanger is 60 % of the size of the large scale component and the evaporator / condenser is only 30 % of the size of the large scale component. Here, we present new measurement data of the small scale module and relate it to the data of the larger module. The evaluation on the component level shows that the downsizing of the evaporator has the advantage of a lower thermal mass, which could improve the efficiency. However, the downsizing has its price in terms of a higher heat and mass transfer resistance which lowers the evaporator power. A systematic study with different evaporator temperatures reveals the strong sensitivity of the module performance on this parameter.

1 Introduction

Wall hung condensing gas boilers are the most widely used technology for domestic heating and hot water supply in Germany and Europe (>4 million units sold per year in Europe) [1]. A reduction of CO₂ emissions can be achieved with further improvement of efficiency. The efficiency of burning gas is at its maximum – it cannot be improved further. With gas driven sorption heat pumps the efficiency can be improved – resulting need for this market segment: compact, efficient and cost-effective adsorption modules.

Several working pairs have been studied for the application in gas heat pumps (e.g. zeolite-water, AC-ammonia) [2], [3]. Adsorption modules with aluminium fiber heat exchangers and a directly crystallized layer of zeotype SAPO-34 with water as refrigerant are a promising candidate for high power density at acceptable efficiency, they were successfully built and evaluated [4]–[6]. The absolute size (and power) developed in the ADOSO project is too big for a wall hung system. Further room for improvement has been identified: thermal mass of evaporator / condenser has been too high in comparison to adsorber, this lowers the efficiency.

In this contribution we show results on a small scale adsorption module with a resized evaporator / condenser. In addition, the temperature conditions presented by [4] are not sufficiently representative for the space heating application, thus we show a systematic evaluation of more relevant temperature conditions.

2 Materials and methods

2.1 Adsorption module

The adsorption module in this study consists of two heat exchanger based on fibrous structures as described earlier by Wittstadt et al. [4]. The main dimensions of the module presented here (“Size S”) and the module measured by Wittstadt et al. (“Size L”) are listed in Table 1. Size S is based on a previous design study (“Size S design”), but due to production limitations not all design features could be realized. The thermal capacity for both the adsorption heat exchanger (adHX) and the combined evaporator / condenser (evco) including the heat transfer fluid (HTF) was calculated according to a recent publication of Gluesenkamp et al. [7]. The results are shown in Figure 1. The thermal mass relative to the adsorbent mass is 5.6 kJ/(kg ads·K) for size L and 9.4 kJ/(kg ads·K) for size S. This is a remarkable difference due to manufacturing limitations and has a negative impact on the efficiency. On the other hand, the lower thermal mass of the evaporator of the size S module will increase the efficiency. It can be calculated with the thermal mass of the components and the temperature difference between evaporation / condensation and adsorption / desorption that the efficiency (COP) of the “Size

S” module could be increased by 0.04 up to 0.08 in absolute numbers if the thermal mass relative to the adsorbent mass of the “Size S” module was 5.6 kJ/(kg·K) instead of 9.4 kJ/(kg·K).

Table 1 – Main dimensions and parameters of the adsorption modules

Quantity	Size L	Size S
Adsorption heat exchanger		
Adsorbent mass in kg	3.3±0.3	1.5±0.2
Heat exchanger dimensions in mm with headers	700x313x45	450x185x80
w/o headers	600x313x45	400x185x80
Volume in dm ³ with headers	9.9±0.1	5.7±0.1
Evaporator / condenser		
Heat exchanger primary area in m ²	43±2	14±1
Heat exchanger dimensions in mm with headers	700x313x45	450x158x45
w/o headers	600x313x45	400x158x45
Volume in dm ³ with headers	9.9±0.1	3.2±0.1
Module		
Dimensions in mm (w/o insulation)	730x320x147	474x169x188
Volume in dm ³ (w/o insulation)	34±0.2	15±0.2

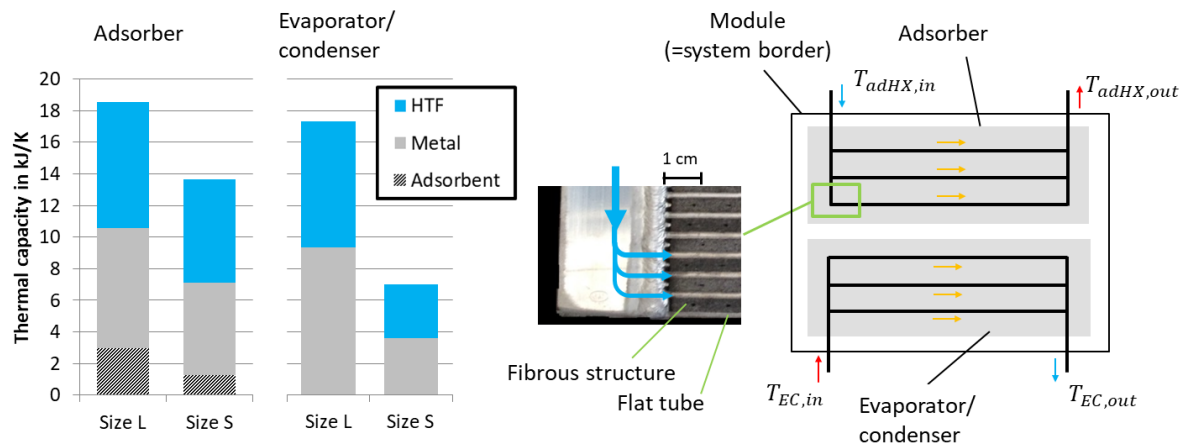


Figure 1 – Thermal capacities of the adsorber and the evaporator / condenser for two modules with different size (left), picture of a fiber heat exchanger (middle), schematic drawing of an adsorption module with fiber heat exchangers (right)

2.2 Experimental set-up for characterization of adsorption modules

The experimental set-up consists of three storage tanks (approx. 500 dm³) at three different temperature levels (5-10 °C, 20-60 °C, 70-110 °C) and controlled mixing units. The inlet temperature of the adsorption heat exchanger and the evaporator / condenser is changed periodically with this set-up in order to trigger the adsorption and the desorption process. The inlet- and outlet temperature of these two components is measured with Pt-100 sensors (+/- 0.01 K), the volume flows are measured with two magnetic-inductive flow sensors (Proline Promag 50P, Endress + Hauser, Germany, +/- 0.5 % relative uncertainty). The sub-atmospheric pressure in the module is measured with a capacitive pressure sensor (MKS Baratron, 0-100 mbar, approximately 1% relative uncertainty). Within just a few seconds, the supply temperature can be switched from e.g. ad- to desorption temperature level, and supply temperature can be kept stable with temperature fluctuations < 0.5 K.

2.3 Evaluation

The heat flows transferred into the components during desorption and evaporation as well as the heat flows extracted from the components during adsorption and condensation are calculated with the energy balance equations (2.1) and (2.2).

The data for the enthalpy h_L , are calculated with the IAPWS 97 formulation [8] with a script implemented by Holmgren [9].

$$\dot{Q}_{EC} = \dot{M}_{HTF,EC} \cdot (h_L(T_{EC,out}) - h_L(T_{EC,in})) \quad (2.1)$$

$$\dot{Q}_{adHX} = \dot{M}_{HTF,adHX} \cdot (h_L(T_{adHX,out}) - h_L(T_{adHX,in})) \quad (2.2)$$

The amount of heat released by the module during adsorption and condensation and the amount of heat transferred into the module during desorption and evaporation can be calculated by integrating equation (2.1) and (2.2). The efficiency for the heating application is the ratio between the heat extracted from the module during adsorption and condensation and the heat transferred to the module during desorption.

The power density is defined according to equation (2.3) with Q_{ads} being the amount of heat released during adsorption and Q_{cond} being the amount of heat released during condensation. The cycle time t_{cyc} is the time needed for one adsorption and one desorption half cycle. The volume of the module V_{module} is listed in Table 1.

$$\frac{P_{heat}}{V_{module}} = \frac{Q_{ads} + Q_{cond}}{V_{module} \cdot t_{cyc}} \quad (2.3)$$

An overall UA-value (i. e. the inverse of the overall transport resistance) for the evaporator / condenser can be calculated with equation (2.4) according to Wittstadt et al. [4]. The underlying assumption of this approach is that the (logarithmic mean) temperature difference between the saturation temperature of the module pressure $T_{sat}(p_{mod})$ and the temperature of the heat transfer fluid (HTF) $T_{EC,in/out}$ drives the evaporation and condensation processes.

$$(UA)_{EC} = \frac{\dot{Q}_{EC}}{\Delta T_{log}} = \frac{\dot{Q}_{EC}}{T_{EC,in} - T_{EC,out}} \cdot \ln \frac{T_{EC,in} - T_{sat}(p_{mod})}{T_{EC,out} - T_{sat}(p_{mod})} \quad (2.4)$$

In order to compare the performance of the two components (“Size S” and “Size L”) on the same basis, the overall UA-value in equation (2.4) can be calculated relative to the heat exchanger primary area A_p . The heat exchanger primary area is defined as the area of the heat exchanger that is in contact with the working fluid (water), i. e. fibrous structures, flat tubes, and headers. The contact area of the fibrous structure is the surface area of the fibers, which mainly depends on the diameter of the fibers and the porosity of the structure [10].

3 Results

More than 20 measurements at different temperature conditions and cycle times have been performed. The results proved to be reproducible after 7 months: absolute difference in COP was below 0.01, the relative deviation of the power density was below 2 %. The results for efficiency and power density of the two modules are shown in Figure 2. The temperature levels for evaporation, adsorption/condensation and desorption, the half cycle times and the numbering of points 2-6 are similar to the measurements of Wittstadt et al. [4].

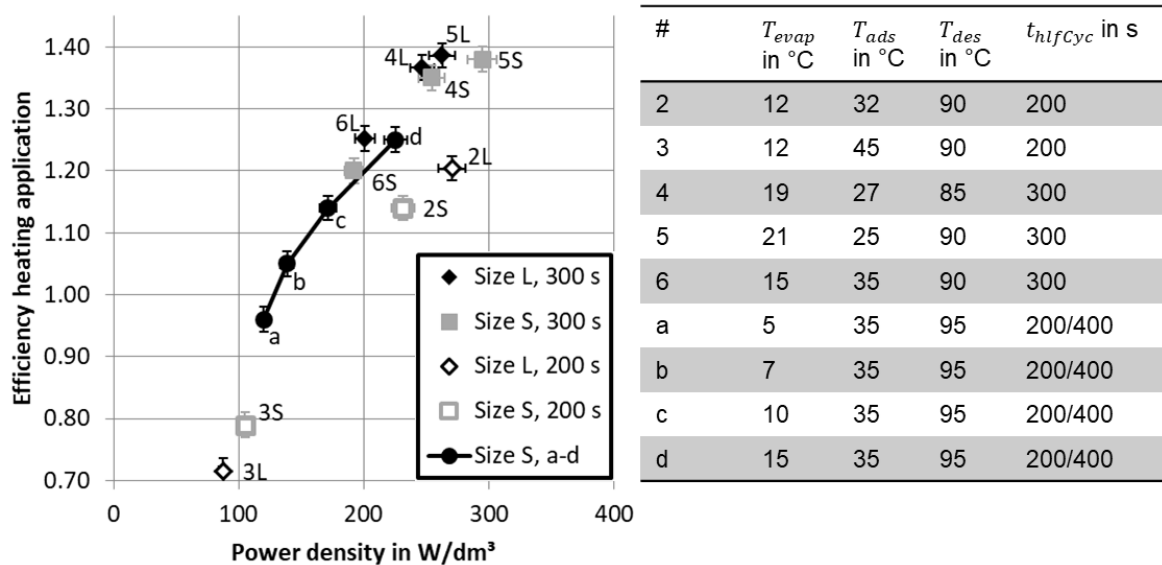


Figure 2 – Efficiency and power density for different temperature conditions and half cycle times. In points a-d the desorption half cycle time (200 s) is shorter than the adsorption half cycle time (400 s).

Points a-d were measured with the “Size S” module only, this is a variation of the evaporator temperature from 5 °C to 15 °C with constant adsorption/condensation temperature. The comparison of “Size S” and “Size L” results shows that the “Size S” module has a slight advantage in terms of power density in points 4 and 5 but a lower efficiency in points 2, 4-6. The lower efficiency in points 4 and 5 can be explained with the higher ratio of thermal mass to adsorbent mass of the “Size S” module. In points 2 and 6 the evaporator temperature is lower and the half cycle time shorter (only point 2). This further decreases the efficiency and the power density of the “Size S” module. It was observed that the “Size S” module needs at least 300 s (better 400 s) for evaporation / adsorption half cycle with reasonable efficiencies, whereas the desorption half cycle is finished after 200 s. Thus, asymmetric half cycle times (desorption shorter than adsorption) are chosen in points a-d. From the results of points a-d it can be clearly seen that the evaporator temperature has a strong impact on efficiency and power density.

The analysis of the time-dependent temperature curves of evaporator / condenser of the “Size S” module shows that the condensation process happens very fast, e. g. there is no temperature difference at the end of the desorption half cycle. The evaporation instead requires relatively large temperature differences over the whole cycle, even at the end. Thus, the evaporation seems to be the limiting process in the module. Out of the temperatures and the module pressure an overall UA-value for the evaporator is calculated according to equation (2.4). For the „Size S“ module these values are in the range of 400 W/K and 1600 W/K for the “Size L” module. It can be clearly seen that the downsizing of the evaporator / condenser has a strong impact on the UA-value. However, if we relate these figures to the primary area of the evaporator / condenser this yields 14...40 W/(m²K) for the „Size S“ component and 27...45 W/(m²K) for the „Size L“ component, i. e. not only the absolute UA-value is lower for „Size S“ but also the specific UA-value. Thus, the module performance suffers not only from the downsizing of the evaporator / condenser but also from the higher heat and mass transfer resistance of this component. A targeted component design requires much more data and a better understanding about the dependence of the heat and mass transfer resistances on the geometric parameters of the fibrous structures.

4 Conclusions

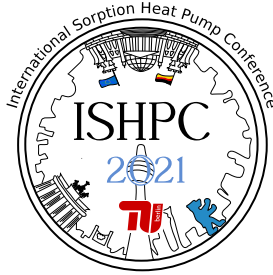
Systematic measurements revealed a strong sensitivity of dynamics of the adsorption module on evaporator temperature. The newly designed and downsized adsorption module with smaller evaporator/condenser yielded a good overall performance, however some issues showed to be problematic: The overall thermal mass of the adsorption heat exchanger relative to adsorbent mass is higher in comparison to Wittstadt et al. (downsize problem), the evaporator performance not sufficient for low temperatures (< 10 °C), and overall thermal mass relative to heat exchanger area is also higher in comparison to component presented by Wittstadt et al. (downsize problem). Still, the measured power density is definitely high enough to consider this technology for a wall-hung gas heat pump application. To achieve useful power output and acceptable performance, a low temperature heat source with temperatures >8°C is helpful. Buildings ventilation exhaust air could be considered as source. General feasibility of a gas heat pump based on such modules also depends on long-term stability and on production cost.

5 Acknowledgment

We would like to acknowledge that Marc Möllers organized the manufacturing process together with Fraunhofer IFAM. The funding of the Fraunhofer Zukunftsstiftung within the project HARVEST is gratefully acknowledged.

6 List of references

- [1] R. Kemna, M. van Elburg, A. Corso, J. Vigand, and V. Maagoe, Space and Combination Heaters - Market Analysis: Ecodesign and Energy Labelling, European Commission Brussels (BE), VHK Delft (NL), BRG Building Solutions London (UK), 2019.
- [2] B. Dawoud and Y. Aristov, Experimental study on the kinetics of water vapor sorption on selective water sorbents, silica gel and alumina under typical operating conditions of sorption heat pumps, *Int. J. Heat Mass Tran.*, vol. 46, no. 2, pp. 273–281, 2003.
- [3] S. J. Metcalf, R. E. Critoph, and Z. Tamainot-Telto, Optimal cycle selection in carbon-ammonia adsorption cycles, *International Journal of Refrigeration*, vol. 35, no. 3, pp. 571–580, 2012.
- [4] U. Wittstadt, G. Földner, E. Laurenz, A. Warlo, A. Große, R. Herrmann, L. Schnabel, and W. Mittelbach, A novel adsorption module with fiber heat exchangers: Performance analysis based on driving temperature differences, *Renewable Energy*, vol. 110, pp. 154–161, 2017.
- [5] U. Wittstadt, G. Földner, O. Andersen, R. Herrmann, and F. Schmidt, A New Adsorbent Composite Material Based on Metal Fiber Technology and Its Application in Adsorption Heat Exchangers, *Energies*, vol. 8, no. 8, pp. 8431–8446, 2015.
- [6] U. Wittstadt, A. Velte, M. Kleinstück, R. Volmer, C. Kostmann, and O. Andersen, Entwicklung einer Gasadsorptionswärmepumpe mit einem aufkristallisierten Adsorptionswärmeübertrager und einem neuartigen Verdampfer/Kondensator-Apparat (ADOSO), Teilvorhaben A: Entwicklung des Gesamtsystems der Adsorptionswärmepumpe, Teilvorhaben C: Aufkristallisation und Weiterentwicklung Zeolith auf Metallfaserstrukturen, gemeinsamer Abschlussbericht, Laufzeit des Vorhabens: 01.05.2013-31.10.2016, TIB - Technische Informationsbibliothek Universitätsbibliothek Hannover, 2016.
- [7] K. R. Gluesenkamp, A. Frazzica, A. Velte, S. Metcalf, Z. Yang, M. Rouhani, C. Blackman, M. Qu, E. Laurenz, A. Rivero-Pacho, S. Hinners, R. Critoph, M. Bahrami, G. Földner, and I. Hallin, Experimentally Measured Thermal Masses of Adsorption Heat Exchangers, *Energies*, vol. 13, no. 5, p. 1150, 2020.
- [8] W. Wagner, J. R. Cooper, A. Dittmann, J. Kijima, H.-J. Kretzschmar, A. Kruse, R. Mares, K. Oguchi, H. Sato, I. Stöcker, O. Sifner, Y. Takaishi, I. Tanishita, J. Trübenbach, and T. Willkommen, The IAPWS Industrial Formulation 1997 for the Thermodynamic Properties of Water and Steam, *Journal of Engineering for Gas Turbines and Power*, vol. 122, no. 1, pp. 150–184, 2000.
- [9] M. Holmgren, *XSteam*. Available: https://www.academia.edu/download/39720574/X_Steam_for_Matlab.pdf (2020, Mar. 10).
- [10] M. Fink, O. Andersen, T. Seidel, and A. Schlott, Strongly Orthotropic Open Cell Porous Metal Structures for Heat Transfer Applications, *Metals*, vol. 8, no. 7, p. 554, 2018.



Determination of heat and mass transfer parameters of adsorption dynamics in MOF aluminium fumarate coatings with volume swing frequency response measurements

Laurenz, Eric^{1*}, Velte, Andreas¹, Schnabel, Lena¹, Földner, Gerrit¹, Schmitz, Gerhard²

¹ Fraunhofer Institute for Solar Energy Systems (ISE), Heidenhofstr. 2, 79111 Freiburg

*Corresponding authors: eric.laurenz@ise.fraunhofer.de, gerrit.foldner@ise.fraunhofer.de

²Technical University Hamburg, Institute for Technical Thermodynamics (M-21), Denickestr. 17, 21073 Hamburg

Abstract:

In this contribution we focus on the differentiation and quantification of different heat and mass transfer phenomena governing the overall sorption dynamics for the example of a binder based aluminium fumarate coating for heat transformation applications with water as refrigerant. The methodological emphasis is on extending the volume swing frequency response (FR) method to problems which are dominated by heat transfer. Finally, the transfer parameters are mapped to sample's temperature and loading state in order to be able to reproduce the non-linear behaviour exhibited under application conditions. Based on a model with space discretised heat transfer and linear driving force (LDF) simplified micro pore diffusion, the thermal conductivity of the samples was identified to about 0.07 W/(m K) and the micro pore transport diffusivity between 3×10^{-12} and 1×10^{-10} m²/s at 40 °C, with a characteristically U-shaped loading dependency. The heat transfer coefficient h for the contact between coating and support was identified to $\geq 4 \times 10^3$ W/(m²K). The model is validated with a non-linear simulation, informed solely by parameters obtained from the new FR-based method, which is compared to results from a large temperature jump experiment.

1 Introduction

Adsorption chillers are an environmentally friendly solution for the valorisation of waste or solar heat for cooling demands. The working principle allows a simple, robust and scalable design. Adsorption chillers and heat pumps have been applied successfully for different applications like solar thermal cooling of buildings [1], gas adsorption heat pumps [2] and more [3]. A possible application that has attracted rising interest in recent years is the provision of data centre cooling driven by heat yielded from water cooled CPUs. Current high performance CPUs allow cooling water temperatures of up to 60 °C or more [4] that can be used to drive adsorption chillers.

Development of new adsorbent materials has been a research interest for many years. Aluminium fumarate, a metal-organic framework (MOF) that attracted increasing interest for thermal applications in recent years, exhibits adsorption equilibrium properties that fit well to the boundary conditions of this cycle [5]. Due to its beneficial stepwise isotherm it allows considerably more efficient cycles compared to the state of the art material silica gel with a good hydrothermal cycle stability [6]. The material is potentially a low cost material due to widely available educts (Al-salts and fumaric acid) and water based synthesis route [7].

The increase of volume specific cooling power (VSCP) – thus reduction of specific costs – while keeping a reasonably high COP is one of the major development challenges for adsorption chillers [8]. Typical values for COPs of market available adsorption chillers are in the order of 0.5 to 0.65 [9]. In the case of data centre cooling the target COP is determined by the ratio of low temperature cooling demand and available waste heat from CPUs which typically is in the same range [4]. A promising approach to increase VSCP is to use binder based adsorbent coatings to allow for a substantially better heat transfer to the heat exchanger structure in comparison to loose grain bed, the state of the art solution [10]. Further performance increase can be reached through model based design and optimization which is more cost-effective than empiric trial-and-error prototyping [11]. However, model based design requires detailed knowledge of a) relevant physical heat and mass mechanisms and the corresponding transfer coefficients, b) the adsorption equilibria, c) the adsorption enthalpy and d) the specific heat capacities, allowing for models with explicit dependency on design parameters like heat exchanger

geometry, layer thicknesses and particle sizes. In this work we propose a comprehensive approach to gain most of this data from small representative Ad-HX cutouts based on the frequency response (FR) analysis.

Moreover, the volume swing FR apparatus used here also allows for measurements of the differential adsorption equilibrium, i.e. the slopes of the isotherm and the isobar, through the equilibrium response for small step experiments. Both slopes can be directly combined to determine the differential adsorption enthalpy.

In the following, a brief summary of experimental set-up and measured quantities is given. Main focus is then on actual results from the measurement and validation of a dynamic model of overall adsorption dynamics which makes use of the measured parameters.

2 Materials and methods

Aluminium sample plates (5x5 cm²) were partly coated ($A_{ct} = 18.9$ cm²) with different thicknesses d_{ct} (0.14, 0.24, 0.61 mm) in a specific process and characterised as described before [12] resulting in different coating dry masses (134, 217, 563 mg). The particle size of the initial adsorbent powder was measured to 18 μ m on average.

2.1 Experimental set-up

Frequency response measurements are done with a custom setup detailed earlier [16]. In addition, this setup allows large temperature jump (LTJ), large pressure jump (LPJ) and small pressure jump (SPJ) experiments with water [13–15]. The closed measurement chamber volume ($\bar{V} = 885.4 \pm 1.3$ ml) is varied sinusoidally by 4.12% with a flexible bellow that is driven by a stepper motor. The bellow position is recorded and calibrated to the chamber volume. The sinusoidal response of the chamber pressure is recorded simultaneously with two pressure transducers. Additionally, the sample's surface temperature is recorded with an IR temperature sensor through a ZnSe vacuum viewport.

Thus, this volume swing thermal FR inspired by approaches from other authors [16–20] is extended by a thorough control of the sample's thermal contact and a temperature response measurement in order to discriminate between heat and mass transfer effects.

2.2 Model

The framework for FR modelling is mainly based on the transfer function approach suggested by Wang and LeVan [21]. The principal assumptions are:

1. Perturbations of loading, pressure and temperature are sufficiently small to allow the linearization of all equations with constant coefficients. These coefficients are assumed local for the given mean state but may be different for different mean state, i.e. different experiments.
2. The pressure in the chamber is uniform.
3. The temperature of the gas in the chamber is constant and equal to the sample support's.
4. Adsorption occurs only on the sample and not on the chamber walls.
5. The chamber contains a pure working fluid atmosphere (single component adsorption).
6. The gas may be described as ideal gas which is a very good approximation for water in the pressure (< 100 mbar) and temperature (20–100 °C) region of interest here.

More in depth information on the FR modelling will be published in a journal publication.

For modelling of macro pore diffusion in even layers of adsorbent coating and intra crystalline (micro pore) diffusion in non-isotropic materials with a single preferred diffusion direction like aluminium fumarate [22] the diffusion equation needs to be solved on an even plate or slab geometry. Moreover, to model the heat transfer effect of coating thickness a 1D-heat-transfer model with contact resistance is required.

For this work we developed the FR solutions for differently simplified heat and mass transfer models describing the coupled adsorption dynamics and then found which model would best describe the actual situation.

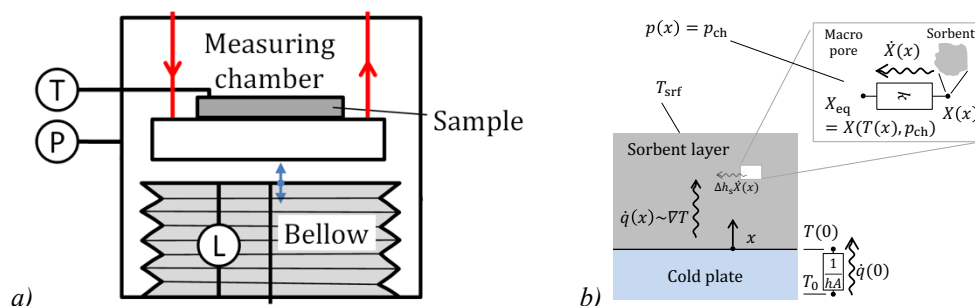


Figure 1: Principles of a) the measurement set-up and b) the best fitting model (discretised heat transfer and LDF-simplified micro pore diffusion) developed amongst others for FR parameter identification

2.3 Evaluation

Most model parameters can be determined externally or in the first part of the measurement procedure [12], whereas the parameters for heat and mass transfer are identified through a generalised weighted least squares method following an approach from Marsili-Libelli [23]. The value for the error functional of the best estimate of the parameter vector is an average relative deviation between the fitted model and the experiment.

3 Results

Sorption equilibria and enthalpy have been evaluated with a separate procedure within the same set-up [12]. The isotherm confirms the step-like form known for aluminium fumarate with a temperature dependent inflection point at $p_{\text{rel}} \approx 0.25, 0.28$ and 0.33 for $30, 40$ and 60 °C. The differential enthalpy of adsorption calculated from the measurements is 2.90 ± 0.05 MJ/kg (52.2 ± 1.0 kJ/mol) on average which is about 10–15% higher than expected by a simple Dubinin approximation.

3.1 Transport parameters

Based on the model with discretised heat transfer through the composite layer and LDF-simplified micro pore diffusion assuming a diffusion length of 9 μm based on adsorbent particle size distribution (1DHT_miLDF, Figure 1b) the thermal conductivity of the samples was identified to about 0.07 W/(m K) and the micro pore transport diffusivity between 3×10^{-12} and 1×10^{-10} m^2/s at 40 °C. The characteristically U-shaped loading dependency, i.e. the transport diffusivity is small for intermediate loadings and large for low/high loadings, may be explained with the pronounced change of the Darken factor due to the step-like isotherm [24]. After Darken correction, the self-diffusivity is roughly estimated to about $2\text{--}7 \times 10^{-12}$ m^2/s at 25 °C. The heat transfer coefficient h for the contact between coating and support was identified to $\geq 4 \times 10^3$ W/(m^2K). An upper boundary for h cannot be given, as it showed to be irrelevant for the overall transport process (non-identifiable).

3.2 Validation with LTJ results

By Pulsed Field Gradient Nuclear Magnetic Resonance (PFG-NMR) a value of $3\text{--}5 \times 10^{-10}$ m^2/s at 25 °C has been found for the micro pore self-diffusivity of water in aluminium fumarate [25] which differs from our results by about two orders of magnitude. To achieve this value for the micro pore diffusion, a diffusion length of about 100 μm needs to be assumed. Since the length scale relevant for micro pore diffusion in the coated layers can only be guessed, FR is the method of choice for the determination of the relevant heat and mass transfer coefficients. The results obtained by FR are validated by comparison to available results from LTJ measurements on the same samples [26]. Thus, an accurate prediction of the LTJ validates the parameters obtained as a basis for application oriented component design and optimisation. To this end, the transport and thermodynamic parameters, identified by the FR-method, were used for a non-linear simulation of an LTJ response, using an existing implementation of the 1DHT_miLDF model (Figure 1b) in the time domain [15]. The simulation is based on loading and temperature dependent micro pore diffusivity and constant thermal conductivity, obtained by FRA, a constant adsorption enthalpy and the fitted adsorption equilibrium, identified in-situ for the same samples through an extended procedure [12]. The simulation is solely based on parameters identified by FRA, without any fitting in the time domain.

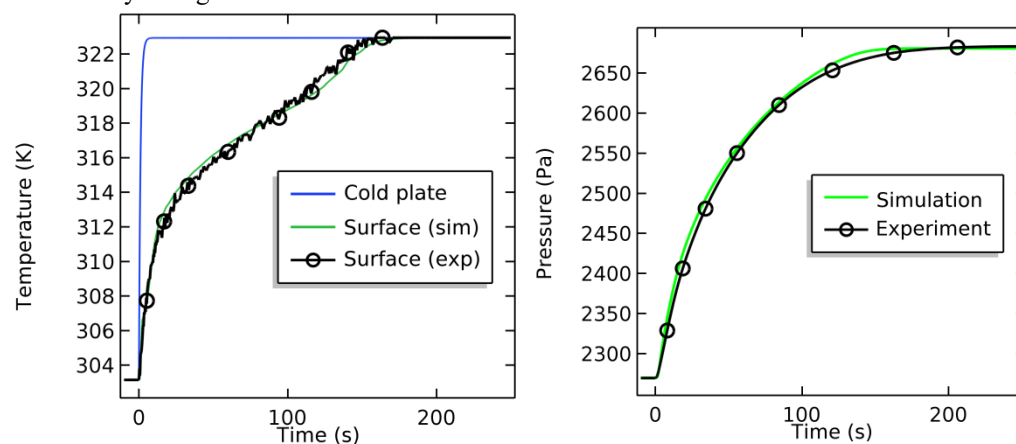


Figure 2: Response of surface temperature (left) and chamber pressure (right) on a large jump of the cold plate temperature (desorption) measured (exp) for sample Ct_610 and simulated with the T, X -dependent transport and equilibrium parameters identified in this work (sim).

The results show very good agreement (Figure 2), validating the aforementioned procedures and identification results. The deviation between measurement and simulation show an improvement compared to previous work where similar transport models were fitted directly in the time domain [15,27]. Our results indicate that the deviation observed before was rather due to the incompletely mapped state dependency of the transfer coefficients than to the general model simplifications, like the reduction of particle size and layer thickness distributions to single values. Obtaining precise state dependent transfer coefficients on samples of relevant scale for practical component design is a specific feature of the FR method, distinguishing it from methods based on fits in the time domain as well as from direct measurements e.g. for diffusion coefficients like PFG-NMR.

4 Conclusions

We developed and validated a method for local (in the thermodynamic state space) measurements of the sorption dynamics based on the frequency response analysis (FRA). Combined with linearized heat and mass transfer models in the Laplace domain, physical transport coefficients can be determined. These coefficients with their state dependency allow precise non-linear modelling of application-relevant processes in the time domain. As these models are explicitly including geometrical parameters they may be directly used for design and optimisation of adsorber heat exchangers (Ad-HX) for adsorption heat pumps and chillers. In particular, a model was developed that takes the spatial temperature distribution into account.

The coated samples showed a high performance. Due to the sorption equilibrium of aluminium fumarate this performance can be achieved under very favourable temperature conditions with low driving temperature. Further improvement is expected by more compact coatings with smaller adsorbent particles.

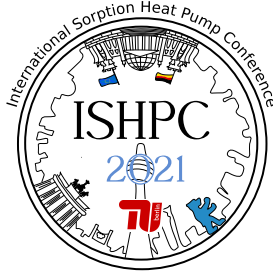
5 Acknowledgment

This work resulted widely from the PhD project of Eric Laurenz for which funding by Heinrich Böll Stiftung is gratefully acknowledged. In addition, funding by BMBF for project WasserMod2 (FKZ 03ET1554A) is gratefully acknowledged.

6 List of references

- [1] F. Meunier, Adsorption heat powered heat pumps, *Appl. Therm. Eng.* 61 (2013) 830–836. <https://doi.org/10.1016/j.applthermaleng.2013.04.050>.
- [2] U. Wittstadt, G. Földner, E. Laurenz, A. Warlo, A. Große, R. Herrmann, L. Schnabel, W. Mittelbach, A novel adsorption module with fiber heat exchangers: Performance analysis based on driving temperature differences, *Renewable Energy* 110 (2017) 154–161. <https://doi.org/10.1016/j.renene.2016.08.061>.
- [3] D.C. Wang, Y.H. Li, D. Li, Y.Z. Xia, J.P. Zhang, A review on adsorption refrigeration technology and adsorption deterioration in physical adsorption systems, *Renewable and Sustainable Energy Reviews* 14 (2010) 344–353. <https://doi.org/10.1016/j.rser.2009.08.001>.
- [4] T. Wilde, M. Ott, A. Auweter, I. Meijer, P. Ruch, M. Hilger, S. Kuhnert, H. Huber, CoolMUC-2: A supercomputing cluster with heat recovery for adsorption cooling, in: *Thirty-third Annual Semiconductor Thermal Measurement and Management Symposium*, San Jose, CA, USA, IEEE, Piscataway, NJ, U.S.A., 2017, pp. 115–121.
- [5] D. Lenzen, J. Zhao, S.-J. Ernst, M. Wahiduzzaman, A. Ken Inge, D. Fröhlich, H. Xu, H.-J. Bart, C. Janiak, S. Henninger, G. Maurin, X. Zou, N. Stock, A metal-organic framework for efficient water-based ultra-low-temperature-driven cooling, *Nat. Commun.* 10 (2019) 3025. <https://doi.org/10.1038/s41467-019-10960-0>.
- [6] H. Kummer, F. Jeremias, A. Warlo, G. Földner, D. Fröhlich, C. Janiak, R. Gläser, S.K. Henninger, A Functional Full-Scale Heat Exchanger Coated with Aluminum Fumarate Metal-Organic Framework for Adsorption Heat Transformation, *Ind. Eng. Chem. Res.* 56 (2017) 8393–8398. <https://doi.org/10.1021/acs.iecr.7b00106>.
- [7] C. Kiener, U. Müller, M. Schubert (BASF SE) WO/2007/118841.
- [8] L. Schnabel, G. Földner, A. Velte, E. Laurenz, P. Bendix, H. Kummer, U. Wittstadt, Innovative Adsorbent Heat Exchangers: Design and Evaluation, in: H.-J. Bart, S. Scholl (Eds.), *Innovative Heat Exchangers*, Springer International Publishing, Cham, 2018, pp. 363–394.

- [9] ASUE, Marktübersicht Gaswärmepumpen 2017/18, 2017.
https://asue.de/sites/default/files/asue/themen/gaswaermepumpe_kaelte/2017/broschueren/ASUE_Marktuebersicht-Gaswaermepumpen_2017.pdf (accessed 6 February 2019).
- [10] A. Freni, B. Dawoud, L. Bonaccorsi, S. Chmielewski, A. Frazzica, L. Calabrese, G. Restuccia, Adsorption Heat Exchangers, in: A. Freni (Ed.), Characterization of zeolite-based coatings for adsorption heat pumps, Springer, Cham, 2015, pp. 35–53.
- [11] S. Graf, S. Eibel, F. Lanzerath, A. Bardow, Validated Performance Prediction of Adsorption Chillers: Bridging the Gap from Gram-Scale Experiments to Full-Scale Chillers, *Energy Technol.* (2020) 1901130. <https://doi.org/10.1002/ente.201901130>.
- [12] E. Laurenz, G. Földner, L. Schnabel, G. Schmitz, A Novel Approach for the Determination of Sorption Equilibria and Sorption Enthalpy Used for MOF Aluminium Fumarate with Water, *Energies* 13 (2020) 3003. <https://doi.org/10.3390/en13113003>.
- [13] L. Schnabel, Experimentelle und numerische Untersuchung der Adsorptionskinetik von Wasser an Adsorbens-Metallverbundstrukturen. Dissertation, Berlin, 2009.
- [14] G. Földner, Stofftransport und Adsorptionskinetik in porösen Adsorbenskompositen für Wärmetransformationsanwendungen. Dissertation, Universität Freiburg, Freiburg, 2015.
- [15] A. Velte, G. Földner, E. Laurenz, L. Schnabel, Advanced Measurement and Simulation Procedure for the Identification of Heat and Mass Transfer Parameters in Dynamic Adsorption Experiments, *Energies* 10 (2017) 1130. <https://doi.org/10.3390/en10081130>.
- [16] M.D. Turner, L. Capron, R.L. Laurence, W.C. Conner, The design and construction of a frequency response apparatus to investigate diffusion in zeolites, *Review of Scientific Instruments* 72 (2001) 4424–4433. <https://doi.org/10.1063/1.1408931>.
- [17] D. Shen, L.V.C. Rees, Study of fast diffusion in zeolites using a higher harmonic frequency response method, *Journal of the Chemical Society, Faraday Transactions* 90 (1994) 3011–3015.
- [18] L. Song, L.V.C. Rees, Frequency Response Measurements of Diffusion in Microporous Materials, in: H.G. Karge, J. Weitkamp (Eds.), *Adsorption and Diffusion*, Springer Berlin Heidelberg, Berlin, Heidelberg, 2008, pp. 235–276.
- [19] S.C. Reyes, J.H. Sinfelt, G.J. DeMartin, R.H. Ernst, E. Iglesia, Frequency modulation methods for diffusion and adsorption measurements in porous solids, *The Journal of Physical Chemistry B* 101 (1997) 614–622.
- [20] Mohammad Iftekhar Hossain, Volume Swing Frequency Response Method For Determining Mass Transfer Mechanisms in Microporous Adsorbents. Doctoral dissertation, 2014.
- [21] Y. Wang, M.D. LeVan, Master curves for mass transfer in bidisperse adsorbents for pressure-swing and volume-swing frequency response methods, *AIChE Journal* 57 (2011) 2054–2069. <https://doi.org/10.1002/aic.12420>.
- [22] E. Alvarez, N. Guillou, C. Martineau, B. Bueken, B. Van de Voorde, C. Le Guillouzer, P. Fabry, F. Nouar, F. Taulelle, D. de Vos, J.-S. Chang, K.H. Cho, N. Ramsahye, T. Devic, M. Daturi, G. Maurin, C. Serre, The Structure of the Aluminum Fumarate Metal-Organic Framework A520, *Angew. Chem. Int. Ed.* 54 (2015) 3664–3668. <https://doi.org/10.1002/anie.201410459>.
- [23] S. Marsili-Libelli, *Environmental Systems Analysis with MATLAB®*, CRC Press, Boca Raton, 2016.
- [24] J. Kärger, C. Chmelik, L. Heinke, R. Valiullin, A new view of diffusion in nanoporous materials, *Chemie Ingenieur Technik* 82 (2010) 779–804. <https://doi.org/10.1002/cite.201000038>.
- [25] T. Splith, D. Fröhlich, S.K. Henninger, F. Stallmach, Development and application of an exchange model for anisotropic water diffusion in the microporous MOF aluminum fumarate, *Journal of magnetic resonance* 291 (2018) 40–46. <https://doi.org/10.1016/j.jmr.2018.04.009>.
- [26] E. Laurenz, A. Velte, H. Kummer, G. Földner, L. Schnabel, Adsorption dynamics of MOF coatings for waste heat driven cooling, in: *Proceedings of the 25th IIR International Congress of Refrigeration*, Montréal Canada, France, 2019.
- [27] A. Frazzica, G. Földner, A. Sapienza, A. Freni, L. Schnabel, Experimental and theoretical analysis of the kinetic performance of an adsorbent coating composition for use in adsorption chillers and heat pumps, *Applied Thermal Engineering* 73 (2014) 1022–1031. <https://doi.org/10.1016/j.applthermaleng.2014.09.004>.



A 3D printed capillary-assisted low-pressure evaporator, CALPE, for sorption systems cooling and heat pumps

G. Bamorovat Abadi and Majid Bahrami

Laboratory for Alternative Energy Conversion (LAEC), School of Mechatronic Systems Engineering,
Simon Fraser University, BC, Canada V3T 0A3, mbahrami@sfu.ca

Abstract:

The main obstacles preventing the commercialization of waste-heat driven sorption systems are their low performance, large weight, and high cost. Capillary-assisted low-pressure evaporators (CALPEs) are a compact solution for increasing the power density of closed-cycle adsorption systems including heat pumps, heat transformers, desalination, and thermal energy storage systems. This paper presents experimental results for a 3D printed metallic CALPE and compares its performance with analytical models available in the literature. Tests are performed with water vapor pressure of 0.87 – 3.17 kPa and a 5-25 °C heat transfer fluid (HTF) inlet temperature.

1. Introduction

The commercialization of waste-heat driven solid sorption cooling systems (SCS) using water as refrigerant faces major challenges, including: i) low operating pressure, leading to sealing and associated maintenance issues; ii) low specific cooling power (SCP), due to poor heat (and/or mass) transfer in heat exchangers; and iii) low coefficient of performance (COP), partly due to the high thermal inertia of heat exchangers (HEXs). These, in turn, make the current SCS costly, bulky and unreliable. To address these issues, heat/mass exchangers need to be specifically designed and optimized for SCS. A solution to address some of these issues is to use a compact capillary assisted low pressure evaporator (CALPE) to reduce the overall size. A CALPE eliminates the need for a circulating pump in the low-pressure evaporator taking advantage of the capillary effect. Thimmaiah et al. [1, 2] studied the performance of a CALPE for SCS using water as the refrigerant. Xia et al. [3, 4] considered a series of enhanced heat transfer tubes featuring circumferential rectangular micro-grooves for experimental investigation and provided an analytical model. They summarized different approaches for predicting the performance of CALPE evaporators. In terms of modeling, the focus has been on the thin film evaporation. Several papers have dealt with this topic [5, 6]. In this study, an experimental approach is undertaken to investigate the performance of a new CALPE, which is 3D printed from stainless steel. The existing heat transfer models are applied to predict the performance of the present 3D CALPE and compared against data collected in our lab.

2. Experimental Study

A custom-made gravimetric large pressure jump (G-LPJ) test bed was re-configured to investigate the heat and mass transfer performance of the present CALPE, as shown in Figure 1. Heat transfer fluid (HTF) was pumped through the evaporator by a Cole-Parmer Polystat thermal bath with controllable temperature. The evaporator was placed inside a vacuum chamber which was connected to a condenser (vapor collector). The entire test bed was vacuumed for 6 hours using a vacuum pump to dry the surfaces. The vacuum chamber was then placed on a precision balance (ML4002E, Mettler Toledo) with an accuracy of 0.01 g to measure its weight. Four T-type thermocouples with an accuracy of 0.5 °C were passed via a feedthrough in the vacuum chamber to measure the temperature of evaporator's wall and the pool of water. The contribution of connecting tubes and sensors are deducted by running the tests first without the evaporator and measuring their evaporation contribution. The pressure of the evaporator was measured using a 722B Baratron pressure transducer (MKS instruments) with an accuracy of 0.5%. 200 ml of distilled water was used for this experiment. The absolute values for weight are unimportant. After placing the evaporator chamber on the scale, the scale was zeroed, the distilled water was added and then during the evaporation, the rate in decrease of overall weight was understood to be the evaporation rate. A schematic diagram of our G-LPJ test bed is shown in Figure 1. It also shows the 3D printed CALPE and its geometry, compared with a Canadian quarter.

3. 3D Printed CALPE

The tested CALPE was made using an AM 400 RENISHAW metal 3D printer and from 316L SST stainless steel. It had a height of 6 cm and length of 10 cm as shown in Figure 1. The fins were 100 μm thick and 100 μm apart, totaling roughly 1000 capillary channels available. The fin height was 1.5 mm. The evaporator weighed 300 grams and had a total volume of 48 cm^3 . On the HTF side, it had 28 parallel 1-mm-radius channels inside. The inlet and outlet of the evaporator were $\frac{1}{4}$ " (6.35 mm inner diameter) ports that acted as a header for the parallel micro-channels.

Table 1 – Three relevant heat transfer mechanisms present in a capillary evaporator. The total cooling power is the result of these three phenomena acting together [3,4].

Natural convection	Thin film evaporation	2D heat conduction
$Q_{nc} = h_{nc} A_{nc} \Delta T$ (1)	$P_v - P_l = \sigma \kappa - \frac{A}{\delta^3}$ (5)	$\frac{\partial^2 T}{\partial x^2} + \frac{\partial^2 T}{\partial y^2} = 0$ (8)
$h_{nc} = \frac{k Nu}{D}$ (2)	$\delta_0 = \left(\frac{-bA}{a(T_{wall} - T_v)} \right)^{1/3}$ (6)	$q''(\xi) = -\frac{k(T_{wall} - T_{lv})}{W} *$
$Nu = 0.48(Gr \cdot Pr)^{0.25}$ (3)	$\frac{1}{\delta^*} \frac{d^2 \delta^*}{dz^*} - \frac{1}{\delta^{*2}} \left(\frac{d\delta^*}{dz^*} \right)^2$ (7)	$\sum_{n=1}^{\infty} \frac{2n-1}{2} \pi C_n \sin\left(-\frac{2n-1}{2} \pi\right)$
$Gr = \frac{g\eta\Delta T D^3}{\nu^2}$ (4)	$= \frac{1}{1 + \lambda\delta^*} \left(1 - \frac{1}{\delta^{*3}}\right)$	$* \sinh\left(\frac{2n-1}{2} \pi \xi\right)$ (9)

4. Results

There are three heat transfer mechanisms present in a CALPE: i) natural convection from the walls to the pool of water, Eqs. 1-4; ii) thin film evaporation, which is directly related to and occurs in the thin film area, Eqs. 5-7; and iii) 2D heat conduction from the walls to the bulk fluid in the capillary meniscus, Eqs 8 and 9 (x and y denote the geometry of a rectangular cross section between two fins). A summary of governing equations for each mechanism is given in Table 1. In the literature, it is assumed that the total heat transfer rate is the summation of these three mechanisms [3, 4]. In a non-capillary low-pressure evaporator, the only considered heat transfer mechanism is the natural convection, which has a direct relationship with the heat transfer area submerged in water. Therefore, in a non-capillary evaporator, the cooling power decreases with decreasing water height; thus, the active heat transfer area. However, in a CALPE, the dominant heat transfer mechanism is the thin film evaporation which keeps the cooling power constant even when the water height decreases. Moreover, in a non-capillary low-pressure evaporator, the saturation pressure difference between the surface of the pool of water and its bottom leads to lowered cooling power, whereas in a CALPE, it is possible to keep a low water height and utilize the capillary action to keep the rest of the evaporator wet. In this experiment, the starting water height was 6.5 mm for 200 ml of distilled water and experiments continued until the evaporator ran out of water. Based on the existing theoretical models available in the literature, a new analytical model is developed in this study. Figure 2 shows G-LPJ data and analytical results from the models summarized in Table 1 for the cooling density of the present 3D printed CALPE vs the pressure difference between the evaporator and condenser (vapor collector). It is expected that the cooling capacity of the evaporator increases as the driving force, the pressure difference between two chambers, is increased. Additionally, a comparison is made between the proposed design and a CALPE designed in our lab [2] (on a per volume basis), showing considerable improvement if off-the-shelf tubes were replaced with the present design. It is also seen that the model is capable of capturing data within 10%. Figure 2 also provides the transient data from the experiments showing constant evaporator pressure and constant rate of weight change during evaporation. In this example, a constant pressure of 2.65 kPa and a constant evaporation rate of 2.1 g/min, associated with evaporation at 25 $^{\circ}\text{C}$, was observed. Data for higher and lower evaporation temperatures are omitted for brevity.

5. Conclusions

A new CALPE was designed, and 3D printed from stainless steel to increase its cooling power which would have been otherwise limited by off-the-shelf tubes. The fine features of the proposed CALPE, namely the fin spacing and thickness of 100 μm , led to a significant increase in surface-area-to-volume ratio. Moreover, the 1-mm micro-channels on the HTF side decreased the internal thermal resistance considerably. As a result, the present 3-D printed CALPE showed a notable per volume cooling capacity improvement, i.e., 4 vs 0.88 kW/m^3 compared to a CALPE made from off the-shelf tubes in our previous study [2]. The experimental data are compared with a new

analytical model developed here. Overall, a good agreement between the proposed model and the experimental data was observed with an averaged relative difference of 10%. This work will be continued by exploring other parameters that impact the cooling capacity of CALPEs, such as channel cross sections and alternative materials. Moreover, the share of improvement from the evaporation side versus the HTF side will be investigated.

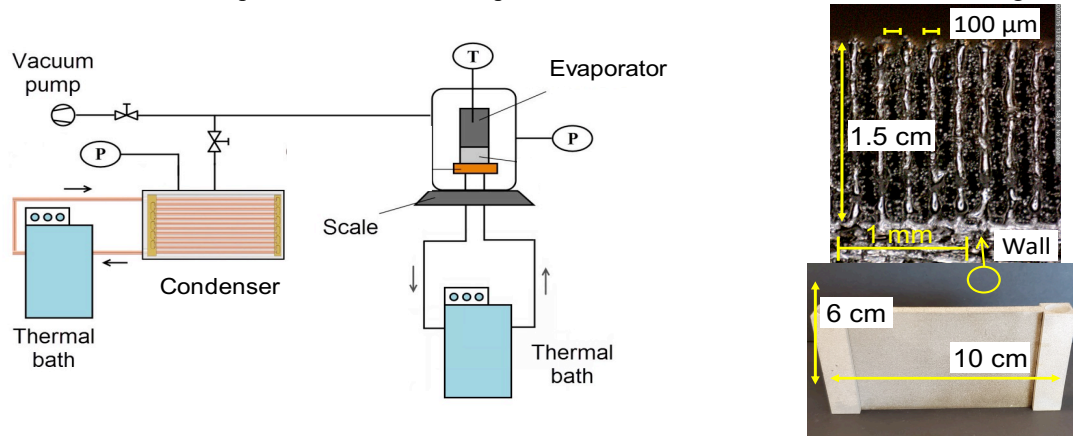


Figure 1 - A schematic diagram of G-LPJ test bed. Left: The G-LPJ test setup showing the evaporator chamber, condenser (vapor collector) and thermal baths. Right: The 3D printed CALPE and its geometry (fin spacing and a thickness 100 μm , height 5cm and length 10 cm), compared with a Canadian quarter. Tests were performed with a 5-25 $^{\circ}\text{C}$ heat transfer fluid (HTF) inlet temperature.

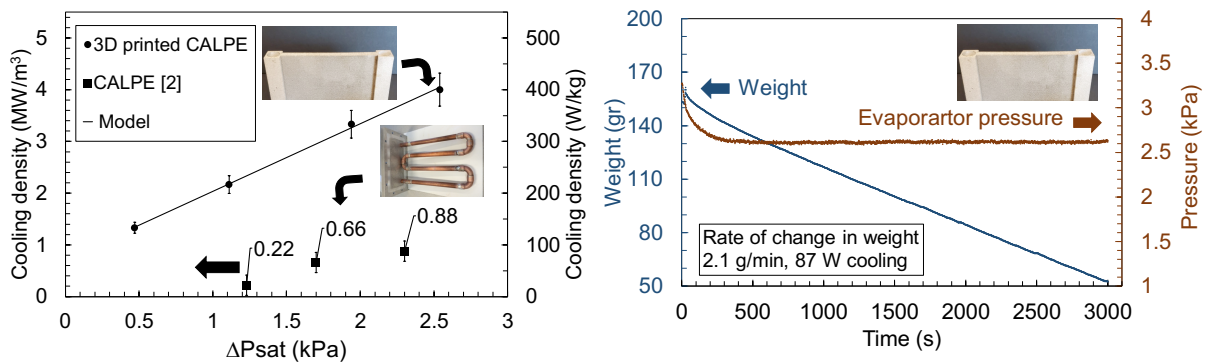


Figure 2 – Left: Experimental and analytical results for cooling density of 3D printed CALPE vs pressure difference between the evaporator chamber and condenser (vapor collector) chamber, compared to a previous CALPE's performance [2]. Right: real time data from experiments showing constant evaporator pressure and constant rate of weight change during evaporation at 25 $^{\circ}\text{C}$ as an example.

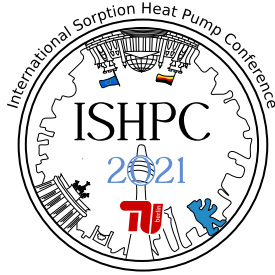
6. Acknowledgment

The authors are thankful for the financial support provided by the Natural Sciences and Engineering Research Council of Canada under the NSERC Idea to Innovation Grant (I2IPJ)#: 530368-2018.

7. List of References

- [1] Thimmaiah PC, Sharafian A, Huttema W, Osterman C, Ismail A, Dhillon A, et al. Performance of finned tubes used in low-pressure capillary-assisted evaporator of adsorption cooling system. *Appl Therm Eng* 2016;106:371–80.
- [2] Thimmaiah PC, Sharafian A, Huttema W, McCague C, Bahrami M. Effects of capillary-assisted tubes with different fin geometries on the performance of a low-operating pressure evaporator for adsorption cooling system applications. *Appl Energy* 2016;171:256–65.
- [3] Xia ZZ, Yang GZ, Wang RZ. Experimental investigation of capillary-assisted evaporation on the outside surface of horizontal tubes. *Int J Heat Mass Transf* 2008;51:4047–54.
- [4] Xia ZZ, Yang GZ, Wang RZ. Capillary-assisted flow and evaporation inside circumferential rectangular micro groove. *Int J Heat Mass Transf* 2009;52:952–61.

- [5] Potash and Wayner, Evaporation from a two-dimensional extended meniscus, *int. J. Heat Mass Transfer*. Vol. 15, pp. 1851-1863. 1972
- [6] Wayner et al., The interline heat-transfer coefficient of an evaporating wetting film, *Int. J. Heat Mass Transfer*. Vol. 19, pp. 487-492. 1976



Development of novel sorber bed heat and mass exchangers for sorption cooling systems

Bahremand, Hesam, Bahrami, Majid

Laboratory for Alternative Energy Conversion (LAEC), School of Mechatronic Systems Engineering, Simon Fraser University, 250-13450 102 Avenue, Surrey, BC, V3T 0A3, Canada; Tel.: +1 (778) 782-8538; E-mail addresses: sbahreham@sfu.ca (H. Bahremand) and mbahrami@sfu.ca (M. Bahrami)

Abstract:

Using our 2-D analytical model, an analysis of variance (ANOVA) is carried out to find the level of contribution and significance of design parameters, namely, fin height, fin thickness, sorbent thickness, graphite flake content in the sorbent, cycle time and fluid channel height to specific cooling power (SCP) and coefficient of performance (COP) of sorber bed heat and mass exchanger (S-HMX). It is shown that the components of S-HMX, consisting of the sorbent, heat exchanger (HEX) and the heat transfer fluid (HTF), should be optimized simultaneously to achieve optimal SCP and COP. Thus, using our closed-form analytical solution and a multi-objective genetic algorithm, an optimization study is conducted on the geometry, heat transfer characteristics and cycle time of S-HMX to acquire optimal SCP and COP. A design with SCP of 976 W/kg and COP of 0.60 was selected; i.e. a compromise between SCP and COP. Based on the optimization results, a novel S-HMX is designed and built. The experimental results show that the present S-HMX has achieved an SCP of 1,005 W/kg sorbent, and a COP of 0.60 which are higher than previously published results in the literature. The present S-HMX has been tested under various operating conditions: i) desorption temperatures, 60 to 90 °C, ii) ambient temperatures (sorption and condenser temperature, 20–40 °C), iii) evaporator temperature (5–20 °C), and iv) cycle time (10–20 min). SCP in the range of 320–1,230 W/kg and COP of 0.40–0.80 were measured in our testbed over the range of targeted operating conditions.

1. Introduction

Two of the major limitations facing the commercialization of sorption air conditioning systems (S-AC) include: i) Low SCP, resulting from low sorbent thermal diffusivity and use of the off-the-shelf heat exchanger designs that are not optimized for S-AC. The low thermal conductivity is a direct result of the high porosity of the sorbent materials, which is crucial for the sorption mass transfer. ii) Low COP, in part due to high thermal inertia of the current off-the-shelf heat exchangers used in S-AC.

This study aims to address these limitations by providing a specific design and optimization of S-HMX for S-AC, while minimizing the S-HMX thermal inertia. A number of researchers have proposed S-HMX to tackle the low performance of S-AC. A summary of the available studies with a reasonable compromise between SCP and COP, is presented in Table 1. It can be seen that the performance has been enhanced considerably over the past decade. However, the performance enhancement has been mainly due to the utilization of zeolite-based sorbents, such as SAPO-34 and AQSOA FAM Z02, which are expensive due to their synthesis process [1]. Furthermore, most of the sorption by zeolite-based sorbents occur in a narrow range of p/p_0 , which limits the application to relatively high desorption temperature, i.e. heat source of 80–90 °C, and low ambient temperature, about 30 °C. In the present study, a novel S-HMX is developed that provides high SCP and COP over a large range of operating conditions. The sorbent composite is made from silica gel and CaCl_2 , graphite flakes as thermally-conductive additive and PVA as binder. The selected composite is cost-effective and is readily-available in the market compared to the zeolite-based sorbents [2]. Moreover, the uptake of the selected composite takes place over the entire range of $0.06 < p/p_0 < 0.4$, suitable for air-conditioning applications [3].

Table 1. A summary of the available studies with a reasonable compromise between SCP and COP

Ref.	Sorption pair	S-HMX	τ (min)	Q_{evap} (kW)	SCP (W/kg)	COP
[4]	Coating silica gel+ CaCl_2 (SWS-1L)/water	Aluminum finned tube	10	0.48	137	0.15

[5]	Coating AQSOA-FAM-ZO2/water	Extruded aluminum finned-tube heat exchanger	–	0.442	294.67	0.21
[6]	Silica gel/water	Aluminum finned tube	6	1.9	158	0.29
[7]	Loose grain LiNO ₃ –Silica KSK/water (SWS-9L)	Aluminum finned flat tube	6.4		318	0.176
[8]	Loose grain AQSOA-FAM ZO2/water	Aluminum finned flat tube	7	0.155	394	0.6
[9]	Coating zeolite, SAPO-34/water	Aluminum finned flat tube	5		675	0.24
[10]	Coating SAPO-34/water	Aluminum sintered metal fiber structures soldered on flat fluid channels	10	5	852	0.4
[11]	Coating AQSOA-FAM-ZO2/water	Finned tube (copper)	1.5	1.5	872	0.27
[12]	Coating silica gel+CaCl ₂ /water	Aluminum finned-copper tube engine oil cooler	10	0.306	235	0.2

2. Background/Fundamentals/Experimental Set-up

Using our 2-D analytical model [12] and a multi-objective genetic algorithm, the geometry, heat transfer characteristics and cycle time of S-HMX are determined in this study to optimize SCP and COP. The constraints are defined based on the parametric study performed and include: i) fin height 1–3 cm, ii) fin thickness 1–3 mm, iii) sorbent thickness 1–3 mm, iv) graphite flake content 0–20 wt.%, v) cycle time 10–20 min, and vi) fluid channel height 4–8 mm. Using the multi-objective genetic algorithm in MATLAB, the SCP and COP of S-HMX are optimized. The set of optimum solutions for S-HMX, i.e. the trade-off between SCP and COP, is presented in Figure 1. The design that can achieve SCP of 976 W/kg and COP of 0.60, shown with pentagram in Figure 1, is selected, due to an optimal compromise between SCP and COP. It can be seen that before and after this point, either COP or SCP decreases significantly. The proposed S-HMX was built based on the optimization study. Figure 2 shows the assembled S-HMX coated with the optimum composite sorbent. The spacing between the fins, the serpentine fluid channels and the half-circle regions for the aluminum tube were machined out of two aluminum 6061 plates using our CNC milling machine in the machine shop in our university. After that, two halves of S-HMX and two aluminum tubes were welded together. Subsequently, the fin spacing of the HEX was filled with the slurry solution of the optimum composite sorbent consisting of 39 wt.% CaCl₂, 39 wt.% silica gel B150, 10 wt.% PVA, and 12 wt.% graphite flakes according to the optimization study. The composite sorbent was dried at 80 °C and then cured at 180 °C in the oven.

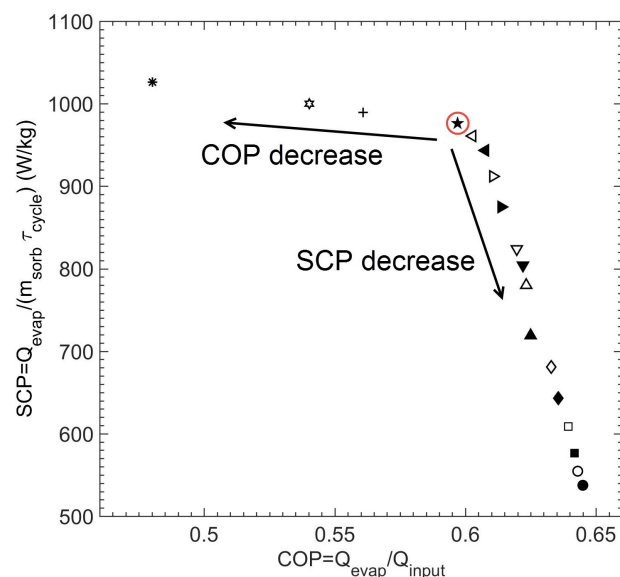


Figure 1. Set of optimum solutions for S-HMX, trade-off between SCP and COP. Each point represents a S-HMX design specification.

Figure 3 shows a picture of the custom-built two-sorber bed sorption test bed in our lab. A custom-designed capillary-assisted evaporator and a helical coil shell and tube HEX were used as the evaporator and the condenser, respectively. The S-HMXs and the evaporator were placed inside the vacuum chambers. Check valves were installed between the S-HMXs and the condenser and gate valves were installed between the evaporator and the

beds. A needle valve with high precision flow adjustment (Speedivalve SP16K, Edwards) and a U-tube were installed between the condenser and the evaporator. The whole system was vacuumed for 6 hours before the tests. Two temperature control systems were used to keep the evaporator at 15 °C and the condenser at 30 °C. Furthermore, two temperature control systems, Julabo LH50 Plus, were set to 90 °C and 30 °C for desorption and adsorption processes, respectively. Two four-way valves were employed to switch the heat transfer fluid between two S-HMXs for desorption and adsorption processes. RTD (PT100) temperature sensors (Omega, model #PR-13-2-100-1/8-6-E) with accuracy of 0.15 °C and pressure transducers with 0-34.5 kPa operating range (Omega, model #PX309-005AI) and 0.4 kPa accuracy were installed to monitor and record the temperature and pressure variations in each component of the sorption test bed over time. Positive displacement flow meters (FLOMEC, Model # OM015S001-222) with accuracy of 0.5% of reading were installed to measure the flow rate of the heat transfer fluid. The instruments were interfaced with a PC through a data acquisition system and in-house software built in the LabVIEW environment. Experiments were performed continuously until the system reached an oscillatory steady state. The maximum uncertainties in the measured COP and SCP were calculated to be 12.5% and 10.6%, respectively.



Figure 2. S-HMX coated with the composite sorbent, silica gel, CaCl_2 , PVA and graphite flakes

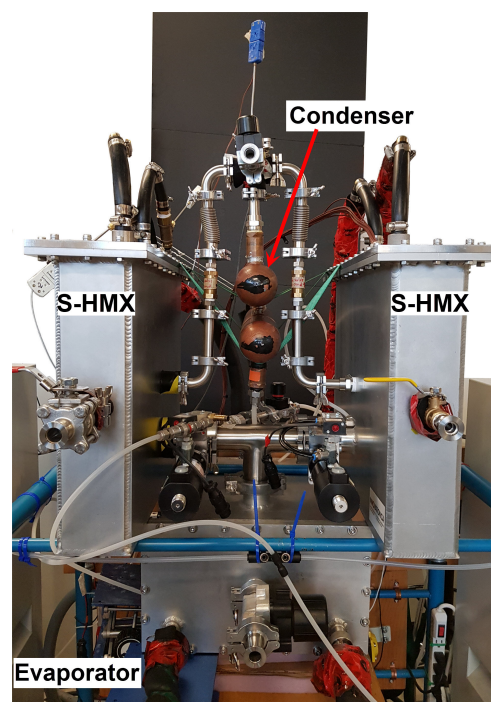


Figure 3. Picture of the two-sorber bed sorption test bed

3. Results

Figure 4 shows the performance of the present S-HMX versus the published values in the literature in Table 1. It can be seen that the present design provides the highest SCP and COP using the specific design and optimization of S-HMX.

4. Conclusions

A multi-objective optimization study was performed on the geometry, heat transfer characteristics and cycle time of S-HMX to find the optimal SCP and COP. A design with SCP of 976 W/kg and COP of 0.60 was selected to achieve an optimal compromise between SCP and COP. A novel S-HMX was designed and built based on the present optimization study. It was shown that the present S-HMX provides an SCP of 1,005 W/kg sorbent, and a COP of 0.60; which is a large improvement compared to the literature.

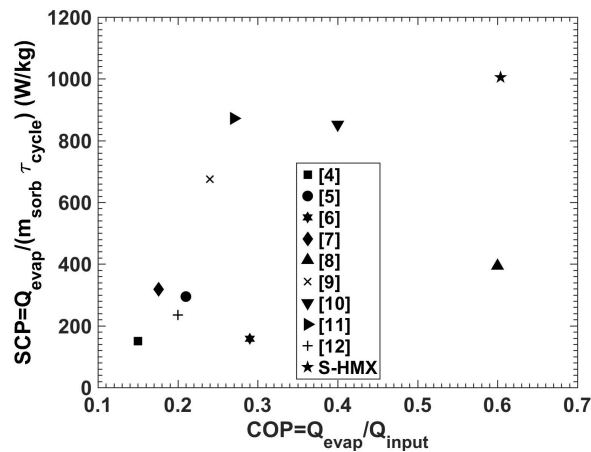


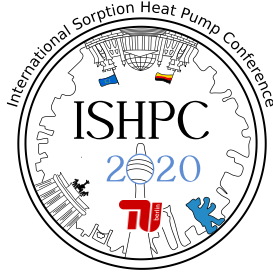
Figure 4. S-HMX versus state-of-the-art in terms of SCP and COP

5. Acknowledgment

The authors gratefully acknowledge the financial support of the Natural Sciences and Engineering Research Council of Canada (NSERC) through Idea to Innovation Grant No. I2IPJ 530368-2018.

6. List of References

- [1] A. Freni *et al.*, *Characterization of Zeolite-Based Coatings for Adsorption Heat Pumps*. SPRINGER BRIEFS IN APPLIED SCIENCES AND TECHNOLOGY, 2015.
- [2] A. Freni, L. Calabrese, A. Malara, P. Frontera, and L. Bonaccorsi, "Silica gel micro fibres by electrospinning for adsorption chillers," *Energy*, vol. 187, p. 115971, 2019.
- [3] H. Bahrehmand, M. Khajepour, and M. Bahrami, "Finding optimal conductive additive content to enhance the performance of coated sorption beds: An experimental study," *Appl. Therm. Eng.*, vol. 143, no. July, pp. 308–315, 2018.
- [4] A. Freni, F. Russo, S. Vasta, M. Tokarev, Y. Aristov, and G. Restucci, "An advanced solid sorption chiller using SWS-1L," *Appl Therm Eng*, vol. 27, pp. 2200–2204, 2007.
- [5] B. Dawoud, P. Höfle, and S. Chmielewski, "Experimental investigation of the effect of zeolite coating thickness on the performance of a novel zeolite-water adsorption heat pump module," in *Tenth international conference enhanced building operations*, 2010, pp. 1–8.
- [6] M. Verde, J. M. Corberan, R. de Boer, and S. Smeding, "Modelling of a waste heat driven silica gel/water adsorption cooling system comparison with experimental results," in *ISHPC conference, Padua, Italy*, 2011, pp. 7–8.
- [7] Y. Aristov, A. Sapienza, D. Ovoshchnikov, A. Freni, and G. Restuccia, "Reallocation of adsorption and desorption times for optimisation of cooling cycles," *Int J Refrig*, vol. 35, pp. 525–31, 2012.
- [8] A. Sapienza, S. Santamaria, A. Frazzica, and A. Freni, "Influence of the management strategy and operating conditions on the performance of an adsorption chiller," *Energy*, vol. 36, pp. 5532–5538, 2011.
- [9] A. Freni, L. Bonaccorsi, L. Calabrese, A. Capri, A. Frazzica, and A. Sapienza, "SAPO-34 coated adsorbent heat exchanger for adsorption chillers," *Appl. Therm. Eng.*, vol. 82, pp. 1–7, 2015.
- [10] U. Wittstadt *et al.*, "A novel adsorption module with fiber heat exchangers: Performance analysis based on driving temperature differences," *Renew. Energy*, vol. 110, pp. 154–161, 2017.
- [11] Z. He *et al.*, "Study on the performance of compact adsorption chiller with vapor valves," *Appl. Therm. Eng.*, vol. 126, pp. 37–42, 2017.
- [12] H. Bahrehmand and M. Bahrami, "An analytical design tool for sorber bed heat exchangers of sorption cooling systems," *Int. J. Refrig.*, vol. 100, pp. 368–379, 2019.



Vertical U-pipe Two-phase Flow Characteristics and Refrigerant Vapor Bypass in Absorption Heat Pump and Absorption Heat Exchanger

Zhu, Chaoyi¹, Xie, Xiaoyun^{1,*}, Jiang, Yi¹

¹ Building Energy Research Center, Department of Building Science, Tsinghua University, Beijing 100084, China

* Corresponding author: Xie, Xiaoyun, Email: xiexiaoyun@tsinghua.edu.cn, Tel.: +86-10627935917

Abstract:

The absorption heat pump and absorption heat exchanger are widely applied in space heating system to recover waste heat as heat source. U-pipe is the pressure separation device between the condenser and the evaporator to meet the wide pressure difference change demand during the whole heating season. Current studies in this area paid few attention to the flow inside U-pipe. The designed U-pipe cannot supply stable pressure separation and fluid flow rate when working condition changes. This study experimentally investigate the two-phase flow phenomenon inside U-pipe under vacuum condition. The bubbles generated under the surface on downward side supply nuclei for flashing. The two-phase flow will undermine the pressure separation ability of a given U-pipe and cause vapor bypass from condenser to evaporator. The vapor bypass mass flow rate is tested. The vapor bypass will reduce the cooling COP of single-stage absorption heat pump by 10%.

1 Introduction

The absorption heat exchanger (AHE) is the key equipment in novel district heating system of China [1]. The AHE replaces the conventional plate heat exchanger to complete the heat exchange from the primary water to the secondary water. The AHE consists of a hot-water driven lithium-bromide absorption heat pump (AHP) and a plate heat exchanger (HEX). Although the structure of the AHE is quite similar to the absorption chiller, the working condition is quite different. The pressure range of the AHP inside AHE is much wider than the absorption chiller. This is a huge challenge to the pressure separation device that connects the condenser and the evaporator.

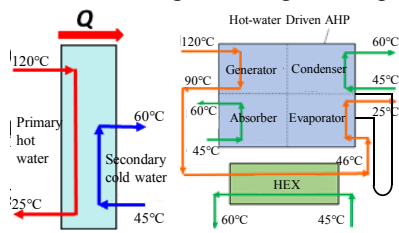


Figure 1: Principle of AHE

Table 1- Condition of absorption chiller and AHPs/AHEs

Parameters	Absorption Chiller	AHPs in AHEs
Condensing Pressure [kPa]	5.6~7.5	5.6~25
Evaporating Pressure [kPa]	0.9~1.2	1.2~4.2
Pressure Difference [kPa]	4.7~6.3	4.4~20.8

The orifice plate and the expansion valve are the early choices of pressure separation device in absorption chiller. The flow rate through these devices are closely related to the pressure difference, making them less convenient to be applied in equipment with wide pressure difference change range. That is why the U-pipe is more commonly used in AHPs and AHEs nowadays instead. The main contribution to pressure drop in a U-pipe is the gravitational pressure drop caused by the liquid level difference between downward and upward side. The flow rate can be stable even if the pressure difference changes a lot. Although the U-pipe seems to be a suitable option for AHPs and AHEs, some unexpected fluid flow problems still happen in real applications that undermine the performance of the equipment. The understanding of the fluid flow inside U-pipe is not sufficient to guide the design.

In previous studies and equipment development, the flow on the upward side of the U-pipe is simply considered to be pure liquid or bubbly two-phase flow [2]. Therefore, the required length of the U-pipe was set equal to the rated pressure difference divided by the product of density of the liquid and the gravitational acceleration. However, we discovered that the fluid on the upward side can flash and develop into churn flow [3]. The change of flow pattern will increase the void fraction to over 0.7 which reduces the overall fluid density. The U-pipe pressure separation capability will be reduced given the designed pipe length. The downward side liquid surface is very low and finally disappear. The liquid seal function of the U-pipe is failed and the vapor channel between two chambers is opened, causing refrigerant vapor bypass from condenser to evaporator..

The U-pipe is a widely used device in areas like chemical engineering, nuclear energy, boiler, and refrigeration [4-6]. It is commonly used to redirect the flow instead of separating the pressure. Previous studies focus on the two-phase flow of U-pipe under ambient or high pressure system. In AHPs, however, the absolute pressure is

under 20kPa. Very few studies focus on this pressure range. In upward flow, the static pressure of fluid decreases and leads to a higher superheat temperature difference under vacuum than under higher-pressure condition. Therefore, phenomena that cannot or rarely exist under higher pressure conditions may be observed inside the U-pipe of AHPs. Meanwhile, the refrigerant vapor bypass is a special condition in pressure separation device. Current studies haven't discussed this condition. This study aim to find the two-phase flow characteristics inside U-pipe of AHPs and AHEs under vacuum condition and to find the effect of vapor bypass on the performance of AHPs and AHEs.

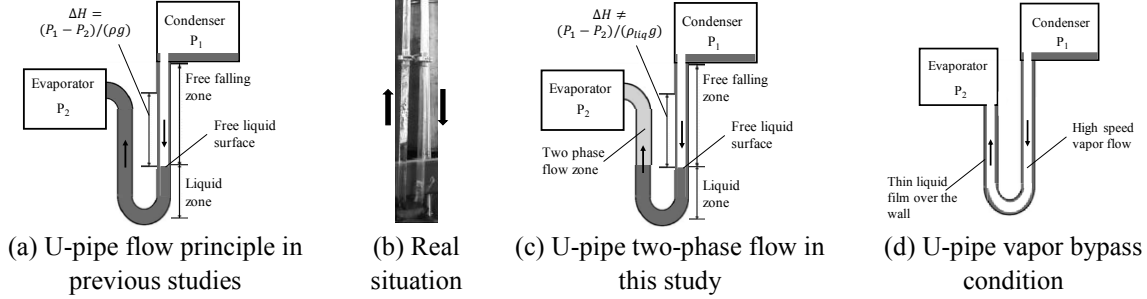


Figure 2: U-pipe flow principle

2 Two-phase Flow Experiment and Vapor Bypass Calculation

2.1 Experiment Setup

To observe the U-pipe flow phenomenon under vacuum and to study the flow characteristic, an experimental unit that is visible and has good vacuum performance with less than 10^{-7} Pa.m³/s gas leakage rate is developed. The experimental unit consists of a high-pressure chamber, a low-pressure chamber, and a PMMA material U-pipe (of 19 mm inner diameter and 1.5 m height) connecting two chambers. The unit can imitate the flow from condenser to evaporator inside AHPs. More detailed description of the unit set up can be found in the authors' work [3].

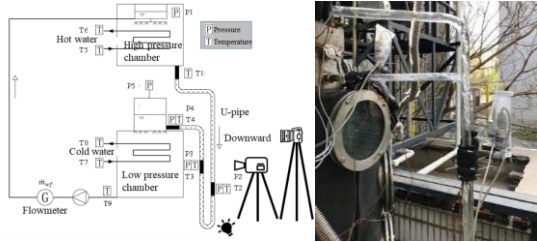


Figure 3: Experimental system

Table 2- Test conditions

Parameter	Range
Internal flow velocity	0–0.7 [m/s]
Inlet pressure	2–26 [kPa]
Outlet pressure	2–6 [kPa]
Inlet/outlet pressure difference	0–20 [kPa]

The pressures of two chambers are controlled by the input heat or cold source fluid temperature and flow rate as well as the flow rate of working fluid which is pure water in this experiment. The working condition shown in Table 2 covers the condition of most absorption chillers, AHPs and AHEs. The two phase flow temperature and pressure change, the flashing evaporation mechanism, and the vapor bypass special condition are discussed.

2.2 Vapor Bypass Flow Rate Calculation

For an AHP, the bypassed vapor will carry part of the heat from generator-condenser unit (GC). This heat \dot{q}_{bp} can be calculated by the heat balance in the unit, as shown in Eq. (1). \dot{q}_{hw} is hot water input heat to genertor. \dot{q}_s , \dot{q}_{cw} , and \dot{q}_{cond} are the heat reject from GC to solution, condenser cooling water, and condensing water. The \dot{q}_s can be calculated by the inlet and outlet solution property shown in Eq. (2). The condensing water flow rate is calculated by \dot{q}_{cw} divided by condensing enthalpy change Δh_{cond} . Then the vapor bypass flow rate ratio of AHP MR_{AHP} is derived by Eq. (4). It is the inlet vapor mass fraction of U-pipe from condenser to evaporator.

$$\dot{q}_{bp} = \dot{q}_{hw} - \dot{q}_s - \dot{q}_{cw} - \dot{q}_{cond} \quad (1) \quad \dot{m}_{cond} = \frac{\dot{q}_{cw}}{\Delta h_{cond}} \quad (3)$$

$$\dot{q}_s = \dot{m}_{s,g,out} h_{s,g,out} - \dot{m}_{s,g,in} h_{s,g,in} \quad (2) \quad MR_{AHP} = \frac{\dot{m}_{bp}}{\dot{m}_{cond} + \dot{m}_{bp}} \quad (4)$$

3 Results

3.1 Two-phase flow phenomenon and fluid status

The main phenomenon and profile of the U-pipe flow are discussed using the experimental result with internal flow velocity of 0.3 m/s. More experimental results can refer to [3]. From case 1 to case 6 in Fig. 4 and Table 3, the pressure difference between the inlet and outlet of the U-pipe changes from 0 to 18 kPa. The flashing happens in the upward side just above the downward side liquid surface. The downward side liquid surface is lower and lower. The two-phase flow zone length increases. Table 3 lists the temperature and pressure change through the flow direction. It also lists the saturated temperature of fluid. The shaded data is in two-phase zone. The underlined data is in downward side free falling zone above the liquid surface. The fluid status can be described as follows:

- The fluid enters the U-pipe in a saturated state. This fluid flows through a free-falling zone on the downward side of the U-pipe with unchanged temperature and pressure before hitting the free liquid surface of the U-pipe.
- Under the free liquid surface of the downward side, the fluid flows as full pipe flow. The static pressure rises as the fluid flows down and the temperature of the fluid remains unchanged. The fluid remains in the liquid state.
- On the upward side of the U-pipe, the fluid pressure decreases. The temperature of the fluid is unchanged. It is lower than the local saturated temperature until the fluid reaches the same height of the downward side free liquid surface.
- As fluid flows upward above the free liquid surface height at the downward side, the local saturated temperature decreases and is below the temperature of the fluid. At this point, flashing evaporation occurs. The fluid temperature decreases to near the local saturated temperature to provide heat for the evaporation.
- As the fluid flows upward, its pressure decreases. Evaporation continues until the fluid leaves the U-pipe. A two-phase flow zone is formed on the upward side of the U-pipe. The void fraction rises as flashing continues.

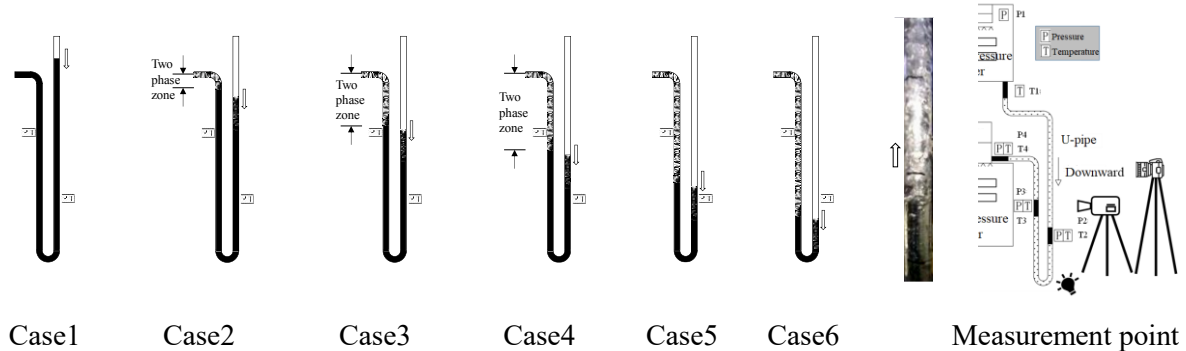


Figure 4: Basic phenomenon

Table 3- Test data

Case no.	#1	#2	#3	#4	#5	#6	Note:
U-pipe inlet pressure P1 [kPa]	2.0	8.9	11.1	14.5	20.2	<u>22.8</u>	^a Liquid level: The height from the downward-side liquid surface to the bottom of the U-pipe.
Pressure point P2 [kPa]	12.7	17.8	19.7	20.1	21.9	<u>22.8</u>	
Pressure point P3 [kPa]	5.1	10.5	11.6	12.9	N/A	N/A	
U-pipe outlet pressure (before) P4 [kPa]	2.5	6.9	8.4	10.1	13.3	14.4	
U-pipe outlet pressure (after) [kPa]	2.4	2.3	3.7	2.5	3.2	4.5	
U-pipe inlet temperature T1 [°C]	16.3	42.5	46.9	52.3	59.2	62.8	
Downward fluid temperature T2 [°C]	16.4	42.4	46.9	52.2	59.2	<u>62.8</u>	^b Flashing start level: The height from the start point of flashing to the bottom of the U-pipe.
Saturated temperature at T2 point [°C]	50.6	57.6	59.7	60.1	62.0	<u>62.9</u>	
Upward fluid temperature T3 [°C]	16.4	42.3	46.7	50.7	55.6	57.5	
Saturated temperature at T3 point [°C]	33.2	46.8	48.7	50.8	N/A ^c	N/A ^c	
U-pipe outlet temperature (before) T4 [°C]	16.4	39.0	42.5	46.0	51.1	52.9	
Saturated temperature at T4 point [°C]	21.1	38.6	42.5	46.1	51.5	53.1	
U-pipe mass flow rate [kg/h]	302.5	311.3	301.7	313.8	309.1	306.9	
Downward-side liquid level [m] ^a	1.505	1.350	1.315	1.010	0.580	0.330	
Upward-side flashing start level [m] ^b	N/A ^d	1.405	1.380	1.055	0.680	0.425	

Note:

^aLiquid level:
The height from the downward-side liquid surface to the bottom of the U-pipe.

^bFlashing start level: The height from the start point of flashing to the bottom of the U-pipe.

^cPressure transducer outranged.

^dNo flashing evaporation.

3.2 Flashing evaporation mechanism

The flashing evaporation process inside the fluid starts in the bubble growth around the nucleus. The bubble growth requires a super heat pressure difference (SHDP) between the inside and outside to overcome the surface tension. Smaller the bubble, higher is the SHDP needed for the growth. In the experiment, several small bubbles formed under the free liquid surface on the downward side when the falling liquid hit the surface and entrained vapor. The bubbles flowed with the liquid into the upward side of the U-pipe and grew larger immediately when flashing occurred. The bubbles are large enough to be observed; their diameter vary between 0.5 and 3 mm. Fig. 6 shows the calculated connection between bubble diameter and the SHDP. When the diameter of bubble is larger than 0.25mm, the flashing required SHDP is lower than 1 kPa. The starting point of flashing is no more than 0.1 m higher than the downward-side surface. This is consistent with the observed phenomenon, proving that the small bubbles caused by the free surface vapor entrainment provide the nuclei for the U-pipe flashing process.

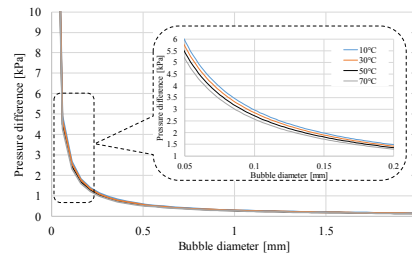
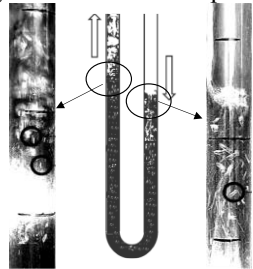


Figure 5: Bubble formation and movement Figure 6: Bubble diameter and pressure difference

3.3 Refrigerant vapor bypass problem and the effect on COP

The vapor bypass problem is found and measured in an on-site AHP applied in Chifeng city for district heating. The working conditions are listed in Table 4. G, E, A, C, and T stand for generator, evaporator, absorber, condenser, and temperature. The bypass vapor mass flow rate ratio (MR_{AHP}) can be calculated by Eq. (1) to (4).

Table 4- Test condition for each case

G/E inlet flow rate [kg/s]	G inlet T [°C]	E inlet T [°C]	A/C inlet flow rate [kg/s]	A inlet T [°C]	C inlet T [°C]
0.86	90.4	42.4	2.20	40.3	44.8
0.83	81.3	41.9	1.70	40.6	44.7
0.83	88.2	41.8	1.87	39.9	44.4
0.84	90.7	41.4	2.92	40.0	40.0
0.83	91.5	42.3	2.05	40.5	44.1
0.82	80.6	41.8	1.84	40.6	44.4
0.83	91.5	41.9	1.98	40.7	45.6
0.83	89.6	41.9	2.07	40.1	43.8
0.82	80.1	41.4	1.81	39.9	44.0

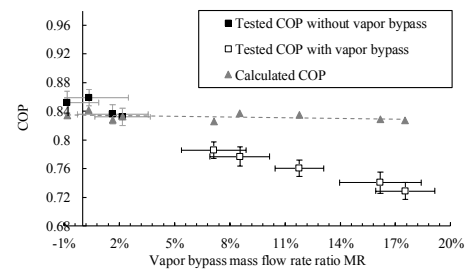


Figure 7: Measured COP with and without vapor bypass problem

The measured COP and simulation calculated COP using parameters in Table 4 and model in [1] are shown in Fig. 7. The MR_{AHP} can be over 10%. The calculated COP is the performance an AHP can reach given the inlet parameters. When vapor bypass happens, the tested COP is 5% to 10% lower than the calculated COP.

4 Conclusions

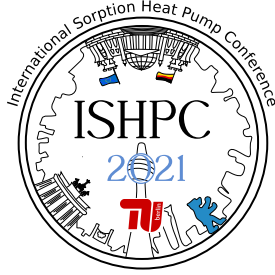
In this study, the two-phase flow inside U-pipe under vacuum condition is experimentally observed and tested. The study on this topic in AHP area is blank in the past. The phenomenon and fluid status is described based on test data. The bubble generated below the downward side liquid surface serves as the flashing nuclei. The refrigerant vapor bypass between condenser and evaporator is a newly found condition when two-phase flow happens inside U-pipe. It happens easily and commonly in present running AHPs since the effect of two-phase flow on void fraction and fluid density inside U-pipe is not found or considered in the past design of U-pipe length. The bypassed vapor can be over 10% of U-pipe mass flow rate. The cooling COP is reduced by 5% to 10% when this happens. There is a good potential to improve the COP of AHPs by solving this problem.

5 Acknowledgment

The authors gratefully acknowledge support from the National Natural Science Foundation of China (Grant numbers 51306098, 51138005), the Innovative Research Group of the National Natural Science Foundation of China (Grant number 51521005), the Tsinghua University Initiative Scientific Research Program (Grant number 20151080470), Graduate Education Innovation Grants, Tsinghua University (Grant number 53812001018), Beijing Municipal Science and Technology Project (No. Z181100005418005), and China Postdoctoral Science Foundation (Grant number BX20190178, 2019M660655).

6 References

- [1] Zhu, C., Xie, X., & Jiang, Y. (2016). A multi-section vertical absorption heat exchanger for district heating systems. *International Journal of Refrigeration*, 71, 69-84.
- [2] Shin, Y., Seo, J. A., Cho, H. W., Nam, S. C., & Jeong, J. H. (2009). Simulation of dynamics and control of a double-effect LiBr-H₂O absorption chiller. *Applied Thermal Engineering*, 29(13), 2718-2725.
- [3] Zhu, C., Xie, X., & Jiang, Y. (2020). Vertical U-pipe flow characteristics in absorption heat pump: Experimental study under vacuum conditions. *Applied Thermal Engineering*, 115164.
- [4] Andrzejczyk, R., & Muszynski, T. (2018). Experimental and comparative study on the two-phase pressure drop of air-water mixture in U-bend and straight pipe annuli. In *Journal of Physics: Conference Series* (Vol. 1101, No. 1, p. 012002). IOP Publishing.
- [5] Aliyu, A. M., Almabrok, A. A., Baba, Y. D., Lao, L., Yeung, H., & Kim, K. C. (2017). Upward gas-liquid two-phase flow after a U-bend in a large-diameter serpentine pipe. *International Journal of Heat and Mass Transfer*, 108, 784-800.
- [6] Ma, X., Tian, M., Zhang, J., Tang, L., & Liu, F. (2018). Flow pattern identification for two-phase flow in a U-bend and its contiguous straight tubes. *Experimental Thermal and Fluid Science*, 93, 218-234.



Experimental investigation on the dynamic performance of desiccant coated microchannel heat exchangers under condensation conditions

Liang, Caipeng¹, Ture, Feyzican¹, Ge, Tianshu^{1,2}

¹ Institute of Refrigeration and Cryogenics, Key Laboratory for Power Machinery and Engineering of M.O.E, Shanghai Jiao Tong University, 800 Dongchuan Road, Shanghai 200240, China

² E-mail: baby_wo@sjtu.edu.cn

Abstract:

A microchannel heat exchanger coated with silica gel is investigated in this paper, and a series of condensation experiments are implemented under the simulated high temperature and high humidity conditions to analyze the dynamic performance of the microchannel desiccant coated heat exchanger (DCMHE). The sign of judging the presence of condensation is found during the process of changing cooling water temperature. The influence differences of desiccant coating under condensation and non-condensing conditions are compared and it is seen that condensation dehumidification plays a leading role under condensation conditions. Besides, the performance of DCMHE is stable in continuous operation under condensation conditions.

1 Introduction

In the past years, the research on desiccant coated heat exchangers mainly put emphasis on experimental research [1], [2] and mathematical model [3],[4]. It can be found that quantities of work have been done to discover the performance of fin-tube heat exchangers under non-condensing conditions. In some cases, condensation conditions appear but are ignored. However, one potential issue with the DCHE system is that condensation may happen after the desiccant coating is saturated. The temperature of the desiccant layer on the surface of the circulating dehumidification evaporator is about 16~18°C, while the outdoor dew point in summer is usually above 20°C, and the indoor return air dew point under the standard working condition is 17°C [5],[6]. Therefore, in-depth research on the performance of dehumidification heat exchanger under condensation conditions should be put on the agenda. In recent years, the desiccant coated microchannel heat exchanger (DCMHE) derived from DCHE has attracted people's attention due to its advantages of light weight, great efficiency and high compactness [7]. The objective of this research is to analyze the performance of DCMHE under condensation conditions. The dynamic characteristics of DCMHE and microchannel heat exchanger (MHE) are compared under various cooling water temperature. With diverse operating conditions, the influences of inlet air velocity and fluid temperature on the moisture and heat transfer and pressure drop performance of DCMHE are analyzed.

2 Experimental Set-up

2.1 Experimental system description

The whole experimental system which is made up of three sub arrangements; air circulation loop, water circulation loop, and control unit has been designed as an open-loop flow system. Fig.1 (a) sketches the simplified experimental setup and (b) is the actual view.

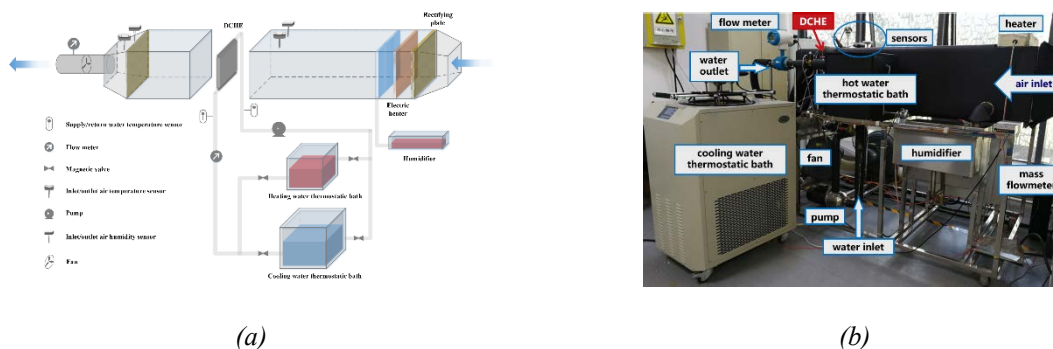


Figure 1 - (a) Schematic diagram and (b) actual view of the experimental system.

The air circulation loop subsystem consists of two air duct sections whose profile areas are $50 \times 50 \text{ cm}^2$. The tested heat exchanger is placed on the rim of the massive section, and the other section which can be moved via slideway installed below gets closed over the massive one. The inlet air comes from the head of the massive duct section to the head of another. A centrifugal fan is installed at the outlet to drive airflow. Furthermore, air ducts have been wrapped with heat insulation foam to reduce heat loss.

The water circulation loop includes two fluid circulation units those are the hot water loop and the cooling water loop. Each has a centrifugal pump, a thermostatic tank, and conventional and magnetic valves. The magnetic valves get opened-closed according to the certain circulation.

The control unit subsystem includes the cabinet fan with variable speed (the maximum the volumetric flow rate of $800 \text{ m}^3/\text{h}$), sensors, magnetic valves, relays, and console data acquisition devices. Besides, the electric heater, cooler, and the humidifier have been installed to control the inlet air conditions of temperature and humidity via the panels.

2.2 Desiccant coated microchannel heat exchanger (DCMHE)

Microchannel heat exchanger coated with 0.15 mm particle diameters is kept into solid silica gel with liquid glue and baked. The detailed views of coated and uncoated are exhibited by Fig.2.

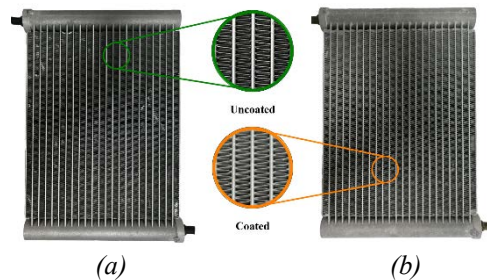


Figure 2 - Photograph of an MHE(a) and DCMHE(b).

3 Results

3.1 Judgment mark of condensation phenomenon found during cooling water temperature change

In order to explore the dynamic characteristics of the outlet air under condensation conditions, the operating conditions chosen are as follows: 27°C , $80\% \text{ RH}$ inlet air (23.3°C dew point), 60°C hot water temperature and 1.5 m/s inlet air velocity. The average values of inlet water temperature in the steady-state of the dehumidification process are adopted as the cooling water temperature, which varies from 9°C to 38°C . The sampling interval is 1 s . Considering that the long cycle time is conducive to observing condensation, the cycle switch time is set to 40 min . The outlet air temperature, humidity ratio and relative humidity of DCMHE in one cycle time at the aforementioned operating conditions are individually plotted in Fig. 3 (a), (b) and (c). In the process of cooling water temperature transition from above dew point (38°C , 32°C , 25°C) to below dew point (16°C , 9°C), significant curve characteristics were found with the generation of condensation. It is obvious that no matter the outlet temperature, humidity ratio or relative humidity in a cycle, the dynamic curves higher than the dew point show the same trends with varying degrees of regular changes, which is consistent with the previous research results [8], while the dynamic curves lower than the dew point have different trends.

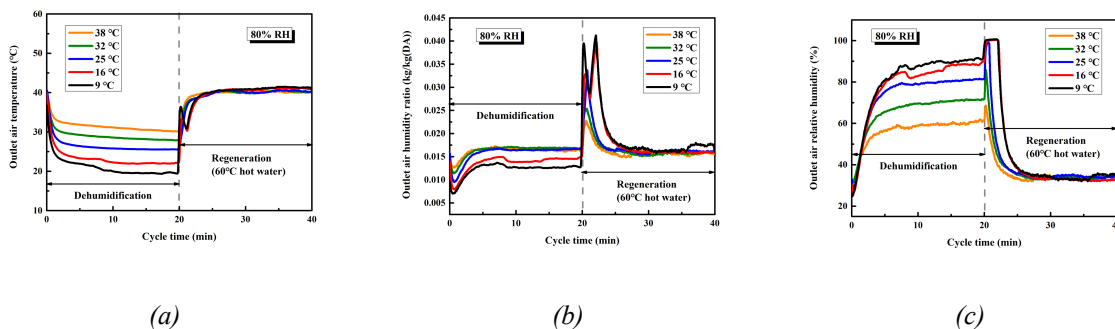


Figure 3 - (a) Outlet air dry bulb temperature, (b) humidity ratio and (c) relative humidity of DCMHE with different cooling water temperatures (1.5 m/s inlet velocity).

During the dehumidification process, the cooling water quickly flows into the heat exchanger and mixes with the residual hot water, resulting in the outlet air temperature drops at a very high slope (0~1 min), then slowly drops and keeps basically stable (1~20 min). As the desiccant is still in full regeneration state under the initial switching state, the outlet humidity ratio drops sharply (0-1 minute) because of the high humidity difference, then rises slowly and restores stability (1-20 minutes) during the process of desiccant adsorption saturation. However, when the cooling water temperature is lower than the dew point, the condensed water is generated and accumulated on the surface of the heat exchanger as the desiccant adsorption saturates at the same time, and finally drops to the ground. Therefore, the outlet air humidity ratio drops suddenly in about 7 minutes in Fig. 3 (b), which is caused by the beginning of the condensation water dropping. Correspondingly, the outlet air temperature and relative humidity also show a trend of a sudden drop in Fig. 3 (a) and 3 (c).

The humidity ratio of outlet air in a stable state is approximately equal to that of inlet air when there is no condensation. When the cooling water temperature is lower than the dew point, adsorption dehumidification and condensation dehumidification are both involved in the dehumidification process. Due to the continuous occurrence of condensation, the steady-state humidity ratio at the outlet of the dehumidification process cannot be consistent with that at the inlet. And the lower the temperature of cooling water, the more condensate produced, the more obvious the difference. But whether there is condensation or not, the instant maximum moisture removal at the outlet increases with the cooling water temperature decreasing, which indicates that the lower temperature of the cooling fluid is helpful to promote dehumidification.

The outlet air temperature deviates from the previous trend and suddenly drops to form a trough (20.5~24 min) when the cooling water temperature is lower than the dew point, which is caused by the evaporation and heat absorption of condensate on the surface of the heat exchanger. As the condensed water changes from liquid to gas, the outlet air humidity ratio increases rapidly, which deviates from the previous trend and presents a new peak (about 23 min). Besides, a large amount of water vapor flows into the outlet since the evaporation and the desorption occur simultaneously at this stage, so the sensor detects that the relative humidity at the outlet reaches 100%.

3.2 Effects of desiccant coating on dynamic curves under condensation and non-condensing conditions

The similarities and differences of heat transfer performance between DCMHE and MHE under condensation and non-condensing conditions are shown in Fig. 4 (a) and 4 (b), separately.

It is thus clear that the temperature difference between the inlet and outlet air of DCMHE is smaller than that of MHE owing to the thermal resistance of desiccant. In both condensing and non-condensing conditions, the heat transfer performance of DCMHE is reduced, and the regeneration process is more obvious. Therefore, under the same relative humidity, the higher outlet air temperature of MHE in the steady-state stage of the regeneration process makes its outlet air humidity ratio higher than that of DCMHE. Furthermore, when the dehumidification is stable under condensation conditions, the curves of the humidity ratio at the outlet of MHE and DCMHE almost coincide, which are far lower than the inlet air humidity ratio. Hence it can be concluded that condensation dehumidification plays a leading role under condensation conditions.

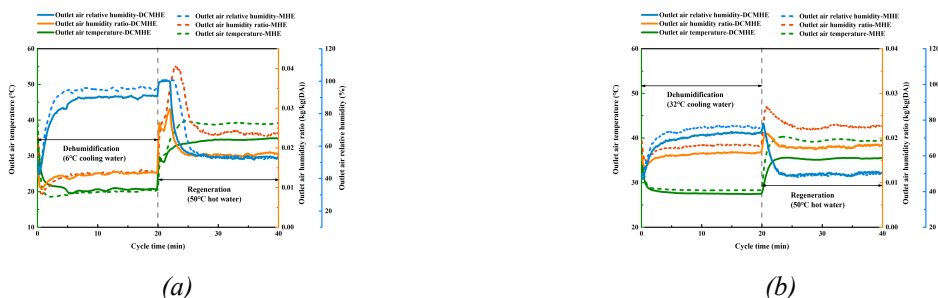


Figure 4 - Outlet air conditions of DCMHE and MHE under (a) condensation (6°C cooling water, 50°C hot water, 2.4 m/s inlet velocity) and (b) non-condensing conditions (32°C cooling water, 50°C hot water, 2.4 m/s inlet velocity).

3.3 Stability of desiccant coated microchannel heat exchanger under condensation conditions

Given that the condensate produced in the dehumidification process will stay on desiccant surface of the heat exchanger and may have a negative influence on the function of desiccant, variation of instantaneous

dehumidification capacity in three continuous dehumidification-regeneration cycles is drawn in Fig. 5 to check whether the performance of DCMHE will be affected. It is evident that three cycles have almost the same change trend and peak value. Therefore, the performance of DCMHE is stable in continuous operation under condensation conditions.

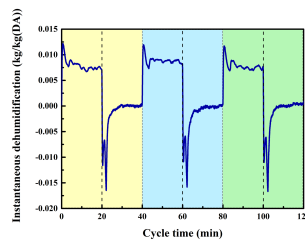


Figure 5 - Instantaneous dehumidification of DCMHE in three cycles time.

4 Conclusions

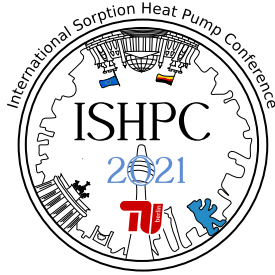
The sudden drop of temperature and humidity in the dehumidification process, the temperature trough in the regeneration process, the double peaks of humidity ratio and 100% relative humidity can be used as the sign to judge the existence of condensation. Condensation dehumidification plays a leading role under condensation conditions. The lower temperature of the cooling fluid is helpful to promote dehumidification. The decisive factor of the outlet air temperature is the internal cooling source temperature. The performance of DCMHE is still stable in continuous operation under condensation conditions.

5 Acknowledgment

This research work is supported by the National Natural Science Foundation of China (Grant No. 51922070).

6 List of References

- [1] Higashi T, Zhang L, Saikawa M, Yamaguchi M, Dang C, Hihara E. 2017. Theoretical and experimental studies on isothermal adsorption and desorption characteristics of a desiccant-coated heat exchanger. *International Journal of Refrigeration*: S0140700717303547
- [2] Jagirdar M, Lee PS. 2018. Mathematical modeling and performance evaluation of a desiccant coated fin-tube heat exchanger. *Applied Energy* 212: 401-15
- [3] Jiang Y, Ge TS, Wang RZ, Huang Y. 2014. Experimental investigation on a novel temperature and humidity independent control air conditioning system – Part I: Cooling condition. *Applied Thermal Engineering* 73: 784-93
- [4] Oh SJ, Ng KC, Chun W, Chua KJE. 2017. Evaluation of a dehumidifier with adsorbent coated heat exchangers for tropical climate operations. *Energy* 137: 441-48
- [5] Sun XY, Dai YJ, Ge TS, Zhao Y, Wang RZ. 2018. Investigation on humidification effect of desiccant coated heat exchanger for improving indoor humidity environment in winter. *Energy and Buildings* 165: 1-14
- [6] Tu YD, Wang RZ, Ge TS, Zheng X. 2017. Comfortable, high-efficiency heat pump with desiccant-coated, water-sorbing heat exchangers. *Scientific Reports* 7: 40437
- [7] Vivekh P, Bui DT, Wong Y, Kumja M, Chua KJ. 2019. Performance evaluation of PVA-LiCl coated heat exchangers for next-generation of energy-efficient dehumidification. *Applied Energy* 237: 733-50
- [8] Xu B, Zhang C, Wang Y, Chen JP, Xu KH, et al. 2015. Experimental investigation of the performance of microchannel heat exchangers with a new type of fin under wet and frosting conditions. *Applied Thermal Engineering* 89: 444-58



Heat Transfer and Frictional Pressure Drop Characteristics of H₂O/LiBr Solution in Plate Heat Exchanger for Triple Effect Absorption Cycle Application

Song, Joo Young¹, Park, Joon Ho¹, Kang, Yong Tae[†] (Corresponding author)

¹ Graduate school of Mechanical Engineering, Korea University, 145, Anam-ro, Seongbuk-gu, Seoul 02841, Republic of Korea

[†] Department of Mechanical Engineering, Korea University, 145 Anam-ro, Seongbuk-gu, Seoul 02841, Republic of Korea

Abstract:

In this study, single-phase H₂O/LiBr solution heat transfer and frictional pressure drop characteristics in plate heat exchanger (PHE) for the widest range of LiBr concentration are experimentally evaluated for triple-effect H₂O/LiBr absorption chiller applications. The test PHE is single-pass heat exchanger with 78.5° chevron angle. Heat transfer experiment in the PHE was conducted with LiBr concentration ranging from 50.21% to 64.92%, solution Reynolds number from 35.01–475.30, and Prandtl number from 3.83 to 24.40, in which the obtained Nusselt number was from 7.40 to 29.10. Frictional pressure drop experiments in the PHE was conducted with LiBr concentration ranging from 50.21% to 62.05%, solution Reynolds number from 52.68 to 536.90, in which the calculated friction factor was from 3.53 to 8.69. All experiments were conducted within ±3% energy balance error range, and the heat transfer and pressure drop correlations developed are applicable within ±10% and ±5% error ranges, respectively.

1. Introduction

The H₂O/LiBr absorption system was firstly developed in the mid-20th century. A low operating pressure of the H₂O/LiBr system allows high-temperature heat sources to be used multiple times. An absorption system that separates refrigerants from absorbents using heat energy multiple times in multiple generators is called a multi-effect absorption system. In 2005, a Japanese manufacturer released the world's first triple-effect absorption system. Then, in 2020, a Korean manufacturer is preparing to enter the market by completing the development of a triple-effect absorption system with a coefficient of performance (COP) of 1.65 and IPLV of 1.75. The H₂O/LiBr triple-effect absorption systems operate with a wider LiBr concentration range than double-effect absorption systems due to the additional refrigerant generation process.

In consideration of various international policies [1, 2] and energy consumption efficiency, absorption systems have been extensively paid attention; hence, studies on absorption systems and their components are being actively conducted. A solution heat exchanger is located between an absorber and a generator, which reduces the driving thermal energy required in the generator and the cooling load of the absorber. A solution heat exchanger is essential for improving the COP of absorption systems [3]; however, studies pertaining to it are insufficient.

Plate heat exchanger (PHE) has been adopted in refrigeration and heat pump systems since its development in the 1920s. A PHE with multiple stacks of wave patterns, despite their small size, has an extremely large heat transfer area. When the PHE is applied to refrigeration systems, both system performance and system volume reduction can be achieved easily. In the development of the triple-effect absorption refrigerator, high performance and compactness of the system are required simultaneously, therefore the application of the PHE to the system is essential. Few researchers evaluated the performance of the PHEs as the solution heat exchanger, but the concentration range of the solution was not wide enough [3-5].

The objectives of this study are to evaluate the single-phase heat transfer and frictional pressure drop characteristics of the H₂O/LiBr solution in the PHE. The findings are then applied to the triple-effect H₂O/LiBr absorption cooling system; hence, experiments were performed for the widest range of LiBr concentration compared with that of other relevant studies.

2. Experiment

Figure 1(a) shows the schematics of the experimental apparatus. The experimental apparatus consisted of two solution loops; a high-temperature solution and a low-temperature solution. Both solution tanks were equipped with three heaters; one 3 kW heater and two 5 kW heaters. The temperature of hot side solution was controlled by only the heaters. The temperature of the cold-side solution was controlled by heaters, followed by the secondary fine adjustments in an auxiliary PHE. In the auxiliary PHE, the heat exchange between the cold-side solution and cooling water occurs; therefore, the cold-side solution releases additional thermal energy. Figure 1(b) shows the schematics of the test PHE, and the specifications of the PHE are summarized in Table 1.

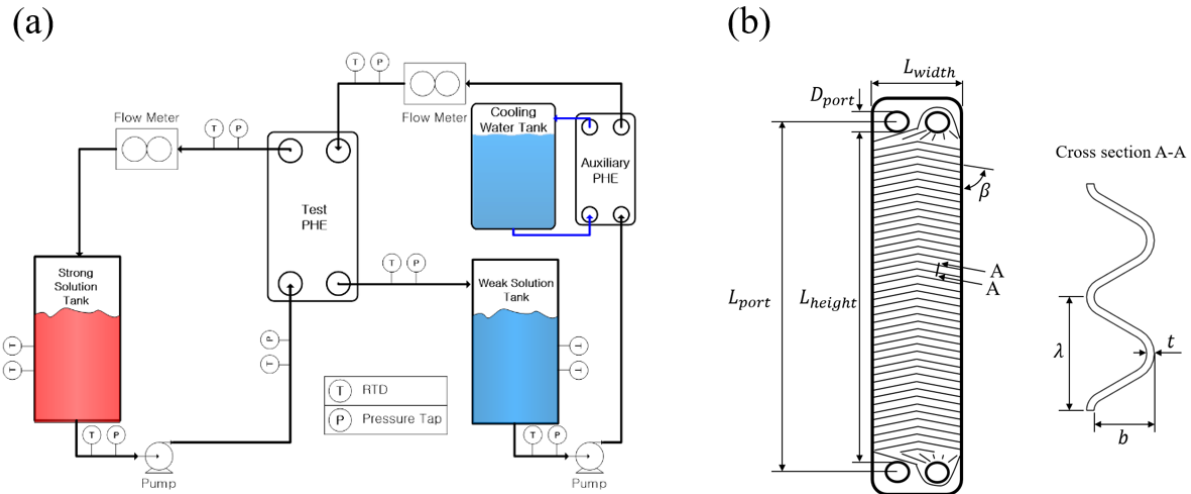


Figure 1 – Schematics of experimental apparatus(a) and test plate heat exchanger(b)

Table 1 – Geometric conditions of the test plate heat exchanger

Port to port length, m	L_{port}	0.466
Plate height, m	L_{height}	0.4315
Plate width, m	L_{width}	0.111
Plate thickness, m	t	0.0004
Corrugation depth, m	b	0.002
Corrugation length, m	λ	0.007
Port diameter, m	D_{port}	0.0345
Chevron angle, $^{\circ}$	β	78.5

RTDs and pressure sensors were installed as close as possible to the inlet and outlet of the test PHE. The hot-side solution flows from the bottom to the top, whereas the cold-side solution flows from the top to the bottom; both solutions were arranged with a single pass and a counter flow in the test PHE. The volumetric flow rate of the cold-side solution was measured before entering the test PHE. The experiment was conducted for more than 20 min under steady state, and all measured data were recorded every 5 s. All heaters were on/off controlled with the solution temperature, and the pumps were controlled by inverters. To ensure a safe experiment, tank sight glasses were installed at a height where the solution soaked all three heaters inside the tanks to ensure that the level of the solution could be verified continuously.

The concentration of the solution was controlled by refrigerant absorption and generation. When distilled water was added to the low-temperature solution in a vacuum state, the concentration of the solution was reduced. By contrast, when steam was released from the solution by heating, the concentration of the solution increased. The concentration, which is a function of temperature and pressure, was calculated using the measured temperature and pressure of the solution in the tank. The properties of the solution were calculated using an Engineering Equation Solver (EES).

3. Results

Energy balance error refers to the difference in heat transfer rate between the hot- and cold-side solution in the PHE. In this study, heat transfer experiments were conducted within $\pm 3\%$ energy balance error in the PHE. Figure 2(a) shows the Nusselt numbers with various Reynolds numbers in the PHE. As shown in Figure 2(a), Nusselt number increased with Reynolds number. Prandtl number of the solution increased as the LiBr concentration increased and the temperature decreased. A high Prandtl number indicates a high Nusselt number within a similar Reynolds number range. The heat transfer experiment in the test PHE shown in Figure 2(a) was conducted with the wide LiBr concentration ranging from 50.21% to 64.92%. The Nusselt numbers obtained were between 7.40 and 29.10 in the PHE. The experimental conditions for heat transfer test in the PHE are summarized in Table 2.

Table 2 – Experimental conditions (Heat transfer test)

	test PHE
LiBr Concentration, %	50.21-64.92
Inlet Solution Temperature, °C	23.16-149.82
Inlet solution Flow Rate, 10^{-3} kg / s	4.88-31.03
Reynolds Number	35.01-475.3
Prandtl Number	3.83-24.40

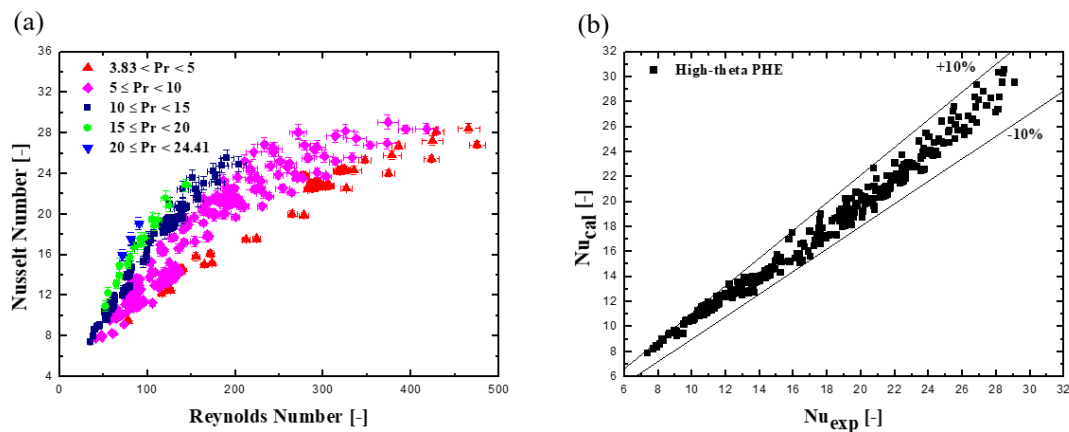


Figure 2 – Nusselt numbers with various Reynolds numbers in the PHE(a) and comparisons between experimental and calculated Nusselt numbers in the PHE(b)

Figure 2(b) compares the experimental and calculated Nusselt numbers in the PHE, obtained by the Wilson plot method [6, 7]. The accuracy of the solution heat transfer correlation of the PHE was estimated to be $\pm 10\%$.

Figure 3(a) shows the friction factor with various Reynolds number in the PHE. As shown in Figure 3(a), the friction factor decreased as the Reynolds number increased, indicating that the frictional pressure drop increased with the flow rate. The frictional pressure drop experiment in the PHE was conducted with the side LiBr concentration ranging from 50.21% to 62.05%. The friction factor obtained was between 3.63 and 8.69. The experimental conditions for pressure drop test in the PHE are summarized in Table 3.

Table 3 – Experimental conditions (Pressure drop test)

	test PHE
LiBr Concentration, %	50.21-62.05
Inlet Solution Temperature, °C	133.81-149.80
Inlet solution Flow Rate, 10^{-3} kg / s	5.21-30.43
Reynolds Number	52.68-536.90

Figure 3(b) compares the experimental and calculated friction factors in the PHE. The form of the friction factor correlation was selected, according to Focke et al. [8]. The accuracy of the frictional pressure drop correlation of the PHE were estimated to be $\pm 5\%$.

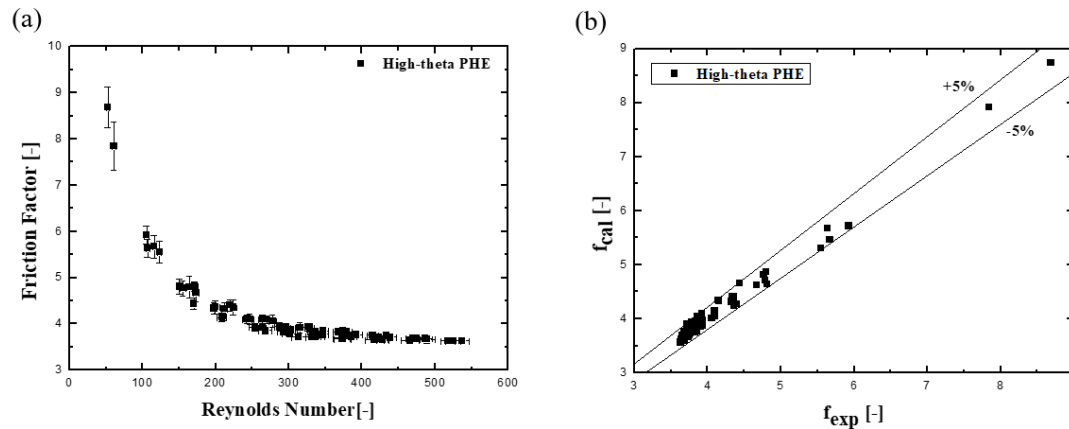


Figure 3 – Friction factor with various Reynolds number in the PHE(a) and comparison between experimental and calculated friction factor in the PHE(b)

4. Conclusions

In this study, the heat transfer and frictional pressure drop characteristics of a H₂O/LiBr solution in the PHE were evaluated with wide LiBr concentration range for the triple-effect absorption refrigerator applications. New experimental heat transfer and frictional pressure drop correlations were developed. All experiments were carried out within $\pm 3\%$ energy balance error range.

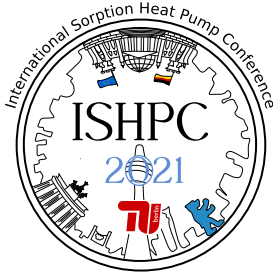
- (1) Based on the experimental results, the new heat transfer correlation was developed and was applicable within $\pm 10\%$ error range for the plate heat exchangers as $Nu = 0.2597 Re^{0.677} Pr^{0.413}$.
- (2) Based on the experimental results, the new frictional pressure drop correlation was developed and was applicable within $\pm 5\%$ error range for the plate heat exchangers as $f = 3.124 + 461.6/Re^{1.112}$.

5. Acknowledgment

This work was supported by the Korea Institute of Energy Technology Evaluation and Planning(KETEP) and the Ministry of Trade, Industry & Energy(MOTIE) of the Republic of Korea (No. 10060218).

6. List of References

- [1] Secretariat, O. (2000): The Montreal protocol on substances that deplete the ozone layer. *United Nations Environment Programme*, Nairobi, Kenya.
- [2] Grubb, M., Vrolijk, C., & Brack, D. (1999): The Kyoto Protocol. a guide and assessment. *Royal Institute of International Affairs*, London, UK.
- [3] Song, J.Y., Lee, J.W., Kang, Y.T. (2019): Comparisons of Nu correlations for H₂O/LiBr solution in plate heat exchanger for triple effect absorption chiller application, *Energy*.
- [4] Kim, H.J., Kim, J.H., Kim, S.S., Jeong, J.H., Kang, Y.T. (2005): Heat Transfer and Pressure Drop Characteristics of Plate Heat Exchangers for Absorption Application, *Proceedings of the SAREK Conference*.
- [5] Kwon, O.K., Cha, D.A., Yun, J.H., Kim, H.S. (2009): Performance Evaluation of Plate Heat Exchanger with Chevron Angle Variations, *Transactions of the Korean Society of Mechanical Engineers B*.
- [6] Wilon, E.E. (1915): A basis for rational design of heat transfer apparatus. *The Journal of American Society of Mechanical Engineers*.
- [7] Fernandez-Seara, J. Uhía, F.J., Sieres, J. Campo, A. (2007): A general review of the Wilson plot method and its modifications to determine convection coefficients in heat exchange devices. *Applied Thermal Engineering*.
- [8] Focke, W.W., Zachariades, J., Oliver, I. (198): The effect of the corrugation inclination angle on the thermohydraulic performance of plate heat exchangers. *International Journal of Heat and Mass Transfer*.



Capillary-assisted evaporation of water from finned tubes: Impacts of dynamics and experimental setups

Seiler, Jan¹, Volmer, Rahel², Krakau, Dennis¹, Pöhls, Julien², Ossenkopp, Franziska², Schnabel, Lena² and Bardow, André^{1,3*}

¹ Institute of Technical Thermodynamics, RWTH Aachen University, 52062 Aachen, Germany

² Department Heating and Cooling Technologies, Fraunhofer Institute for Solar Energy Systems ISE, Heidenhofstr. 2, 79110 Freiburg, Germany

³ Institute of Energy and Climate Research (IEK-10), Forschungszentrum Jülich, 52425 Jülich, Germany

⁴ Energy & Process Systems Engineering, ETH Zurich, 8092 Zürich, Switzerland

* Corresponding Author: abardow@ethz.ch

Abstract:

Capillary-assisted thin-film evaporation has attracted increased attention recently to efficiently evaporate the natural refrigerant water at low pressures. Although capillary-assisted evaporators have been studied in many publications, it remained unclear if published results can be compared. Respective measurements are often conducted under different conditions in terms of setup, procedure and evaluation, and potentially important factors are not specified or disregarded. In this work, we compare experimental setups and procedures. Experiments with finned copper tubes are conducted at RWTH Aachen and Fraunhofer ISE. A set of requirements is identified to ensure good agreement of the overall heat transfer coefficients. Major requirements are the specification of the heat exchanger's surface properties, analysis of measurement uncertainty, well-specified input conditions, and control of non-condensable gases (NCG). Furthermore, dynamic experiments with continuously decreasing filling levels prove to be well-suited to quickly assess the heat transfer at all filling levels in a single experiment. Thus, this work identifies approaches for fast, reproducible and comparable characterization of capillary-assisted evaporation.

1 Introduction

Due to its environmental friendliness, broad availability and high enthalpy of evaporation, water is often used as refrigerant in thermally driven heat pumps. However, low-pressure evaporation of water at low temperatures is challenging since the favourable nucleate boiling regime can only be achieved by high superheats [1] which can usually not be provided in thermally driven heat pumps. To overcome this drawback, capillary-assisted thin film evaporation has been intensively investigated recently [2-6]. However, published measurement results occasionally differ strongly in their underlying experimental setup, instrumentation, procedures, and definition of evaluation quantities. So far, it has not been investigated to what extent these factors affect measurement results and thus if published results are comparable.

In this work, we investigate if capillary-assisted evaporation is affected by the experimental procedure (decreasing vs. constant filling levels) and by experimental setups (setup A at RWTH¹ vs. setup B at ISE²). We identify requirements for obtaining comparable results. Contents of this work have also been published in [7].

2 Experimental setup and data reduction

The geometry of the investigated finned copper tubes (Table 1) was chosen to create strong capillary action for thin-film evaporation. An internal structure of the tube prevents limitations of the overall heat transfer coefficient on the inside.

Table 1 – Details of finned tube investigated in this work.

Tube property	Value	Sketch of tube	Tube in setup
Material	Cu (C12200)		
Tube inner diameter d_{in}	9.6 mm		
Tube outer diameter d_{out}	13.2 mm		
Fin spacing	56 fpi		
Fin width w_{fin}	0.15 mm		
Fin height h_{fin}	0.8 mm		
Tube inner fluid side	Internal structure		
Total length of tubes L	2 m		

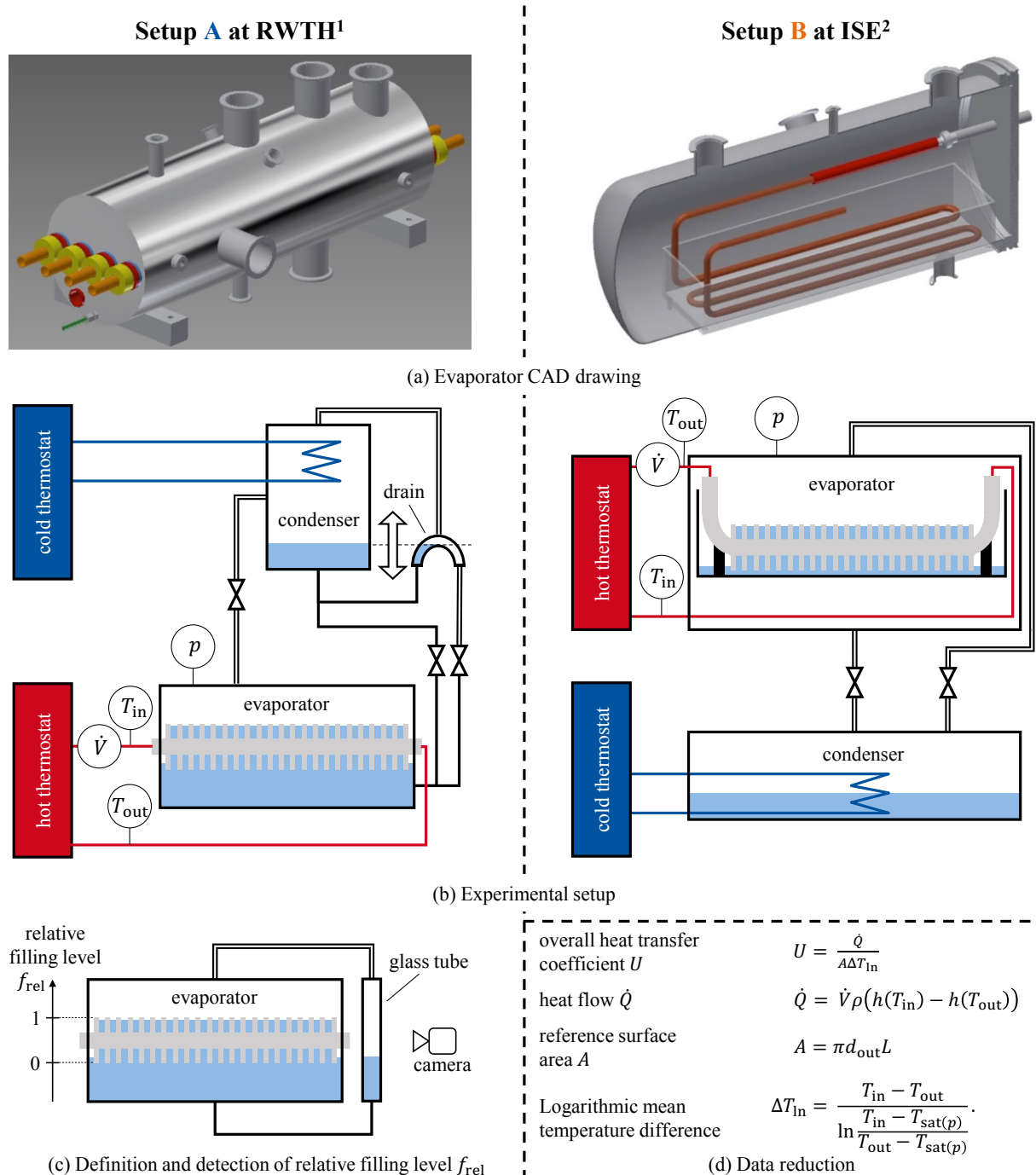


Figure 1 – Employed experimental setups **A** (left) and **B** (right). (a) CAD drawing of evaporator chambers with installed finned tubes. (b) Sketches of experimental setups with installed sensors for temperature (T), volume flow rate (\dot{V}) and pressure (p) in evaporator and condenser. (c) Definition and detection of relative filling level in communicating pipe of experimental setup **A**. (d) Data reduction which is identical for both setups. Refrigerant and secondary fluids are water and its physical properties (density ρ , specific enthalpy h and saturation temperature T_{sat}) are calculated by RefProp using the equation of state “IAPWS-95” [8].

Four identical tubes were serially connected and installed in the vacuum-tight evaporator chambers in the experimental setups **A** and **B**. Details of the similar setups along with the employed data reduction are given in Figure 1. The setups differ in condenser (type and position), the way the refrigerant is supplied to the evaporator (liquid reflux in setup **A** vs. condensed in setup **B**), connection of the tubes (outside in setup **A** vs. within vacuum chamber in setup **B**) and the measurement uncertainty of the used sensors [7].

Both setups measure at decreasing filling levels, thereby determining the overall heat transfer coefficient U at all filling levels within a single experiment. Additionally, the setup **A** also allows experiments at any constant filling

level in steady-state condition. The desired constant filling level in the evaporator can be changed by adjusting the height of the drain without affecting the vacuum in the experimental setup (cf. Fig. 1 (b), left). A camera and an image analysis algorithm automatically determine the filling level. Knowledge of the uncertainty of the conducted measurement is important for the evaluation of low-pressure evaporation. Therefore, the whole measurement chain including data reduction was analysed regarding uncertainty u according to GUM [9] with the “law of propagation of uncertainty” for uncorrelated input quantities x_i

$$u_{f(x_i)} = \sqrt{\sum_i \left(\frac{\partial f}{\partial x_i}\right)^2 u_{x_i}^2} \quad (1)$$

using a coverage factor of $k = 1$. The calculated uncertainties for the U -values are shown in Figure 3.

2.1 Experimental procedure

The following experimental procedure was employed to ensure comparable experiments: Since surface condition affects wetting of the tubes [7], the tubes were cleaned with isopropanol before installation. The refrigerant was degassed, deionized/bi-distilled water. Control of non-condensable gases (NCG) dissolved in the refrigerant or attached to surface is crucial since NCGs affect condensation, evaporation and the evaluation of the saturation temperature by pressure measurement. Thorough evacuation after the installation of the tubes (until experimental results did not change anymore) and additional evacuation prior to (in setup B) or during (in setup A) each experiment ensured no impact from NCGs. Before the experiments started, the tubes were submerged in refrigerant to fully wet their surface. The thermostats were set to constant inlet conditions (cp. boxes in Figure 2 and Figure 3). The inlet conditions of the condenser were set to obtain identical pressure in the evaporation chamber during the experiment. Measured inlet conditions were identical within uncertainty of measurement during all experiments [7].

3 Results

3.1 Impact of dynamics - decreasing vs. constant filling levels

In Figure 2, the results for experiments with decreasing filling level versus 6 constant filling levels and identical inlet conditions (given in blue box in the figure) are presented. Reproducibility of both types of experiments is very good. Although measured U -values at constant filling levels are generally 5-10 % lower than measured U -values at decreasing filling level, they mostly coincide within uncertainty of measurement. Detachment occurs at

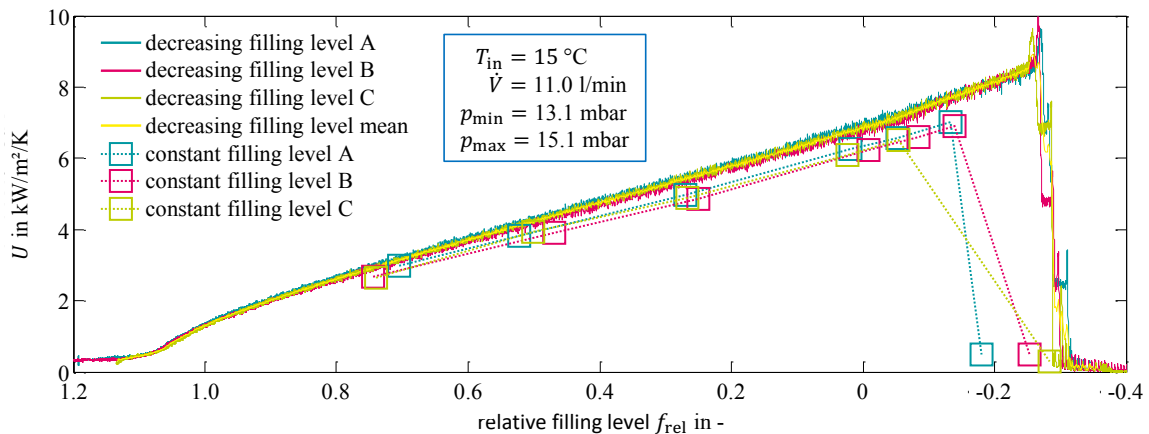


Figure 2 – Overall heat transfer coefficient U for decreasing and constant filling levels in setup A.

higher f_{rel} for constant filling levels, which is probably caused by difficulties to precisely set low constant filling levels due to a meniscus in the drain. Since the menisci between the tubes and the refrigerant in the evaporator are very fragile at filling levels below the tube, these filling levels will probably not be used in real-world applications anyway. Thus, experiments with decreasing filling levels are well-suited to quickly assess the U -values at all filling levels in a single experiment. Furthermore, operating capillary-assisted thin-film evaporator with decreasing filling levels might enhance the U -value by up to 10 %.

3.2 Impact of experimental setups

In general, the results in setups **A** and **B** are very similar (Figure 3). For low driving force (low ΔT_{in} , Figure 3, left), the measured U -values coincide within uncertainty of measurement, while the measured U -values differ up to 24 % for high driving forces (Figure 3, right). Overall, the agreement of the experiments is very good and shows that obtaining comparable results with different experimental setups is possible. The remaining difference can be explained by 3 effects: (1) Capillary action might have deteriorated due to altered surface properties of the tubes in setup **B** caused by necessary brazing for vacuum-tight connection of the tubes. (2) The configuration of the refrigerant pool differs in setup **A** and **B** (Figure 1): in setup **A**, the evaporator contains more refrigerant which is also thermally connected to the metal vessel. Therefore, its thermal mass is increased which leads to comparably lower evaporating temperatures in setup **B** which in turn lead to lower U -values. (3) Unknown measurement uncertainties and/or distorting effects could also have caused the observed differences.

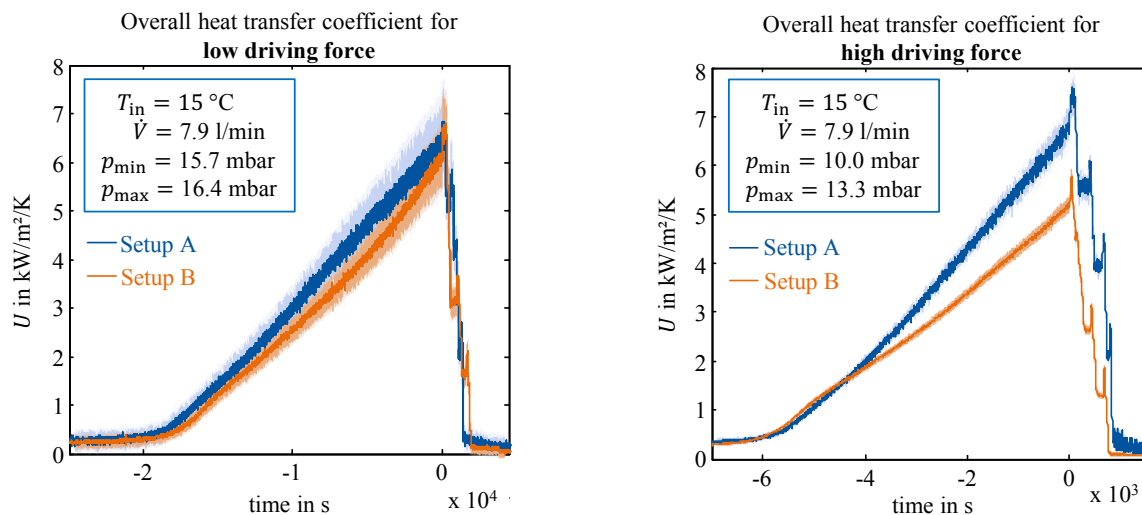


Figure 3 - Overall heat transfer coefficient U shown with uncertainty (as shade in light colour in the background) plotted over time for decreasing filling levels for low driving force (left) and high driving force (right). As can be seen in both plots, measurement uncertainty is lower at high driving force (right), yet similar in both setups (A and B). Both experiments (in setups A and B) are synchronized at the end of the experiment ($t=0$) when the first tube loses contact to the refrigerant pool.

4 Conclusions

The results demonstrate that experiments with continuously decreasing filling levels are well-suited to quickly assess the U -values at all filling levels in one single experiment. Furthermore, experiments in two different setups **A** and **B** can produce identical results within uncertainty of measurement. The following aspects should be considered to ensure reproducible and comparable experiments of capillary-assisted thin-film evaporation: (1) exact definition of the investigated heat exchangers' surface properties is important; (2) analysis of uncertainty of measurement and accordingly choice of appropriate sensors and design of experiment; (3) input conditions need to be identical and if possible constant; and (4) vacuum tightness and control of NCGs are crucial for reproducibility. Our work indicates that measurement results from different laboratories probably allow for a good comparability if the stated aspects are taken into account.

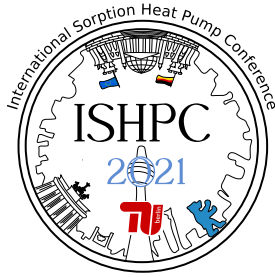
5 Acknowledgment

We thank Wieland Werke AG for providing the heat exchanger tubes. RWTH Aachen and Fraunhofer ISE gratefully acknowledge the financial support from the German Federal Ministry for Economic Affairs and Energy (BMWi) in the "7th Energy Research Programme of the Federal Government" (03EN2002A & 03EN2012A). The work at Fraunhofer ISE was supported by Fraunhofer Zukunftsstiftung in the context of the project HArVest.

6 List of References

- [1] Giraud, F., Rullière, R., Toubanc, C., Clause, M., Bonjour, J. (2015): Experimental evidence of a new regime for boiling of water at subatmospheric pressure. *Exp. Therm. Fluid Sci.*, vol.60, pp.45–53.
- [2] Seiler, J., Lanzerath, F., Jansen, C., Bardow, A. (2019): Only a wet tube is a good tube. *Appl. Therm. Eng.*, vol.147, pp.571–578.

-
- [3] Volmer, R., Eckert, J., Földner, G., Schnabel, L. (2017): Evaporator development for adsorption heat transformation devices. *Renew. Energy*, vol.110, pp.141–153.
- [4] Thimmaiah, P.C., Sharafian, A., Huttema, W., Osterman, C., Ismail, A., Dhillon, A., Bahrami, M. (2016): Performance of finned tubes used in low-pressure capillary-assisted evaporator of adsorption cooling system. *Appl. Therm. Eng.*, vol.106, pp.371–380.
- [5] Lanzerath, F., Seiler, J., Erdogan, M., Schreiber, H., Steinhilber, M., Bardow, A. (2016): The impact of filling level resolved. *Appl. Therm. Eng.*, vol.102, pp.513–519.
- [6] Xia, Z. Z., Yang, G. Z., Wang, R. Z. (2008): Experimental investigation of capillary-assisted evaporation on the outside surface of horizontal tubes. *Int. J. Heat Mass Transf.*, vol.51, pp.4047–4054.
- [7] Seiler, J., Volmer, R., Krakau, D., Pöhls, J., Ossenkopp, F., Schnabel, L., Bardow, A. (2020): Capillary-Assisted Evaporation of Water from Finned Tubes. *Appl. Therm. Eng.*, vol.165, 114620.
- [8] Wagner, W., Pruß, A. (2002): The IAPWS Formulation 1995 for the Thermodynamic Properties of Ordinary Water Substance for General and Scientific Use. *J. Phys. Chem. Ref. Data*, vol.31, pp.387-535.
- [9] Joint Committee for Guides in Metrology (2008): Evaluation of measurement data - Guide to the expression of uncertainty in measurement (GUM). http://www.bipm.org/en/publications/guides/gum_print.html



Absorption of high concentration $\text{NH}_3/\text{H}_2\text{O}$ in a plate heat exchanger

Tao, Xuan¹, Infante Ferreira, Carlos¹

¹Delft University of Technology, Process and Energy Department

Leeghwaterstraat 39, Delft, 2628 CB, the Netherlands, (x.tao@tudelft.nl)

Abstract:

High concentration $\text{NH}_3/\text{H}_2\text{O}$ is suitable for Kalina cycles used for the recovery of low grade heat. Plate heat exchangers (PHEs) are compact and reduce the charge of working fluid. This work investigates the absorption of $\text{NH}_3/\text{H}_2\text{O}$ in a PHE, which has a weight concentration of 96%. Being different from normal absorption systems, the concentration difference between vapor and liquid is small, and apparent heat transfer coefficients (HTCs) are used to interpret the phase change process, which assumes that the vapor and liquid are in equilibrium state. The apparent HTCs and frictional pressure drop of $\text{NH}_3/\text{H}_2\text{O}$ are presented and are compared with those of NH_3 . The mass transfer resistance has noticeable influences on heat transfer depending on the flow patterns, while the influence on frictional pressure drop is minor.

1. Introduction

The utilization of low grade heat is a promising approach to increase the sustainability of energy systems. The recovery of low grade heat can be implemented making use of Organic Rankine Cycles or Kalina Cycles. During evaporation and condensation, Kalina Cycles utilize the temperature glide of mixtures to match the temperature change of the secondary fluid. $\text{NH}_3/\text{H}_2\text{O}$ is a suitable working fluid because of the large latent heat. $\text{NH}_3/\text{H}_2\text{O}$ can be combined with PHEs to transfer large heat loads with compact structures and reduced charge. The condensation of $\text{NH}_3/\text{H}_2\text{O}$ is characterized by a large temperature glide. This process is also referred to as absorption. In order to obtain uniform temperature difference between $\text{NH}_3/\text{H}_2\text{O}$ and the secondary fluid, the bulk weight concentration is required to be higher than 80%. Thus it is different from the phase change process in normal absorbers where the liquid concentration is in the range of 25%~50% and the vapor concentration is >98% [1].

The absorption of $\text{NH}_3/\text{H}_2\text{O}$ within PHEs has been investigated experimentally. The driving potential for the external heat transfer is the temperature difference between the $\text{NH}_3/\text{H}_2\text{O}$ liquid and secondary fluid. The vapor is almost pure NH_3 and is absorbed into the liquid, releasing heat. The corresponding heat transfer correlations available in the literature are only applicable in the original operating ranges. The analysis of mass transfer is limited to the overall absorbed mass flow rate, which determines the heat generation and is sensitive to the two-phase concentration difference [1-3]. The temperature glide of $\text{NH}_3/\text{H}_2\text{O}$ changes significantly with concentration, making it difficult to develop widely applicable predicting models. This paper addresses the absorption of $\text{NH}_3/\text{H}_2\text{O}$ with an average weight concentration of 96%.

The authors have studied NH_3 condensation in a PHE including flow patterns, heat transfer and frictional pressure drop [4, 5]. The fluid properties of high concentration $\text{NH}_3/\text{H}_2\text{O}$ are slightly different from NH_3 . The pure refrigerant and mixture have similar momentum transport characteristics, but the energy transport characteristics are different owing to the simultaneous heat and mass transfer taking place in the $\text{NH}_3/\text{H}_2\text{O}$ process [6]. This paper experimentally investigates the absorption of high concentration $\text{NH}_3/\text{H}_2\text{O}$ in a PHE, and compares the results with NH_3 condensation to analyse the influence of mass transfer resistance.

2. Background

The determination of bulk concentration is key for the design of Kalina Cycles operating with $\text{NH}_3/\text{H}_2\text{O}$. The temperature glide is required to match the temperature change of the secondary fluid from heat source and heat sink. Figure 1 shows the temperature glide of $\text{NH}_3/\text{H}_2\text{O}$, with fluid properties calculated using Refprop [7]. When the concentration is close to 100% and the fluid becomes almost pure NH_3 , the temperature glide of $\text{NH}_3/\text{H}_2\text{O}$ is so small that the advantage of Kalina Cycles cannot be fully exploited. When the concentration is too low, the temperature of $\text{NH}_3/\text{H}_2\text{O}$ changes more than the secondary fluid. Moreover, lower concentration brings about larger mass transfer resistance. Thus an optimum concentration exists and is expected to be located in the range of

80%~100%. As shown in Figure 1, the temperature glide between bubble point and dew point is large in this range, while the temperature glide between bubble point and the point of 0.5 vapor quality is relatively small. The available range is in low and intermediate vapor qualities of high concentration. In real operating conditions of Kalina Cycles, the process starts from two phase and ends up with subcooling. Thus the temperature change of $\text{NH}_3/\text{H}_2\text{O}$ depends on the inlet vapor quality. The optimum concentration is determined by the heat capacity of the secondary fluid and the inlet vapor quality of the condenser. The value is sensitive to the cases and needs to be discussed in the specific conditions. This work investigates the condensation of high concentration $\text{NH}_3/\text{H}_2\text{O}$, also referred to as absorption. The bulk weight concentration of 96% is presented in this paper, with other concentrations being followed up. This process is different from normal absorption since no rectification is involved in the system. Consequently, the vapor and liquid are close to thermodynamic equilibrium.

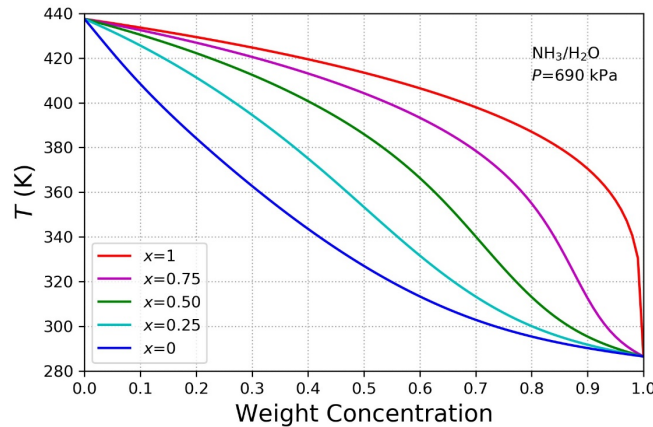


Figure 1 – Temperature glide of $\text{NH}_3/\text{H}_2\text{O}$ with varying weight concentrations. The equilibrium temperatures of bubble point, dew point and three vapor qualities are indicated.

3. Experimental Set-up and Data Reduction

The detailed descriptions of the experimental setup and test section are given in a previous paper [4]. The test section is a gasketed plate heat exchanger with a hydraulic diameter of 2.99 mm and a chevron angle of 63° . The $\text{NH}_3/\text{H}_2\text{O}$ has a bulk weight concentration of 96%. The working fluid is two-phase at the inlet and outlet of the test section. The two phases are mixed at the inlet by spraying the liquid into the vapor flow. The liquid has relatively low NH_3 concentration, while the vapor is almost pure NH_3 . $\text{NH}_3/\text{H}_2\text{O}$ flows from the top to the bottom of the test section, and is cooled by cold water flowing upward. Vapor is absorbed into liquid within the test section, releasing heat to the cold water [6].

The bulk NH_3 concentration is determined by measuring the density of the $\text{NH}_3/\text{H}_2\text{O}$ at liquid state together with the local temperature and pressure [6]. In Eq. (1), the heat transfer rate, Q_{test} , is calculated using the energy balance of the water. The apparent HTC of $\text{NH}_3/\text{H}_2\text{O}$, α_a , is determined by referring to the equilibrium temperature of $\text{NH}_3/\text{H}_2\text{O}$, T_a . Apparent HTC identifies the deterioration of heat transfer owing to mass transfer, but the mass transfer resistance is not calculated directly. Apparent HTC is more relevant for high concentration $\text{NH}_3/\text{H}_2\text{O}$ at low and intermediate vapor qualities, where the concentration difference between the vapor and liquid is small. Compared with intermediate concentrations or complete phase change from vapor to liquid, the temperature glide during partial phase change within two-phase region is relatively small. Additionally, apparent HTC is comparable with the HTC of NH_3 .

$$\begin{aligned}
 Q_{test} &= \dot{m}_w c_{p,w} (T_{w,out} - T_{w,in}) = \dot{m}_a (h_{a,in} - h_{a,out}) \\
 &= UA \frac{(T_{a,in} - T_{w,out}) - (T_{a,out} - T_{w,in})}{\ln \frac{T_{a,in} - T_{w,out}}{T_{a,out} - T_{w,in}}} = \frac{A}{\frac{1}{\alpha_a} + \frac{d_p}{\lambda_{wall}} + \frac{1}{\alpha_w}} \frac{(T_{a,in} - T_{w,out}) - (T_{a,out} - T_{w,in})}{\ln \frac{T_{a,in} - T_{w,out}}{T_{a,out} - T_{w,in}}} \quad (1)
 \end{aligned}$$

In Eq. (2), the frictional pressure drop, $\Delta P_{fri,a}$, is calculated by subtracting the other components from the measured pressure drop, $\Delta P_{exp,a}$, including the pressure drops of inlet and outlet ports, $\Delta P_{in\ port,a}$ and $\Delta P_{out\ port,a}$, the deceleration pressure rise, $\Delta P_{de,a}$, elevation pressure rise, $\Delta P_{ele,a}$, and the mixing pressure drop, $\Delta P_{mix,a}$ [6].

$$\Delta P_{fri,a} = \Delta P_{exp,a} - \Delta P_{in\ port,a} - \Delta P_{out\ port,a} - \Delta P_{mix,a} + \Delta P_{de,a} + \Delta P_{ele,a} \quad (2)$$

4. Experimental Results and Discussion

According to the visualization experiments of NH_3 condensation in PHEs, the flow patterns are full film flow at large liquid mass fluxes and partial film flow at small liquid mass fluxes [4]. During full film flow, the wall surface of the PHE is completely wetted by the liquid film. For partial film flow, parts of the wall are dry. Flow patterns are the function of two-phase fluid properties, operating conditions and channel geometries. The flow patterns for $\text{NH}_3/\text{H}_2\text{O}$ are considered to be the same as for NH_3 . The fluid properties change continuously with concentration, and the properties of high concentration $\text{NH}_3/\text{H}_2\text{O}$ approximate to those of NH_3 . The $\text{NH}_3/\text{H}_2\text{O}$ experiments have been operated at the same ranges of mass fluxes and vapor qualities as the NH_3 experiments. Additionally, the same test section has been used. Both full film flow and partial film flow are separated flow, and the influences of liquid and vapor mass fluxes are investigated separately.

Figure 2(a) presents the apparent HTC of $\text{NH}_3/\text{H}_2\text{O}$ with varying liquid and vapor mass fluxes, whose averaged bulk weight concentration is 96%. The saturated pressure is 690 kPa. The ratio of vapor mass flow rate to liquid mass flow rate is in the range of 0.17-1.78. The liquid weight concentration is above 90% at the inlet and above 94% at the outlet. The vapor weight concentration is higher than 99%. The HTCs of NH_3 are shown for comparison in Figure 2(b), which have been published in our previous paper [4]. In Figure 2(a), the apparent HTCs increase with increasing liquid mass fluxes at small values, and stay almost constant at larger values. The change of the slopes indicates the transition of flow patterns. The value of liquid mass flux for this change is almost the same as that for NH_3 shown in Figure 2(b). The flow patterns for high concentration $\text{NH}_3/\text{H}_2\text{O}$ are expected to be the same as for NH_3 [4].

As reported in [4], partial film flow happens at small liquid mass fluxes. The wall is composed of wetted zones and dry zones. In the wetted zones, the vapor contacts the two-phase interface and is absorbed by the liquid. Heat and mass are transported through the liquid film. In the dry zones, the vapor is in contact with the wall directly. The phase change takes place since the wall temperature is lower than the bubble point of $\text{NH}_3/\text{H}_2\text{O}$. The heat transfer performance at the wall is inferior to that at the two-phase interface where the two-phase concentration difference drives the mass transfer. The area of the wetted zones increases with liquid mass fluxes, promoting the overall HTCs. Full film flow applies at a certain liquid mass flux when the wall gets wetted completely. All the heat is transferred through the two-phase interface. The apparent HTCs become almost constant. The slope of HTCs is different from that of NH_3 in Figure 2(b). For partial film flow, the heat transfer at the dry zones can be regarded as mixture condensation. The concentration of vapor is higher than 99%. According to the experimental results, even minor H_2O brings about noticeable mass transfer resistance and deteriorates the phase change heat transfer at the wall surface. Consequently, the apparent HTCs of $\text{NH}_3/\text{H}_2\text{O}$ are significantly smaller than the HTCs of NH_3 . For full film flow and the wetted zones of partial film flow, the mass transfer resistance hinders the heat transfer. Nevertheless, the concentration difference of NH_3 promotes the absorption of NH_3 vapor into the liquid, which simultaneously drives the heat transfer. These two effects counteract each other. Thus the apparent HTCs of $\text{NH}_3/\text{H}_2\text{O}$ are slightly smaller than the HTCs of NH_3 . Larger vapor mass fluxes enhance the heat transfer, which is the same as for NH_3 .

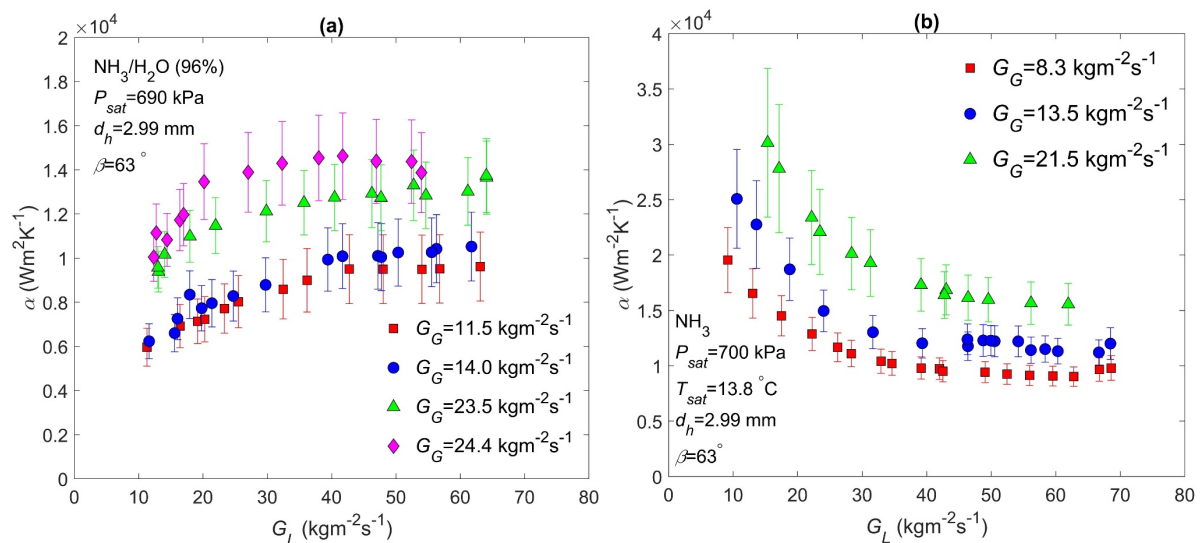


Figure 2 - HTCs with varying liquid and vapor mass fluxes: (a) apparent HTCs of $\text{NH}_3/\text{H}_2\text{O}$, (b) HTCs of NH_3 [4]

The model of $\text{NH}_3/\text{H}_2\text{O}$ absorption has been widely developed. Many researchers neglected the mass transfer resistance for simplification. Some neglected the mass transfer resistance of liquid phase, while others neglected the vapor resistance. When both mass transfer resistances are involved, the dominance of liquid or vapor resistance depends on the operating conditions [8]. In Figure 2, the difference between $\text{NH}_3/\text{H}_2\text{O}$ and NH_3 for partial film flow indicates the vapor mass transfer resistance plays important role. The self-compensating effects of mass transfer for full film flow need to be identified. The prediction of heat and mass transfer should be based on flow patterns.

Larger two-phase mass fluxes increase the flow velocities and enhance the shear force at liquid-vapor interface, which promotes heat transfer. In Figure 2(a), larger vapor mass fluxes significantly increase the apparent HTC. $\text{NH}_3/\text{H}_2\text{O}$ has a large two-phase density ratio. The vapor mass flux contributes noticeably to the flow velocity. However, the influence of liquid mass flux is self-compensating. Apart from enhanced shear force, larger liquid mass fluxes hinder the heat transfer because of thicker liquid film, which acts as heat transfer resistance. Consequently, for full film flow, the apparent HTCs stay almost constant with increasing liquid mass fluxes. The increase of the apparent HTCs for partial film flow is attributed to wetting characteristics.

During the absorption of $\text{NH}_3/\text{H}_2\text{O}$ within PHEs, larger vapor qualities increase the apparent HTCs [6]. In tubes, the apparent HTCs decrease or remain unchanged with increasing vapor qualities [9]. Different channel geometries affect the wetting characteristics [5].

Figure 3 shows the influence of liquid and vapor mass fluxes on frictional pressure drop. For $\text{NH}_3/\text{H}_2\text{O}$, the frictional pressure drop increases monotonously with both mass fluxes, which is the same as NH_3 [4]. The change of flow patterns does not affect the trend of frictional pressure drop. The sharp trend indicates separated flow. Mass transfer resistance has negligible effects on momentum transport characteristics, which further confirms that the flow patterns of $\text{NH}_3/\text{H}_2\text{O}$ are the same as for NH_3 . The flow pattern based model of NH_3 is expected to be also applicable for high concentration $\text{NH}_3/\text{H}_2\text{O}$ [5].

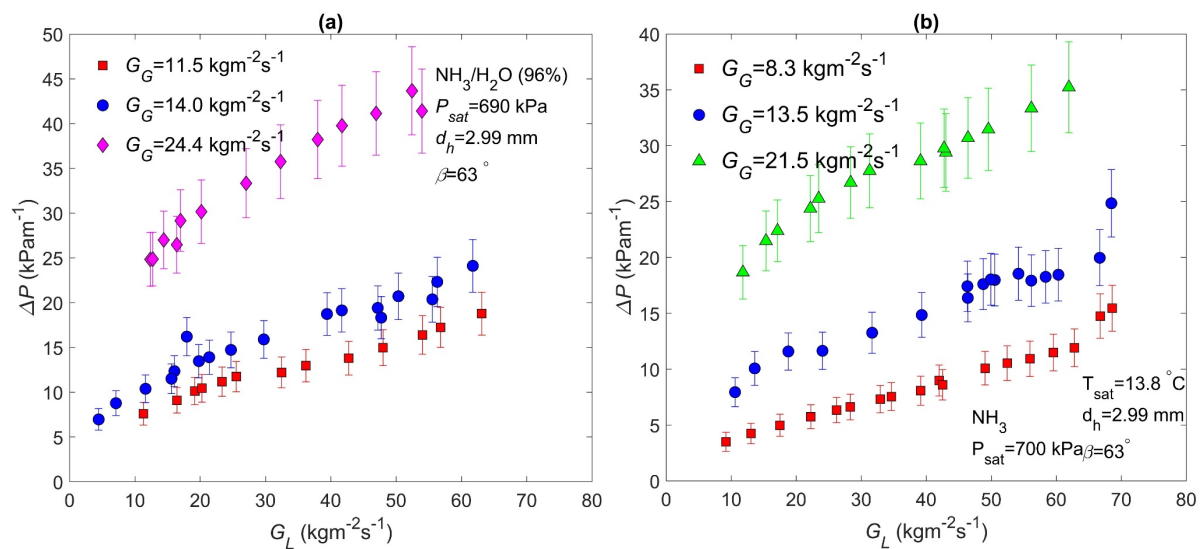


Figure 3 - Frictional pressure drop with varying liquid and vapor mass fluxes: (a) $\text{NH}_3/\text{H}_2\text{O}$, (b) NH_3 [4]

5. Conclusions

This paper discusses heat transfer and frictional pressure drop during $\text{NH}_3/\text{H}_2\text{O}$ absorption in a PHE, and compares the experimental results with pure NH_3 condensation. The bulk weight concentration is 96% and will be extended to larger ranges in the follow-up work. The flow patterns are considered to be the same as for NH_3 condensation because the fluid properties only change slightly. For full film flow, the phase change takes place at the two-phase interface. The apparent HTCs of $\text{NH}_3/\text{H}_2\text{O}$ are slightly smaller than the HTCs of NH_3 . On the one hand, the mass transfer resistance deteriorates the heat transfer. But on the other hand, the two-phase concentration difference of NH_3 drives the mass transfer and promotes the absorption of NH_3 vapor into the liquid. The process is the same at the wetted zones of partial film flow. At the dry zones, the phase change takes place directly at the wall surface. The apparent HTCs of $\text{NH}_3/\text{H}_2\text{O}$ are much smaller than the HTCs of NH_3 because of the mass transfer resistance. The frictional pressure drop of $\text{NH}_3/\text{H}_2\text{O}$ increases sharply with both liquid and vapor mass fluxes, showing the same flow characteristics as for NH_3 . The frictional pressure drop is not affected by mass transfer resistance or the

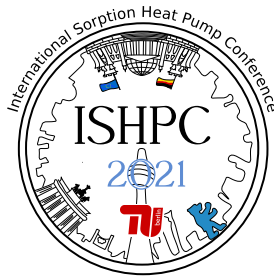
change of flow patterns. Flow pattern based models of heat transfer need to be developed identifying the mass transfer resistance. The frictional pressure drop model of NH₃ is expected to be applicable for NH₃/H₂O [5].

6. Acknowledgment

This project has been developed in cooperation with Allseas Engineering B.V. The authors acknowledge the financial support from the China Scholarship Council and from the Koude Groep Delft / Wageningen.

7. List of References

- [1] D. Triché, S. Bonnot, M. Perier-Muzet, F. Boudéhenn, H. Demasles, N. Caney, Experimental and numerical study of a falling film absorber in an ammonia-water absorption chiller, *International Journal of Heat and Mass Transfer*, 111 (2017) 374-385.
- [2] J. Cerezo, M. Bourouis, M. Vallès, A. Coronas, R. Best, Experimental study of an ammonia–water bubble absorber using a plate heat exchanger for absorption refrigeration machines, *Applied Thermal Engineering*, 29(5) (2009) 1005-1011.
- [3] C.W. Jung, S.S. An, Y.T. Kang, Thermal performance estimation of ammonia-water plate bubble absorbers for compression/absorption hybrid heat pump application, *Energy*, 75 (2014) 371-378.
- [4] X. Tao, E. Dahlgren, M. Leichsenring, C.A. Infante Ferreira, NH₃ condensation in a plate heat exchanger: Experimental investigation on flow patterns, heat transfer and frictional pressure drop, *International Journal of Heat and Mass Transfer*, 151 (2020) 119374.
- [5] X. Tao, C.A. Infante Ferreira, NH₃ condensation in a plate heat exchanger: Flow pattern based models of heat transfer and frictional pressure drop, *International Journal of Heat and Mass Transfer*, 154 (2020) 119774.
- [6] X. Tao, E. Dahlgren, C.A. Infante Ferreira, Condensation heat transfer and pressure drop of NH₃ and NH₃/H₂O within a plate heat exchanger, in: *The 25th IIR International congress of refrigeration*, Montreal, Canada, 2019.
- [7] E.W. Lemmon, I.H. Bell, M.L. Huber, M.O. McLinden, NIST Standard Reference Database 23, Reference Fluid Thermodynamic and Transport Properties (REFPROP), version 10.0, National Institute of Standards and Technology, See <http://www.nist.gov/srd/nist23.cfm>, (2018).
- [8] J.D. Killion, S. Garimella, A critical review of models of coupled heat and mass transfer in falling-film absorption, *International Journal of Refrigeration*, 24(8) (2001) 755-797.
- [9] B.M. Fronk, S. Garimella, Condensation of ammonia and high-temperature-glide ammonia/water zeotropic mixtures in minichannels–Part I: Measurements, *International Journal of Heat and Mass Transfer*, 101 (2016) 1343-1356.



Vertical tube evaporator and thermosiphon desorber for a flue gas-condensing heat pump

Hermann, Tina¹, Dürndorfer, Lena¹, Glöckner, Dominik², Bauer, Marco², Schweigler Christian¹

¹ CENERGIE Research Center Energy-efficient Buildings and Districts

Munich University of Applied Sciences, Department of Building Services Engineering,

Lothstr. 34, 80335 Munich, Germany – tina.hermann@hm.edu

² SCHERDEL Energietechnik GmbH, Scherdelstraße 2, 95615 Marktredwitz

Abstract:

Condensing boilers are widely applied for optimal fuel utilization, but the targeted increase of boiler efficiency by extracting heat from the hot flue gas is often limited by high return temperatures of the heating system. This research investigates the use of an absorption heat pump (AHP) for flue gas condensation of biomass-fired boilers. Sensible and latent heat obtained by cooling the flue gas down to temperatures around 25 °C is upgraded for further utilization in conventional heating systems. Aiming at robust operation and reduced electric energy input, the concept of an AHP with a thermosiphon desorber and a falling film evaporator without refrigerant recirculation is investigated. An experimental setup has been designed to investigate refrigerant evaporation at a vertical tube bundle. The setup aims at characterizing the wetting behavior of tubes with structured surfaces. Heat transfer coefficients around 3.3 kW/(m² K) are expected for lowest mass flow rates per unit wetted perimeter of 0.0076 kg/(m s). The thermodynamic modelling of the thermosiphon desorber predicts comparatively high heat transfer coefficients for the boiling of the sorbent solution, indicating a limitation of the heat transfer through the external heating cycle. Temperature and pressure profiles in the boiling tube are strongly influenced by the operating conditions. Hence, the results of the experimental investigations and the modelling are essential for the final design of the AHP.

Keywords: absorption heat pump, water-lithium bromide, falling film evaporation, thermosiphon desorber

1 Introduction

Cooling the flue gas down below the dew point with release of sensible and latent heat leads to an increase of boiler efficiency over 100%. Utilization of heat pumps for flue gas condensation can provide low cooling temperatures that are independent from return flow temperatures of the heating network. An AHP needs, unlike compression heat pumps, only a fraction of electrical energy for operating the heat pump cycle.

This research investigates the integration of an AHP into the heating system of a woodchips fired boiler. The driving heat to run the sorption cycle can be supplied by the biomass-fired boiler, and consequently, operation of the heat pump cycle is almost completely based on renewable energies. The temperature levels of boiler and heating network are decisive for the performance of the AHP. In previous studies the concept of the heat pump cycle for integration in the biomass heating system has been developed, as illustrated in Figure 1 [1].

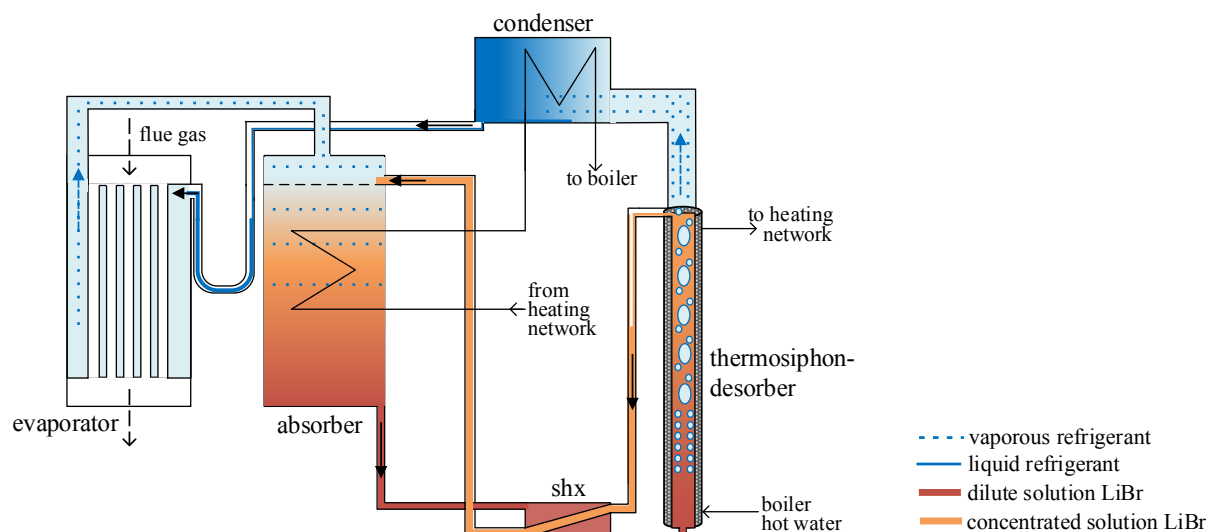


Figure 1: concept of the heat pump cycle

A biomass boiler which provides supply water temperatures of 95 °C is considered to achieve the highest possible temperature level for heat input into the thermosiphon desorber. In the evaporator, heat is transferred to the refrigerant from the flue gas that is cooled down from 140 °C to 25 °C. The extracted heat is upgraded from the low temperature level to release it to a standard heating network with return temperatures of 50 °C by absorber and condenser. Conventional falling film apparatuses are applied for absorber and condenser. Avoiding electrical consumption of a solution pump, natural circulation of sorbent between generator and absorber shall be accomplished by means of a thermosiphon desorber and the evaporator is operated without a pump for refrigerant circulation.

This research paper focuses on experimental investigations of the evaporator and thermodynamic modelling supporting the design of the thermally driven thermosiphon desorber.

2 Experimental investigations of Evaporator

The flue gas-coupled evaporator is designed as falling film evaporator with flue gas directed downstream inside the tube bundle and shell-side evaporation of the refrigerant. Tubes with structured surfaces are used, aiming at complete wetting and evaporation of refrigerant over the whole length of the evaporator. For investigation of the evaporation heat transfer coefficient, a test rig with 2 x 2 vertical evaporator tubes has been erected. For experimental reasons the test tubes are heated by a hydronic heating circuit. The schematic diagram of the setup is shown in Figure 2.

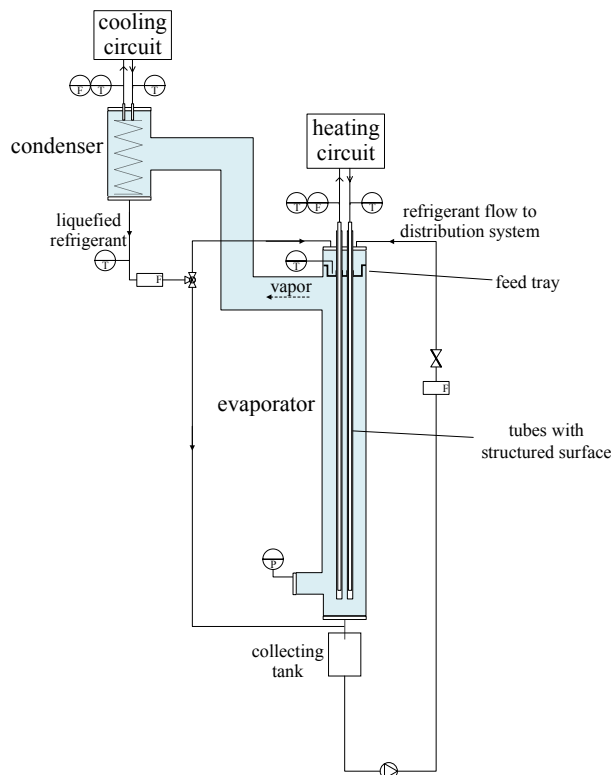


Figure 2: Experimental setup

Aiming at flue gas condensation at about 25 °C, the experiment will be operated at saturation pressure around 25 mbar. The refrigerant is supplied to the top end of the evaporator tubes by a feed tray, serving for even distribution of the refrigerant. The capillary structure of the tubes is expected to assure a complete wetting of the tube surface. The resulting vapor is liquefied by a condenser and flows back to the distribution system of the evaporator by gravity. To adjust the amount of circulating refrigerant, a tank below the evaporator collects and stores excess refrigerant. Thermodynamic modelling of the falling film evaporation indicates heat transfer coefficients around 3.3 kW/(m² K) [1], which shall now be proved experimentally. With a wettable tube length of 4 x 1.5 m an evaporation capacity of 6 kW is expected, which correspond to a refrigerant mass flow rate per unit wetted perimeter of 0.0076 kg/(m s).

3 Thermodynamic modelling of the thermosiphon

3.1 Fundamentals

The thermosiphon desorber serves both the circulation of sorbent solution between absorber and condenser, and the desorption of the refrigerant. The solution enters the bottom end of the vertical boiling tubes and external heat input drives vaporization of the refrigerant, inducing an upward two-phase-flow. The desorption process and the fluid-dynamic situation of the LiBr/water sorbent solution inside the boiling tubes is modelled using the software EES. Over the length of the boiling tube, mass flow rate, heat transfer and pressure losses of the two-phase flow are strongly interdependent. So, the balance equations can only be solved iteratively. Characteristic pressure profiles of the boiling tubes show high pressure at the inlet of the tube which decreases with continuous heat supply due to transition from a single phase to a two phase flow [2]. Given the dependence of the equilibrium temperature of the sorbent solution on pressure and concentration, a variation of the boiling temperature along the boiling tube is found. Pressure loss in the two-phase flow of the solution results from acceleration, friction and change of hydrostatic height. The frictional pressure drop is calculated according to the Lockhart-Martinelli-method [3]. Pre-heating of the solution entering the thermosiphon desorber is analyzed separately and it is assumed that the sorbent solution enters the vertical tube under boiling conditions. Heat is transferred from hot water entering at the bottom of the boiling tube and streaming in upward direction. Thereby a high temperature difference is provided at the inlet, where the highest boiling temperature is expected. Heat transfer is calculated based on correlations for nucleate boiling, according to Steiner and Taborek [4]. The boiling tube is divided into ten sections and within each, energy, mass and pressure balances are solved to characterize fluid properties and flow conditions.

3.2 Results

Results of the modelling are discussed in the following charts. A boiling tube with an internal diameter of 10 mm and a height of 1.5 m has been chosen. Sorbent solution of 54 % mass fraction LiBr enters at an inlet pressure of 19.5 kPa; outlet pressure is 12.35 kPa.

The following charts show the profiles of solution concentration and temperature, and pressure drop over the length of the boiling tube.

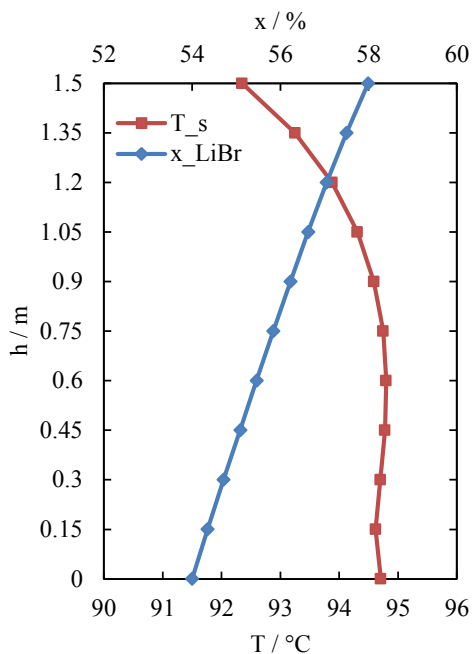


Figure 3: saturation temperature (T_s) and concentration of LiBr solution (x_{LiBr})

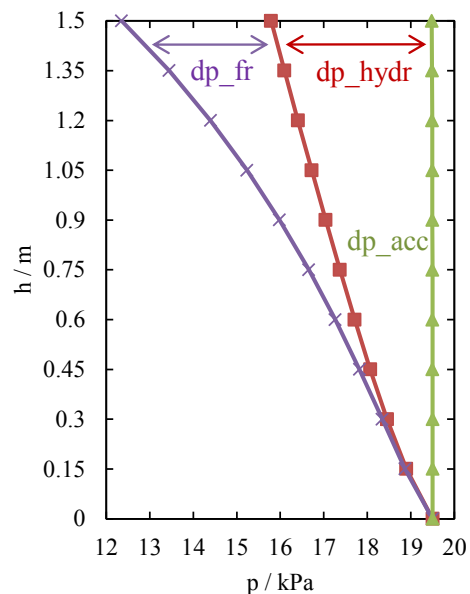


Figure 4: pressure drop due to acceleration (dp_{acc}), friction (dp_{fr}) and hydrostatic (dp_{hydr})

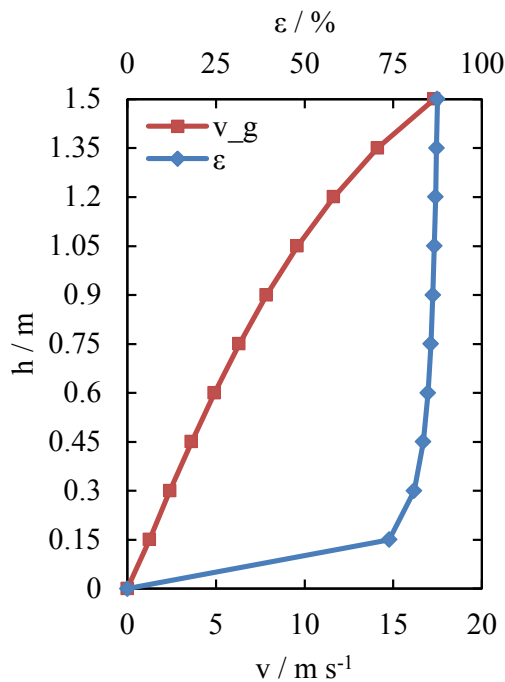


Figure 5: volumetric vapor content (ε) and vapor velocity (v)

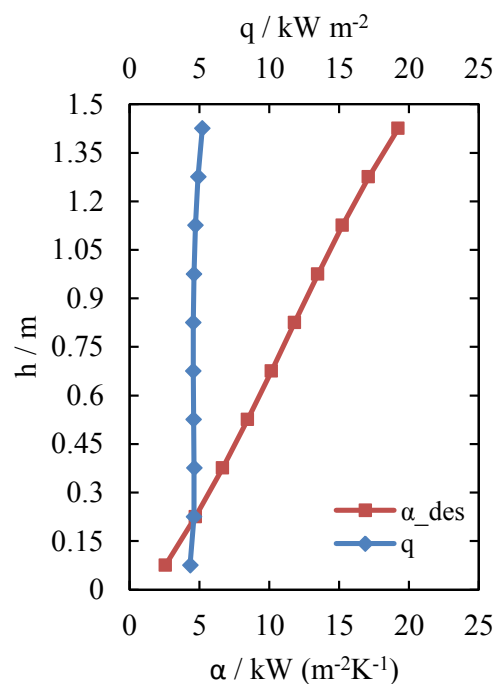


Figure 6: heat transfer coefficient (α) and heat flux density (q)

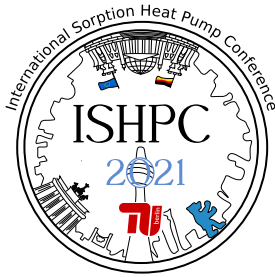
Figure 3 shows high saturation temperature at the inlet of the boiling tube that decreases over the height of the boiling tube. The concentration of the sorbent solution increases constantly. Figure 4 illustrates the pressure drop originating from acceleration, hydrostatic and friction of the two-phase flow. Losses originating from acceleration stay negligibly small. At the inlet, hydrostatic pressure losses are dominating but with increasing height, friction gains importance and results in higher pressure drop values. This corresponds to the rising vapor velocity, as can be seen in Figure 5. Starting from the outlet of the lowest tube section, the volumetric vapor content exceeds 75 % and vapor velocity rises significantly. Figure 6 shows average values for the heat transfer coefficient of the ten modelled tube sections. With progressing desorption and increasing flow velocity, the heat transfer coefficient rises significantly. However, heat flux density stays nearly constant. This indicates that heat transfer is limited by the external heating characteristics. In total, the generated vapor flow and the obtained degasification width reach the required values for implementation of the flue gas fired heat pump.

4 Conclusions

A vertical tube evaporator and a thermosiphon desorber are developed for a sorption heat pump which shall be applied for flue gas condensation of a biomass boiler. Theoretic modeling yields promising results for practical implementation. The contribution will include further results for varying input parameters of the thermosiphon desorber and first experimental data of the evaporator experiment.

5 List of References

- [1] T. Hermann, J. Geier-Pippig, C. Schweigler: Sorption heat pump for flue gas condensation of biomass-fired boilers. International Congress of Refrigeration 2019, Montréal, Canada
- [2] K. Dialer: Die Wärmeübertragung beim Naturumlaufverdampfer. Eidgenössische Technische Hochschule Zürich, Dissertation, 1983
- [3] R. W. Lockhart, R. C. Martinelli: Proposed correlation of data for isothermal two-phase, two-component flow in pipes. Chemical Engineering Progress 45.1 (1949), S. 39–48.
- [4] D. Steiner, J. Taborek: Flow Boiling Heat Transfer in Vertical Tubes Correlated by an Asymptotic Model. Heat Transfer Engineering 13.2 (1992), S. 43–69.



Heat Transfer and Flow Characteristics in Thermosiphon Regenerators of Multi-Stage LiBr/Water-Absorption Heat Pumps

Riepl, Manuel¹

¹Bavarian Centre for Applied Energy Research (ZAE Bayern), Division Energy Storage, Walther-Meissner-Str. 6, 85748 Garching, Germany, manuel.riepl@zae-bayern.de

Abstract

For an efficient, safe and reliable design of direct fired or exhaust gas fired regenerators for multi-stage water/LiBr absorption heat pumps the exact knowledge of local heat transfer coefficients on the solution side is crucial due to high gas temperatures, and high heat loads to the heat exchanger tubes exposed to the corrosive LiBr solution. A promising type of regenerator type is a natural convection boiler - a thermosiphon regenerator. Within this work experimental series have been carried out with detailed results of local solution side heat transfer coefficients and natural circulation flow characteristics. It could be shown experimentally that the heat transfer coefficients (h_{tc}) are only weakly dependant on the circulation mass flow rate but directly and positively dependent on the heat flux. This allows for the application of even very high heat fluxes as they occur in gas fired regenerators.

1. Introduction

Multi-stage absorption heat pumps enable high efficiencies (COP) and/or high temperature lifts and thus enable a wide range of applications, such as high-temperature heat pump applications or simultaneous heating and cooling. However, high temperatures for driving the heat pump process are required which can be found in hot exhaust gases. The input of high-temperature driving heat from exhaust gases into the absorption heat pump process requires a reliable and efficient heat exchanger, called high temperature regenerator. Previous studies (e.g. [1]) have shown that a natural circulation boiler design of the regenerator (*thermosiphon regenerator*) with vertical boiling tubes has significant advantages. The heat transfer on the flue gas side in the boiling tube regenerator type is up to twice as high compared to the shell boiler type - allowing for the same flue gas side pressure drop. That implies that the required heat exchanger surface can be halved.

The *thermosiphon regenerator* type enables compact designs and thus high heat fluxes from high exhaust gas temperatures, gas velocities and thus high exhaust gas-side heat transfers. LiBr solution is highly corrosive, especially at elevated temperatures ($>140\text{ }^{\circ}\text{C}$), so that the temperature of the inner tube wall in contact with the solution should be kept as low as possible to ensure the stability of the heat exchanger. Hence, the decisive parameter for the resulting local tube wall temperature is the local solution-side heat transfer coefficients.

2. Fundamentals

Within the frame of the research work [2] summarized in this paper, the thermo-hydraulic operating principle of natural circulation regenerators has been outlined and an extensive literature research has been carried out on available correlations and calculation approaches for both fluid dynamics and heat transfer. A large number of different empirical approaches are available to calculate the processes in such boiling tubes. Particularly worth mentioning here are: correlations for convective heat transfer, pool boiling (e.g. [3]), flow boiling (e.g. [4, 5, 6]) and frictional pressure loss in two-phase flows (e.g. [8, 9]). The empirical data of all these correlations are largely based on water as process fluid above atmospheric pressure, whereas in the present application aqueous LiBr solution is used under sub-atmospheric pressure conditions. Therefore, the suitability of the existing correlations for this application is questionable and has to be verified. Furthermore, the scattering range of the results from the different correlations and approaches is very high. A challenge in quantifying the processes in such boiling tubes is the thermally driven natural circulation. The supply of heat into the boiling tube - also called riser tube - causes the evaporation (*regeneration*) of refrigerant (water vapour) resulting in a two-phase mixture with a density lower than the density of the single-phase solution in the unheated down comer tube. A circulating mass flow results from this

density difference (see fig. 1a). This mass flow is expected to influence the heat transfer by e.g. its flow velocity, the local vapour contents and the resulting fluid temperature profile in the riser tube. The coupling of heat transfer and fluid dynamics is an implicit problem. The circulating mass flow can not be determined *a priori* and therefore must be determined iteratively. These boundary conditions led to the conclusion that own experimental investigations on fluid dynamics and heat transfer within the boiler tubes are necessary for a reliable and safe design of thermosiphon regenerators.

2.1. Experimental Setup

An experimental test rig has been designed and set up in the laboratory, which enables to determine height-resolved solution side heat transfer coefficients along the upward flow in the boiling tube and to measure the mass flow rate of the natural circulation between riser and down comer tube (see fig. 1a). The core of the experimental setup is the exchangeable electrically variably heated boiling tube. It is included in the vacuum-tight apparatus and is connected to the down comer tube, a sump container which connects both tubes at the bottom, a head container at the top in which the generated steam and liquid solution are separated. In the externally cooled condenser heat exchanger the generated water vapour condenses and the process pressure can be adjusted during operation. The circulation mass flow rate can be determined by measuring the volume flow rate in the down comer tube by the means of a magnetic inductive volume flow meter.

The local solution side htc can not be measured directly but can be determined by the local heat flux (by measuring the electrical power of each local heating clamp), the local tube wall temperature and the local solution temperature in each height element. The tube wall temperatures (12 or 18 depending on the different boiling tube lengths) are determined by means of resistance thermometers axially recessed in the middle of the thick tube shell in deep hole borings (see fig. 1b). Also, the solution temperatures are not measured directly but can be determined by the first of two software models specifically designed for this purpose.

The first model - based on Excel-VBA - calculates the natural convection flow by means of a height segmented calculation of (given) temperatures, local pressure, pressure drops, saturation temperatures, and so forth. The second model calculates the heat conduction in the thick experimental boiling tube (FEM-modelling in *Engineering Equation Solver*). Both models combined lead to the target values - the height-resolved local solution side htc. The experimental setup has been validated by a series of pre-experiments.

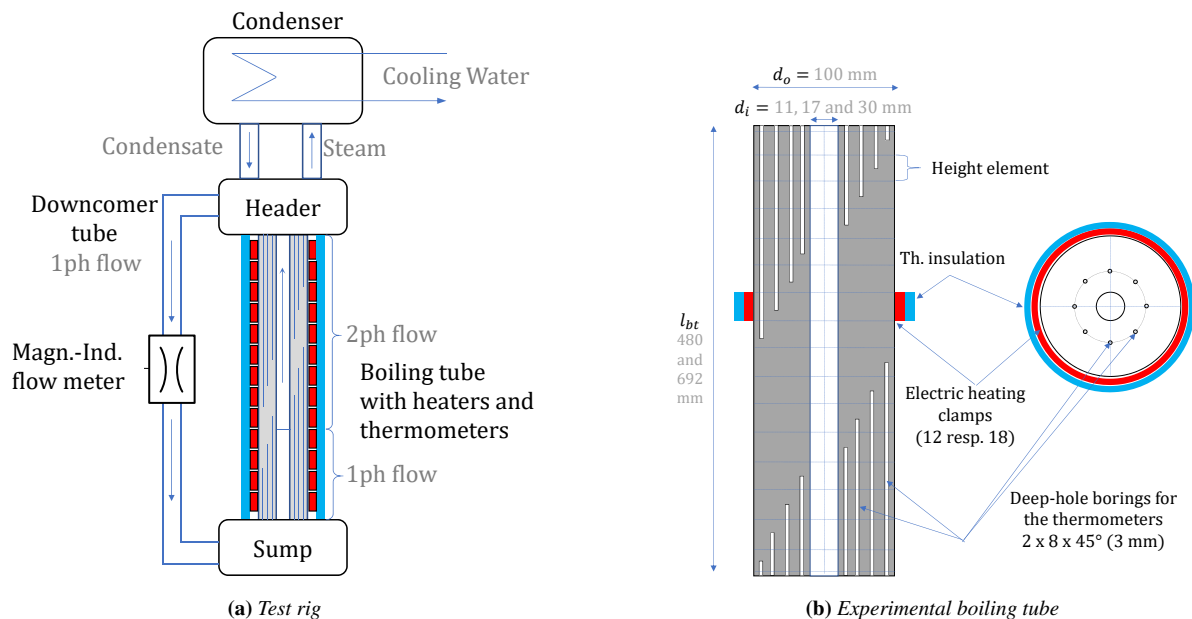


Figure 1: Schematic drawings of experimental test rig (a) and boiling tube (b).

2.2. Experiments

In the main experiments a wide variation of different parameters has been carried out to analyse their effects on both flow characteristics in natural circulation and heat transfer. Six boiling tubes with typical dimensions for regenerators have been investigated, which differed in length and inner diameter and represented typical dimensions in such regenerators (3 tubes with a length l_{bt} of 480 mm each and inner diameters d_i of 11, 17 and 30 mm as well as 3 tubes with the same inner diameter but the tube length l_{bt} of 692 mm). For all tubes, typical parameters for exhaust driven regenerators have been applied. Heating rates (heat flux density at the inner wall $\dot{q} = 5 - 321 \text{ kW m}^{-2}$, for a more detailed distinction, see table 1), global process pressure (expressed by the condensation temperature of the generated steam $\vartheta_C = 60-95 \text{ }^\circ\text{C}$, resulting in pressures of approx. 200-850 mbar_{abs}) and solution concentration ($w_{LiBr} = 55-63 \text{ wt. } \%$) have been varied in narrow steps. The application of electrical heating of the tubes represents the boundary condition of *forced heat flux*, $\dot{q} = \text{constant}$. This boundary condition can be found in exhaust driven regenerators as the highest heat flux resistance lies on the exhaust gas side of the tubes. The inner htc - on the LiBr-side - is at least one magnitude higher. Thus, the heat flux is forced onto the tubes. A total of 2,122 test series for the local htc are available. The detailed measurement and result uncertainty check yielded satisfactory average uncertainties in the mass flow of less than 5%, for the local htc clearly below 20%.

3. Results

3.1. Flow characteristics in natural circulation

The influences of the varied parameters on the characteristics of the natural circulation mass flow have been analysed. The result is a uniform and generally valid picture for all varied parameters. The natural circulation mass flow rate is strongly influenced by the applied heat flux. Starting with small heat fluxes, the mass flow rate increases steeply with increasing heat flux, reaches a maximum and decreases flatly with increasing heat flux (see a typical result for a specific test series in figure 2). These typical characteristics for natural circulation boilers could be shown. Although increased steam quantities - as a result from higher heating rates - cause higher driving forces for the natural circulation they are overcompensated by disproportionately increasing irreversible frictional and acceleration pressure losses in the two-phase flow after having reached the point of the mass flow maximum. Over all test series, mass flow densities ($\dot{m} = \dot{M}/A$, with A being the cross sectional area of the boiling tube) of approx. 200-1000 $\text{kg s}^{-1} \text{ m}^{-2}$ have been observed. The larger the inner diameter of the boiling tube, the larger is the circulating mass flow rate at otherwise identical boundary conditions. Another important parameter influencing the circulation rate is the global process pressure. At the lowest process pressure (equals to a condensation temperature of $\vartheta_C = 60 \text{ }^\circ\text{C}$), the circulation has been up to 30% lower than at the highest process pressure $\vartheta_C = 95 \text{ }^\circ\text{C}$ (see again fig. 2). That can be explained by the lower steam densities and higher volumetric vapour quantities at lower pressures and the associated higher friction and acceleration pressure losses in the two-phase flow region. Further varied parameters (concentration, tube length) are of minor importance. The natural circulation software model could be validated by means of the experimental results and can be used for hydraulic design purposes of such regenerators.

3.2. Heat transfer

At the bottom of the boiling tube there is always a section with sub-cooled single-phase fluid. The solution enters the riser tube with its equilibrium temperature from the header. The liquid head adds pressure to the liquid and that causes higher eq. temperatures which is the reason for the sub-cooled state. With rising height in the tube static pressure decreases and increasing solution temperatures by the applied heat lead to an equilibrium state from where the two-phase flow starts. It has been expected that the single-phase region is characterized by convective heat transfer which is mainly influenced by the flow properties of the fluid namely flow velocity, Re numbers, etc. In the two-phase section additionally heat transfer by flow boiling is expected to occur. In the two-phase region the correlations available in the literature predict higher htc compared to the single-phase region, since the presence of steam promises turbulence-enhancing effects and the influence of bubbly boiling improves heat transfer. In the two-phase region an additional direct heat flux dependency of the htc (by means of pool boiling effects) can be expected.

However, the experiments have shown that the solution side htc - found in all test series and independent of the state of phase - does not significantly depend on the mass flow rate while the htc is positively and continuously dependent on the local heat flux - both for single- and two-phase flow - meaning that increasing heat flux constantly

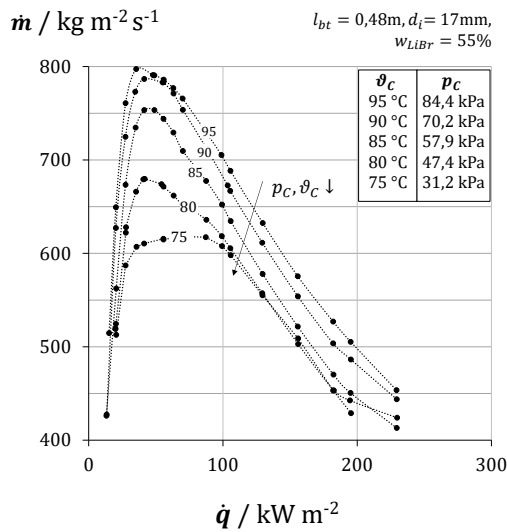


Figure 2: Experimental mass flux density of solution in the natural circulation \dot{m} in dependency of the mean heat flux density \dot{q} and different operational pressures p_c .

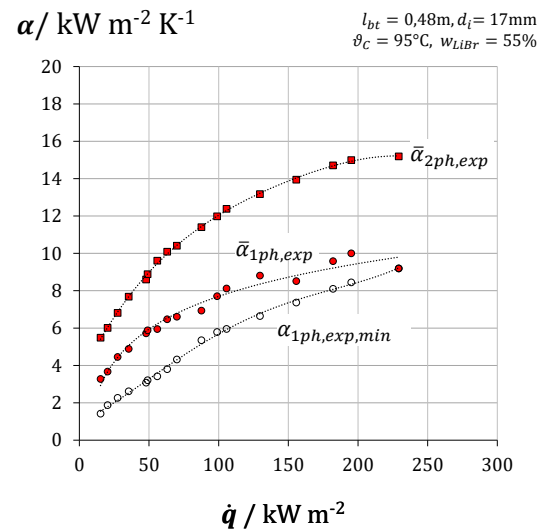


Figure 3: Experimentally height averaged htc for the single-phase $\bar{\alpha}_{1ph,exp}$ and two-phase region $\bar{\alpha}_{2ph,exp}$ and the respective height-minimum htc in the one-phase region $\alpha_{1ph,exp,min}$ in dependency of the mean heat flux density \dot{q} .

leads to increasing htc (see figure 3).

The dependency of the htc on the heat flux in the single-phase region can be explained by the occurrence of sub-cooled flow boiling. The positive dependency of the htc on the heat flux described in the literature could thus be experimentally confirmed. For the present application, however, much higher minimal heat flux densities had been expected for the onset of sub-cooled boiling (e.g. [7]).

In the two-phase region a similar dependence could be shown throughout. Here, the htc there also depends directly on the heat flux density ($\alpha \propto \dot{q}^{0.5 \dots 0.8}$) - as expected qualitatively (e.g. [3]). In addition, the local steam content has a strengthening effect on the htc: the higher the local steam content, the higher the htc.

Over all test series, the average htc in the two-phase region are about 2 times higher than in the single-phase region. Htc between 0.2 and 15 $\text{kW m}^{-2} \text{K}^{-1}$ have been observed in the single-phase region and htc between 1.0 and 20 $\text{kW m}^{-2} \text{K}^{-1}$ in the two-phase region.

As an important result of this work, a simple but reliable estimation of the minimum achievable htc for the investigated operating range in the boiling tube as a function of heat flux density can be given. By means of the following simple equation the minimum achievable htc α_{min} can be calculated by $\alpha_{min} = \frac{\dot{q}}{\Delta\vartheta_{max}}$ as a function of the heat flux density \dot{q} and the maximum wall overtemperature $\Delta\vartheta_{max} = \vartheta_{wall,max} - \vartheta_{fluid}$ which has been detected in the experiments. The maximum resulting wall overtemperatures vary depending on the phase state and pressure range. Table 2 lists the maximum wall overtemperatures one can use for calculating the respective htc applying heat flux density (use table 1 accordingly). At the highest examined pressure ($\vartheta_c = 95 \text{ °C}$) wall overtemperatures $\Delta\vartheta_{max} = 20 \text{ K}$ for one-phase flow region respective $\Delta\vartheta_{max} = 25 \text{ K}$ for two-phase flow can be used. For the lowest pressure examined ($\vartheta_c = 70 \text{ °C}$) a continuous maximum wall overtemperature of $\Delta\vartheta_{max} = 30 \text{ K}$ can be used. The maximum wall overtemperatures for pressures that lie between the two extremes can be estimated by linear interpolation. There are regions of smaller heat fluxes where the maximum wall temperature even is smaller and the htc are higher. The use of this simple estimation does not necessarily lead to the optimum design, as often higher htc can result than calculated by the minimum estimation, it can yet be used to reliably derive a safe design of such regenerators. The use of the available correlations for the htc is not recommended as high scattering of values can be found. Possible reasons are the differences in operating pressure and the use of LiBr solution (e.g.) which has not been in the scope of examination in the literature so far. The influence of the tube roughness especially on nucleate boiling is significant (compare e.g. [3]), therefore the use of tubes as rough as possible is recommended. Although the roughness has an influence on the achievable circulation mass flow - the rougher the pipe the smaller the circulation rate - it has no significant influence on the htc within wide limits. The advantage of improving the htc by a rough tube clearly outweighs here.

Table 1: Heat flux densities \dot{q} applied to each experimental boiling tube (bt)

l_{bt} mm	d_i mm	\dot{q} kW m^{-2}
480	11	13-321
	17	13-321
	30	8-215
692	11	21-152
	17	14-143
	30	5-110

Table 2: Maximum wall overtemperatures $\Delta\vartheta_{max}$ of all experimental data for both phase states and the two extreme operating pressures - all heat flux densities \dot{q} in kW m^{-2} .

ϑ_C in $^{\circ}\text{C}$	one-phase	two-phase
95	$\Delta\vartheta_{max}(\dot{q} \geq 50) = 20 \text{ K}$	$\Delta\vartheta_{max}(\dot{q} \geq 80) = 25 \text{ K}$
	$\Delta\vartheta_{max}(\dot{q} < 50) = 15 \text{ K}$	$\Delta\vartheta_{max}(\dot{q} < 80) = 15 \text{ K}$
		$\Delta\vartheta_{max}(\dot{q} < 50) = 10 \text{ K}$
70		$\Delta\vartheta_{max}(\dot{q} \geq 80) = 30 \text{ K}$
	$\Delta\vartheta_{max}(\dot{q} \geq 7) = 30 \text{ K}$	$\Delta\vartheta_{max}(\dot{q} < 80) = 25 \text{ K}$
		$\Delta\vartheta_{max}(\dot{q} < 50) = 20 \text{ K}$

4. Conclusions

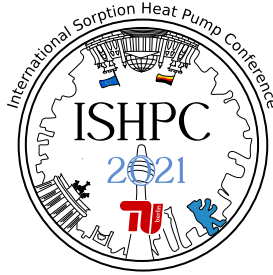
The major conclusion of this work is that the feasible heat transfer on the LiBr solution side is sufficiently high so that the regenerator in thermosiphon design can be exposed to high heat flux densities without violating reliable operating limits with regard to excessive wall temperatures and increased risk of corrosion. A positive dependence of the heat transfer coefficients on the heat flux has been observed throughout, both in the single-phase and the two-phase region within the boiling tube. In the experiments, values of heat transfer coefficients were found to be significantly higher in all operating ranges than would have been expected based on the available literature. The findings shown in this paper extend the understanding and the predictability of the decisive processes in vertical boiling tubes under sub atmospheric pressure conditions and the use of LiBr solution. They allow for the optimisation of the design of high temperature thermosiphon regenerators in absorption heat pumps.

5. Acknowledgment

The outcome of this work could not have been achieved without the funding of the German Ministry of Economics (BMWi) within the research project "Entwicklung eines solarthermischen Waermepumpenheiz- und -kuehlsystems" (FKZ 0325997A). The responsibility for the content of this publication is with the author.

References

- [1] Kren, C., Schweigler, C., Ziegler, F. (2005): Heat Transfer Characteristics in Flue Gas Fired Regenerators of Water/lithium Bromide Absorption Chillers *Proceedings of the International Sorption Heat Pump Conference, Denver, USA, 2005, ISHPC- 072-2005*
- [2] Riepl, M. (2020): Naturumlaufaustreiber für mehrstufige Absorptionswärmepumpen *Doctoral Thesis (under preparation), to be submitted at TUM Department of Mechanical Engineering, Technische Universität München*
- [3] Cooper, M.G. (1984): Heat Flow Rates in Saturated Nucleate Pool Boiling - A Wideranging Examination Using Reduced Properties. *Advances in Heat Transfer 16 (1984), p. 157-239.*
- [4] Kenning, D.B.R. ; Cooper, M.G. (1989): Saturated flow boiling of water in vertical tubes *International Journal of Heat and Mass Transfer 32 (1989), No. 3, p. 445 - 458.*
- [5] Liu, Z. ; Winterton, R.H.S. (1991): A general correlation for saturated and subcooled flow boiling in tubes and annuli, based on a nucleate pool boiling equation *International Journal of Heat and Mass Transfer 34 (1991), No. 11, p. 2759 - 2766.*
- [6] Steiner, D. ; Taborek, J. (1992): Flow Boiling Heat Transfer in Vertical Tubes Correlated by an Asymptotic Model *Heat Transfer Engineering 13 (1992), No. 2, p. 43-69.*
- [7] Hodgson, A. (1986): Forced convection, subcooled boiling heat transfer with water in an electrically heated tube at 100-550 lb/in² *Transactions of the Institution of Chemical Engineers (1968), p. 25-31*
- [8] Mueller-Steinhagen, H. ; Heck K. (1968): Pressure Drop Correlation for Two-Phase Flow in Pipes *Chemical Engineering and Technology (1986), No. 20, p. 297-308*
- [9] Friedel, L. (1979): Improved friction pressure drop correlations for horizontal and vertical two phase pipe flow. *Rohre Rohrleitungsbau Rohrleitungstransport 18 (1979), No. 7, p. 478-491*



Non-absorbable gasses motor-less purge system for absorption heat transformers

Evron, Yigal¹, Gommed, Khaled, Grossman Gershon

¹ Technion – Israel Institute of Technology (shmigal@campus.technion.ac.il)

Abstract:

Non-absorbable gasses in absorption heat pumps are well known to significantly hamper their performance. It is hard to prevent the presence of non-absorbable gasses; therefore, regular purging is required. Publications describing earlier work on purge systems for absorption heat transformers (or type II absorption heat pumps) are relatively scarce. The goal of this work has been to design a motor-less purge system that continuously collects and evacuates non-absorbable gasses. This system was installed and tested on our laboratory scale 10 kW LiBr-H₂O absorption heat transformer. The measurements indicate that system performs well and successfully removes non-absorbable gasses.

1 Introduction

This paper details the concept and measurement results of a motor-less system for purging Non-Absorbable Gasses (or Non-Condensable Gases, NCGs) from an Absorption Heat Transformer (AHT, or type II absorption heat pump). The presence of NCGs in an absorption machine reduces its performance mainly due to their entrainment by the refrigerant/absorbate vapor flow towards the absorbing/condensing surfaces where they accumulate and create a mass transfer resistance for the vapor flow. Typically, in LiBr-H₂O absorption machines, the operating pressure is sub-atmospheric, and penetration of the ambient air is the significant source of contamination. The problem of NCGs is well recognized and any absorption heat pump system should address it.

Some publications predict a severe performance penalty due to the mere presence of NCGs, while others predict a performance reduction somewhat proportional to the percentage of NCG content in the vapor volume. An example of the latter was recently published [1], and includes an informative literature review regarding the performance penalty incurred by NCGs in absorption systems, of both theoretical and experimental results, including the authors' own. Their results are relevant for a rather substantial presence of NCGs (up to more than 30% volume), but not for minute amounts of less than 1% in volume, which might explain the discrepancy with publications which focus on the very minute presence of NCGs [2].

Dozens of publications and hundreds of patents regarding NCG purging from sub-atmospheric pressure refrigeration systems are available since at least the 1920s; with growing interest in the 1940s which is also around the time aqueous LiBr absorption chillers technology was pioneered in the USA [3]. Many relevant patents were later granted to US firms in the late 1960s, and, according to Google Patents, in the late 1980s there was a growing number of relevant Chinese patents.

Some concepts use a cold trap (or a variation thereof) to collect the NCGs. Some use ejectors (or eductors, exhausters, etc.) to entrain NCGs by a motive stream branching from an already available higher-pressure source. After collection, the NCGs are periodically evacuated from the system, along with some vapor (refrigerant). Relatively recently, a non-ejector-based motor-less NCG collection method for AHPs was patented [4]. It is similar to ejector-based systems except that the suction is not produced by high velocity liquid, but by creating a so-called *contraction turbulence* that captures gas in the liquid flow through a dedicated vertical conduit, delivering it to a separate container where the NCGs are trapped.

Another NCGs collection method uses an additional smaller dedicated absorber. This absorber uses a fraction of the solution stream delivered from the desorber and is cooled to be slightly colder than the main absorber to maintain a lower pressure and thus NCGs suction. This method, or a variant of it, was detailed in several patents in the field of absorption refrigeration NCGs separation and collection [5], [6].

2 Background/Fundamentals/Experimental Set-up

We installed and tested a moto-less purge system on an experimental laboratory scale, single-effect LiBr-H₂O AHT system described elsewhere [7]. Figure 1 includes a schematic diagram thereof, where the AHT is faded out to visually highlight the purge system. It is assumed that the reader understands the fundamentals of absorption heat pumps technology, hence the following is just a brief overview.

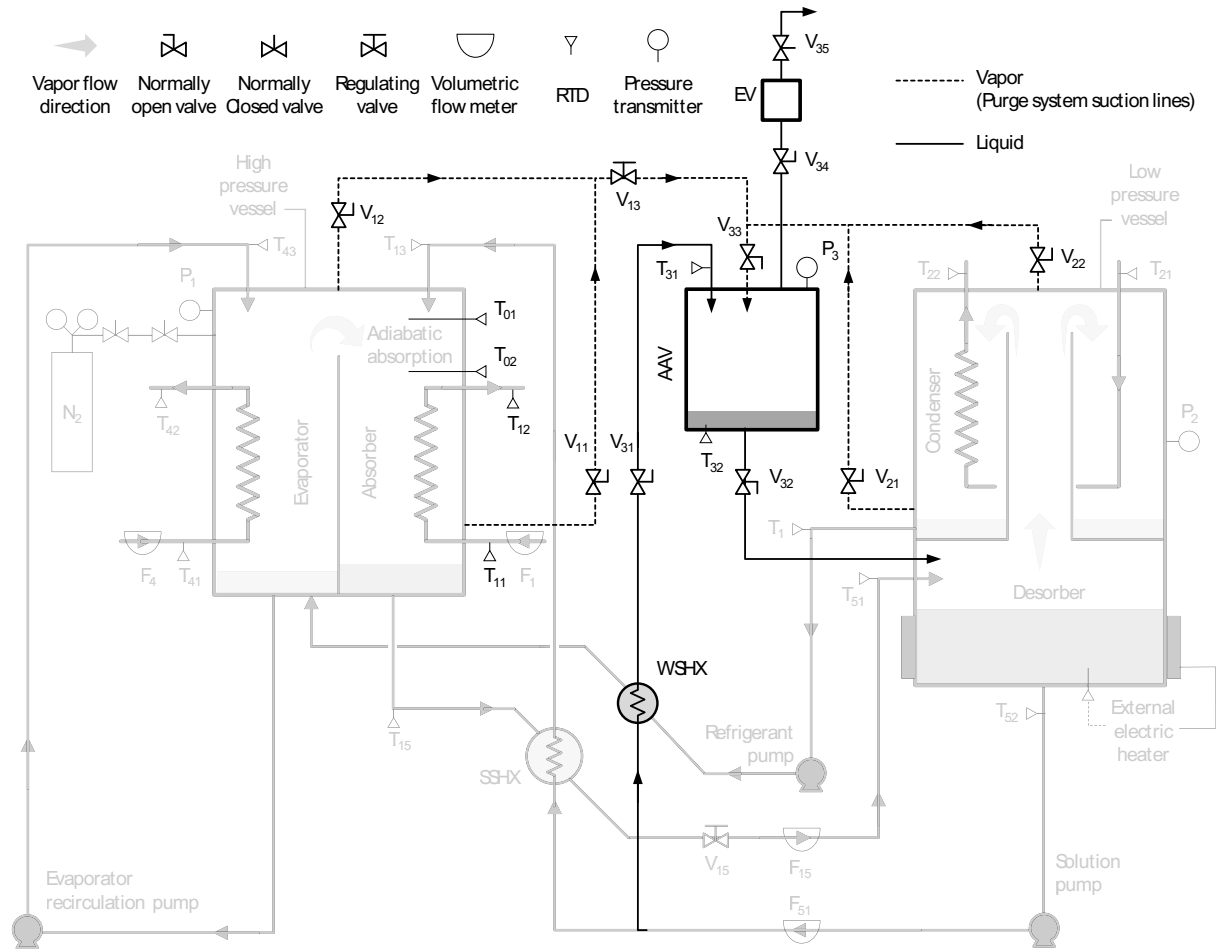


Figure 1 - Non-absorbable purge system diagram superimposed on a faded AHT diagram. Solid arrow lines indicate liquid tubing, dashed lines indicate vapor tubing.

The high-pressure vessel (HPV, on left) is supplied with hot water at about 95°C generated by a dedicated 10 kW in-line water heater. This hot water source powers the evaporator and the absorber. A portion of the temperature-boostered water leaving the absorber is recirculated back to the absorber to maintain its higher temperature, and the rest returns to the in-line heater. The pressure within the HPV (P_1) is measured at the top of the evaporator. The refrigerant and the solution are distributed over the evaporator and absorber tube bundles using spray nozzles. The absorber's spray nozzles atomize the liquid solution to increase its surface area in contact with the surrounding vapor and thus enhance the adiabatic absorption process. To measure this, two RTD probes are used: One (T_{01}) measuring the solution temperature soon after leaving the nozzle, and the other (T_{02}) below it, immediately before the solution contacts the tube bundle.

The absorber power is calculated according to the measured external water temperature difference ($T_{12} - T_{11}$), volumetric flow rate F_1 (the water density and specific heat capacity are estimated according to the measured temperature and pressure in the water line). The low-pressure vessel (LPV, on right) contains the desorber and the condenser. The pressure within the LPV (P_2) is measured at the condenser. The refrigerant in the evaporator pool is continuously recirculated to wet the evaporator tube bundle, and the strong solution in the desorber is continuously pumped, through the cold side of the recuperative solution-to-solution heat exchanger (SSHX), to wet the absorber tube bundle.

The purge system operates in two stages: collection and evacuation. To collect and trap the NCGs, an adiabatic absorption vessel (AAV) is used. The lowest pressure in the system is maintained within the AAV by spraying a pre-cooled small fraction of the pumped concentrated solution from the desorber outlet. It is cooled using a water-solution heat-exchanger (WSHX) which recuperates heat between the solution leaving the desorber and the water leaving the condenser. As the cooled solution is sprayed into the AAV, its vapor pressure is lower than the LPV's, allowing it to absorb vapor from the LPV adiabatically. It is important to emphasize that the WSHX heat is recuperated and not considered a heat loss.

In normal operation, this system continuously collects and traps NCGs in the main volume of the AAV and in the Evacuation vessel (EV, similar in principle to an airlock), while absorbent solution exits from the bottom of the AAV. After sufficient time, the presence of NCGs in the AAV may prevent further absorption, which is manifested by diminished pressure difference between the AAV and the LPV. Also, given that the solution heating effect by absorption is diminished, the solution may leave the AAV colder than it had entered it due to heat losses. Either of these measured indications can be used to determine that it is time to exhaust the EV content to the ambient, by the following steps:

- (1) Isolate the purge system vessels from the AHT except for the solution inlet - allowing the solution to continue entering the AAV. This will cause the solution liquid level to act as a rising piston pressurizing the trapped NCGs at the top of the EV to a pressure similar to the solution pump outlet pressure, which must be above ambient pressure.
- (2) Isolate the EV from the AAV.
- (3) Open the EV outlet to allow the pressurized NCGs to exhaust to the atmosphere.
- (4) Close the EV outlet. Either return to (1), or continue.
- (5) Open to solution outlet to allow the liquid level to recede well below the AAV vapor inlet port.
- (6) Return to normal operation by opening the AAV vapor inlet line.

To demonstrate the purge system operation, while the system operates at a relatively steady state, a measured amount of NCGs (in the form of N_2) is injected into the system, and the performance before and after this deliberate contamination is measured. Then, purging is periodically performed while the AHT performance is monitored. It is difficult to maintain a steady state in our system because the cooling tower power is too low, which causes to cooling water temperature to steadily rise over the course of several hours. However, the injection and purging of NCGs very noticeably impacts the AHT performance almost immediately.

3 Results

To demonstrate the presence of NCGs effect on the absorber performance, Figure 2 presents relevant measurements before and during N_2 injection, and during evacuation. In this experiment, purging was tested from the HPV only, and only from the bottom suction port (V_{12} , V_{21} and V_{22} always closed). During the time prior to evacuation (point 'e'), V_{35} was closed, and the AHT was disconnected from the purge system (V_{11} closed), except for the solution inlet and outlet (V_{31} and V_{32}). The performance is almost immediately reduced as the N_2 is injected at the times indicated as 'a', 'b', 'c', and 'd'. The injected N_2 occupied roughly 0.2% of the HPV volume each time. The absorber power clearly drops as a consequence, each time by roughly 2%. The drop in external water inlet and outlet temperatures T_{11} and T_{12} , and the adiabatic absorption temperatures T_{01} and T_{02} , are also presented.

At the time indicated as 'e', the AAV was connected to the HPV line (V_{33} and V_{11} opened, while V_{12} remains closed), and then a series of purge cycles started. Consequently, the performance recovered as indicated by the increase in absorber power and temperature. The performance in this example does not fully revert to the level it was at before N_2 contamination. This is partly because the purging was performed from the HPV alone, and some NCGs make their way to the LPV over time by dissolving in the solution.

It is important to note a specific inherent problem with this purging method – the potential crystallization risk due to subcooling the solution leaving the desorber. If the machine operates close to the crystallization line, using this purge system may require adjustment of the operating point or stricter control.

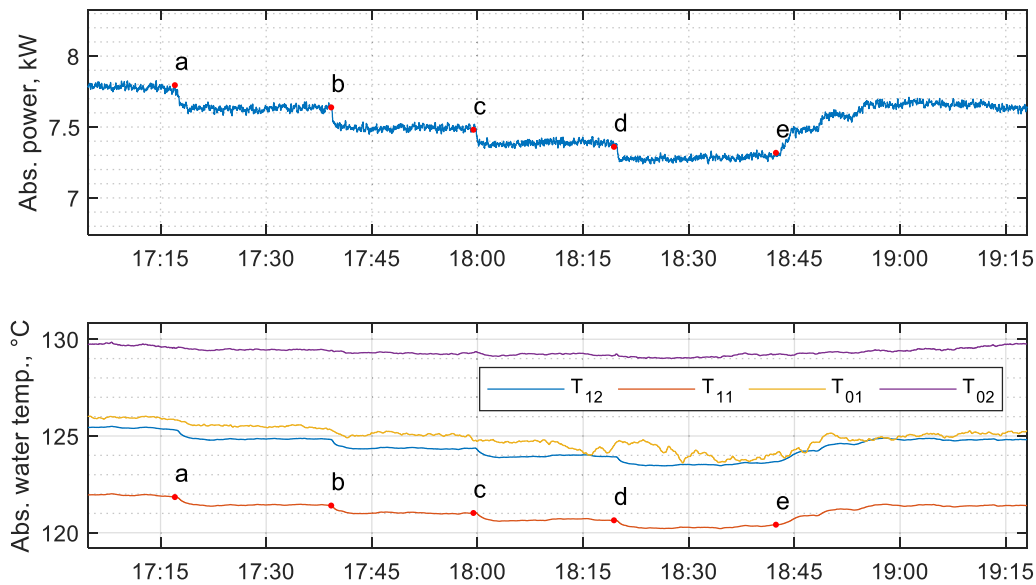


Figure 2 - relevant AHT and purge system measurements before and during NCGs injection, and during their purging. The abscissa indicates the time of day.

4 Conclusions

The proposed AHT motor-less non-absorbable gasses (or non-condensable gasses, NCGs) purge system design was built and operated. This system can potentially operate in a fully automated mode. It demonstrated its ability to collect NCGs, and then remove them from the AHT. This was demonstrated by reversing the performance penalty associated with our deliberate NCGs (N_2) injection. An important observation is that, for a purge system to function properly, it is crucial to design the interior of the AHT volumes to promote sufficiently high vapor velocities to entrain the NCGs to designated removal points, and to place the purge system suction points accordingly to remove them from where they accumulate.

5 Acknowledgment

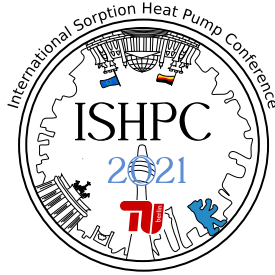


This work has been conducted under the project “Indus3Es: Industrial Energy and Environmental Efficiency” funded by the Horizon 2020 framework of the European Union, Project No. 680738. <http://www.indus3es.eu/>

We are thankful for the support of the Israeli Ministry of Energy in partially funding this work under contract number 216-11-018.

6 List of References

- [1] E. García-Rivera, J. Castro, J. Farnós, and C. Oliet, “Numerical and experimental study of absorption of H_2O vapor in wavy falling film of $LiBr$ aqueous solution in vertical tubes and in presence of non-absorbables,” *Int. J. Refrig.*, vol. 100, pp. 184–195, 2019, doi: 10.1016/j.ijrefrig.2019.01.022.
- [2] G. Grossman and K. Gommed, “Heat and mass transfer in film absorption in the presence of non-absorbable gases,” *Int. J. Heat Mass Transf.*, vol. 40, no. 15, pp. 3595–3606, Oct. 1997, doi: 10.1016/S0017-9310(97)00002-1.
- [3] K. E. Herold, “Design challenges in absorption chillers,” *Mech. Eng.*, vol. 117, no. 10, pp. 80–83, 1995.
- [4] Petersen Stefan, “Method for discharging a gas from a heat pump, and heat pump,” WO Patent 2007006289A1, 11-Jul-2006.
- [5] T. Kazumi, “Device for separating, removing, and storing non-condensable gas in absorption-type refrigerators,” US Patent 3309894A, 1967.
- [6] P. P. Anderson, “Refrigeration,” US Patent 2374521A, 1945.
- [7] Y. Evron, K. Gommed, and G. Grossman, “Adiabatic absorption by absorbent atomization for improving absorption heat transformer performance,” *ASME. J. Heat Transf.*, doi: <https://doi.org/10.1115/1.4046789>.



Big-data analytics of the thermo-hygrometric conditions inside a desiccant based and a traditional flower greenhouse

Longo Giovanni A.¹, Gasparell, Andrea², Ceccato Riccardo¹, Salmaso Luigi¹

¹ University of Padova, Department of Management and Engineering, I-36100, Vicenza, Italy

² Free University of Bozen, Faculty of Science and Technology, I-39100, Bozen, Italy

Abstract:

This paper presents a three-year experimental comparative analysis of a desiccant based and a traditional flower greenhouse in winter mode operation, with particular reference to the thermo-hygrometric conditions inside the greenhouse. The innovative greenhouse allows a primary energy saving with respect to the traditional one ranging from 9.6% in 2010 to 15.1% in 2012. Moreover, it exhibits more stable thermo-hygrometric patterns and it maintains thermo-hygrometric optimum ranges (16-20 °C temperature and 60-80% relative humidity) more times than the traditional greenhouse. In particular the innovative greenhouse operated with H₂O-LiCl desiccant in 2010 exhibited the best humidity control.

1. Introduction

The thermo-hygrometric control is fundamental for the management of flower greenhouses as improper values of temperature and humidity content might cause damage to the plants increasing also the energy consumption.

In the traditional greenhouse air-conditioning system the humidity control is obtained through ventilation with outdoor air, while the temperature level is adjusted by unit heaters, generally fed by hot water or steam.

Sorption technology provides a new technique for controlling the thermo-hygrometric conditions inside the greenhouse based on the use of desiccant. The energy cost of this process is due to the regeneration of the desiccant, when the moisture ab/adsorbed is removed from the solution, and it may be consistently reduced by a proper heat recovery, such as, for example, in multi-effect techniques [1]. The desiccants have also a direct sanitising effect on the air by removing dusts and microbial content [2].

In a previous work [3], the authors carried out an experimental comparative energy analysis between a traditional and an innovative flower greenhouse equipped with a liquid desiccant based air-conditioning system in the winter season. Three different desiccants were tested: H₂O/LiCl in 2010, H₂O/KCOOH in 2011 and H₂O/LiBr in 2012. The primary energy saving of the innovative greenhouse was of 9.6% with H₂O/LiCl in 2010, 11.7% with H₂O/KCOOH in 2011 and 15.1% with H₂O/LiBr in 2012. No corrosion or carry over phenomena were observed during the three years of experimental campaign.

This work reports a comparative analysis aiming at investigating the thermo-hygrometric conditions inside the traditional and the innovative greenhouses by means of big-data analytics techniques to highlight additional benefits of the desiccant based air-conditioning system, beyond the simple energy saving.

2. Background/Fundamentals/Experimental Set-up

Two identical flower greenhouses in northern Italy were provided with a traditional and a desiccant based air-conditioning system, respectively. Both the greenhouses are equipped with unit heaters driven by hot water, for temperature control, and an automatic roof opening system, for humidity control by ventilation with outside air. The innovative greenhouse is also equipped with a Ventilated Latent Heat Converter (VLHC) AGAM 1020 [4] that directly dehumidifies around one third of the air inside the greenhouse by using a hygroscopic salt solution. The hygroscopic solution, after the dehumidification process, is heated by hot water coming from a gasoline boiler and regenerated by scavenger air evolving in a closed loop. Heat recovery is performed on the desiccant regeneration process by condensing part of the humidity content of the scavenger air at the outlet of the regeneration unit, thus recovering the corresponding latent heat to warm up the dehumidified air, before re-entering the greenhouse. The VLHC unit is directly controlled by a hygrometer inside the greenhouse. The total energy demand of the innovative greenhouse includes the thermal energy for driving the unit heaters and the regeneration process in the VLHC unit, while the traditional greenhouse only requires heat to operate the unit heaters. The relative humidity RH and temperature T inside the greenhouses were measured by using a capacitive hygrometer (uncertainty ($k=2$) = ± 1.8 %) and a band-gap thermometer (uncertainty ($k=2$) = ± 0.3 K) integrated within a single measuring probe. Each greenhouse was instrumented with eight probes uniformly distributed over the space.

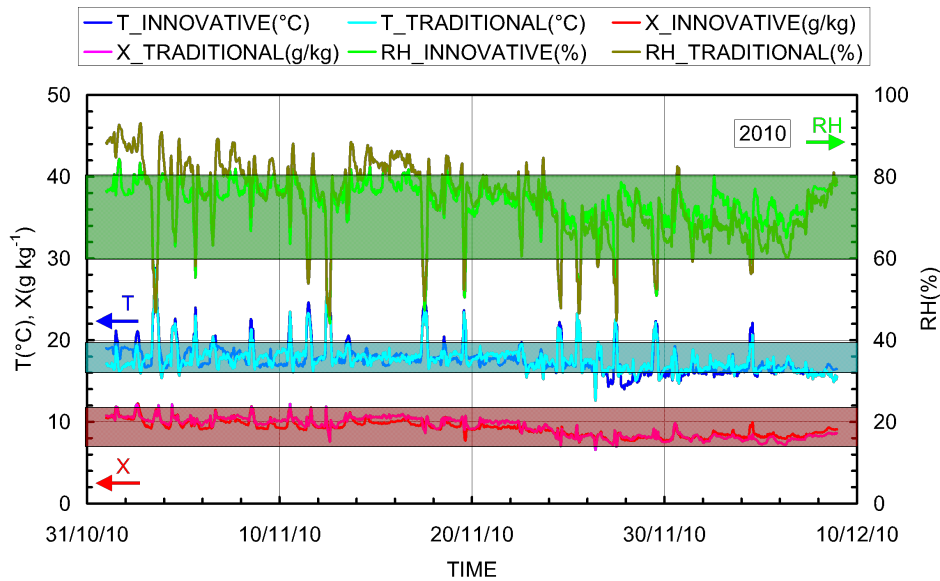


Figure 1 - Hourly average thermo-hygrometric condition inside the greenhouses in 2010 ($H_2O/LiCl$).

3. Results

The relative humidity RH and the temperature T inside each greenhouses were measured over the eight positions six times per hour, from October 31st to December 10th, in 2010, 2011 and 2012, when the greenhouses were filled with Christmas flowers. From the measurement of temperature T and relative humidity RH also the humidity ratio X was computed, therefore the final whole thermo-hygrometric database of the two greenhouses in the three years of experimentation consists of almost 10^6 T , X , and RH data-points. Figures 1, 2, and 3 show the hourly average values for temperature T , humidity ratio X , and relative humidity RH measured inside both the greenhouses in the testing periods of 2010, 2011 and 2012. The hourly averaged air temperature was in general within the optimum range (16-20 °C) for Christmas flowers in both the greenhouses, whereas the hourly averaged relative humidity in the traditional greenhouse in some cases was over the upper limit (80%) selected to prevent the moisture condensation on the plants.

The whole thermo-hygrometric database was processed by big-data analytics and re-sampling techniques. In particular, the adoption of permutation tests, i.e. highly flexible non-parametric testing procedures allowing us to deal with high-dimensional data, and providing some interesting insights on the behaviour of the two greenhouses.

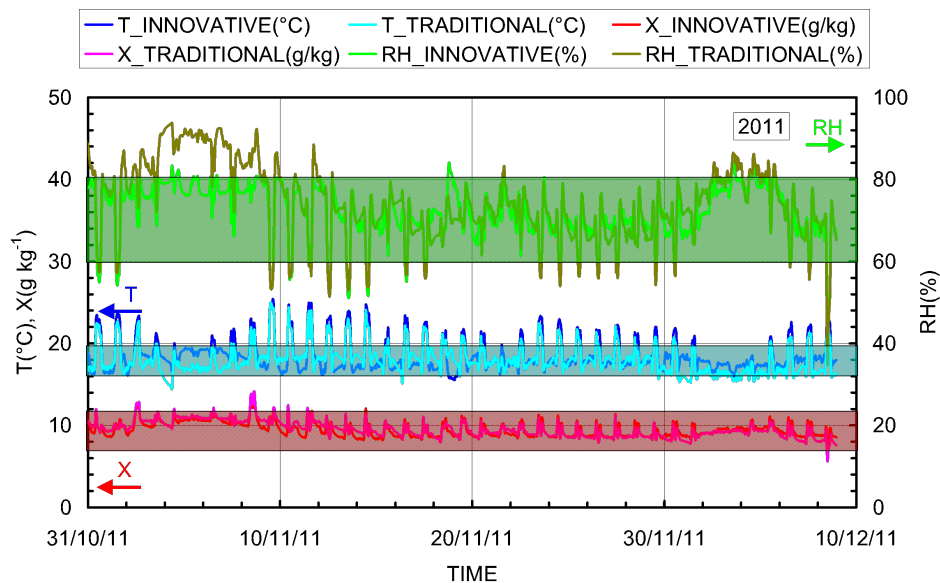


Figure 2 - Hourly average thermo-hygrometric condition inside the greenhouses in 2011 ($H_2O/KCOOH$).

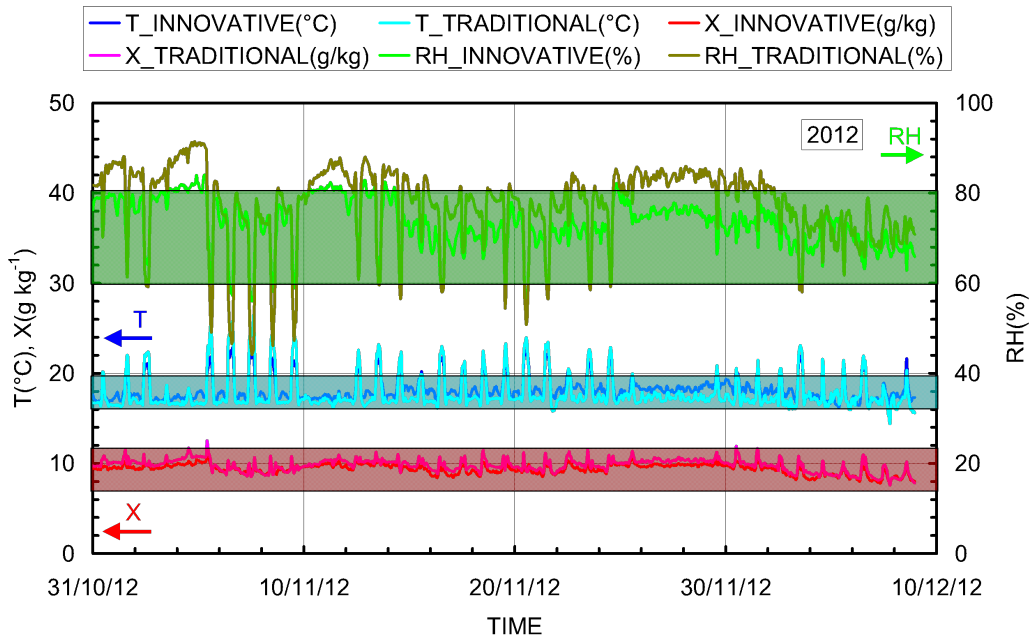


Figure 3 - Hourly average thermo-hygrometric condition inside the greenhouses in 2012 (H₂O/LiBr).

Firstly, we focused on temperature and generated the response variable Y , a binary variable assuming value 0 if temperature T is within the optimum range, 1 otherwise. We then adopted directional permutation tests, using the difference of mean as test statistic and $B=2000$ permutations, in order to identify the measurement occasions in which the innovative greenhouse had a significantly higher number of temperature out-control positions than the traditional one ($H_{1a}: \mu_I > \mu_T$), and vice versa ($H_{1b}: \mu_I < \mu_T$). The numbers of instances in which we concluded in favour of H_{1a} and H_{1b} were then recorded. The same approach was also adopted for the relative humidity. Figure 4 shows the percentage of Temperature out-control ($T > 20$ and < 16 °C) and Relative Humidity out-control ($RH > 80\%$) in the innovative and in the traditional greenhouse in the three years of experimentation. The percentage of RH out-control is always higher for the traditional greenhouse with respect to the innovative one (29.6% vs. 14.1% in 2010, 35.1% vs. 27.6% in 2011 and 47.1% vs. 41.8% in 2012), while in general the percentage of T out-control of the traditional greenhouse is lower than in the innovative (37.8% vs. 35.6% in 2010, 39.8% vs. 43.2% in 2011 and 24.8% vs. 30.6% in 2012).

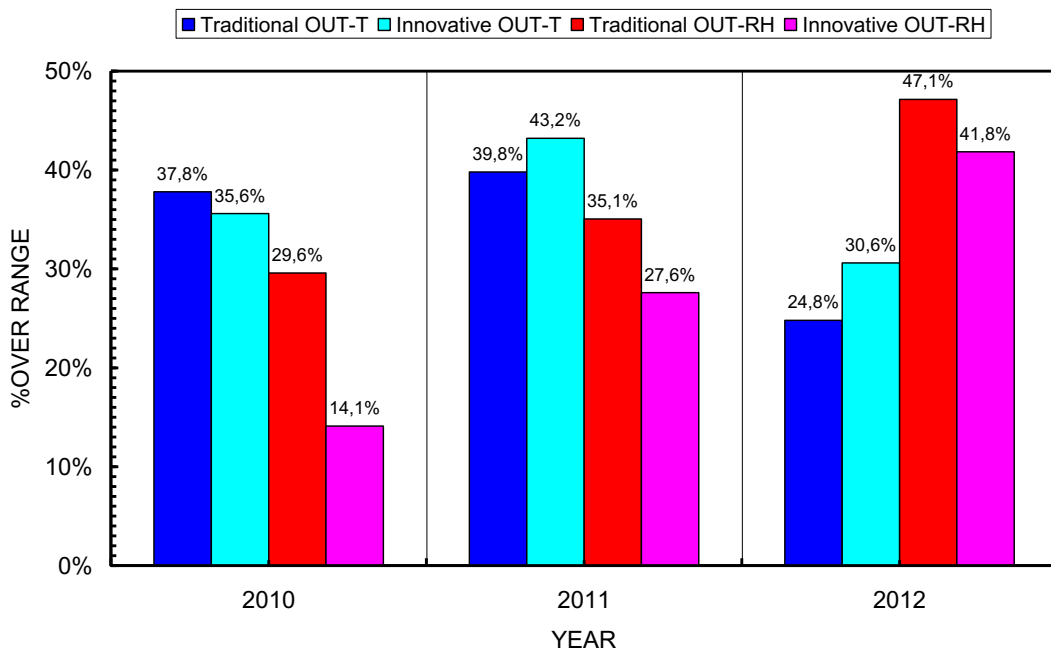


Figure 4 - Percentage of T and RH out-control inside the greenhouses in 2010, 2011 and 2012..

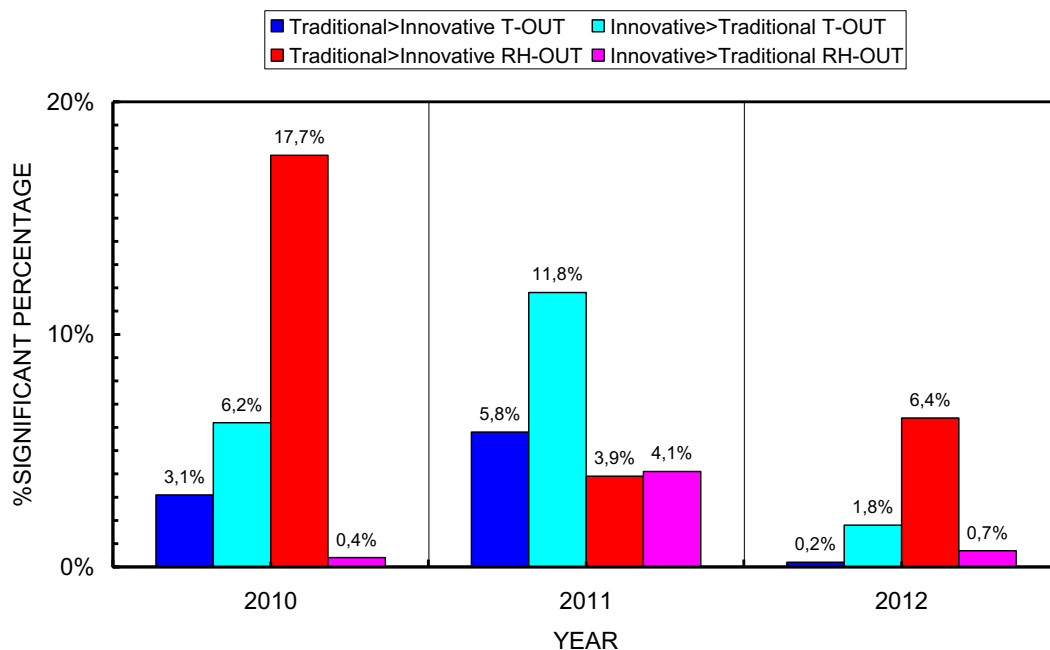


Figure 5 - Percentage of T and RH out-control inside the greenhouses in 2010, 2011 and 2012..

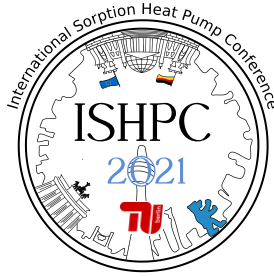
These results are also confirmed by the analysis of the distribution of the significant differences in terms of number of out-control positions for temperature T and relative humidity RH in the innovative and traditional greenhouses illustrated in figure 5. The percentage of occasions in which we conclude in favour of H_{1a} (see column *Traditional < Innovative T-OUT*), i.e. the innovative greenhouse has a significantly larger number of temperature out-control positions than the traditional one, is always higher than its counterpart, the percentage of cases in which data support H_{1b} (see column *Traditional > Innovative T-OUT*): 6.2% vs. 3.1% in 2010, 11.8% vs. 5.8% in 2011 and 1.8% vs. 0.2% in 2012. On the other hand, considering the relative humidity, the percentage of occasions in which the traditional greenhouse has a worse performance than innovative (i.e. data support H_{2b}) is in general higher than the percentage of occasions in which the innovative greenhouse has the highest number of out-control positions (i.e. we conclude in favour of H_{2a}): 17.7% vs. 0.4% in 2010, 3.9% vs. 4.1% in 2011 and 6.4% vs. 0.7% in 2012. These behaviours might be explained considering the different strategy in thermo-hygrometric control of the traditional and the innovative approach. The sorption dehumidification unit controls the moisture content of the greenhouse by introducing hot dehumidified air, therefore it is easy to overcome the optimum thermal range. On the contrary, the traditional system controls the internal humidity level by ventilation with outside dry and cold air, therefore it is easier to overcome the optimum range of relative humidity.

4. Conclusions

The big-data analytics of the thermo-hygrometric database of the two greenhouses in the three years of comparative analysis that consists of almost 10^6 T , X , RH data points, shows that the thermo-hygrometric patterns are more stable and the thermo-hygrometric optimum ranges are maintained more times in the innovative greenhouse than in the traditional one. In particular the innovative greenhouse operated with H_2O - $LiCl$ desiccant in 2010 exhibited the best humidity control. This result highlights additional benefits of the desiccant based air-conditioning system with respect to the traditional one, beyond the simple energy saving. Moreover, no corrosion or carry over phenomena were observed with all the desiccants tested.

5. List of References

- [1] A.Lowenstein. Review of liquid desiccant technology for HVAC applications. *HVAC&R Research* 14(2008) 819-839.
- [2] B.Kovac, P.R.Heimann, J.Hammel. The sanitizing effect of desiccant-based cooling. *ASHRAE J.* 39(1997) 60–64.
- [3] G.A.Longo, A.Gasparella. Three years experimental comparative analysis of a desiccant based air-conditioning system for a flower greenhouse: Assessment of different desiccants. *App.Therm.Eng.* 78(2015) 584–590.
- [4] Agam. VLHC Dehumidifier for Cold-Climate Greenhouses. www.agam-greenhouses.com.



Heating and Cooling of a Building by Absorption Heat Pumps driven by Evacuated Tube Solar Collectors (ETCs)

Lazzarin, Renato¹, Noro, Marco²

¹ Department of Management and Engineering, University of Padova – 36100, Vicenza (Italy),
renato@gest.unipd.it

² Department of Management and Engineering, University of Padova – 36100, Vicenza (Italy),
marco.noro@unipd.it

Abstract

Solar assisted heat pumps till now have used the solar collectors as a cold source. Solar collectors provided when possible direct heating, otherwise they offered temperature levels higher than outside air for the heat pump evaporator. At the same time, solar thermal cooling exploits solar collectors and the absorption chiller only in hot months. The paper considers the possibility of employing ETCs to drive an absorption heat pump that is in summertime the absorption chiller. The cold source is the ground which is recharged by the solar collectors in mid seasons and by the cooling of absorber-condenser in summer. The study analyses the system behavior in yearly operation evaluating also the role of suitable storage capabilities in a temperate climate.

1. Introduction

An interesting option to increase attractiveness of solar thermally driven systems with respect to the actual more competitive PV heating and cooling systems can be the utilization of Evacuated Tube Collector(s) (ETC) as driving energy at the generator of a thermally driven heat pump. This can be nowadays possible thanks to a series of improvements regarding the solar thermal collectors occurred in the last years [1], thus a first order thermal losses coefficient of $1 \text{ W m}^{-2} \text{ K}^{-1}$ or even less is normal in ETC largely available on market. As a matter of fact, thanks to the high thermal efficiency also during colder months, suitable outlet temperature can be reached if a sufficient solar radiation impinges the collectors. Obviously, the performance depends on the climate of the resort considered, in particular on the outside air temperature and the clearness index. For such an annual utilization of solar thermal energy, a thermally driven chiller that can operate as heat pump with the suitable temperatures at the three heat exchangers (generator, evaporator, absorber/condenser) has to be coupled.

In this study, a simulation model of a thermally driven dual-source heat pump/chiller that faces the heating and cooling loads of an existing building is developed. The main novelty of this study is the utilization of thermal energy produced by ETC as both driving and heat source energy of a thermally driven heat pump/chiller.

2. Background

2.1. The simulation model

The case study concerns an existing real building, the F92 sited at ENEA Casaccia Research Centre near Rome (Italy) that houses the “Scuola delle energie” (“Energies School”). It is developed in three-storey (basement, ground floor and first floor, the last two being identical) for a volume of 620 m^3 and a total floor surface of 230 m^2 . The building/plant system has been modelled in Trnsys on the basis of transparent and opaque surfaces characteristics, internal gains and thermal/cooling plant schedules data supplied by ENEA [2]. The heating and cooling loads are calculated on the basis of climatic data of the Italian resort Belluno (46.14° N latitude) [3].

The original feature of the HVAC plant is the solar section composed of ETCs that drive a thermally driven absorption heat pump which satisfies all the loads. Moreover, the ETCs provide direct heating when possible, or act as heat pump cold source. The plant is set up by four main loops, and the various components are connected via suitable storage tanks (Figure 1). The control logic is based on a survey of solar radiation intensity (S), determining an operation threshold of 50 W m^{-2} , and on a comparison between the various suitable tanks set-points and the available temperatures in the different circuits (see next section 2.2).

The ETC considered is a modern collector available on the market, with very low first order heat loss coefficient ($\eta_0=71.8\%$, $a_1=1.051 \text{ W m}^{-2} \text{ K}^{-1}$, $a_2=0.004 \text{ W m}^{-2} \text{ K}^{-2}$). It is modelled by type 71, with a tilt of 30° and an azimuth of 0° . The ground field is modelled by type 557a with a ground thermal conductivity of $2.87 \text{ W m}^{-1} \text{ K}^{-1}$, and a storage heat capacity of $2016 \text{ kJ m}^{-3} \text{ K}^{-1}$. The ground field is composed by $n \times 50$ or $n \times 100 \text{ m}$ in a row vertical tube U heat exchangers (n varying with the ETC field area), with an outer diameter of 32 mm and a thickness of 2.9

mm, distance 6 m. The tanks are modelled by type 4a (Generator Tank, Cold Tank) and type 60d (Heat Source Tank, Hot Tank). Finally, as no specific type is available in Trnsys for modelling a thermally driven heat pump, type 927 is used to model the water-water heat pump based on nominal data from a manufacturer concerning thermal power, cooling power and thermal power consumption at various heat source, heat sink and generator temperatures, considered varying in useful ranges according to source and sink temperatures (respectively $2 \leq T_{source_tank} \leq 20$ °C and Hot Tank or Heat Source Tank max 40 °C), and generator temperature (75-95 °C).

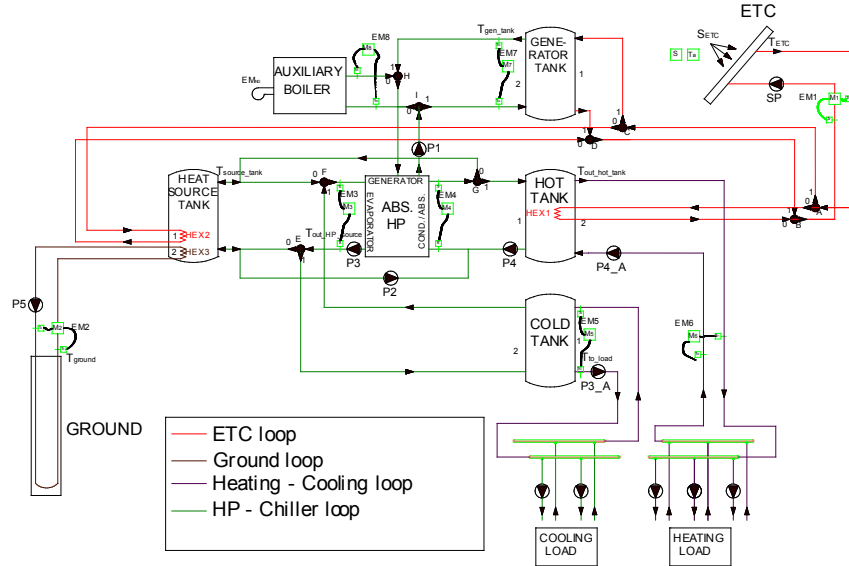


Figure 1 - Schematic of the main equipment of the plant

2.2. Control strategy of the plant

During heating season, the operation of the ETC field is based on the useful thermal energy producible by the plant in correspondence of two values of the reduced temperature T_{red} , defined as a function of the mean temperature of the water entering and leaving the collector (T_m), the air temperature (T_a) and the global solar radiation on the tilted surface (G_β) (Equation (1)):

$$T_{red} = \frac{T_m - T_a}{G_\beta} \quad (1)$$

T_{red1} is calculated as a function of the return temperature from the Generator Tank, whereas T_{red2} in function of the return temperature from the Hot Tank (with $T_{red1} > T_{red2}$). In correspondence of these two values, the thermal efficiency as defined in Equation (2) is calculated (EN ISO 9806:2017):

$$\eta_{th,ETC} = \eta_0 - a_1 T_{red} - a_2 (G_\beta) \cdot T_{red}^2 \quad (2)$$

where η_0 is the optical efficiency, a_1 is the heat loss coefficient, a_2 is the temperature dependence of the heat loss coefficient. The useful thermal energy producible by the plant in the two cases has been then determined (where COP_{HP} is the Coefficient Of Performance of the heat pump, HP):

1. $Q_{us,1} = \eta_{th,ETC,1} \cdot G_\beta \cdot COP_{HP}$ (indirect heating by HP)
2. $Q_{us,2} = \eta_{th,ETC,2} \cdot G_\beta$ (direct heating by ETC)

The ETC field is operated on the basis of the greatest Q_{us} : if $Q_{us,1} > Q_{us,2}$ the ETC field feeds the Generator Tank (A=B=C=D=1 - indirect heating by HP), whereas if $Q_{us,1} < Q_{us,2}$ the ETC field feeds the Hot Tank (A=B=0 - direct heating by ETC). If $T_{red} < T_{red2}$ the ETC field feeds the Heat Source Tank (A=B=1, C=D=0) (Figure 1).

During cooling season, A=B=1 in any case (no direct heating as no heating loads are present). The ETC operation is based on the Generator Tank outlet temperature: if $T_{gen_tank} < 95$ °C, hot water from ETC is supplied to the Generator Tank to feed the absorption HP generator (C=D=1), if $T_{gen_tank} > 95$ °C, hot water from ETC is supplied to the Heat Source Tank to regenerate the ground (C=D=0).

The operation strategy of the HP is based on the Hot Tank outlet temperature during heating season ($COOLING_LOADS = 0$ AND $T_{out_hot_tank} < 40$ °C), and on the Cold Tank outlet temperature during cooling season ($COOLING_LOADS > 0$ AND $T_{to_load} > 12$ °C). In the first case, the machine operates as heat pump (the absorber/condenser heats up the Hot Tank, the evaporator is fed by the Heat Source Tank). In the second case, the equipment can operate as chiller (the evaporator cools down the Cold Tank) with heat recovery (if $T_{out_hot_tank} < 38$

°C the absorber/condenser is connected to the Hot Tank) or without heat recovery (if $T_{out_hot_tank} > 40$ °C the absorber/condenser is connected to the Heat Source Tank). Moreover, when the HP/Chiller is in operation, its generator has to be fed by hot water that is produced by the Generator Tank if $T_{gen_tank} > 75$ °C ($H=I=1$) or by an Auxiliary Boiler (efficiency supposed constant and equal to 0.9) if $T_{gen_tank} < 75$ °C ($H=I=0$).

3. Results

As the Authors already proved ([4]-[6]), the length of the ground probes can be reduced when increasing the solar field as the contribution of the solar energy to recharge the ground during summer months is greater. This feature is here considered also in the following economic analysis. Furthermore, the capacity of the Hot Tank and the Heat Source Tank is fixed at 0.8 and 1.5 m³ respectively, whereas the Cold Tank capacity is fixed at 0.75 m³.

Many different combinations of ETC area, Generator Tank capacity and length of the ground probes have been simulated. For the sake of brevity, only the ones described in Table 1 are compared in Figure 2(a) on a yearly basis in terms of no-renewable primary energy consumption EP_{annual} (divided into two contributes relative to heating and cooling seasons), each with the counterpart of a traditional solution (NG Boiler for heating + a/w Chiller for cooling). The yearly primary energy ratio ($PER_{plant,nren}$) is reported as well. It is calculated on the basis of the no-renewable primary energy consumption of the whole plant (Auxiliary Boiler and parasitic power of pumps with the primary energy factors as defined by Italian Decree DM 26/06/2015: $f_{p,nren}$ (NG) = 1.05; $f_{p,nren}$ (electricity from the grid) = 1.95).

Table 1 – ETC area, ground probes number and length, and Generator Tank capacity for the main alternatives simulated – CAPEX of the main equipment

	ETC (m ²)	Ground (n x m)	GenT (m ³)	CAPital EXpenditures (CAPEX)	
1	60	2 x 100	4	Variable Ground Bor. cost (€ m ⁻¹)	25
2	60	2 x 50	4	Fixed Ground Bor. cost (€)	10000
3	80	2 x 50	4	ETC cost (€ m ⁻²)	300
4	80	2 x 50	5	Adsorption HP/Chiller (€ kW ⁻¹)	600
5	100	2 x 50	6	El. Trad. Sol. a/w Chiller (€ kW ⁻¹)	300

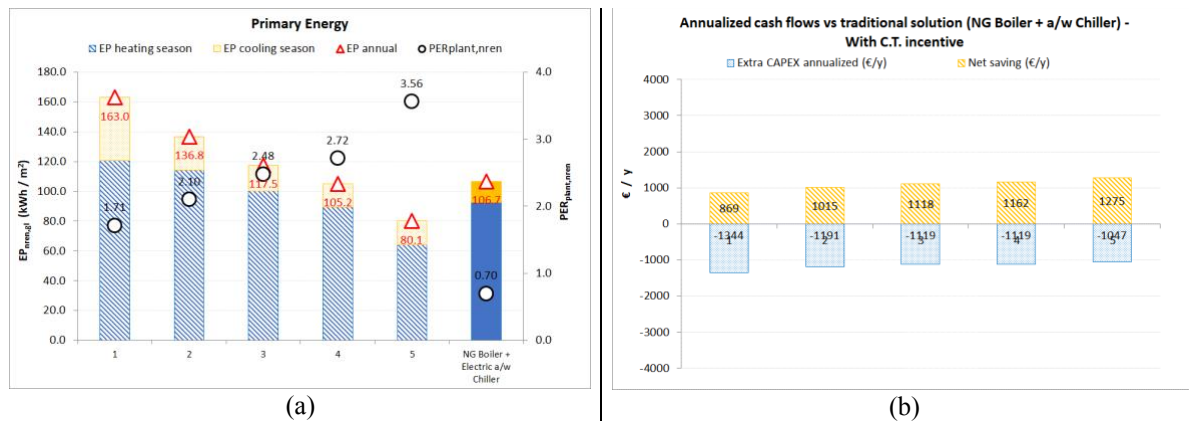


Figure 2 - Comparison between the different alternatives compared with the conventional one, on the base of annual no-renewable primary energy consumption ($EP_{nren,gl}$) and primary energy ratio ($PER_{plant,nren}$) (a), and on the base of annual discounted saving and extra-CAPEX (b)

Comparing solutions 1 and 2 in Figure 2(a) reveals that a correct balance between the solar and the ground fields is necessary in order to improve energy performance of the plant. Moreover, increasing the ETC area is beneficial as EP_{annual} (red triangle) decreases: looking at solutions 1-3-5, the increase of the ETC area decreases the no-renewable primary energy consumption of the plant both in heating season (blue line bars) and in cooling season (orange line bars) as more thermal energy for driving the HP/Chiller is produced thus reducing the NG consumption of the Auxiliary Boiler. Increasing the capacity of Generator Tank has a similar effect, that is the plant EP_{annual} decreases (comparison between solutions 3 and 4). When EP_{annual} decreases, $PER_{plant,nren}$ increases. For the BL climate here considered, it is not advantageous to have lower than 60 m² of ETC field, as in this case EP_{annual} would be in any case greater than the traditional solution. The best solution appears to be the number 5

(100 m² ETC, 2x50 m ground probes, 6000 L Generator Tank), with an EP_{annual} of 80.1 kWh m⁻² year⁻¹ and a $PER_{plant, nren}$ equal to 3.56.

In terms of economic analysis, besides the CAPEX reported in Table 1, an extra investment cost of 6000 € for the innovative solutions is considered (for Generator and Heat Source tanks, pumps, etc.) with respect to the traditional one. Operating Expenses (OPEX) are determined on the basis of a price of 0.9 € Sm⁻³ for NG, and 0.2 € kWh⁻¹ for electricity from the grid. The results of the comparison of the five alternatives here considered with the “traditional” solution are reported in Figure 2(b) (interest rate 2%, time period 20 years). The figure reports both the net saving (calculated on the basis of the OPEX) and the extra-CAPEX annualized discounted cash flows: the economic viability is assured when the former are greater than the latter. As a matter of fact, the economic viability of all the five alternatives is allowed only considering the presence of the Italian economic incentive “Conto Energia Termico”, that is determined on the basis of the standard performance of the considered ETC in the Wurzburg location (552 kWh m⁻²), the ETC area, and the economic incentive by the Italian Decree DM 16/02/2016 (0.13 € kWh⁻¹). Figure 3(a) reports the annual discounted cash flows with respect to the traditional solution: even the best solution from the energy point of view (5) allows a discounted payback of 16 years. A turnaround of this conclusion cannot be excluded, if an important falling price of solar collectors takes place (Figure 3(b)). This would be not unexpected, as an investigation on market price of ETCs in China and India reveals prices already less than a half of current European price lists.

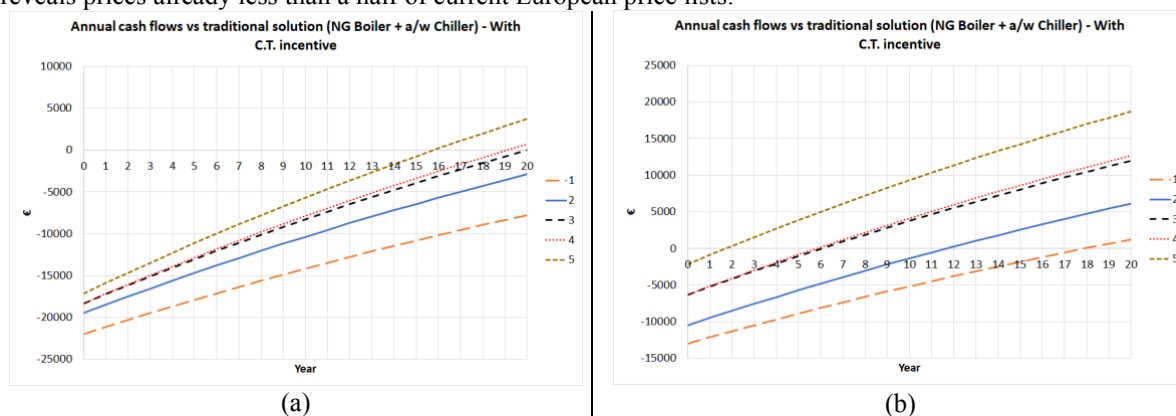


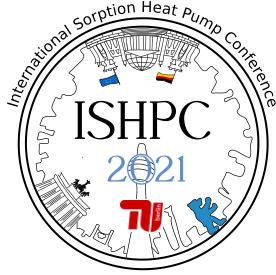
Figure 3 - Annual discounted cash flows of the different alternatives compared with the conventional one with 300 € m⁻² (a) and 150 € m⁻² (b) ETC investment cost

4. Conclusions

The use of modern high efficiency ETC offers a technical solution really suitable in view of solar heating and cooling systems with high energy performance. This study allows to understand the reasoning of the optimum sizing strategies and annual utilization of the equipment in dual-source (ground+ETC) thermally driven heat pump/chiller. The design of the plant by means of dynamic simulation considers different alternatives by varying the solar ETC field, the ground field, and the Generator Tank capacity, revealing that the most efficient solution features 25% saving of no-renewable primary energy consumption compared to a traditional one. A future decrease in ETC cost could make this kind of solar heating and cooling plant competitive with the actual more advantageous PV driven electric HP/chiller solution.

5. List of References

- [1] Lazzarin, R., Noro, M. (2018): Past, present, future of solar cooling: technical and economical considerations. *Solar Energy*, vol. 172, pp. 2-13.
- [2] Noro, M., Lazzarin, R., Busato, F. (2014): Solar cooling and heating plants: an energy and economic analysis of liquid sensible vs phase change material (PCM) heat storage. *International Journal of Refrigeration*, vol. 39, pp. 104-116.
- [3] EN ISO 15927-4:2005. “Hygrothermal performance of buildings - Calculation and presentation of climatic data - Part 4: Hourly data for assessing the annual energy use for heating and cooling”.
- [4] Busato, F., Lazzarin, R., Noro, M. (2015): Ground or solar source heat pump systems for space heating: Which is better? Energetic assessment based on a case history. *Energy and Buildings*, vol. 102, pp. 347-356.
- [5] Lazzarin, R., Noro, M. (2018): Lessons learned from long term monitoring of a multisource heat pump system. *Energy and Buildings*, vol. 174, pp. 335-346.
- [6] Lazzarin, R., Noro, M. (2020): Photovoltaic/Thermal (PV/T) / ground dual source heat pump: optimum energy and economic sizing based on performance analysis. *Energy and Buildings*, vol. 211, 109800.



Application of the two-stage absorption heat exchanger in district heating

Yi Yuhao¹, Xie Xiaoyun^{1, *}, Jiang Yi¹

¹ Building Energy Research Center, Tsinghua University, Beijing, 100084, People's Republic of China

Xiaoyun Xie

Building energy research center, Tsinghua University, Beijing, China, 100084;

86-010-62793591, xiexiaoyun@tsinghua.edu.cn

Abstract:

The absorption heat exchanger (AHE) plays an important role in the district heating system in China, increasing the temperature difference between the supply and return water of the primary network and improving the heating capacity. The two-stage AHE is proposed and systems of different capacities are applied in Taiyuan. The operation performances of different capacities in the heating season in 2018-2019 are tested. The units operate stably and efficiently at the load rate of 5%-98%, and the tested heat exchange efficiency is from 1.2 to 1.43. Furthermore, the system can also operate stably when the inlet water temperature of the primary network is as low as 65 °C. The results show that the two-stage AHE has a remarkable effect on improving the heating capacity in district heating.

1 Introduction

The temperature difference between the inlet and outlet of the primary network is generally 50-60 K in the traditional district heating system of China. Increasing the temperature difference is conducive to increasing the heat supply scale of the system, which has caused extensive research. The first type AHE system proposed by Li et al. [1] can effectively reduce the return water temperature of the primary network without changing the supply water temperatures of the primary and secondary networks, resulting in increasing the heat supply scale. Moreover, the low-temperature return water of the primary network allows improving the waste heat recovery, which contributes to energy saving. Therefore, the AHE system has been widely studied and applied in different engineering situations.

The process of the basic first type AHE system is shown in Fig. 1. The first type AHE consists of a first type absorption heat pump (AHP) using LiBr/H₂O as working fluids and a plate heat exchanger (PHE). This system can realize the heat exchange between the heat source with the large temperature difference, low flow rate and the heat sink with the low temperature difference and large flow rate. When the inlet water temperatures of the primary network and secondary network are 110 °C and 40 °C respectively, the outlet water temperature of the primary network in the conventional PHE system is higher than 40 °C, while that in the AHE system can be reduced to 20 °C. The heat supply of the AHE system is 1.3 times higher than that of the PHE system under the same flow rate of the primary network, which has the apparent advantage.

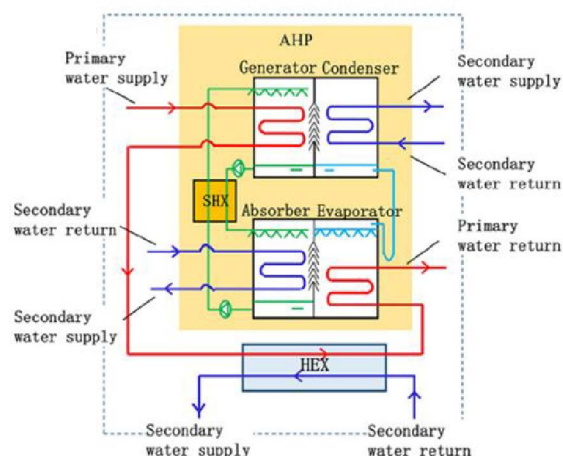


Figure 1 – The process of basic first type AHE.

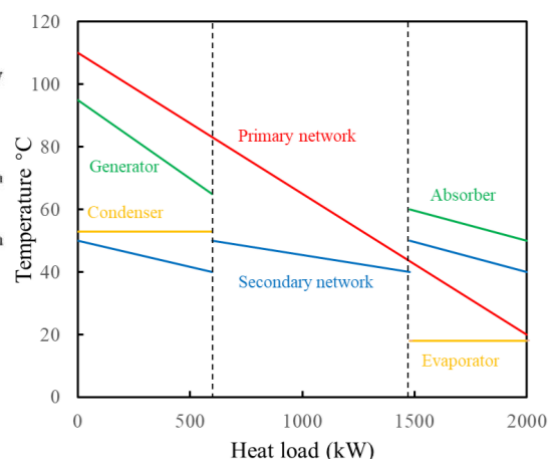


Figure 2 – The T-Q chart of basic first type AHE.

The basic AHE system has been utilized in district heating [2], but the tested heat exchange efficiency is 1.14-1.2, which leaves room for improvement. The T-Q chart of the basic AHE system is shown in Fig. 2. The temperature changes significantly in the process, which leads to the immense heat transfer triangle in the heat exchanger of the

system, thus leading to the dissipation [3]. Therefore, the emphasis of researches is to reduce the heat transfer dissipation, which refers to the irreversible loss of energy grade due to the heat transfer temperature difference between the two fluids in the heat transfer process. Wang et al. [4] optimized the flow rate distribution of the secondary network and determined the process under the minimum dissipation. The method based on the entransy dissipation analysis was proposed by Wang et al. [5], and the multi-section AHE system was designed to reduce the irreversibility. A multi-section unit of 180 kW capacity was made by Zhu et al. [6] based on the result. The tested heat exchange efficiency rose to 1.2-1.3. Furthermore, a two-stage AHE system of 6 MW capacity was proposed by Yi et al. [7] and applied in Taiyuan for district heating. The heat exchange efficiency rose to 1.25-1.41.

Therefore, the operation performance can be effectively improved by reducing the dissipation. The two-stage system has the best performance. A batch of two-stage AHEs with different capacity play a practical role in district heating in Taiyuan. In this paper, five units with capacities of 1, 2, 3, 6, 8 MW are selected for the operation performance test. The critical parameters of the system, including the heat load rate, flow rate ratio and heat exchange efficiency are tested to evaluate the performance of the two-stage AHE systems with different capacities.

2 Process and evaluation parameters

2.1 Process of the two-stage AHE.

The process of the two-stage AHE is shown in Fig. 3(a), and the T-Q chart is shown in Fig. 3(b). This system consists of two AHPs and a PHE. The water of the primary network flows through the corresponding heat exchanger in series, and the water of the secondary network is divided into three currents flowing separately into different heat exchangers to realize the heat exchange process. The corresponding pressures of the heat exchangers in different AHPs are different, which matches the temperature of the fluid flowing through the heat exchanger respectively, resulting in the heat transfer process with less irreversibility. Compared with the basic AHE system, the two-stage AHE system changes the heat transfer triangle in the condenser and evaporator into two steps, which reduces the heat transfer dissipation in condenser and evaporator. Thus, the performance of the system has been improved.

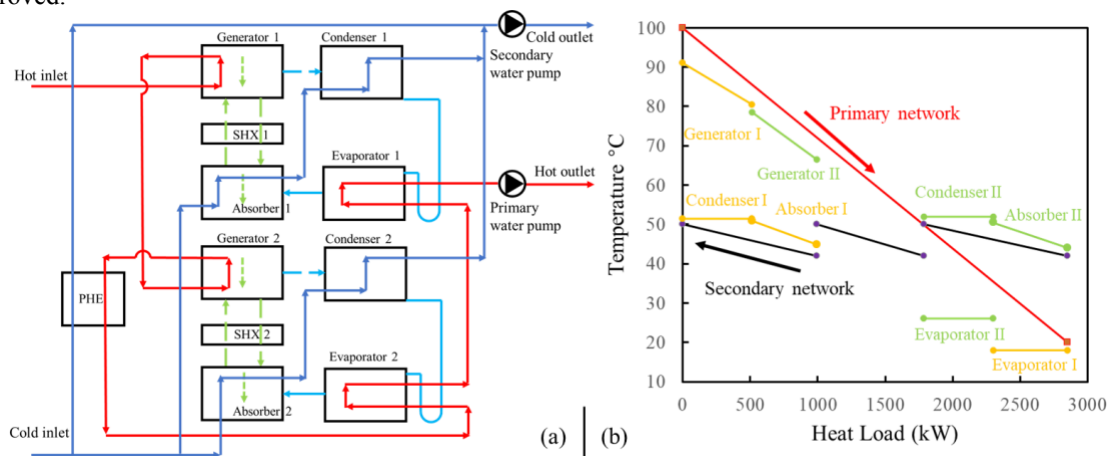


Figure 3 – The (a) process; (b) T-Q chart of the two-stage AHE system.

2.2 Evaluation parameters.

The processes of the AHEs with different capacities are the same, but the design parameters including the area of the heat exchangers and the flow rate etc. are different. The heat exchanger areas per stage of different systems are shown in Table 1. The temperature before and after each heat exchangers and the flow rate of water are tested to calculate and analyze the performance of the system. The temperature measuring instrument is the copper-constantan thermocouple, and the flow rate measuring instrument is XCT-2000 ultrasonic flowmeter. The accuracies of the instruments are ± 0.2 °C and $\pm 0.5\%$ FS respectively. The critical parameters to evaluate the performance include the heat load rate, flow rate ratio and heat exchange efficiency. The heat load rate is the ratio of the actual load to the design load of the system. The flow rate ratio is the ratio of the flow rate of the secondary network to the flow rate of the primary network. The definition of the heat exchange efficiency ε is as follows:

$$\varepsilon = \frac{t_{pri,in} - t_{pri,out}}{t_{pri,in} - t_{sec,in}} \quad (1)$$

Where $t_{pri,in}$, $t_{pri,out}$ and $t_{sec,in}$ are the inlet water temperature of the primary network, the outlet water temperature of the primary network and the inlet water temperature of the secondary network respectively. The heat exchange efficiency of the AHE system is obtained by analogy with that of the PHE. By dividing the molecular denominator of the expression of the PHE's heat exchange efficiency by the flow rate of the fluid with low flow rate, the heat exchange efficiency expressed by temperature is obtained. For the PHE, the fluid temperature on one side is higher than that on the other side in all positions in the heat exchange process, so the heat exchange efficiency must be less than 1. For the AHE, if it is regarded as a black box model, the outlet water temperature of the primary network is lower than the inlet water temperature of the secondary network, so the heat exchange efficiency is greater than 1. This parameter is equivalent to the degree that the system reduces the temperature of the primary network under given conditions, which can be used to evaluate the performance of the AHE [3,6,7]. All of the critical parameters can be calculated by the measured temperature and flow rate.

Table 1 – The heat exchanger area per stage of different systems.

System capacity	A_g (m ²)	A_c (m ²)	A_a (m ²)	A_e (m ²)
1 MW	9.23	5.91	13.45	5.46
2 MW	24.11	15.52	37.22	13.56
3 MW	35.57	22.91	52.90	20.35
6 MW	69.98	37.28	80.01	40.79
8 MW	92.44	60.32	134.50	53.62

3 Results

3.1 Test results

The heat load rate ranges of systems with 1, 2, 3, 6, 8 MW are 10%-30%, 15%-32%, 55%-98%, 5%-47.5% and 26%-51.4% respectively. The heat load rates of different capacity systems are different, and the degrees of the change are also different, which are 17%-43%. In terms of all the systems, the overall heat load rate ranges from 5% to 98%, and the system can operate stably. Therefore, in the range of full heat load rate, the system can achieve the heat exchange and obtain the low outlet water temperature of the primary network. The test results of the flow rate ratio and heat exchange efficiency of different systems are shown in Table 2. The overall heat exchange efficiency is high, ranging from 1.2 to 1.43. In early or late winter, both of the heat load rate and the inlet water temperature of the primary network are low, resulting in the high flow rate ratio and the high heat exchange efficiency. In harsh winter, when the heat load rate and the inlet water temperature of primary network increase, the flow rate ratio becomes lower and so as the heat exchange efficiency.

Table 2–The flow rate ratio and heat exchange efficiency of different systems.

System capacity	Early/late winter		Harsh winter	
	Flow rate ratio	Heat exchange efficiency	Flow rate ratio	Heat exchange efficiency
1 MW	16-24	1.3-1.34	14-18	1.2-1.28
2 MW	14-20	1.33-1.37	12-14	1.3-1.35
3 MW	10-12	1.28-1.33	8-10	1.25-1.3
6 MW	10-15	1.35-1.4	8-12	1.3-1.35
8 MW	12-16	1.38-1.43	9-12	1.33-1.38

3.2 Analysis

Some typical conditions are selected for correlation analysis of different critical parameters. The relationship between the heat load rate and the flow rate ratio under the typical condition of different systems is shown in Fig. 4(a). It can be seen that the higher the heat load rate of the same system, the lower the flow ratio. This is caused by the regulation mode of the system. When the heat load increases, the method is to increase the flow rate of the primary network and keep the flow rate of secondary network unchanged to meet the heat demand, resulting in the decrease of the flow rate ratio. The relationship between the heat exchange efficiency and the flow rate ratio under typical conditions of different systems is shown in Fig. 4(b). For different systems, the temperature increases with the increase of flow rate ratio, which is the same as the result proposed by Yi et al. [7]. Under the same flow rate ratio, the larger the system capacity, the higher the heat exchange efficiency. Furthermore, the larger the system capacity, the lower the slope of the curve between the heat exchange efficiency and the flow rate ratio.

3.3 Performance under the extreme condition

In order to further verify the operation performance of the system under all operating conditions, the performance of the 1 MW system is tested under the extreme condition that the inlet water temperature of the primary network is lower than 70 °C in late winter. The temperature curves of the primary and secondary networks are shown in Fig. 5. When the inlet water temperature of the primary network drops below 70 °C, the system can reduce the outlet water temperature of the primary network to a level lower than 10 K of the inlet water temperature of the secondary network. And the heat exchange efficiency reaches the level of 1.24. Therefore, under the extreme conditions of low heat load and low inlet water temperature of the primary network, the two-stage AHE can keep operating normally.

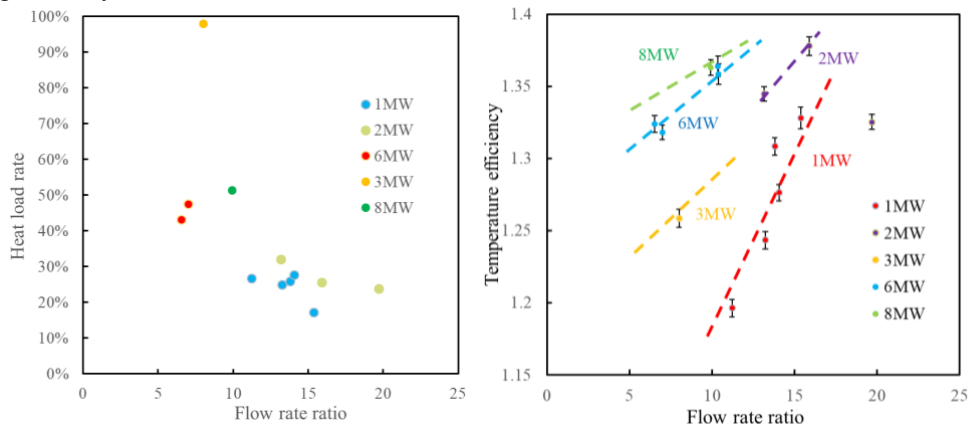


Figure 4 – The relationship between the (a) heat load rate; (b) heat exchange efficiency and the flow rate ratio.

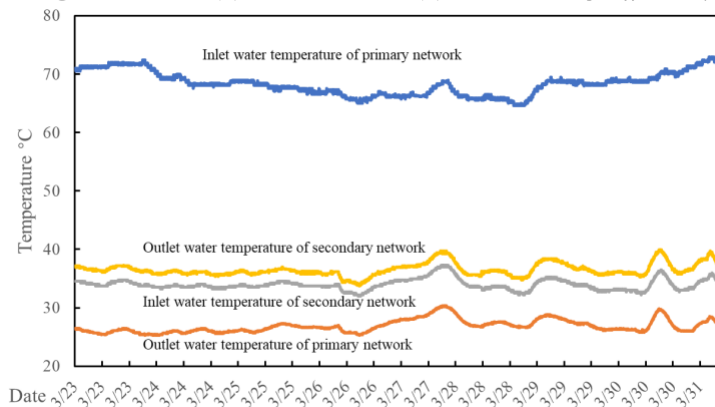


Figure 5 – The temperature curves of the primary and secondary network under the extreme condition.

4 Conclusions

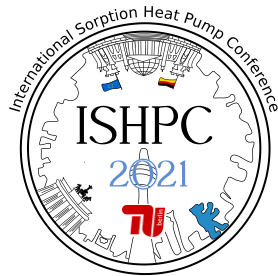
The AHE system plays an important role in the development of district heating. Several two-stage AHE systems with different capacity utilized in Taiyuan are tested in the whole heating season. The critical parameters are calculated and analyzed to evaluate the performance of the system. The systems with different capacity can operate normally, the measured overall heat load rate is 5% - 98%. The heat exchange efficiency is 1.2 - 1.43. Furthermore, the system can operate stably under the extreme condition that the inlet water temperature of the primary network is lower than 70 °C, resulting in the great capacity of load regulation. The heat exchange efficiency of the system is about 0.15 higher than that of the conventional AHE system, and about 0.1 higher than that of the two-section AHE system. The test results of the two-stage AHE systems show the superiority of the performance, which has an important guiding significance for further optimization.

5 Acknowledgment

The authors gratefully acknowledge the support from the Innovative Research Group Project of National Natural Science Foundation of China (Grant number 51521005) and National key research and development program of China (Grant number 2019YFE0102700).

6 List of References

- [1] Li, Y., Fu, L., Zhang, S., Jiang, Y., Xiling, Z. (2011): A new type of district heating method with co-generation based on absorption heat exchange (co-ah cycle). *Energy Conversion and Management*, vol. 52, pp. 1200-7.
- [2] Sun, J., Ge, Z., Fu, L. (2017): Investigation on operation strategy of absorption heat exchanger for district heating system. *Energy and Buildings*, vol. 156, pp. 51-7.
- [3] Xie, X., Jiang, Y. (2017): Absorption heat exchangers for long-distance heat transportation. *Energy*, vol. 141, pp. 2242-50.
- [4] Wang, X., Zhao, X., Fu, L. (2018): Entropy analysis of secondary network flow distribution in absorption heat exchanger. *Energy*, vol. 147, pp. 428-39.
- [5] Wang, S., Xie, X., Jiang, Y. (2014): Optimization design of the large temperature lift/drop multi-stage vertical absorption temperature transformer based on entropy dissipation method. *Energy*, vol. 68, pp. 712-21.
- [6] Zhu, C., Xie, X., Jiang, Y. (2016): A multi-section vertical absorption heat exchanger for district heating systems. *Int. Journal of Refrigeration*, vol. 71, pp. 69-84.
- [7] Yi, Y., Xie, X., Jiang, Y. (2020): A Two-stage Vertical Absorption Heat Exchanger for District Heating System. *Int. Journal of Refrigeration*.



Process design and analysis of the zonal absorption heat exchanger for high-rise buildings

Yi Yuhao¹, Xie Xiaoyun^{1,*}, Jiang Yi¹

¹ Building Energy Research Center, Tsinghua University, Beijing, 100084, People's Republic of China

Xiaoyun Xie

Building energy research center, Tsinghua University, Beijing, China, 100084;

86-010-62793591, xiexiaoyun@tsinghua.edu.cn

Abstract:

In terms of the high-rise buildings with large areas, the heating system of the vertical zone is generally considered to prevent the problems of hydraulic imbalance and bearing pressure. In practical application, the plate heat exchanger (PHE) is utilized in the zonal heating system and the parameters are designed in different zones. A zonal absorption heat exchanger (AHE) utilized in the heating station for high-rise buildings is proposed in this paper to realize the function of the zonal PHE heating system, heating for each zone independently. Furthermore, this system can reduce the outlet water temperature of the primary network to 15 K lower than the inlet water temperature of the secondary network. The low water outlet water temperature of the primary network contributes to the waste heat recovery and improves the heating scale. The heat load adaptability and the regulating ability of the process are analyzed. The results contribute to the energy saving of the zonal heating system.

1 Introduction

More and more clusters of high-rise buildings have been established in China, which are characterized by a high number of floors and large heat load demand. The problems of overpressure and vertical hydraulic imbalance will occur if utilizing the general heating system [1]. At present, there are mainly three directions to solve this problem: the direct heating system, the indirect heating system and the zonal heating system. The characteristic of the direct heating system is that all heat users are connected in the same set of pipelines. The problems are solved by adding the valve, pump and the pipes [2]. However, the self-regulation ability of the direct heating system is weak, which leads to the extremely high requirements of the operation regulation. The indirect heating system is characterized by multiple sets of heating pipes, and the heat exchange between different sets of pipes is through the PHE [1]. However, the indirect heating system is still not independent. A disturbance of heating will happen in the high zone when a problem occurs in the low zone. The zonal heating system is a system designed for the high-rise buildings with large areas (such as a community), the equipment of which is generally in the heating station [3]. This system divides the high-rise buildings into two or more heating areas in the vertical direction, called different heating zones and heated by different equipment respectively. The zonal heating system not only solves the problems, but also realizes the independence of different heating zones, which is widely utilized in the district heating of high-rise buildings.

The first-type AHE utilized in the heating station is proposed by Fu et al. [4] in 2011 to effectively reduce the outlet water temperature of the primary network to 10 K lower than the inlet water temperature of secondary network, which contributes to the waste heat recovery and improve the heating capacity of the system. The first-type AHE consists of a first-type absorption heat pump and a PHE. The water of primary network flows in series through the generator, the PHE and the evaporator for heat exchange. The water of the secondary network is divided into three currents flowing separately into the condenser, the absorber and the PHE to exchange heat. Compared with the system utilized the PHE, the heat load of this system is 1.3 times higher under the condition of the constant flow rate of the primary network [5]. The heat exchanger in the current zonal heating system is the PHE system, in which the outlet water temperature of the primary network is higher than the inlet water temperature of the secondary network. Thus, the current zonal heating system leaves room for improvement.

A zonal AHE system is proposed to replace the current PHE in the zonal heating system. This process retains the characteristics of the AHE which can reduce the outlet water temperature of the primary network to 10 K lower than the inlet water temperature of the secondary network. Furthermore, the pipes of secondary network in different heating zones are independent to ensure that different heating zones don't influence each other. In this paper, the performance, heat load adaptability and the regulating ability of the process under an actual condition are simulated and analyzed. The results show the feasibility of the zonal AHE system.

2 Process design

The process of the zonal AHE with two zones are shown in Fig. 1. The red curve represents the primary network. The dark and light blue curves represent the secondary network in two different zones respectively.

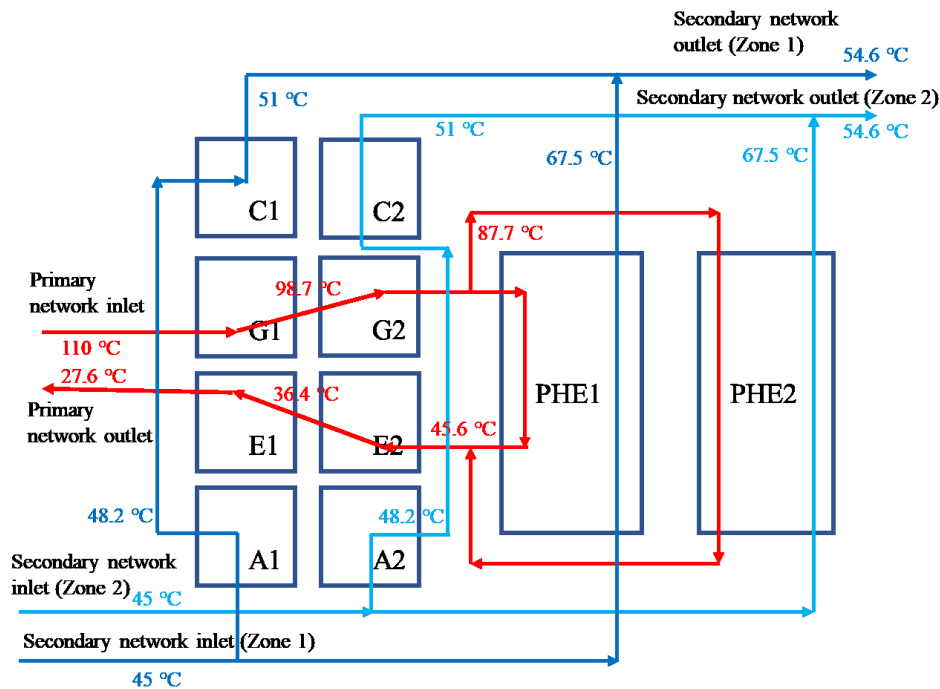


Figure 1 – The process of the zonal AHE with two zones.

This process is equal to the process of the two-stage AHE system [5], which consists of two AHPs with different pressures and two PHEs. The C, G, E, A represents the condenser, generator, evaporator and absorber respectively, and the follow-up 1 and 2 represent different stages. The primary network water flows through the high-pressure generator of the first stage AHP and the low-pressure generator of the second stage of AHP. Then, it is divided into two currents flowing into PHE1 and PHE2 separately. The two branches are mixed after the heat exchange in the PHEs. Then, it flows through the high-pressure evaporator of the second stage AHP and the low-pressure evaporator of the first stage AHP and finally to be cooled to the outlet temperature. The secondary network in different zones flows through the same heat exchangers at different levels to obtain heat according to the same flow process. Take the secondary network of zone 1 as an example. The secondary network water is divided into two currents flowing into the PHE1 and the first stage AHP respectively. In terms of the branch into the AHP, the water first flows into the absorber, then flows through the condenser and finally flows out. The two branches are finally mixed after finishing heat exchange and flow to the user of zone 1.

This process continues the characteristic of the AHE, which can realize heat exchange between fluids with the unmatched flow rate and reduce the outlet water temperature of the primary network to the level that lower than the inlet water temperature of the secondary network. Furthermore, in terms of the secondary network, the heat exchange processes of different zones are symmetric. The parameters of the system can be determined separately based on the corresponding heat load of different zones in the system design. The heat exchange processes between the two zones are independent, which can effectively replace the PHE of the current zonal heating system.

3 Analysis

3.1 Parameter introduction

The related parameters of the zonal AHE system are designed based on the heat load requirement of an actual zonal heating system. This system is divided into the high zone and low zone. The design heating loads of both zones are 960 kW. The inlet water temperature of the primary network is 110 °C, and the inlet water temperatures of the secondary network of the two zones are both 45 °C. The flow rate, heat exchanger capacity of the zonal AHE system designed for this condition is shown in Table 1. The simulation model of the zonal AHE system is established. The one-dimensional three-fluid heat transfer model [6] is utilized in the heat transfer processes of generator and absorber, and the logarithmic average temperature difference model is utilized in other heat

exchangers. The specific assumptions and equations are introduced in the published research [5]. The simulation model is calculated by the Engineering Equation Solver [7].

The simulation results under the design condition are shown in Fig. 1, including different water temperatures of the primary and secondary networks. Both of the outlet water temperatures of secondary network in zone 1 and zone 2 are 54.6 °C. The heat loads of different zones are 959 kW and 962 kW respectively. The outlet water temperature of the primary network is 27.6 °C, which is 17.4 K lower than the inlet water temperature of the secondary network. The performance of the zonal AHE system is satisfactory.

Table 1–The parameters of the zonal AHE system designed for the specific condition.

Flow rate ($\text{m}^3 \cdot \text{h}^{-1}$)		Heat transfer capacity (KA) ($\text{kW} \cdot \text{K}^{-1}$)			
Primary network	20.1	Generator (per stage)	36.17	PHE1	86.18
Secondary network (zone 1)	86	Condenser (per stage)	34.15	PHE2	86.18
Secondary network (zone 1)	86	Absorber (per stage)	48.40	Solution HEX1	10
Solution (generator inlet)	3	Evaporator (per stage)	24.42	Solution HEX2	10

3.2 Heat load adaptability

Such a situation often occurs in the actual condition that the actual heat load is lower than the design heat load. Adjusting the corresponding flow rate of primary and secondary networks can solve this problem for the conventional heating system. However, in terms of the zonal AHE system, it may appear that the actual heat load of one zone is the same as the design heat load, but the actual heat load of another zone is lower than the design heat load. At this time, the same adjustment method as the convention system is required to achieve this requirement. The heat supply of one zone is unchanged and that of another zone is reduced by adjusting the total flow rate of the primary network and secondary network.

The simulation results of the heat load adaptability are shown in Fig. 2. In Fig. 2(a), the heat load of zone 1 is reduced and the heat load of zone 2 is unchanged, while in Fig. 2(b), the heat load of zone 2 is reduced and the heat load of zone 1 is unchanged. The $m_{w,pri}$, $m_{w,sec}$, $m_{w,pri}^0$, $m_{w,sec}^0$ are the actual flow rate of the primary network, the actual flow rate of the secondary network, the design flow rate of the primary network and the design flow rate of the secondary network. The change trends of the two figures are almost the same, which verifies the symmetry of heat exchange in different zones of the system. Take the results of Fig. 2(a) as examples, the heat load of zone 1 is reduced and the heat load of zone 2 is slightly increased if only reducing the secondary network flow rate of zone 1. This is because the flow rate of the primary network is given based on the design heat load, but the actual heat load is reduced. Therefore, it's necessary to slightly reduce the flow rate of the primary network to keep the heat load of zone 2 unchanged. When the secondary network flow rate of zone 1 is reduced to 20% of the design flow rate, the heat load rate of zone 1 is reduced to 53.7% after adjustment, and the outlet water temperature of the primary network increases to 35 °C. That is, in terms of the zonal AHE system, when the heat load rate of one zone is reduced to about 50%, and the heat load rate of another zone is unchanged, the heating requirement can be realized by adjusting the total flow rate of primary and secondary networks. Meanwhile, the outlet water temperature of the primary network is still 10 K lower than the inlet water temperature of the secondary network. As a result, the zonal AHE system has excellent heat load adaptability.

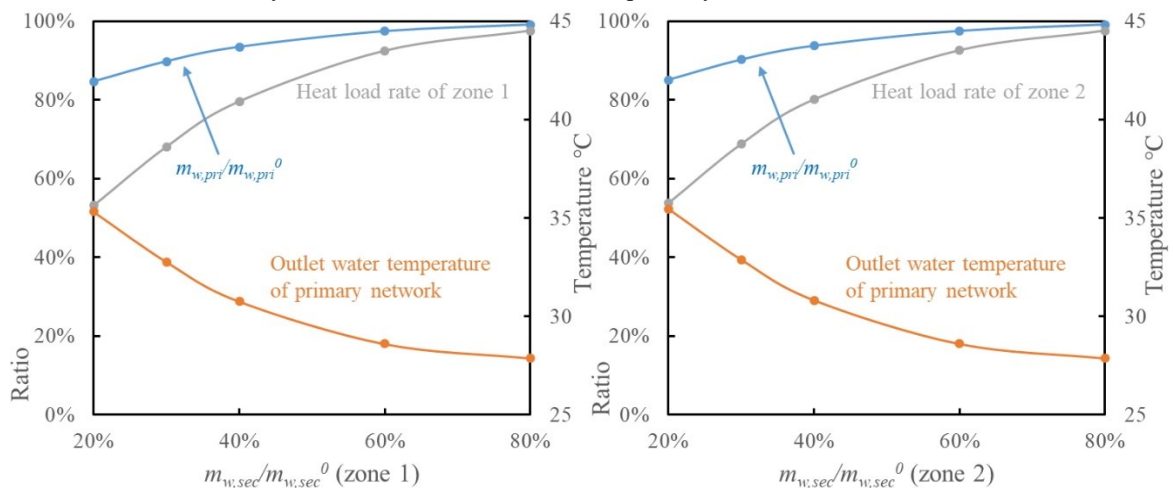


Figure 2 – The simulation result of the heat load adaptability: change the flow rate of: (a). zone 1; (b) zone 2.

3.3 Regulating ability in partial load

The regulating ability in partial load is also required when the system is in normal operation under the design parameters. Consistent with the conventional system, when the heat load on the user side drops in the early or late winter, the heat load of different zones is required to drop in the same proportion by only reducing the flow rate of the primary network, so as to meet the corresponding heat demand of each zone. The simulation result of the regulating ability in partial load by reducing the flow rate of the primary network is shown in Fig. 3. Four conditions that the ratios of the actual and the design flow rate of the primary network are 0.4, 0.6, 0.8 and 1.0 respectively are simulated. The flow rates of the secondary network under different conditions are the same, and the inlet water temperatures of the secondary network under different conditions are 36 °C, 39 °C, 42 °C and 45 °C respectively. According to Fig. 3, when the ratio of primary network is reduced from 100% to 40%, the heat load rates of zone 1 and zone 2 decrease almost the same, from 100% to 51.7% and 49.7% respectively. That is, in terms of the zonal AHE system, the heat load of different zones can be reduced in the same proportion only by reducing the flow rate of the primary network in partial load. As a result, the zonal AHE system also has an excellent regulating ability in partial load.

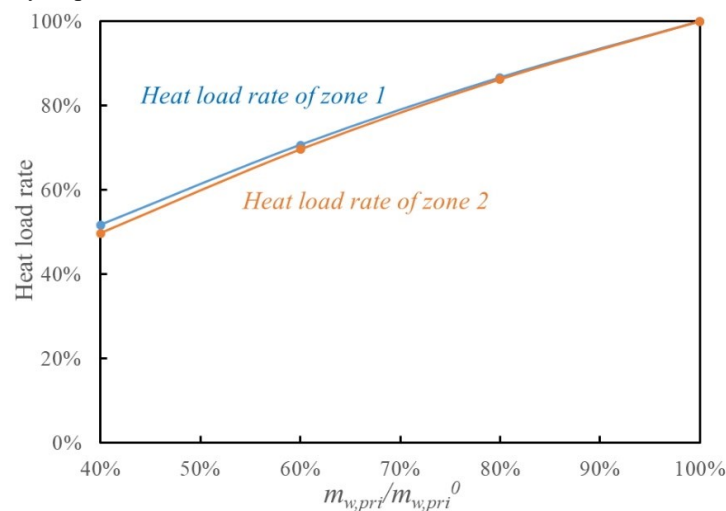


Figure 3 – The simulation result of the regulating ability in partial load.

4 Conclusions

The zonal AHE system is proposed in this paper aiming at the zonal heating system for the existing high-rise buildings with large areas. The system can not only meet the function of the existing system, but also realize the function of AHE to reduce the outlet water temperature of the primary network. Based on the two-stage AHE, the secondary network is designed as the symmetrical heat exchange process. The simulation model of this system is established and analyzed. The system can reduce the outlet water temperature of primary network 17.4 K lower than the inlet water temperature of the secondary network under design condition. Furthermore, the zonal AHE system has both excellent heat load adaptability and regulating ability in partial load, which can effectively replace the current PHE zonal heating system. The results contribute to the energy saving of the zonal system in district heating.

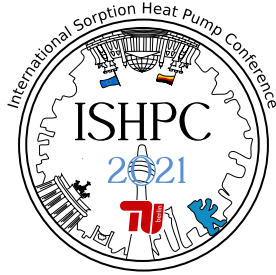
5 Acknowledgment

The authors gratefully acknowledge the support from the Innovative Research Group Project of National Natural Science Foundation of China (Grant number 51521005) and National key research and development program of China (Grant number 2019YFE0102700).

6 List of References

- [1] GB 50019-2003. (2004): Code for design of heating ventilation and air conditioning (In Chinese).
- [2] Sheng, X. (1998): Hot water heating system of high-rise building and its connection mode. *Applied energy technology* (In Chinese), vol.4, pp. 5-8.
- [3] Xiao, X. (2019): Analysis and optimization of vertical imbalance in high-rise heating system. *Symposium on construction and efficient operation of heating engineering* (In Chinese).

-
- [4] Li, Y., Fu, L., Zhang, S., Jiang, Y., Xiling, Z. (2011): A new type of district heating method with co-generation based on absorption heat exchange (co-ah cycle). *Energy Conversion and Management*, vol. 52, pp. 1200-7.
- [5] Yi, Y., Xie, X., Jiang, Y. (2020): A Two-stage Vertical Absorption Heat Exchanger for District Heating System. *Int. Journal of Refrigeration*.
- [6] Hu, T., Li, J., Xie, X., Jiang, Y. (2019): Match property analysis of falling film absorption process. *International Journal of Refrigeration*, vol. 98, pp. 194-201.
- [7] Klein, S.A. (2010): Engineering Equation Solver. *Software available at <http://www.fchartsoftware.com/ees/>.*



Experimental study on liquid distribution and horizontal motions of droplets in a tube bundle

Yang, Yueting¹, Xie Xiaoyun¹, Jiang Yi¹

¹ Building Energy Research Center, Department of Building Science, Tsinghua University, Beijing, 100084, China, xiexiaoyun@tsinghua.edu.cn

Abstract:

Liquid distribution effectiveness on horizontal tubes directly influences falling film heat and mass transfer efficiency in falling film absorbers. Droplets spreading and horizontal motions at tube bottoms directly influence liquid distribution. This paper studies phenomena of LiBr/H₂O solution droplets spreading and horizontal motions on horizontal tubes, and investigates heat and mass transfer characteristic of smooth copper and enhanced copper tube bundles in falling film absorption. A vacuum experimental unit is built and set up on a vacuum test bench. Horizontal motion distances on pre-wetting tubes are larger than those on no pre-wetting tubes. Droplets horizontal motion is related to propagation of liquid film wave on the fully wetted falling film. Horizontal motions distances decrease when Reynolds number rises. In the range of Reynolds number between 87~228, horizontal motion distances on enhanced copper tube are between 0.99~1.30cm. Wettability on enhanced tubes is relatively higher than that on smooth copper tubes under the same Reynolds number.

1. Introduction

Effectiveness of liquid distribution of falling film directly influences the performance of heat and mass transfer process of absorption heat pumps and absorption heat exchangers, especially under low Reynolds numbers [1]-[4]. Two influential phenomena of falling film distribution are discovered in practical falling film absorption heat exchangers: dry patches on the tube surface (with no liquid on the tube surface), and droplets horizontal motions at horizontal tube bottoms, as shown in Fig.1 and Fig.2. Dry patches occur when the flow rate is low, or misdistribution of falling film. Fig. 2 shows pictures of a droplet horizontal motion. The droplet at the first tube bottom changed its position before it jumps off from the first tube to the next tube row by time series. Firstly, the droplet forms from a breaking liquid bridge. After the bridge breaks, the droplet jumps off to the next tube. At this time, there is not enough residual liquid at tube bottom to produce another droplet immediately, and waves at the tube bottom push the next droplet to form at another site near the first droplet. There is a horizontal distance between jumping off sites of the two continuous droplets. This process lasts less than one second, and is very hard to recognize with naked eyes. It is so fast that it seems to be a “horizontal motion” of droplets. Droplets horizontal motions at tube bottoms lead to redistribution of droplets on the next row. The two flow phenomena directly affect the effectiveness of heat and mass transfer processes of liquid film on horizontal tubes, especially in tube bundles.

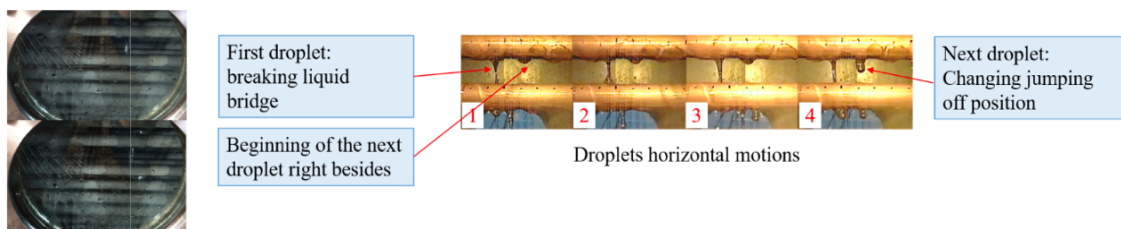


Figure 1 Dry patches on tubes

Figure 2 Droplets horizontal motions at the bottom of the first row

Researches on falling film liquid distribution on horizontal tubes define falling flow regime into droplets, jets, and sheets modes, depending on different Reynolds numbers[5]. Hu and Jacobi [6][7] describe the distance between adjacent liquid droplets and liquid jets λ_T as the “departure site spacing”. Wang [8] describes the phenomenon that during the formation of a droplet, the upper part of the liquid column rebounds back to the tube bottom once the liquid bridge breaks, and waits for enough liquid refilling for the formation of the next droplet. Killion and Garimella[9][10] describe the phenomenon of droplets horizontal motions at tube bottoms, named as “axial translation”. Axial motion of the liquid on the tube bottom due to propagating waves is described, and it is stated that it may generate a local excess of liquid that can develop into a formation site. Killion states that these waves

at the tube bottom can disturb the formation of neighbouring droplets, and affect the mixing in the film. Above all, there are a few research focusing on phenomena of droplets horizontal motions at tube bottoms. However, there are limited quantities researches. This paper is going to study the liquid spreading and horizontal motions of aqueous Lithium Bromide solution on falling film horizontal tube bundles based on experiments using an absorption-evaporation experiment unit on a vacuum test bench, and try to define the scale of droplets horizontal motions, and the effect to falling films.

2. Background/Fundamentals/Experimental Set-up

The experiment was carried out on a test bench for vacuum falling film heat and mass transfer process [11]-[13]. The structure of the test bench was shown in Fig. 3. In the absorber, a horizontal orifice divided the absorber into the upper liquid distribution chamber and the lower absorption chamber. Diameters of the holes in the orifice liquid distributor were 1.5 mm, and spacing between each hole was 30mm. Properties of the tube bundle were given in Table 1. Two kinds of tubes were applied to the experiment, the smooth copper tube and the enhanced copper tube, as shown in Fig.4. The tube spacing was 16 mm. There was only one tube on each altitude, so that movements of droplets on the tube bundle were be well observed from both sides of the tube bundle through sight windows. Images and films of horizontal motions of droplets were collected by a high speed camera. Both mass flow rate and densities of inlet and outlet solution were measured separately by two Coriolis flow meters. Pressure of the experimental unit was measured by a high precision vacuum pressure sensor (0-200Torr). Solution temperatures inside the unit were measured by T type copper-constantan thermocouples. All the parameters were measured after they were stable. In order to compare the wettability under for pre-wetted tubes and the no pre-wetting tubes, the pre-wetting treatment was conducted. During the pre-wetting treatment, large flow rate of solution was applied to tubes. We made sure that the tube surface was completely wetted by solution by observing through sight windows. The large flow rate of solution remained over 10mins, and then the flow rate was reduced to the normal flow rate range. Later, layers of the tube bundle were increased to observe droplets spreading, tube bundle wettability and droplets horizontal motions in tube bundles. There were over 18 layers on tube bundles, and were named as tube diameter d (mm)x tube spacing s (mm) x the distance between the bottom of the tube-type liquid distributor (as shown in fig.5) and the top of the first layer h (mm). The wettability of tube bundles were calculated using image capture tools from the video during the experiment.

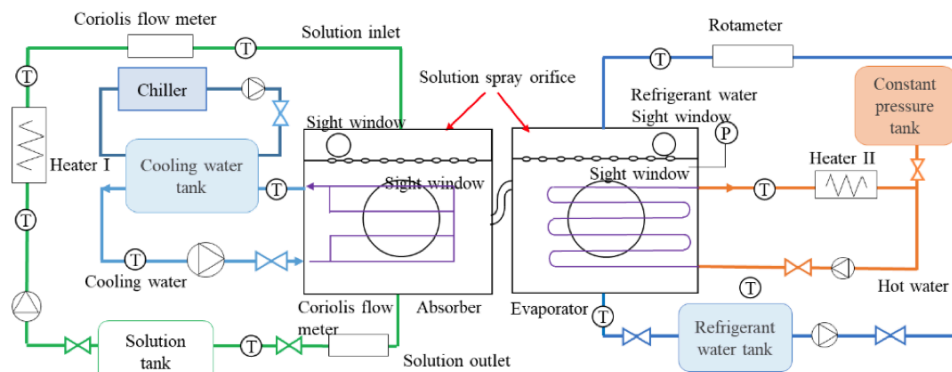


Figure 3 the vacuum test bench

Table 1 Properties of tubes

	External diameter of smooth part /mm	Wall thickness/mm	External diameter of enhanced part /mm	Tooth height/mm	Tooth bottom thickness/mm	Teeth per inch
smooth tube	16.0	0.96	-	-	-	-
enhanced tube	15.9	0.71	15.6	0.35	0.45	26

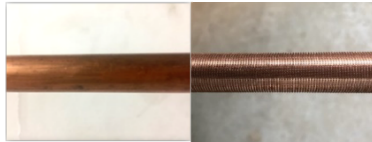


Figure 4 the smooth copper tube (L), the enhanced tube (R)

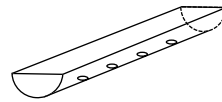


Figure 5 The tube-type liquid distributor

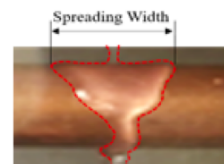


Figure 6 Spreading width

3. Results and Discussions

3.1 Observation results

During the experiment, fully wetted liquid film at tube bottoms are wavy during falling film, and these waves produce droplets for the next tube. However, when there are dry patches at tube bottom, as shown in fig.7, the uneven distribution of film waves at the tube bottom produces droplets horizontal motions. This dry patch stops the wave propagation in the liquid film, and is the “disturbance “of steady falling film flow. Disturbances in the falling film process, especially at the tube bottom, were essential conditions to droplets horizontal motions. Disturbances include uneven distribution of liquid from the distribution orifice, the droplet not spreading on the very central point on top of the tube, or the uneven distribution of roughness on the tube. These errors are common in manufacturing. These disturbances result in film waves propagating transversely at the bottom of the tube, and change the liquid amount of different sites at the tube bottom. Therefore, droplets jump off the tube bottom at different times and different sites, and is observed as “droplets horizontal motions” .

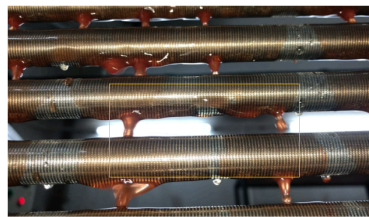


Figure 7: Dry patches at the bottom of a tube

Based on the observation during the experiment, horizontal motion distance is defined as follows:

$$d_{hm} = l_{t(i)} - l_{t(i-1)}$$

where d_{hm} is the horizontal motion distance in cm, $t(i)$ is the droplet jumping off time, and l is the droplet jumping off site at the tube bottom.

3.2 Quantities results

Fig. 8 shows total spreading widths of 10 droplets on different horizontal rows under different solution flow rates. The spreading width is the length of top of each spreading area of the droplets, as shown in Fig. 6. There is a clear trend that as the solution flow rates increases, the total spreading width of droplets increases. Total spreading widths of droplets on the second tube are generally larger than the first tube. However, as the solution falls to the lower horizontal tubes, spreading widths tend to be stable. Under the experiment conditions, in which the tube diameter is 16mm and axis spacing is 32mm, spreading widths on the third and the fourth tube are almost the same. This means the axis spacing limits spreading of the liquid film. As the film continues falling down, flow regimes are more complicated, and there is higher possibility that dry patches occur on the film in practical engineering. Therefore, the effective heat and mass transfer areas on lower layers are lower. In order to find a higher wetting ratio, it is important to find out the best row number and tube spacing for a tube bundle.

Fig. 9 shows droplet horizontal motion distances on pre-wetting copper tubes and no pre-wetting tubes. Under different Reynolds numbers, horizontal motion distances of pre-wetting tubes are larger than that of no pre-wetting tubes. Horizontal motion distances are on the same order of magnitude with droplet departure site spacing. Fig. shows droplet horizontal motion distances under different liquid spray densities. As solution mass flow rate rises, liquid spray density rises, and droplet horizontal motion distances decrease. This trend is relatively easy to explain that as flow rate rises, Re number rises, and falling film regime tends to transfer to jets mode. In the jets mode, gravity dominates the falling film regime, and there are seldom any horizontal motions.

Fig.10 shows horizontal motion distances of enhanced tubes under different Re numbers. Under the Re range of 87-227, droplets horizontal motion distances on smooth copper tubes are between 0.4-0.8cm, and droplets horizontal motion distances on enhanced tubes are between 0.9-1.2cm. As Re increases, droplets horizontal motion distances on both tubes decreases. Fig.11 shows wettability on smooth and enhanced copper tube bundles. Under the same tube spacing (10mm) and distribution height from the orifice to the top of the first tube (6mm), the enhanced copper tube bundles had higher wettability than the smooth copper tube bundle. As the distribution height increases from 6mm to 32mm, wettability on both smooth tube and enhanced tube bundle also increases.

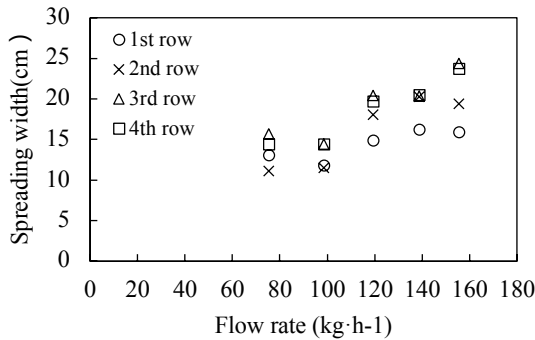


Figure 8: Total spreading width droplets on different rows

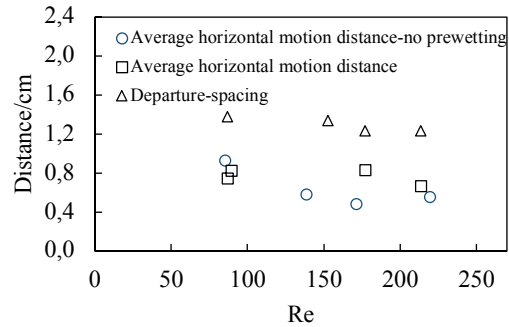


Figure 9: Horizontal motions on pre-wetting copper tubes and no pre-wetting tubes

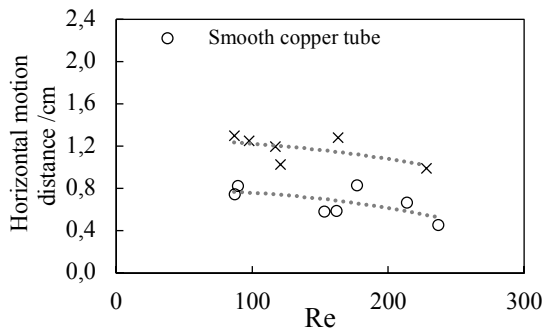


Figure 10: Horizontal motion distances of enhanced tubes under different Re numbers

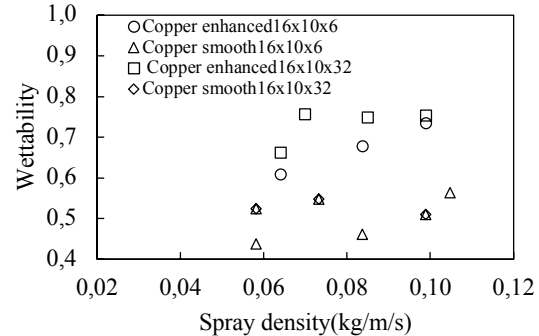


Figure 11: Wettability on smooth and enhanced copper tubes

4. Conclusions

Falling film LiBr flow experiments are conducted on droplets spreading and horizontal motions. The conclusions are as follows:

1. Spreading widths of droplets increase with solution flow rates. Low row spacing limits spreading widths of the liquid film, and spreading widths of droplets do not increase apparently on lower layers.
2. Horizontal motion distances of pre-wetting tubes are larger than that of no pre-wetting tubes;
3. LiBr/H₂O solution droplets horizontal motion distances on a 16mm diameter smoother copper tube are between 0.45~0.83cm in the range of Reynolds number between 87~237, and it decreases when liquid spray density rises;
4. In the range of Re between 87~228, horizontal motion distances on enhanced copper tube are between 0.99~1.30cm, higher than horizontal motion distances on smooth copper tubes.
5. Wettability on enhanced tubes are relatively higher than that on smooth copper tubes. The essence of the phenomenon is the same as that of the upper layer, which is caused by the disturbance of the liquid film. It is transmitted to the lower layer of the tube bundle to form the liquid drop displacement. Wettability is necessary for droplets horizontal motions.

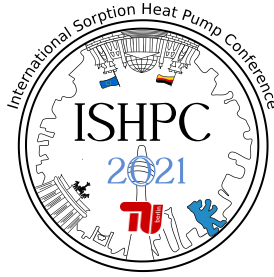
5. Acknowledgment

The authors gratefully acknowledge the support from the Innovative Research Group Project of National Natural Science Foundation of China (Grant number 51521005), and the International Cooperation Project in Innovation,

Science and Technology between Governments of the National Key Research and Development Program (No.2019YFE0102700).

6. List of References

- [1] Yung, D., Lorenz, J., Ganic, N. (1980): Vapor/liquid interaction and entrainment in falling film evaporators. *J. Heat Transfer*, vol.102 (1), pp.20-25.
- [2] Parken, H., Fletcher, S., et al., (1990): Heat transfer through falling film evaporation and boiling on horizontal tubes. *J. Heat Transfer*, vol.112 (3), pp.744.
- [3] Ribatski, G., Jacobi, M., (2005): Falling-film evaporation on horizontal tubes—a critical review. *Int. J. Refrig.* Vol: 28(5), pp.635-653.
- [4] Mitrovic, J., Ricoeur, A.,(1995): Fluid dynamics and condensation-heating of capillary liquid jets. *Int. J. Heat and Mass Transfer*, vol.38 (8), pp.1483-1494.
- [5] Hu, X., Jacobi, M., et al., (1996): The intertube falling film: part 2—mode effects on sensible heat transfer to a falling liquid film. *J. Heat Transfer*. vol.118 (3), pp.626-633.
- [6] [Hu, X., Jacobi, M., (1998): Departure-site spacing for liquid droplets and jets falling between horizontal circular tubes. *Exp. Therm. Fluid. Sci.* vol.16 (4), pp.322–331.
- [7] Subramaniam, V., Garimella, S., (2009): From measurements of hydrodynamics to computation of species transport in falling films. *Int. J. Refrig.* vol.32 (4), pp.607-626.
- [8] Killion, J., Garimella, S., (2003): A review of experimental investigations of absorption of water vapor in liquid films falling over horizontal tubes. *Hvac & R Research* vol.9 (2), pp.111-136.
- [9] Killion J D, Garimella S., (2003b): Gravity-driven flow of liquid films and droplets in horizontal tube banks [J]. *Int. J. Refrig.* vol.26 (5), pp.516-526.
- [10] Hu, T., Xie, X., Jiang, Y., (2019): A detachable plate falling film generator and condenser coupling using lithium bromide and water as working fluids. *Int. J. Refrig.* vol.98, pp.120-128.
- [11] Li, J., Xie, X., Jiang, Y., (2015): Experimental study and correlation on the falling column adiabatic absorption of water vapor into LiBr–H₂O solution. *Int. J. Refrig.* vol.51, pp.112–119.
- [12] Zheng, S., Xie, X., Jiang, Y., (2016): Experimental study on the flash evaporation process of LiBrH₂O solution in an absorption heat pump. *Int. J. Refrig.* vol.61, pp.117–126.



Transforming Heat From 90 °C to 110 °C: Demonstration of a Lab-Scale Adsorption Heat Transformer (AdHT)

Engelpracht, Mirko¹, Driesel, Jannik¹, Jürgens, Boyung¹, Seiler, Jan¹, Bardow, André^{1,2,3 *}

¹ Institute of Technical Thermodynamics, RWTH Aachen University, 52062 Aachen, Germany

² Institute of Energy and Climate Research (IEK-10), Forschungszentrum Jülich, 52425 Jülich, Germany

³ Energy & Process Systems Engineering, ETH Zurich, 8092 Zurich, Switzerland

* Corresponding Author: abardow@ethz.ch

Abstract:

Industry requires mainly heat above 100 °C, but waste heat is mostly available at temperatures below 100 °C. To close this temperature gap, Adsorption Heat Transformers (AdHTs) are particularly promising and, therefore, recently discussed in the literature. However, an experimental feasibility study of closed AdHTs is currently lacking for temperatures around 100 °C. Therefore, we present an experimental setup for a lab-scale cyclic operating prototype of a closed AdHT in one-bed configuration that uses TiAPSO-34 & H₂O as working pair. For the AdHT prototype, we demonstrate that heat transformation from 90 °C to 110 °C is experimentally feasible, while achieving a Coefficient Of Performance (COP) of 0.136 and a Specific Heating Power (SHP) of 32.4 W/kg. Moreover, we identify main challenges of the AdHT cycle that limit the AdHT performance and need to be resolved.

1. Introduction

To reduce greenhouse gas emissions from industry, the decrease of energy consumption to generate heat is key since heat accounts for 71% of the industrial energy demand [1-2]. According to a study, the heat demand is 2.2 EJ (27%) between 100 °C and 400 °C for the European industry [3], whereas 8.7 EJ (27%) of the global industrial waste heat is available between 60 °C and 100 °C [4]. Thus, most waste heat cannot be integrated directly into industrial processes but needs to be transformed to temperatures of industrial heat demand first.

For heat transformation, three thermally driven technologies have been discussed in literature: (1) thermochemical heat transformers; (2) absorption heat transformers; and (3) adsorption heat transformers. The concept of thermochemical heat transformers has proven to be experimental feasible for operating temperatures around 100 °C, with COPs reported up to 0.38 and heating capacities reported up to 50 kW [5]. However, major open issues are the selection of stable working pairs [6], with high reaction kinetics [5-6], and the enhancement of currently low gas permeabilities [7]. Absorption heat transformers have already been shown to be experimental feasible by both several lab-scale prototypes and first industrial prototypes [8-9]. For operating temperatures around 100 °C, reported COPs range from 0.15 to 0.50 and reported heating capacities range from 0.7 kW up to 6700 kW [8-9]. However, non-toxic working pairs, which do not corrode, are stable, and have good thermodynamic properties, are still missing for higher temperatures [8]. In contrast to thermochemical and absorption heat transformers, AdHTs are particularly promising due to non-toxic environmentally friendly working pairs that are well-known, characterized by good reaction kinetics, and have great material stability [9].

For the interesting operating temperatures around 100 °C, open AdHTs have already been proven to be experimental feasible [10], whereas closed AdHTs have only been investigated by steady-state analysis [11], showing e.g. promising COPs up to 0.49 for heat transformation from 85 °C to 110 °C. However, the experimental feasibility of closed AdHTs has been proven for operating temperatures around 20-30 °C using methanol as refrigerant [12]. For example, Gordeeva et al. built a first prototype in one-bed configuration and generated an averaged useful heat flow of 350 W for heat transformation from 20 °C to 29 °C [13]. For both the same operating temperatures and the same prototype, Tokarev et al. have increased the averaged useful heat flow from 350 W to 670 W when changing the sorbent [14-15]. Furthermore, Tokarev build another prototype of a closed AdHT in two-bed configuration to transform heat from 20 °C to 30 °C, releasing waste heat at -30 °C [16]: He reported a COP of 0.44 and a SHP, which he normalized to the sorbent mass, of 350 W/kg for the working pair LiCl/SiO₂ & CH₃OH. Thus, closed AdHTs are already known to be promising for low-temperature heat transformation when using methanol as refrigerant.

However, the experimental feasibility of a closed AdHT has not yet been demonstrated for operating temperatures around 100 °C and, thus, an experimental assessment of the potential is still missing. To close this gap, we present an experimental setup for a closed AdHT in one-bed configuration that uses TiAPSO-34 & H₂O as working pair (Section 2). In Section 3, we assess the performance for heat transformation from 90 °C to 110 °C. In Section 4, we draw conclusions.

2. Experimental Set-up

We investigated the cyclic operation of a closed AdHT (Fig. 1). Main components of the AdHT were a finned-tube evaporator, a double helix condenser, and a finned-tube adsorber that were all made from copper and placed into vacuum-tight steel vessels. Besides the main components, the AdHT consisted of a reservoir for condensed water, various valves to connect the components, and an orifice between the evaporator and the adsorber for smooth pressure equalization. The heat transfer fluid was water, and inlet temperatures of the water were kept constant by thermostats. To ensure easy reproducibility of experiments, the experimental setup was completely automated.

As working pair, we selected TiAPSO-34 & H₂O based on a previously performed analysis of equilibrium data of different sorbents. We used TiAPSO-34 as sorbent due to its high working capacity for water compared with classical sorbents such as Zeolite 13X or Silica Gel 123 for the investigated operating temperatures around 100 °C. We used water as refrigerant since it is environmentally friendly, has no global warming potential, and offers a high enthalpy of evaporation.

To assess the AdHT performance, all heat transfer circuits of the main components were equipped with measurement sensors. We measured the temperatures of the heat exchanger inlets (T_i) and outlets (T_o), of the sorbent (T_s), and the volume flows at heat exchanger inlets (\dot{V}). Furthermore, we measured the absolute pressures (p) in all main components. Based on the measurements, we calculated the COP and the SHP. The COP describes the efficiency of the AdHT, depends only on transferred energy amounts, and is given by

$$\text{COP} = \frac{\int_{\tau_{\text{start}}}^{\tau_{\text{end}}} \dot{Q}_{\text{ads}} d\tau}{\int_{\tau_{\text{start}}}^{\tau_{\text{end}}} \dot{Q}_{\text{evap}} + \dot{Q}_{\text{des}} d\tau}, \quad (1)$$

where \dot{Q}_{ads} is the adsorption heat flow, \dot{Q}_{des} the desorption heat flow, \dot{Q}_{evap} the heat flow supplied for evaporation, τ_{start} the start time of the cycle, and τ_{end} the end time of the cycle. The SHP describes the power density of the AdHT, depends on the sorption dynamics and system size, and is given by

$$\text{SHP} = \frac{\int_{\tau_{\text{start}}}^{\tau_{\text{end}}} \dot{Q}_{\text{ads}} d\tau}{(\tau_{\text{end}} - \tau_{\text{start}})(m_{\text{sor}} + m_{\text{hx}})}, \quad (2)$$

where m_{sor} is the mass of the sorbent (2.18 kg) and m_{hx} the mass of the adsorber heat exchanger (3.35 kg). To calculate the heat flows \dot{Q}_j , we applied energy balances to the heat exchangers of the main components and neglected changes of inner energies of the heat transfer fluids. Thus, the energy balances read

$$\dot{Q}_j = \rho_j \dot{V}_j (h_{\text{in},j}(T_{i,j}) - h_{\text{out},j}(T_{o,j})), \quad (3)$$

where ρ_j describes the density at the heat exchanger inlets, $h_{\text{in},j} / h_{\text{out},j}$ the specific enthalpy of the heat transfer fluids at the heat exchanger inlets / outlets. To calculate physical properties of water, we used RefProp with equation of state ‘‘IAPWS-95’’ [17].

We only present results once we had reproduced the AdHT cycle at least 4 times. Here, the AdHT cycle consisted of 5 phases: (1) pressure equalization, (2) use phase, (3) cooling phase, (4) condensate reflux, and (5) desorption.

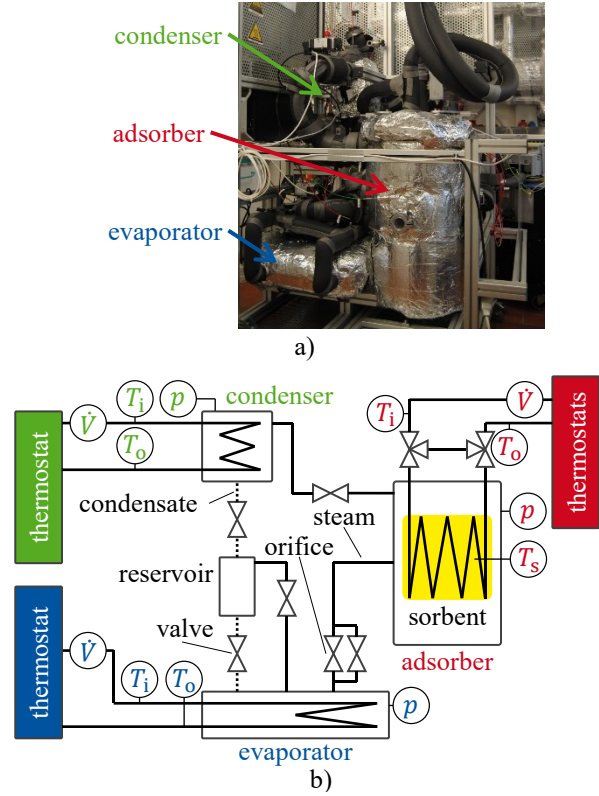


Figure 1 – a) Photograph of the lab-scale adsorption heat transformer. b) Scheme of experimental setup of the adsorption heat transformer with measurement sensors (circles): pressure (p), temperature (T), volume flow (\dot{V}) located at inlet (i), outlet (o), sorbent (s).

- 1) During the pressure equalization phase (here: 270 s), the adsorber started at desorption temperature T_{des} and condensation pressure p_{cond} , whereas evaporation temperature T_{evap} and evaporation pressure p_{evap} were kept constant by supplying a heat flow to the evaporator. The evaporator was connected to the adsorber by an orifice that smoothens the pressure equalization between the two components. Thereby, we avoided dragging liquid water from the evaporator into the adsorber that would have been caused otherwise due to the huge pressure difference between both components (here: $p_{evap} - p_{cond} > 650$ mbar). During the smooth pressure equalization, vapor flowed from the evaporator into the adsorber and was adsorbed by the sorbent. Thus, the heat of adsorption was released and heated up the adsorber heat exchanger from desorption temperature T_{des} to adsorption temperature T_{ads} since the adsorber heat transfer fluid did not flow through the adsorber.
- 2) During the use phase (here: 350 s), the evaporator was connected directly to the adsorber and the adsorber heat transfer fluid flowed through the adsorber. Since the inlet temperature of the adsorber heat transfer fluid was set to adsorption temperature T_{ads} , the adsorber discharged a useful heat flow at temperature T_{ads} .
- 3) During the cooling phase (here: 50 s), the adsorber was disconnected from all components and the inlet temperature of the adsorber heat transfer fluid was switched from adsorption temperature T_{ads} to desorption temperature T_{des} . Thus, the adsorber was cooled down at isosteric conditions. The isosteric cooling phase was introduced to imitate the influence of a heat recovery phase that would possibly be used for a 2-bed AdHT.
- 4) During the condensate reflux phase (here: 30 s), the reservoir was first disconnected from the condenser. Then, the vapor phases of the reservoir and of the evaporator were connected for pressure equalization. Subsequently, the liquid phases of the reservoir and of the evaporator were connected and, thus, condensed refrigerant flowed into the evaporator due to gravity. Thus, we avoided using a mechanical pump for condensate reflux.
- 5) During the desorption phase (here: 600 s), the adsorber was connected to the condenser and the condenser was connected to the reservoir. By supplying a desorption heat flow to the adsorber at temperature T_{des} , the sorbent desorbed water vapor. The vapor flowed into the condenser and condensed at condensing temperature T_{cond} . The temperature T_{cond} was kept constant by releasing a condensing heat flow to the ambient.

The phase times were selected exemplary to demonstrate the experimental feasibility of the AdHT cycle. To investigate impacts of the operating temperatures on the AdHT performance, we evaluated three temperature triples. The reference temperature triple was $T_{cond} = 35$ °C / $T_{evap/des} = 90$ °C / $T_{ads} = 110$ °C according to the objective of waste heat transformation presented in Section 1. We used a relatively high condensing temperature to imitate the ambient temperature of a hot summer day, which is typically used for recooling. Besides, we reduced the adsorption temperature from 110 °C to 105 °C to see an impact of the gross temperature lift, and we reduced the condensing temperature from 35 °C to 30 °C to see an impact of the ambient temperature.

3. Results

The results demonstrate that adsorption heat transformation is possible for operating temperatures around 100 °C when using water as refrigerant (Fig. 2). For the reference case 35/90/110 °C, the COP is 0.136 and the SHP is 32.4 W/kg. When reducing the adsorption temperature by 5 K, the COP and the SHP increase by about 22% and 34%, respectively, because less heat of adsorption is required to heat up the adsorber heat exchanger. Thus, more released heat of adsorption is available to generate useful heat. When reducing the condensing temperature by 5 K, the COP and the SHP increase by about 4% and 20%, respectively, because the usable working capacity increases. Thus, more heat of adsorption can be spent to generate useful heat. Overall, the operating temperatures influence the AdHT performance as expected and as derived from the behavior of adsorption chillers. However, the COPs are about 70% lower compared to the state-of-the-art absorption heat transformers for operating temperatures around 100 °C (cf. Section 1) [8-9]. Moreover, the COPs and the SHPs are about 66% or 72% lower than the values reported by Tokarev for the closed AdHT in two-bed configuration (cf. Section 1) [16]. To

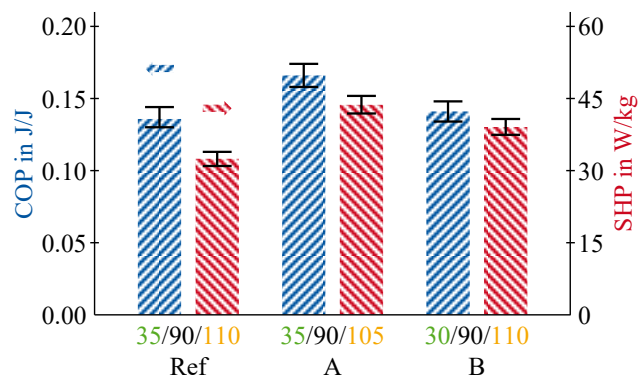


Figure 2 – Comparison of Coefficient Of Performance (COP) and Specific Heating Power (SHP) for three AdHT cycles with different operating temperature triples condensation / evaporation / adsorption in °C.

identify reasons for the low performance indicators as well as main characteristics and challenges of the AdHT cycle, we analyze pressures in the main components, adsorber temperatures, and the difference in the enthalpy flow of the adsorber heat transfer fluid over time for the reference operating temperatures 35/90/110 °C:

1) The pressure equalization (Fig. 3 a) to overcome the pressure difference between the evaporator and the adsorber (> 650 mbar) is very slow and, thus, limits the mass flow. Consequently, the pressure equalization also limits the adsorption-based heating (Fig. 3 b), increases the cycle time, and thus decreases the SHP. However, the SHP could be increased by 16% if the phase time of the pressure equalization were decreased by 80%.

2) The cooling phase (Fig. 3 b-c) is not suitable for a 1-bed AdHT since we lose the sensible heat of the adsorber, which is stored in the adsorber heat exchanger after adsorption, to the ambient, instead of using it for desorption. Therefore, we suggest using the sensible heat of the adsorber for desorption for a 1-bed AdHT or for heat recovery for a 2-bed AdHT. For example, the COP could be increased by 17% if all sensible heat (here 224 kJ, cf. Fig. 3 c) could be used for desorption.

3) Due to the huge pressure difference between the condenser and the evaporator (> 650 mbar), condensate cannot be returned to the evaporator by gravity only. Therefore, we propose to use a condensate reflux based on gravitation-supported pressure equalization (Fig. 3 a). When using the proposed condensate reflux, the subsequent desorption is not limited by the pressure increase of the condenser (Fig. 3 a). Thus, we show that the proposed condensate reflux is applicable for the AdHT cycle.

Overall, the results show the experimental feasibility of a closed AdHT transforming heat around 100 °C. However, we expect to achieve higher COPs and SHPs at optimal control of the AdHT cycle in future, since the performance of sorption systems is known to strongly depend on the control [18]. Moreover, higher temperature lifts may be achievable when using other working pairs with tailor-made equilibrium properties for heat transformation applications at specific temperatures.

4. Conclusions

We demonstrated the experimental feasibility of a lab-scale cyclic operating prototype of a closed AdHT in one-bed configuration. For the operating temperature triple 35/90/110 °C, we obtained a COP of 0.136 and a SHP of 32.4 W/kg. When reducing the condensing or the adsorption temperature by 5 K, COP and SHP increased by 4% to 34%. Furthermore, we proposed and experimentally demonstrated a gravitation-supported pressure equalization for the condensate reflux from the condenser to the evaporator. Thereby, we could avoid a mechanical pump, which is often suggested in the literature, for the condensate reflux. This work thus provides the experimental starting point to investigate closed adsorption heat transformers around 100°C to exploit waste heat.

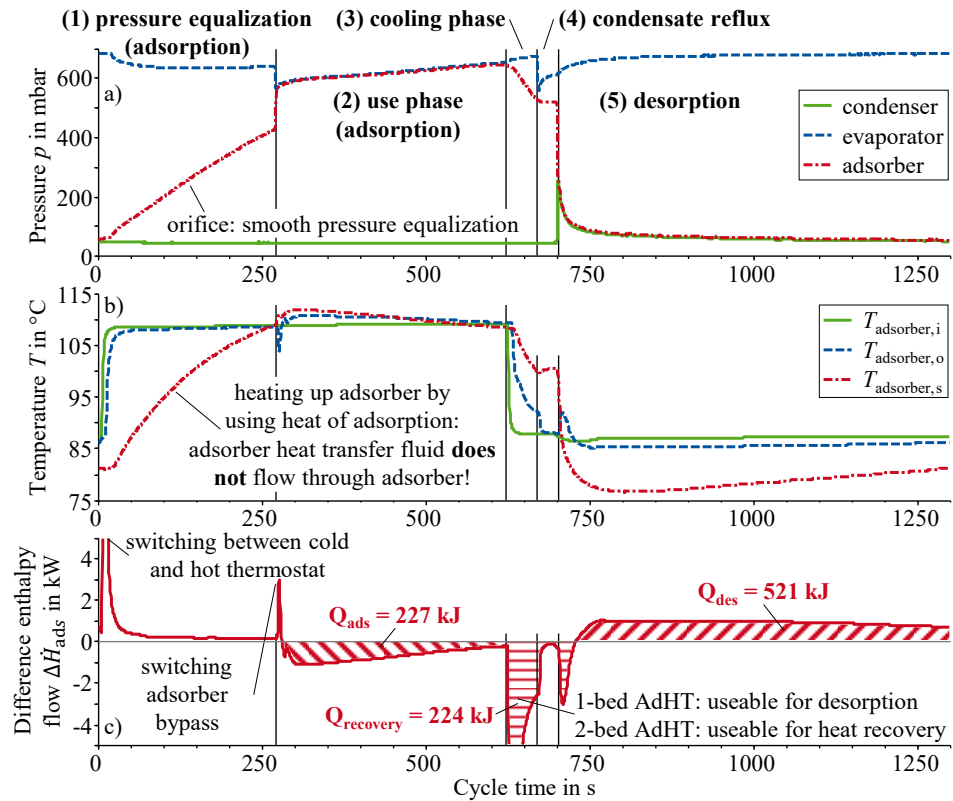


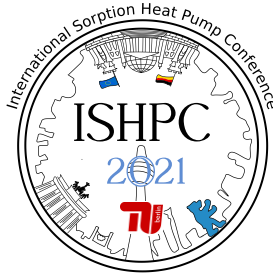
Figure 3 – Time evolution of a) pressure, b) temperature, and c) difference in the enthalpy flow of the adsorber heat transfer fluid for an adsorption heat transformer cycle at operating temperature triple 35/90/110 °C.

5. Acknowledgment

This study was founded by Excellence Initiative of the German federal and state governments.

6. List of References

- [1] Eisentraut, A., Brown, A. (2014): Heating without global warming – Market Developments and Policy Considerations for Renewable Heat. <https://www.ourenergypolicy.org/wp-content/uploads/2014/06/heating-cooling.pdf>, accessed 29 February 2020.
- [2] International Energy Agency (2012): Data and statistics. <https://www.iea.org/data-and-statistics/data-tables?country=WORLD&energy=Balances&year=2012>, accessed 29 February 2020.
- [3] Naegler, T., Simon, S., Klein, M., Gils, H. C. (2015): Quantification of the European industrial heat demand by branch and temperature level. *Int. J. Energy Res.*, vol.39, pp.2019–2030.
- [4] Forman, C., Muritala, I. K., Pardemann, R., Meyer, B. (2016): Estimating the global waste heat potential. *Renew. Sustain. Energy Rev.*, vol.57, pp.1568–1579.
- [5] Yu, Y. Q., Zhang, P., Wu, J. Y., Wang, R. Z. (2008): Energy upgrading by solid–gas reaction heat transformer: A critical review. *Renew. Sustain. Energy Rev.*, vol.12, pp.1302–1324.
- [6] Richter, M., Habermann, E.-M., Siebecke, E., Linder, M. (2018): A systematic screening of salt hydrates as materials for a thermochemical heat transformer. *Thermochim. Acta*, vol.649, pp.136–150.
- [7] Richter, M., Bouché, M., Linder, M. (2016): Heat transformation based on $\text{CaCl}_2/\text{H}_2\text{O}$ – Part A: Closed operation principle. *Appl. Therm. Eng.*, vol.102, pp.615–621.
- [8] Xu, Z., Wang, R. (2017): Absorption heat pump for waste heat reuse: Current states and future development. *Front. Energy*, vol. 4, pp. 414–436.
- [9] Rivera, W., Best, R., Cardoso, M. J., Romero, R. J. (2015): A review of absorption heat transformers. *Appl. Therm. Eng.*, vol.91, pp.654–670.
- [5] Goyal, P., Baredar, P., Mittal, A., Siddiqui, A. R. (2016): Adsorption refrigeration technology – An overview of theory and its solar energy applications. *Renew. Sustain. Energy Rev.*, vol.53, pp.1389–1410.
- [10] Xue, B., Ye, S., Zhang, L., Wei, X., Nakaso, K., Fukai, J. (2019): High-temperature steam generation from low-grade waste heat from an adsorptive heat transformer with composite zeolite-13X/ CaCl_2 . *Energ. Convers. Manage.*, vol.186, pp.93–102.
- [11] Frazzica, A., Dawoud, B., Critoph, R. E. (2016): Theoretical analysis of several working pairs for adsorption heat transformer application. In *Heat Powered Cycles*, England.
- [12] Aristov, Y. I. (2019): A new adsorptive cycle "HeCol" for upgrading the ambient heat: The current state of the art. *Int. J. Refrig.*, vol. 105, pp. 19–32.
- [13] Gordeeva, L. G., Tokarev, M. M., Aristov, Y. I. (2018): New Adsorption Cycle for Upgrading the Ambient Heat. *Theor. Found. Chem. Eng.*, vol.52, pp.195–205.
- [14] Tokarev, M. M., Gordeeva, L. G., Grekova, A. D., Aristov, Y. I. (2018): Adsorption cycle "heat from cold" for upgrading the ambient heat. The testing a lab-scale prototype with the composite sorbent CaClBr/silica . *Appl. Energ.*, vol.211, pp.136–145.
- [15] Tokarev, M. M., Gordeeva, L. G., Shkatulov, A. I., Aristov, Y. I. (2018): Testing the lab-scale "Heat from Cold" prototype with the "LiCl/silica – methanol" working pair. *Energ. Convers. Manage.*, vol.159, pp.213–220.
- [16] Tokarev, M. (2019): A Double-Bed Adsorptive Heat Transformer for Upgrading Ambient Heat: Design and First Tests. *Energies*, vol. 12, pp. 4037–4050.
- [17] Wagner, W. and Pruß, A. (2002): The IAPWS Formulation 1995 for the Thermodynamic Properties of Ordinary Water Substance for General and Scientific Use. *J. Phys. Chem. Ref. Data*, vol.31, pp.387–535.
- [18] Bau, U., Baumgärtner, N., Seiler, J., Lanzerath, F., Kirches, C., Bardow, A. (2019): Optimal operation of adsorption chillers: First implementation and experimental evaluation of nonlinear model-predictive-control strategy. *Appl. Therm. Eng.*, vol.149, pp.1503–1521.



Ammonia-salt Large Temperature Jump Experimental Technique Advances

Hinners, Samuel^{1*}, Critoph, R.E.¹, Atkinson, George¹, Locke, Jake¹.

¹University of Warwick, School of Engineering, CV4 7AL UK
(*s.hinners@warwick.ac.uk.)

Abstract

Halide salts reacting with ammonia have been tested using the Large Temperature Jump (LTJ) method. To date the experiments have revealed much about the nature of the reversible sorption reaction. The tests showed some gaps in the knowledge as well as highlight the importance of LTJ experimentation to understand the sorption behaviour. The LTJ tests enable the salts to be tested in realistic conditions like those in a sorption machine, with rapid reactions while monitoring conditions in the salt, and the system pressure. This can illustrate far more than traditional gravimetric testing methods. A major unknown, was the percentage conversion of ammoniated salt to pure salt and vice versa in desorption and adsorption respectively (per cycle). It was observed that the temperature sampling method failed to enable accurate modelling within the heat transfer model and with the unknown percentage of ammonia reacting during a cycle, the reaction engineering was unclear. Steps have now been taken to improve the temperature sampling to ensure a simple heat transfer model while Rubotherm magnetic suspension balance tests can enhance understanding of overall conversion of ammoniate during reactions.

1 Introduction

Resorption systems utilising the reversible reactions of ammonia and two halide salts, present an opportunity for the recovery of waste heat. Resorption is a well explored method, which can provide cooling, heat pumping, or heat transforming [1-4]. The aim of this project is the development of a resorption heat transformer; the premise is a simple system which can recover low grade heat with limited use of electricity, upgrading to a useable temperature is an attractive prospect and will increase efficiencies of industrial processes. This will facilitate a switch from current fossil fuel energy supplies, to renewable alternatives as part of the *Energiewende*. Resorption also creates an opportunity for better integrated heat networks.

To design a machine with a coefficient of performance (COP) great enough to make a case for support, it is necessary to understand the behaviour of the salt materials during cycles. This required the use of Large Temperature Jump (LTJ) tests. The monovariant nature of the salt-ammonia reactions show a desorption or adsorption of salt is a transition between ammoniate phases, only occurring when certain pressure or temperature conditions are exceeded. The representation of the phase changes are seen in a Clausius-Clapeyron diagram as equilibrium lines. Work by Neveu and Castaings, reviews and presents a huge number of these from the literature [5]. The data collected shows a single line for the phase changes, but when LTJ testing one can observe that adsorption and desorption occur at different conditions. This is observed by Goetz and Mazet, they describe the region between the two as an area of pseudo-equilibrium in which the reaction rate is zero [6]. The salt is also observed to form a metastate before the reaction initiates; this is measured as the conditions exceed those of the phase change, before returning to the phase change, further explained in section 2.

An LTJ machine has been developed at the University of Warwick to measure the reaction conditions. The design has gone through several iterations and initial tests have proven insightful leading to some published data. What is clear, is the requirement to improve the design and the data recording. This paper will detail the past experiments and the design, before elucidating the issue and improvements made to address these. The experiments provide a basis for constructing an empirical model which simulates reaction rate, it will also provide an insight into the heat transfer of the reactive material. Details of the empirical model are found in the work by Hinners and Critoph [7].

2 Background and Experimental Set-up

2.1 Large Temperature Jump

Large temperature jump experiments are well documented [8-11], they test a sorbent material under real cycle conditions. The LTJ design rig is documented by Hinners and Critoph [7], the simple design mimics a heat exchanger bed that would be packed with the sorbent material and is subjected to rapid heating and cooling, where the conditions in the system are measured to attain data on performance, reaction rate, and pressure rise. The reaction material used is an expanded natural graphite (ENG) matrix, hosting a halide salt. The matrix avoids the effects of agglomeration of the salt crystals, and the high conductivity ensures a rapid reaction. A relatively high conductivity is necessary as when small salt crystals are hosted in a matrix the reaction is limited by the rate of heat transfer. The initial test reactor can be seen in Figure 1.

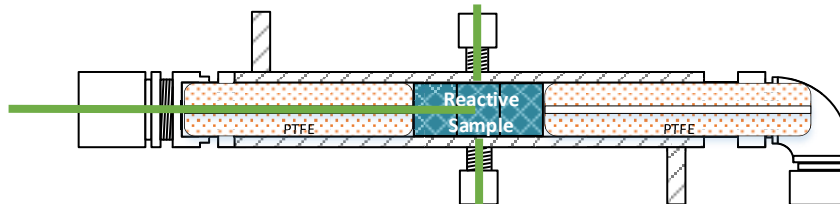


Figure 1 Initial LTJ design [7] Thermocouple positions indicated by green lines, heat transfer fluid passes through jacket via inlet and outlet perpendicular to reactor axis.

The initial LTJ focussed on simplicity, as a single double pipe heat exchange, comprised of an inch outer diameter pipe and half inch inner diameter pipe. The heat transfer fluid (silicone oil) flows through the annulus, providing the driving force for the reaction. The fitting on the left hosted a long 1mm K type thermocouple that fed down the centre into the middle sample of ENG indicated in figure 1. Two fittings on the top and bottom of the outer tube house the thermocouple sheaths used to measure the temperature of the outer wall of the inner tube. They are K type sheathed thermocouples. To fill dead volume in the reactor, polytetrafluoroethylene (PTFE) fillers were machined with a 1.2mm diameter central hole. The ENG was drilled with a 1mm central hole before salt dosing. The reactor is connected to a pressure vessel which limits the pressure rise during the process.

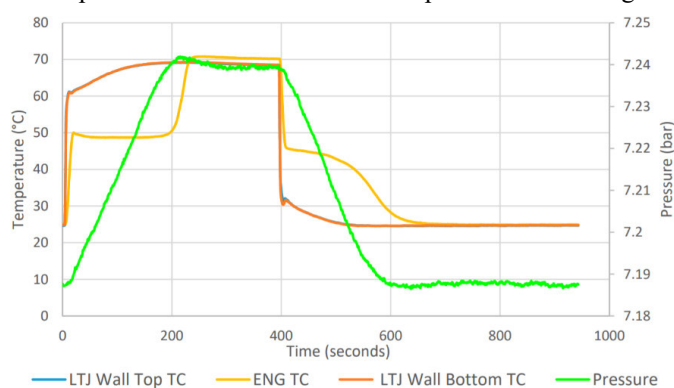


Figure 2 Initial LTJ result for barium chloride, desorption cycle followed by an adsorption cycle [7]. The wall temperature (perpendicular thermocouples figure 1) rises, causing the phase change to occur at around 50°C, the desorption causing the pressure rise in the system. The reverse happens around 400 seconds, where the wall is cooled and desorption occurs at around 45°C. This behaviour is described by Hinners and Critoph [7]. ENG TC describes the central thermocouple figure 1.

The first set of results were promising, and an example can be seen in Figure 2. The yellow line is the central thermocouple, which measures the temperature at the centre of the salt-ENG composite. The orange line, and blue line (behind and not visible) are the top and bottom wall temperatures (identical). Overlaid is a green line which is the system pressure recorded on the right-hand scale. The reaction occurs both when the sample temperature is steady and when the pressure changes due to devolution or evolution of ammonia. The large temperature jump occurs shortly after time zero creating the step change in wall temperature. As the reaction progresses ammonia is desorbed causing the linear pressure rise. This is reversed in adsorption, beginning just before 400 seconds. The linear pressure change shows the reaction is heat transfer limited, since concentration and pressure have no effect on rate of reaction; it is constant until completion. The metastate discussed earlier is seen as the peak in the yellow line as the sample superheats before returning to the isothermal phase change.

The initial data enabled modelling to be done which identified the order of the reactions using an empirical form presented by Mazet [12] and can be seen in the paper by Hinners and Critoph [7]. This may present enough data to design with, but some shortfalls were observed in the measurements. The thermocouple having a sheathed tip meant it was insulated from the steel of the reactor wall, the heat transfer resistance between the tip and the wall impeded accurate wall measurement, giving a reading more akin to the oil temperature. The conversion of ammoniate during a cycle is also an unknown, this reduces the effectiveness of the model as the heat transfer and the total percentage reacted are integral in calculating the reaction rate. The pressure rise within the system can give a guide to the ammoniate mass change but some of the gas and pipework is heated so there is error in any calculation. To more accurately measure the wall temperature and predict the heat transfer a new design has been proposed. Furthermore, to give an indication of the percentage conversion some Rubotherm magnetic suspension balance tests will be performed to see how much ammoniate reacts. The cycles in a magnetic suspension balance are much longer but this will give us an indicative value.

The new design uses custom made thermocouples from TC. These are sheathed k-type thermocouples with an exposed junction at the end. The exposed junction is placed in contact with the pipe and gives a more accurate wall reading but with a small contact area there is still a difference. To further improve this, a thermocouple on each side of the pipe has one connection from each so that the contact point is now the pipe itself and the reading is the average temperature of that section of pipe radius. This can be seen in Figure 3. One wire colour from each thermocouple is seen.

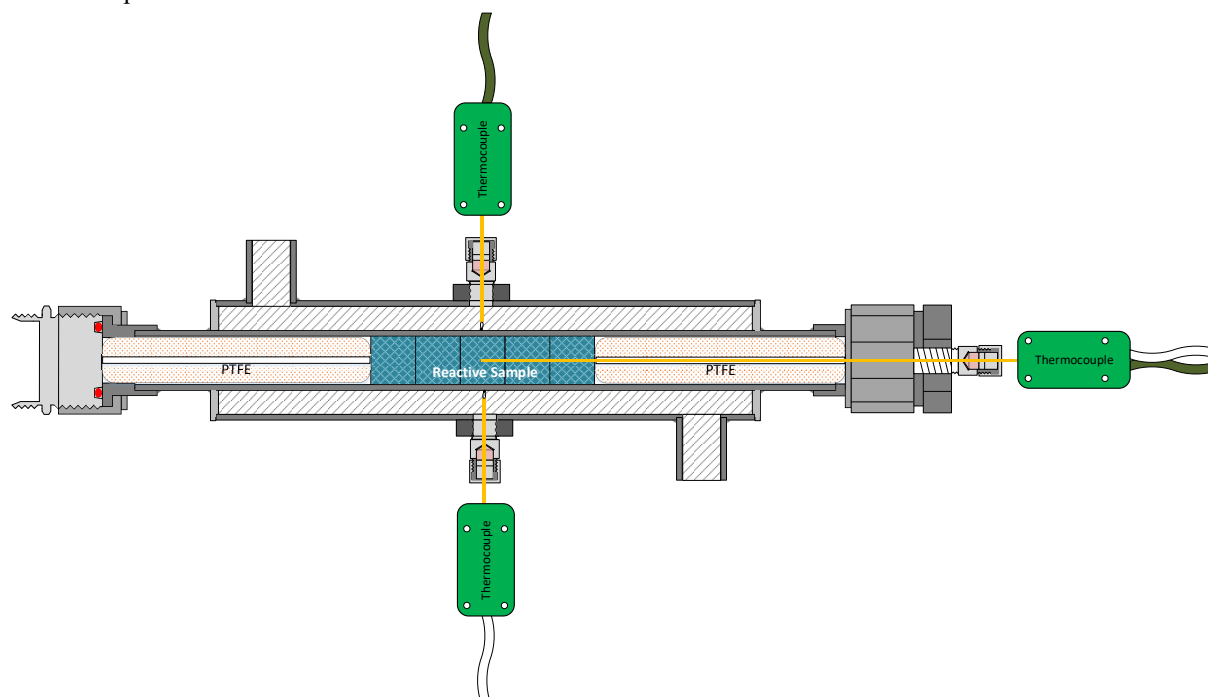


Figure 3 New reactor design

Initial tests are promising, but large temperature jumps for extended periods can cause thermocouple contact loss. Future work will consider the longevity of this set up considering options to solder the thermocouple tip to the pipe with a small amount of tin/silver solder. To be able to monitor the position of the tip and to enable future soldering or adjusting of pipe surface, a boss has been manufactured which hosts a thermocouple fitting with a PTFE olive rather than a stainless-steel olive to increase flexibility, and to enable monitoring of tip or to attempt soldering. Other adjustments have been to use O-ring Swagelok face seal fittings, these make taking apart of the reactor very easy and reduce effects of pinching of the inner pipe which can occur with standard fittings opened and closed many times. The pinching reduces the inner diameter and affects the insertion of samples.

The new design has improved the quality of results enabling formulation of a reliable reaction model. Next steps will look to review the behaviour of halide salts like calcium chloride and manganese chloride and retest barium chloride. This will build on that by Spinner, Mazet and Amaroux and provide data which can be used to model the next generation of ammonia-salt adsorption machines.

3 Conclusions

A number of improvements have been made to the large temperature jump test rig at the University of Warwick. The new design addresses the issue of accurate wall temperature readings by the novel use of the reactor as the contact for two thermocouple wires. Further modifications to improve reactor reliability have been considered. Accurate data for ammonia-salt reactions under conditions similar to those within a working sorption machine are yet to be published. Finalising this data can provide the basis to model the next generation of sorption machines.

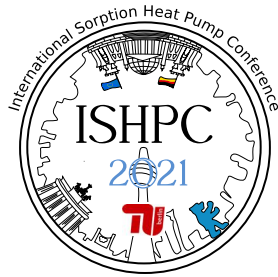
4 Acknowledgment

This work is funded by EPSRC, TNO and InnovateUK via T-ERA. Many thanks to Charles Joyce for technician support throughout manufacture of components.

5 List of References

- [1] H. S. Bao, R. G. Oliveira, R. Z. Wang, L. W. Wang, and Z. W. Ma, "Working pairs for resorption refrigerator," *Applied Thermal Engineering*, vol. 31, no. 14, pp. 3015-3021, 2011/10/01/ 2011, doi: <https://doi.org/10.1016/j.applthermaleng.2011.05.035>.
- [2] H. S. Bao, R. Z. Wang, R. G. Oliveira, and T. X. Li, "Resorption system for cold storage and long-distance refrigeration," *Applied Energy*, vol. 93, pp. 479-487, 2012/05/01/ 2012, doi: <https://doi.org/10.1016/j.apenergy.2011.12.022>.
- [3] L. L. Vasiliev, D. A. Mishkinis, A. A. Antukh, A. G. Kulakov, and L. L. Vasiliev, "Resorption heat pump," *Applied Thermal Engineering*, vol. 24, no. 13, pp. 1893-1903, 2004/09/01/ 2004, doi: <https://doi.org/10.1016/j.applthermaleng.2003.12.018>.
- [4] Y. I. Aristov, "'Heat from Cold' – A new cycle for upgrading the ambient heat: Adsorbent optimal from the dynamic point of view," *Applied Thermal Engineering*, vol. 124, pp. 1189-1193, 2017/09/01/ 2017, doi: <https://doi.org/10.1016/j.applthermaleng.2017.06.107>.
- [5] P. Neveu and J. Castaing, "Solid-gas chemical heat pumps: Field of application and performance of the internal heat of reaction recovery process," *Heat Recovery Systems and CHP*, vol. 13, no. 3, pp. 233-251, 1993/05/01/ 1993, doi: [https://doi.org/10.1016/0890-4332\(93\)90014-M](https://doi.org/10.1016/0890-4332(93)90014-M).
- [6] V. Goetz and A. Marty, "A model for reversible solid-gas reactions submitted to temperature and pressure constraints: simulation of the rate of reaction in solid-gas reactor used as chemical heat pump," *Chemical Engineering Science*, vol. 47, no. 17, pp. 4445-4454, 1992/12/01/ 1992, doi: [https://doi.org/10.1016/0009-2509\(92\)85122-R](https://doi.org/10.1016/0009-2509(92)85122-R).
- [7] S. Hinners and R. E. Critoph, "Modelling the Ammoniation of Barium Chloride for Chemical Heat Transformations," vol. 12, no. 23, p. 4404, 2019. [Online]. Available: <https://www.mdpi.com/1996-1073/12/23/4404>.
- [8] Y. I. Aristov, B. Dawoud, I. S. Glaznev, and A. Elyas, "A new methodology of studying the dynamics of water sorption/desorption under real operating conditions of adsorption heat pumps: Experiment," *International Journal of Heat and Mass Transfer*, vol. 51, no. 19-20, pp. 4966-4972, 2008, doi: 10.1016/j.ijheatmasstransfer.2007.10.042.
- [9] J. V. Veselovskaya and M. M. Tokarev, "Novel ammonia sorbents "porous matrix modified by active salt" for adsorptive heat transformation: 4. Dynamics of quasi-isobaric ammonia sorption and desorption on BaCl₂/vermiculite," *Applied Thermal Engineering*, vol. 31, no. 4, pp. 566-572, 2011, doi: 10.1016/j.applthermaleng.2010.10.018.
- [10] Y. I. Aristov, "Adsorptive transformation and storage of renewable heat: Review of current trends in adsorption dynamics," *Renewable Energy*, vol. 110, pp. 105-114, 2017/09/01/ 2017, doi: <https://doi.org/10.1016/j.renene.2016.06.055>.
- [11] Y. I. Aristov, "Optimal adsorbent for adsorptive heat transformers: Dynamic considerations," *International Journal of Refrigeration*, vol. 32, no. 4, pp. 675-686, 2009/06/01/ 2009, doi: <https://doi.org/10.1016/j.ijrefrig.2009.01.022>.

-
- [12] N. Mazet and M. Amouroux, "ANALYSIS OF HEAT TRANSFER IN A NON-ISOTHERMAL SOLID-GAS REACTING MEDIUM," *Chemical Engineering Communications*, vol. 99, no. 1, pp. 175-200, 1991/01/01 1991, doi: 10.1080/00986449108911586.



Integration of absorption chillers in centralized solar heating systems of multifamily buildings.

Belmonte, J.F.^{1,2}, Salgado, R.³, and Almendros-Ibáñez, J.A.^{1,2}

¹Renewable Energy Research Institute, Castilla-La Mancha University, Albacete, 02071, Spain.

²School of Engineering. Castilla-La Mancha University, Campus universitario s/n, Albacete, 02071, Spain.

³Universidad Interamericana de Puerto Rico, Recinto de Bayamón. 500 Carretera Dr. John Will Harris, Bayamón, Puerto Rico, 00957.

Abstract

A significant number of multifamily buildings constructed in Spain during the last years have been provided with centralized heating systems, typically achieving the required domestic hot water (DHW) solar fraction by oversizing collector fields, with the aim of reducing the winter auxiliary consumption (typically, natural gas) of the heating demand. This sizing criteria of the solar system generates some problems during summer operation, when no space heating load has to be met and DHW demand is also low, requiring the operation of heat dissipators connected to the solar loop (or other methods, none of them energy efficient) during a significant number of hours to prevent overheating problems. One of the purposes of this work is to estimate the cooling fraction that the integration of an absorption chiller can provide in a multifamily building located in Madrid without modifying any major aspect of the existing solar system (maintaining the same conventional flat-plate solar collectors, collectors arrangement and slope, volume of the thermal storage tank (TES), etc.), only including an additional loop in the TES to drive the absorption chiller. TRNSYS simulation results have shown that this solution is only capable of providing a limited cooling fraction (less than 15%), as the absorption chiller operates more efficiently at high temperatures (90 – 95°C), a range of temperatures that conventional flat-plate collectors connected in parallel are not able to supply during prolonged periods even on the hottest summer days, as these high operation temperatures reduce significantly collectors thermal efficiency, and may also lead to excessive thermal stresses on solar system components (pumps, tanks, pipes, etc.).

1. Introduction

The required DHW renewable fraction required by the Spanish building codes is typically covered by solar flat-plate collectors in multifamily buildings [1]. When these buildings are air-conditioned by centralized heating systems, modern HVAC schemes may also include the possibility of providing a solar fraction of the heating demand (normally not higher than the 30% for sizing and economic reasons) by the solar system. In these cases, overheating problems during summer operation (from June to September) can be especially severe due to the low heating demand (as no space heating is required, and DHW demand is relatively low). Additionally, as most centralized conditioning systems installed in multifamily buildings are not able to provide cooling, only heating, the installation of unitary split-system air conditioners to meet the cooling needs during summer is a practice that completely dominates the residential market. In this context, the integration of absorption chillers fired by hot water from the surplus solar energy in summer, may arise as a solution to utilize the full potential of the solar field during the entire year (avoiding the intense operation of heat dissipators connected to solar loops, as depicted in Figure 1-Right), for two main reasons: the excess of solar production (wasted heat) during summer months, and the good match (synchronicity) between the solar radiation and cooling load profiles.

The following study differs from other research approaches [2] carried out in Spain on two main aspects: (1) the absorption chiller size has to be sufficiently small to be fired by the actual solar collectors field of the multifamily building (considering a typical range between 2 to 3 m² of solar field per kW of cooling capacity, which gives rise to a downsized chiller to meet the building peak cooling load), and (2) no modifications of the solar system are permitted because of the integration of the absorption chiller (collector technology, collectors arrangement or slope, TES volume, etc.), in order to realistically evaluate the absorption chiller performance.

In the following sections, the TRNSYS [3] modeling of the base case building and its centralized HVAC system including the solar collectors field is described. Next, simulation results for the heating and cooling seasons are presented and discussed. Finally, the main conclusions are summarized.

2. Base Case Building Model/TRNSYS Simulations/Absorption Chiller

A 32-flat multifamily building has been chosen as building base case. Table 1 summarises the most relevant characteristics of the building model. Building comprises of four identical, single-level floors containing eight apartments each floor (four apartments perfectly oriented to the South while the other four to the North). Figure 1-Left shows the South facade of the base case building. In an initial approach, the building was modeled using the component Type 12, based on the simplified ASHRAE energy/degree-day methodology, considering a single lumped capacitance model, which estimates the space heating and cooling loads with a low computation effort. Solar gains transmitted through the windows were computed using the TRNSYS component Type 687, being linked to the building model. Because a simplified component (Type 12) was used to model the thermal behavior of the building, it was assumed that building floor area coincides with the actively conditioned area (considering both heating and cooling services), according to the parameters shown in Table 1.

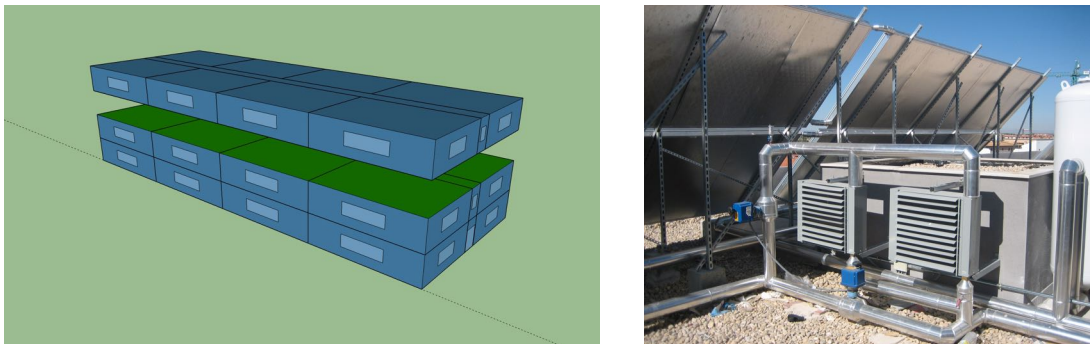


Figure 1: Left: Schematic of the multifamily building model analysed. Right: Photograph of dissipators connected to the solar loop.

Table 1: Main characteristics of building base case model

Parameter	Value	Units
Floor area per flat (x32)	88.24	m^2
Building envelope area	1988	m^2
Walls overall U-value	0.41	W/m^2K
East (or West)/ South (or North) Window area	26.72/83.20	m^2
Glass U-factor	3.809	W/m^2K
Total building thermal capacitance	248000	kJ/K
Heating/Cooling setpoints	20/26	$^{\circ}C$

Main solar collector field characteristics are presented in Table 2. These values are able to provide a solar DHW fraction slightly higher than the strictly mandatory values (60 %) for the weather conditions of Madrid, being able, at the same time, to provide a fraction of the building heating demand of the multifamily building (around 30 %). A relatively large TES volume/collectors area ratio equal to 100 $liters/m^2$ is considered in the study. Although the building has a single HVAC system, two different TRNSYS schemes were considered in the study: one for the heating season (from October to May), and another for the cooling season (from June to September). This modeling approach should not add any error to our simulation results, considerably simplifying the TRNSYS modeling task. The cooling scheme (illustrated in Figure 2) only differs from the heating scheme in the absorption chiller and its associated heat rejection loop (cooling tower and condensing loop). Considering the collectors area available, a hot water single-effect chiller Yazaki WFC-SC10, with a nominal cooling capacity of 35.2 kW has been included in the simulation scheme. TRNSYS component Type 107 was used to model the absorption machine, using the operational performance curves from the work of [4]. To simulate both TRNSYS schemes a short time step of 2 min was chosen to prevent instability and convergence problems.

3. Results

Table 3 summarises the most relevant TRNSYS simulation results for the heating and cooling seasons and the weather conditions of Madrid. The effect of the absorption chiller on the collectors efficiency and average operating

Table 2: Main characteristics of solar system

Parameter	Value	Units
Collectors Orientation	South	-
Collectors Slope	40	°
Collectors Area	80	m ²
Collectors Optical efficiency	0.8	-
Collectors slope efficiency	3.611	W/m ² K
Collectors curvature efficiency	0.013	W/m ² K ²
Solar loop flow rate	4000	l/h
Solar Tank Volume	8	m ³
HXs effectiveness	0.7	-

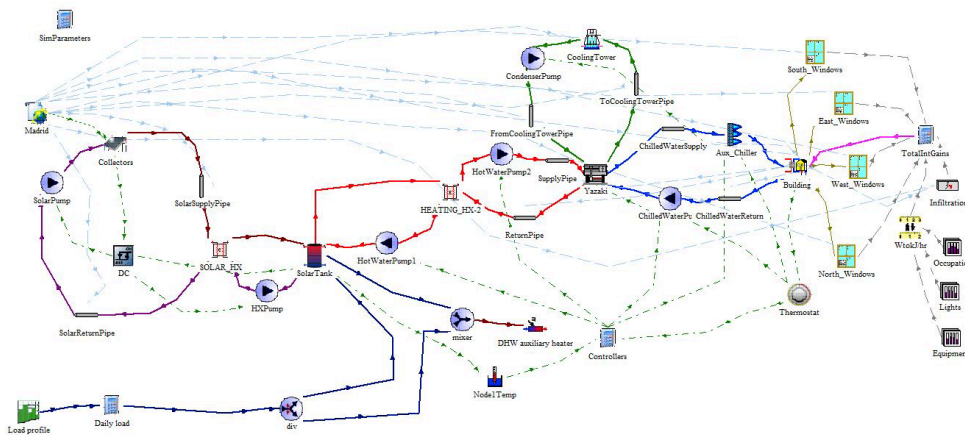


Figure 2: TRNSYS simulation scheme of the solar system for the cooling season.

temperatures is examined in Figure 3. Absorption chiller increases collectors efficiency lowering at the same time its operating temperatures during summer, these beneficial effects are caused by the increment in the useful energy delivered by the solar field, from 15587.75 to 21222.69 kWh (approximately a 35% greater).

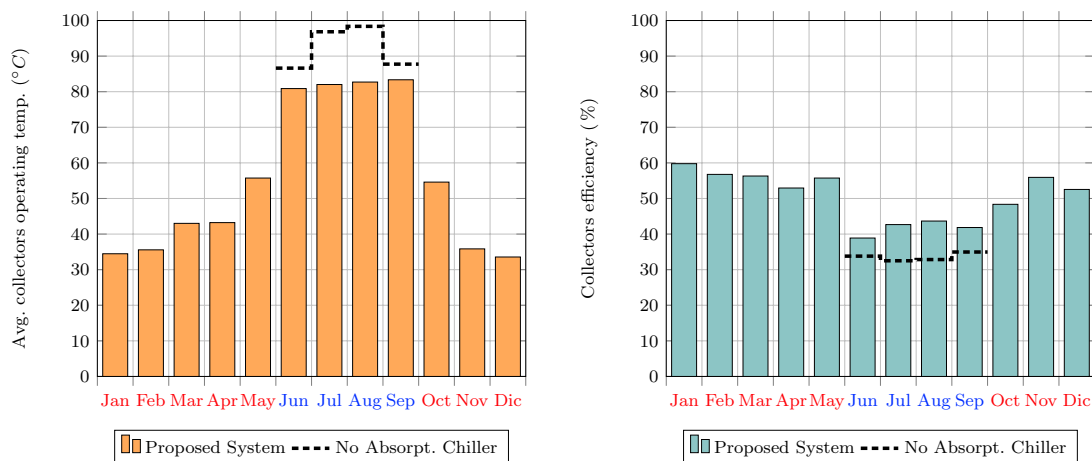


Figure 3: Average operating temperatures and efficiency of collectors for the proposed system, and with no absorption chiller.

4. Conclusions

TRNSYS Simulation results have shown that multifamily buildings for the weather conditions of Madrid having an oversized solar field with the aim of providing a greater solar fraction than that strictly established by building codes, and additionally a portion of the heating demand (around 25-30%), can only provide a limited fraction of the cooling

Table 3: Heating and cooling season operation. Most relevant TRNSYS Simulation results.

HEATING SEASON		
Performance Indicator	Value	Units
Total solar energy delivered to TES	38098.74	kWh
Solar energy supplied to DHW service	16494.39	kWh
Solar energy supplied to building space heating	16691.39	kWh
Auxiliary DHW energy	7866.36	kWh
Auxiliary space heating energy	42377.43	kWh
DHW solar fraction (F_{DHW})	0.67	-
Space heating solar fraction ($F_{Heating}$)	0.28	-
COOLING SEASON		
Performance Indicator	Value	Units
Total solar energy delivered to TES	18637.12	kWh
Solar energy supplied to DHW service	5260.31	kWh
Solar energy supplied to absorption chiller	6945.23	kWh
Auxiliary DHW energy	796.57	kWh
Chilled water energy produced by chiller	4101.05	kWh
Auxiliary chilled water energy	32763.14	kWh
DHW solar fraction (F_{DHW})	0.87	-
Space cooling solar fraction ($F_{Cooling}$)	0.11	-
Average Coefficient of Performance (COP)	0.59	-

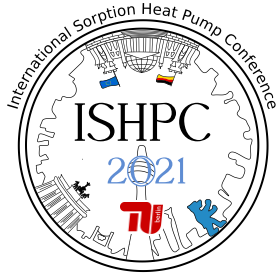
demand (below 15%) when it is integrated into the centralized HVAC system an absorption chiller for summer cooling. Unless profound modifications were incorporated into the solar system (used of evacuated collectors, a different arrangement in series, etc.), an economic analysis (not conducted in this work) would probably conclude that the proposed system is not economically feasible.

5. Acknowledgment

This work was partially funded by the Ministry of the Economy and Competitiveness (Project ENE2016-78908-R) of the Spanish Government, the Regional Government of Castilla-La Mancha (project SBPLY/17/180501/000412) and the Ministry of Science, Innovation and Universities – State Research Agency (AEI) (RED2018-102431-T).

References

- [1] Ministerio de Fomento (2019): Documento Básico HE de Ahorro de Energía *HE4: Contribución mínima de energía renovable para cubrir la demanda de agua caliente sanitaria*.
- [2] ARFRISOL PROJECT (2005): PSE-ARFRISOL 2005-2012. www.arfrisol.es [last accessed on March 2020].
- [3] Klein, S., Beckman, W., Mitchell, J. (2019): TRNSYS 18. *Solar Energy Laboratory, University of Wisconsin-Madison*.
- [4] Venegas, M., Rodríguez-Hidalgo, M.C., Salgado, R., Lecuona, A., Rodríguez, P. Gutiérrez, G. (2011): Experimental diagnosis of the influence of operational variables on the performance of a solar absorption cooling system *Applied Energy*, vol.88, Issue 4, pp.1447-1454.



Building-level Absorption Heat Exchange Substation Applied in District Heating System

Zhu, Chaoyi¹, Xie, Xiaoyun^{1,*}, Jiang, Yi¹

¹ Building Energy Research Center, Department of Building Science, Tsinghua University, Beijing 100084, China

* Corresponding author: Xie, Xiaoyun, Email: xiexiaoyun@tsinghua.edu.cn, Tel.: +86-10627935917

Abstract:

The novel district heating system applies absorption heat exchanger (AHE) to realize low return primary water temperature to collect low-grade waste heat for heating. However, current applications only replace the plate heat exchanger (HEX) in group substation (GS) with large scale AHE. The limitations of GS mode still exist, including complicated secondary network, imbalanced flow rate distribution to each building, and high secondary water pump energy consumption. The building-level substation (BLS) mode is the way to solve the problems of conventional GS mode. However, current BLSs applies HEX that cannot reduce return primary water temperature for waste heat collection. This study proposes a new mode called building-level absorption heat exchange substation (AHE-BLS) that combines the benefits of current modes. A small scale vertical multi-segment AHE is designed and tested for the AHE-BLS. The performance of AHE-BLS in real application is tested. The heating rate control of AHE-BLS is tested and proved to be better than conventional BLS.

1 Introduction

The novel district heating (DH) system applying waste heat from power plants and factories as heat source is developing rapidly in China to reduce fossil energy consumption and realize clean-energy heating [1]. The heat source site is usually far away from city. The primary district heating network connecting the heat source with the group substation (GS) around terminal users is running at large temperature difference and low flow rate condition to reduce long-distance heat transportation energy consumption. While the secondary district heating network connecting each GS with terminal buildings and rooms prefer to run at small temperature difference and large flow rate condition to overcome hydraulic imbalance. In a GS, the heat exchange from primary water to secondary water is a process with two fluids of extremely different flow rate. The heat source should be over 115 °C to meet the demand. Most low grade waste heat cannot reach this high temperature. The absorption heat exchanger (AHE) is proposed to solve this problem [2]. The AHE is a combination of a hot-water driven lithium bromide absorption heat pump (AHP) and a plate heat exchanger (HEX). The primary water flows through generator, HEX, and evaporator in series to release heat. The secondary water flows in multiple branches into HEX, condenser, and absorber to be heated. Generally speaking, the AHE realizes the heat exchange from the primary to the secondary water. The merit is that the outlet hot fluid (return primary water) temperature is lower than the inlet cold fluid (return secondary water). The heat source temperature requirement is lower. More low grade waste heat can be collect for heating.

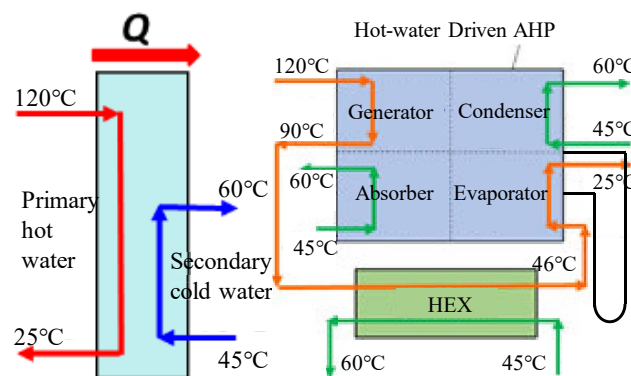


Figure 1: Principle of AHE

At the meantime, the building-level substation (BLS) heating mode is quite commonly used in European countries like Finland, Germany, and France [3]. Each building has one BLS. The primary hot water flows directly to each BLS instead of a GS which supplies heat to 5-20 buildings. Compared with the traditional GS mode in China, the BLS mode has simple secondary network, less hydraulic imbalance problem, and low energy consumption for

secondary network. However, the conventional BLS applies HEX inside. The heat source temperature is still too high to apply waste heat. We propose the building-level absorption heat exchange substation (AHE-BLS) that replaces the HEX with AHE to combine the advantage of AHE and BLS together.

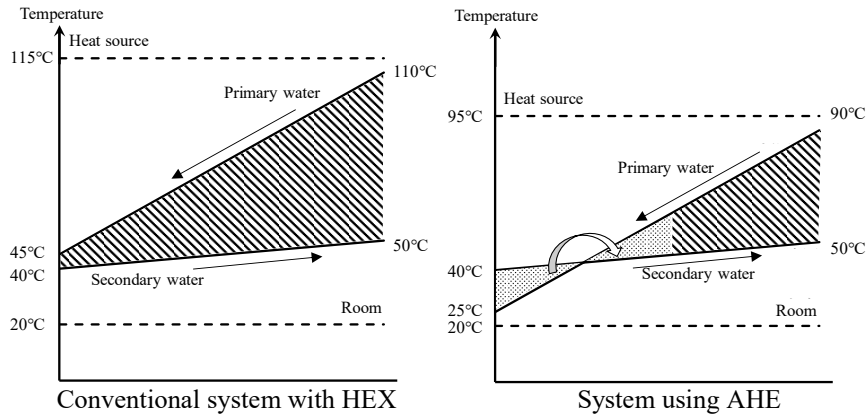


Figure 2: Comparison of system with/without AHE

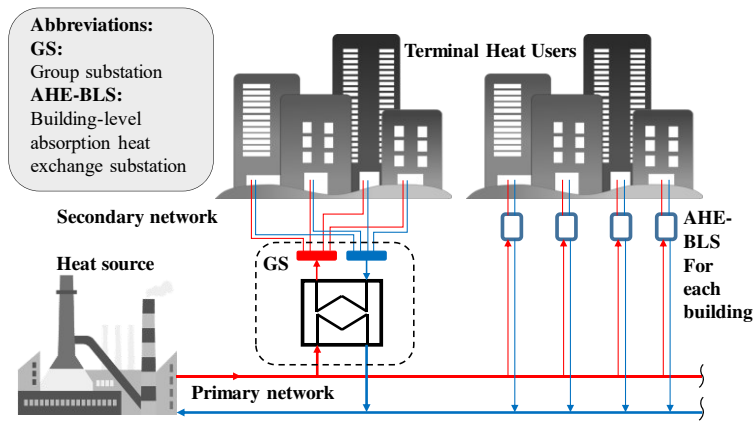


Figure 3: Conventional GS mode vs. AHE-BLS mode

The AHE used in heating system has 15K-20K hot or cold fluid temperature difference in condenser and evaporator, larger than the 5K design difference in conventional absorption chiller. This will undermine the performance of condensing and evaporating processes [4]. Meanwhile, the AHE used in GS has large site area and heat exchange rate of over 2MW. For the use of AHE-BLS, the heat exchange rate is usually 0.2MW-0.4MW. The site area should also be reduced. Advanced cycles and structures are applied in the design of AHE used in AHE-BLS to improve the performance, reduce the site area, and to realize compact design for small heat exchange rate. The first one applies multi-segment design of generator, condenser, absorber, and evaporator [4]. The second one applies multiple absorption cycles [5]. The first design is developed, tested, and applied in AHE-BLS project. The second one is still under development. In this study, we will introduce the development of the small scale AHE inside AHE-BLS and discuss the field test result of the AHE-BLS.

2 Development of AHE-BLS

2.1 Design and development of vertical multi-segment AHE

The designed AHE is for the application in Chifeng city. The designed heat capacity is 200kW. The inlet/outlet temperature of heat source water (primary water) is 90°C/30°C. The inlet/outlet temperature of heat sink water (secondary water) is 40°C/50°C. The designed condition is controlled by the field application, which is a little different from Fig. 1.

The absorber and evaporator are divided into three segments from top to bottom to provide three evaporating processes for the 15K~20K inlet/outlet water temperature difference in evaporator. Since the secondary water design temperature is only 40°C/50°C, we let the secondary water flow through absorber and condenser in series. In this way, the inlet/outlet water temperature difference in condenser is 5K. There is no need to use multi-segment generator and condenser for this working condition. U-pipes are applied to let the solution or refrigerant water

flow from the upper section to the lower section and maintain the pressure gradient between the two sections. The design modeling process is similar to that mentioned in [4]. EES was used to finish the calculation.

2.2 AHE-BLS design

In the development of vertical multi-segment AHE, we integrated necessary devices to realize the function of a heating substation, including primary water pump, secondary water pump, flowmeters, temperature and pressure sensors, filters, buffer tank, water supply and pressure stabling system, and remote monitor-control system. The total dimension of the AHE-BLS equipment is 1.2 m × 1.3 m × 3.0 m (L × W × H). The AHE-BLS can be placed on the ground or in parking lot near each building. Only four connectors are designed to connect the inlet/outlet of primary and secondary water. There is no need for substation construction or complicated pipework.

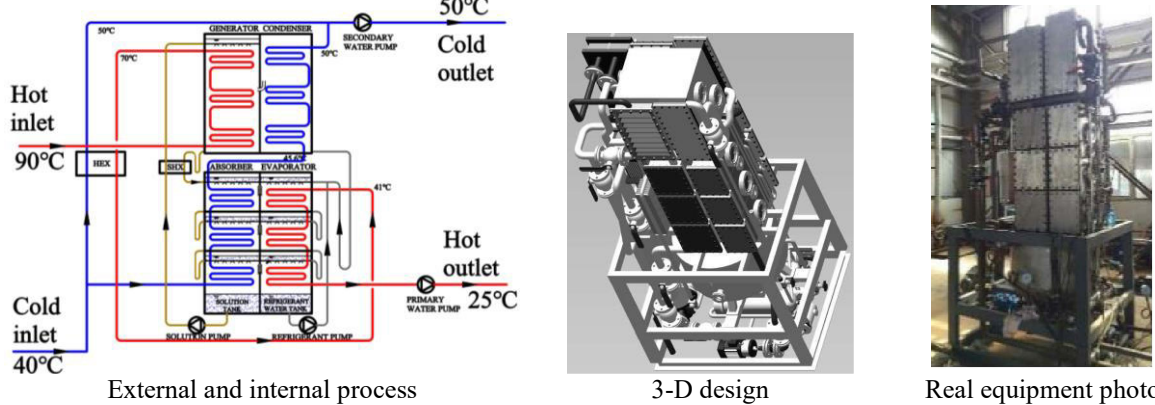


Figure 4: Vertical multi-segment AHE development

3 Results

3.1 Performance test of vertical multi-segment AHE

The performance of this AHE under various conditions were tested. The outlet primary water temperature was below 30°C in all conditions. The results were better than design condition.

Table 1- Condition of absorption chiller and AHPs/AHEs

Parameters	Design	Case1	Case2	Case3	Case4	Case5	Case6
Hot side inlet/outlet /°C	90/30	91.3/28.7	90.1/26.5	91.0/29.4	90.5/29.2	91.0/29.9	85.2/27.3
Cold side inlet/outlet /°C	40/50	39.3/48.4	39.0/44.1	40.1/50.8	40.0/49.3	41.0/51.0	40.2/45.5
Heating rate /kW	200	200.8	223.3	219.2	196.7	173.9	105.1

3.2 Application of AHE-BLS

The AHE-BLS is applied in Chifeng city of China to supply heating for community and government buildings. The AHE-BLSs are installed next to each building. No separate building is required for each heating substation. The primary water is directly connected to each AHE-BLS. Each AHE-BLS can supply heat to a building or heating zone with heating area of 5000-8000 m². The performance of each AHE-BLS can be controlled and monitored remotely. No staff is needed on site during the whole heating season.

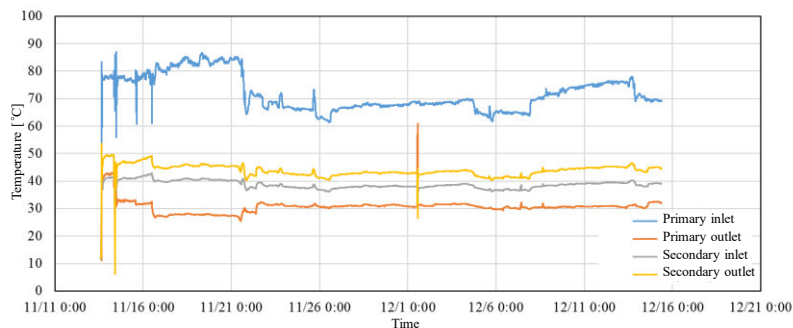


Figure 5: Heating season running performance of AHE-BLS

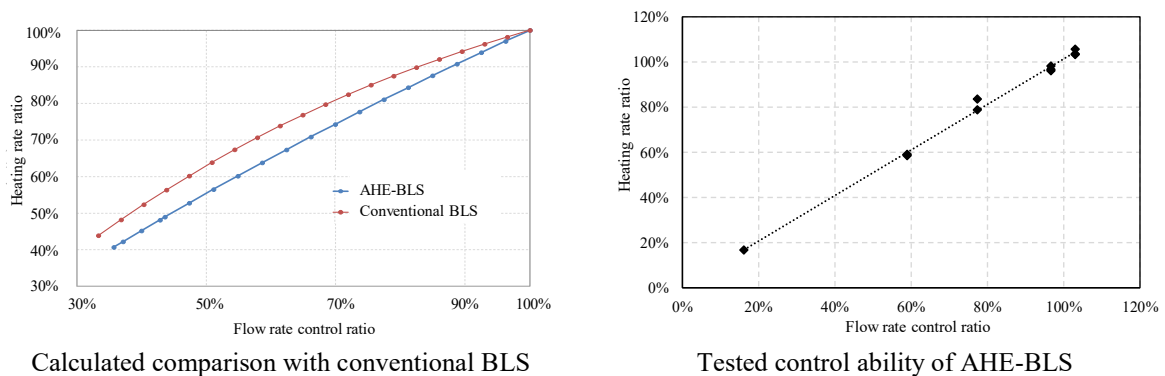


Figure 6: AHE-BLS applications

From long-time performance test of AHE-BLS in real project, we found that the outlet primary water temperature can remain below 30°C under large change of condition. This is enough to use low grade waste heat as heat source.

3.3 Heat exchange rate control ability of AHE-BLS

One benefit of the AHE-BLS is that the flexibility of heating rate control is improved since the change of flow rate or secondary water temperature of one single building has less effect on other buildings compared to GS system. Usually the heating rate is controlled by the flow rate of primary water. The control ability of AHE-BLS and conventional BLS is compared in Fig. 7. The heating rate of AHE-BLS has a good linear relationship with flow rate of primary water. This is better than conventional BLS applying HEX inside.



Calculated comparison with conventional BLS

Tested control ability of AHE-BLS

Figure 7: AHE-BLS heat exchange rate control ability

4 Conclusions

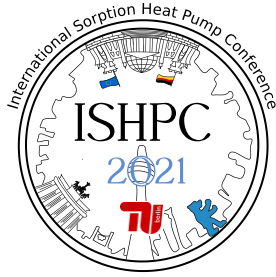
In this study, a novel mode of heating system, the AHE-BLS mode, is proposed. This mode combines the advantage of BLS mode and AHE heat exchange process. On the one hand, the outlet primary water temperature is reduced from 50° C-60° C to 20° C-30° C to collect low grade waste heat. On the other hand, it can simplify the secondary network, reduce hydraulic imbalance, decrease secondary water pump energy consumption, and improve single building heating control ability. A 200kW heating rate small scale vertical multi-segment AHE is developed and tested. The AHE is integrated with substation functions and developed into a small scale AHE-BLS. The AHE-BLS is applied in several projects. The outlet primary water temperature keeps lower than 30° C during the long time running test. The heat exchange rate control ability of AHE-BLS is tested. It is better than conventional BLS because of the linear relationship between primary water flow rate and heating rate.

5 Acknowledgment

The authors gratefully acknowledge support from the National Natural Science Foundation of China (Grant numbers 51306098, 51138005), the Innovative Research Group of the National Natural Science Foundation of China (Grant number 51521005), the Tsinghua University Initiative Scientific Research Program (Grant number 20151080470), Graduate Education Innovation Grants, Tsinghua University (Grant number 53812001018), Beijing Municipal Science and Technology Project (No. Z181100005418005), and China Postdoctoral Science Foundation (Grant number BX20190178, 2019M660655).

6 List of References

- [1] Li, Y., Chang, S., Fu, L., & Zhang, S. (2016). A technology review on recovering waste heat from the condensers of large turbine units in China. *Renewable and Sustainable Energy Reviews*, 58, 287-296.
- [2] Xie X, Jiang Y. Absorption heat exchangers for long-distance heat transportation [J]. *Energy*, 2018, 141.
- [3] Sipilä Kari, Nuorkivi Arto, Pietiläinen, Jorma. Building level substation—the innovation of district heating system [M]. VTT Technical Research Centre of Finland Ltd, 2015.
- [4] Zhu, C., Xie, X., & Jiang, Y. (2016). A multi-section vertical absorption heat exchanger for district heating systems. *International Journal of Refrigeration*, 71, 69-84.
- [5] Yi, Y., Xie, X., & Jiang, Y. (2020). A Two-stage Vertical Absorption Heat Exchanger for District Heating System. *International Journal of Refrigeration*.



A miniature 3D printed sorption heat transformer

AL-Hasni, Shihab¹, Olkis, Christopher¹, Freni, Angelo², Santori, Giulio^{1*}

¹ The University of Edinburgh, School of Engineering, Institute for Materials and Processes, Sanderson Building, The King's Buildings, Mayfield Road, EH9 3BF, Edinburgh, Scotland, UK.

² Consiglio Nazionale Delle Ricerche, Istituto di Chimica Dei Composti Organometallici (CNR-ICCOM), Via G. Moruzzi, 1, Pisa, 56124, Italy.

*Corresponding author. Email: g.santori@ed.ac.uk; Tel: +44 (0)131 651 9043

Abstract: Despite their enormous potential in primary energy saving and emissions reduction, sorption heat transformers are not in practice commercially viable yet. In the past, a good number of commercialization attempts have been discontinued and the remaining players struggle to find a market niche. The units currently marketed are more similar to R&D prototypes than commercial devices and are available at prices which cannot compete with vapor compression systems yet. In conclusion, AHTs have great potential for the decarbonisation of heating and cooling but still suffer from an apparent stage fright, a consequence of a number of technological shortcomings, among which their manufacturing process. In this investigation we have experimentally confirmed that it is possible to manufacture pressure- and vacuum-tight polymer components with commercial 3D printing. This discovery unlocks many of the usual manufacturing limitations which are preventing sorption heat transformers from reaching higher technology readiness levels and allows to reduce the cost of manufacturing of about 3.9 times.

1 Introduction

Sorption heat transformers (SHTs) are usually heavyweight and require special manufacture. Vacuum SHTs follow strict vacuum standards and rely on machined and special-welded metal components. Pressure SHTs use steel, resulting in heavy components. These characteristics ultimately lead to high production costs.

3D printing is a rapid prototyping manufacturing process having lower cost compared to a number of other established processes. 3D printing starts from a 3D computer model, therefore objects of any shape can be created. So far, 3D printed objects are deemed unsuitable for the containment of fluids as well as vacuum applications because the final objects are porous. The two most popular 3D printing techniques are fused deposition modelling (FDM) and stereolithography (SLA). This investigation focuses on SLA, where a layer of epoxy-based resin is polymerized by a focused laser beam. In [1], the Sustainable Emerging Technologies Research Group at The University of Edinburgh has already proved that SLA can be used to produce vacuum-tight vessels. In this contribution we show the design and realization of first 3D printed sorption heat transformer at miniature scale. The selection of 3D printing and the decision to produce miniature heat transformer was based on the synergies between the flexibility in product design, techno-economical attributes of SLA 3D printing technology and moderate installation cost.

2 Experimental set-up design, manufacture and description

2.1 3D printer and resin specifications

A SLA 3D printer SL1 (Prusa Research, Czech Republic) was used for manufacturing all the plastic components of this investigation. This printer uses a high-resolution LCD panel and a UV LED to cure thin layers of resin. The 3D printer was operated using transparent Tough Resin (Prusa Research, Czech Republic), a high-quality UV photosensitive 405nm liquid resin for 3D printing composed by epoxy resin (40-50%w), methacrylate monomer and oligomer (20-40%) and a photo-initiator in traces.

2.2 Design for additive manufacturing

The utilization of 3D printers instead of traditional manufacturing methods is fascinating but several factors should be taken into account in order to produce flawless 3D printed components. These factors eventually reduce the initial degrees of freedom, especially those related to the complexity of the manufactured parts. Table 1 discusses the main factors that have been considered in this investigation before starting the printing process. The miniature heat transformer is manufactured aiming at minimal part cost which can be realized by faster printing time and high printing success rate. This was achieved by acting on the following aspects: i) elimination of all support structures during printing through proper orientation of the printed part and smart CAD design; ii) reduction of the printing time by designing the part with one flat surface and use of transparent resin; iii) all details such as holes, grooves and connections are realized by 3D printing, minimizing the need for extensive post-processing of the part.

Table 1: Factors influencing the 3D printing manufacturing process of vacuum tight components.

3D Printing factor	Description
Selection of the 3D Printing resin	The choice of a transparent resin is to allow direct observation of the internal hydraulics.
3D printing support	The SHT is designed in a way that no support is required during printing, therefore no wasted material is produced in the end of the process.
3D printing orientation	The choice is based on manufacturability (printing time, capability to the 3D printer to withstand the component weight) as simulated in the 3D printing slicer software.
Layer height	0.05 mm. This option controls the thickness of each layer being cured
Faded layers	Initial layers that work as a backbone for the other layers (10 in this study).
UV-resin exposure initial time	15 seconds of UV light exposure time for faded layers.
UV-resin exposure time	7 seconds of UV light exposure time for each layer after the faded layers.

2.3 Cost of manufacturing

The cost of manufacturing is one of the issues in preventing adsorption chillers being brought to market. Although there are no specific studies on the subject, it is well known that the manufacturing of metal vacuum-tight vessels is expensive, especially because it requires skilled workforce for welding and special vacuum fittings. Being a different manufacturing process, 3D printing shows different types of manufacturing costs. A comparison between manufacturing of a Stainless Steel vessel and manufacturing of a SLA 3D-printed vessel is reported in Table 2. The comparison refers to the vessel shown in Fig. 1 and is realized by using the CALC4XL tool [2]. Among the main findings from Table 2, the direct material cost can be reduced by fifty percent and the direct labor expenses of the steel vessel is a cost driver by 10 times compared to the SLA 3D printing technology. The cost analysis shows also that 3D printing technology can significantly reduce the vessel total weight 55 times compared to a metal steel vessel. Overall, 3D printing can decrease the total cost of manufacturing down to 3.88 times compared to conventional manufacturing.

Table 2: Breakdown of cost of manufacturing of the vessel in Fig. 1 (dimensions: 9.5 cm X 11.7 cm X 5.4 cm)

The vessel type	Stainless Steel vessel	SLA vessel	Ratio
Direct Material cost (Euro)	26.11	12.54	2.08
Direct Labor cost (Euro)	147.56	14.24	10.37
Manufacturing Overhead cost (Euro)	93.52	42.06	2.22
Manufacturing location	Contractor/Factory	The university lab	
Final weight of the vessel (kg)	5.22	0.094	55.65
Cost of Manufacturing (Euro)	267.19	68.83	3.88

2.4 SHT system description and testing process

The 3D printed miniature SHT in Fig 1 has an internal volume of 385 cm³ and is designed to use ultra-low grade heat in range of 30-60 °C. It comprises three aluminum heat exchangers (RC Racing Radiators, Italy), as evaporator (40.67 g), condenser (45.39 g) and adsorber (47.09 g), which are all connected to three separate thermostatic baths (Julabo, Germany). The heat exchangers have identical dimensions and arranged as illustrated in Fig. 2. Temperatures are acquired from thermocouples (Omega Engineering, USA, 0.4% accuracy) located at the inlet and outlet of each heat exchanger. The internal pressure is monitored using on vacuum sensor (WIKA, Germany, 0.25 % accuracy). The water flow rate through each heat exchangers is adjusted by setting constant values on manual flowmeters (Nixon Flowmeters, UK, 1.6% accuracy). The approach described in [1] was adopted to assure vacuum tightness. An acetoxysilicon rubber sealant (Dow Corning 732 Multi-Purpose Sealant, USA) was used to seal the connection between 3D printed parts such as the vessel and its front cover. This sealant cures when it is exposed to moisture in the air with operational temperature range from -60°C to 180°C.

Water was degassed to get rid from any trapped gas-bubbles in an ultrasound degassing unit (Branson 2800 cpxh ultrasonic cleaner 2.8 l, Italy). Non degassed water could increase the overall system pressure and therefore decrease the performance of SHT. Water degassing is also important to increase shelf life of the polymeric 3D printed parts and metal heat exchangers. The miniature SHT goes under cyclic thermal swing by using the same set of automatic valves and data acquisition and control system used in [3].

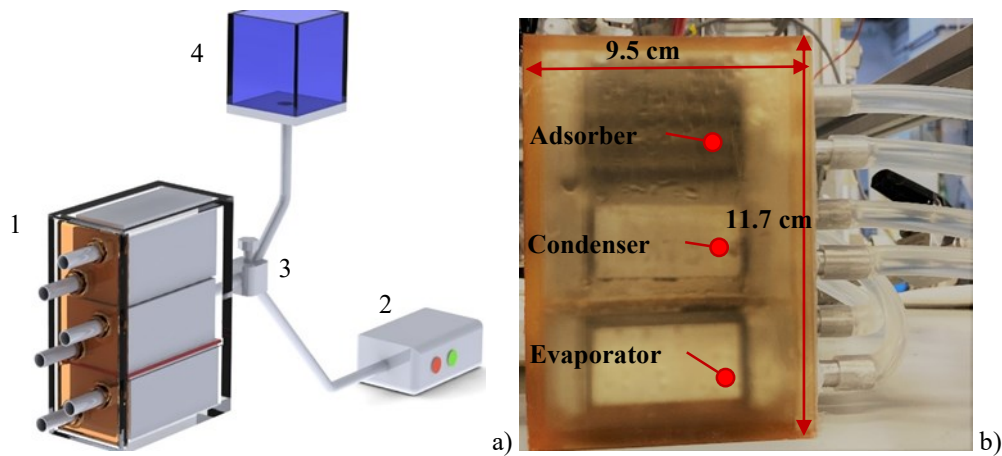


Figure 1: a) CAD model of the sorption heat transformer and its auxiliary components: (1) the single-bed miniature heat transformer comprising of evaporator, condenser and adsorber; (2) vacuum pump including a liquid nitrogen trap; (3) isolation valve to feed in water from the water reservoir (4) and to isolate the system from ambient pressure. b) 3D-printed miniature sorption heat transformer (outer dimensions are 11.7 cm X 9.5 cm X 5.4 cm)

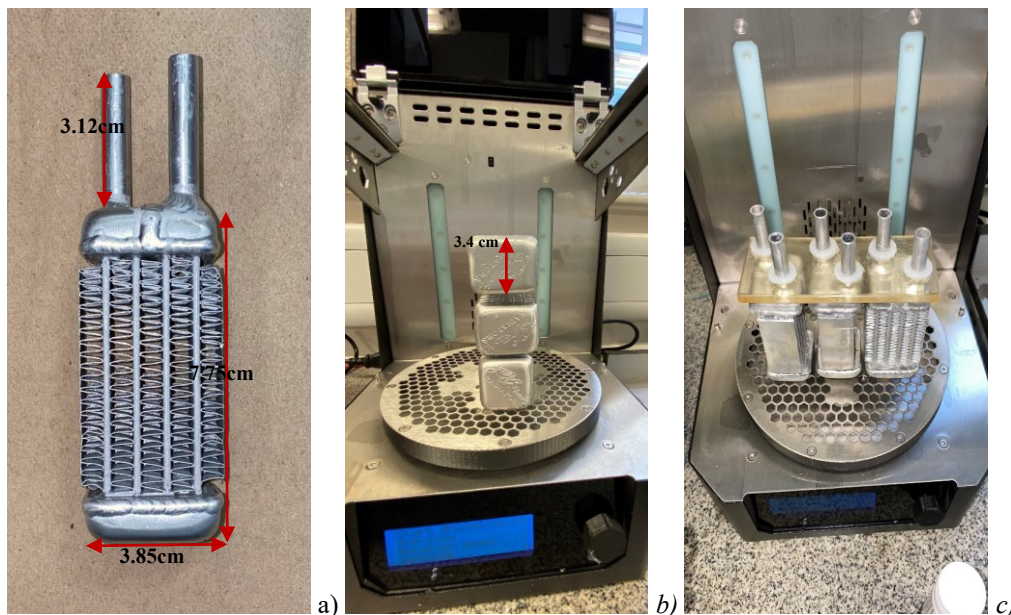


Figure 2: a) Top view and the dimensions of one of the heat exchanger used in the prototype. b) Back view of the heat exchangers inside the 3D-printing washing and curing machine; c) Side view of the assembled heat exchangers with the 3D printed cover sheet.

3 Results

The device was initially tested without sorption material first at desorption temperature ($T_{\text{ads,in}}$) of 42 °C, condensing temperature ($T_{\text{cond,in}}$) of 19 °C and evaporator temperature ($T_{\text{evap,in}}$) of 14 °C. Fig. 3 shows the temperatures measured at the outlets of each heat exchanger during this preliminary investigation. Vacuum was stable throughout the test. The adsorber heat exchanger underwent heating and cooling with a half cycle time of 300 seconds.

Cycling a blank adsorber with water is a crucial first step to quantify the sensible heat of the metal mass of the heat exchanger without adsorption material. In the following steps, this allows to detach the heat to the sorption material from the heat to the heat exchanger and thus in part distinguish the heat of adsorption from the blank experiment. This strategy is described in detail in [3]. Fig. 4 shows that the adsorber heat exchanger needs 50.8 ± 5 kJ with a heating peak at 375 W and cooling peak at 348 W.

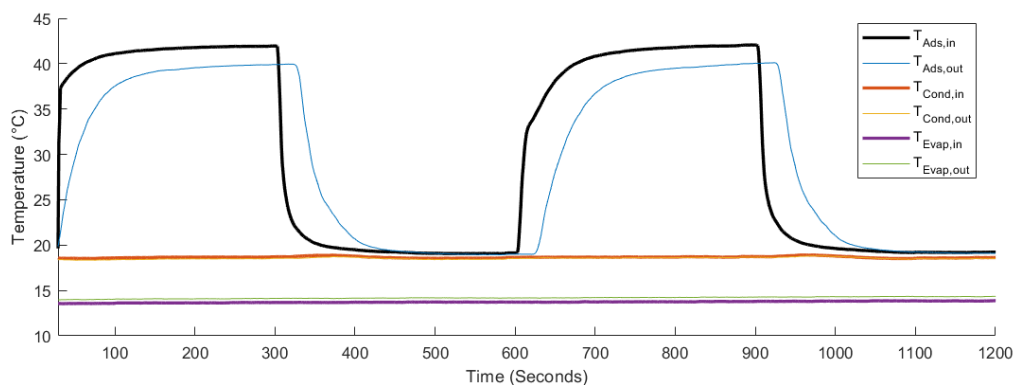


Figure 3: Temperature evolution in the miniature heat transformer without sorption material.

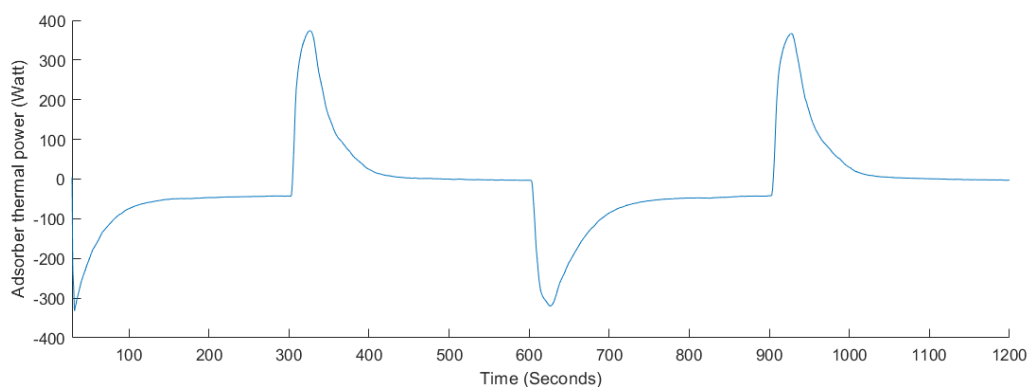


Figure 4: Blank experiment showing heating and cooling curves of the empty adsorber heat exchanger.

4 Conclusions

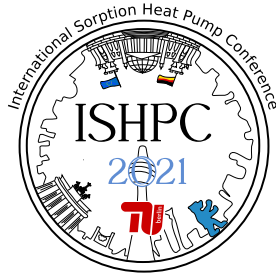
This investigation showed the development of a single-bed 3D printed miniature heat transformer and demonstrated the feasibility of using stereolithography 3D printing to produce a miniature-scale sorption device. Stereolithography 3D printing can produce vacuum tight parts and has the benefit of moderate manufacturing costs (3.88 times less than conventional metal manufacturing) which can significantly help taking the sorption heat transformers to the market. This investigation has shown pressure stability of vacuum level while conducting temperature swings and temperature stability up to 42 °C. Furthermore, the analysis of the temperatures has shown that the amount of energy required to heat the empty adsorber of 47.09 g equals 50.8 ± 5 kJ. In the next steps the adsorber will be filled with silica gel an advanced ionic-liquid based sorption material and tested at higher regeneration temperatures [4].

5 Acknowledgment

The authors declare that they have no known competing financial interests or personal relationships that could have appeared to influence the work reported in this paper.

6 List of References

- [1] S. AL-Hasni, G. Santori, 3D printing of vacuum and pressure tight polymer vessels for thermally driven chillers and heat pumps, *Vacuum*. 171 (2020) 109017. doi:10.1016/j.vacuum.2019.109017.
- [2] Product-Cost-Calculation for EXCEL. <https://www.calc4xl.com/en/home/> (accessed July 2, 2020).
- [3] C. Olkis, S. Brandani, G. Santori, Design and experimental study of a small scale adsorption desalinator, *Appl. Energy*. 253 (2019) 113584. doi:10.1016/j.apenergy.2019.113584.
- [4] A. Askalany, C. Olkis, E. Bramanti, D. Lapshin, L. Calabrese, E. Proverbio, A. Freni, G. Santori, Silica-Supported Ionic Liquids for Heat-Powered Sorption Desalination, *ACS Appl. Mater. Interfaces*. (2019) acsami.9b07602. doi:10.1021/acsami.9b07602.



Directly Biomass-fired Absorption Heat Pump

KAUSCHE Manuel, HELM Martin, RIEPL Manuel

Bavarian Centre for Applied Energy Research (ZAE Bayern)

Walther-Meissner-Strasse 6, D-85748 Garching, Germany

Manuel.Kausche@ZAE-Bayern.de +49 89 329442-90

Abstract:

The development and design of a flexible two-stage absorption heat pump system comprising a directly biomass-fired desorber is presented. A nominal heating capacity of 100 kW is provided with a performance factor (PF) up to $PF_{\text{heat}} \approx 2$, what in this context is the supplied heat referred to the lower heating value of the ligneous biomass input. For this purpose, the integrated sorption process replaces valuable renewable biomass energy with thermally upgraded heat from any additional low-temperature source. A steady-state simulation-study with input and output parameters close to reality was conducted. The results lead to an optimized design and partition of heat exchanger area and fluid circuits. The subsequent engineered system-unit allows for several operation-modes, such as double-effect and double-lift. The chosen design temperatures fit to common ambient heat-sources, new and old buildings and industrial processes, as the heat-input can be lowered to 4 °C and the output can reach 90 °C. Additionally, the system directly provides cold from biomass-combustion with a performance factor up to $PF_{\text{cold}} \approx 1.1$. Based on the simulations, a pilot-plant was manufactured and commissioned in a test-rig setup. The automated operation under laboratory conditions will show, if the distribution of the concept is economically and ecologically justified.

1 Introduction

Completive to wind and solar, biomass represents one of the most important renewable energy resources and already contributes substantially to a climate-neutral energy supply. Although there is further development perspective, for instance regarding residual and waste materials, respecting the available state of the art, the economic potential is limited and almost fully tapped. Therefore, highly efficient usage is eminent.

Beside the use of the energy stored in ligneous biomass for electricity generation, it was particularly the heat supply from district heating stations and smaller scaled boiler, which covered the heat demand in Germany by 10.7% in the year 2016 [1]. For nominal conditions, heat units reach a performance factor of approximately $PF_{\text{heat}} \approx 0.9$. By application of innovative flue gas condensation, this value rises to $PF_{\text{heat}} \approx 1.1$ [2]. A thermally driven, two-stage heat pump process enables an even better utilisation of the exergy from the biomass.

Starting with a simple Proof of Concept in the joint German-Finish SET-plan research project “Solar Heating and Cooling for Northern and Central Europe” [3], the development of the directly biomass-fired absorption heat pump here is continued in cooperation with a biomass boiler manufacturer. The research project focuses on an economic and reliable heat pump design and performance tests under lab conditions. This paper describes the basic sorption process design and results of the simulation of the research. Furthermore, the pilot-plant and test rig setup as well as defined key figures for testing are shown.

2 Fundamentals and experimental setup

The combination of a biomass combustion and sorption process offers a quite efficient way for low temperature heat supply with a certain share of ambient heat and minimal consumption of electricity. Multi-staging reduces the biomass input significantly. Nevertheless, its pros and cons have to be carefully balanced regarding economic feasibility as well as a simple, robust and reliable system design.

2.1 Advantages of a two-stage heating and cooling system with biomass-combustion

The benefits of multi-stage absorption heat pumps have been theoretically investigated sufficiently and are well known. For instance, Ziegler [4] has shown, that using the driving energy in a cascade leads to a significant higher efficiency. Coming along with that, the feasibility is limited by the necessarily rising temperatures of the driving energy source and of the working fluids. The fluid used in the apparatus presented in this essay is aqueous lithium bromide ($\text{H}_2\text{O}/\text{LiBr}$) with water as refrigerant. It has a common upper range for application temperatures between 150 °C and 170 °C, regarding rising corrosivity. Carrying out a multistage concept therefore is limited by economical acceptable variety and uncomplicated availability of construction materials. Moreover, an increasing quantity of stages rises the complexity and expense for heat exchangers, piping valves and instruments. As the

refrigerant H₂O limits the evaporation temperature to 1 °C to avoid internal freezing, ambient heat-sources seem to be limited for H₂O/LiBr-heat-pumps. In fact, the potential of ambient heat-sources delivering temperatures higher than 8 °C, such as groundwater, wastewater or geothermal probes is notable. Here it also has to be considered, that in rural areas, where biomass as fuel is more common and available than in cities, these kind of ambient heat-sources also are more probable. Additionally, in current research projects reliable and sufficiently efficient evaporator-systems for modified refrigerants are investigated. Presuming successful research, ambient heat sources delivering energy with temperatures below the freezing point of water could be integrated.

Respecting these constraints, a two-stage concept was chosen for the system presented here as a good compromise of performance, cost and complexity. Regarding the Coefficient of Performance (COP) as the quotient of net energy and driving energy, the increase in efficiency is evident: Modern absorption single-stage heat pumps enable a COP_{SE} ≈ 1.8, relating to the generation of heat. A two-stage type enables values up to COP_{DE} ≈ 2.4.

Commercial two-stage units typically range in capacities of a megawatt. Beside directly gas- and oil-fired systems, an implementation of steam-driven or pressurised hot water is economically justifiable in this higher capacity class. In general, one falls back to single-stage hot-water-driven absorption heat pumps for lower capacities. To replace fossil energy sources in smaller systems, the attention has to be turned to waste heat, solar heat or on the best storable, locally available fuel biomass for directly driving absorption heat pumps. Ligneous biomass here succeeds as standardised fuel and its combustion is technically mature.

Without the detour of the initial generation of hot water, a directly biomass-fired two-stage heat pump in the medium capacity range is viable, respecting an increase of efficiency (COP_{DE}/COP_{SE}) up to 33%. The additional expenses by purchasing an absorption heat pump (AHP) are even more accommodated for the two-stage system: A rough estimate shows that the capital investment in the biomass direct-fired, two-stage absorption heat pump (bioSHC-system) is nearly the same as for a single-stage AHP connected to a biomass-fired boiler. Additionally, the efficiency of the combustion unit concerning the provided fuel is equal for both systems. The common exhaust temperature for wood firing at nominal operating conditions is set to 160°C or higher, which enables to use most of the smokestacks installed in buildings. Concerning the maximum working-fluid temperatures, the exhaust temperature of the two-stage heat pump-system is similar.

The bioSHC-system reaches a performance factor (PF) up to PF_{heat} ≈ 2 referred to the lower heating value (LHV) of the fuel and the heat from an ambient low temperature reservoir included. With halve of the conventional fuel input providing the same amount of useable heat, emissions (dust, CO₂, etc.) may be reduced in the same scale. The following section implicates, that the multi-stage structure induces further advantages regarding variety of operation modes.

2.2 Implemented modes of operation

The bioSHC-system has been developed based on the analysis of appropriate ambient heat sources for absorption heat pumps, so the goal was to utilize the lowest possible temperature of the refrigerant.

Substantially the system consists of three main subsystems - a directly biomass-fired second-stage desorber plus condenser, a single-effect absorption heat pump and a pre-fabricated hydraulic-system, which helps for an easy implementation and interaction in buildings and their control systems. The guideline for engineering was the double-effect-mode (DE). For this operation mode, the realised concept requires six main heat exchangers.

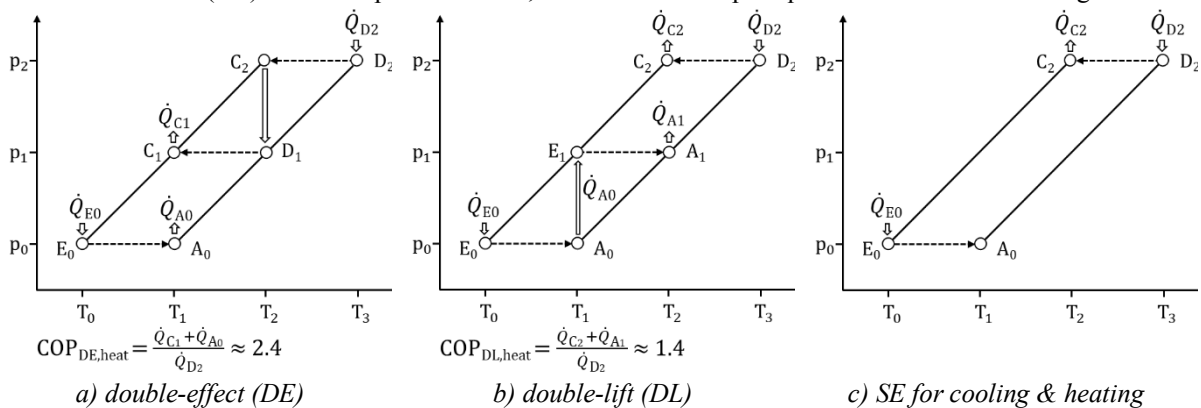


Figure 1 – schematic diagram of the three main operating modes of the bioSHC-system

The lower four exchangers evaporator (E₀), absorber (A₀), condenser (C₁) and desorber (D₁) are realised as tube bundles in two vessels and form a separate entity, that could be operated as a single-stage or single-effect-system

(SE). A high-temperature-desorber (D_2) and a second condenser (C_2) are added for building a double-effect-system (DE). The second desorber D_2 herein is the innovative core piece. It is a directly biomass-fired desorber with a driving capacity of about 50 kW and a combustion power of 55 kW.

The cascade of energy-use from the combustion is carried out by coupling C_2 and D_1 via an external heat carrier. In Figure 1a) this external heat transport is displayed as a double line arrow between these main components. The connecting, continuous lines follow the logarithmic depiction of the pressure curve (ordinate) for constant salt concentrations depending on equilibrium-solution-temperatures (abscissa). Dashed lines represent the vapour flow of the refrigerant between the components. Therefore, the resulting four temperature- and three pressure-levels of the bioSHC-system are visible. These levels are quite similar for the three suggested modes of operation. Comparing Figure 1a) and Figure 1b) it can be seen, that the external circuit between C_2 and D_1 allows an additional mode for an efficient and very high temperature-lift, by lifting the heat \dot{Q}_{E0} coupled into the evaporator E_0 two times. This double-lift-mode (DL) requires the condenser C_1 to operate as a second evaporator (E_1) and the D_1 as another absorber (A_1) at a higher pressure-level. A further operation mode named “single effect for cooling and heating” is also possible within the bioSHC-system. Figure 1c) shows that in this case, cooling and higher temperatures as in common single-effect AHP can be provided at the same time without the need of a middle pressure stage.

3 Results

3.1 Modelling of the heating and cooling system

The shown system-concept was modelled in a component-based simulation on physical property data and balances of mass, sorbent and energy. The steady-state simulation-study with the Engineering Equation Solver (EES) leads to an optimum of heat-and-mass-transfer-area by variation of temperature spread as well as different internal and external hydraulics. The main results of theoretical capability, coefficient of performance, design temperatures and the performance factor for the double-effect and double-lift mode at nominal conditions are given in table 1:

Table 1 – Key figures of the bioSHC-System

Key figure	Abbreviation and/or Equation	Unit	Efficiency mode	Temperature-lift mode
			<i>double-effect-mode</i>	<i>double-lift-mode</i>
chilled water	$T_{\text{cold}} (\text{supply} \text{return})$	$^{\circ}\text{C}$	4 8	4 8
heating water	$T_{\text{heat}} (\text{supply} \text{return})$	$^{\circ}\text{C}$	41 31	90 70 ^(a)
temperature lift	$T_{\text{lift}} = T_{\text{heat supply}} - T_{\text{cold supply}}$	K	37	86
nominal capacity	$\dot{Q}_{\text{heat}} \dot{Q}_{\text{cold}}$	kW	111 62	66 16
$\text{COP}^{(b)}_{\text{heat/cold}}$	$\dot{Q}_{\text{heat}} \cdot \dot{Q}_{D2}^{-1} \dot{Q}_{\text{cold}} \cdot \dot{Q}_{D2}^{-1}$	-	2.22 1.23	1.31 0.3
Performance Factor	$\dot{Q}_{\text{heat}} \cdot (\dot{m}_{\text{fuel}} \cdot \text{LHV})^{-1}$	-	1.99	1.18
$\text{PF}^{(c)}_{\text{heat/cold}}$	$\dot{Q}_{\text{cold}} \cdot (\dot{m}_{\text{fuel}} \cdot \text{LHV})^{-1}$	-	1.10	0.27

^(a) max. 85 °C feasible

^(b) Coefficient of Performance

^(c) Reference lower heating value (LHV)

As boundary conditions, the maximum allowable salt-concentration and temperature of the solution, external and internal temperatures, realistic heat transfer rates and heat-exchanger-efficiency were set. In addition, the wetting of the tube bundles and therefore the solution- and refrigerant-circuits have been considered based on measurements. Depending on whether the required continuous solution-flow through the desorber D_1 and D_2 is parallel or serial, pros and cons vary in operation, efficiency and partitioning of area over all heat exchangers. To check the theoretical values, the solution-flow can be switched in the test-rig between serial- and parallel-flow.

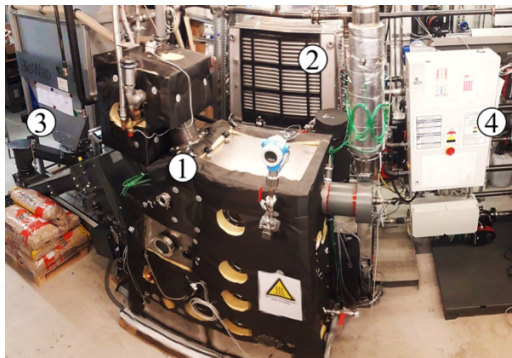
The key figures in table 1 are gained from the series-flow-model, as it was the guideline for engineering.

Considering that the design-point in practice may not always perfectly match, for example in external conditions, the system has to be resilient especially to changing supply-temperatures of the fluid-circuits. A variation of temperatures and their spread in the cold- or cooling-water shows a low sensitivity regarding the cooling-performance and COP. As the temperature T_{cold} is varied from 3 °C to 6 °C as well as the temperature-spreads from 3 K up to 10 K, the cooling-capacity and the COP change merely 2% regarding to the nominal conditions. The temperature-variation of T_{heat} from 38 °C to 44 °C and a change in temperature-spreads from 5 K up to 12 K show the same results.

3.2 Developed plant and test-rig setup

As mentioned before, the innovative core piece of the system is the desorber D_2 . It was drafted based on an existing combustion chamber geometry. The layout as a pool-desorber with natural circulation enables a homogenous

allocation of temperature and solution-concentration. The design of the heat exchanger on the solution-side was based on extensive research. In the zone of the combustion-chamber a heat flux up to $80 \text{ kW}\cdot\text{m}^{-2}$ may appear, which will not cause critical wall-temperatures above $180 \text{ }^\circ\text{C}$ due to best heat transfer resulting from flow-boiling, following evaluations from Riepl [5][6]. Nevertheless, the design of the desorber D2 seems very similar to any standard wood-chip-boiler with flue-tubes, except the built-in components supporting natural convection and vapour-flow and the mounted condenser C₂. Therefore, it was fabricated with the conventional methods of a boiler manufacturer. Due to the effective remodelling, the D₂ can be produced with similar costs regarding to a commercially available hot-water boiler of the same combustion capacity.



- (1) Biomass-fired desorber D2
- (2) Absorption heat pump (AHP)
- (3) Storage, supply and scale for biomass-fuel
- (4) Control and hydraulic system

Figure 2 – Picture of the system-setup integrated in a HIL-laboratory environment

The single-stage absorption heat pump unit (AHP) has been realised for a perfect match to the high-temperature-desorber D2. As shown in Figure 2 the entire installation of the components was assembled in a laboratory. With the aid of a hardware-in-the-loop-test-rig (HIL), measuring of the bioSHC-system is carried out close to reality.

3.3 Upcoming measurements

The new setup of the bioSHC-system has already been commissioned, so new and promising measurement data is currently gathered and going to be presented at the coming up ISHPC. Particular attention to precise sensors and data acquisition ensures accurate scientific measurement. For instance, less than 10 % error in COP is expected, despite the less homogenous fuel regarding mass flow and heating value. By means of extensive consideration of possible sources of error, a meaningful comparison with conventional SHC-systems and common electrical heat pumps is possible.

4 Conclusions and outlook

The presented directly biomass-fired absorption heat pump system doubles the heat-output compared to conventional biomass boilers, fired with ligneous biomass. Essential precondition is a sufficiently available low temperature heat reservoir (e.g. geothermal probes), feeding the implemented sorption heat pump process. The modular design of the three main components allows for switching between operation modes such as single-effect, double-effect, double-lift or the “single-effect for cooling & heating”. Thus, a high performance factor and/or high temperature lift for solely or simultaneous heating and cooling is obtained.

In addition, the system can directly and highly efficient convert biomass energy into useable cold for cooling purposes. Furthermore, the overall very low electricity consumption relieves the electrical grids. The chosen design temperatures fit the requirements of new building-standards but are also appropriate to old buildings. This enables prospective numerous applications in real buildings or industrial processes.

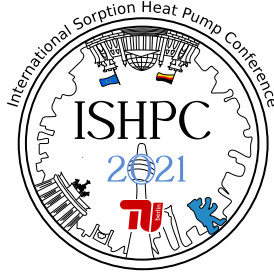
The combination of biomass-combustion and heat pump technology offers further applications such as extracting heat from flue gas by utilisation of condensing. Referring to Hermann [2], cooling the flue gas of a wood chips fired desorber down to 25°C , the gained sensible and latent heat may reduce the required ambient low temperature heat source by 18% in double-effect setup and 70 % in double-lift setup respectively.

5 Acknowledgment

This research was supported by the German Federal Ministry for Economic Affairs and Energy (BMWi). We also greatly thank HDG Bavaria GmbH for additional financial support. The authors furthermore thank our colleagues from HDG Bavaria GmbH, especially W. Aich, who provided insight and assisting expertise.

6 List of References

- [1] Pelkmans, L. (2018): Germany – 2018 update, Bioenergy policies and status implementation. *Country Reports. IEA Bioenergy: 09 2018*, p. 8
- [2] Hermann, T., Geier-Pippig, J., Schweigler, C. (2019): Sorption heat pump for flue gas condensation of biomass-fired boilers. *25th IIR International Congress of Refrigeration, Montréal*
- [3] Sipilä, K. Reda, F. Pasonen, R. Löf, A. Viot, M. Pischow, K. Helm, M. Möckl, M. Menhart, F. Kausche, M. Osgyan, P. Streib, G. (2017): Solar heating and cooling in Northern and Central Europe. *VTT Technology 287. ISBN 978-951-38-8510-6. VTT Technical Research Centre of Finland Ltd, Finland*, pp. 69 - 77.
- [4] Ziegler, F. (1997): Sorptionswärmepumpen. *Forschungsberichte des Deutschen Kälteund Klimatechnischen Vereins, 1997 (Nr. 57). – 978-3-932715-60-0 (ISBN)*, pp. 7, 16, 209
- [5] Riepl, M. (2020): Naturumlaufaufstreiber für mehrstufige Absorptionswärmepumpen. *Thesis (under preparation), to be submitted at TUM Department of Mechanical Engineering, Technische Universität München, Munich*.
- [6] Riepl, M. (2020): Heat Transfer and Flow Characteristics in Thermosiphon Generators of Multi-Stage LiBr/Water-Absorption Heat Pumps. *Research Paper (under preparation), to be submitted to International Sorption Heat Pump Conference 2020, Berlin*.



Energy efficient cooling with absorption chillers in a field test

Paitazoglou, Christopher¹, Albers, Jan¹, Graf, Rupert¹, Hausherr, Carsten¹, Hüls, Walther¹, Lanser, Wolfgang¹, Petersen, Stefan¹

¹ Technische Universität Berlin, Institute of Energy Engineering, Marchstraße 18 D-10587, Berlin
Tel: +49 30 314 25183, christopher.paitazoglou@tu-berlin.de

Abstract:

The absorption chiller types Bee and Bumblebee, which have been developed by the Technische Universität Berlin (TU Berlin) in cooperation with Vattenfall Europe Wärme AG and the Bavarian Center for Applied Energy Research (ZAE Bayern), are installed in 16 field tests in Germany [1]. The heat driven absorption chiller is based on the non-ozone depleting and climate-friendly working pair water/lithiumbromide and has a high potential for decreasing indirect/direct greenhouse emissions without the use of fluorinated gases like in conventional cooling technologies. Values for the daily average electrical efficiency higher than 30 kWh₀/kWh_{el} have been reached for state of the art field tests.

1 Introduction

The installation of the 25 absorption chillers in Germany took place within the framework of the project FAKS, funded by the Federal Ministry for Economic Affairs and Energy (BMWi). Further involved as scientific partners in the collaborative research project were the German Heat and Power Association (AGFW), the Federal Industrial Association for technical building equipment (BTGA), the Technische Universität Dresden and the Institut für Luft und Kältetechnik Dresden (ILK). TU Berlin had a supportive, accompanying and managing role in the planning, installation, operation, monitoring and optimization. The installation and commissioning of the absorption chillers took place between 2011 and 2017. In some field tests a combination of up to three absorption chillers can be found. District Heating (DH) systems, Combined Heat and Power plants (CHP) or solar collector systems serve as a heat source for the driving heat.

A brief overview of the field test results regarding the operation of absorption chillers will be given. The focus is on the thermal coefficient of performance (COP_{th}) of the absorption chillers and the electrical/primary energy efficiency of the absorption chiller cooling assemblies (ACCA). An ACCA takes into account the energy demand of peripheral components, such as pumps and reject heat devices, allowing not only an overall comparison of the energy efficiency for the various ACCAs and additional back-up chillers or alternative cooling modes [2], but provides an energy based assessment around the peripheral components and their specific energy demand as well. Moreover, the aspects of system integration into DH systems or heating networks supplied by decentralized CHP-units are addressed as much as the wide operation field and the flexibility that can be reached in the heating circuit of the absorption chillers. Especially the requirements of CHP-units on the narrow variability with regard to the return (hot water for absorption unit / cooling water for CHP-units) temperature have proven a strong demand of the implemented absorption chiller control while fulfilling simultaneously an energy efficient cooling operation. The so-called CE-controller uses an improved characteristic equation (CE) method [3].

A generalized system setup to characterize each field test has been defined. It is further used for evaluating energetically and in a comprehensive way the various chillers and cooling systems that are monitored in the research project FAKS. Moreover, key figures for assessing the energy efficiency of installed chillers allow a comparison of the field tests for which an allocation methodology of the electrical and primary energy demand have been developed. This allocation takes into account the different operating modes and site specific features found in the external circuits of the ACCA. Those key figures express the ratio of the generated cooling to either the thermal energy (thermal efficiency), electrical energy (electrical efficiency) or primary energy (primary energy efficiency) within an observed time period.

2 Operation Results

2.1 ACCA electrical efficiency and primary energy efficiency

A thermally driven absorption chiller cooling assembly (ACCA) uses primarily heat as a driving energy source, while an electrically driven compression chiller cooling assembly (CCCA) uses electricity. To evaluate and

compare cooling systems an integral characterization of the energy efficiency based on primary energy figures is made. For the electrical energy input a primary energy factor of $1.8 \text{ kWh}_{PE}/\text{kWh}_{el}$ (valid since January 1st 2016 according to German Energy Saving Ordinance *EnEV* [4]) is applied, whereas for the thermal energy input the corresponding certified primary energy factor (f_{H1}), provided by each operating DH company, is taken into account. For heat from decentralized CHP-units the primary energy factor is assessed with monitoring data according to the “displacement” method described in the German Rules [5] and [6].

With the control of the absorption chillers a partial load from approx. 110 % down to 5 % with respect to the nominal cooling capacity was covered. This is equivalent to a part load ratio of approx. 175 % to 10 % with respect to the design cooling capacity that varies from site to site.

Yearly average values for the thermal efficiency above $0.7 \text{ kWh}_0/\text{kWh}_2$ were monitored in several installations. Efficient cooling is still feasible with values for the thermal efficiency over $0.6 \text{ kWh}_0/\text{kWh}_2$ and at a part load ratio of 30 % [7]. During the last cooling period (2017) in some few field tests values for the electrical efficiency from 6 to $10 \text{ kWh}_0/\text{kWh}_{el}$ proved insufficient mainly due to design misfit of pumps and reject heat devices. In other field tests, with better designed and operated peripheral ACCA components, values for the electrical efficiency of $20 \text{ kWh}_0/\text{kWh}_{el}$ and in certain sites even up to $30 \text{ kWh}_0/\text{kWh}_{el}$ were monitored. In most ACCAs the operation of the pump in the cooling water circuit and the reject heat device is responsible for approx. 70 % of the electrical energy demand (Figure 1). In terms of primary energy, the driving energy source of several of the installations in FAKS causes approx. 70 % to 95 % of the total primary energy demand (Figure 1, Figure 2 bottom)¹.

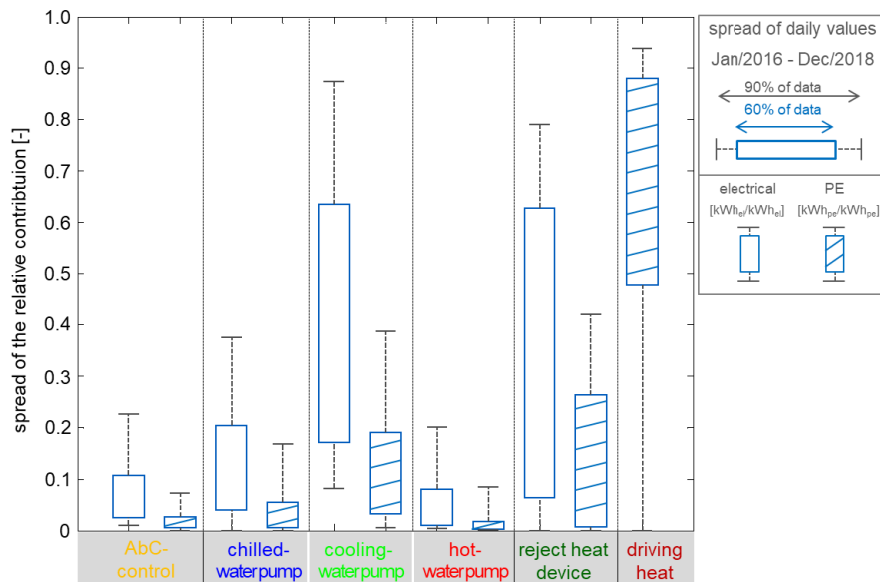


Figure 1: Relative contribution of peripheral components in terms of electricity and primary energy

Figure 2 (top) gives a detailed overview of the distribution of daily values for the primary energy efficiency for each ACCA and each location (BOLY, TUEW, etc.) taking into account the site specific factor f_{H1} . The majority of the values for the primary energy efficiency in FAKS range between $0.8 \text{ kWh}_0/\text{kWh}_{PE}$ and $2.6 \text{ kWh}_0/\text{kWh}_{PE}$. Field tests with a lower primary energy factor for the thermal energy input due to utilization of renewable energy sources in the CHP-units or abundant industrial heat in the DH networks (down to $0 \text{ kWh}_{PE}/\text{kWh}_2$) can reach a primary energy efficiency up to $7 \text{ kWh}_0/\text{kWh}_{PE}$. It should be mentioned that more than 50% of german DH networks provide heat with a factor below $0.4 \text{ kWh}_{PE}/\text{kWh}_2$ (see Figure 3).

The operation of compression chiller cooling assemblies (CCCA) and the operation mode “Free Cooling” (also known as “Direct/Ambient Cooling”) were additionally monitored and evaluated. “Free Cooling” uses low ambient air temperatures to directly cool the chilled water network without the need for any chillers. In FAKS field tests, where the reject heat devices of installed absorption chillers were used for “Free Cooling”, an electrical efficiency between $6 \text{ kWh}_0/\text{kWh}_{el}$ and $36 \text{ kWh}_0/\text{kWh}_{el}$ was monitored. The pumps are responsible for 80-90 % of the overall electricity demand for this operating mode. The evaluation of the electrical energy efficiency of CCCA showed values in the range of $2.1 - 4.0 \text{ kWh}_0/\text{kWh}_{el}$. In comparison to CCCA, higher values for the primary energy

¹ Subscripts: Wh_{PE} : primary energy related unit, Wh_{el} : electrical energy unit

Wh_0 : (thermal) energy unit related to cooling, Wh_2 : (thermal) energy unit related to driving heat

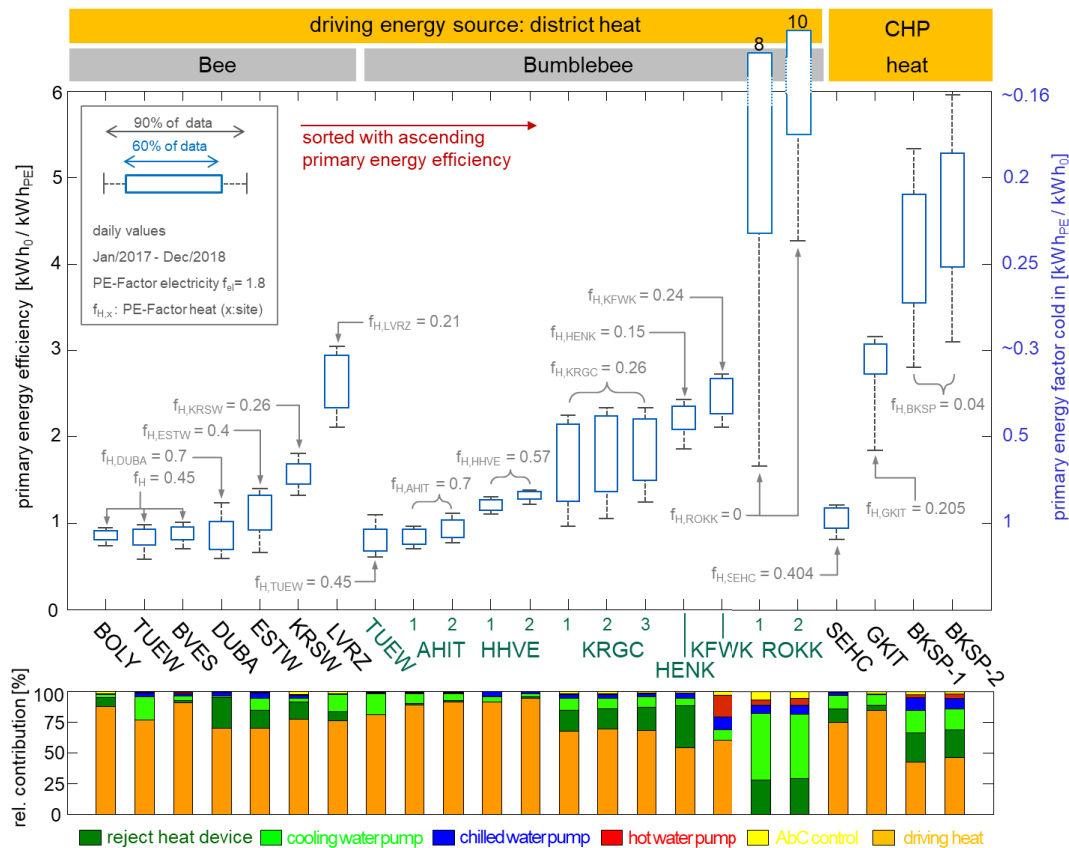


Figure 2: Primary energy efficiency in the field test (up) and relative contribution of each peripheral component in terms of primary energy (down)

efficiency of ACCA can be reached when the primary energy factor for the thermal energy input is below $0.4 \text{ kWh}_{\text{PE}}/\text{kWh}_2$. This shows the high potential of primary energy savings and a change towards a market diversification as approx. 50 % of the DH networks in Germany have low primary energy factors and almost 40 % of the networks provide district heat with a primary energy factor even below $0.2 \text{ kWh}_{\text{PE}}/\text{kWh}_2$ (see Figure 3).

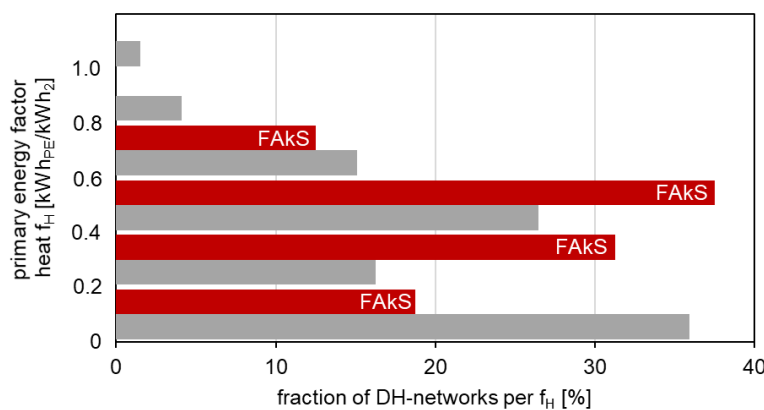


Figure 3: Distribution of primary energy factors in FAKS and Germany

2.2 Operation flexibility on the hot water / driving heat side

Monitoring data from field test partners show that DH networks operate at a very low load during summer. Typically, the monthly heat supply at that time is only 10 to 20% of the peak supply during winter [7,8]. As a result, the capacities of efficient CHP-units are hardly used due to the lack of heat demand. Thermally driven chillers support thus a better and evenly utilization of heat from DH and local heating networks. The total heat used as driving energy source in the summer in all field tests accounts up to 700 MWh per month in 2017. Without the installations of FAKS absorption chillers the return temperatures during summer are at a range of $60 \text{ }^\circ\text{C}$ to $70 \text{ }^\circ\text{C}$ and are hence approx. 10 K higher than during winter time [8]. Therefore, demands and expectations from

DH-network operators forced absorption chiller return temperatures in FAKS in the range of 60 °C or even lower [9]. This project goal of system integration of absorption chillers is met hence completely. Apart from covering the cooling demand the absorption chillers provide thus a further benefit by promoting the operation of efficient CHP-units by smoothing the district heat load curves. In addition, they can be used to reduce the average return temperature in the DH networks if the heat sink temperature is moderate and additional CCCA are able to cover the peak load. This is shown in Figure 4 (left hand), where low cooling water from a river allows to be counterbalanced by low driving temperatures.

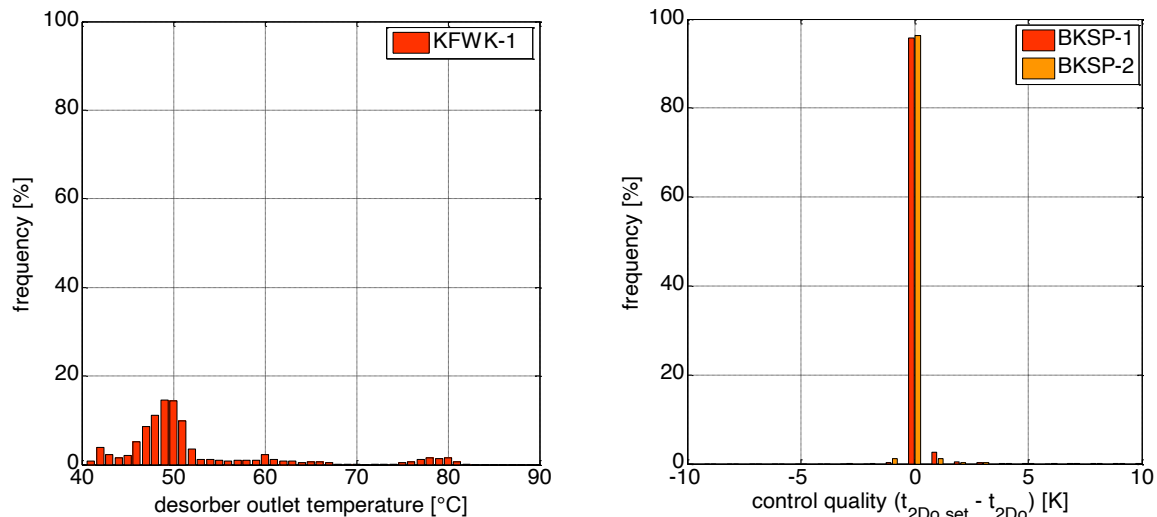


Figure 4: Desorber outlet temperatures and control quality for the hot water outlet temperature in two field tests (KFWK and BKSP) with heat from CHP-units

In this special case a hot water outlet temperature of less than 50 °C is possible. The installed thermally driven chillers can be further characterized by their high level of control quality regarding the hot water outlet temperature (see Figure 4 right hand).

By prioritizing the “hot water outlet” instead of “chilled water outlet” the CE-controller manages to control hot and cooling water inlet temperatures in a way that the real temperature meets the set value for the hot water outlet in 99 % of the annual operating hours with an absolute deviation of maximal ± 1 K [10] (see Figure 4). As a result, the absorption chillers *Bee* and *Bumblebee* are an optimal completion for decentralized CHP-units that have the highest requirements on stable and not deviating return temperatures and need a high degree of capacity utilization, in order to be economically beneficiary.

These qualities show an extended operation field of the installed absorption chillers that have already been proven initially in the laboratory [11]. Verifying this experimentally in the field test makes the technology accessible for new application fields that so far have been unknown or uncertain for absorption chillers.

3 Conclusions

ACCA, based on *Bee* and *Bumblebee*, in combination with a model based multivariable control for the control of ab- and adsorption chillers, which has been developed during the research project, are beneficial in terms of primary energy efficiency, when the primary energy factor of the driving heat is below 0.4 kWh₀/kWh_{PE}. In field tests with a satisfactory operation of peripheral ACCA components, daily values for the electrical efficiency of 20 kWh₀/kWh_{el} and in certain sites even up to 30 kWh₀/kWh_{el} were monitored. Furthermore, a high level of control quality on the hot water outlet temperature, a feature strongly needed by decentralized CHP-units, is reached and demands on low DH return temperatures are simultaneously met. More detailed insight is given in the final project report [7].

4 Acknowledgment

We acknowledge financial support by the EnEff: Wärme Projects 03ET1171A and 03ET1583 grant funded by the Federal Ministry for Economic Affairs and Energy (BMWi).

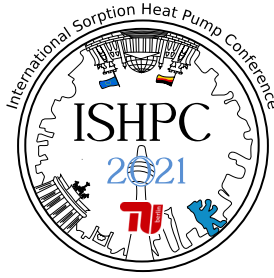
Supported by:



on the basis of a decision
by the German Bundestag

List of References

- [1] C. Paitazoglou, S. Petersen, S. Hunt, W. Lanser, J. Albers, A. Hansske, C. Hennrich, W. Hüls, M. Schröder and F. Ziegler. Möglichkeiten und Einsatzpotentiale neuer Absorptionskälteanlagen. In *Tagungsband Deutsche Klima-Kälte-Tagung*, Hannover, November 2013.
- [2] C. Paitazoglou and S. Petersen. Energy Efficient Cooling with new Absorption Chiller Technology in Solar Cooling Systems and CHPC-Plants. In *Proc. of the 6th International Conference ENERGY in BUILDINGS 2017*, pages 1–13. ASHRAE HELLENIC CHAPTER and Technical Chamber of Greece (TEE), Athens, October 2017.
- [3] Jan Albers. *Improvement of a calculation method for the control of absorption chillers*. PhD thesis, in German, TU Berlin, Fakultät III Prozesswissenschaften, Institut für Energietechnik, 2018.
- [4] EnEV 2007 (Änderung zum 01.05.2014). *Energieeinsparverordnung - EnEV 2007, Anlage 1, Nummer 2.1.1.* https://www.gesetze-im-internet.de/enev_2007/EnEV.pdf
- [5] DIN18599-1. Energetische Bewertung von Gebäuden - Berechnung des Nutz-, End- und Primärenergiebedarfs für Heizung, Kühlung, Lüftung, Trinkwarmwasser und Beleuchtung - Teil 1: Allgemeine Bilanzierungsverfahren, Begriffe, Zonierung und Bewertung der Energieträger, September 2018.
- [6] AGFW FW 309-1. AGFW-Regelwerk: Arbeitsblatt FW 309-1, Energetische Bewertung von Fernwärme - Bestimmung der spezifischen Primärenergiefaktoren für Fernwärmeversorgungssysteme - Mai 2014.
- [7] S. Petersen, J. Albers, R. Graf, C. Hausherr, C. Hennrich, W. Hüls, S. Hunt, W. Lanser, C. Paitazoglou, M. Schröder and F. Ziegler. EnEff:Wärme - Feldtest Absorptionskälteanlagen für KWKK Systeme. Technical Report FKZ 03ET1171A (Schlussbericht), TU Berlin, Institut für Energietechnik, FG Maschinen u. Energieanlagentechnik, 2019.
- [8] C. Schweigler. Kälte aus Fernwärme - Konzept, Auslegung und Betrieb der Single-Effect/Double-Lift-Absorptionskälteanlage, TU München, 1998.
- [9] C. Hennrich, R. Graf and S. Petersen. Absorptionskälteanlagen am Fernwärmerücklauf - Betriebsergebnisse aus dem FAKS-Projekt. In *Tagungsband Deutsche Klima-Kälte-Tagung*, Kassel, November 2016.
- [10] W. Lanser, J. Albers, W. Hüls, C. Paitazoglou, S. Hunt and S. Petersen. Systemintegration von Absorptionskälte: Erste Betriebserfahrungen aus einem Feldtest für KWKK-Systeme. In *Tagungsband Deutsche Klima-Kälte-Tagung*, Dresden, November 2015.
- [11] S. Petersen, A. Hansske, C. Hennrich, W. Hüls, J. Stangl, M. Mittermaier, Helm. M., P. Zachmeier, S. Natzer, W. Lanser and F. Ziegler. Development of a 50 kw absorption chiller. In *23rd IIR Int. Congress of Refrigeration, Prague, Czech Republic*, paper-ID 951, August 2011.



Electrical, environmental and economic optimal operation of an absorption heat transformer based industrial heat recovery and upgrade system

Corrales Ciganda, J. L.¹, Cudok, F.¹, Martinez-Urrutia, A.², Ramirez, M.², Gavaldà, O.³, and Pérez-Ortiz, A.³

¹TU Berlin, Institut für Energietechnik, 10587 Berlin, Germany

²Tecnalia, Energy and Environment Division, 20730 Azpeitia, Spain.

³Aiguasol Enginyeria, 08009, Barcelona, Spain.

Abstract

The performance of a heat recovery and upgrade system based on a 200 kW absorption heat transformer (AHT) is studied with a focus on its electrical consumption. The analyzed system has been installed in the power plant of an oil refinery. The system is fully monitored allowing comparison between measured and simulated data. The electrical energy consumption needed for heat recovery and upgrade is studied for three different system boundaries: the AHT with its internal pumps; the heat upgrade device including all minimal electrical consumption needed for its operation; and the complete heat upgrade system, including the power consumption needed to circulate the heat carriers between the AHT and the heat sources and sinks. Using a model validated with experimental measurements, a study is performed to evaluate the electrical energy efficiency of the system and its economic and environmental optimal operating point, depending on the selected external heat carriers flow rates. The results show that for the present boundary conditions, both economic and environmental performance are better for high external heat carrier flow rates, even at the price of higher electrical consumption.

1. Introduction

The electrical consumption of sorption systems is often regarded as negligible. Field results of sorption cooling systems, however, have shown that due to a suboptim hydraulic design, an inadequate control strategy and/or an oversized system that works mostly under low loads, the electrical consumption can be a significant contributor to the total primary energy input. [1] Sorption heat transformers upgrade available waste heat above its recovery temperature. Around half of the waste heat is upgraded to a higher temperature, while the other half is released to a lower temperature sink (mostly the ambient air through a heat rejection device). Such systems have been presented in the literature upgrading industrial waste heat from 60-100 °C to temperatures up to 140-150 °C. In the frame of the European Indus3Es project a similar system has been installed in a power plant inside an oil refinery in Izmit, Turkey. Low pressure steam with a temperature around 100 °C is used to drive an AHT and increase the temperature of a demineralized water stream from 95 up to 130-140 °C. The system is presented in Figure 1.

2. Pilot plant, electrical consumers and balance boundaries

As shown figure 1 there are 5 main electrical consumers in the system.

The first one includes the consumption of the pumps inside the AHT, $P_{el,int}$. The AHT operates with constant flow rates of solution and refrigerant pumps and constant electrical consumption .

Consumers two, three and four are the electrical driven pumps of the external circuits of the AHT: one at the intermediate temperature level, $P_{el,GE}$, another at the high temperature level, $P_{el,A}$, and a third one at the low temperature level, $P_{el,C}$, circuits. Each of these pumps circulates glycol-water or water through the AHT, through the pipes connecting AHT and the heat sources or sink, and through the source/sink itself. Simplifying the hydraulic circuits the electrical consumptions are calculated with the following expression.

$$P_{el,X} = (\dot{V}_X^3) \cdot \rho \cdot (R_{X,AHT} + R_{X,pipes} + R_{X,HX}) / 3600 / 10 / \eta_{el} \quad (1)$$

In this equation the flow rates are expressed in m^3/h and the hydraulic resistances in $mbar/(m^3/h)$. For each main heat exchanger of the AHT, hydraulic resistances to the flow of the external heat carrier $R_{X,AHT}$, are obtained using an analytic model validated for a 30 kW AHT prototype ([3]. The hydraulic resistances to the flow through the heat source and high temperature heat sink, $R_{X,HX}$, are taken from the manufacturer data of the heat exchangers. The hydraulic resistances to the flow through the piping systems, $R_{X,pipes}$, are obtained indirectly with the flow

rate measured at the plant for maximum pump speed and the corresponding head from the pump curves from manufacturer.

The fifth term corresponds to the power consumption of the heat rejection system $P_{el,HR}$. The power plant inside the refinery uses forced draught cooling towers in the capacity range of MW. The literature [1] reports specific electrical consumption between 0.008 and 0.02 kW_{el}/kW_{HR} for cooling towers of these type. A value of 0.01 is used in the present study for the ones at the power plant.

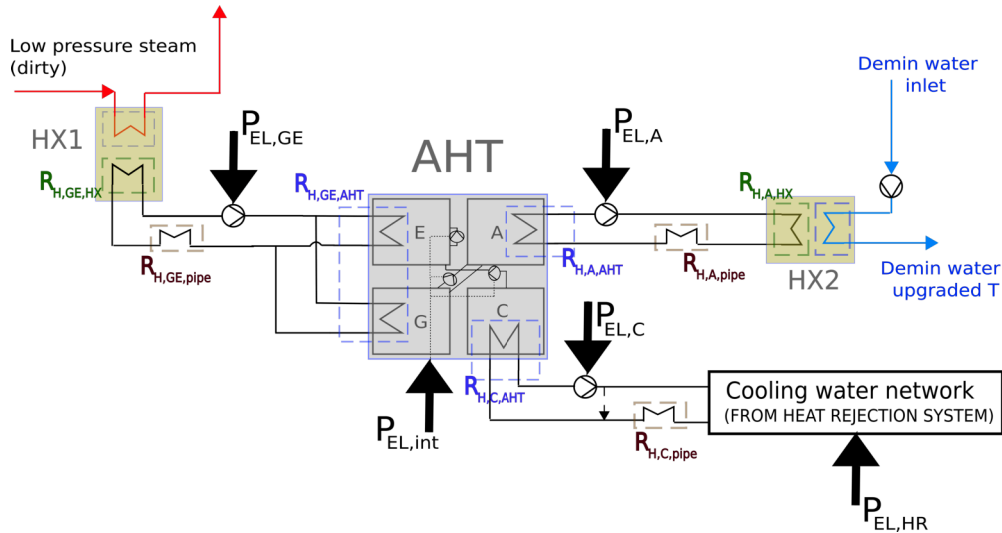


Figure 1: System description

COP_{el} indicates the amount of electrical energy necessary to upgrade a unit of heat. The majority of studies regarding COP_{el} of absorption chillers [1], follow their own methodology for the boundary definition for its calculation. Here, we distinguish between three boundaries that lead to three different electrical COP values:

- $COP_{el,int}$: internal electrical COP.
Is the electrical COP of the internal process. This includes electrical consumption of the pumps inside the AHT, circulating solution and refrigerant between the falling film heat exchangers. ($COP_{el,int} = \dot{Q}_A / P_{el,int}$)
- $COP_{el,device}$: the electrical COP of the heat upgrade device.
It includes also the electrical consumption of the pumps used to circulate the external heat carriers through the AHT heat exchangers, and the amount of electrical energy needed for the heat rejection. ($COP_{el,device} = \dot{Q}_A / (P_{el,int} + \sum P_{el,X,AHT} + P_{el,HR})$ with $X=A, G, E$ or C)
- $COP_{el,system}$: the electrical COP of the heat upgrade system.
It includes the internal consumption of the AHT, the consumption of the heat rejection system and that of the external pumps for the circulation of the heat carriers between the heat sources, sinks and the AHT. ($COP_{el,system} = \dot{Q}_A / (P_{el,int} + \sum P_{el,X} + P_{el,HR})$ with $X=A, GE$ or C)

Table 1: Auxiliary equipment characteristics

Component	\dot{V}_{design} [m ³ /h]	$P_{EL@ \dot{V}_{design}}$ [kW]	\dot{V}_{max} [m ³ /h]	$P_{EL@ \dot{V}_{max}}$ [kW]	η_{EL} [-]
$P_{el,int}$ Internal Pumps	-	2.13	-	2.13	-
$P_{el,GE}$ GE Pump (H Source)	74	4.42	96.2	9.70	0.78
$P_{el,A}$ A Pump (HT H Sink)	17.7	1.18	24	2.96	0.50
$P_{el,C}$ C Pump (HT H Sink)	38	-	?	?	0.72
$P_{el,HR}$ Heat Rejection ($P_{el,HR}$)	-	$\dot{Q}_C \cdot 0.01$	-	3.42	-

Because of the high feed pressure of the cooling water at the power plant network, the additional pump in the condenser circuit is not being used, and for the $COP_{el,system}$ calculations $P_{el,C} = 0$.

3. Measurement results and optimization study

Figure 2 shows the values for \dot{Q}_A and COP_{el} from measured and simulated data. The point series correspond to average values of quasi-steady state measurements of at least 30 minutes. In addition, the lines present the simulation results obtained using the characteristic equation model as presented in [2]. Two different lines resulting from this $\Delta\Delta T$ model are included for each variable: a solid line for a value of \dot{V}_{GE} of $74 \text{ m}^3/\text{h}$, and a dashed line for a flow rate reduced to $60 \text{ m}^3/\text{h}$. The characteristic equation coefficients of the AHT result from overall heat transfer coefficients k_X calculated as a function of the flow rate of the external heat carriers. For its calculation, the external heat transfer coefficients $\alpha_{A,ext}$ are calculated according to Dittus-Boelter, while the heat transfer coefficients between solution/refrigerant film and the heat exchanger tube wall are assumed to be constant. The latter are taken from laboratory measurements of a 40 kW prototype: $\alpha_{A,int}=800 \text{ W/m}^2\text{K}$, $\alpha_{G,int}=400 \text{ W/m}^2\text{K}$, $\alpha_{E,int}=1200 \text{ W/m}^2\text{K}$, $\alpha_{C,int}=2000 \text{ W/m}^2\text{K}$ [3].

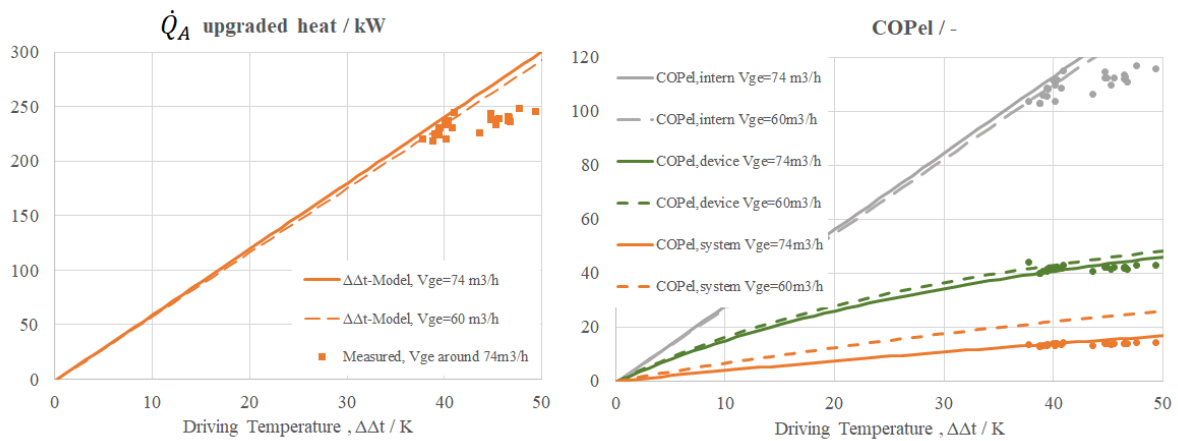


Figure 2: Upgraded Heat \dot{Q}_A and COP_{el} vs $\Delta\Delta t$ from measured and simulated data

The value for $COP_{el,system}$ is half the value for $COP_{el,device}$ because of the extra consumption at the two intermediate circuits with water-glycol. The main electricity consumer is $P_{el,GE}$. Reducing the flow rate in this circuit from the design one, $74 \text{ m}^3/\text{h}$, down to $60 \text{ m}^3/\text{h}$, $COP_{el,system}$ can be increased from 15-22 up to 18-28. ($P_{el,GE}$ decreases from 4.42 to 2.35 kW). $COP_{el,device}$ is also slightly higher when \dot{V}_{GE} decreases. $COP_{el,int}$ however, decreases when \dot{V}_{GE} sinks, as it does the amount of upgraded heat, \dot{Q}_A .

COP_{el} values alone do not give sufficient information to determine the optimal operation value for \dot{V}_{GE} . Two additional indicators are calculated: the operational savings of the plant compared to a situation with no heat upgraded in both economic (savings in euro/h) and environmental (savings in kg CO₂/h) terms. Using the parameters provided by the plant operator, and the characteristic equation method for changing flow rates, the operation savings are calculated with the following expression. (C_X are the costs per unit of energy for X=fuel, electricity or CO₂ emissions and η_{boiler} is the efficiency of the fuel furnace).

$$OperationSavings = \dot{Q}_A / \eta_{boiler} \cdot (C_{fuel} + C_{CO2}) - (\dot{Q}_A / COP_{el,system}) \cdot C_{el} \quad (2)$$

An analogue equation is used to calculate the savings in CO₂ emissions in (kg CO₂)/h.

In figure 3 \dot{V}_{GE} varies between the minimal flow rate for turbulent flow, ($Re=4000$) and maximum flow rate that the pump can provide for the driving heat circuit. The calculations have been made for two sets of boundary conditions, differing only on the cooling water inlet temperature changing from 15°C to 28°C . The resulting driving temperature differences $\Delta\Delta T$ are presented on top of the figures, together with the corresponding upgraded heat \dot{Q}_A and $COP_{el,system}$. The bottom figures present the economic and CO₂ savings per hour of operation. The figures show that although reducing the flow rate \dot{V}_{GE} can make $COP_{el,system}$ increase up to 25, both the economic and CO₂ savings are larger for higher flow rates. For the two set of conditions the optimal economic operating point (independent of CO₂ price) is for \dot{V}_{GE} values above the design one. The hourly savings increase between 2 and 5% compared to operating with the design and reduced flow rate respectively. Increasing \dot{V}_{GE} leads to an increase of

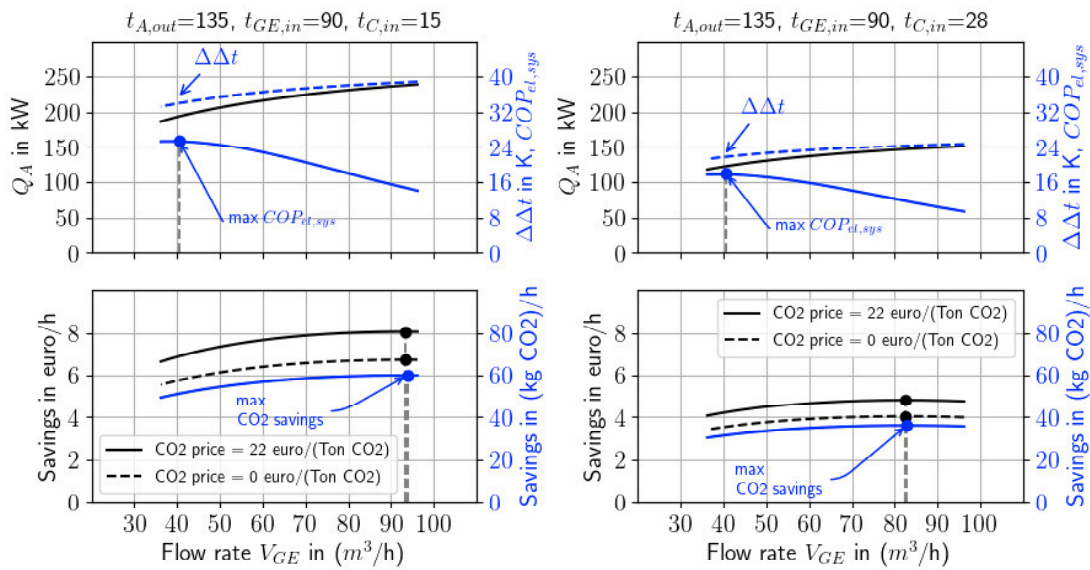


Figure 3: Electrical performance and operation costs of the heat upgrade system for \dot{V}_{GE} variations

\dot{Q}_A , and for its optimal value the marginal extra cost for fuel savings is the same as the marginal extra cost of the electricity. The optimal \dot{V}_{GE} value for the reduction of CO₂ emissions is in both cases very close to the value for optimal economic operation.

4. Conclusions

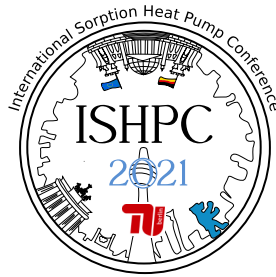
The obtained COP_{el} of an AHT pilot plant for heat upgrade is in the range 80-120 just considering the internal process, 35-45 for the minimal possible configuration of a heat upgrade device, and 15-22 for the heat upgrade system working with design flow rates. This value for $COP_{el,system}$ can be improved from 15 to 25 reducing \dot{V}_{GE} by 20%. However, taking into account the operation costs and CO₂ factors of the site, it is better to increase \dot{V}_{GE} up to 25% from the design value when heat is upgraded from 90 to 135 °C, although the value for $COP_{el,system}$ is reduced to 16 or even 10 for cooling water temperatures of 15 °C to 28 °C respectively.

5. Acknowledgment

This work has been developed under the project "Indus3Es: Industrial Energy and Environmental Efficiency" funded by the Horizon 2020 framework of the European Union, Project No. 680738.

References

- [1] Eicker, U., Pietruschka, R., Pesch R. (2012): Heat rejection and primary energy efficiency of solar driven absorption cooling systems. *Int. Journal of Refrigeration*, vol.35, pp.729-738.
- [2] Cudok, F., Ziegler, F., (2015): Absorption heat converter and the characteristic equation model *Proceedings of 24th IIR International Congress of Refrigeration*, vol.1.
- [3] Corrales Ciganda, J., Cudok, F., Kononenko, N. (2017): Experimental Results of an absorption heat transformer *Proceedings of 12th IEA Heat Pump Conference*, vol.1.



Development and experimental validation of a linear state-space model for absorption heat pumping systems for model-based control strategies

Sandra, Zlabinger^{1,2}, Unterberger, Viktor^{1,2}, Gölles, Markus^{1,2,*}, Horn, Martin^{1,2}, Wernhart, Michael³, and Rieberer, René³

¹BEST - Bioenergy and Sustainable Technologies GmbH, Inffeldgasse 21b, 8010 Graz

²Institute for Automation and Control, Graz University of Technology, Inffeldgasse 21b, 8010 Graz

³Institute of Thermal Engineering, Graz University of Technology, Inffeldgasse 25b, 8010 Graz

*Corresponding author: Phone: +43 5 02378-9208, E-Mail: markus.goelles@best-research.eu

Abstract

Control strategies of absorption heat pumping systems (AHPS, comprising heat pumps and chillers) often perform insufficiently well, since they usually do not explicitly consider the systems' dynamics and cross-coupling effects. One promising approach to improve their performance is to apply model-based control strategies since they would allow for an explicit consideration of these system characteristics. Therefore, mathematically simple models of the system to be controlled are required. This contribution proposes a new approach for such a model for a H₂O-LiBr AHPS. The model results from the linearization of a more complex, nonlinear simulation model, leading to a simple, but physically still meaningful linear state-space model structure. The experimental validation shows that the developed model describes the system's dynamics and cross-coupling effects sufficiently well and indicates that it is suitable to serve as a basis for the development of a model-based control strategy for AHPS.

1. Introduction

Absorption heat pumping systems (AHPS, comprising heat pumps and chillers) have great potential to increase the share of renewable energy in the heating and cooling sector. However, many potential applications remain unused since the performance of the control strategies currently applied is often insufficient. The extensive literature review given in [1] specifically examines the performance of existing AHPS control strategies and concludes that most are either only valid for a very narrow operational range, ignore internal control parameters (e.g. solution flow rate), lack experimental validation and/or neglect cross-coupling effects (i.e. controlled variables which actually have strong interactions are not controlled with one multivariable controller, but with multiple individual (decoupled) single-variable controllers instead). Advanced, typically model-based, control strategies have the potential to overcome these deficiencies. When developing these advanced control strategies the control design process is usually supported by means of two types of models of the system to be controlled. The first one (subsequently referred to as *simulation model*) serves the purpose of a virtual testbench. It is usually implemented in a simulation environment like Simulink[®] or Dymola[®] and is used to get an understanding of the dynamic system behavior and to test newly developed control strategies in simulation (e.g. [2]). The second one (subsequently referred to as *controller design model*) is applied for the development of model-based control strategies where the mathematical description of the system is used to explicitly consider the system's characteristics in the design of the controller. Unfortunately, most of the available mathematical models for AHPS cannot serve as a general basis for model-based control strategies, since they are either too complex (e.g. based on partial differential equations) or too simple (e.g. steady-state mass and energy balances). The linearized Dymola[®] simulation model in [3] could be a viable controller design model but the paper presents only limited information on the model structure and the validation results. Therefore, this paper presents a new, promising approach for developing a linear controller design model for model-based control on the basis of a H₂O-LiBr AHPS. In the oral presentation, the derived model and an extensive experimental validation will be discussed in detail.

2. Experimental setup

The proposed model was developed on the basis of a single stage H₂O-LiBr AHPS. A schematic representation of the AHPS including all sensor installations at the testbench is depicted in Figure 1. The main components include heat exchangers in the upper shell (i.e. generator and condenser), heat exchangers in the lower shell (i.e. absorber and evaporator), a solution heat exchanger for heat recovery between rich and poor solution, a solution pump between absorber and generator, a circulation pump in the evaporator and fixed refrigerant and solution expansion valves. The testbench setup was implemented in such a way that the rich solution volume flow rate and all inlet

temperatures and mass flow rates of the external hydraulic circuits (hot, cool and cold water circuit) can be adjusted precisely and independently, and internal and external variables - like temperatures, flow rates, pressure and levels - are measured, thus enabling comprehensive test runs and an experimental model validation.

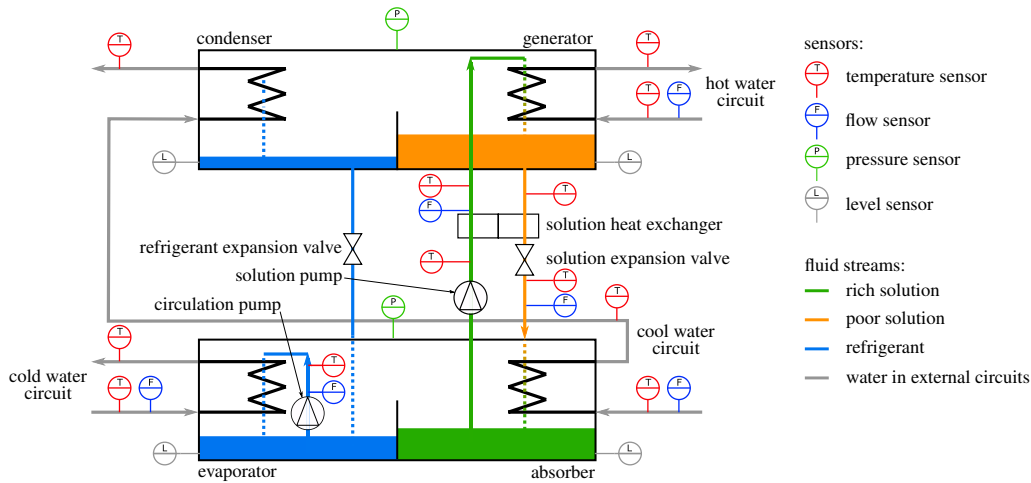


Figure 1: H_2O -LiBr AHPS and sensor installations

3. Modeling approach

The modeling approach is divided into two parts. First, a physically motivated simulation model is derived. Then, this simulation model is used as a basis for the development of a controller design model by systematically simplifying the simulation model through linearization and linear algebra. Both models will be briefly discussed in the following two sections. For clarity, the used nomenclature shall be explained before. Variables that influence the system from the outside will be referred to as *input variables* u_i . For this AHPS there are seven input variables - the rich solution volume flow rate and the three inlet temperatures and mass flow rates in the external hydraulic circuits. The states of mass and energy storages will be referred to as *state variables* x_i , which are stored masses and internal energies for this system. Their change over time is mathematically described by means of first-order differential equations, which in turn can be subject to certain constraints in the form of algebraic equations. For the formulation of these constraints additional variables are necessary which will be referred to as *algebraic variables* z_i (e.g. system pressure, internal temperatures, mass fractions etc.).

3.1. Simulation model

The simulation model is based on a lumped component approach, which means that the individual components are not spatially discretized but considered as lumped nodes with concentrated properties (like temperature, mass etc.). The dynamic system behavior is described by ordinary differential equations in the form of differential energy and mass balances for the fluid in the sumps of the generator, condenser, evaporator and absorber. The simulation model further contains property data equations (e.g. for the correlation between specific enthalpy and temperature), correlations for heat transfer and assumptions concerning saturation conditions at the outlet of the heat exchangers. These are algebraic equations (i.e. not containing derivatives), which describe static correlations between the state, input and algebraic variable vectors \mathbf{x} , \mathbf{u} and \mathbf{z} . Hence, the resulting model contains differential and algebraic equations, leading to a so-called system of *differential-algebraic equations* (DAE model). Both, the differential and the algebraic equations are in general not linear (e.g. even the simple multiplication of a non-constant mass and a non-constant specific energy to calculate the total energy is already a nonlinear term). The mathematical structure can be summarized as

$$\frac{d\mathbf{x}}{dt} = \mathbf{f}(\mathbf{x}, \mathbf{u}, \mathbf{z}) \text{ (differential equations),} \quad \mathbf{0} = \mathbf{g}(\mathbf{x}, \mathbf{u}, \mathbf{z}) \text{ (algebraic equations),} \quad (1a-b)$$

with \mathbf{f} and \mathbf{g} being vector functions. The resulting simulation model consists of a coupled, nonlinear system of ten differential and 47 algebraic equations. This model is very suitable for simulation purposes, as will be shown later, but still very complex and therefore less suitable as a basis for model-based control strategies. Thus, further simplifications are necessary to derive a viable controller design model.

3.2. Controller design model

The high complexity of the simulation model in section 3.1 can be attributed to (i) its non-linearity, (ii) the presence of both differential and algebraic equations, and finally (iii) the large number of equations in general. This section describes how these three issues are addressed to derive a suitable controller design model.

The first step consists of linearizing the DAE model. For this, at first a reference operating point is chosen. This reference operating point consists of a set of state, input and algebraic variables \mathbf{x}_{ref} , \mathbf{u}_{ref} and \mathbf{z}_{ref} where the system is in steady state, i.e. where the derivatives $\frac{d\mathbf{x}}{dt}$ equal zero. For this purpose a representative set of input variables \mathbf{u}_{ref} is chosen and the resulting \mathbf{x}_{ref} and \mathbf{z}_{ref} are calculated by means of the DAE model (equation (1)). Next, all differential and algebraic equations of the DAE model are approximated at the chosen reference operating point by a first order Taylor expansion (i.e. omitting all terms with a higher order than one), yielding a linear DAE model for the deviations $\Delta\mathbf{x}$ ($=\mathbf{x}-\mathbf{x}_{ref}$), $\Delta\mathbf{u}$ ($=\mathbf{u}-\mathbf{u}_{ref}$) and $\Delta\mathbf{z}$ ($=\mathbf{z}-\mathbf{z}_{ref}$)

$$\frac{d\Delta\mathbf{x}}{dt} = \left. \frac{\partial \mathbf{f}}{\partial \mathbf{x}} \right|_{ref} \Delta\mathbf{x} + \left. \frac{\partial \mathbf{f}}{\partial \mathbf{u}} \right|_{ref} \Delta\mathbf{u} + \left. \frac{\partial \mathbf{f}}{\partial \mathbf{z}} \right|_{ref} \Delta\mathbf{z}, \quad \mathbf{0} = \left. \frac{\partial \mathbf{g}}{\partial \mathbf{x}} \right|_{ref} \Delta\mathbf{x} + \left. \frac{\partial \mathbf{g}}{\partial \mathbf{u}} \right|_{ref} \Delta\mathbf{u} + \left. \frac{\partial \mathbf{g}}{\partial \mathbf{z}} \right|_{ref} \Delta\mathbf{z}, \quad (2a-b)$$

where $\left. \frac{\partial \mathbf{f}}{\partial \mathbf{x}} \right|_{ref}$ refers to a Jacobian matrix, i.e. a matrix containing the first-order partial derivatives of \mathbf{f} with respect to \mathbf{x} , evaluated at the chosen reference operating point. The same applies to the other Jacobian matrices in equations (2a) and (2b). This results in a linear DAE, hence issue (i) is resolved.

The second step consists of eliminating the set of linearized algebraic equations (equation (2b)). When the set of algebraic equations of the original DAE model (equation (1b)) is well posed and does not contain redundant or conflicting equations, the resulting (quadratic) Jacobian matrix $\left. \frac{\partial \mathbf{g}}{\partial \mathbf{z}} \right|_{ref}$ is regular and can therefore be inverted. This allows solving equation (2b) for $\Delta\mathbf{z}$,

$$\Delta\mathbf{z} = - \left(\left[\left. \frac{\partial \mathbf{g}}{\partial \mathbf{z}} \right|_{ref} \right]^{-1} \left. \frac{\partial \mathbf{g}}{\partial \mathbf{x}} \right|_{ref} \Delta\mathbf{x} + \left[\left. \frac{\partial \mathbf{g}}{\partial \mathbf{z}} \right|_{ref} \right]^{-1} \left. \frac{\partial \mathbf{g}}{\partial \mathbf{u}} \right|_{ref} \Delta\mathbf{u} \right), \quad (3)$$

which is further inserted into equation (2a),

$$\frac{d\Delta\mathbf{x}}{dt} = \left(\left. \frac{\partial \mathbf{f}}{\partial \mathbf{x}} \right|_{ref} - \left. \frac{\partial \mathbf{f}}{\partial \mathbf{z}} \right|_{ref} \left[\left. \frac{\partial \mathbf{g}}{\partial \mathbf{z}} \right|_{ref} \right]^{-1} \left. \frac{\partial \mathbf{g}}{\partial \mathbf{x}} \right|_{ref} \right) \Delta\mathbf{x} + \left(\left. \frac{\partial \mathbf{f}}{\partial \mathbf{u}} \right|_{ref} - \left. \frac{\partial \mathbf{f}}{\partial \mathbf{z}} \right|_{ref} \left[\left. \frac{\partial \mathbf{g}}{\partial \mathbf{z}} \right|_{ref} \right]^{-1} \left. \frac{\partial \mathbf{g}}{\partial \mathbf{u}} \right|_{ref} \right) \Delta\mathbf{u}, \quad (4)$$

resulting in a model form, where the system is described by a set of linear ordinary differential equations only, with the state vector $\Delta\mathbf{x}$ and the input vector $\Delta\mathbf{u}$. Hence, also issue (ii) and (iii) are resolved. The resulting model in equation (4) has the mathematical structure of a linear state-space model, which is highly favorable from a control engineering point of view, since this allows applying a vast number of methods from linear control theory. The absolute values for \mathbf{x} can be easily determined by adding the (known) values \mathbf{x}_{ref} to $\Delta\mathbf{x}$.

3.3. Output equations

The equations in equation (1) (for the nonlinear simulation model) or respectively equation (4) (for the linear controller design model) each describe the temporal development of the state variables in dependence of the seven input variables and therefore describe the system's dynamic behavior. However, often one is not only interested in state variables but in variables depending on several state and input variables, e.g. heat flows or outlet temperatures. These will be collectively referred to as output variables \mathbf{y} and can be described by correlations between state, input and algebraic variables \mathbf{x} , \mathbf{u} and \mathbf{z} in the form of algebraic output equations. For the nonlinear simulation model in section 3.1 the output equations are in general nonlinear, their mathematical structure can be outlined as

$$\mathbf{y} = \mathbf{h}(\mathbf{x}, \mathbf{u}, \mathbf{z}), \quad (5)$$

with \mathbf{h} being a vector function. It shall be stressed at this point, that neither equation (1) nor (4) contain the output variables \mathbf{y} . Equation (1) and (4) are therefore independent of the formulation of equation (5) - output variables do not influence the system's state variables and dynamic behavior.

To derive the linear output equations for the controller design model from section 3.2 the same method as described in section 3.2 is used and yields linear output equations with the mathematical structure

$$\Delta \mathbf{y} = \left(\frac{\partial \mathbf{h}}{\partial \mathbf{x}} \Big|_{ref} - \frac{\partial \mathbf{h}}{\partial \mathbf{z}} \Big|_{ref} \left[\frac{\partial \mathbf{g}}{\partial \mathbf{z}} \Big|_{ref} \right]^{-1} \frac{\partial \mathbf{g}}{\partial \mathbf{x}} \Big|_{ref} \right) \Delta \mathbf{x} + \left(\frac{\partial \mathbf{h}}{\partial \mathbf{u}} \Big|_{ref} - \frac{\partial \mathbf{h}}{\partial \mathbf{z}} \Big|_{ref} \left[\frac{\partial \mathbf{g}}{\partial \mathbf{z}} \Big|_{ref} \right]^{-1} \frac{\partial \mathbf{g}}{\partial \mathbf{u}} \Big|_{ref} \right) \Delta \mathbf{u}, \quad (6)$$

which is also consistent with the mathematical structure of linear state-space models mentioned in section 3.2.

4. Experimental validation

For a controller design model accuracy is often not as important as it is for a simulation model - it's rather its mathematical structure that is crucial in order to be able to use it for specific control design methods. Nevertheless, the more accurate a controller design model is, the more likely it can be used for successful controller design. To evaluate the model's accuracy, both the nonlinear simulation model and the linear controller design model were implemented in the simulation environment Simulink[®] and compared with measurement data from the AHPS described in section 2. Figure 2 shows exemplary results from a test run where the hot water inlet temperature was changed in a step-wise manner while the remaining six input variables were kept constant at the chosen reference operating point. The three sub-figures on the left show inlet temperatures in solid grey and outlet temperatures (output variables) in solid green (measured), dotted dark blue (simulated with nonlinear model) and dashed bright blue (simulated with linear model) for the three water circuits (hot, cool and cold water). Analogously, the three sub-figures on the right show the resulting heat flows (output variables) in the three circuits. These results indicate that both models agree well with measurement data and that the linearized model approximates the nonlinear one very well in the depicted operating range.

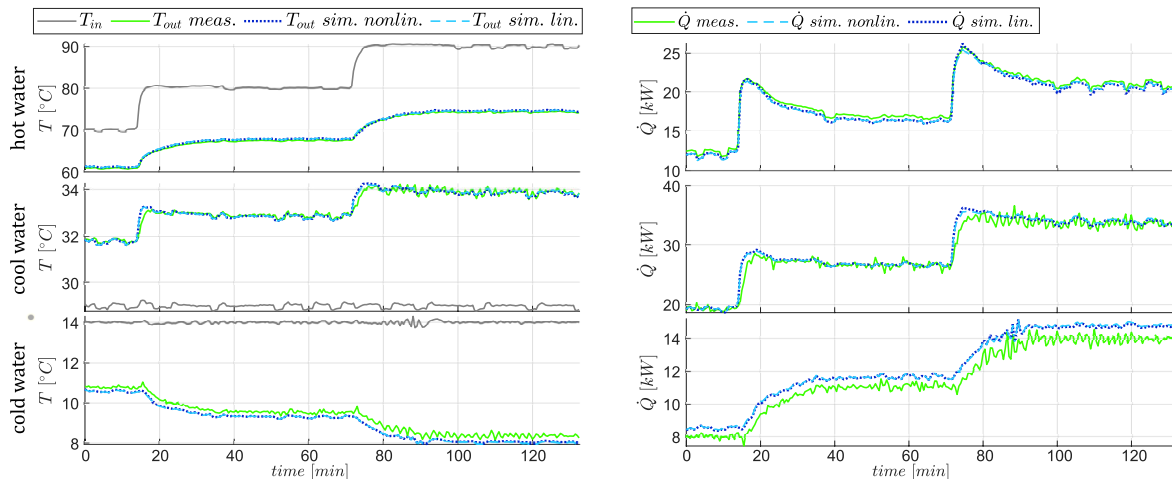


Figure 2: Comparison of measurement and simulation data

The excellent validation results depicted in figure 2 may raise the question why the more complex simulation model is necessary at all, which shall be briefly discussed. First, the linear controller design model can only be derived with the help of the more complex simulation model if one does not want to resort to black box approaches, since only the simulation model is based on physically motivated considerations. Second, a more extensive validation may show that the linear model is too inaccurate for large deviations from the chosen reference operating point. In this case the linearization in several reference operating points - instead of in just one - could be an option, for which again the complex simulation model serves as a basis.

5. Conclusion and outlook

First experimental validations indicate that the developed simulation model and controller design model describe system dynamics sufficiently well. Furthermore, the controller design model has the favorable mathematical structure of a linear state-space model, thus being a promising basis for the design of a model-based control. In the oral presentation, both models and an extensive experimental validation, including an analysis for large deviations

from the chosen reference operating point for all seven input variables, will be discussed. Using the proposed controller design model to develop model-based control strategies for AHPS is part of the authors' current research.

6. Acknowledgment

This project is funded by the Austrian Climate and Energy Fund and carried out in the framework of the *Energiforschungsprogramm 2017* program in cooperation with our project partners *AEE - Institut für Nachhaltige Technologien*, *EAW Energieanlagenbau GmbH Westenfeld*, *Pink GmbH* and *SOLID Solar Energy Systems GmbH*.

References

- [1] Goyal, A., Staedter, M. A., Garimella, S. (2019): A review of control methodologies for vapor compression and absorption heat pumps. *International Journal of Refrigeration*, vol. 97, pp. 1-20.
- [2] Ochoa, A., Dutra, J., Henríquez, J., dos Santos, C. (2015): Dynamic study of a single effect absorption chiller using the pair LiBr/H₂O. *Energy Conversion and Management*, vol. 108, pp. 30-42.
- [3] Vinther, K., Nielsen, K. M., Andersen, P., Pedersen, T.S., Bendtsen, J.D. (2015): Absorption Cycle Heat Pump Model for Control Design. *2015 European Control Conference (ECC)*, pp. 2228-2234.



Explicit calculation of flow rate set values for absorption chiller control

Albers, Jan¹ ORCID: 0000-0002-1134-1025

¹ Technische Universität Berlin, Institut für Energietechnik, Sek. KT 2, jan.albers@tu-berlin.de

Abstract:

By active control of the supply flow rates for an absorption chiller a considerable reduction of auxiliary electricity demand is possible. For this purpose, a calculation method is derived which allows an explicit determination of the necessary set values for the flow rates in hot, cooling and chilled water circuit at given inlet temperatures and desired cooling capacity. An improved method of characteristic equations from open literature is used in combination with additional approximations. The deviation in cooling capacity calculated with explicit set values is below 10 %.

1. Introduction

Recently an improved calculation method for the part load behaviour of single stage H₂O/LiBr absorption chillers has been published [1]. The related source code is available at [2]. This method is used by commercial absorption chillers in a model predictive control strategy to ensure low hot water return temperatures t_{Do}^{set} in addition to match the cooling load \dot{Q}_E^{set} and chilled water set value t_{Eo}^{set} [3], [4]. Although the method is able to handle variable flow rates of hot, cooling and chilled water they are not yet controlled actively. On the other hand it has been shown in [5] that the auxiliary electricity demand of an absorption chiller assembly including the reject heat device can be reduced by approx. 60 % under part load condition when the set values \dot{Q}_E^{set} , t_{Eo}^{set} and t_{Do}^{set} are adjusted by flow rate control (and not by the inlet temperatures of hot and cooling water, i.e. t_{Di} , t_{Ai}). In this contribution the explicit calculation of the necessary flow rate set values will be derived in detail. In contrast the whole methodology and derivation of coefficients is referenced to literature [1], [2]. Only absorption chillers with a serial cooling water flow from absorber to condenser and without solution recirculation in the absorber will be considered.

2. Methodology

Unlike the established characteristic equation method where arithmetic mean temperatures $t_X = (t_{Xi} + t_{Xo})/2$ of the external flow rates are combined to a characteristic temperature difference $\Delta\Delta t$ [6], the improved method combines the independent inlet temperatures t_{Xi} to an effective characteristic temperature difference $\Delta\Delta t_i^*$. The index $X = D, E, C, A$ holds for the main heat exchangers desorber, absorber, evaporator and condenser and $X = S$ for the solution heat exchanger. The effective characteristic temperature difference

$$\Delta\Delta t_i^* = t_{Di} \cdot (1 - K_1) - t_{Ai} \cdot (1 - K_2) + t_{Ei} \cdot (1 - K_3) \quad (1)$$

includes the variable but load independent losses. Hereby the loss parameter $\Delta\Delta t_{min}$ of the established method is avoided (which is indicated by the asterisk), and the cooling capacity reads (cf. [1], [2]):

$$\dot{Q}_E = K_4 \cdot \Delta\Delta t_i^* \quad (2)$$

The slope parameter K_4 consists of four coefficients K_{XQ} (where $X = D, E, C, A$)

$$K_4 = (K_{DQ} + K_{AQ} + K_{CQ} + K_{EQ})^{-1} \quad (3)$$

which include the dimensionless temperature glides P_X , e.g. for the desorber ($X = D$):

$$K_{DQ} = \frac{K_{D2} + K_{D1s}}{\dot{W}_D \cdot P_D} - \frac{K_{D2} + 2 \cdot K_{D1s}}{2 \cdot \dot{W}_S} \quad (4)$$

The determining equations of all coefficients K_{XN} and K_{XNx} with $N = 1,2,3$ and $x = r, s$ (where r is used for coefficients describing load independent effects and s for load dependent effects) can be found in [2] or [7].

For a counter flow heat exchanger X the dimensionless temperature glide P_X depends on the heat capacity flow rate ratio R_X and the dimensionless heat transfer capability $NTU_X = Y_X/\dot{W}_X = U_X \cdot A_X/\dot{W}_X$. Consequently, P_X depends on the external heat capacity flow rate $\dot{W}_X = \dot{m}_X \cdot c_{p,X}$ or volume flow rate $\dot{V}_X = \dot{W}_X/(c_{p,X} \cdot \rho_X)$, respectively.

$$P_X = \frac{1 - \exp((R_X - 1) \cdot NTU_X)}{1 - R_X \cdot \exp((R_X - 1) \cdot NTU_X)} = \frac{1 - \exp((R_X - 1) \cdot Y_X/\dot{W}_X)}{1 - R_X \cdot \exp((R_X - 1) \cdot Y_X/\dot{W}_X)} \quad (5)$$

To control the cooling capacity e.g. by a variable set value for the hot water flow rate \dot{V}_D^{set} , eq. (2) has to be solved for \dot{W}_D together with eq. (3), (4) and (5). Unfortunately an analytical, explicit solution for \dot{W}_D is yet unknown. However, instead of eq. (5) an approximation P'_X of P_X can be used to avoid the exponential function.

$$P_X \approx \left(1 + \frac{\dot{W}_X}{\dot{W}_{X,0}} \cdot \left(\frac{1}{P_{X,0}} - 1 \right) \right)^{-1} = P'_X \quad (6)$$

In this equation $\dot{W}_{X,0}$ holds for the capacity flow rate at nominal condition (Index 0) and $P_{X,0}$ is calculated with $\dot{W}_{X,0}$ (i.e. also at nominal condition). Thus, at normalized flow velocity $\gamma_X = \dot{W}_X/\dot{W}_{X,0} = 1$ the approximation P'_X equals $P_{X,0}$ (i.e. the exact value). For $\gamma_X = 0$ eq. (6) converges to the same limit value $P'_X = 1$ as P_X in eq. (5). Between $\gamma_X = 0$ and $\gamma_X = 1$ – and also beyond – the exponential dependency is considered by a reciprocal approach. By introducing a term $d_X = (1 - P_{X,0} \cdot R_{X,0}) \cdot f_X$ approximation (6) can be improved. By means of $R_{X,0} = \dot{W}_{X,0}/\tilde{W}_{X,0}$ the internal, pseudo specific heat capacity flow rates $\tilde{W}_X = \tilde{c}_{p,X} \cdot \dot{m}_X$ under nominal conditions are incorporated. In evaporator and condenser (i.e. $X = E, C$) there is no internal temperature glide. Thus the pseudo specific heat capacity $\tilde{c}_{p,X}$ is infinite and $R_{X,0} = 0$. In addition a value $f_X = 1$ is used. For ab- and desorber (i.e. $X = A, D$) values of $\tilde{c}_{p,X} \approx 25$ kJ/kgK and $f_X = 2$ are suitable. Thus the improved approximation P''_X of P_X reads:

$$P_X \approx \left(d_X + \frac{\dot{W}_X}{\dot{W}_{X,0}} \cdot \left(\frac{1}{P_{X,0}} - d_X \right) \right)^{-1} = P''_X \quad (7)$$

On the left hand side of Figure 1 both approximations P'_X and P''_X are shown in comparison to the exact values for an absorption chiller of type FM160v2.1 or Bumblebee, respectively (cf. [4] for further details). On the right hand side the deviations $\epsilon_X''' = P_X'''/P_X - 1$ are depicted for the same flow rate variation $0.01 < \gamma_X < 2$. In practice a range of $0.2 < \gamma_X < 1.5$ is of interest. Here the deviations ϵ_X'' of P''_X from eq. (7) are below 10 %.

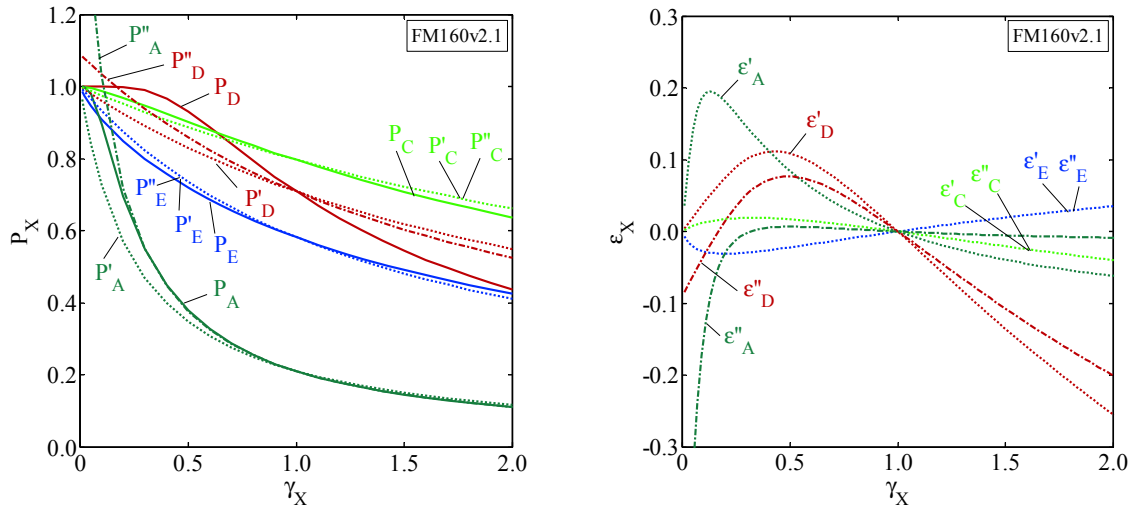


Figure 1 – Approximations and their deviation for the dimensionless temperature glide.

Applying approximation (7) to all coefficients K_{XQ} of the slope parameter in eq. (3) simultaneously (i.e. for $X = D, E, C, A$), leads to an approximated characteristic equation for the cooling capacity

$$\dot{Q}_E \approx \left[K_{VD} \cdot \frac{1}{\dot{W}_D} - K_{VH} \cdot \frac{1}{\dot{W}_H} + K_{VE} \cdot \frac{1}{\dot{W}_E} + K_{V0} \right]^{-1} \cdot \Delta \Delta t_i^* = K'_4 \cdot \Delta \Delta t_i^* \quad (8)$$

with an approximated slope parameter $K'_4 \approx K_4$ and the coefficients

$$K_{VD} = (K_{D2} + K'_{D1s}) \cdot d_D \quad (9)$$

$$K_{VH} = (K_{A2} + K'_{A3s}) \cdot d_A + K_C \cdot B_{X2} \cdot d_C \quad (10)$$

$$K_{VE} = B_{X2} \cdot d_E \quad (11)$$

$$K_{V0} = \frac{K_{D2} + K'_{D1s}}{\dot{W}_{D,0}} \cdot \left(\frac{1}{P_{D,0}} - d_D \right) - \frac{K_{D2} + 2 \cdot K'_{D1s}}{2 \cdot \tilde{W}_D} - \frac{K_{A2} + K'_{A3s}}{2 \cdot \dot{W}_{H,0}} \cdot \left(\frac{1}{P_{A,0}} - d_A \right) - \frac{K_{A2} + 2 \cdot K'_{A3s}}{2 \cdot \tilde{W}_A} + \frac{K_C \cdot B_{X2}}{\dot{W}_{H,0}} \cdot \left(\frac{1}{P_{C,0}} - d_C \right) + \frac{B_{X2}}{\dot{W}_{E,0}} \cdot \left(\frac{1}{P_{E,0}} - d_E \right). \quad (12)$$

For serial cooling water flow through absorber and condenser (where $\dot{W}_A = \dot{W}_C = \dot{W}_H$) an index $X = H$ is used for the related coefficients. Unfortunately also the coefficients K_1, K_2 and K_3 of the characteristic temperature difference $\Delta\Delta t_i^*$ depend on the heat capacity flow rates \dot{W}_X (with $X = D, E, H$), either directly via \dot{W}_H or indirectly via slope parameter K_4 , process parameter B^* and K_{A3s} .

$$K_1 = \frac{B^*}{B^* - \frac{K_{A3r} + \dot{W}_H}{K_4 \cdot (K_{A2} + K_{A3s})}} \quad K_2 = K_1 \cdot \left(1 + \frac{\dot{W}_H}{K_4 \cdot (K_{A2} + K_{A3s})}\right) \quad K_3 = 1 - K_1 + K_2 \quad (13)$$

The process parameter $B^* = B_{X2} + K_{Dt} + K_{At}$ is calculated from the Dühring-parameter $B_{X2} = 1,15$ and two coefficients K_{Xt} which hold for the effect of solution inlet sub-cooling (or super-heating) in ab- and desorber, cf. [1]. If \dot{W}_E is the only unknown (or desired) flow rate K_{Dt} and K_{At} can be calculated exactly. If \dot{W}_D or \dot{W}_H are unknown an approximation $K_{Xt} \approx K'_{Xt}$ is used where the nominal flow rate is applied, e.g. for $X = D$:

$$K_{Dt} = \frac{K_{D1r}}{\dot{W}_D \cdot P_D} - \frac{K_{D1r}}{\tilde{W}_D} \approx \frac{K_{D1r}}{\dot{W}_{D,0} \cdot P_{D,0}} - \frac{K_{D1r}}{\tilde{W}_D} = K'_{Dt} \quad (14)$$

The same procedure (i.e. replacing the unknown flow rate \dot{W}_X and dimensionless temperature glide P_X by its nominal value) is performed for K_{At} , K_{A3s} and K_{D1s} . Since the coefficients K_{A3r} , K_{D1r} are independent of the external flow rates an approximated value for $K'_1 \approx K_1$ can be calculated by applying the approximated slope parameter K'_4 .

$$K'_1 = \frac{B^{**}}{B^{**} - \frac{K_{A3r} + \dot{W}_H}{K'_4 \cdot (K_{A2} + K'_{A3s})}} = \frac{B^{**}}{B^{**} - \frac{K_{A3r} + \dot{W}_H}{(K_{A2} + K'_{A3s})} \cdot \left(\frac{K_{VD}}{\dot{W}_D} - \frac{K_{VH}}{\dot{W}_H} + \frac{K_{VE}}{\dot{W}_E} + K_{V0}\right)} \quad (15)$$

In the same way also $K'_2 \approx K_2$ and $K'_3 \approx K_3$ can be determined from eq. (13) as function of the external flow rates.

3. Flow rate set values

Inserting the approximated coefficients K'_1, K'_2 and K'_3 into the characteristic temperature difference in eq. (8) leads to a representation which can be solved explicitly for the external heat capacity flow rates \dot{W}_X necessary for a certain cooling capacity $\dot{Q}_E = \dot{Q}_E^{set}$ at given inlet temperatures t_{Xi} .

Finally, the formula for hot and chilled water (i.e. $X = D$ or $X = E$) reads

$$\dot{W}_X^{set} = \frac{K_{VX}}{\frac{1}{\dot{Q}_E} \cdot \left((t_{Di} - t_{Ai}) - \frac{\dot{W}_H \cdot B^{**}}{K_{A3r} + \dot{W}_H} \cdot (t_{Ai} - t_{Ei}) \right) - K_{V0} + \frac{B^{**} \cdot (K_{A2} + K'_{A3s})}{K_{A3r} + \dot{W}_H} + \frac{K_{VH}}{\dot{W}_H} - \frac{K_{VZ}}{\dot{W}_Z}} \quad (16)$$

where $Z = E$ if $X = D$ and $Z = D$ if $X = E$ in the last term of the denominator.

The formula for the cooling water flow rate (i.e. $X = H$) looks different, because inserting K'_1, K'_2 and K'_3 into $\Delta\Delta t_i^*$ in eq. (8) results in a fractured rational function of second order in \dot{W}_H :

$$\dot{Q}_E = \frac{\dot{W}_H^2 \cdot (t_{Di} - t_{Ai} - B^{**} \cdot (t_{Ai} - t_{Ei})) + \dot{W}_H \cdot K_{A3r} \cdot (t_{Di} - t_{Ai})}{\dot{W}_H^2 \cdot K_{V0}^H - \dot{W}_H \cdot (K_{VH} + B^{**} \cdot (K_{A2} + K'_{A3s})) - K_{A3r} \cdot K_{V0}^H} - K_{A3r} \cdot K_{VH} \quad (17)$$

where

$$K_{V0}^H = K_{V0} + \frac{K_{VD}}{\dot{W}_D} + \frac{K_{VE}}{\dot{W}_E} \quad (18)$$

To solve for the necessary flow rate $\dot{W}_H = \dot{W}_H^{set}$ at $\dot{Q}_E = \dot{Q}_E^{set}$ and given inlet temperatures t_{Xi} eq. (17) is transformed to the normal form of a quadratic equation $\dot{W}_H^2 + \dot{W}_H \cdot p + q = 0$ with the well-known solution

$$\dot{W}_H^{set} = -p/2 \pm \sqrt{p^2/4 - q} \quad (19)$$

and

$$p = \frac{K_{VH} - K_{A3r} \cdot K_{V0} + B^{**} \cdot (K_{A2} + K'_{A3s}) - \frac{K_{A3r}}{\dot{Q}_E} \cdot \left(\frac{K_{VD}}{\dot{W}_D} + \frac{K_{VE}}{\dot{W}_E} - (t_{Di} - t_{Ai})\right)}{\frac{1}{\dot{Q}_E} \cdot (t_{Di} - t_{Ai} - B^{**} \cdot (t_{Ai} - t_{Ei})) - K_{V0}^H} \quad (20)$$

$$q = \frac{K_{A3r} \cdot K_{VH}}{\frac{1}{\dot{Q}_E} \cdot (t_{Di} - t_{Ai} - B^{**} \cdot (t_{Ai} - t_{Ei})) - K_{V0}^H} \quad (21)$$

Calculations with different values and different distributions of heat transfer capabilities $Y_{X,0}$ (where $X = D, E, C, A, S$) and solution flow rates (i.e. different sizes and types of absorptions chillers) have been shown, that only the solution of eq. (19) using the positive square root provides technical sensible results for \dot{W}_H . Nevertheless, a mathematical substantiation for this finding is still owing.

In Figure 2 the part load behaviour of an absorption chiller type FM160v2.1 is shown as function of the characteristic temperature difference $\Delta\Delta t_i^*$. The change of cooling capacity $\dot{Q}_E(\dot{W}_H)$ is a result of a cooling water flow rate variation between $\gamma_H = 0.2$ and 2.0 at constant driving temperature $t_{Di} = 75^\circ\text{C}$. The same load variation $\dot{Q}_E(t_{Di})$ between 49 and 112 kW can be achieved by keeping $\dot{W}_H(t_{Di}) = 0.8 \cdot \dot{W}_{H,0}$ constant and controlling the driving temperature in a range $59^\circ\text{C} < t_{Di} < 79^\circ\text{C}$. In both cases the flow rates in hot and chilled water are constant at $\dot{W}_X = 0.8 \cdot \dot{W}_{X,0}$ and the inlet temperatures at $t_{Ai} = 27^\circ\text{C}$ and $t_{Ei} = 14^\circ\text{C}$, respectively. The results of $\dot{Q}_E(t_{Di})$ and $\dot{Q}_E(\dot{W}_H)$ have been derived by applying the function *CE_method* [1] with the provided values for t_{Xi} and \dot{W}_X .

To check the explicit but approximated method of set value calculation at constant $t_{Di}/t_{Ai}/t_{Ei} = 75/27/14^\circ\text{C}$ the load variation $\dot{Q}_E(\dot{W}_H) = \dot{Q}_E(t_{Di})$ between 49 and 112 kW is now used as set value \dot{Q}_E^{set} to calculate the values \dot{W}_H^{set} according to eq. (19). Due to the approximations for P_X and the coefficients K_1 to K_3 the deviation $\epsilon(\dot{W}_H) = \dot{W}_H^{set}/\dot{W}_H - 1$ is up to 20 %. Thus, using the approximated but explicitly calculated set values \dot{W}_H^{set} to control the chiller at the same temperatures $t_{Di}/t_{Ai}/t_{Ei} = 75/27/14^\circ\text{C}$ the resulting cooling capacity $\dot{Q}_E(\dot{W}_H^{set})$ – again calculated with *CE_method* [1] – also deviates from $\dot{Q}_E^{set} = \dot{Q}_E(\dot{W}_H) = \dot{Q}_E(t_{Di})$. Since the heat transfer improvement diminishes at high flow rates the effect of deviations $\epsilon(\dot{W}_H) > 10\%$ at $\dot{W}_H^{set} > 45\text{ kW/K}$ is dampened and the deviation $\epsilon(\dot{Q}_E) = \dot{Q}_E^{set}/\dot{Q}_E - 1$ stays below 10 %.

4. Conclusions

The described explicit calculation procedure to determine flow rate set values \dot{W}_X^{set} for the control of commercial absorption chillers leads to deviations below 10 % between the set value \dot{Q}_E^{set} and the controlled cooling capacity $\dot{Q}_E(\dot{W}_X^{set})$. This enables the application in control strategies aiming at a reduced auxiliary electricity demand.

5. Acknowledgment

We acknowledge financial support by the EnEff:Wärme Project 03ET1583 grant funded by the Bundesministerium für Wirtschaft und Energie (BMWi).

6. List of References

- [1] Jan Albers. *Enhancement of a calculation method for the control of absorption chillers*. PhD thesis in German, TU Berlin, Fakultät III Prozesswissenschaften, 2019. <http://dx.doi.org/10.14279/depositonce-8708>
- [2] J. Albers. *CE_Method*. A MATLAB function for calculating the part load behaviour of absorption chillers and heat pumps based on (C)haracteristic (E)quations, Sep. 2017. <http://dx.doi.org/10.14279/depositonce-6164>
- [3] J. Albers and F. Ziegler. Control Strategies for Absorption chillers in CHPC-plants ensuring low hot water return temperatures. In *Proc. of Heat powered cycles conference*, Nottingham, 27–29 Jun. 2016, paper-ID: 800.
- [4] BINE. Cooling with heat - A new generation of compact chillers cools and heats with low-temperature heat. http://www.bine.info/fileadmin/content/Presse/Projektinfos_2012/Projekt_07-2012/ProjektInfo_0712_engl_internetx.pdf (01.03.2020)
- [5] S. Petersen, W. Hüls, C. Paitazoglou, and J. Albers. Active control of external volume flow rates for single effect absorption chillers. In *Proc. of 25th Int. Congr. of Refrigeration, IIR*, 2019, paper-ID: 1287.
- [6] F. Ziegler, H. M. Hellmann, and C. Schweigler. An approximative method for modelling the operating characteristics of advanced absorption chillers. In *20th Int. Congr. of Refrigeration, IIR*, 1999, paper-ID: 600.
- [7] J. Albers. Präzisierungen zur Methode der charakteristischen Gleichungen. In *Tagungsband Deutsche Klima-Kälte-Tagung*, paper-ID: AA.II.1.15, Bremen, 22. Nov –24. Nov. 2017. DKV. ISBN: 978-3-932715-93-8.

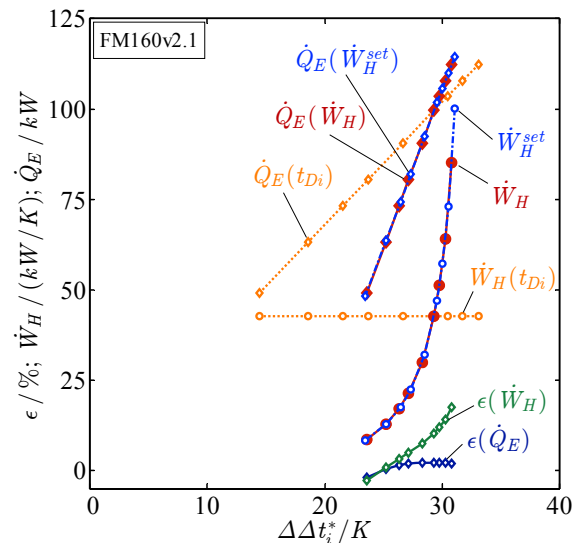
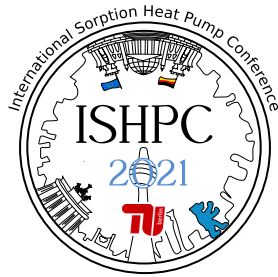


Figure 2 – Load variation due to temperature and flow rate changes in comparison to load control with flow rate set values calculated explicitly.

Gefördert durch:



aufgrund eines Beschlusses
des Deutschen Bundestages



Chilled Water Flow Rate Control for Chillers in Multiple Producer Cooling Plants.

Walther Hüls¹, Rupert Graf¹, and Stefan Petersen¹

¹Technische Universität Berlin, Institut für Energietechnik

Abstract

This paper introduces a control strategy for chilled water supply pumps to increase the energy efficiency and match the chilled water temperature set-point even in overload situations allowing the parallel operation of several chillers. It, therefore, ensures a hydraulic balance between consumer and producer circuits, using only temperature probes without the need for further flow meters. The paper shows the concept by means of a simulation and practical use in a real central air-conditioning application.

1. Introduction

Central air-conditioning (AC) cooling plants often consist of a chilled water production system (producer), a distribution system (consumer) and a hydraulic separator, e.g. a storage tank (see figure 1) or a bypass. The main distribution pump P_{PC} in state-of-the-art applications are variable-frequency drive (VFD) controlled to ensure adequate efficiency for varying loads [1]. The overall flow rate in the consumer circuit \dot{V}_C , as a general rule of thumb, increases with the cooling demand due to ambient conditions among other factors. In contrast, a constant volume flow rate for each chiller and/or in the production system \dot{V}_P is often accepted, especially when chillers only operate in on-off mode. Moreover, investment costs for constant speed pumps P_{P1} are lower. This discrepancy between variable and constant speed pumps may lead to one of three flow regime situations shown in the storage tank or hydraulic separator.

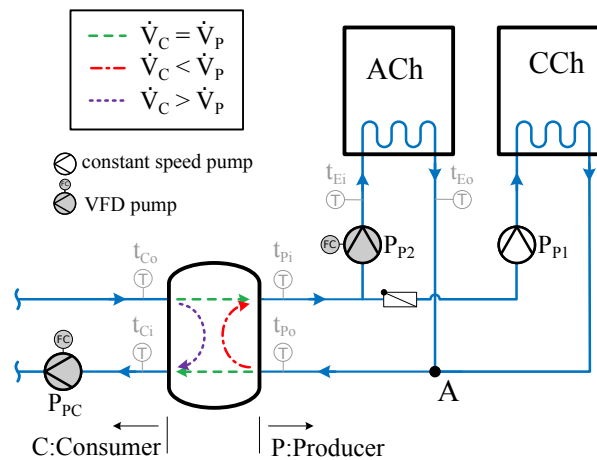


Figure 1: P&ID scheme of an AC central cooling plant.

Ideally, the flow rate between the producer \dot{V}_P and consumer \dot{V}_C circuits are identical¹ in order to avoid losses due to mixing effects (see green dashed line). In this case the inlet matches the outlet temperatures ($t_{Co} = t_{Pi}$ and $t_{Po} = t_{Ci}$). In case of a considerably high consumer flow rate ($\dot{V}_C > \dot{V}_P$, see purple dotted line), the producer circuit is partly by-passed and the consumer inlet temperature increases ($t_{Ci} > t_{Po}$). In case of a considerably high producer flow rate ($\dot{V}_P > \dot{V}_C$, see red dashed-dotted line), the consumer circuit is partly by-passed and the producer inlet temperature decreases ($t_{Pi} < t_{Co}$). Hence, with modern, variable-capacity controllable chillers and in systems with a high share of part load operation it is often advisable to control the pump speed (see P_{P2}) to reduce the auxiliary energy consumption and to avoid the temperature mixing effect by ensuring hydraulically balanced overall systems [1], [3]. Consequently, the producer flow rate continuously has to be adapted to the consumer flow rate.

¹In praxis for heating systems a 10-30% higher producer flow rate is allowed in order to charge the storage tank[2]. This setting is also applicable for cooling systems. For a hydraulic separator, this difference practically does not exist.

This study introduces a chilled water flow rate strategy for variable-capacity controlled absorption chillers (ACh). Typically, due to economic and primary energy saving reasons, ACh in AC applications are used to cover the base load. During peak load hours, it is assumed that an additional compressor chiller (CCh) covers the total load. Nevertheless, due to the previous reasons, it is advisable to increase the load share of the ACh through parallel operation, which also helps to reduce the size of the CCh. However, during parallel operation and peak load, the base load producer (ACh) may not be able to hold the evaporator outlet set-point² $t_{Eo\text{set}}$, increasing the overall producer outlet temperature at the mixing point A (see figure 1).

2. Control Algorithm

The flow rate control strategy (FCS) adapts the chilled water flow rate to match the temperature set-point $t_{Eo\text{set}}$. Thereby, an increased mixing temperature at point A can be prevented independently of the load conditions (first objective: T_{obj}). Consequently, a parallel operation is possible, which increases the overall cooling load share of the base load ACh. Another requirement is the continuous adjustment of the overall chilled water flow rate to the consumer flow rate \dot{V}_C (even if unknown) to avoid undesirable flow regimes in the hydraulic separator (second objective: F_{obj}). Finally, the strategy should not limit the chiller's cooling capacity in comparison to the operation without FCS (third objective: \dot{Q}_{obj}).

$$\dot{V}_C = \dot{V}_{E\text{set}}^{FCS} = \dot{V}_E \frac{(t_{Ei} - t_{Eo})}{\max(t_{Ei}, t_{Ei\text{set}}^{FCS}) - (t_{Eo\text{set}}^{FCS})} \quad (1)$$

In equation 1 the physical correlations between the temperatures and the flow rates are used to obtain the set-point flow rate $\dot{V}_{E\text{set}}^{FCS}$ for the speed control of the chiller supply pump. If available, the consumer outlet temperature t_{Co} may replace the chilled water inlet set-point $t_{Ei\text{set}}^{FCS}$. This relation originates from the load and capacity balance between consumer and producer. The $\max()$ function is introduced to avoid $t_{Ei} < t_{Co}$, which would imply bypassing of the consumer. The consumer temperature set-point fixes the lower temperature level and if $t_{Ci\text{set}} = t_{Ci} = t_{Eo\text{set}}^{FCS} = t_{Eo}$ the producer bypass is avoided (F_{obj}). It is important to emphasize, that the presented strategy operates in addition to the load-controller of a chiller, which has a lower but close chilled water temperature set-point $t_{Eo\text{set}}^{FCS} > t_{Eo\text{set}}$ in order to work with the FCS.

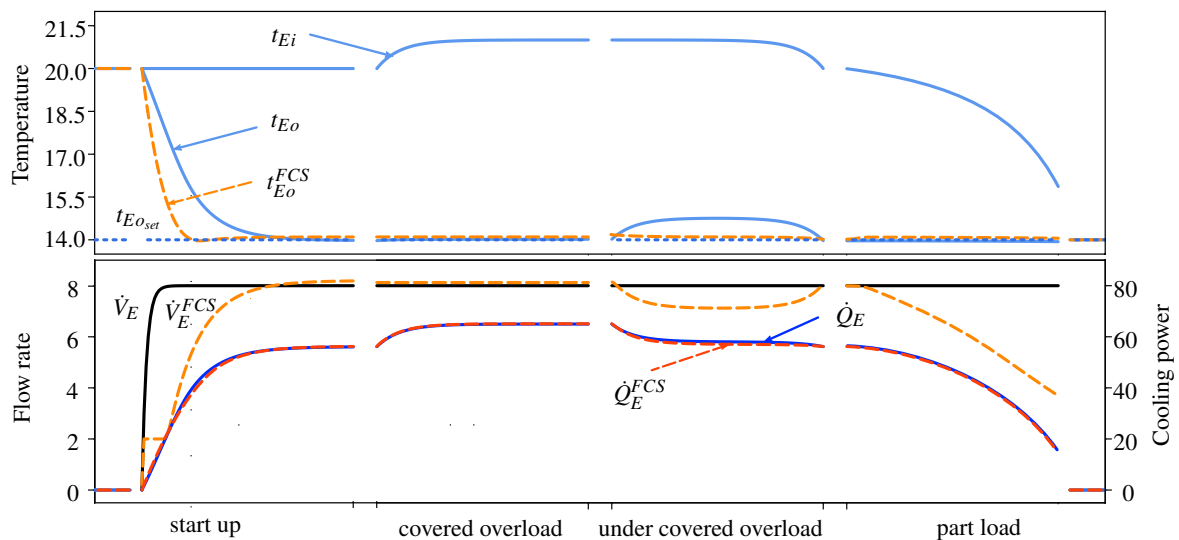


Figure 2: Simulation and comparison of the FCS strategy in 4 load conditions with $t_{Ei\text{set}}^{FCS} = 20^\circ\text{C}$ and $t_{Eo\text{set}}^{FCS} = 14.1^\circ\text{C}$.

Figure 2 shows results of a process simulation based on the characteristic equation method [4]. The variable-capacity controlled ACh adapts the hot and cooling water temperatures (not displayed) in order to achieve the chilled water cooling capacity and temperature set-point $t_{Eo\text{set}} = 14^\circ\text{C}$. The shown conditions correspond to a fictive operation day and are the result of changing the load, e.g., due to varying ambient temperatures (not displayed). Note, that the periods focus on a load condition despite the duration of it. Thus, each period has the same length. Covered

²Temperatures and the flow rate around the ACh are related now to the evaporator $t_{Ei}, t_{Eo}, t_{Eo\text{set}}, \dot{V}_E$, and not to the producer

overload of a chiller is defined either the load above the nominal conditions that the specified chiller can still cover. Under-covered overload refers to situations, where shortage occurs and additional producers are required to cover the entire load.

In consequence, the strategy: a) raises the flow rate, when the chiller is capable to increase the cooling capacity (see start up and second half of under-covered overload); b) reduces the flow rate in order to enable high temperature differences (see beginning of the start up and part load phase), which leads to a faster match of the set-point temperatures in start up and adapts \dot{V}_P to \dot{V}_C in part load (F_{obj}); and c) reduces the flow rate to achieve $t_{Eo_{set}}$ (T_{obj}) when the demand cannot be covered (see beginning of under-covered overload). This allows the base load ACh to be operated in parallel with a peak load CCh and, by that, to increase the overall cooling load share of the base load ACh.

During covered overload, when the system is hydraulically balanced, the resulting flow rate in both cases (with FCS and without) is the same. The increasing consumer load, which results in an increase of t_{Ei} is compensated by the load-controller of the ACh. Note, that \dot{V}_E^{FCS} is somewhat higher than \dot{V}_E due to the slightly different set-points ($t_{Eo_{set}}^{FCS} > t_{Eo_{set}}$) and, consequently, the smaller temperature difference between in- and outlet. Finally, as shown in the simulation, the strategy does not affect the cooling capacity \dot{Q}_E (\dot{Q}_{obj}).

3. Experimental Results

The FCS was developed under laboratory conditions and then tested in an existing AC application in Rosenheim, Germany. The production system consists of two absorption chillers (ACh-1 and ACh-2) with a design capacity of each 90kW and a CCh with a capacity of 250kW to cover the peak load. In addition, the system is equipped with a storage tank to reduce high frequent on-off behavior. The absorption chillers are driven by the city's district heating grid, which provides a driving heat temperature of about 90°C. All three chillers use the same dry cooling tower to remove heat. The distribution system was designed for cold-water temperatures of 10°C / 16°C. A building automation system (BAS) requests the chillers in the following sequence, when the consumer inlet temperature or the storage temperature succeed thresholds: ACh-1 → ACh-2 → CCh. The shutdown sequence is in reverse order.

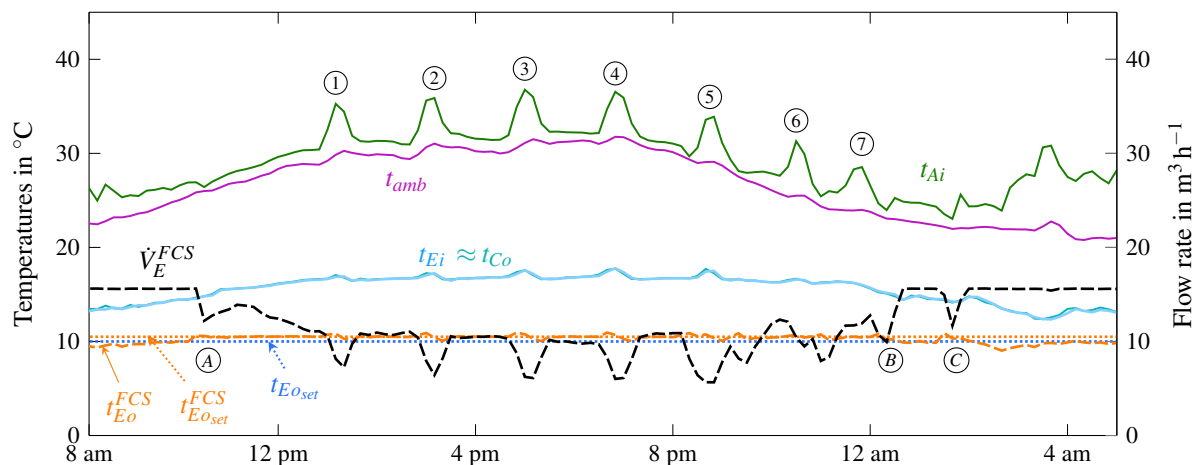


Figure 3: Measurement results on July 22nd, 2019

Figure 3 shows measurement data of one absorption chiller (ACh-1) on a warm day with ambient temperatures t_{amb} reaching close to 32°C in the late afternoon. The increasing ambient temperature leads to an increase of the cold-water return temperature t_{Co} and, consequently, to an increased cooling demand. Note, that the chiller inlet temperature matches the producer outlet temperature $t_{Co} \approx t_{Ei}$. Until around 11 a.m. the load-control of the ACh is able to compensate the increasing demand (compare covered overload in figure 2). Thereafter, the flow rate controller detects a cooling capacity shortage (compare undercovered overload) and adapts the cold-water flow rate \dot{V}_E to maintain the cold-water outlet temperature t_{Eo} at the set point $t_{Eo_{set}}$.

Shortly after 1 p.m. the CCh is requested by the BAS for about 40 min. Due to the sudden increase of waste heat for the shared dry cooling tower, the cooling water temperature t_{Ai} increases (see label 1 in figure 3), which further reduces the cooling capacity of ACh-1. Consequently, the flow rate controller further adapts the flow rate \dot{V}_E to keep

the set-point $t_{Eo, set}$, which allows ACh-1 to stay in operation. Interesting here is the fact, that the FCS improves the time of response of the ACh due to the sudden increase of CCh cooling share. After the BAS turns the CCh off, the cooling tower is able to provide lower temperatures and the flow rate is increased due to the ACh's capability to increase capacity. Throughout the day, this behavior can be observed several times (1-7), while the cold-water outlet temperature t_{Eo} stays constant. During three events (see labels A, B and C), fluctuations in the district heat supply cause a reduced cooling capacity of ACh-1, which is also detected and compensated by the FCS.

Overall, the flow rate controller successfully allows parallel operation of absorption chillers with dry cooling towers during peak load hours, without affecting the cold-water temperatures. Throughout the day the chiller inlet temperature matches the producer outlet temperature $t_{Ei} \approx t_{Co}$, indicating a well-balanced flow rate between producer and consumer. In contrast, before the FCS strategy, the ACh worked with a constant flow rate of $\dot{V}_{E, set, old} = 11 \text{ m}^3 \text{ h}^{-1}$ and later, in order to adapt it to the expected load profile, set to $8 \text{ m}^3 \text{ h}^{-1}$. Comparing both strategies (FCS and constant flow rate) during the shown time period in figure 3, the ACh is able to provide a higher cooling capacity during $\dot{V}_{E, set} : 16 \text{ m}^3 \text{ h}^{-1} > \dot{V}_{E, set, old}$ (see. begin and end of the period). During $\dot{V}_E^{FCS} < \dot{V}_{E, set, old}$ (see. middle period) in constant flow rate operation the BAS withdraw the request of the ACh due to the mismatch of the set temperature, leading to the standalone operation of the CCh. Consequently, for the displayed time period, the new FCS leads to an increase of the cooling load share provided by the ACh of 40% compared to a constant flow rate of $8 \text{ m}^3 \text{ h}^{-1}$ and 60% compared to a constant flow rate of $11 \text{ m}^3 \text{ h}^{-1}$.

4. Conclusion

The presented strategy shows the feasibility to control the chilled flow rate in central AC applications to match the overall consumer flow rate leading to hydraulically balanced systems. During overload, the parallel operation of several chillers leads to cover the cooling demand and mixing temperatures after the producer outlet can be avoided. Moreover, the overall cooling load share of the base load chillers is increased, which contributes to further savings. Adapting the flow rate also results in a smoother chilled water temperature outlet even during suddenly start/stop cycles of the CCh. Further, planned tests include stand-alone control in VFD supply pumps for CCh and strategies to adapt the temperature set-point during charging/discharging cycles of chilled water storage tanks.

5. Acknowledgment

We acknowledge financial support by the EnEff:Wärme Projects 03ET1171A and 03ET1583 grant funded by the Federal Ministry for Economic Affairs and Energy (BMWi)



References

- [1] ASHRAE (2016): ASHRAE HANDBOOK-HVAC Systems and Equipment Atlanta: American Society of Heating, Refrigerating and Air-Conditioning Engineers, Inc. ISBN: 1-931862-47-8
- [2] Recknagel Hermann, Sprenger Eberhard (2011/2012): Taschenbuch für Heizung + Klimatechnik. Deutscher Industrieverlag Vol.75, pp. 683.
- [3] Petersen, S., Albers, J., Graf, R., Hausherr, C., Hennrich, C., Hüls W., Hunt, S., Lanser, W., Paitazoglou. C., Schröder, M., Ziegler, F. (2019): EnEff: Wärme - Feldtest Absorptionskälteanlagen für KWKK Systeme. Technical Report FKZ 03ET1171A (Schlussbericht) TU Berlin, Institut für Energietechnik, FG Maschinen u. Energieanlagentechnik
- [4] Albers, J., Ziegler, F., (2016): Control strategies for absorption chillers in CHPC-plants ensuring low hot water return temperatures. Proc. of Heat powered cycles conference

List of Authors

Name	Title	Page
Albers, J.	Energy efficient cooling with absorption chillers in a field test (#61)	181
Albers, J.	Explicit calculation of flow rate set values for absorption chiller control (#66)	196
AL-Hasni, S.	A miniature 3D printed sorption heat transformer (#55)	172
Almendros Ibañes, J.	Integration of absorption chillers in centralized solar heating systems of multifamily buildings. (#27)	162
Altamirano, A.	Experimental characterization by thermal and mass effectivenesses of plate heat exchangers in NH ₃ -LiNO ₃ absorption chillers (#59)	56
An, G.	Kinetics research of single/multi-halide sorbents and their simulation comparison in continuous refrigeration cycle (#09)	5
Atkinson, G.	Ammonia-salt Large Temperature Jump Experimental Technique Advances (#24)	157
Atkinson, G.	Modelling ammonia (re-)sorption cycles: An abridged literature review and introduction to an ammonia salt MATLAB model for use in (re) sorption heat pumping (#47)	41
Bahrami, M.	Improved coefficient of performance in sorption systems (#07)	1
Bahrami, M.	A 3D printed capillary-assisted low-pressure evaporator, CALPE, for sorption systems cooling and heat pumps (#08)	84
Bahrami, M.	Development of novel sorber bed heat and mass exchangers for sorption cooling systems (#13)	88
Bahrehand, S.	Improved coefficient of performance in sorption systems (#07)	1
Bahrehand, S.	Development of novel sorber bed heat and mass exchangers for sorption cooling systems (#13)	88
Bamorovat Abadi, G.	A 3D printed capillary-assisted low-pressure evaporator, CALPE, for sorption systems cooling and heat pumps (#08)	84
Bardow, A.	Transforming Heat From 90 °C to 110 °C: Demonstration of a Lab-Scale Adsorption Heat Transformer (AdHT) (#22)	152
Bardow, A.	Water and ethanol as refrigerant mixture: Towards adsorption cooling below 0 °C (#25)	19
Bardow, A.	Computationally efficient, experimentally validated adsorption chiller model using a plug-flow-based modelling approach (#26)	24
Bardow, A.	Experimental Validation of a Dynamic Adsorption Chiller Model Using Optimal Experimental Design (#30)	28
Bardow, A.	SorpPropLib: An Open-Source Database for Sorption Equilibrium Properties (#31)	33
Bardow, A.	Capillary-assisted evaporation of water from finned tubes: Impacts of dynamics and experimental setups (#44)	105
Bardow, A.	Heat and Mass Transfer Kinetics of MOF-Coatings from Al-fumarate and CAU-10(Al)-H from IR-LTJ experiments: The Impact of Characteristic Times (#67)	65
Bauer, M.	Vertical tube evaporator and thermosiphon desorber for a flue gas-condensing heat pump (#52)	115
Belmonte Toledo, J.	Integration of absorption chillers in centralized solar heating systems of multifamily buildings. (#27)	162
Castano Parga, S.	Compact cold storage by means of a closed absorption process with H ₂ O/LiBr and crystallization of the strong absorbent (#54)	51
Ceccato, R.	Big-data analytics of the thermo-hygrometric conditions inside a desiccant based and a traditional flower greenhouse (#16)	129
Choi, H.	Experimental study on diffusion absorption refrigeration cycle with a low GWP refrigerant-R1234ze(E) (#37)	37

Ciganda, J.	Electrical, enviromental and economic optimal operation of an absorption heat transformer based industrial heat recovery and upgrade system (#62)	186
Coronas, A.	Experimental characterization by thermal and mass effectivenesses of plate heat exchangers in NH ₃ -LiNO ₃ absorption chillers (#59)	56
Critoph, R.	Ammonia-salt Large Temperature Jump Experimental Technique Advances (#24)	157
Critoph, R.	Modelling ammonia (re-)sorption cycles: An abridged literature review and introduction to an ammonia salt MATLAB model for use in (re) sorption heat pumping (#47)	41
Cudok, F.	Electrical, enviromental and economic optimal operation of an absorption heat transformer based industrial heat recovery and upgrade system (#62)	186
Davidesko, A.	A numerical study on heat and mass transfer dynamics in sorption cells (#11)	10
Demir, H.	Isotherm relations and COP analysis on silica gel RD with two different adsorptive; acetone and ethanol (#15)	14
Driesel, J.	Transforming Heat From 90 °C to 110 °C: Demonstration of a Lab-Scale Adsorption Heat Transformer (AdHT) (#22)	152
Dürndorfer, L.	Vertical tube evaporator and thermosiphon desorber for a flue gas-condensing heat pump (#52)	115
Engelpracht, M.	Transforming Heat From 90 °C to 110 °C: Demonstration of a Lab-Scale Adsorption Heat Transformer (AdHT) (#22)	152
Engelpracht, M.	Experimental Validation of a Dynamic Adsorption Chiller Model Using Optimal Experimental Design (#30)	28
Engelpracht, M.	SorpPropLib: An Open-Source Database for Sorption Equilibrium Properties (#31)	33
Entrup, M.	Water and ethanol as refrigerant mixture: Towards adsorption cooling below 0 °C (#25)	19
Ernst, S.	Heat and Mass Transfer Kinetics of MOF-Coatings from Al-fumarate and CAU-10(Al)-H from IR-LTJ experiments: The Impact of Characteristic Times (#67)	65
Evron, Y.	Non-absorbable gasses motor-less purge system for absorption heat transformers (#63)	125
Ferreira, C.	Absorption of high concentration NH ₃ /H ₂ O in a plate heat exchanger (#49)	110
Fink, M.	Experimental investigation of an adsorption module based on heat exchangers with fibrous aluminium structures and the SAPO-34 / water working pair for gas-driven adsorption heat pumps (#70)	74
Freni, A.	A miniature 3D printed sorption heat transformer (#55)	172
Földner, G.	Experimental investigation of an adsorption module based on heat exchangers with fibrous aluminium structures and the SAPO-34 / water working pair for gas-driven adsorption heat pumps (#70)	74
Földner, G.	Determination of heat and mass transfer parameters of adsorption dynamics in MOF aluminium fumarate coatings with volume swing frequency response measurements (#71)	79
Furuya, K.	Measurement of Time Constants of Water Vapor Adsorption Reaction on a Consolidated Silica-gel micro particles using QCM method (#53)	46
Gasparella, A.	Big-data analytics of the thermo-hygrometric conditions inside a desiccant based and a traditional flower greenhouse (#16)	129
Gavaldà, O.	Electrical, enviromental and economic optimal operation of an absorption heat transformer based industrial heat recovery and upgrade system (#62)	186
Ge, T.	Experimental investigation on the dynamic performance of desiccant coated microchannel heat exchangers under condensation conditions (#35)	97
Gediz Ilis, G.	Isotherm relations and COP analysis on silica gel RD with two different adsorptive; acetone and ethanol (#15)	14

Gibelhaus, A.	Computationally efficient, experimentally validated adsorption chiller model using a plug-flow-based modelling approach (#26)	24
Gibelhaus, A.	Experimental Validation of a Dynamic Adsorption Chiller Model Using Optimal Experimental Design (#30)	28
Gilges, M.	Heat and Mass Transfer Kinetics of MOF-Coatings from Al-fumarate and CAU-10(Al)-H from IR-LTJ experiments: The Impact of Characteristic Times (#67)	65
Glöckner, D.	Vertical tube evaporator and thermosiphon desorber for a flue gas-condensing heat pump (#52)	115
Gluesenkamp, K.	SorpPropLib: An Open-Source Database for Sorption Equilibrium Properties (#31)	33
Godefroy, A.	Hybrid thermochemical cycles for power and cold cogeneration: thermodynamic analysis and dynamic performances (#64)	61
Goerdten, P.	Performance evaluation of a double-lift concept for an adsorption refrigerator for high ambient temperatures (#69)	69
Göller, C.	Performance evaluation of a double-lift concept for an adsorption refrigerator for high ambient temperatures (#69)	69
Gölles, M.	Development and experimental validation of a linear state-space model for absorption heat pumping systems for model-based control strategies (#65)	191
Gommed, K.	Non-absorbable gasses motor-less purge system for absorption heat transformers (#63)	125
Graf, R.	Energy efficient cooling with absorption chillers in a field test (#61)	181
Graf, R.	Chilled Water Flow Rate Control for Chillers in Multiple Producer Cooling Plants. (#68)	200
Grossman, G.	Non-absorbable gasses motor-less purge system for absorption heat transformers (#63)	125
Habash, R.	Isotherm relations and COP analysis on silica gel RD with two different adsorptive; acetone and ethanol (#15)	14
Hamamoto, Y.	Measurement of Time Constants of Water Vapor Adsorption Reaction on a Consolidated Silica-gel micro particles using QCM method (#53)	46
Hausherr, C.	Energy efficient cooling with absorption chillers in a field test (#61)	181
Helm, M.	Directly Biomass-fired Absorption Heat Pump (#57)	176
Henninger, M.	Heat and Mass Transfer Kinetics of MOF-Coatings from Al-fumarate and CAU-10(Al)-H from IR-LTJ experiments: The Impact of Characteristic Times (#67)	65
Hermann, T.	Vertical tube evaporator and thermosiphon desorber for a flue gas-condensing heat pump (#52)	115
Himmers, S.	Ammonia-salt Large Temperature Jump Experimental Technique Advances (#24)	157
Himmers, S.	Modelling ammonia (re-)sorption cycles: An abridged literature review and introduction to an ammonia salt MATLAB model for use in (re)sorption heat pumping (#47)	41
Horn, M.	Development and experimental validation of a linear state-space model for absorption heat pumping systems for model-based control strategies (#65)	191
Hüls, W.	Energy efficient cooling with absorption chillers in a field test (#61)	181
Hüls, W.	Chilled Water Flow Rate Control for Chillers in Multiple Producer Cooling Plants. (#68)	200
Jiang, Y.	Application of the two-stage absorption heat exchanger in district heating (#19)	137
Jiang, Y.	Process design and analysis of the zonal absorption heat exchanger for high-rise buildings (#20)	142
Jiang, Y.	Experimental study on liquid distribution and horizontal motions of droplets in a tube bundle (#21)	147

Jiang, Y.	Vertical U-pipe Two-phase Flow Characteristics and Refrigerant Vapor Bypass in Absorption Heat Pump and Absorption Heat Exchanger (#33)	92
Jiang, Y.	Building-level Absorption Heat Exchange Substation Applied in District Heating System (#34)	167
Joonho, P.	Heat Transfer and Frictional Pressure Drop Characteristics of H ₂ O/LiBr Solution in Plate Heat Exchanger for Triple Effect Absorption Cycle Application (#42)	101
Joos, L.	Experimental investigation of an adsorption module based on heat exchangers with fibrous aluminium structures and the SAPO-34 / water working pair for gas-driven adsorption heat pumps (#70)	74
Jürgens, B.	Transforming Heat From 90 °C to 110 °C: Demonstration of a Lab-Scale Adsorption Heat Transformer (AdHT) (#22)	152
Kang, Y.	Experimental study on diffusion absorption refrigeration cycle with a low GWP refrigerant-R1234ze(E) (#37)	37
Kang, Y.	Heat Transfer and Frictional Pressure Drop Characteristics of H ₂ O/LiBr Solution in Plate Heat Exchanger for Triple Effect Absorption Cycle Application (#42)	101
Kappelhoff, C.	Water and ethanol as refrigerant mixture: Towards adsorption cooling below 0 °C (#25)	19
Kausche, M.	Directly Biomass-fired Absorption Heat Pump (#57)	176
Kim, G.	Experimental study on diffusion absorption refrigeration cycle with a low GWP refrigerant-R1234ze(E) (#37)	37
Kostmann, C.	Experimental investigation of an adsorption module based on heat exchangers with fibrous aluminium structures and the SAPO-34 / water working pair for gas-driven adsorption heat pumps (#70)	74
Krakau, D.	Capillary-assisted evaporation of water from finned tubes: Impacts of dynamics and experimental setups (#44)	105
Kühn, R.	Performance evaluation of a double-lift concept for an adsorption refrigerator for high ambient temperatures (#69)	69
Lanser, W.	Energy efficient cooling with absorption chillers in a field test (#61)	181
Laurenz, E.	Determination of heat and mass transfer parameters of adsorption dynamics in MOF aluminium fumarate coatings with volume swing frequency response measurements (#71)	79
Lävemann, E.	Compact cold storage by means of a closed absorption process with H ₂ O/LiBr and crystallization of the strong absorbent (#54)	51
Lazzarin, R.	Heating and Cooling of a Building by Absorption Heat Pumps driven by Evacuated Tube Solar Collectors (ETCs) (#17)	133
Le Pierrès, N.	Experimental characterization by thermal and mass effectivenesses of plate heat exchangers in NH ₃ -LiNO ₃ absorption chillers (#59)	56
Lee, G.	Experimental study on diffusion absorption refrigeration cycle with a low GWP refrigerant-R1234ze(E) (#37)	37
Lee, J.	Experimental study on diffusion absorption refrigeration cycle with a low GWP refrigerant-R1234ze(E) (#37)	37
Liang, C.	Experimental investigation on the dynamic performance of desiccant coated microchannel heat exchangers under condensation conditions (#35)	97
Locke, J.	Ammonia-salt Large Temperature Jump Experimental Technique Advances (#24)	157
Longo, G.	Big-data analytics of the thermo-hygrometric conditions inside a desiccant based and a traditional flower greenhouse (#16)	129
Mähne, K.	Performance evaluation of a double-lift concept for an adsorption refrigerator for high ambient temperatures (#69)	69
Martinez Urrutia, A.	Electrical, environmental and economic optimal operation of an absorption heat transformer based industrial heat recovery and upgrade system (#62)	186

Mazet, N.	Hybrid thermochemical cycles for power and cold cogeneration: thermodynamic analysis and dynamic performances (#64)	61
Miyata, K.	Measurement of Time Constants of Water Vapor Adsorption Reaction on a Consolidated Silica-gel micro particles using QCM method (#53)	46
Neveu, P.	Hybrid thermochemical cycles for power and cold cogeneration: thermodynamic analysis and dynamic performances (#64)	61
Noro, M.	Heating and Cooling of a Building by Absorption Heat Pumps driven by Evacuated Tube Solar Collectors (ETCs) (#17)	133
Olkis, C.	A miniature 3D printed sorption heat transformer (#55)	172
Ossenkopp, F.	Capillary-assisted evaporation of water from finned tubes: Impacts of dynamics and experimental setups (#44)	105
Paitazoglou, C.	Energy efficient cooling with absorption chillers in a field test (#61)	181
Pérez Ortiz, A.	Electrical, enviromental and economic optimal operation of an absorption heat transformer based industrial heat recovery and upgrade system (#62)	186
Perier-Muzet, M.	Hybrid thermochemical cycles for power and cold cogeneration: thermodynamic analysis and dynamic performances (#64)	61
Petersen, S.	Energy efficient cooling with absorption chillers in a field test (#61)	181
Petersen, S.	Chilled Water Flow Rate Control for Chillers in Multiple Producer Cooling Plants. (#68)	200
Pöhls, J.	Capillary-assisted evaporation of water from finned tubes: Impacts of dynamics and experimental setups (#44)	105
Postweiler, P.	Computationally efficient, experimentally validated adsorption chiller model using a plug-flow-based modelling approach (#26)	24
Postweiler, P.	Experimental Validation of a Dynamic Adsorption Chiller Model Using Optimal Experimental Design (#30)	28
Preßl, D.	Compact cold storage by means of a closed absorption process with H ₂ O/LiBr and crystallization of the strong absorbent (#54)	51
Ramirez, M.	Electrical, enviromental and economic optimal operation of an absorption heat transformer based industrial heat recovery and upgrade system (#62)	186
Rieberer, R.	Development and experimental validation of a linear state-space model for absorption heat pumping systems for model-based control strategies (#65)	191
Riepl, M.	Heat Transfer and Flow Characteristics in Thermosiphon Regenerators of Multi-Stage LiBr/Water-Absorption Heat Pumps (#56)	119
Riepl, M.	Directly Biomass-fired Absorption Heat Pump (#57)	176
Römer, J.	Performance evaluation of a double-lift concept for an adsorption refrigerator for high ambient temperatures (#69)	69
Rustam, L.	Heat and Mass Transfer Kinetics of MOF-Coatings from Al-fumarate and CAU-10(Al)-H from IR-LTJ experiments: The Impact of Characteristic Times (#67)	65
Salgado, R.	Integration of absorption chillers in centralized solar heating systems of multifamily buildings. (#27)	162
Salmaso, L.	Big-data analytics of the thermo-hygrometric conditions inside a dessicant based and a traditional flower greenhouse (#16)	129
Santori, G.	A miniature 3D printed sorption heat transformer (#55)	172
Schmidt, M.	Compact cold storage by means of a closed absorption process with H ₂ O/LiBr and crystallization of the strong absorbent (#54)	51
Schmitz, G.	Determination of heat and mass transfer parameters of adsorption dynamics in MOF aluminium fumarate coatings with volume swing frequency response measurements (#71)	79
Schnabel, L.	Capillary-assisted evaporation of water from finned tubes: Impacts of dynamics and experimental setups (#44)	105
Schnabel, L.	Determination of heat and mass transfer parameters of adsorption dynamics in MOF aluminium fumarate coatings with volume swing frequency response measurements (#71)	79

Schrecker, S.	Performance evaluation of a double-lift concept for an adsorption refrigerator for high ambient temperatures (#69)	69
Schweigler, C.	Vertical tube evaporator and thermosiphon desorber for a flue gas-condensing heat pump (#52)	115
Seiler, J.	Transforming Heat From 90 °C to 110 °C: Demonstration of a Lab-Scale Adsorption Heat Transformer (AdHT) (#22)	152
Seiler, J.	Water and ethanol as refrigerant mixture: Towards adsorption cooling below 0 °C (#25)	19
Seiler, J.	Computationally efficient, experimentally validated adsorption chiller model using a plug-flow-based modelling approach (#26)	24
Seiler, J.	Experimental Validation of a Dynamic Adsorption Chiller Model Using Optimal Experimental Design (#30)	28
Seiler, J.	SorpPropLib: An Open-Source Database for Sorption Equilibrium Properties (#31)	33
Seiler, J.	Capillary-assisted evaporation of water from finned tubes: Impacts of dynamics and experimental setups (#44)	105
Seiler, J.	Heat and Mass Transfer Kinetics of MOF-Coatings from Al-fumarate and CAU-10(Al)-H from IR-LTJ experiments: The Impact of Characteristic Times (#67)	65
Song, J.	Heat Transfer and Frictional Pressure Drop Characteristics of H ₂ O/LiBr Solution in Plate Heat Exchanger for Triple Effect Absorption Cycle Application (#42)	101
Stutz, B.	Experimental characterization by thermal and mass effectivenesses of plate heat exchangers in NH ₃ -LiNO ₃ absorption chillers (#59)	56
Tao, X.	Absorption of high concentration NH ₃ /H ₂ O in a plate heat exchanger (#49)	110
Ture, F.	Experimental investigation on the dynamic performance of desiccant coated microchannel heat exchangers under condensation conditions (#35)	97
Turnaoglu, T.	SorpPropLib: An Open-Source Database for Sorption Equilibrium Properties (#31)	33
Tzabar, N.	A numerical study on heat and mass transfer dynamics in sorption cells (#11)	10
Unterberger, V.	Development and experimental validation of a linear state-space model for absorption heat pumping systems for model-based control strategies (#65)	191
Velte, A.	Heat and Mass Transfer Kinetics of MOF-Coatings from Al-fumarate and CAU-10(Al)-H from IR-LTJ experiments: The Impact of Characteristic Times (#67)	65
Velte, A.	Experimental investigation of an adsorption module based on heat exchangers with fibrous aluminium structures and the SAPO-34 / water working pair for gas-driven adsorption heat pumps (#70)	74
Velte, A.	Determination of heat and mass transfer parameters of adsorption dynamics in MOF aluminium fumarate coatings with volume swing frequency response measurements (#71)	79
Volmer, R.	Capillary-assisted evaporation of water from finned tubes: Impacts of dynamics and experimental setups (#44)	105
Wang, L.	Kinetics research of single/multi-halide sorbents and their simulation comparison in continuous refrigeration cycle (#09)	5
Wernhart, M.	Development and experimental validation of a linear state-space model for absorption heat pumping systems for model-based control strategies (#65)	191
Xie, X.	Application of the two-stage absorption heat exchanger in district heating (#19)	137
Xie, X.	Process design and analysis of the zonal absorption heat exchanger for high-rise buildings (#20)	142
Xie, X.	Experimental study on liquid distribution and horizontal motions of droplets in a tube bundle (#21)	147

Xie, X.	Vertical U-pipe Two-phase Flow Characteristics and Refrigerant Vapor Bypass in Absorption Heat Pump and Absorption Heat Exchanger (#33)	92
Xie, X.	Building-level Absorption Heat Exchange Substation Applied in District Heating System (#34)	167
Yang, Y.	Experimental study on liquid distribution and horizontal motions of droplets in a tube bundle (#21)	147
Yang, Z.	SorpPropLib: An Open-Source Database for Sorption Equilibrium Properties (#31)	33
Yi, Y.	Application of the two-stage absorption heat exchanger in district heating (#19)	137
Yi, Y.	Process design and analysis of the zonal absorption heat exchanger for high-rise buildings (#20)	142
Zhu, C.	Vertical U-pipe Two-phase Flow Characteristics and Refrigerant Vapor Bypass in Absorption Heat Pump and Absorption Heat Exchanger (#33)	92
Zhu, C.	Building-level Absorption Heat Exchange Substation Applied in District Heating System (#34)	167
Zlabinger, S.	Development and experimental validation of a linear state-space model for absorption heat pumping systems for model-based control strategies (#65)	191